به نام خدا

مرکز دانلود رایگان
مهندسی متالورژی و مواد

www.Iran-mavad.com

ELSEVIER

CORROSION INDUCED BY LOW-ENERGY RADIONUCLIDES

MODELING OF TRITIUM AND ITS RADIOLYTIC AND DECAY PRODUCTS FORMED IN NUCLEAR INSTALLATIONS

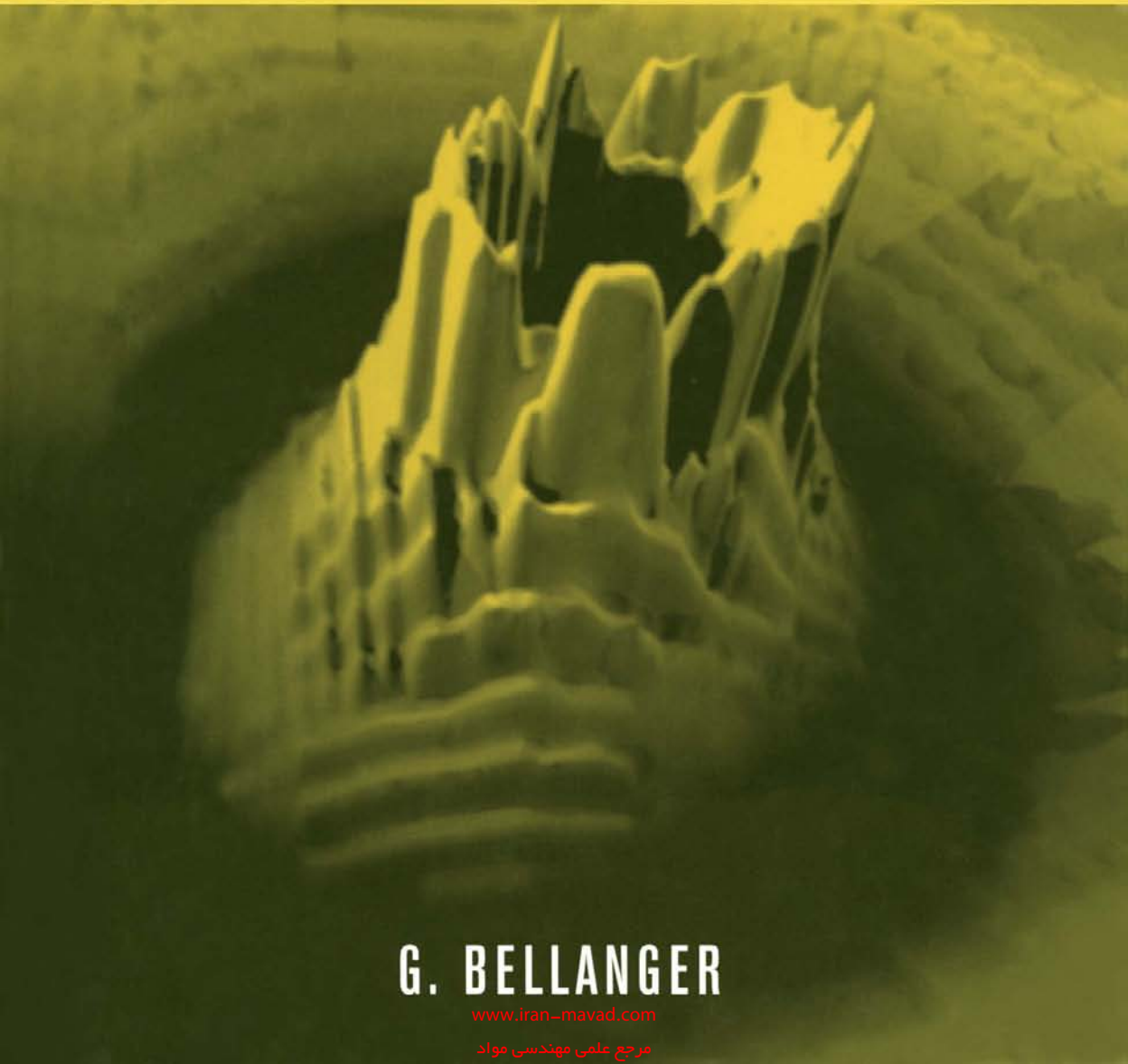

G. BELLANGER

CORROSION INDUCED BY LOW-ENERGY RADIONUCLIDES

Modeling of Tritium and Its Radiolytic and Decay Products Formed in Nuclear Installations

Elsevier Internet Homepage—http://www.elsevier.com

Consult the Elsevier homepage for full catalogue information on all books, journals and electronic products and services including further information about the publications listed below.

Elsevier titles of related interest

Books

VARGEL
Corrosion of Aluminium
2004. ISBN: 0080444954

DECHEMA: Corrosion Handbook
Corrosive Agents and their Interaction with Materials
Part 1, 2 and Combined
2001. ISBN: 0-444-50819-8, 0-444-508295 and 0-444-508309

Elsevier author discount

Elsevier authors (of books and journal papers) are entitled to a **30% discount** off the above books and most others. See ordering instructions below.

Journals

Sample copies of all Elsevier journals can be viewed online for FREE at www.sciencedirect.com, by visiting the journal homepage.

Journals of Alloys & Compounds
Corrosion Science
Journal of Nuclear Materials
Acta Materialia
Materials Science and Engineering A

To contact the Publisher:

Elsevier welcomes enquiries concerning publishing proposals: books, journal special issues, conference proceedings, etc. All formats and media can be considered. Should you have a publishing proposal you wish to discuss, please contact, without obligation, the publisher responsible for Elsevier's material science programme:

David Sleeman
Publishing Editor
Elsevier Science Ltd
The Boulevard, Langford Lane
Kidlington, Oxford
OX5 1GB, UK

Phone: +44 1865 843265
Fax: +44 1865 843920
E.mail: d.sleeman@elsevier.com

General enquiries, including placing orders, should be directed to Elsevier's Regional Sales Offices—please access the Elsevier homepage for full contact details www.elsevier.com

CORROSION INDUCED BY LOW-ENERGY RADIONUCLIDES

Modeling of Tritium and Its Radiolytic and Decay Products Formed in Nuclear Installations

Gilbert Bellanger

Selongey, France

2004

ELSEVIER

Amsterdam • Boston • Heidelberg • London • New York • Oxford
Paris • San Diego • San Francisco • Singapore • Sidney • Tokyo

ELSEVIER B.V.
Sara Burgerhartstraat 25
P.O. Box 211, 1000 AE Amsterdam
The Netherlands

ELSEVIER Inc.
525 B Street, Suite 1900
San Diego, CA 92101-4495
USA

ELSEVIER Ltd
The Boulevard, Langford Lane
Kidlington, Oxford OX5 1GB
UK

ELSEVIER Ltd
84 Theobalds Road
London WC1X 8RR
UK

First edition 2004

Library of Congress Cataloging in Publication Data
A catalog record is available from the Library of Congress.

British Library Cataloguing in Publication Data
A catalog record is available from the British Library.

ISBN: 0-08-044510-1

♾ The paper used in this publication meets the requirements of ANSI/NISO Z39.48-1992 (Permanence of Paper).
Printed in The Netherlands.

PREFACE

Nuclear power plants produce radionuclides emitting radiation and particles with a range of energies. Energy deposition on and in the materials can therefore be very different depending on the type of emitter. Gamma rays and neutrons have the highest energies and penetrate the interior of metals by breaking the metal bonds, thus leading to their degradation. They have been the origin of one of the problems in the construction of nuclear power plants and consequently their effects have been studied widely and discussed in numerous scientific publications in order to select the most suitable alloy. This is not the case for the low energy nuclide environment. Here the β^- particle can be taken as a model and although it has a low energy, it will be the source of problems that are both different and appreciable. These are degradation of the passive oxide layers protecting the metals. Without this protective layer, the metals are easily corroded. Particular charge transfers result in excitation by β^- particles giving birth to special electrochemical reactions in the oxide. However, while the reactions are in generally classical the particular effects are produced in conditions energetically favored by the energy brought by the radiation. Excitation creates holes in the oxide lattice leading to broken valence bond between two neighbor atoms. Moreover, electrons move out and become holes that lead to unoccupied orbitals that can receive an electron from a neighbor atom. It can be also noted for constant β^- particles flow that the equilibrium state is not obtained, but a stationary state can be established. This is characterized by a charge carrier density different from that obtained in the unexcited state. Among the low energy radionuclides present in nuclear power stations, tritium is of major importance due to its physical-chemical properties. Tritium is also found at different concentrations in plants for fuel reprocessing and military and civilian applications. Moreover, very large amounts of this low decay energy element is used in controlled fusion reactors. Due to its properties it can be substituted for the bound hydrogen in the molecules. This characteristic makes it possible to elucidate more easily the different types of corrosion of oxide layers than with another low energy nuclide, which is why tritium was chosen. In discussing tritium we must also discuss tritiated water since it is not possible to have tritium without tritiated water in such installations. The tritium in tritiated water always causes difficulties in these installations, including equipment corrosion. Moreover, with tritiated water there are, in addition, the radiolytic products. Special emphasis is given to aqueous corrosion which is the most important. The discussions include comments on tritiated water, radiolytic products and decay helium using aqueous corrosion models and

a model taking account of metal embrittlement. With regard to tritium installations, there were too many errors made to render it possible to exploit them. This is due to the fact that in most cases, persons in charge lacked solid knowledge of fluid flow, heat exchange, gas diffusion in materials and of materials resistance. In order to avoid these problems courses should be given, or books written, in these fields. Until the present there has not been a book devoted to corrosion by low energy radionuclides and consequently, there was a need to fill this vacancy concentrating on the effects of tritium and tritiated water. This book does not provide a course on corrosion, but is aimed at the specialists working in the nuclear field and scientists in electrochemistry and corrosion. This book is a reference tool of interest to post-graduates because of the concise examples treated in different chapters. Equipment manufacturers also may be interested by the choice of alloys and their characteristics.

In common with my previous publications and my conferences, this book has required support from individuals and organizations from different continents to whom I am very grateful. These include my friend, Professor Jean Jacques Rameau (University of Grenoble, France), who has motivated me to publish my results. He was there whenever I needed scientific help and advice. There are researchers who have unfailingly supported my conferences. Most particularly, I would like to thank the President of the International Society of Electrochemistry, previously Member of the Executive Committee and Officer of the Scientific Division of Corrosion: Professor Kálmán (Academy of Sciences, Budapest, Hungary). Special thanks also are due to the Officer of the Scientific Division of Industrial Electrochemistry and Electrochemical Engineering, Professor Matsunaga (Kyushu Institute of Technology, Kitakyusu, Japan), who sustained my project for the ISE Meeting in Japan, and also to the French Secretaries: Dr. Deslouis (University of Jussieu, Paris, France) and Professor Savall (University of Toulouse, France). I would like to thank Professor Ali Ben Bachir Hassani (University of Mohammed V, Rabat, Morocco), who is also Scientific Adviser in the Moroccan Government for his support in Marrakech. I would like to thank Professor Ives (Mc Master University, Hamilton, Canada) and Professor Savadogo (Ecole Polytechnique de Montréal, Canada) and especially to the Managers of UKAEA JET (United Kingdom Atomic Energy Authority—Joint European Torus) for their proposal to work as a consultant testing equipment. Thanks are also due to Professor Su-Il Pyun (Korea Advanced Institute of Science and Technology, Daejon, South Korea) and Dr. Varga (Department of Radiochemistry, University of Veszprém, Hungary) for their proposal in scientific collaboration in nuclear corrosion. I would also like to express my gratitude to many expert friends who helped me during the Meetings of The Electrochemical Society (USA) and those of EuroCorr (European Community of Anticorrosion). My writing was guided step by step by my friend, Allan William Boyd, who helped to turn the scientific English style into intelligible and engaging literature. Without his tireless efforts my publications would not have seen the light of day. Most of all, I must give my sincerest thanks to my wife Marie Claude and I dedicate this book to her patience and understanding in accepting the financial outlay, making it all possible.

The book is supported by the accompanying CD-ROM, which contains the pdf, slides files and 3D views for the appreciation of the text and figures as a reference source. It makes possible interlaced interactive links (more than 5000) acting on the figures, photographs, tables, bibliography...

About the Author

Dr. Bellanger obtained an engineering diploma in Electrochemistry and Engineering of Nuclear Materials from the Conservatoire National des Arts et Métiers in Paris, having studied the retreatment of tritiated water by diffusion metal electrodes. Following this, Dr. Bellanger received a Doctorate in Electrochemistry and Engineering of Nuclear Materials. His studies for this degree involved the decontamination of metals by electrochemistry.

His early contributions in research were in the development of isotopic separation of uranium hexafluoride by gaseous diffusion, on which he worked from 1962 to 1965. From 1965 to 1985, he headed the Plutonium Analysis Laboratory at the Commissariat à l'Energie Atomique and he has been responsible for the analysis of impurities present in aqueous solutions and plutonium metal. He has over 20 years of solid experience in physical chemistry analysis to his credit. He has also worked on the diffusion of radioactive tritium in metals and the decontamination of tritiated steels by isotopic exchange with electrolytic hydrogen.

Dr. Bellanger has been the Director of the Materials and Corrosion Laboratory since 1985. Within the past ten years he has authored approximately 65 technical papers and articles published in international journals such as Fusion Technology, the Journal of Nuclear Materials, the Journal of Materials Science, Corrosion Science, the Canadian Journal of Chemical Engineering and Electrochimica Acta, and in the proceedings of international conferences held in Europe, Japan and North America. He has published two chapters of a book on the passivity of metals and holds two international patents concerning the retreatment of radioactive water and decontamination of steels. His published work mainly concerns the effects of tritiated water on metal corrosion that is induced by released energy. Dr. Bellanger has studied the effects of radiolytic species on the corrosion of super-alloys and has over 10 years of experience in materials, corrosion and electrochemistry; he has carried out research and written extensively in these subject areas.

Dr. Bellanger was elected the member responsible for corrosion conferences for the scientific committee of the Electrochemistry Days Meeting held at Strasbourg, Montréal and Toulouse. He served in this position for 6 years, until the year 2000, organizing 450 people at each meeting. He has also been a guest speaker several times at present plenary and thematic conferences, and chair of several international conferences organized in foreign countries. He has also been a member of several international scientific societies, including the International Society of Electrochemistry, the Electrochemical Society Inc., the Institute of Corrosion, and Nace International Corrosion. Dr. Bellanger is now a senior consultant for a number of companies.

CONTENTS

Part IV. APPENDIX

INTRODUCTION

Aspects for understanding corrosion induced by low energy nuclide—modeling to tritium and tritiated water

The tritiated media are very reactive and their properties are extremely interesting. Tritium decays as follows:

$$^{3}H \rightarrow {}^{3}He^{+} + \beta^{-} + \nu_{e} \quad (0.1)$$

A positively charged ^{3}He, β^{-} particle and the antineutrino, ν_e are formed. Table 1 gives the nuclear data for tritium decay. Electrons of 18.6 keV per atom have sufficient low energy deposition to induce radiolysis phenomena in the hydrated oxide and in tritiated water leading to a blue luminescence (chapter 25 and Fig. 1). Radiolysis of the oxide, i.e. damage of an ionic lattice by β^{-} radiation, results in an increase in defects as free electrons, anion holes and vacancies. This increase has a direct impact on the oxidation kinetics if the limiting step in the oxidation process involves the mobility of the O^{2-} vacancies or electrons. In addition, water radiolysis induces the formation of unstable radical or molecular species at high concentrations such as $O^{3}H^{\bullet}$, $^{3}H^{\bullet}$, $^{3}H_2O_2$ [1–3], modifying the oxidizing character of this medium and is thus able to influence the oxidation kinetics of steels or stainless steel alloys.

Due to its unfilled electron shell, tritium reacts with almost all chemical species by ionic or covalent bonds. However, its reactivity is not limited to this behavior; it can replace hydrogen atoms in various chemical bonds by isotopic exchange. As tritium has extremely high mobility, and if the chemical compound is not stable enough to resist the low energy released with the β^{-} particle, chemical bonds are broken along the chains during its transit, first giving transient chemical species then stable compounds over a wide concentration

Table 1. Characteristic data of tritium

Radiation	β^{-}
Half-life ($\tau_{1/2}$)	12.3 yr.
Decay product	^{3}He and ν_e
Maximum β^{-} energy	18.6 keV
Energy produced by tritium decay	1.95 W mol^{-1} $^{3}H_2$
Activity per mole of tritium	1075 TBq

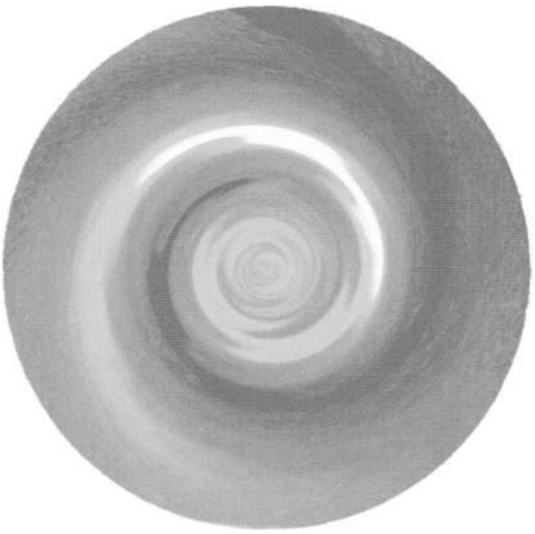

Figure 1. Spacial blue luminescence of tritiated water due to the presence of unstable free radicals on a disk electrode during convective stirring. The blue spiral pattern is representative for the displacement of radiolytic products and tritium at the surface of metal indicating thereby dynamic corrosion.

range. Chloride, fluoride, carbonate and nitrate are formed with pH modification by degradation of organic materials [1–3]. The transient species and stable compounds will react in various ways with the metal oxide layers thus producing corrosion.

In contrast to tritium, helium atoms are very stable and helium forms only a limited number of compounds. Therefore, other chemical species do not bond to it. Moreover, its recoil energy of about 0.4 eV is negligible as is the radiation due to the antineutrino. Therefore, due to its stability, helium is not involved in corrosion in the same way. It has extremely low solubility and can be easily trapped in metals, and as a result it and tritium induce metal embrittlement.

The damaging action of tritiated water and tritium on the corrosion resistance of the stainless steels is a very real problem. As these attacks lead to severe damage of metals, it is essential to know the effects of this complex medium in order to interpret the mechanisms in passivation or localized corrosion. To avoid these attacks, the corrosion tests must make it possible:

- to analyze tritiated water and tritium for its radiolytic and decaying species,
- to study the initiation and evolution of corrosion phenomena in the presence of tritium, tritiated water and various radiolytic species,
- to identify defects on the passivating oxide layers,
- to understand their behavior,
- to select the best adapted materials.

Table 2. Composition of gases above and dissolved in tritiated water

Radiolytic gas	O_2	^3He	H_2	$^2H_2$	$^3H_2$
mmol gas above 1 dm^3 ^3H_2O	50	150	10	8	0.8
mmol gas dissolved in 1 dm^3 ^3H_2O	1	1.5	1	0.5	0.05

Table 3. Composition of radiolytic species and corrosion species dissolved in tritiated water

Aqueous species	O, $^3H_2O_2$	NO_3^-	CO_3^{2-}	Cl^-	F^-	$^3H^+$	Fe^{3+}, Fe^{2+}	Ni^{2+}	Cr^{3+}, Cr^{6+}
mmol dm^{-3} ^3H_2O	6	70	50	50	5	1	1.5	1	0.3

First of all, for a good understanding of corrosion phenomena, we need to know what there is in tritiated water and in tritium, i.e. their composition. Analysis of various tritiated water samples include determination of the tritium content and identification of the radiolytic species and their respective concentrations. The radiolytic gases dissolved in and above tritiated water (Table 2) were analyzed by mass spectrometry. The tritium and the low energy discharged in tritiated water were determined by calorimetric measurements. The radiolytic species and corroded metals were analyzed by laboratory methods (Table 3). These species will be considered together or separately to ascertain their mutual influence on corrosion.

Corrosion tests must also meet the selection criteria for new materials. These concern laboratory examinations of new super-alloys or stainless steels such as super-austenitic and Duplex stainless steels and nickel and/or cobalt base super-alloys, hardened or ductile stainless steels, or the exotic alloys of zirconium or titanium. Materials selection is a difficult, complex but essential process, and many problems are caused by an inappropriate choice leading to corrosion-related failures. To carry out this study in a hot laboratory, we have essentially made use of the results of cyclic voltammetry, electrochemical impedance spectroscopy, Dispersive X-ray and Scanning Electron Microscopy, autoradiography and the scanning Reference Electrode Technique. To quantify the potential influences of tritiated water and radiolysis on oxides and the oxidation process, the electrochemical cell and analyzer chambers were arranged in a glove box in order to ensure the protection against tritium contamination. The presence of transients influences the results and can drastically modify them, making the results difficult to analyze. Thus, the results are based on these research methods with the use of rotating disk electrodes that are very sensitive for determining the effects of the transients formed in tritiated water. These measurements provide information in real time on corrosion systems to investigated the processes and the research techniques are also employed for studying passive oxide layers. Finally, the corrosion parameters obtained are then used to provide the required information for improving corrosion resistance of metals and determining the most suitable alloy.

Before discussing the corrosion problems, it is necessary to describe the operation of fusion reactors and the preparation of tritium and its processing in current operations. This is extremely useful because the technology now employed in tritium plants is directly applicable to recycling tritium in future reactors because the basic principles of both processes are identical and, since the technologies are identical, there are no problems in

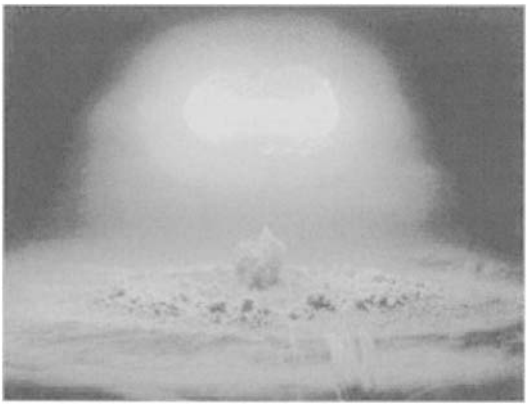

Figure 2. Thermonuclear fusion weapon fireball resulting in the formation of an extremely hot incandescent mass of gas (U.S. Army photograph, Marshall Islands).

applying the same anti-corrosion measures. Man-made tritium is generated on the industrial scale by bombarding lithium with neutrons, which also produces helium-4 generating α particles.

Tritium is also important in research and industry in the following applications: in producing luminous paint, in cancer treatment with the indirect generation of neutrons, in physico-chemical analysis and recently for ceramic electrolytes in hydrogen isotope separation as shown by Mukundan et al. [4]. The increasing amount of man-made tritium for consumer products and nuclear reactors requires more research into the techniques of analysis, disposal and recycling of tritium. For example, in analysis helium-4 and tritium can be easily detected using high sensitivity mass spectrometers and ionization chambers, respectively. The detection limit for tritium is far lower than that for hydrogen or deuterium due to tritium's radioactive decay. Tritium is thus employed as a label and tracer for hydrogen by nuclear-physical methods, and is the most versatile β^--emitting radionuclide for use in chemical and biological research. Due to this large range of uses, high purity tritium is industrially available in large quantities. The half-life for tritium decay is twenty years. This signifies that five years after preparation of nuclear weapon, helium 3 content is large and there remains about 80–85% of tritium. In this condition, detonating does not work and therefore nuclear weapons must be recycled. Moreover, the nuclear weapons are made of three charges: tritium, plutonium 239 and uranium 235. In addition to this composition, lithium-6 compounds (deuteride or deutero-tritide) in a warhead avoid the necessity of replacing tritium periodically. The presence of lithium and neutrons during predetonation increase the quantity of available tritium and boost the primary and secondary stages and the nuclear fireball (Fig. 2). Lithium-6 is a critical material and does not require the use of liquid deuterium and tritium liable for corrosion. Plutonium can be fissioned with slow neutrons. Because this material is fissionable, careful planning must be exercised in its handling and machining. The critical mass of plutonium varies over a wide range depend-

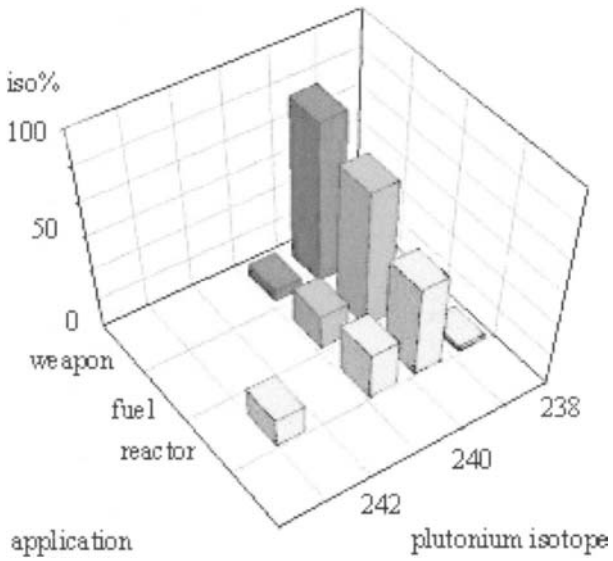

Figure 3. Isotopic composition of plutonium according to its use.

ing on such factors as geometry, reflectors (beryllium), material mass or density, neutron absorbers (boron-10) and the effect of diluents. Plutonium metal in the form of a powder or when finely divided is pyrophoric. Therefore, machining and manufacturing are usually conducted in a dry inert gas atmosphere. The isotopic composition of plutonium furnished by the manufacturer depends on its use (Fig. 3). A nuclear weapon needs more than 93% plutonium 239.

After several years of storage, the proportion of plutonium 239 decreases through decay, whereas that of plutonium 241 is increasing (about 12–15% for 5 years). Plutonium 241 is transmuted into americium 241 which produces gamma rays used in metal radiography for determining cracks and internal geometry in three dimensions. This ray is dangerous to humans, provoking burning and cancer. Moreover, this radiation destroys sensitive materials such as electronic components and organic materials. Consequently, plutonium 239 must also be periodically recycled to eliminate americium 241. The properties of unalloyed plutonium are a function of the six allotropes it forms during cooling from the melt (640°C) to room temperature.

Plutonium has electrons residing in the 7s, 6d and 5f states. Migration from the outer electron shells to the inner 5f causes contraction of the atom. Moreover, most of the phase transformations result in large volume changes and produce crystal structures that have different physical properties. These unusual characteristics have made the metallurgy of plutonium and its alloys particularly challenging. For example, the mechanical properties of plutonium indicate marked changes ranging from high strength, extremely brittle properties of the low temperature α-phase (monoclinic and martensitic) to the low strength,

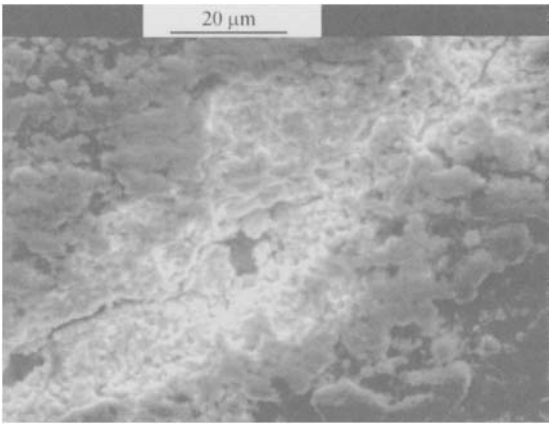

Figure 4. Embrittlement accompanied by cracking of pure plutonium.

high ductility properties exhibited by the δ-phase at temperatures 320 to 450°C. Thus the α-phase is a strong brittle phase due to the large volume reductions produced during cooling from the melt, and does not often attain the full density of 19.8 g cm^{-3}. This is caused by microcracking due to transformation by stresses (stress corrosion, Fig. 4). Cracks are formed, firstly in the body of the metal then progresses to the surface (Fig. 5). Fabrication of unalloyed α-phase plutonium to complex shapes also presents difficulties due to residual amounts of high temperature phases which make engineering tolerances difficult to achieve and to maintain over long periods. These high temperature phases tend to be retained by small amounts of impurity elements. The addition of 2 at.% Ga stabilizes the face-centered cubic δ structure, a phase with superior mechanical properties when compared to the α-phase (Fig. 6). Other elements can act as δ stabilizers, but the Pu-Ga system has been studied in much more detail than others.

The δ-phase alloys exhibited properties more suitable to fabrication techniques, exhibiting ductility and good forming properties that permitted the metal to be rolled into sheet and formed and machined in a conventional way. One of the key issues in understanding the phase stability of Pu-2 at.% Ga alloy is the solid-state microsegregation that occurs during cooling from the melt. This process results in a microstructure consisting of δ-phase grains with Ga-rich cores and Ga-poor edges. Alloys produced by casting or during cold working are not homogeneous. To ensure a uniform gallium content across the grains, heat treatment is undertaken to cause gallium diffusion and to achieve complete δ-phase stabilization. This needs to be performed below the $\delta \rightarrow \varepsilon$ transformation boundary; the coring being produced at this interface originally during the cooling period. Employing extended homogenization treatments makes it possible to stabilize Pu-Ga alloys for long periods at room temperature. These alloys are relatively easy to cast as the liquid is more dense than the δ-phase.

Aging has significant impact on the nuclear weapons programs and weapon systems need to remain in service for very large periods. Plutonium itself suffers internal degen-

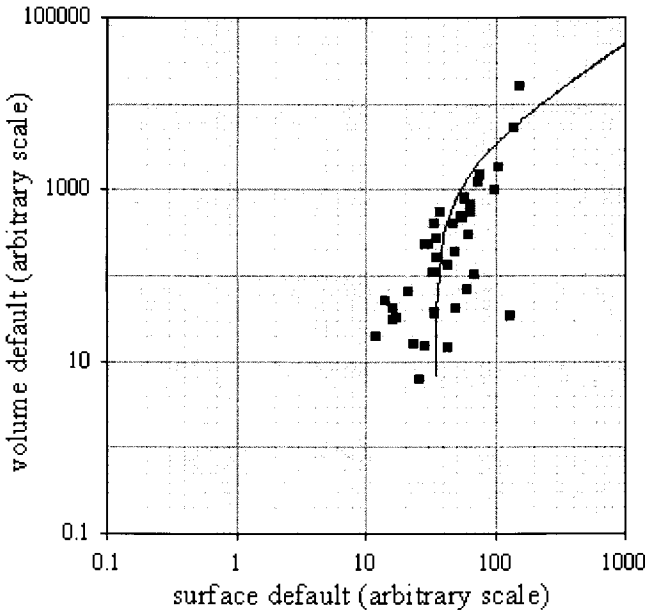

Figure 5. Cracking evolution in the bulk and at the surface of pure plutonium.

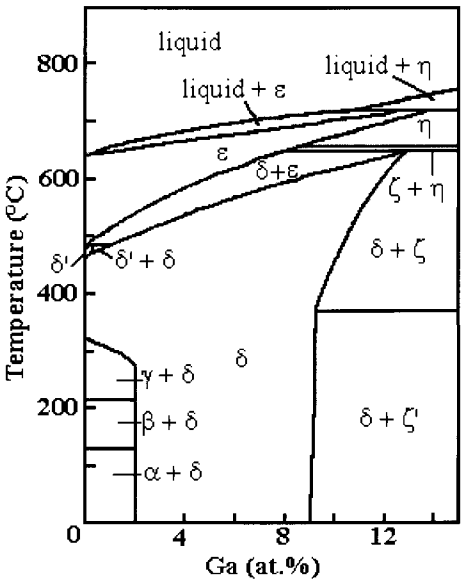

Figure 6. Gallium–plutonium alloy diagram showing the different allotropic domains.

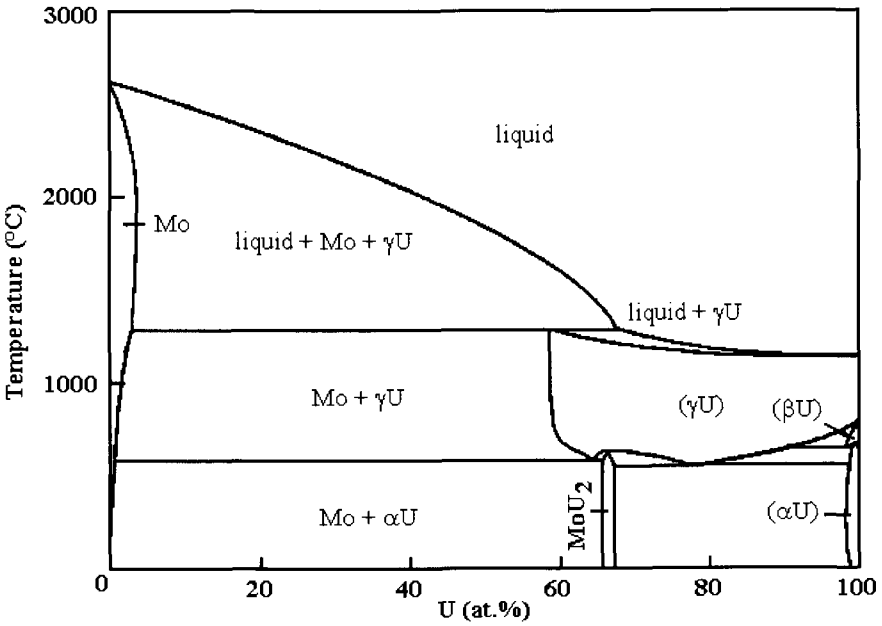

Figure 7. Molybdenum–uranium alloy diagram showing the different allotropic domains.

eration due to radioactive decay. The recoiling uranium nucleus and the smaller He ion cause considerable damage in the immediate area. The 'cannon ball' of the uranium nucleus causes about 2500 Pu atoms to be displaced and creates a large number of residual and interstitial vacancies at the periphery of its damage spike to such an extent that it can be calculated that statistically in 10 years time all the Pu atoms will have been forced from their original sites. Likewise, the He ion, having captured two electrons from the plutonium, comes to rest in the lattice as a helium atom with the potential for it to diffuse to create bubbles of helium in the metal, reducing the density, increasing the strength, and having significant effects on the implosion performance.

For implosion, subcritical masses of 235U (and body-centered-cubic γ-phase Mo-235U and Ta-235U alloys) and 239Pu are compressed to produce a mass capable of supporting a supercritical chain reaction. These uranium alloys are stabilized in the γ-phase (Fig. 7) by rapid cooling and are less sensitive to classical and stress corrosion and their mechanical properties are enhanced.

One obstacle to recycling uranium is that repeated casting with graphite crucible causes an accumulation of carbon in ingots which has a deleterious effect on casting properties. The procedure used to reduce carbon content before electrorefining is that of adding trace amounts of niobium that combines with the carbon. The resulting carbide is less dense than is the liquid uranium. Buoyancy forces would tend to transport it toward the top of the casting where, after solidification, the carbon-rich portion could be removed. Furthermore,

alloying niobium prevents oxidation and causes change in crystalline structure making the alloy brittle.

The compression is achieved by the detonation of specially designed high explosives surrounding a subcritical sphere of fissionable material. When the high explosive is detonated, an inwardly directed implosion wave is produced. This wave compresses the sphere of fissionable material. The decrease in surface to volume ratio of compressed mass and the increased density are such as to make the mass supercritical for a nuclear explosion. Boosting fission and predetonation are essential. This is done by insertion of a thin beryllium reflector and a neutron emitter of sufficient strength. Consider a spherical implosion, where Δ represents the change in system dimension (i.e. size of radius) along the axes of compression in three dimensions, then the compression C achieved by the implosion is represented in the simplified equation:

$$C = \left(\frac{r_0}{r_0 - \Delta}\right)^3 \tag{0.2}$$

Agglomeration and bubble formation lead to significant dilation of aged plutonium. Not only can the helium atoms agglomerate but the vacancies produced at the periphery of the damage spikes can diffuse and form voids. These voids could grow at an accelerated rate. Thus the original δ-plutonium alloy is continually changing, He content is increasing with time and then has an impact on phase stability, density, and strength of the δ-phase material. In addition other isotopes of plutonium, namely ^{241}Pu, are decaying to americium at a rate concomitant with a half-life of 13 years. This has significant implications for phase stability and also enhanced γ radiation output which will affect radiation dose levels to operations during the process. Finally, plutonium is rapidly corroded in moist atmospheres containing relatively small amounts of oxygen. In aqueous solutions, plutonium may exist in all four valency states (3, 4, 5 and +6) depending on radiolysis. The +4 valency is the most stable oxidation state.

Tritium is a crucial component of thermonuclear weapons in enhancing their explosive yield. A typical thermonuclear device consists of two stages, a primary where the explosion is initiated and focused to the inner by plutonium and uranium fission trigger (X-rays), and a secondary where the main thermonuclear explosion takes place (fusion) to form helium. The yield of the primary stage, and its effectiveness in driving the secondary to explode, is aided (boosted) by tritium gas which undergoes a nuclear reaction with deuterium, and generates a large amount of high-speed neutrons to 'boost' the nuclear burn-up of the plutonium or highly enriched uranium. Instant fusion reactions will not begin until the nuclei involved have been heated to very high temperatures, and pressures, by fission reactions. The reason is that the nuclei are positively charged (strong electrical repulsion) and repel one another strongly up until the moment they stick, collide and fuse, thereby releasing enormous amounts of energy and radiation. Incidentally, it is puzzling why a full and small palladium ball cathode using pure tritiated water, as made in the 'Cold Fusion' is not used to charge the tritium. Hyperconcentrated tritium in the ball center should release a few neutrons.

An optimally efficient fission explosion requires the implosion of the fissile core in a very short time (hundreds of nanoseconds) from shock waves produced by explosive when the neutron multiplication rate is at a maximum. Creating a symmetric implosion wave requires close synchronization in firing the detonators, because only they can be fired by very powerful and fast current surges. The normal method of providing the power supply for the detonator system is to discharge a high capacitance very rapidly at high voltage. The capacitor must be matched with a switch that can handle high voltages and currents without adding undue inductance to the circuit. A variety of technologies are available: triggered spark gaps, krytrons and thyratrons. More recently, laser detonating systems have been developed. These use a high power solid state laser to deliver sufficient energy in the form of a short optical pulse to initiate a primary or booster explosive. The laser energy is conducted to the detonator by a fiber optic cable. Finally, a miniature linear particle accelerator called a 'pulse neutron tube' can provoke collisions between deuterium and tritium nuclei to generate high energy neutrons through a fusion reaction. The tube has an ion source at one end, and an ion target at the other. The target contains one of the hydrogen isotopes adsorbed on its surface as a titanium hydride. When a current surge is applied to the ion source, an electrical arc creates a dense plasma of hydrogen isotope ions. This cloud of ions is then extracted from the source, and accelerated to an energy of 100–170 KeV by the potential gradient created by a high voltage acceleration electrode. Slamming into the target, a certain percentage of the ions fuse to release a burst of 14.1 MeV neutrons. These neutrons do not form a beam but are emitted isotropically. High explosives are designed to compress the core. To create a spherical implosion wave, inward facing explosive ring lenses need to be arranged on the surface of the sphere assembly so that the convergent spherical segments produced merge into one wave. It is a substantial advantage to use lenses with a small thickness to produce a wave with a smaller curvature. Powerful shock waves can dissipate significant amounts of energy in entropic heating. Energy that contributes to entropy increase is lost in compression. This problem can be overcome by using a shock buffer; this is a layer of low impedance or low density material that separates two denser layers. When a shock is driven into the buffer from one of the dense layers, a weaker shock of low pressure (but higher velocity) is created. This shock is reflected at the opposite interface, driving a shock of increased pressure into the second dense layer. This shock is weaker than the original and dissipates much less entropy. Two likely low density materials for use as buffers are graphite and beryllium. The term 'tamper' has long been used to refer both to the effects of hydrodynamic confinement in assembling and to neutron reflection. One must be careful to distinguish between these effects. The term 'tamper' refers exclusively to the confinement of the expanding fissile mass. Tamping is provided by a layer adjacent to the fissile mass. This layer dramatically reduces the rate at which the heated core material can expand by limiting its velocity to that of a high pressure shock wave. Two physical properties are required to accomplish this role: high mass density, and optical opacity to the thermal radiation emitted by core. High mass density requires both a high atomic mass and a high atomic density. Dense materials for use as tampers are natural or depleted uranium, tantalum and tungsten carbide. Any neutron that reaches the surface of the core is lost for ever to the reaction. A reflector around the core scatters

the neutrons to force some fraction of them to re-enter the surrounded fissile mass. Ideally the reflector is a layer of low-Z material. Beryllium and graphite are excellent neutron reflectors.

Safety is a serious problem with high yield fission weapons. Since several critical masses are present, simply collapsing the hollow space inside the core can render it highly supercritical. This does not require accurate implosion. Any accidental detonation of the explosive layer would squash a hollow core like a squashed tennis ball, and could lead to a very powerful explosion. Much milder accidents could also create serious criticality events such as a local region of criticality in the sphere. Several approaches are available to reduce these problems:

- keep the weapon core partially disassembled, with the fissile material brought into its 'implosion ready' configuration shortly before detonation,
- fill the hollow core with something that will prevent its collapse, then remove the material as part of the arming sequence,
- fill the core cavity with tritium and deuterium as part of the arming sequence,
- fill the core cavity with a good fast neutron absorber (i.e. something containing boron-10) to provide an additional margin of critical safety before arming,
- insert a continuous neutron emitter of sufficient strength to guarantee early predetonation,
- use locking mechanisms requiring special keys or codes,
- employ sophisticated fuzing systems to detonate the device at the proper place and time,
- resist malicious tampering, human error, component or systems failure (either inside or outside the weapon) and accidental damage,
- avoid inappropriate activation of the weapon's firing system and detonation of the high explosives by means other than the firing system (e.g. physical damage through fire or impact),
- use multiple and redundant safety systems requiring cooperation by more than one person to complete weapon arming.

After this brief description of tritium and nuclides used with it and their military applications, we will describe the organization of this book that is in three parts.

- In chapter 1 general aspects of fusion reactors using tritium are given. Chapter 2 describes methods for preparing tritium from lithium blankets. A variety of techniques for tritium handling and processing of highly tritiated wastes are described in chapter 3.
- In chapter 4 and chapter 5 we present the strategy for controlling corrosion in tritium-tritiated water, theoretical recall of characteristics of super-alloys and stainless steels and typical corrosion examples in installations in various parts of the world.
- Finally, results obtained in our laboratory are discussed and analyzed in the next chapters. Chapters 6 to 9 and chapter 23 describe the corrosion obtained directly from discharged low energy, tritiated water, tritium and helium. Corrosion by the primary aqueous radiolytic products (peroxides) and the effects of changes in pH are detailed in chapters 10 to 12. The corrosion problems due to the indirect radiolytic species (Cl^-, F^-, CO_3^{2-}, NO_3^- and ^2H_2O) are presented in chapters 13 to 21. Chapter 22 deals with

temperature effects. Finally, chapter 24 summarizes the findings and gives practical applications. In the annexe, 3D surface topographies show aspect of corroded metals in tritiated media (chapter 25) and fractal representation shows the modification of tritiated oxide layers leading to breakdown (chapter 26). These views of corrosion problems are significant and show the usefulness of this book. Because the book contains an unusually large number of corrosion terms a glossary is presented in the introductory material.

GLOSSARY

a = constant
$_{abs}$ = absorbed species
$_{ads}$ = adsorbed species
$_{aq}$ = aqueous solution
A = electrode surface (cm^2)
A = constant phase element (CPE)
B = rate coefficient for oxide layer corrosion or constant
b = constant
C = species concentration ($mol\,dm^{-3}$) or capacitance ($\mu F\,cm^{-2}$)
C = parameter depending on excitation and ionization in oxide or weapon compression factor
C_{ox} = oxide capacitance ($\mu F\,cm^{-2}$)
C_{dl} = double layer capacitance ($\mu F\,cm^{-2}$)
C_p = pore capacitance ($\mu F\,cm^{-2}$)
C_{hl} = Helmholtz layer capacitance ($\mu F\,cm^{-2}$)
$C_{V_{O^{2-}}}$ = concentration of O^{2-} vacancy
$C_{V_{Me^{n+}}}$ = concentration of Me^{n+} vacancy
{oxide-^3H_2O} = interface ^3H_2O–oxide
D = diffusion coefficient ($cm^2\,s^{-1}$)
d = depth of weld (mm)
d = oxide layer thickness (nm)
$d_{k,l}$ = deformation reaction of a metal to twinning
e = electron charge (1.602×10^{-19} C)
$e^{p}_{i,k}$ = irreversible part of a strain rate tensor where the subscript p is for elastic and plastic parts
E = electrochemical potential (V)
E_a = activation energy (J)
E_{corr} = corrosion potential (V)
E_{rep} = repassivation potential (V)
E_{pit} = pitting potential (V)
$E_{breakdown}$ = breakdown potential (V)
$E_{n...}$ = energy released in oxide by β^- particle

f, f = frequency (Hz)
F = Faraday constant (96 500 C)
F = free energy correlated to martensitic transformation
i = current ($A\,cm^{-2}$)
$i_{a,c}$ = anodic or cathodic current ($A\,cm^{-2}$)
i_{corr} = corrosion current ($A\,cm^{-2}$)
i_p = peak current ($A\,cm^{-2}$)
$i_{passive}$ = passivity current ($A\,cm^{-2}$)
I = ionization energy in oxide
j = imaginary operator
J_0 = parameter depending on thermodynamic constant
J_m = rate of submergence of the metal cation vacancy
K_w = dissociation constant
k = Boltzmann constant ($1.38 \times 10^{-23}\,J\,K^{-1}$) or rate constant
k = interaction parameter
$k_a, k_{c...}$ = rate constant of a reaction ($mol\,cm^{-2}\,s$)
l = cavity radius
L = inductance (H)
M = oxide mean molecular weight (g)
Me = metal
m = mass of β^- particle
n = neutron
n = number of electrons transferred in an electrochemical reaction
n_d = donor density ($n\,cm^{-3}$)
n_i = number of impacts in oxide by tritium decay
of = oxide layer formation
om = oxide layer modification
pd = primary depassivation
sd = secondary depassivation
p = pressure (Pa)
P_s = entropy production, positive for stable phases and negative for unstable phases
Q = electrical charge (C)
r = adsorption site
r = roughness factor or radius of the weapon-grade fissile material
$\bar{r}$ = corrosion rate ($\mu m\,yr^{-1}$)
R = molar gas constant ($8.314\,J\,mol^{-1}\,K$)
$R_{1,2...}$ = resistance ($\Omega\,cm^2$)
R_{ct} = charge transfer resistance ($\Omega\,cm^2$)
R_{el} = electrolyte resistance ($\Omega\,cm^2$)
R_{ox} = oxide resistance ($\Omega\,cm^2$)
R_{pit} = pitting resistance ($\Omega\,cm^2$)
R_p = polarization resistance ($\Omega\,cm^2$)
R_{lc} = localized corrosion resistance ($\Omega\,cm^2$)

R_{im} = imaginary resistance ($\Omega\,cm^2$)
R_{real} = real resistance ($\Omega\,cm^2$)
R_D = diffusion resistance ($\Omega\,cm^2$)
s = Laplace operator
$s_{i,k}$ = independent thermodynamic variable
t, T = time (s)
$\tau_{1/2}$ = half life for tritium (yr.)
T = temperature (K: Kelvin degree, C: Celsius degree)
V_m = measured potential (V)
V_{fb} = flatband potential (V)
$V_{O^{2-}}$ = oxygen vacancy
$V_{Me^{n+}}$ = metal vacancy
V = helium atom volume
v = scan rate (V/s)
ν = electrochemical reaction order
$\overline{v}$ = travel speed during welding ($cm\,min^{-1}$)
V_{fb} = flatband potential (V)
w = width of weld (mm)
w = equivalent weight of metal (g)
W = Warburg impedance (Ω)
W = energy carried out during welding (W)
X^- = halide
x = angular frequency or adsorbate or numerical value
y = numerical value
Z = atomic number of element
Z = impedance (Ω)
Z_r = real impedance (Ω)
Z_i = imaginary impedance (Ω)
Z_{ou} = outer oxide impedance (Ω)
Z_{in} = inner oxide impedance (Ω)
Z_D = diffusion impedance (Ω)
Z_L = Laplace impedance (Ω)
Z_{CPE} = constant phase element impedance (Ω)
Z_F = faradaic impedance (Ω)
$|Z|$ = impedance modulus ($|\Omega|$)
ΔG = standard Gibbs energy (J)
$\Delta\Phi$ = potential drop into oxide (V)
α, (1α) = symmetry factors
α = constant
β^- = negative particle emitted during tritium decay
γ = surface tension on wall
v_e = antineutrilo particle emitted during tritium decay
φ = parameter

Υ = dynamic viscosity (P)
δ = diffusion-layer thickness (μm)
Δ = change in dimension of the weapon-grade fissile material
ε = relative dielectric constant
ε_0 = permittivity of free space (8.854×10^{-14} F cm^{-1})
θ = fractional surface coverage or t/T (stepped potentials) or phase angle (°)
κ = conductibility (S cm^{-1}), or parameter depending on energy absorbed in oxide
σ = Warburg coefficient (Ω^{-1} cm^{-1})
$\sigma_{i,k}$ = macroscopic stress tensor
η = overpotential (V)
Φ = electrical field inside an oxide layer (V)
$\overline{\mu}$ = shear modulus
ρ = solid density (g cm^{-3})
ω = angular frequency (rad) or electrode rotation rate (n min^{-1})
Ψ = function related to fractal polynomial
υ = parameter of β^- particle
ς = parameter of β^- particle
Γ = concentration of adsorbed species
rpm = rotation per minute
$*$ = excited species

Part I

THE ROLE OF TRITIUM IN THE NUCLEAR INDUSTRY

This Page Intentionally Left Blank

Chapter 1

THERMONUCLEAR FUSION REACTOR

1. Thermonuclear fusion reactor overview

Controlled nuclear fusion can be defined as the process by which tritium and deuterium nuclei combine at very high temperatures to produce ^{4}He and fast neutrons releasing a large amount of energy that can be recuperated as electrical power. The latest experimental machine, which is a joint undertaking of the European Union, Japan, the Russian Federation and the USA, is known as ITER (International Thermonuclear Experimental Reactor). The overall view of ITER is given in Fig. 1.1, as shown by Rebut and Keen [5]. The facility consists essentially of a vacuum and plasma vessel containing tritium and deuterium and magnetic field generators to confine the nuclei. In the reactor, the ignition of ^{2}H-^{3}H must be maintained in the plasma over long pulse times during the thermonuclear reaction for the stationary state.

Here the deuterium-tritium nuclear reaction is:

$$^2\mathrm{H} + {}^3\mathrm{H} \rightarrow {}^4\mathrm{He}\ (3.5\ \mathrm{MeV}) + n\ (14.3\ \mathrm{MeV}) \tag{1.1}$$

Scientific aspects of thermonuclear reactors have been detailed by Dautray [6] and Dautray and Watteau [7]. As seen in the equation above large amounts of energy are released. To make this ignition reaction take place in a nuclear fusion reactor, the ^{2}H and ^{3}H ion fuel must be fused. This is achieved under the action of electromagnetic forces and extremely high temperatures overcoming the electrostatic Coulomb repulsion between positively-charged nuclei and bringing them close enough together for fusion to occur at a sufficient rate. For this, a temperature of around 10^7 °C and an ordered magnetic field of ten Tesla are needed in the plasma core of the reactor. At this temperature, the gas is a plasma and the ions and electrons form a macroscopically neutral fluid. Also, using magnetic confinement fields makes it possible to keep the plasma thermally insulated in the core. The fusion energy in this device would amount to several gigawatts. In practice, the confined radioactive ^{4}He, formed in eq. (1.1), would heat, during its removal, the fresh fuel and then, once it has cooled, would be extracted from the core for its eventual sale. A 1000 MW fusion reactor will require about 3×10^{20} fusion reactions per second and produce about 10^{19} 14.3 MeV neutrons/s and would require several kilograms of tritium per year, equivalent to a fuel burn-up of about 3.6 g of deuterium and 5.4 g tritium per hour. This shows that tritium is

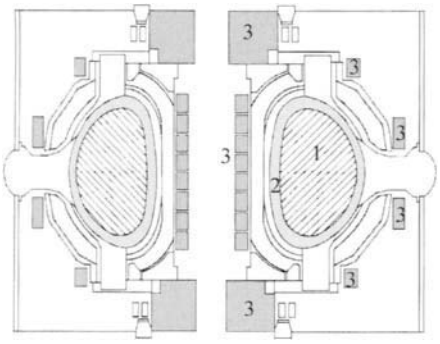

Figure 1.1. Cross-sectional view of the International Thermonuclear Experimental Reactor, 1: ^{2}H-^{3}H plasma torus, 2: vacuum vessel, 3: magnetic field generators (coils, transformers).

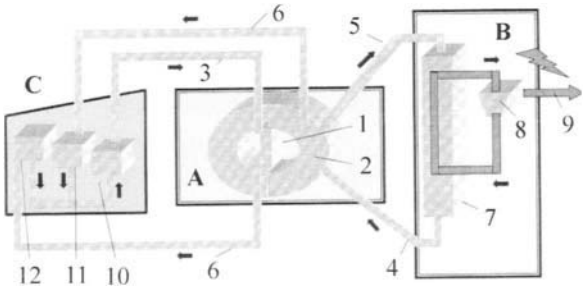

Figure 1.2. Schematic of the elements of the Fusion Energy Power Plant, A—fusion reactor, 1: torus, 2: blanket, 3: ^{2}H-^{3}H fuelling, 4: coolant inlet, 5: coolant outlet, 6: ^{3}H outlet tritium, B—electrical power, 7: steam generator, 8: turbine, 9: electric output, C—tritium recycling, 10: ^{2}H-^{3}H fuel preparation, 11: recovery, 12: clean up and recovery.

needed to keep the plasma burning. The major tritium inventories will be in the plasma, impurity processing, lithium blanket, isotope separation, fuel storage as metal tritides and tritiated water recycling. Since tritium and deuterium are such important components, their supply for the nuclear reactor must be anticipated (Fig. 1.2).

Deuterium is abundant in the Earth, but tritium is radioactive, with a half-life of 12.3 years and therefore does not occur naturally. It has to be manufactured, and breeding tritium in situ is an interesting possibility. In meeting this objective, some fast neutrons are used to breed enough tritium from a lithium blanket material adjacent to the nuclear reactor. For this process, 14.3 MeV neutrons pass through the nuclear reactor wall then interact with the lithium in the reactor blanket before being transported to a conventional power plant.

$$^{6}\mathrm{Li} + n \rightarrow {}^{4}\mathrm{He} + {}^{3}\mathrm{H}\ (4.85\ \mathrm{MeV}) \tag{1.2}$$

$$^{7}\mathrm{Li} + n \rightarrow {}^{4}\mathrm{He} + {}^{3}\mathrm{H} + n - (2.5\ \mathrm{MeV}) \tag{1.3}$$

The basic material for this reaction, natural lithium, consisting of 92.5% ^{7}Li and 7.5% ^{6}Li is found in large quantities in the earth. Primary 14.3-MeV neutrons from the fusion plasma are slowed down in the blanket that must be sufficiently thick to generate a large quantity of tritium and slow neutrons. Slowing the neutrons heats the blanket and a coolant flowing through it and so the blanket in the fusion reactor serves a second function, i.e. it converts the released energy into useful heat.

In practice there are several options. Due to its low melting point the liquid lithium-breeding blanket can be used as coolant, as in the Phoenix type super-generators, to thermalize the neutrons. In this case, the bred tritium is transported with the liquid lithium stream and is separated externally. The blanket design can include, to be more efficient, the addition of beryllium to lithium for neutron multiplication; however, the compatibility of beryllium with the other materials and the coolant medium is a sensitive issue. Moreover, multiplied neutrons have lower energies. A second choice has been made between burning more lithium and the greater recuperation of energy for heating the blanket. In using solid lithium, three options have been examined for the blanket-support: lithium-ceramic (solid breeder), lithium-salts (aqueous salt) and lithium-lead eutectic. Key design issues for the lithium-ceramic are to maintain the breeder material at a temperature high enough in the presence of hydrogen to enhance tritium release at 400–1000 °C, while having a low temperature water-cooled steel structure. The bred tritium contains $O^{3}H^{-}$ ions, $LiO^{3}H$ and $H^{3}HO$-$^{3}H_2O$ moisture. Tritium recovery is strongly dependent upon the activity of these species. The key issue for the lithium-salt option is the corrosion of the coolant channels. Lithium-lead alloys such as $Li_{17}Pb_{83}$ with a melting point at 235 °C and a high breeding rate due to the neutron multiplying element, lead, have been also studied. The key property of the lithium-lead eutectic is the extremely low solubility of tritium in it leading to chemical reactions and high permeation through the hot stainless steel walls inducing material damage.

Moreover, the thermonuclear fusion reactor has specific advantages and disadvantages:

- a runaway fusion reaction is intrinsically impossible. Furthermore, once the supply of fresh fuel is cut off the reactor can continue operating for only a few tens of seconds and no melting of critical components would occur. In addition, major explosions similar to nuclear explosions cannot occur in fusion reactors because the total amount of reacting fuel in the plasma is unable to maintain full power operation for more than a few tens of seconds and any disturbance leads to loss of plasma confinement and hence terminates the fusion reaction,
- there are radioactive wastes, unburnt tritium and tritiated water to be treated in the tritium processing installations. Structural components of the nuclear reactor which have become radioactive through exposure to the neutrons will have to be stored for a long time.

2. Requirements for controlled nuclear fusion

Nuclear reactors produce a large amount of energy at very high temperatures and require, paradoxically, the provision of external energy. To control the energy balance, the conditions must be such that the thermonuclear fusion reaction delivers more energy by confinement than it consumes. Also, in a nuclear reactor burning a ^{2}H-^{3}H fuel, the reaction can be partially self-sustaining by the 4.5-MeV kinetic energy to maintain the combustion temperature. The best performance obtained for a ^{2}H-11% ^{3}H combustion expressed by $Q_i \tau_E n^{-1}$ is 9×10^5 EeV s m^{-3} where Q_i is the ignition energy in the center of the plasma, τ_E energy confinement time and n the density of the ^{2}H-^{3}H fuel contained in the plasma. To obtain this performance, the reactor specifications including reactor vessel toroid (made of stainless steel) must be taken into account. According to the specifications, the ignition chamber steel underwent various treatments where surface cleanliness was at a premium. Baking to 500 °C took place under vacuum-removed gas and impurities adsorbed on the inner wall surface were removed. This made it possible to achieve the specified vacuum of about 10^{-7} Pa required for correct fusion operation with the ^{2}H-11% ^{3}H mixture without the presence of impurities. As the stainless steel vessel which is several tens of centimeters thick is the primary containment for plasma where there are high radiation levels, corrosion fatigue tests have been made. These verify that the stainless steel used meets the specifications of the loads both for fusion operation and also for accident conditions where there could be irradiation. To avoid tritium leakage and external contamination, double containment is provided between the plasma vacuum chamber and the external torus wall. It is clear that the vessel assembly due to its complexity and thickness is subjected to mechanical stresses that can lead to plastic deformation mechanisms and rupture following the cracking of the steel. This is an additional reason for carrying out these corrosion fatigue tests in a Pressurized Water Reactor.

The other components within the vacuum vessel are also subject to fatigue stress by irradiation. Since components have limited lifetimes, it must be possible to replace them quickly. In addition, the layout of the cooling pipes was designed to reduce the number of welds to a minimum in the most vulnerable regions where localized stresses, ruptures and induced corrosion can occur.

The best energy balances, plasma density, ignition temperature and pulse time have been obtained after applying these specifications and after applying the tests in selecting materials. The energy obtained by fusion of ^{2}H-11% ^{3}H is about 10.5 MW. It is hoped that, in the future, break even will be reached with ^{2}H-50% ^{3}H.

It is foreseen that in this thermonuclear fusion the tritium is not completely consumed. Its inventory is thus important for following the recuperation and recycling operations. The recycling of tritium is well understood and controlled in specialized tritium-handling plants that use methods such as tritium isotope cryodistillation, uranium storage beds, gas chromatography and metal diffusion membranes for purifying the tritium gas to maintain tritium at a high standard of purity in the torus and annex facilities. Recycling will be discussed in the chapter that describes tritium processing.

3. Plasma confinement

Plasma confinement is necessary and is achieved by magnetic fields. Other modes for confinement are possible such as the inertial thermonuclear fusion confinement by laser beams. In confinement, a fuel capsule is heated and highly compressed to obtain a very high liquid density until ignition occurs in the center by implosion, then the explosion carries the energy outside the reactor for recuperation in the power plant. Ignition lasts as long as the fuel remains confined by its own inertia. This technology is not yet optimized and will not be described further. Nevertheless, if it is adopted in the future, the same lithium blanket, tritium reprocessing or recycling will be applied and so the tritium processing problems will be the same.

In the absence of magnetic confinement, the ^{2}H and ^{3}H ions in hot plasma tend to spread and fill the space available because of the collisions between ions. The plasma in this condition is not confined and the thermonuclear reaction cannot occur. If a linear, perpendicular magnetic field is applied, ^{2}H and ^{3}H ions move in helical paths around the magnetic field lines and thus remain radially confined and the hot plasma forms a magnetic trap for the ^{2}H and ^{3}H ions. The stationary burn is thus possible for as long as the magnetic confinement is maintained. The particles of plasma cannot reach the side walls of vessel, but they will strike the ends of the vessel and thermonuclear fusion is limited. To prevent the particles coming into contact with the ends of the vessel, toroidal configurations have been realized. In these configurations, a toroidal field has the perpendicular poloidal field superimposed upon it. The ^{2}H and ^{3}H ions trajectories thus take spiral paths along and around the plasma. The toroidal field magnet includes several water-cooled coils to maintain the necessary toroidal trajectory. The shape of these is chosen to reduce mechanical stresses because they are subjected to the forces due to magnetic pressure and control of the mechanical stresses is important to avoid stainless steel cracking and tritium leakage. The poloidal field coils are the primary windings of a transformer, and their main role is to induce the current flowing through the plasma. They create field components that control the equilibrium, position and shape of the plasma.

Three types of system produce a spiral path:

- the Tokamak consists of a series of coils spaced around the torus to generate the toroidal magnetic field with the transformer to produce an electric current flowing through the plasma creating the poloidal field. The transformer also serves to heat the plasma resistively. The transformer improves the magnetic coupling between the primary windings and the secondary plasma to create a demagnetizing effect. This produces the required voltage for gas breakdown in the vessel and maintains the plasma current to heat it ohmically. The values of the toroidal field and plasma current are about 3.45 T and 4.8 MA, respectively. An important parameter of the machine is the ratio of the major radius to the minor radius of the torus. Theoretical studies and experiments have shown that a ratio of about 1.5 provides the best plasma performance.
- the Stellarator is formed by a series of external coils to produce the spiral magnetic field lines. No current is induced in the plasma. The Stellarator can operate continuously

avoiding disruptions responsible for mechanical stresses in the stainless steel structures and walls.
- the Reversed Field Pinch device has the toroidal and poloidal configuration with a very high current so that the direction of the toroidal field at a certain radius within the plasma is reversed.

4. Plasma heating

In Tokamak devices, the current flowing through the plasma also serves to heat the plasma by the Joule effect until a high temperature is reached. Beyond this point the resistivity of the plasma is too low so that additional heating systems are needed to bring the plasma to the temperatures required for thermonuclear fusion.

In the case of Stellarators, these heating systems have to supply all the energy needed since there are no current flows induced within the plasma. The main methods of additional heating selected for controlled thermonuclear fusion systems are essentially injection of high-energy neutral beams, dissipation of radiofrequency waves in the plasma, adiabatic compression and the use of electrical transformers.

- neutral injection heating is achieved by injecting an intense beam of energetic neutral atoms across the confining magnetic field into the plasma. There, the neutral particles are ionized and confined by the magnetic field. The resulting energetic ions give up their energy to the bulk plasma via collisions, thus increasing its temperature. The beams are generated by the electrostatic acceleration of positive ions, which subsequently are neutralized in a gas cell since charged particles are unable to penetrate the magnetic fields of the torus. The neutralization efficiency is quite low and the remaining ion beams are deflected and dumped.
- additional radiofrequency generators dissipate energy which is absorbed by the plasma, and thus heating occurs for a long time.
- adiabatic compression of the plasma involves the plasma moving and changing shape from a region affected by a weak magnetic field towards a region where there is a strong magnetic field. In this method, heating occurs during all thermonuclear fusion time.
- transformers induce a heating inductive current on the plasma for only a short time.

Chapter 2

THE PREPARATION OF TRITIUM

Obtaining background information for the industrial production of tritium by a lithium blanket is an important point for its use in a fusion reactor. Tritium is prepared by neutron activation of ^{7}Li-7.5% ^{6}Li. Neutrons with sufficiently high energy activate ^{6}Li, whereas ^{7}Li requires more energy for activation. Due to the fact that ^{6}Li has a low concentration, a larger fraction of the neutron trajectories will encounter ^{7}Li and therefore, neutrons with energies well above 2.9 MeV are required. In previous studies as reported by Johnson [8], it has been seen that tritium breeding materials are attractive because of their overall excellent tritium release, chemical inertness and thermophysical and thermomechanical properties with a stable phase under irradiation. Li_2O, Li_2AlO_2, Li_2TiO_3, Li_2ZrO_3 have been selected from a choice of several ceramics.

The work done has shown that the rate-limiting mechanism for tritium transport into the ceramic and its release must be known. A full understanding of processes is critical for achieving an efficient production of tritium fuel to sustain the fusion reaction. In fact, the mechanisms are complex and involve tritium diffusion and trapping in the ceramic grain, grain boundary diffusion, adsorption reactions on the grain surface, tritium desorption, gas-solid equilibration by bulk solubility and molecular diffusion in the gas phase. Diffusion should be the rate-limiting mechanism. However, it was shown that the rate-controlling step changed from diffusion to surface phenomena as the ceramic grain size decreased and/or temperature increased.

Also, oxygen activity controls the released oxidized and reduced tritium forms, the amount of tritium retained in the condensed phase, and the amount of blanket transported as $LiO^{1}H/LiO^{3}H$ vapor. If oxygen activity is reduced sufficiently, it is possible for tritide dissolved in the bulk to become an important species in the condensed phase and tritium release is slow. The result will be an increase in the tritium inventory in the blanket that is unacceptable from both an economic and safety viewpoint. For this, oxygen activity depends on the used ceramic type. Recent tests indicated excellent tritium release behavior of Li_2ZrO_3 and Li_2TiO_3 ceramics over the temperature range of 350–1100°C. Insensitivity to moisture or vapor for Li_2ZrO_3 ceramic was also observed. Fortunately for safety, activation by radiation of zirconium-ceramic is small in comparison with that from currently used structural steel materials. Postirradiation examination of the Li_2ZrO_3 pebble bed showed very low tritium inventory, about 0.05 ppm, and excellent release comparable with that of Li_2TiO_3 pebbles.

Helium-4 generated in ceramic breeder materials during neutron irradiation has also a significant impact on the durability of materials by its diffusion in the grains and release from the surface. Data indicate that helium-4 release is much lower than tritium and, therefore, can cause a blanket swelling problem if helium gas does not escape from the ceramic. Ceramics in small grain form do not represent too great a problem, and no fractures have been observed in the breeder Li_2ZrO_3 ceramic.

In the process, tritium outgassing from the ceramic compounds will be transported from the blanket in a helium or argon-stream and recovered externally. It has been noted that tritium release is very much easier with about 1000 vpm hydrogen. This particularity has been used in tritium-piles for several years. However, the addition of hydrogen to the purge gas imposes a multiple-stage tritium purification for isotope separation. Also, the species released have been found in two forms, H^3H and H^3HO, so that the tritiated water must be separated from the tritium-hydrogen mixture by alumina-ceramic desiccating beds. The presence of tritiated water in these beds could be a source of equipment corrosion. In addition, using hydrogen requires understanding of the tritium processes in the lithium ceramic. For this, the surface-to-volume ratio of the ceramic grains is an important parameter for diffusion and desorption. With large grains, the bulk diffusion will determine the release rate. For smaller grains, the surface reaction becomes important with respect to the role that hydrogen plays. For tritium release, there are two mathematical formulations depending on whether hydrogen is present or not. Irradiation of lithium by neutrons with no hydrogen in the helium purge gas creates tritium in the form of $^3H^+$ inside the ceramic at a few tens of ppm. The probability of forming $^3H_2$ or ^3H_2O is very small, and the release rate is proportional to the square of the low molecular tritium concentration in the lithium-based solid breeder ceramic. With hydrogen present, there is chemisorption of OH^- and $Li_2^+H^-$ on the lithium ceramic surfaces and two possible reactions with $^3H^+$:

$$Li_2^+H^- + {}^3H^+ \rightarrow 2Li^+_{solid} + H^3H \tag{2.1}$$

$$OH^- + {}^3H^+ \rightarrow H^3HO + V_{O^{2-}} \tag{2.2}$$

where $V_{O^{2-}}$ indicates oxygen vacancy. Tritium release rates are proportional to the product of the surface coverage of the chemisorbed hydrogen and the tritium concentration; the former is usually much larger than the latter. Therefore, in the second mathematical formulation, the tritium release rate is directly proportional to the tritium concentration and not to its square, as is the case in the absence of hydrogen. This is the basic reason that the addition of hydrogen to the purge gas leads to an enhancement of the tritium release rate. The model thus suggests that the tritium release rate should be enhanced by increasing hydrogen concentrations in the helium purge gas. But experiments have shown that majority of the surface sites are not available for hydrogen chemisorption with only a small number of sites such as step ledges and point defects being favorable. Once these sites are all occupied, further increases in the hydrogen concentrations would not be useful.

As a final point, the ceramic Li_2ZrO_3 is thermally stable and has satisfactory behavior under neutron irradiation. However, the consumption of lithium in the irradiation that can

reach 10 to 20% will lead to a two-phase ceramic made up of both zirconia, ZrO_2, and zirconate, Li_2ZrO_3. The appearance of zirconia is liable to embrittle this ceramic by degrading the grain cohesion. As shown by Abraham et al. [9], it is of interest to note that the introduction of copper in this substance as a solid solution makes it possible to conserve the lithium zirconate structure in the consumption of lithium by the creation of cationic vacancies favoring ion mobility. This presence of copper in the ceramic structure also enables improvement of its tritium release capacity by lowering the temperature at which it is produced. The resulting ceramic has the formula $Li_2ZrCu_yO_{3+y}$ with $0 < y \leqslant 0.06$.

The experimental campaign of ITER involves the introduction of tritium in torus. For reasons of safety, both the gas introduction system and gas collection system are confined inside ventilated enclosures. The cleaning system by ventilated air depends on the flow rate in each enclosure, the cross-section for blowing or extraction in pipes, the velocity rate for extraction or blowing, and the depression in regard to the atmospheric pressure.

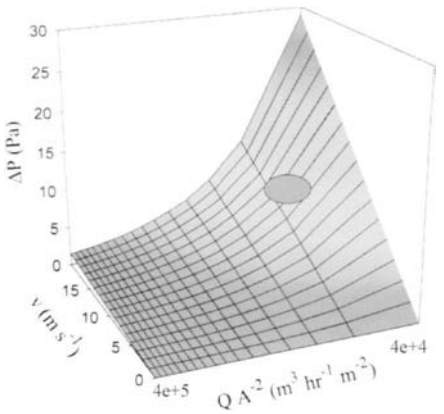

Figure 2.1. Mutual effects between depression, velocity rate and flow rate with the cross-section to eliminate tritium by ventilation.

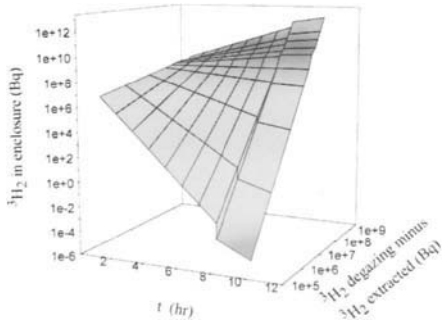

Figure 2.2. Air decontamination by extraction and blowing in force in regard to time.

Each parameter is dependent on others (Fig. 2.1). Good cleaning is obtained for a velocity rate of 10 $m\,s^{-1}$, a depression of 15 Pa and an air flow of 4500 $m^3\,h^{-1}$. Extraction in force can be also used up to 50000 $m^3\,h^{-1}$ to decontaminate a particular area. Decontamination is effective after several hours (Fig. 2.2).

Chapter 3

TRITIUM RECYCLING

According to Hircq [10], in the thermonuclear fusion excess tritium will not be burned and will be present in addition to the pure tritium that is supplied continuously. A gas clean up exhaust system working by pulses will remove the excess tritium isotopes with radioactive ^4He into a gaseous stream. For this, the gases containing about 2% of unburned tritium will have to be processed for each pulse of about 5000 dm^3. Moreover, this clean up exhaust will also be used to process tritiated gases produced during maintenance of the torus. The design of the tritium pulsing system is based on a daily processing by pumping the gases. High pumping speeds can be obtained with cryosorption and turbomolecular pumps. Fusion reactions also produce gaseous impurities such as CO_2, N_2, O_2, H_2, N^3H_3 and C^3H_4. Therefore, in addition to their excellent pumping properties, cryopumps can be also used to partially separate the gases. For this, all gases are condensed in the cryopump, with the exception of helium. The cryosorption pump releases the free pure helium with a minimum of tritium carry-over. At 20 K the tritium and deuterium gases are separated from the other impurities by freezing. Tritium and deuterium are subsequently separated in a gas chromatography or cryodistillation unit in the tritium plant for recycling. Gaseous impurities still containing a little tritium are processed in another unit of the tritium plant. A disadvantage of the cryopumps is that the tritium inventory is large and requires periodic removal of the trapped gases. With turbomolecular pumps, the tritium gas is in contact with the lubricating oil and may undergo isotope exchange reactions with the H atoms in the oil. Due to the radiation, the viscosity of the oil and the operating life-time of the pump change. Moreover, there is tritiated water formed by cracking of the oil and chlorides from the breaking of the carbon chains of oil constituents. This is an example, among others, showing the necessity of a better understanding of tritium chemistry in order to improve the technology. Improving the technology for extracting tritium from the torus has required studies including those of corrosion to ascertain the compatibility of any form of new materials with tritium and tritiated water containing impurities. The difficulties inherent in selecting new materials are directly related to the β^- emission which includes intrinsic energy. These difficulties are due to:

- helium-4 and -3 generation permanently modifying the gas composition and pressure as well as thermodynamic and physico-chemical properties of the medium,
- tritium oxidation leading to tritiated water and organic effluents that exhibit radiolysis phenomena depending on the β^- density responsible for corrosion,

- isotopic exchanges with hydrogenated molecules,
- degradation of organic materials that have a complex radical chemistry making them incompatible with tritium.

In addition, tritium exhibits the general properties of hydrogen including permeation through metals for the first containment leading to consequences on several levels:

- tritium leakage and safety and tritium recovery problems,
- helium-3 and -4 in confinement materials leading to metal embrittlement and weldability problems resulting from coalescing,
- tritium in materials leading to contaminated wastes that are to be stored, degassed and eventually to be processed.

Therefore, tritium recuperated from the gas clean up exhaust system is recycled by the tritium plant processes in making allowance for the difficulties inherent to tritium. The primary function of the tritium plant is to purify and separate hydrogen isotopes for recycling and store them. Also, considering the large amounts hydrogen isotopes of circulating in the torus, high capacity tritide storage systems are needed. The second function of the tritium plant is to treat depleted tritiated gaseous, rich and depleted tritiated liquid and solid wastes to minimize tritium release and to recycle it. Tritiated water will undoubtedly be present in all parts of this plant. Considering its high activity level compared to tritium gas, its radiolysis properties and its corrosion effects on materials highly concentrated tritiated water must be processed.

Tritium treatments require the use of numerous processes with all their components, such as transfer pumps, absorbent beds and purification catalysts for satisfactory operation. Consequently, the materials of tritium processes have to be tritium compatible and keep their functional integrity under all operational conditions during aging and retain their physico-chemical and thermodynamical properties. Also, compatibility studies are required for materials, such as stainless steels for which tritium permeation, embrittlement by ^{3}He and weldability can represent severe problems. Aged steel with ^{3}He generation showed helium coalescence along the welding bead. Moreover, independently of work undertaken for gas process optimization, studies of material corrosion have been made with the same objective; one such was to test the super-alloys and stainless steels.

The basic operations for tritium treatments are represented by the diagram, Fig. 3.1. These include removal of impurities, hydrogen isotope separation, metal tritide storage and tritium recovery from tritiated water. As can be seen, numerous processes are involved.

1. Production of pure tritium and its storage

The tritium facility's mission is first to produce pure tritium gas. Due to the decay of the tritium to ^{3}He, to successive improvements, over the years, in the manufacturing process and to equipment maintenance and waste processing, concentrated tritium gas quantities are gradually being depleted or mixed with impurities in a broad concentration range. Separation is defined here as the process of removing unwanted gas from hydrogen isotopes.

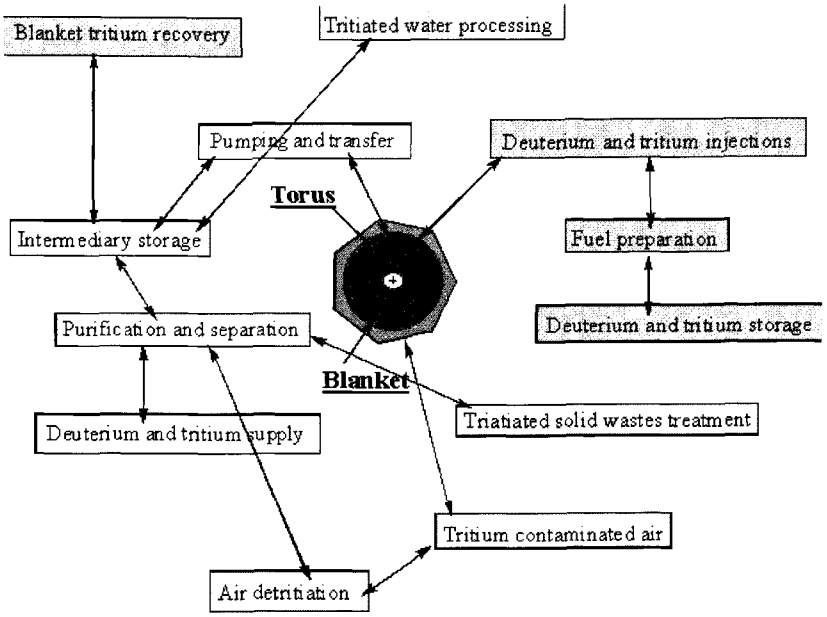

Figure 3.1. Overall tritium handling schematic.

The technologies used to accomplish this mission are divided into three main sectors as shown by Chabot et al. [11]:

- gaseous impurities separation,
- hydrogen isotope separation,
- tritium storage on tritide metals before reusing.

1.1. Impurity processing loops

Purification of tritium-deuterium gas is realized by permeation through 100 μm thickness palladium-silver membranes at high temperature as shown in Fig. 3.2 and [12]. Separation of 10^5 vpm of O_2, N_2, N^3H_3, C^3H_4, CO_2 impurities from tritium gas at low pressure showed no poisoning effect. For a high flow rate, the permeation module includes numerous hollow pins of Pd-25% Ag alloy. This module can supply about 700 dm^3/h of pure deuterium-tritium gas for a continuous process. After purification, hydrogen isotopes are transferred by cryotransfer pump to the isotopic separation loop.

Tritium-deuterium gas can also be purified by absorption of impurities in hot uranium beds between 500 and 900°C. After absorption, an accumulation panel pumps all impurities by cryocondensation at a temperature (< 100 K) while helium is trapped on activated

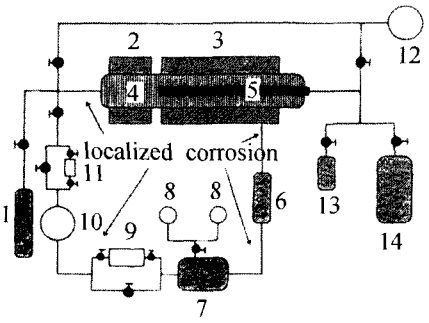

Figure 3.2. Schematic of thermal diffusion-purification loop process, 1: gas supply, 2: preheater, 3: furnace, 4: permeation cell, 5: Pd-Ag membrane, 6: cooler, 7: reservoir tank, 8: thermometer and manometer, 9: chromatograph analyzer, 10: circulator pump, 11: flow meter, 12: vacuum pump, 13: mass spectrometer, 14: reservoir tank.

charcoal at 4 K. The level of the resulting purification is altogether satisfactory (< 1 vpm starting from 1 vol% for each impurity such as O_2, N_2, N^3H_3, C^3H_4, CO_2).

After these processes, the recovered impurities still contain a little tritium; this trace level tritium is oxidized to tritiated water for storage.

1.2. Hydrogen isotope separation

Once the impurities of the plasma exhaust have been removed, it is necessary to separate deuterium and tritium in the pure gas stream. One possibility is hydrogen isotope separation by cryogenic distillation using the difference in the boiling points of these gases. The least volatile gas is $^3H_2$ with a boiling point of 25 K, whereas the most volatile gas is H_2 with a boiling point of 20 K. Thus, the more volatile isotope can be obtained at the head of the separation column, whereas the less volatile isotope can be obtained at the bottom of the column. The cryodistillation unit is designed for reprocessing the large tritium-deuterium amounts that are produced.

Another technique is gas chromatographic separation (Fig. 3.3). The purification process involves taking the hydrogen isotope stream and separating these, i.e. tritium, deuterium and hydrogen. This is carried out by a thermal cycle adsorption process using palladium hydride grains to perform the gas chromatography separation as reported by Botter et al. [13]. Depending on the composition of the gas phase in equilibrium (H^3H, $^2H^3H$, H^2H, H, ^2H and ^3H) with the hydride phase in solution, several equilibria are taken into account to obtain the appropriate isotopic separation. Also, the operating parameters (i.e. column capacity, column temperature, displacement velocity, pressure, hydrogen supply and eluent gas, etc.) must be correctly selected for separating pure tritium. This method is effective and gives separation levels above 99%. A disadvantage of this method is that a carrier gas, such as He, Ne or Ar, must be used and the hydrogen eluent makes it more difficult to separate small amounts of an isotope in the mixture.

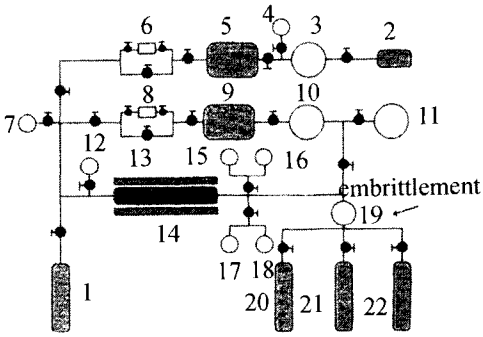

Figure 3.3. Schematic of tritium chromatographic isotope separation loop process, 1: H_2, $^2H_2$ and $^3H_2$ gases supply, 2: H_2 loading/eluent gas supply, 3: circulator pump, 4: manometer, 5: reservoir tank, 6: pressure regulator valve, 7: mass spectrometer, 8: pressure regulator valve, 9: reservoir tank, 10: circulator pump, 11: vacuum pump, 12: manometer, 13: heater, 14: chromatographic column, 15: differential thermometer, 16: manometer, 17: ionization chamber, 18: cathetometer, 19: circulator pump, 20-21-22: H_2, $^2H_2$ and $^3H_2$ gases storage.

In the separation and purification, the compression and pumping (turbomolecular pump) processes are mechanical operations. Compressors produce the high pressures desired for filling containers and gas circulation. Periodically, pumps and compressors are corroded leading to the breakage of mechanical parts. Over the years, oil pumping media have been partly eliminated from these systems, thus greatly reducing the amounts of organic liquids requiring reprocessing. Overall, these processing systems, when correctly coordinated, provide a very effective tritium handling system. They have evolved over many years with emphasis on improving worker safety, reducing environmental impact and effectively meeting their production mission. Note that these systems, operating exclusively in the gas phase under high or low tritium pressures or in tritiated water containing dissolved tritium gas (Table 2, in the Introduction), can induce embrittlement followed by cracking of the stainless steel or titanium alloy components (Fig. 3.4) and cause breakdown in the oxide layers both by tritium and the decay helium, as well as release of the decay gases (thermally induced effect, Fig. 3.5). In general, tritium and helium lead to greater embrittlement of metals than does hydrogen.

1.3. Tritium storage as metal tritides

Due to the use of large quantities of tritium in future fusion reactors, metals are employed for tritium storage. Metal tritides are very suitable materials for the reversible storage, pumping, compression, purification, isotope enrichment and transport disposal of tritium. Metal tritides can be produced by similar physical procedures and techniques as those used for metal protides and metal deuterides. There are three tritium-charging techniques as indicated by Lässer [14]:

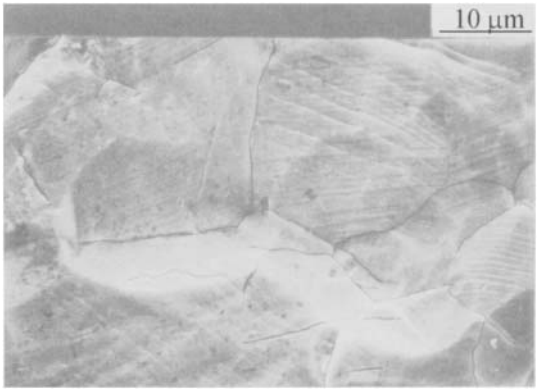

Figure 3.4. Embrittlement accompanied by cracking at the titanium grain boundaries and fine striations resembling cleavage by tritium gas dissolved in tritiated water.

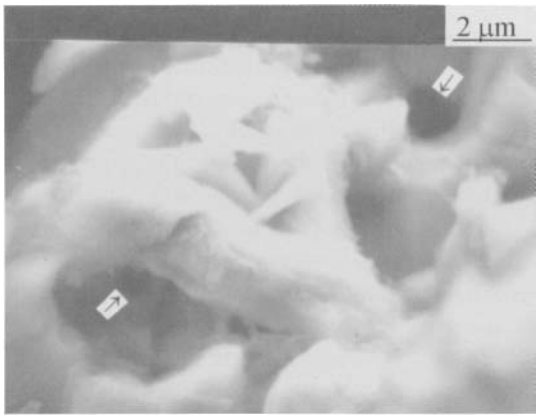

Figure 3.5. Thermally induced cavities (arrows) in stainless steel formed during the decay gas release (^{3}He) (sample heated at 1000°C for 3 h).

- charging the cathode metals with tritium is an easy procedure and requires only a simple setup for high tritium concentrations. This procedure leads to a pure mixture of hydrogen, deuterium and tritium atoms in the cathode metals and these have to be separated isotopically during the release,
- production of metal tritides from the gas phase is realized under high vacuum by an ion getter pump. In this way, the amount of tritium absorbed in the metal can be varied by changing the temperature and the tritium pressure,
- tritium charging of metals by metal tritides can be used to extract tritium from a metal tritide by a metal with a higher affinity for tritium. Host and donor metal tritides have to be activated to obtain high adsorption and desorption rates. In this case, the surfaces

of these metals must not be covered with oxide layers that prevent the adsorption or desorption of tritium atoms on catalytic sites. To circumvent this problem, metals have to be treated at high temperature in high vacuum or hydrogen gas. As a result, more catalytic metal atoms are obtained to dissociate tritium molecules and absorb tritium atoms into the lattice.

A very important advantage of storage of tritium in metals is the small dimensions of the metal tritide storage containers in comparison with storage of tritium gas because the latter should be stored only at a pressure below 10^5 Pa for safety. The second advantage is that metal tritides possess a low equilibrium pressure reducing the permeation of tritium through the container walls into the environment. A final advantage is that due to the very small solubility of the ^{3}He in metals, this is not trapped during operation and only the tritium gas will be absorbed. The unabsorbed ^{3}He gas will be removed from the metal tritide storage container.

Uranium can be used to produce metal tritides. Its main advantages are:

- very low tritium equilibrium pressures of about 2×10^{-3} Pa at 20°C; this means that the uranium acts as a getter at low temperatures,
- at about 400°C, and 550°C the equilibrium pressure is about 10^5 and 10^6 Pa, respectively. Therefore, the storage container can release tritium when uranium tritide is heated,
- uranium disintegrates to powder after reaction with tritium. Due to the powdering, the surface area capable of reacting with tritium increases, resulting in very short absorption or desorption times,
- the uranium powder also reacts easily with oxygen, nitrogen and hydrocarbons in a large temperature range and, therefore, works as a gas purification system,
- a very high tritium storage capacity of, in principle, three tritium atoms per uranium atom.

Disadvantages of the use of uranium are its radioactivity and the high pyrophoricity of the powder when exposed to air.

Alloyed palladium tritides play a special role because they are resistant to passivation due to the catalytic nature of their surface. For this reason palladium is used in cases where other metal hydrides easily become poisoned leading to a drastic reduction of absorption capacity and requiring a heat treatment for reactivation. Thin films of palladium coated on kieselguhr have a large surface area and are used for high pumping speeds and are especially suited to absorbing tritium from gas mixtures.

The main reason for using $LaNi_{5-x}Al_x$ tritides is that this material does not show significant disproportionation after many charging and temperature cycles in contrast with other metals. The prevention of disproportionation is very important in the case of tritium storage because otherwise tritium would become trapped in one component with a very low equilibrium pressure. $LaNi_4Mn$ tritides are very advantageous for tritium storage with an acceptable capacity of 0.15 dm^3/g for a storage pressure of $< 10^3$ Pa at 20°C and desorption temperature of $\sim$ 150°C at 10^5 Pa. Furthermore, aging studies involving 5 g tritium trapped have indicated that such products exhibit a total ^{3}He retention above 99%. These

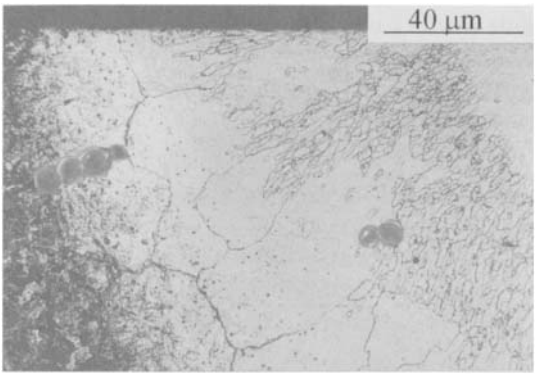

Figure 3.6. Formation of sub-critical microscopic helium bubbles in metal.

results are of great interest because they prove that large tritium amounts can be stored over long periods while maintaining a low storage pressure.

Another choice is that of Zr-Co alloys that are very attractive due to their capacity of ~ 0.2 dm^3/g for low storage pressures of $< 10^{-2}$ Pa at 20°C and their relatively low temperature for tritium recovery at 330°C for 10^5 Pa.

Metal tritides at high tritium concentration have high helium production rates. For several metal tritides, the extremely low solubility of helium in these leads to helium diffusion, lattice damage, disordered structure, cracks, microscopic cavities (Fig. 3.6) and conversion to metal powder on aging. Thus the tritium causes changes in the physical properties and influences the lifetime of metal tritides. Moreover, when helium accumulation occurs, several tritium concentrations coexist in the metal. Helium cavity formation requires two diffusion types. Due to the large binding energy between helium atoms and defects, diffusion cannot occur by defects at low temperature. Helium can diffuse via jumps between interstitial sites. Migration can also occur by a vacancy mechanism. In this case, helium migrates from a vacancy towards the immediate neighborhood until it is accumulated in a defect leading to a cavity as in the case of jumping diffusion. These two diffusion types depend on a physical equilibrium between a vacancy or interstitial site and cavity formation. For this, the necessary condition for diffusion is that the pressure, p_d, inside the existing cavities, which can be interconnected, does not exceed a threshold value [14] given by:

$$p_d \leqslant \frac{2\gamma}{l} + \frac{E_a}{V} \tag{3.1}$$

where γ is the surface tension of the cavity wall, E_a the activation energy between helium in the cavity and that adsorbed on the cavity wall, l the cavity radius, and V the helium atom volume. In fact, p_d may reach values of up to 10^{11} Pa.

Independently of the previous equation, after reaching a certain pressure depending on the increasing cavity size, ^{3}He-filled cavity loops are formed and connected by channels.

The threshold pressure is:

$$p_c \geqslant \frac{(2\gamma + \bar{\mu} b)}{l} \tag{3.2}$$

where $\bar{\mu}$ is the isotopic average of the shear modulus, and b the Burgers vector of the ^{3}He-filled cavity loop.

Channels can reach the outside surface of the metal tritides and thus release helium at its generation rate. The release rate depends strongly on grain-size and temperature, e.g. U^3H_3 with a surface area of 0.6 m^2/g, released 4% of ^{3}He, whereas with a surface area of 3.0 m^2/g, the release is 21% after 650 days. Increasing temperature accelerates the release rate. An extrapolation of the behavior shows that after aging, about 70% to 90% of the helium is released after external rupture of ^{3}He-filled cavity loops. Rupture is accompanied by tritium discharge to the outside.

To show the effects of helium on the palladium-silver alloy, this was charged with tritium to form two α-β tritide phases. After aging, the results show strong evidence of coexistence of two regions depending on the ^{3}He density distribution. In the β phase, which is richer in tritium, ^{3}He-filled small isolated cavities and a dense distribution of ^{3}He-filled cavity loops are observed at 6000-ppm concentration. The number of loops increased after long aging. Also, an interconnected system of ^{3}He-filled cavity loops is visible on aging. Whereas in the α phase palladium-silver depleted in tritium, the ^{3}He generation rate is lower and no ^{3}He cavity loops are found. The β phase is the dominant site for helium clustering. Cavity diameters in loops increase approximately as the cube root of the aging time indicating constant helium density in the cavities with no helium release and high internal pressure above 2×10^9 Pa. Nevertheless, for longer aging, connection of the cavity loops to the external surface releases ^{3}He to the outside leading to a pressure drop in the interconnected system. Conceivably, this high pressure drop may cause the loop-channels to close as seen by experiments. Re-opening of the loop channels is only possible after refilling with ^{3}He atoms. Thus, three different states on aging may be distinguished:

- generation of cavities,
- growth of the ^{3}He-filled cavity loops,
- development of interconnecting ^{3}He loop-channels towards outside surfaces thus allowing the release of helium and tritium after aging.

2. Tritiated waste processing

The above operations and nuclear fusion reactors produce tritiated wastes. A particular feature of tritiated wastes compared with other radionuclides is that they exist in three different forms:

- gas: effluents composed mainly of gaseous tritium and tritiated water vapor,
- liquid: basically tritiated water at different concentrations; there are also tritiated oils,

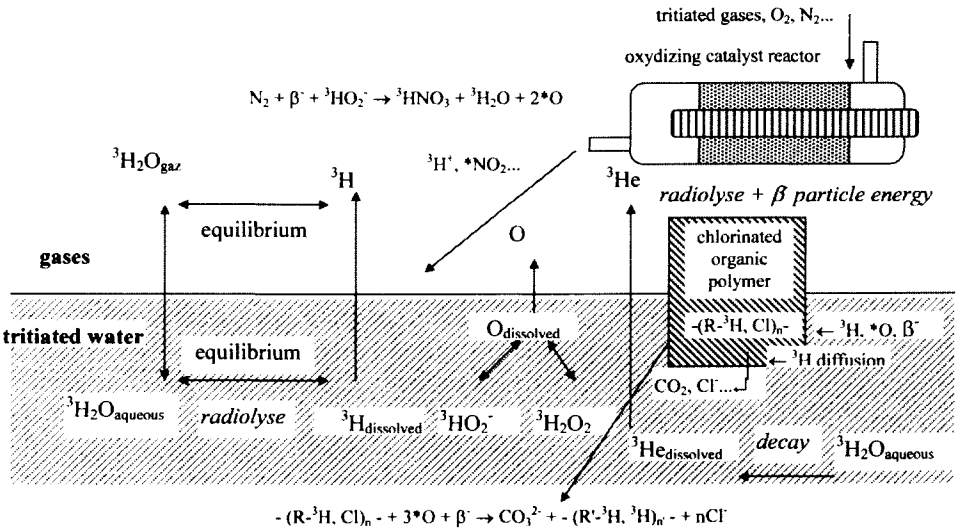

Figure 3.7. Self-radiolytic mechanisms with formation of CO_3^{2-}, Cl^-, NO_3^-, $^3HO_2^-$, $^3H_2O_2$, $^3H^+$, $O_{dissolved}$ and $^3H_{dissolved}$.

– solid: metals (mainly steels), organic and inorganic materials. The inorganic products such as concrete are subjected to heat-treatment at low pressure with an argon sweep in a graphite resistance furnace at > 800°C and do not cause any decontamination problem.

All three categories of waste may be stored in stainless steel vessels. A special feature of solid and liquid tritiated wastes is degassing, i.e. they permanently emit gaseous wastes:

– either by desorption of volatile compounds (for the most part these are on the surface),
– or by self-radiolysis (Fig. 3.7).

Consequently, wastes are stored on the basis of three main criteria:

– degassing rate,
– surface contamination.

Surface decontamination of metals can be carried out by electrolysis with cathodic hydrogen charging for an isotopic exchange (Fig. 3.8) [15]. The steels to be used for the decontamination contain tritium both on the surface and in the bulk. The tritium on the surface is easier to remove than from the bulk. The tritium depth profile can be evaluated by taking a sample using the slicing technique followed by full dissolution in acid or by melting and full oxidation of the produced slices,

– tritium concentration in the bulk.

The range of tritium contents of gaseous, liquid and solid waste is extremely wide and varies from 10 to 10^9 MBq/kg. The main hazard of stored tritium waste is container leakage. Storage containers must be able to withstand corrosion damage as well as the increase of internal pressure resulting from the decay of tritium to helium-3.

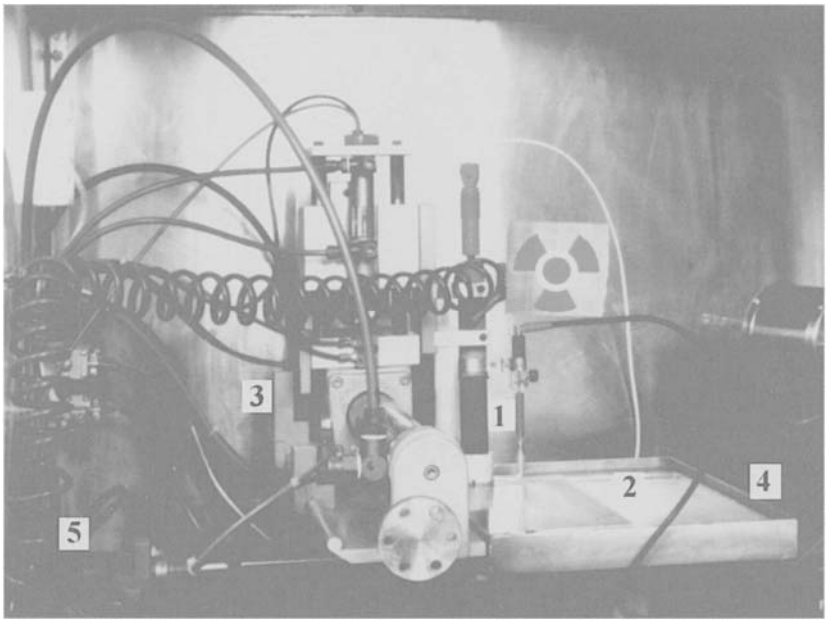

Figure 3.8. Robot electrolyzer for surface decontamination, 1: bielectrode body for charging hydrogen, 2: steel to be decontaminated, 3: device for displacement of the bielectrode on the steel surface with the use of a remote control, 4: operating floor, 5: pneumatic control system.

In the last point, during any tritiated waste treatments, the recovered tritium is conveyed by collectors towards the air detritiation and processing plant vacuum units. Maintenance operations are periodically required in these different units due to corrosion-induced breakdowns.

2.1. *Electrolysis of highly concentrated tritiated water*

The chemical properties of tritium are very similar to those of deuterium and hydrogen since these depend mainly on the characteristics of the unpaired electron of each isotope. But, due to the β^- decay energy, thermodynamic equilibria can be reached faster when tritium atoms are present. The result is that tritium gas can be easily transformed into tritiated water by oxidation with air and by isotope exchange with water. The rates of the tritiated water formation are slow at room temperature, but can be increased by the presence of catalysts or ionizing radiation. For example, the equilibrium constant of the exchange reaction is about 6.3 at 20°C and 3.4 at 130°C, showing that tritium prefers to be in the water molecule. Also, the tritium-contaminated organic impurities will be catalytically oxidized, reduced or destroyed to form $^2H^3HO$, $^2H^3HO_2$, CO_3^{2-}, $N^3H_4^+$ and Cl^-. This impure tritiated water, which is a source of corrosion, must be electrolyzed for recycling tritium. In

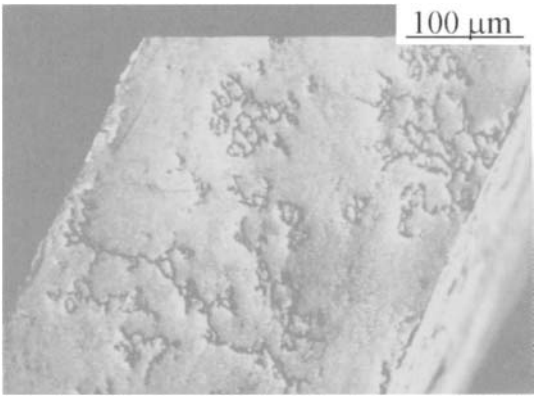

Figure 3.9. Embrittlement of Pd-Ag by tritium.

addition, estimates based on existing equipment show that tritium release is about 450 TBq H^3HO and 350 TBq H^3H/yr. This means that in a fusion reactor, as much tritiated water will be formed as tritium gas demonstrating the need for tritiated water recycling. The standard method uses hot activated uranium beds that react with water forming uranium oxide and uranium tritide. The disadvantages are far from negligible because this makes use of pyrophoric uranium that will generate radioactive solid wastes emitting α and β^- particles.

To avoid these problems, innovative electrolyzers operating with Pd-25%Ag gas diffusion thimbles cathode have been developed and have the specific advantages of a low inventory of tritiated water, a low working temperature and a throughput of 20 cm^3 tritiated water per day [16]. Their function is to convert tritiated water into high purity tritium and its isotopes and they have already processed tritiated water with concentrations of 30 PBq/dm^3.

The four stages in this prototype industrial electrolysis process are the generation of tritium by electrolysis of tritiated water, adsorption of tritium on the palladium-silver alloy cathodic membrane, diffusion of the triton in Pd-Ag and desorption of tritium on the other side of the palladium cathode wall. In addition, a particular effort was made with respect to the nature of the components used: critical studies of materials, to avoid corrosion of steels and embrittlement of Pd-Ag (Fig. 3.9), of the safety of the installation operations and of protection of the environment.

The industrial prototype includes (Fig. 3.10):

- tritiated water circuit:

  This includes the thermostatted electrolyzer using a Pd-25%Ag thimble cathode and operating at temperatures between 80 and 140°C. The conditions in this system can induce embrittlement of the palladium-silver. The thickness, the composition of the cathodic membrane and the temperature are three important parameters for obtaining a good yield of tritium diffusion. In addition, for good diffusion of tritium in the palladium alloy, the metal lattice should not have any electron holes or dislocations as is the case

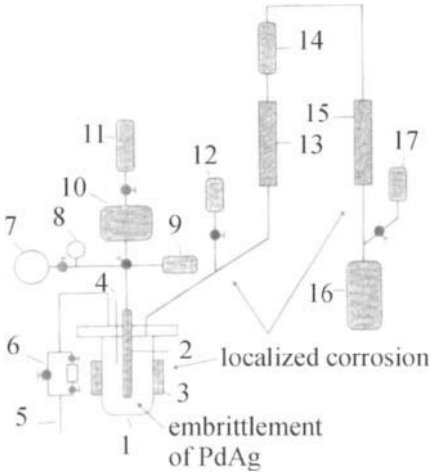

Figure 3.10. Schematic of electrolysis process for tritiated water reprocessing, 1: electrolysis cell, 2: Pd-Ag cathode, 3: heater, 4: tritiated water level controller, 5: argon input, 6: flow regulator valve, 7: vacuum pump, 8: manometer, 9: mass spectrometer, 10: storage tank, 11: palladium black trap, 12: tritiated water tank, 13: condenser, 14: oxidation catalyst, 15: condenser, 16: molecular sieve, 17: gas sampling.

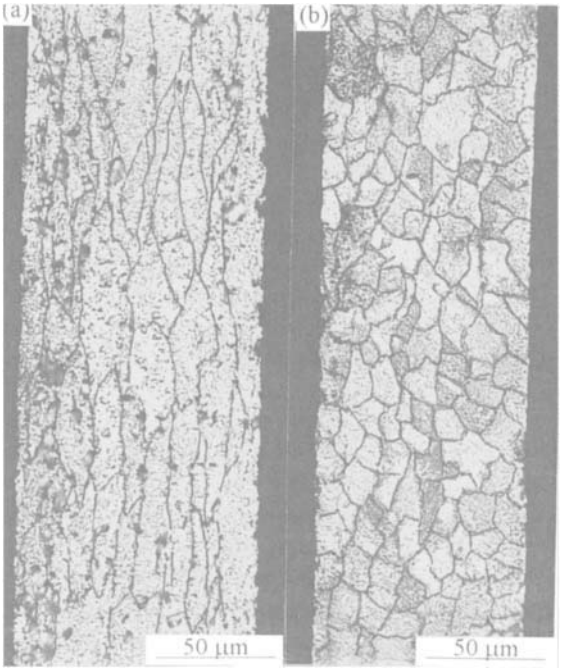

Figure 3.11. Metallography showing the Pd-Ag microstructure before (a) and after (b) annealing (magnitude of 500).

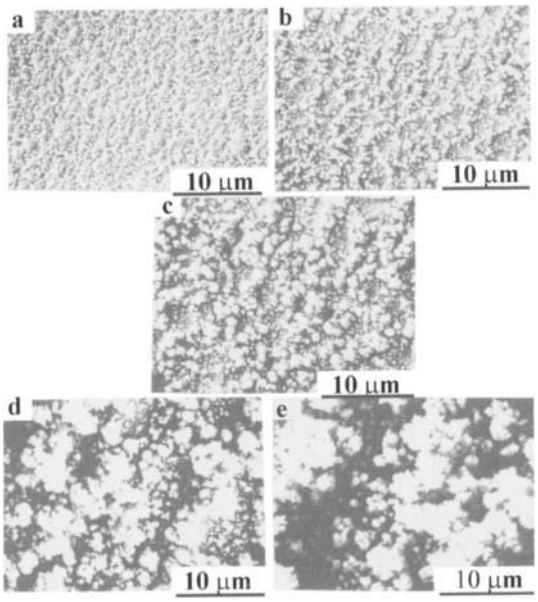

Figure 3.12. Photographs of palladium black deposit on the Pd-Ag membrane entry face, grain size depends on time in reduction of the Pd^{2+} ions, a: 30 s, b: 1 min, c: 2 min, d: 5 min, e: 7'min, optimum is 7 µm (magnitude of 2000).

with membranes received after manufacturing rolling. To limit the diffusion variations, the membranes can be restored by appropriate annealing at 450°C for 30 min (Fig. 3.11). Moreover, diffusion can be enhanced in increasing the number of active centers, which is achieved by covering the entry surface with a thin palladium black deposit. In the case of non-limited diffusion of tritium, this film improves the diffusion yield (Fig. 3.12).

– auxiliary facility for elimination of anodic gases formed in the electrolysis cell:

An upstream condenser on the effluent anodic gas rejection circuit has the function of condensing the tritiated water vapor. As the electrolyzer has a diffusion yield of around 80%, part of the tritium produced at the cathode is mixed in the anodic gas circuit with oxygen. The risks of forming an explosive gas mixture are avoided by sweeping the cell with argon. The anodic gas effluents then pass over an oxidizing precious metal catalyst whose function is to oxidize the tritium that did not diffuse. This reactor is designed to have a yield close to 100%. The operating temperature of the palladium catalyst is naturally maintained by the heat of the tritium oxidation reaction. A downstream condenser condenses the tritiated steam produced by the precious metal-alumina catalyst. The tritiated steam condensed in the second condenser and recovered liquid are reinjected in the electrolyzer. A molecular sieve is placed at the end of the anodic gas rejection line for protecting the installation. All the lines of the anodic gas circuit and the liquid wastes circuit can be connected to a partial vacuum for decontamination. A practical use of the oxygen pump was proposed to separate the non-diffused tritium from oxygen formed

in the anodic compartment. The principle of the oxygen pump is based on the use of the stabilized zirconia membrane, an ionic conductor for O^{2-} at high temperatures. In this case, oxygen is adsorbed, ionized and diffused in the zirconia membrane at a high temperature (1000°C) leading to its impoverishment in the anodic compartment, thus facilitating the treatment of a low grade of tritium gas and decontamination of anodic gases.

- facility for recovery of tritium after diffusion in the cathode:

  A pumping installation makes it possible to obtain the vacuum in the cathodic gas circuit and to trap tritium as tritide on palladium black or to store it in containers. These are fitted with in-line isotope analysis instrumentation for determining concentrations before pumping pure tritiated gases to the isotopic separation process. The electrolyzer module has been tested to compress tritium over a factor of 20 for stocking.

2.2. *Detritiation in bulk metal wastes*

Metal (mainly steels) components from a tritium facility must be detritiated before any type of disposal. The thermal melting process under low pressures with argon sweeping is designed to minimize the activity range of these wastes [17]. Induction heating is preferable because it minimizes the following: heating of the metal framework, thus reducing permeation losses; the amount of tritium remaining in the processing furnace and embrittlement of refractory stainless steel equipment. This method reaches a tritium reduction of 10^5 after detritiation, and has a number of advantages:

- fast detritiation, favored by melt vacuum degassing,
- volume reduction of waste.

Suitable solvent metals should have the following criteria:

- high solubility of the waste metal,
- low melting point (e.g. eutectic mixtures).

The melting process produces decontaminated metal ingots which may be handled without the need for any special precautions in the 'cold' storage. The tritium recovered during this operation is conveyed by collectors to the gas detritiation units and by the processing plant vacuum system. The tritiated gases are transferred by pumping to the palladium-silver thimble diffuser for eliminating the various gas impurities.

2.3. *Detritiation of organic waste*

The reprocessing of tritiated gases, liquids and solids produces large amounts of tritiated organic wastes (gloves, vinyl, polymers, cellulose compounds and oils, etc.). Most wastes will be only very slightly contaminated with tritium, but due to their high tritium-absorbing capability, a small proportion, mostly elastomer seals and oils, may be highly tritiated (~TBq per ton). With high tritium or tritiated water concentrations, organic compounds

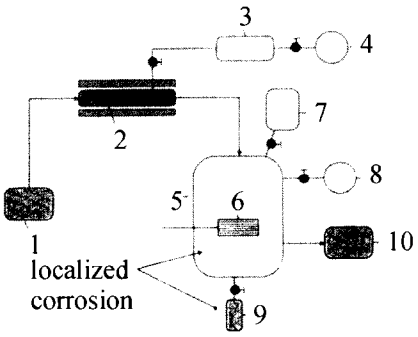

Figure 3.13. Schematic of organic waste reprocessing process, 1: shredding machine, 2: oven for pre-decontamination, 3: condenser, 4: pump, 5: reprocessing oven, 6: heating, 7: light water steam-generating unit, 8: vacuum pump, 9: tritiated steam condenser, 10: detritiated waste compaction.

are decomposed or polymerized as soft wastes by radiolysis with the release of basically tritiated hydrocarbon waste and Cl_2, F_2 and CO_2 that induce corrosion.

With a view to reprocessing the organic products originating in the tritium facilities, an industrial unit was developed (Fig. 3.13) and constructed for specific treatment and packaging of such products so they were not considered as final waste [18]. Decontamination is based on a drying process using steam, which results in a decontamination factor of 80%. Furthermore, the volume of the products to be stored is reduced by a factor of 8 by waste compaction. This industrial unit also cuts down the degassing rates of the stored wastes, which allows placing them in 'cold' sites, thus significantly reducing costs and providing an economic advantage to the management of tritiated wastes.

This is done by direct water extraction with a low vacuum-obtained partial pressure and a specific steam-drying technique. It provides the recovery of small amounts of tritiated water at high concentrations and has the advantage of short processing times.

The reprocessing unit consists of:

- shredding machine,
- oven for pre-detritiation,
- reprocessing oven,
- water steam-generating unit,
- compacting press,
- pumping unit and steam condenser.

After condensation, the acid tritiated water is collected in a neutralization vat for pH adjustment; it is then transferred to a dedicated tank (Fig. 3.14) from which it is sent by heating to the tritiated water reprocessing units, with corrosion problems identical to the above. The recovered detritiated wastes are removed from the reprocessing line and sent to a 'cold' site.

Figure 3.14. Tank for stocking tritiated water.

3. Air detritiation

The tritium plant handles significant quantities of tritiated air and gaseous impurities that generally come from process modifications, equipment maintenance and waste processing in glove boxes. Also, the impure and tritiated air from the gas clean up exhaust system is evacuated into the first containment where tritium circulates. The best available technology (Fig. 3.15) to eliminate undesirable tritium is to convert it to tritiated vapor by oxidation on precious metal-alumina catalysts, followed by tritiated vapor adsorption on a molecular sieve bed throughout a detritiation closed-loop operating in a 'permanent' mode as shown by Bourdon et al. [19] and Chabot et al. [20].

This system provides detritiation of flows up to 300 m^3/h. This process may be accelerated by the tendency of gaseous tritium to be converted to tritiated water vapor by self-radiolysis and isotopic exchange. For this, the tritiated gas entering the detritiation system can flow through the following components:

- a cooler for control of maximum humidity reducing the gas temperature to about 5°C and condensing excess tritiated moisture.
- a first recombiner for the oxidation of tritium at 150°C on a Pd-Rh precious metals/Al_2O_3 catalyst bed and preventing ignition and permeation of tritium in steel at subsequent gas temperatures of 500°C. Getter alloys and Pd-Pt catalysts are also very efficient for decontaminating gases by tritium trapping and conversion into tritiated water.

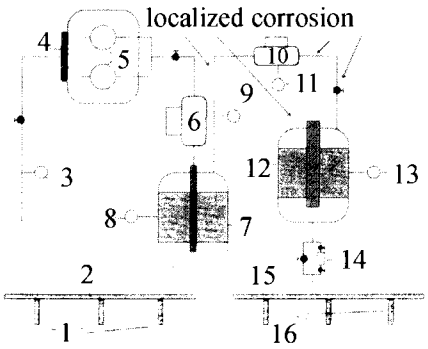

Figure 3.15. Detritiation module for the glove boxes air operating in a closed loop, 1: towards the glove boxes, 2: glove boxes air collector, 3: manometer, 4: filters, 5: turbines, 6: heater, 7: catalytic reactor, 8: thermometer, 9: manometer, 10: cooler, 11: thermometer, 12: drier, 13: hygrometer, 14: pressure regulator valve, 15: glove boxes air collector, 16: return to glove box.

- molecular-sieve beds of alumina grains to trap the tritiated vapor. Absorption on molecular sieves at very low water vapor pressure and room temperature is a widely used method but requires sieve regeneration by heating.
- a second recombiner of, for example, CuO, to oxidize the remaining tritium at 500°C. The global oxidation factor is approximately 10^6.
- a cooler for control of minimum tritiated humidity. This unit decreases gas humidity to a dew point of −20°C to maintain the total detritiation factor about 10^6. Moreover, cold trapping of tritiated water instead of second absorption on the molecular-sieve bed unit would decrease the amount of tritiated solid wastes and facilitate the tritiated water recovery.
- a sweeping and heating unit to displace H^3HO isotopically from molecular sieves. One of the sweeping techniques consists in displacing H^3HO from molecular sieves with recycled H_2O vapor. This technique, operating at 300°C is the most successful on an industrial scale and, in comparison with others, avoids frequent drying of the molecular sieve by high heating with neutral gas sweeping. Water vapor sweeping reduces the concentration of tritium in the residual tritiated water by a factor of 200. Sweeping can be repeated several times at the end of the cooling cycle to form a tritium-free saturated section and in this case there is a further fifty-fold increase in the detritiation factor.

In the presence of gaseous impurities, the results show that precious metal or nickel catalyst beds provide satisfactory efficiency for hydrocarbons, and that for ammonia, a nickel oxide catalyst on alumina is the most efficient.

Moreover, during operation of the ^2H-^3H fuelled fusion reactor, the tritium gas atmosphere contains radioactive ^{16}N, ^{13}N and ^{41}Ar. Thus to optimize detritiation with these gaseous active species present the tritium gas and tritiated water vapor concentrations must be known. ^{16}N, ^{13}N and ^4Ar will interfere in monitoring tritium and tritiated vapor measurements by an ionization chamber. Flow-through ionization chambers cannot differen-

tiate between the various radioactive gases. A three-compartment ionization chamber is useful for solving this problem as shown by Jalbert [21]. The first two compartments are separated by a Nafion® polymer membrane that has the property of retaining water in any form and of being permeable only to gases. The tritiated vapor is trapped as water in the clusters of the membrane in order to be recovered by degassing and analyzed by in-line liquid scintillation spectroscopy. The second and third compartments are separated by a thin wall opaque to tritium β^-. With this arrangement, the total gas activity is measured in the second compartment and in the third the ^{16}N, ^{13}N and ^{41}Ar activities are determined. The ^{3}H and $^{3}H_2O$ activities are obtained by difference.

In the gas circulation in the detritiation system, the flow through the recombiner and the dryer units is kept practically constant facilitating temperature control [22] and [23]. As any contamination of the tritiated gas feed is generally small, the flow in the dryer and recombiner units are recirculated internally by a 100-hour cycle to increase the detritiation rate. Long cycles meet the requirements maintaining the detritiation system in a ready-to-start state and the low contamination in the first containment. Auto-rotation of dryers and coolers is a high priority requirement for long-term operations. It assists in regenerating dryers consistently at programmed conditions to increase the absorption capacity. This unit leads to the multiplication of the amount of water formed in the detritiation system. To limit all this production of concentrated or slightly tritiated water, the size of the glove boxes is a fundamental factor. The disadvantage of detritiation by oxidation into tritiated water is that at high temperatures radiolysis phenomena with air are greater thus leading to nitric acid formation at a pH of around 3–4. This tritiated and acid medium induces corrosion of stainless steel in the installations.

4. Material for the first containment

The materials for the first containment of tritium must be chosen very carefully. The important parameters influencing the choice include tritium solubility, permeability, bakeability, strength, corrosion behavior, stress fatigue and tritium and helium embrittlement. The most commonly used material is stainless steel 316L for the tritium gas. AISI 310 type stainless steel has the advantage of lower tritium permeability at high temperature in comparison with other stainless steels. These stainless steels are not compatible for tritiated water, and the choice was oriented towards the super stainless steels or alloys. These stainless steels appear in the corresponding quality assurance document. Also, stringent quality assurance measures should be taken during and after equipment construction. The treatment of the inner surfaces of the first containment as well as cleanliness are very important for maintaining the tritium gas purity. It is well known that tritium is able to react with organic impurities and that tritiated methane and carbon dioxide are produced. These measures should also include analyzing helium-leak and pressure tests and radiography of all welds. Parts in the process have to be exchanged after a certain operating time by demountable tubing couplings. Organic polymer seals for connecting flanges and valves must be avoided because they degrade under radiation in the presence of concentrated tritium gas or tritiated

water. Helicoflex type (trademark) seals are well suited to these couplings. The resulting joint meets two opposing requirements. These are its plasticity which makes it possible it to be deformed and to fill all the spaces liable to allow the fluid to be sealed to pass and its elasticity which ensures durable compressive strength. In a Helicoflex® joint seal, that consists only of stainless steel, plasticity and elasticity are ensured by three metal components: two internal and external envelopes of stainless steel and a helical spiral spring sandwiched between these two envelopes. In tightening the joint, the spring is compressed and generates, due to its elasticity, a reaction opposing the compressive force. The external envelope which is more ductile than the materials surrounding it is then crushed against the plane made up by the hardened surface of the flange and thus ensures an excellent seal. The internal envelope avoids the direct compression of the external envelope by the spring spirals that would be deformed and no longer provide perfect tightness. Ultra-high vacuum and ultra-high purity are obtained using Helicoflex® seal (Cefilac Inc.) for tritium applications such as heat and cold exchangers, piping and so forth.

Part II

NUCLEAR CORROSION AND METALLURGICAL ASPECTS

This Page Intentionally Left Blank

Chapter 4

STRATEGY FOR CONTROLLING CORROSION

First of all, the following question can be asked: why carry out corrosion tests?

Before answering this question, we must recognize that there are very few laboratories in the world that use highly concentrated tritium and tritiated water. Our laboratory is the only one in France. It is not a question of tritiated water traces present in light water, but the reverse. We do not work with light water as is the case in PWR or other nuclear reactors. No steel or super stainless alloy has been previously tested in this highly concentrated tritiated aqueous medium by anyone in France. By its nature, this medium is very reactive and its properties are completely different from the light water in nuclear power stations, which although it can be activated, contains much lower concentrations of radiolytic hydrogen peroxide, among other species, than in our closed storage units. In addition, we are not confronted with microbial corrosion as in the secondary circuits of PWR power stations. No living species could withstand the tritiated water concentrations we have. The behaviors and the types of corrosion of stainless steels or superalloys are thus completely different in our installations and no comparison is possible. After this digression, in answering the question, our corrosion tests, which are specific to tritium, must make it possible:

- to study the initiation and evolution of corrosion phenomena in the presence of tritium, concentrated tritiated water and radiolytic species,
- to select materials best adapted to the envisaged use in concentrated tritiated media,
- to know and understand their behavior in the various tritiated media,
- to monitor their corrosion resistance in a well-specified tritiated medium.

Finally, to reach the overall goal, the operator of a tritium gas and tritiated water nuclear processing installation, must, to ensure its correct operation and safety, apply a material and equipment maintenance and monitoring policy as well as an on-going survey of new materials for replacing corroded components. If he does not apply this policy and is satisfied with a simple monitored storage system, his installation will soon become obsolete with respect to those of other potential competitors in the tritium market for nuclear fusion. To avoid this, he must implement resources for monitoring and follow-up of the most highly stressed and defective components as well as for specialized examinations that can be directly applied to his installations. Various inspection methods have been extensively used to meet these requirements. These make possible: (1) analysis of tritiated water and tritium for its radiolytic species and impurities. This knowledge makes it possible to determine

their involvement in corrosion, (2) identification of defects on the passivating oxide layers after aging, (3) observation by televisual examination from the interior of the component located in situ in the nuclear installation. These tests are carried out over a long period (several months) and are followed by visual observation. They are not easily exploitable since the samples are either too corroded or the visual observation is not sufficiently detailed.

Monitoring and examinations also meet the need for qualifying new materials for use in future installations. Consequently, in parallel, essential in-depth studies have been carried out that precede the monitoring of new tritium technologies. These concern laboratory examinations of new super-alloys or stainless steels that have not yet been used in the process like super-austenitic and Duplex stainless steels and nickel, cobalt-base super-alloys, hardened or ductile stainless steels or the exotic alloys of zirconium or titanium. Also, besides the traditional and easy methods for following corrosion evolution whose use has developed with industrial requirements, highly specialized examination and study methods have been implemented. These are laboratory techniques adapted at the tritium gas and tritiated water nuclear processing site. It can be seen then that corrosion monitoring and control in a tritiated water facility involves a wide range of techniques.

Here, we propose to describe the techniques currently used. Their application field is discussed in the following chapters with specific examples taken from the examination of tritiated equipment and materials. Although these techniques are used for the follow-up and study of corrosion phenomena in a nuclear environment, the chosen examples correspond to a wide range of material damages. To apply this policy we have carried out examinations of new super-steel or stainless steel alloys in order to determine corrosion mechanisms, types of corrosion and properties of the passivating layers for different tritiated media.

1. Composition of the tritiated products

First of all, for a good understanding of corrosion phenomena, we need to know what there is in the tritiated water, i.e. its composition. Analysis of various tritiated water samples include determination of the tritium content and identification of the impurities and the radiolytic species and their respective concentrations. The tritium in highly concentrated water is determined by calorimetric measurements. Energy release is very important and a blue luminescence caused by free radical reactions can be seen in Fig. 1. If the tritiated water radioactivity is very high, the temperature is much higher than the ambient due to the β^- particle energy, and visible radiolytic gas bubbles quickly form in tritiated water. The radiolytic gases dissolved in and above tritiated water (Table 2) were analyzed by mass spectrometry. Moreover, organic compounds in contact with tritiated water are decomposed and carbonized (Fig. 4.1).

The detailed physicochemical analysis carried out by electrochemical methods and Atomic Absorption Spectroscopy showed the presence of the following ions Cl^-, F^-, CO_2^{2-}, NO_2^-, NO_3^-, $^3H^-$, O^3H^-, with considerable concentrations of metal ions coming from the corrosion of the stainless steels (Table 3). Their presence results from the process itself and from possible accident configurations. These species are responsible for

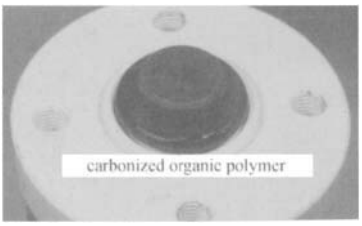

Figure 4.1. Organic compounds carbonized by the release energy.

dramatic effects including corrosion of such equipment as process piping, electrolyzers, catalytic exchange columns, tanks and valves. It is then necessary to determine their respective corrosion effects and to study these under various conditions to evaluate the risks and process reliability and also to make the best choices for materials and technology.

2. Televisual examinations

The first implemented in situ examination is visual observation and is carried out in the majority of the cases by endoscopy (Fig. 4.2). In many cases, where the examinations must be carried out from the interior of the defective part, with risks of contamination, endoscopy allows inspecting hard-to-access sites which otherwise could be observed only following disassembling, thus involving labor costs and expensive down times. These resources are moreover adapted to the interventions in hostile environments and their use in our installations has risen over the years. They originated in the requirements of inspections linked to installation safety. In this, the development of flexible optical fibers to obtain greater miniaturization and performance have brought about the rapid development of high-resolution videoscopy.

It was thus necessary to develop, in particular, equipment for the televisual inspection of the internal surface of the tubes or other components for circulating tritiated water, tritiated steam and tritiated gas and especially in areas where specific zones are more subjected to corrosion. Televisual examination using a micro-camera is thus currently used to characterize these zones in the inside surfaces of the equipment. This examination can be done in a short intervention and requires only the introduction of the fiberscope. It is programmed during a production shutdown and its cost is thus relatively low. The speed and the resolution of the examinations make it possible to avoid extracting tube samples for laboratory tests and it is not necessary to make longitudinal and radial cuts (Fig. 4.3) that destroy the part to be examined.

The implemented equipment includes optical fibers giving access to the zone to be examined. They provide lighting, collect the images and transmit them to the operator and can be used from an indirect access to the internal surface of the examined component. Due to its flexibility, possibility of indirect access and orientation by translating its end unit the fiberscope in this case provides access to a broad field of visual investigations. The beam includes optical fibers having a length of up to 30 meters. The fiberscopes can be oriented

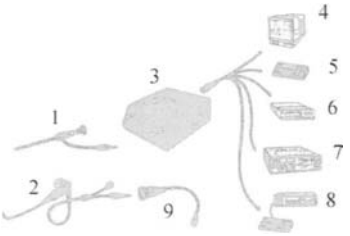

Figure 4.2. Televisual examinations equipment, 1: endoscope, 2: videofiberscope, 3: video light source, 4: monitor, 5: keyboard, 6: video tape recorder, 7: high resolution color printer, 8: computer, 9: optical fibers.

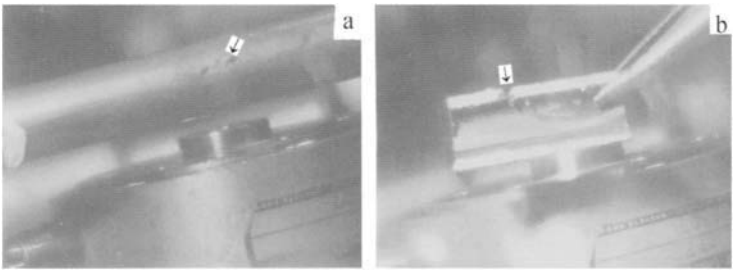

Figure 4.3. Examination of a stainless steel tube showing the presence of corrosion leading to tube perforation (arrow), a: outside view, b: inside view.

in various ways and directions that must be adapted to the specific local configurations. Enlargement of the surface to be examined is not their prime objective. Their main qualities are the extent of the field that can be examined and the viewing angle.

The implemented tools include a very small eyepiece, for hostile environments, that can receive the micro-camera. In practice, examination of the surfaces is carried out with enlargements between 10 and 800. This apparatus allows the examination of small-size irregularities that cannot be studied by standard endoscopes. This micro-camera makes it possible to visualize structural defects $\geqslant 3$ μm. The principal characteristics of these instruments are: 30°–80° field angle, rotary radial head, 5 mm $\rightarrow$ infinity depth of field, minimum inside diameter of tubes that can be examined of 6 mm and 3 lux lighting minimum.

A number of examples of examinations of components in tritium processing installations made using this instrumentation can be selected (chapter 25). These include both unaffected components and those subjected to damage. This damage can cause rupture of the tritium containment in the installations if it is not detected in time (Fig. 4.3). Finally, specific anomalies such as roughness and scratches (Fig. 4.4) can be observed on the inside of tube walls. Scales can be responsible for excessive thickness of oxide (Fig. 4.5). These can be the source of localized corrosion.

It is also noted that this inspection made possible specifying the appearance of the inside wall surface at the connections in welded piping (Fig. 4.6). In this figure, there is

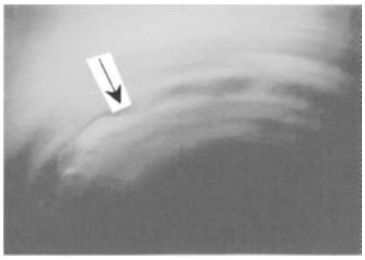

Figure 4.4. Roughness and scratches on the internal wall of a stainless steel tube (arrow).

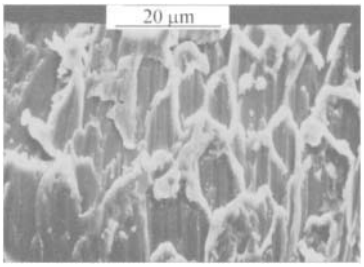

Figure 4.5. Over-oxidized scales (in white).

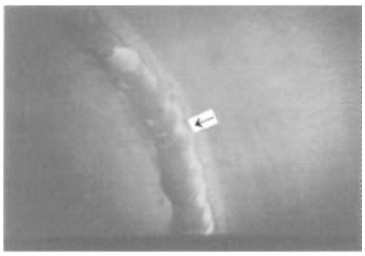

Figure 4.6. Inside wall of a stainless steel tube after welding (arrow).

complete penetration of the weld bead, and the bead material is sound. Finally, the televisual examinations of stainless steel make it possible, in particular, to visualize pitting after enlargement (Fig. 4.7).

3. Laboratory examinations of super-alloys

In tritium decay, electrons with a maximum energy of 18.6 keV per atom are released, making it possible to have sufficient energy deposition and to induce radiolysis phenomena in the oxide being formed and in tritiated water. Radiolysis of the oxide, i.e. damage of an

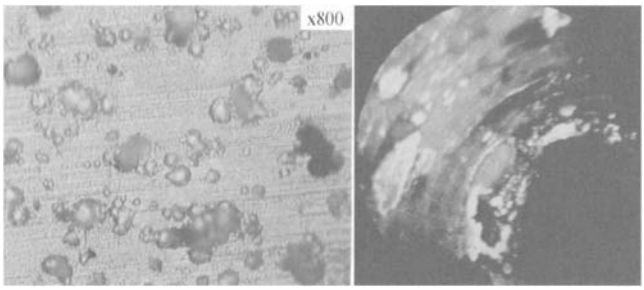

Figure 4.7. Microscopy showing pitting inside of a stainless steel tube.

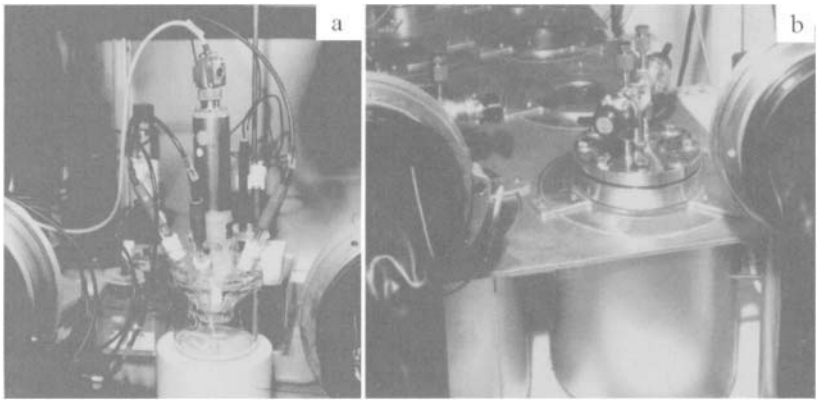

Figure 4.8. Electrochemical cell (a) and corrosion reactor (b) for corrosion tests in glove boxes.

ionic lattice by β^- radiation results in an increase in defects (free electrons, anion holes and vacancies). This increase has a direct impact on the oxidation kinetics if the limiting step in the oxidation process involves the mobility of the O^{2-} vacancies or electrons. In addition, water radiolysis induces the formation of unstable radical or molecular species such as $O^3H^\bullet$, $^3H^\bullet$, $^3H_2O_2$, likely to modify the oxidizing character of this medium and thus able to influence the oxidation kinetics of steels or stainless steel alloys. To quantify these potential influences of radiolysis on oxides and the oxidation process, we developed an electrochemical cell for highly concentrated tritiated water (Fig. 4.8).

This is situated in a detritiated glove box (Fig. 4.9) in order to ensure the protection of the equipment, personnel and the environment from tritium contamination. The samples of super-alloys tested can then be examined by microscopy and by Energy Dispersive X-ray analysis. Analysis showed many modifications in the metal element compositions at various oxide depths before and after tritiated water corrosion. It can be deduced that the inner oxide is enriched in a selective alloying element. In addition, the X-ray Diffraction analysis made it possible to identify martensite on the surface embedded in austenite (Fig. 4.10).

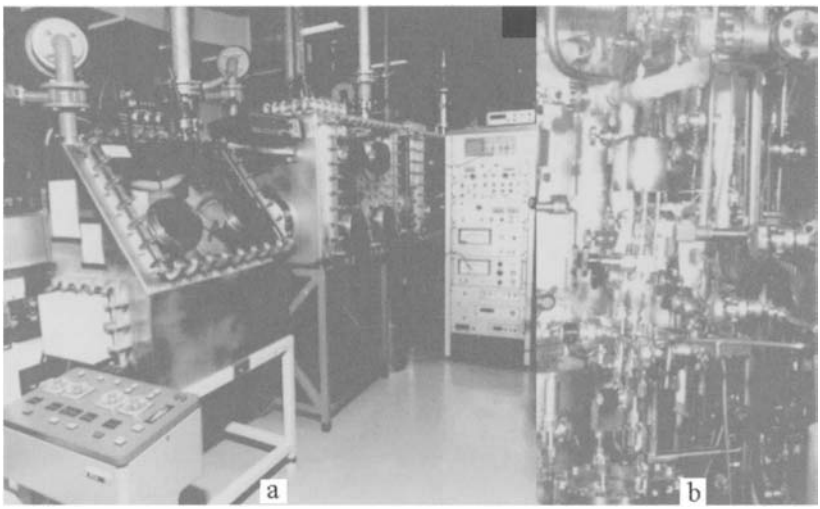

Figure 4.9. Assembly of glove boxes for corrosion tests, tritiated water analysis (a) and dynamic tests by flow loop (b).

This martensite can be formed by the presence of tritium gas, as is often found with hydrogen, and it can be responsible for embrittlement of steels. It should be noted that annealed or welded alloys show depletion of martensite. This depletion depends on welding type and has a beneficial effect (Fig. 4.11). The X-ray Photoelectron Spectroscopy analysis provided a semi-quantitative identification of the atoms in the tritiated oxide layer (Fig. 4.12). This analysis indicates that the alloying element concentrations dropped considerably for alloys in tritiated media whereas for another element, concentration increased.

Our corrosion studies are now in a stage beyond a technological survey. On the basis of this work, we can say that materials selection is a difficult and complex but essential process. In fact, from industrial experience in this field it can be seen that many problems are caused by an inappropriate choice of materials, often leading to corrosion-related failures. The initial selection criteria are, obviously, qualitative. A good material is that which gives satisfaction to its user, or by default to those responsible for the technical and financial choices. These are made after discussions with the suppliers who can provide various types of steel or stainless steel alloys with specifications meeting our equipment dimensions (all-metal valves, stainless steel seals and piping, stainless steel storage units, etc.). This shows the usefulness of the scientific analysis in the presence of tritium or tritiated water in the relevant industrial context.

For more details, the selection criteria for materials also extend to the tritiated corrosive media with their respective impurities. Consequently, for a given material, the initial study concerns a precise definition of the 'material' parameters for an assembly of tritiated corrosive media with varying compositions and concentrations. Subsequently, for a well-defined and stable corrosive tritiated medium, the study involves classification criteria for candi-

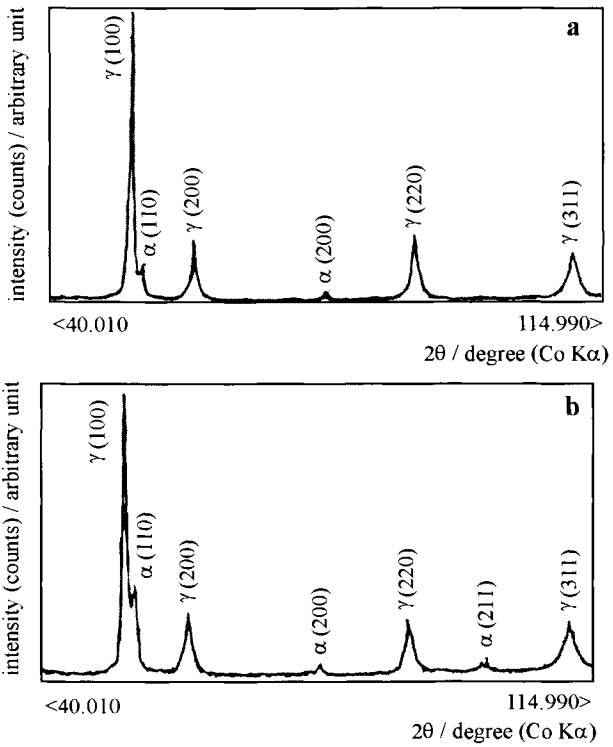

Figure 4.10. Examinations by XRD showing martensite formed in the presence of tritium for fully type 316L stainless steel, a: obtained in the absence of $^3H_2$, b: obtained in the presence of $^3H_2$.

date materials for a single specified medium. Material selection therefore depends on the total validity of an experimental design that is well defined after completion of the study for ascertaining the composition of the tritiated medium. For this, it is also necessary to apply this experimental design over all the study and to evaluate the favorable and unfavorable results. The strength of the method is then based on the accuracy of the evaluation of these results. Conversely, the weakness of the method is that it does not give any indication for the selection nor determine the problems correctly.

Generally, the choice of materials is always expressed in multidimensional spaces. There are at least 9 factors for the corrosive medium (radiolytic ^3H_2O, Cl^-, F^-, CO_3^{2-}, $^3H_2O_2$, NO_3^-, pH, temperature, radiolysis pressure), 5 others for the metal (composition, microstructure, heat treatment, hardness, stresses) and 4 final factors for the risk of corrosion (uniform corrosion, pitting, crevice corrosion, tritium embrittlement), i.e. a total of at least 18 factors. Each of the 200 possible combinations including only one corrosion mechanism and only one metal and medium parameter can provide a selection criterion. In addition, the number goes up to 400 with two medium parameters and one metal parameter, etc. These considerations immediately lead to the following conclusion. Due to

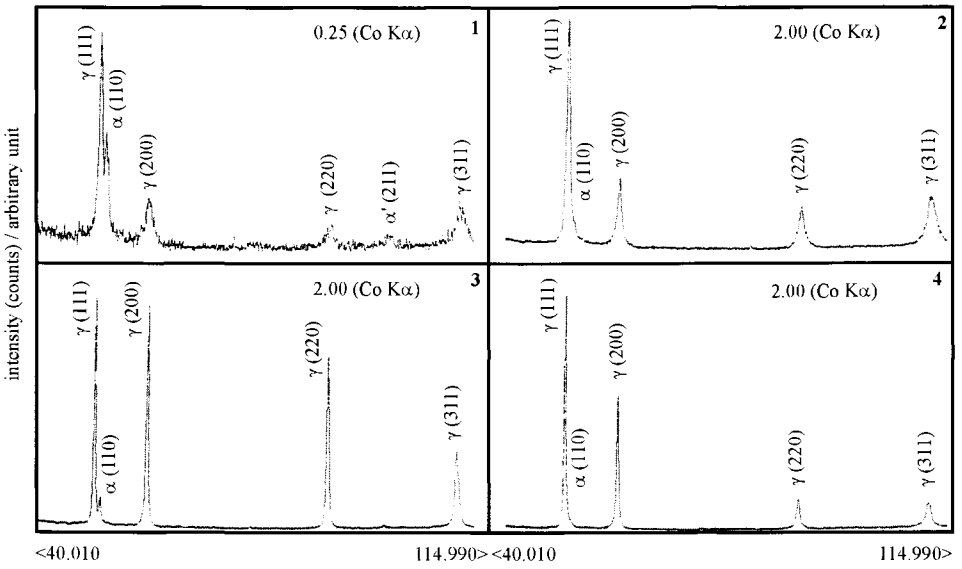

Figure 4.11. Examinations by XRD showing depletion of martensite for welded 316L stainless steel, 1: base 316L stainless steel, 2: weld obtained by laser beam, 3: weld obtained with metal solder, 4: weld obtained without metal solder.

the exponential explosion, the experimental design must be very precisely defined and successive interpretations of the results checked to avoid duplications in the study. If, nevertheless, there are still duplications, the cost of a laboratory study is generally very much less than the costs of in-service corrosion. The laboratory study is thus an extremely profitable investment, provided that the parameters are well-limited and combined. Trying to make savings in the cost of such a selection study would be a false economy. The material selection policy is at the core of corrosion prevention and preventing corrosion is at the core of the process engineering operation and construction of new processing systems. The correct choice of materials is thus a vital requirement for tritiated water reprocessing installations and selecting the final alloy is the responsibility of the operators, after consultation with the laboratory head. But it must be stated that in practice it is necessary to take other factors into account: commercial availability, economic aspects, component construction feasibility, etc. These factors can then contradict an initially judicious choice.

To carry out this study in a hot laboratory we have essentially made use of the electrochemical and surface analysis techniques. The diagrams and photographs made it possible to do the following to examine pitting currents, to interpret the mechanisms in passivation or corrosion, to show corrosion by pitting and/or at the grain boundaries and tritium embrittlement, tritium insertion in the oxide and the formation of micro-cells in the corrosion process. Each of these diagrams or photographs corresponds to a real case in tritiated water media. Results clearly show the advantage in this research on corrosion phenomena in the various processes for treating tritiated products. These analyses have many advantages.

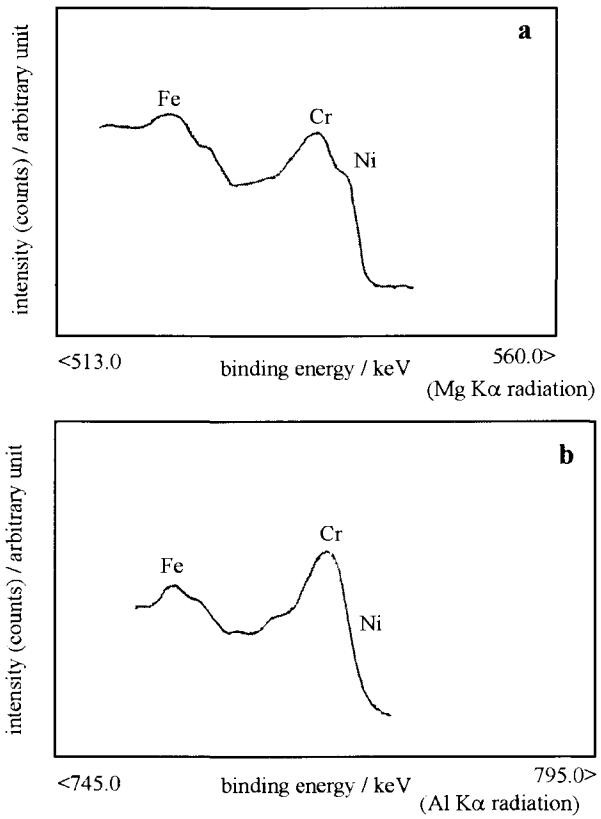

Figure 4.12. Examinations by XPS electron spectroscopy for chemical analysis indicating a depletion in iron and nickel and chromium enrichment in the presence of tritiated water, a: obtained in the absence of ^3H_2O, b: obtained in the presence of ^3H_2O.

They provide information in real time on parallel corrosion systems. From this information it is often possible to distinguish the various corrosion processes, unlike that from complementary physicochemical analysis techniques. The obtained corrosion parameters can be then used to provide the head of the nuclear tritium installation with the required information for improving safety and productivity.

4. Qualitative in situ tests

These tests are required to ascertain the natural corrosion conditions in the presence of the corrosive species generated from tritiated aqueous mixtures in the process. These also must be carried out with the addition of representative impurities that dramatically increase the corrosion phenomena, such as radiolytic redox species and chloride, etc. In these tests, the

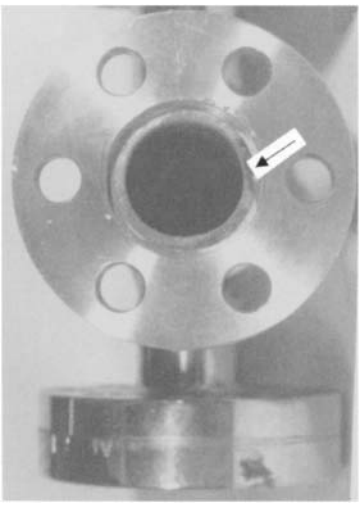

Figure 4.13. Photographs of the corrosion points in tritium installations observed during maintenance or in dismantling. Plate 1: flange elements on which corrosion by recess effect was observed (arrow).

steel samples are placed in holders and the latter are put in a closed container in which the corrosion conditions are obtained by the addition of various successive media corresponding to real process cases. After periodic visual examinations, the samples undergo thorough optical examinations for identifying the surface appearance and for assessing corrosion levels. These long duration qualitative tests make it possible to ascertain the lifetime of an equipment component.

5. Examples of corroded samples

A priori, all the precautions were taken in the various tritium processing installations. This was done from the very start, i.e. the surface quality of the selected material (polishing and passivation) before assembly in the process. Nevertheless, the damaging action of tritiated water and tritium on the corrosion resistance of the stainless steels is a very real problem as observed in maintenance operations or dismantling of the tritium processing circuit. During these interventions, we frequently noted appreciable attacks on the piping and tanks in contact with tritiated water. As these attacks lead to severe damage of the metal parts used for tritium containment, it was essential to have thorough examinations of these.

Plates 1–5 (Figs 4.13–4.18) illustrate corrosion examples in tritiated media taken from the most significant cases observed for various equipment components during processing and dismantling:

- plate 1: flange elements with its all stainless steel joint showing recess corrosion on these two parts (crevice corrosion). In this specific case, this localized corrosion could have

Figure 4.14. Photographs of the corrosion points in tritium installations observed during maintenance or in dismantling. Plate 1: joint elements on which corrosion by recess effect was observed (arrows).

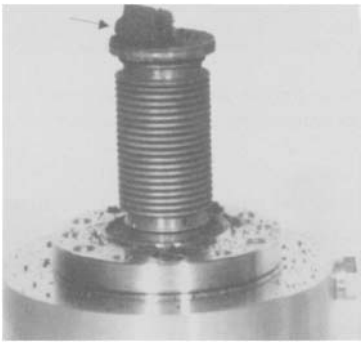

Figure 4.15. Photographs of the corrosion points in tritium installations observed during maintenance or in dismantling. Plate 2: valve metal bellows elements perforated by recess corrosion and corrosive deposits formed during gas and aqueous turbulences (arrow).

Figure 4.16. Photographs of the corrosion points in tritium installations observed during maintenance or in dismantling. Plate 3: galvanic corrosion for the copper seal and stainless steel valve assembly.

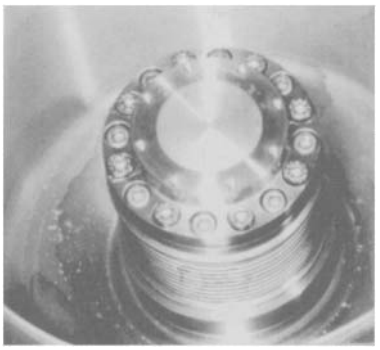

Figure 4.17. Photographs of the corrosion points in tritium installations observed during maintenance or in dismantling. Plate 4: formation of oxide deposits and corrosive substances in the body of a turbomolecular pump that induced pitting corrosion.

Figure 4.18. Photographs of the corrosion points in tritium installations observed during maintenance or in dismantling. Plate 5: pitting corrosion along the heat-affected zone/fusion boundary of the weld (arrow).

been induced by the stagnate tritiated water containing impurities between the flange and its stainless steel joint (Figs 4.13 and 4.14),

- plate 2: all stainless steel valve component showing its metal bellows corroded with perforations. The steel or stainless steel parts or moving parts undergo treatments for giving a combination of properties, i.e. ultra-high strength, toughness or ductility and outstanding corrosion resistance. In spite of its high anti-corrosive characteristics, this super-alloy was corroded by tritiated water and gas to the extent that these could cross this first protection barrier for the processing circuit. This type of corrosion can be explained in various ways: (1) recess effect, (2) deposition of corrosive substances in the bellows cavities assisted by turbulence in the valve body, (3) micro-cells in these due to the use of several 'stainless' alloys in the valve elements, (4) low thickness of the bellows (a few hundreds of μm), therefore a shorter lifetime for this equipment (Fig. 4.15),

- plate 3: galvanic corrosion between a copper gasket and the stainless steel valve body. The presence of green corrosion products indicates that the copper gasket was anodic and attacked by the tritiated medium. We deduce that it was not really a good choice to use this metal for a joint (Fig. 4.16),
- plate 4: stainless steel internal body of the turbomolecular pump body showing oxide deposited by turbulences during suction. Whether they are at points or as a film these deposits are particularly dangerous, for they act as halide traps. They are also hazardous due to the fact that they allow local acidification (pH~3), thus facilitating corrosion by pitting of the internal parts of the pumps (Fig. 4.17),
- plate 5: storage container weld. The photograph shows appreciable corrosion, particularly along the heat-affected zone/fusion boundary of the weld. Welds are an important corrosion attack point due to the electrochemical interaction between the component and the weld material, along with the heat affected and non-heat affected zones (Fig. 4.18). Pitting is clearly visible and in this case, the equipment material breakdown, the final corrosion effect, led to non-scheduled maintenance work, with the resulting productions losses and increase in the costs and a possible direct incidence on safety. Controlling corrosion is thus not only necessary for economic reasons, but also, due to the tritium radioactivity, for ecological reasons.

After having shown these various cases of corrosion, it is seen that the means of avoiding them will depend on a number of factors, and the designer as well the installation operator must be assisted by the specialist in corrosion prevention. At this stage, it can be seen that a list of appropriate and precise specifications is required to avoid new problems in future tritium processing installations. In other words, a quality assurance document containing all detailed specifications or explanations must be available for any in-service or future equipment. In this document, the various equipment units must be identified and classified according to the medium corrosiveness. For each of these units, a data sheet specifying monitoring procedures must also be prepared.

Similarly, the information collected during periodic inspections, preventive tests or incidents must be reported on follow-up forms, which, after analysis, will make possible the appropriate decisions (initiation of repair procedures, damage analysis). Periodic inspections and preventive tests are very useful, when properly carried out, they can avoid leaks or malfunctions in a major components. The incidents due to corrosion are not constant: they vary largely according to the operating conditions and depend on the temperature, pressure, internal humidity, pH and medium composition parameters in the process. Understanding the interrelationships between these various physical and physicochemical parameters makes it possible to reduce the corrosion rates. These physical and physicochemical parameters will also be reported on these various data sheets and forms and must be taken into account in the experimental design. These forms will be used to feed a database for enriching the fault identification tools. This database must be available in a computer-assisted management system for decision making with respect to anti-corrosion measures. Subsequently, programming parts replacements must be done according to this computerized system which will be planned by maintenance. The keystone of the problem thus lies in

the integration of a continuous follow-up of corrosion in the installation monitoring program, and in the overall maintenance, periodic inspections and preventative tests planning. Finally, at the end of the installations programmed lifetime, a very thorough inspection of corrosion must be made as part of the safety audit and risk evaluation program, and the resulting conclusions must appear in each of the preceding documents.

We can recognize that the important participants in the fight against corrosion are actually the designer of future installations, the operator, since he is directly concerned, and the person in charge of equipment maintenance. These persons must listen to the corrosion prevention specialist, who has essentially an advisory role, and rely on him.

6. Types of corrosion in tritium installations

The nuclear industry's primary objective is to construct and operate its installations reliably but it has also objectives of safety and the protection of the environment. The reliability of these installations can be guaranteed by thorough knowledge of the behavior of materials under service conditions, which, for nuclear reactors, correspond to lifetimes of several tens of years. In reprocessing plants for highly radioactive wastes and isotopic separations, materials are subjected to more aggressive media where nuclear chemistry is involved. Nevertheless, interventions for maintenance or repair are generally easier, and the technology for tritium processing changes rapidly, which implies a shorter life for equipment utilization. However, malfunctions are possible at any time. With time the pressure of radiolytic gases is no longer negligible. It increases quickly and if not controlled can lead to deformation of storage tanks (Fig. 4.19) followed by stress corrosion.

Thus to avoid serious incidents the corrosion resistance of materials is highly important. Indeed, aging of materials rarely has sufficient beneficial effects and leads to increasing risks of damage to the assembly. In tritium installations, there are a great number of metallic assemblies, as shown in the photographs (Figs 4.19, 4.20 and 4.21).

The diagrams show the vessels, consisting of tubes, tanks, numerous valves and clamping collars, used to electrolyze tritiated water. This electrolyzer operates with a palladium-silver alloy cathodic membrane, which is less sensitive to embrittlement by tritium, nevertheless, if it is not carefully monitored, damage will occur. It has been observed that the time-dependence of corrosion damage has a statistical character. The assembly lifetime has been obtained by knowledge of occurred incidents, their nature, and their cycle in the operating mode. Only then, knowing the lifetime of a material, can there be preventive maintenance with replacement before an incident occurs. Accidents due to corrosion are more frequent in tritiated water containers; reprocessing equipment, with valves and furnace equipment, are often affected. The lifetime for these components is several months or one or two years, depending on impurities, tritium concentration and inspections.

6.1. Stress cracking corrosion by tritium

It is well established that tritium or hydrogen [24] when present either as an external gas environment or as dissolved ions can result in modifying the plasticity [25] and internal

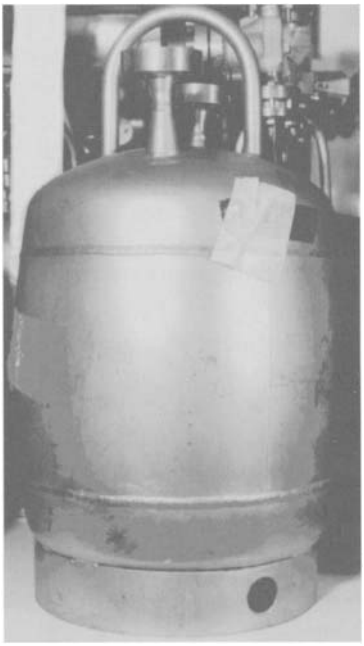

Figure 4.19. Deformation of a storage container by high radiolytic pressure.

cracking [26] or cause a dramatic loss of toughness in a variety of metals. Such behavior has been observed in copper, iron alloys, titanium alloys and nickel alloys. Importantly in a large number of cases, these effects can be facilitated in alloys over a wide range of strength levels, encompassing materials that in the absence of tritium can exhibit brittle fracture modes. An example is given in Figs 4.22a, where materials were exposed to a high shock pressure. In these photographs, the black grains are carbides, that can have dendrite morphology (Fig. 4.23).

It can be seen that there is a crack starting with formation of tritium cavities, that propagates up to the edge of the sound metal (Fig. 4.24). In the next sequence (Fig. 4.22b), propagation continues with new cavities at a velocity of about 10 nm s^{-1}. In order for a secondary crack to initiate in the stress field of the primary crack, it is essential that nucleation and growth should occur in a constant stress field. Tritium susceptibility in the alloy systems can be a sensitive function of both extrinsic and intrinsic variables, such as composition, microstructure, time of exposure and thermal treatment. Manipulation of the latter variables is a most promising way of improving alloy resistance to tritium embrittlement. It is clear that for embrittlement of a material by tritium, it must be present in the host lattice. There is no unequivocal evidence that surface-adsorbed tritium is an embrittling agent. Once tritium enters the material, its transport and subsequent locations are critical. Tritium is seen to move by lattice diffusion and on mobile dislocations that can be obtained after shocks. The former is considered to dominate in the face-centered cubic ferrous materials

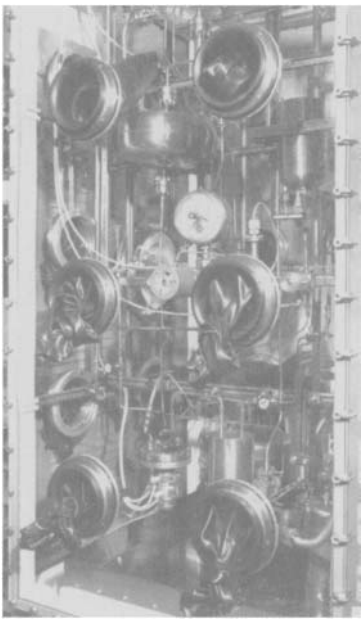

Figure 4.20. Electrolyzer for reprocessing tritiated water in a glove box, general aspect.

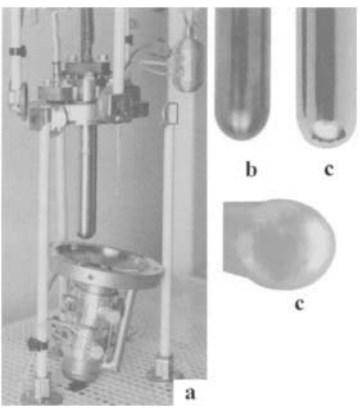

Figure 4.21. a: electrolyzer for reprocessing tritiated water in a glove box, electrolyzer with Pd-Ag cathode, b: Pd-Ag cathode hollow finger made in extruding, c: Pd-Ag cathode finger semi-sphere made in hammering.

which have high tritium diffusivities at ambient temperatures, while the latter is important in lower diffusivity materials, such as for instance, austenitic stainless steels.

Dislocation transport is accelerated in materials exhibiting planar slip (Fig. 4.25). The slip planarity [27] can be either intrinsic or a result of tritium modifying the stacking fault

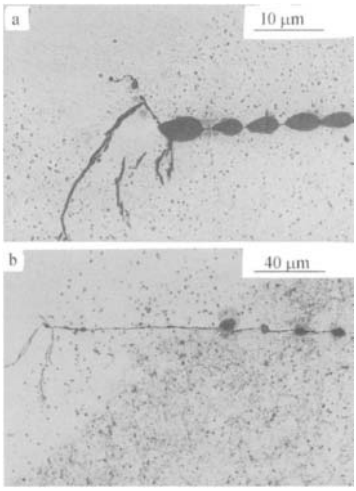

Figure 4.22. Photographs showing tritium cavities accompanied by progressive development of cracks at a velocity of 10 nm s^{-1}, Δt between (a) and (b): 20 h.

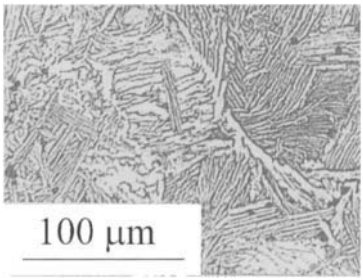

Figure 4.23. Carbides with dendrite morphology.

energy. Tritium is attracted to heterogeneities in the lattice: dislocations, grain boundaries, particles, voids and local stress fields all interact positively. Tritium can also be present in three forms in a metal; as a dissolved atomic species in equilibrium with the local chemical potential, adsorbed on heterogeneities of varying strengths, or recombined in molecular form. Mobile tritium can be rapidly transported to local stress centers, while strongly trapped tritium is immobilized at the original trapping site. The crack path can be either intergranular or transgranular, depending upon thermal aging. Changes have been related to the relative partitioning of solute elements at either the grain boundaries or at sites within the lattice. Carbon segregation at grain boundaries promotes transgranular over intergranular cracking. Another important factor is whether the material is highly plastic or has limited ductility. The transgranular crack planes can be quite different. In highly plastic material, cracking generally appears to be discontinuous by striations. In addition, the crack

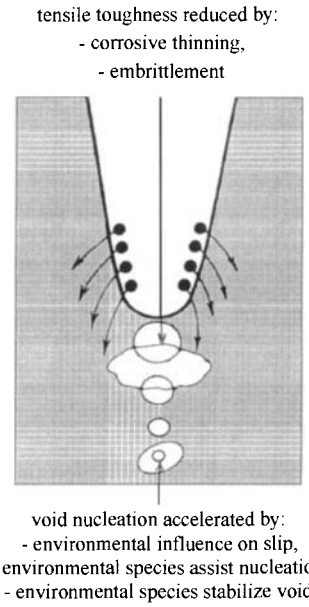

Figure 4.24. Schematic view of cavities propagating by the formation of voids and the rupture of steel.

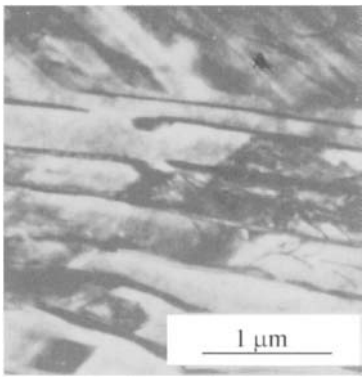

Figure 4.25. Cracking in the form of planar slips.

face will appear to be composed of planar segments, most likely variants of the slip plane on which the major crack lies. In limited ductility material, there is a close connection between the tritium-induced fracture and the adjoining low temperature cleavage crack face, and evidence for discontinuous cracking is not apparent. Cracking should be discontinuous in nature, since a running crack would leave the tritium excess concentration behind, necessitating reaccumulation. As heterogeneities are present in alloys, initially without a

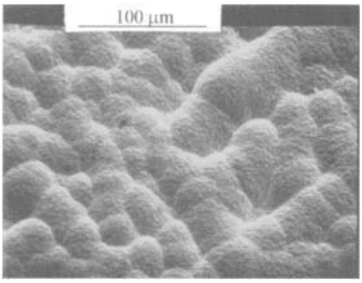

Figure 4.26. Scanning electron microscopy showing blisters on the entry face of a palladium membrane after charging tritium.

significant change in strength level, the cracking becomes a sensitive function of the nature and distribution of reversible and irreversible traps present in the lattice. If produced, generation of localized internal stresses is facilitated by the high pressure developed when tritium recombines at heterogeneities. This situation has been analyzed for the tritium- induced intergranular cracks and it was found that reducing the tritium concentration at grain boundaries reduces the extent of cracking.

Thermal aging at high temperature is characterized by modification of structure with hardening the intermetallic phase leading to local stress. This is the case of ferrite in Duplex stainless steels used in furnaces for cracking tritiated water. Corrosion by thermal aging is characterized by intergranular attack if the carbon concentration is too high as this forms chromium carbide precipitates. Thus minimization of carbon concentration has been an important criterion in the choice of materials. Type 310 stainless steel retains its properties in these furnaces under tritium gas and tritiated water vapor. Moreover, the presence of tritium in the metallic system can entail appreciable deterioration by precipitation of tritides. Tritides are found in palladium membranes operating at cycled high temperatures. Tritium atoms recombine to molecules in the presence of macroscopic or microscopic defects. The effects of defects are discussed in chapters 8, 9 and 23. Molecular tritium leads to a considerable internal pressure resulting in blisters (Fig. 4.26) and cracks in the brazed palladium-stainless steel joint (Fig. 4.27) or slip steps on stainless steel (Fig. 4.28). In this region, molecules of tritium lead to an appreciable decrease in plastic deformation capacity and the metal becomes embrittled.

6.2. Generalized corrosion

The theoretical basis for generalized corrosion testing is derived from the mixed potential theory as reported by Sedriks and Audouard [28] and [29]. In essence this theory separates the oxidation and reduction reactions of corrosion and postulates that the total rates of all the oxidation reactions equal the total rates of all the reduction reactions on a corroding surface. Oxidation reactions, referred to as anodic, because they occur at the anodic sites

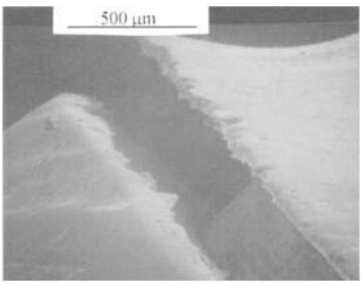

Figure 4.27. Scanning electron microscopy showing rupture formed on palladium-stainless steel braze after charging tritium.

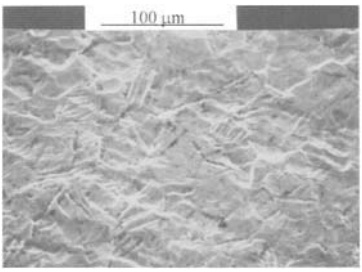

Figure 4.28. Scanning electron microscopy showing slip step zones.

of a corroding metal, can be represented by the reaction:

$$Me \rightarrow Me^{n+} + ne^{-} \tag{4.1}$$

This is the generalized corrosion reaction of a metal atom oxidizing to an ion. The mixed potential theory proposes that all the electrons generated by the anodic reaction are consumed by corresponding reduction reactions. Reduction reactions are known as cathodic, because they occur at the cathodic sites of corroding metal. The more common cathodic reactions are:

$$H^{+} + e^{-} \rightarrow H \tag{4.2}$$

$$O_2 + 2H_2O + 4e^{-} \rightarrow 4OH^{-} \tag{4.3}$$

$$H_2O_2 + 2e^{-} \rightarrow 2OH^{-} \tag{4.4}$$

During corrosion several anodic and cathodic reactions may occur. Removing one of these reactions will reduce the corrosion rate. In generalized corrosion, the mixed potential, also called corrosion potential, is the potential at which the total rates of all the anodic reactions are equal to those of cathodic reactions. The corrosion potential is obtained by

Figure 4.29. Photograph showing salting out phenomena in turbomolecular pump parts.

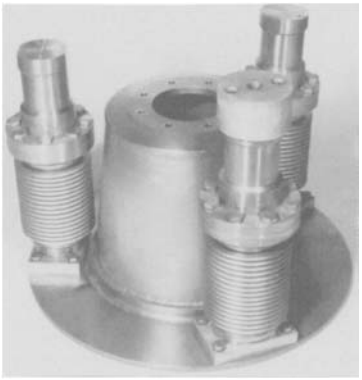

Figure 4.30. Photograph showing settling phenomena in internal pump parts.

linear polarization, and its current is a measure of the corrosion rate. The corrosion current is obtained by extrapolating the anodic and cathodic linear segments of each branch. The intersection of these lines at the corrosion potential yields the value of current, which can be converted to corrosion rate by the equation:

$$\bar{r} = 3.2 i_{\text{corr}} \frac{w}{\rho} \tag{4.5}$$

where $\bar{r}$ is the corrosion rate in μm thickness per year, w the equivalent weight of metal and ρ its density. In installations, r is found, in general, to be 100 μm per year. This indicates

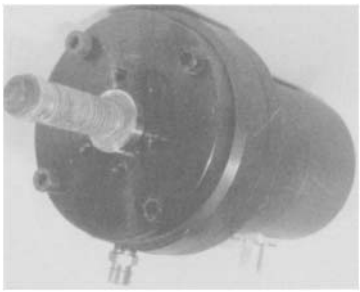

Figure 4.31. Photograph showing settling phenomena on flanges.

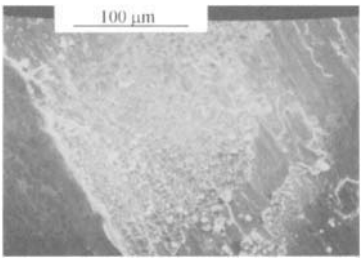

Figure 4.32. Photograph showing settling phenomena on valve bellows.

generalized corrosion is not the limiting factor for the lifetime of tritium installations, if alloys are well chosen and thick enough for storage tanks. The photograph in Fig. 4.29 is of a turbomolecular pump corroded by generalized corrosion.

Generalized corrosion has an indirect effect by thickening the oxide film leading to oxide salting-out phenomena. These phenomena signify that solid particles form in tritiated water and are susceptible to settling in internal tube walls, pumps, flanges or valve bellows (Figs 4.30–4.32) thus entailing corrosion and maintenance difficulties. Transportation and deposition conditions are very dependent on composition of the media, such as pH, and on local temperature. Oxide transport is minimized by correcting the pH by adding small amounts of sodium hydroxide.

6.3. Galvanic corrosion

Galvanic corrosion is the result of contact of two metals or alloys each with its own corrosion potential. If the values of the two corrosion potentials are significantly different, the metal with the more noble value becomes predominantly cathodic and the metal with the more active potential becomes anodic. A measurable current will flow between the anode and the cathode. The corrosion rate of the anode metal will be increased and the corrosion rate of the cathode metal decreased or entirely stopped. A simple practical assessment of whether two different metals are likely to produce galvanic corrosion in a given corrosive

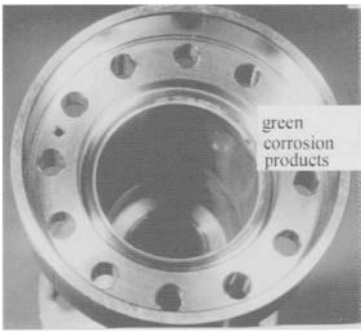

Figure 4.33. Galvanic corrosion between stainless steel flange and copper seal.

medium can be obtained by measuring and comparing the corrosion potential values. If the values differ by hundreds of millivolts, galvanic corrosion is clearly a practical possibility, whereas if the difference is of the order of tens of millivolts, galvanic corrosion is less likely. In reality, assessment of galvanic corrosion risks is more complex, as shown by Mazille [30]. This can be most accurately obtained by taking into account the Butler-Volmer equations and the Tafel curves. These curves lead to a consideration of a minimum of four reactions corresponding to the coupling of the two metals. The polarization resistance, corrosion currents and the solution conductivity are also involved. In practice, the concept of the 'Wagner number' is introduced. If this number is high, the attack is microscopic signifying that the current density is relatively uniform for each metal. On the other hand, if the number is small, the attack is macroscopic, and the current density varies significantly over all the surface of the couple. However, welding of two alloys with small differences in corrosion potential values can lead to increased corrosion of the more active material. Fig. 4.33 illustrates galvanic corrosion of a copper seal attacked in a tritium installation due to the wrong choice of galvanic coupling.

This corrosion has been avoided by choosing metallic couples whose values are identical in the galvanic series, and/or taking a favorable surface ratio. Moreover, in stagnant tritiated water, deposits may form, creating crevices. With crevices, stainless steels exhibit less noble corrosion potential values due to oxygen depletion within the crevice. Under these conditions, galvanic corrosion can occur. A very important factor is the ratio of the areas of the anodic and cathodic materials. An unfavorable area ratio is one which comprises a large cathode and a small anode. A small anode will have a greater current density, and hence a greater corrosion rate, like the copper seal (Fig. 4.34). Finally, tritium embrittlement of high strength stainless steels in contact with more active metals can lead to galvanic corrosion.

6.4. Crevice corrosion

This form of attack is generally associated with the small volume of stagnant solution present in interstices, under deposits or valve seals as shown in this photograph of a tritium installation (Figs 4.35 and 4.36).

Figure 4.34. Galvanic corrosion between stainless steel flange and copper seal.

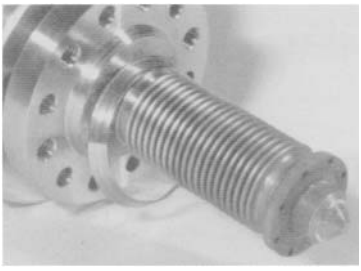

Figure 4.35. Crevice corrosion along valve bellows and flange gap.

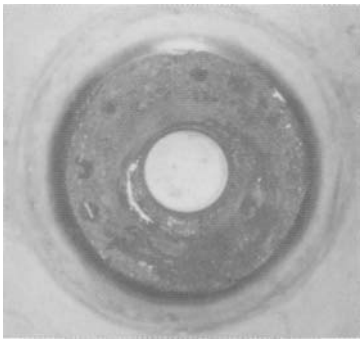

Figure 4.36. Crevice corrosion along valve bellows and flange gap.

Because it can destroy the integrity of mechanical joints in engineering structures, crevice corrosion is generally considered to be a troublesome form of localized corrosion.

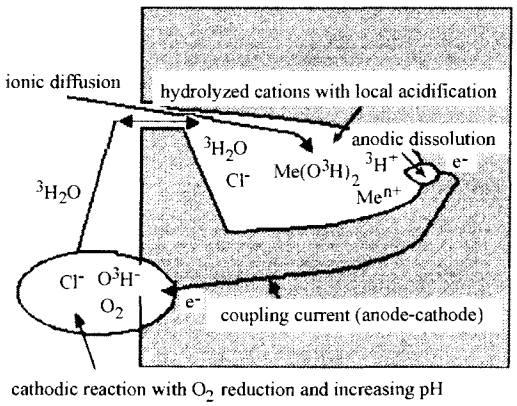

Figure 4.37. Schematic of various reactions in crevices associated with cathodic reactions.

Table 4.1. Effect of tritiated water containing chloride on the probability of crevice corrosion. 30 days exposure

Stainless steels	Type 430	Type 304L	Type 316L	Type N08932
Probability of crevice corrosion	92	75	45	3

To function as a corrosion site, a crevice has to have sufficient width to permit the entry of the aggressive solution, but sufficiently narrow to ensure that the latter remains stagnant (Fig. 4.37).

Accordingly, crevice corrosion usually occurs in gaps a few micrometers wide, and is generally not found in wide grooves in which circulation of the solution is possible. Moreover, the mechanism assumes that the films become unstable in presence of halide and acid pH. In terms of the mixed potential theory, the anodic reaction is balanced by the cathodic reactions (eqs (4.2)–(4.4)). However, because the solution within the crevice is stagnant, the oxidizing species used up in the cathodic reaction is not replenished and this reaction within the crevice ceases to operate. The anodic reaction, however, continues within the crevice, building up a high concentration of metal ions. To balance the charge, negatively charged ions, particularly halides, migrate into the crevice. The resulting metal halide is hydrolyzed by water to free acid in the crevice, while the pH of the solution outside remains neutral. This build-up of acidity is responsible for the breakdown of the passive film and autocatalytic attack. Attempts have been made to identify the hydrolysis reaction responsible for acidification by analyzing the species in the crevice. It was concluded that acidification is essentially dominated by chromic ions. Nickel ion does not hydrolyze to yield significantly acid pH values. Crevice corrosion can be predicted by its effects on the passive and corrosion currents, breakdown and repassivation potentials after reversing the scanning direction as indicated by Sedriks and Combrade [28] and [31]. If the potential difference is small, crevice attack can develop. The crevice corrosion test can also consist in counting the number of sites attacked and measuring the crevice depth. An example is shown in Table 4.1 giving the probability of forming crevices deeper than 0.75 mm

in quiescent tritiated water containing chloride. It is instructive to see that crevice attack resistance is in the order N08932 > 316 > 304 > 430 stainless steel. The present state-of-the-art suggests utilizing high molybdenum stainless steels or higher alloys containing molybdenum. Moreover, this corrosion is fought using welded rather than mechanically joined assemblies, using non-porous seals, and inspecting the internal surfaces of processing installations by endoscopy. Crevice corrosion is described and discussed in chapters 13 and 21.

6.5. *Pitting corrosion*

This form of corrosion is particularly insidious in nuclear installations. The attack is limited to very localized pits that can progress very rapidly in depth by a self-sustaining mechanism while the remaining surface is not attacked. Its mechanism is very similar, in terms of the propagation steps, to that proposed for crevice corrosion. The propagation of pits involves instabilities and dissolution of passive film with a high degree of acidity by hydrolysis at the bottom of pit while the pH of the bulk solution remains unaltered [28] and [32]. Alloy and environment combinations can cause pitting. In acidic oxygenated-chloride solutions, where the likelihood of pitting of stainless steels is a concern, the corrosion potential is nobler than the potential defined at the active-passive transition. The anodic polarization curve, therefore, does not display the active-passive transition. Consequently, pitting will depend on the separation of corrosion, repassivation and pitting potentials. If these potentials are close, any small change in the oxidizing power of the tritiated water can produce attack, otherwise generalized corrosion will occur. Thus, it is accepted that the position of the pitting potential in the transpassive region avoids pitting corrosion. In some cases, the anodic polarization curve does not show a clearly identifiable pitting potential. In such cases, it can be helpful to refine its value by holding the metal at various applied potentials near pitting and monitoring the current decay characteristics. Another technique is based on determining the repassivation potential that avoids pitting. Rapid potential scanning can help to determine the time necessary for developing pitting and crevice corrosion. A ferric chloride test has been standardized. Evaluation includes photographic reproduction of the pitted specimen including pit density, size and depth. Results have shown both chromium, nickel and molybdenum increase resistance to pitting.

An important element increasing resistance to pitting is nitrogen. It should be noted that microstructure plays an important part in determining pitting resistance. Phases, such as ferrite and sigma, sulfide and manganese inclusions, strengthening precipitates in hardened stainless steels, sensitized grain boundaries and welds can all have detrimental effects on pitting resistance. Addition of nitrogen and higher chromium and molybdenum concentrations tend to stabilize austenites and thereby prevent the formation of delta ferrite and sigma phases. For Type 630 stainless steel, the strengthening heat treatment leads to slightly more active pitting potentials, indicating slightly lowered resistance to pitting. Investigations showed that, when present, sensitized grain boundaries act as preferred sites for pit initiation. In martensitic stainless steels the chromium-depleted regions around carbides precipitated at tempering temperature are also thought to act as sites for preferential

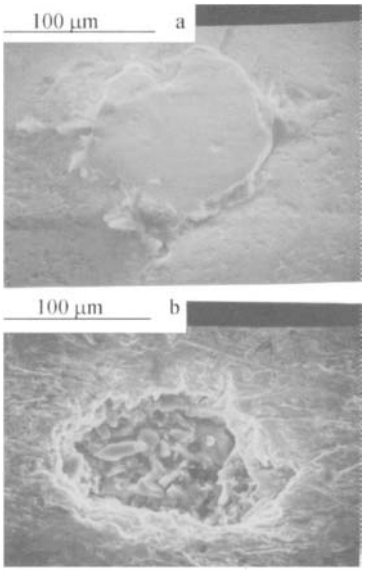

Figure 4.38. Scanning electron microscopy showing inclusion (a) acting as localized corrosion site (b).

attack. In molybdenum-containing stainless steels, another factor reducing pitting resistance is the molybdenum depletion near delta ferrite formed in welds. Other factors affecting the pitting behavior of stainless steels are oxidizers, halides, cupric and ferric ions in solution and acidity. Increasing the temperature favors the tendency to pitting, but this depends on the composition of the alloy. In chloride solutions, no severe corrosion is observed at ambient temperatures. Typical values for critical pitting temperatures are about 50°C for stainless steels and 100°C for nickel-based alloys. The corrosion morphologies at these low temperatures are hemispherical pits in an otherwise unattacked surface. Corrosion products inside the pits are normally enriched in chromium and completely depleted in nickel and iron. High susceptibility to pit nucleation is connected with n-type conductivity of the oxide film, whereas low susceptibility corresponds to p-type conductivity. Among chemical surface treatments aimed at improving pitting resistance is passivation, which consists in immersing the stainless steel in nitric acid solution. The main effect of this treatment is to clean the stainless steel by dissolving surface inclusions and contaminants, such as manganese sulfide particles (Fig. 4.38), which act as pit initiation sites.

From a practical viewpoint, stainless steels can be perforated in some ways as shown in Fig. 4.3 without substantial weight loss. This localized corrosion is avoided by choosing appropriate materials such as super-austenite stainless steels or super-Duplex, and eliminating stagnant zones and deposits. This entails a good design for the processing system. Pitting corrosion is discussed in chapters 13–21.

6.6. Intergranular corrosion

Grain boundaries are disordered, poorly fitting regions separating grains of different crystallographic orientation, and therefore they are favored sites for segregation of various elements or precipitation of metal elements, such as carbides and sigma phases. It is not surprising, therefore, that grain boundaries enriched or impoverished in one of the constituents can be preferentially attacked while the remaining material is not corroded [33]. The usually encountered form of intergranular corrosion is due to sensitization. Sensitization is understood in terms of chromium precipitation, and is generally attributed to chromium depletion in the vicinity of carbides precipitated at grain boundaries (Fig. 4.39).

The alloy disintegrates and loses all mechanical properties leading to tube perforation. To understand the phenomenon in terms of microstructure, it is instructive to examine the carbon solubility relationship in steels [28] as illustrated in Fig. 4.40. This figure shows that in steels containing between 0.03 and 0.7% carbon, the structure at ambient temperature contains austenite, ferrite and carbides. Austenite containing less than 0.03% carbon should be stable. Austenite containing more carbon should precipitate carbides on cooling below the solubility line. However, at relatively rapid rates of cooling this reaction is partially suppressed. The term stabilized implies that carbon remaining in solid solution will be preferentially precipitated as titanium carbide during metallurgical treatment if titanium is added to the alloy.

Our present understanding suggests that intergranular corrosion is primarily under anodic control, i.e. attack is determined by the availability of anodic sites at the grain boundaries. Therefore, it would be expected that the anodic polarization curve of a sensitized stainless steel would be different from that of a non-sensitized material. Taking an example, if sensitization reduces the chromium concentration at the grain boundaries to values below 12% while the grains retain a chromium concentration, there will be a significant potential range over which the boundaries will exhibit active corrosion while the grains remain passive. Therefore, conceptually, it should be possible to define sensitized stainless

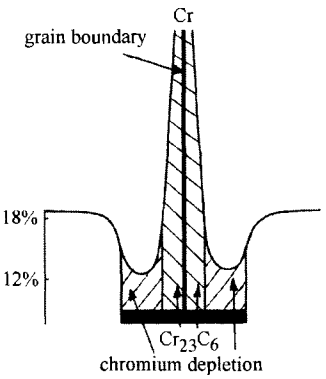

Figure 4.39. Schematic illustration of chromium depletion in the vicinity of grain boundaries.

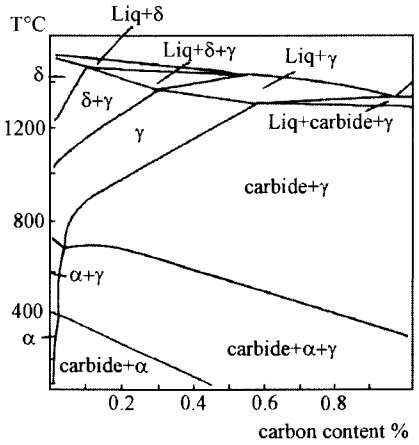

Figure 4.40. Phase diagram for steel with varying carbon concentrations, reprinted from ref. [28].

steel in which intergranular attack is or is not likely to occur as a result of chromium depletion by considering differences in passive potential ranges. Among the polarization curve parameters that are particularly affected by sensitization are the active peak and passive currents. The width of the anodic peak corresponding to the active-passive transition can be used. This method was prompted by the desirability of having a rapid, nondestructive test for determining the degree of sensitization in field-welded components for the nuclear power industry.

Destructive tests by ferric sulfate-sulfuric and boiling nitric acid are also used to detect susceptibility to intergranular corrosion in the submicroscopic sigma phase formed in molybdenum-containing types 316L and N08932. These are recommended for testing weldments of higher alloys, such as Hastelloy and Inconel alloys. The nitric acid-hydrofluoric acid test makes it possible to differentiate the effects of chromium depletion and sigma phase. The composition and structure of bare metal and weld metal, metallurgical condition of the bare metal before welding, the welding process and procedure, shielding gas and size of the welded material can influence weldment corrosion. For austenitic stainless steels, cooling rate and post-welding heat treatment can be useful in minimizing intergranular attack in welds. If the weld is reheated to the temperature in the chromium carbide precipitation range (500–750°C), a very thin zone of sensitized material may develop immediately adjacent to the weld that can be susceptible to intergranular attack (Fig. 4.41).

Because the sensitized region is very narrow, an attack called 'knife-line' is a common occurrence along a thin line just (Fig. 4.42) at the weld-base metal junction in tritiated water containers. Knife-line attack can be eliminated by reheating the welded part to about 1070°C to redissolve chromium carbide and reprecipitate titanium carbide. Knife-line attack is found currently in oxidizing environments, such as radiolytic oxygen and hydrogen peroxide. Therefore, it is possible that in addition to chromium depleted regions, any sigma

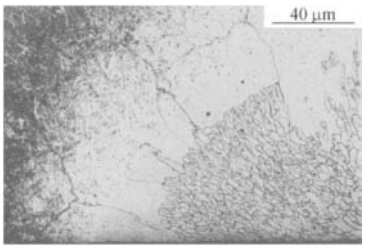

Figure 4.41. Sensitized zone adjacent to the thermally affected zone in a weld.

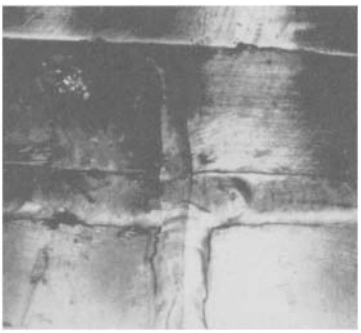

Figure 4.42. Corrosion in the form of a knife-line.

phase present may also be attacked, since oxidizing species are known to attack this phase. Essentially, chromium increases and nickel decreases the solubility of carbon in austenite, so a balance must be struck between the concentrations of these two elements. However, this pattern cannot be extrapolated directly to higher nickel alloys; for example, Inconel alloys cannot be sensitized to show any intergranular attack. The presence of molybdenum reduces the tendency to sensitization. However, the submicroscopic sigma phase is attacked at acid pH when present in austenite stainless steels as an identifiable phase at grain boundaries. Titanium carbide precipitated at grain boundaries could also lead to intergranular attack in oxidizing environments at acid pH. There is some evidence to suggest that increasing grain size increases susceptibility to intergranular attack. This is explained as being due to the fact that in small-grained material there is more grain surface area and therefore less chance for a continuous network of carbides. Type 430 stainless steel can be sensitized by heating to temperatures above 920°C at which there is a significant increase in the solubility of carbon in ferrite. The most effective way to eliminate intergranular attack is to anneal the ferritic stainless steels at 800°C or to cool slowly through the temperature range 700–900°C. At these temperatures chromium rediffuses back into the depleted zones. Moreover, addition of stabilizing elements minimizes intergranular attack. Duplex stainless steels containing both austenite and ferrite phases exhibit high resistance to intergranular corrosion. The presence of small ferrite grains in the structure minimizes the

formation of continuous networks of chromium carbide along the austenite grains. Carbides precipitate around isolated ferrite grains, thus attack will be confined and will not propagate. Grain boundary migration at 600–800°C may also contribute to the prevention of the formation of continuous paths in chromium-depleted material.

To conclude, this form of corrosion is currently an important problem in tritium installations thus limiting their lifetime. This will be met, in the future, in steam generator secondary circuits for controlled fusion facilities. Attack will limit the lifetime for confined zones, such as tube elbows where the local chemistry is modified by copious deposits and oxidizing and acid species sequestration. This sequestration appears to be chemically aggressive and leads to intergranular attack that can also develop in the presence of stress. Studies have been carried out to identify media responsible for this attack. The origin is the presence of concentrated oxidizers and organic pollution produced by radiolytic decomposition in reprocessing. Remedies to delay it are the utilization of radiolytic inhibitors. These should be the combined action of a slightly alkaline pH and peroxide, at low concentrations, and nitrate and carbonate. Results are given in chapters 17, 19 and 20.

6.7. Selective corrosion

This mode of corrosion denotes the dealloying of one element or phase of an alloy if there are several phases. In industrial practice, selective corrosion is often associated with several modes of attack produced by aggressive species which can be distributed in the oxide. Mechanisms have been proposed and, generally, concern the mobility of electronic bilacunes [30] and [34]. The bilacunes allow the formation of a concentration gradient in the oxide, which is accompanied by progressive enrichment of an element or phase. This mechanism explains the phenomenon of oxide sublayer corrosion leading to exfoliation, as observed in tritiated water. In this process the planar diffusion of metal atoms and the germination of islands in oxide sublayer can be involved. The presence of radiolytic peroxide amplifies this mechanism by introducing a supplementary cathodic reaction. This corrosion has been observed for membranes made of cobalt-base alloy equipping valves in tritium installations. In this case, there is cobalt depletion. Results will be discussed in chapter 6.

6.8. Stability of passive films and corrosion by oxide breakdowns

The physical and chemical characteristics of passive layers condition their protective properties and therefore their degree of resistance to corrosion. These characteristics are closely linked to the film composition. The thickness of the film in passivity is, depending on the case, in the order of 1–10 nm. The film consists of hydrated anions and oxidizable metal cations such as iron and chromium. The composition of the passive layer depends both on the metal substrate, surface treatment and the medium where the material is immersed. This shows that the structure and composition of the oxide layer do not have a definitive

character but evolve during all the modifications of the medium. A relative maximum concentration of chromium in the passive film is seen. The role of chromium is essential in the stabilization of passive film, because this element is much more really oxidized than is iron. It is generally considered that steel is called 'stainless' when the chromium concentration is of the order of 12%. It will be recalled that the stability of this layer depends on the corrosive medium. In some media, 17–20% chromium, or more, will prove to be essential. According to the theory of Uhlig [35] the alloy remains passivated so that the five electronic gaps in the 'd' shell of chromium atoms are not completely filled by electrons from iron. Conversely, considering the percolation, the minimum chromium concentration would be such that superficial chromium atom sites would be sufficiently close enough to be connected to adsorbed oxygen atoms. In austenitic steels, it does not seem that nickel participates directly in the composition of passive film. This element acts rather by a moderating role in generalized corrosion. In the case of molybdenum, analysis has shown its presence in the passive film and this element is localized in the external layer of the film.

The driving force providing growth and stability of passive films is due to the presence of a potential drop in the oxide thus inducing a high electrical field. The potential difference can reach very high values, in the order of 10^6 V cm^{-1}. It results in some electrostriction forces that have to be balanced by the intrinsic superficial tension. An order of magnitude of 2×10^7 Pa can easily be reached for usual values of thickness and electrical field in the film. As the ionic species transfer is limited, the passive film acts as a resistance, a capacitance or more generally impedance so that electronic conductivity is largely preponderant. Moreover, in some cases, the film appears to act as a semiconductor. The semi-conducting behavior induces the possibility of a space charge in the two interfaces. A model of oxide defined with point defects has been developed. In this model, the passive film has an electrical field close to that of electrical rupture, where electrons and holes would be in balance. In the proposed model, the process of film growth corresponds to the gap diffusion into the external and internal interfaces [36]. This idea can be generalized for any film. The film would develop from a more or less amorphous and semi-organized film containing water molecules. The metal cations from the substrate are injected into the lattice perturbed by the potential difference, and thus their affinity with the oxygen of water is all the more important. The electrical neutrality of the film would be preserved by ejection of protons towards the electrolyte, and their number should correspond to those of cations injected into the film. The deprotonation would result in the gradual evolution of the film from a hydrated structure to that of an oxide. Moreover, linked water and oxygen ions are found in oxide and hydroxide. Depending on transportation, the internal layer structure of the film will be that of an oxide and the external layer structure will be hydroxide.

Exchanges between the metal and the solution through the passive film occur by ionic transfer processes. These processes will confer fairly substantial protection against corrosion. Even if the ionic conductivity of the film is low, it is not zero and will correspond to a current density of the order of 1 μA cm^{-2}. It will result in some perturbations, even in a film at the stationary state. Several phenomena accompany the cation transfer through the film. The cations should be evacuated, and this will produce a concentration gradient in the solution at the oxide interface vicinity. These cations will hydrolyze and induce local

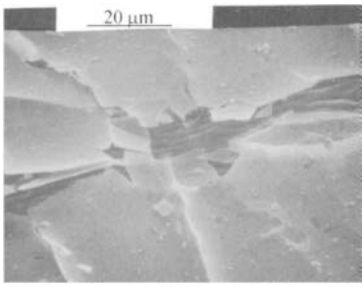

Figure 4.43. Oxide breakdown on the internal surface of a turbomolecular pump.

increase in acidity. Moreover, extraction of cations leads to a gap near the oxide interface. This is interpreted as a point defect called a vacancy. This is plausible because the cations flow across the film is small and its transfer induces only a weak perturbation, consequently the structure of the passive film remains globally unchanged. The gap produced at the interface diffuses under the action of the high electrical field until it reaches the other side. It results in a gap concentration gradient in the passive film. The metal cations of the substrate cross the interface to annihilate gaps present in the film near the metal-oxide interface. Gaps can also cross this interface to diffuse into the substrate resulting in an excess of vacancies at the oxide-metal interface. At the stationary state, the defect concentration increases with the flow of metal cations. An increase in this flow can lead to instability in the dynamic system, leading to rupture of the passive oxide layer. This is a specific degradation when the oxide is subjected to extension constraints by the presence of tritium in radiolyzed oxide. There are several further factors that are responsible for the development of constraints. These can be an internal pressure produced by corrosion (striction), a void in the oxide, a localized expansion with local dissolution of oxide (Fig. 4.43).

Such expansion can be caused by:

- diminution of surface energy,
- decohesion by radiolytic concentration in zones of triaxial constraints,
- cleavage of the oxide, modification of local chemistry in the film,
- effect of localized plasticity.

Several ruptures of oxide leading to holes in steel have been observed in thin membranes and bellows made of 316L stainless steel. These concern elements of the valves or body of turbomolecular pumps, which are expensive parts used in tritium processing (Figs 4.29–4.32). If not carefully monitored, these elements can be destroyed in less than a year thus increasing the maintenance and replacement costs in tritium installations. Our work has led to proposing type N08932 super-stainless steel as a replacement of 316L stainless steel. The resistance to breakdowns has been verified by multiple tests carried out in the presence of tritiated water or gaseous tritium. To increase the reliability of installations, we must understand why the oxide of N08932 super-stainless steel is less sensitive to this attack. We can mention here that the film obtained from the super-stainless steel is richer in chromium.

This leads to better passivity. Corrosion by oxide breakdowns and passivity are studied in chapters 6, 7 and 10–12.

6.9. *Mechanical stress corrosion and fatigue corrosion*

Mechanical stress corrosion results from the combined action of a mechanical stress and an aggressive medium [37]. This photograph (Fig. 4.44) is of a high pressure-pumping system for a gaseous tritium medium. The internal part is made of hardened stainless steel deposited on austenitic stainless steel. Steel layer deposition is of practical importance for ensuring satisfactory pumping, but using more sensitive hardened steel constitutes a risk of localized corrosion.

Fatigue corrosion is distinguished from stress corrosion [37] by the fact that applied mechanical constraints are no longer static but cyclic in the presence of a liquid or gaseous environment that may or may not be particularly corrosive. Increasing the frequency leads to an increase in fatigue corrosion stress, as illustrated by numerous narrow transgranular cracks seen in Fig. 4.45.

These cracks are obtained for 10^3 cycles and a tritium pressure of 5×10^7 Pa. High mechanical-resistance alloys are often sensitive to corrosion fatigue. This is notably the

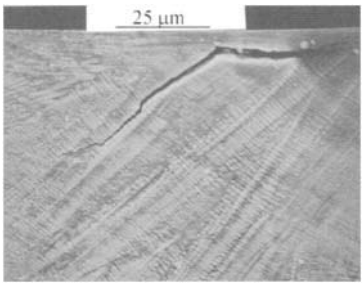

Figure 4.44. Crack produced along a nickel membrane by combined action of mechanical stress and corrosion during pumping at high pressure.

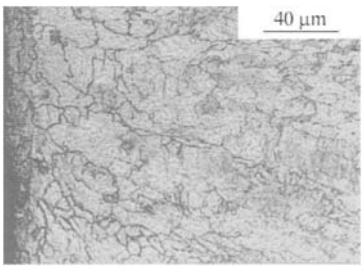

Figure 4.45. Transgranular cracks induced by fatigue corrosion.

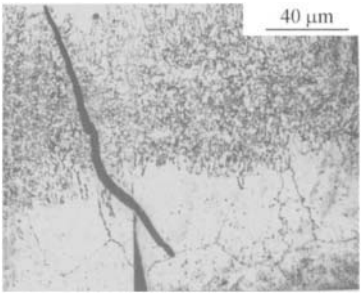

Figure 4.46. Transgranular cracks induced by fatigue corrosion in weld.

case in the damage observed using tubes made of 316Ti stainless steel. The phenomenon intervening in welded junctions is attack by fine titanium carbide precipitate located in cold-hammered zones close to the heat-affected zone. It results in some hardening and loss of ductility of the alloy leading to larger transgranular cracks (Fig. 4.46).

Parameters that increase these effects are:

- too high titanium concentration during welding,
- high dislocation density (cold-hammered zones) that are sites for TiN germination,
- high tensile and precipitation hardening,
- delta ferrite phase,
- residual constraints after welding,
- poorly adapted temperature regulation in precipitation kinetics and relaxation mechanisms for austenitic and martensitic stainless steels.

Fatigue corrosion can be reduced or eliminated in decreasing constraints by relaxation annealing or by mechanical treatment such as shot peening which introduces superficial compression constraints. Another remedy consists in optimizing the processes to reduce the number of cycles (such as pumping tritium at very high pressure). A further remedy lies in decreasing the grain size. It should be emphasized that laboratory tests should not be used directly to predict the lifetime of components. Both the time exposure to the corrosive medium and the frequency of the stress cycles may be significantly different. A popular test is the U-bend test described in ASTM C30-72. It is simple and easy to make and is one of the most severe tests. Figs 4.47 and 4.48 illustrate the result obtained on a foil made of Inconel 690 U-bended in the presence of hot chloride. The specimen contains large helical tearing produced both on the internal face and external face by bending. One can conclude there is no stress corrosion for this alloy.

6.10. Erosion corrosion and cavitation

This corrosion is produced by corrosive fluid displacement which, in some cases, contains solid particles capable of causing erosion in nozzles, elbows, bends, T-joints in tubes,

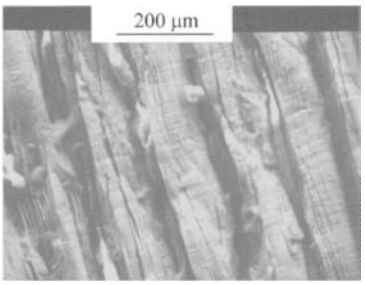

Figure 4.47. External spines induced by bending in the presence of hot chloride.

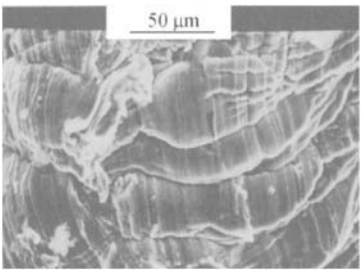

Figure 4.48. Internal spines induced by bending in the presence of hot chloride.

tubes and propeller blades for pumping. In addition, turbulent flow causes greater erosion-corrosion than laminar flow, and can destroy protective films [38] and [39]. Oxidizing species plus acid pH and liquid velocity can significantly increase the corrosion rate. Since a corrosion effect is superimposed on a mechanical erosion process, attack can be limited by factors enhancing resistance to corrosion (Cr, Mo) and erosion (hardening alloy, TiN deposit). Remedies should include the use of more resistant higher alloys, changes in design and removal of suspended solids. We have chosen the nitriding process on stainless steels as an example that combines high superficial hardness and correct corrosion resistance in tritiated water. Titanium nitride was studied in our laboratory and results will be discussed in chapter 14.

Cavitation damage is a form of attack occurring under conditions in which the relative velocity between the liquid and solid material is very high. The collapse of cavities on a solid surface leads to oxide layer rupture and removes material by mechanical erosion. Corrosion should be thereby accelerated. We can note that greater resistance is obtained by using austenitic stainless steels, precipitation hardening stainless steels, higher alloys, such as Inconel, Hastelloy and cobalt base alloys and TiN deposit. While all these materials have good corrosion resistance, they range from ductile to hard and high strength.

6.11. *Irradiation corrosion*

This type of corrosion will not be met in tritium reprocessing installations, but will be present in controlled fusion and fission reactors [36,40,46,47]. The neutron dose will exceed several 10^{19} n cm^{-2} and neutrons will interact with metallic materials creating defects in cascade. This results in zones having weak and high atomic density depending on the extent of interstitials. The creation of defects by irradiation tends to accelerate the formation of intermetallic vacancies and voids. It follows that neutron fluence is the essential parameter for metal damage. Moreover, reactions with neutrons can lead to helium production which regroups defects, generally localized in grain boundaries, thereby entailing a loss of metal ductility. Depending on irradiation conditions, changes of geometry by swelling and particular corrosion phenomena linked to radiolysis can arise. Embrittlement by irradiation could occur and through progressive hardening of structures can lead to the situation where it is not possible to ensure safe operation of the reactor. Therefore, embrittlement of materials composing the core is a key consideration in the lifetime of controlled fusion reactors. Thus representative samples should be irradiated. Rupture tests will make it possible to assess embrittlement and to determine if the fusion reactor is operating safely. Reactor structures should be made of stainless steel, and these will also be subjected to high neutron fluences. These structures, although replaceable, will have lifetimes as long as the core. The behavior of stainless steels under irradiation is considered good, but accumulation of very high neutron doses may lead to hardening and appreciable embrittlement.

Chapter 5

CHARACTERISTICS OF SUPER-ALLOYS

The harmful action of the tritium, tritiated water and radiolytic products in the corrosion of different materials will be established in subsequent chapters. In this section we wish to discuss the principal characteristics of super-alloys, stainless steels and deposits.

1. Austenitic stainless steels

Austenitic stainless steels are extensively used in the nuclear industry because of their excellent corrosion resistance, good mechanical properties, and ease of welding. The different varieties of austenitic stainless steels have been reviewed by Sedriks [28]. Their great structural stability enables their use at both low and high temperatures in heat exchangers and for stocking and transferring gases in tritium reprocessing. Some grades behave better than others do. These differences result from alloying elements and tempering treatment that affect the stability of the microstructure, from physical characteristics at high and low temperatures, suitability for welding and corrosion resistance.

Type 304 is the most popular grade used in applications requiring a good combination of corrosion resistance and formability. Type 304L is a lower carbon grade used in applications requiring welding. The lower carbon concentration minimizes carbide precipitation in the heat-affected zone near welds that can lead to intergranular corrosion. Type 316 contains molybdenum and has a greater resistance to pitting and crevice corrosion than has type 304. Type 316L has a low carbon concentration to increase corrosion resistance. Most tritium equipment is made of 316L stainless steel. Type 316Ti is a grade stabilized with titanium for applications requiring welded structures for elevated temperature service. Type 348 is a nuclear grade of stainless steel with a restricted tantalum and cobalt concentration to limit nuclear activation of the two elements. Type 310 has higher nickel and chromium concentrations to provide oxidation resistance at high temperatures in the presence of tritium. Type 310S is a lower carbon version used to minimize carbide precipitation near welds. Type N08932 is a high grade steel that has had heat treatment at high nitrogen pressure (overhardening) followed by quenching in order to homogenize the face cubic centered austenitic structure. Nitrogen is a highly effective element for generating an austenite structure in steel and can replace carbon and form metal nitrides. Depending on the heat treatment, nitrogen is found in grain boundaries and manganese is added to in-

crease its solubility. Incorporating nitrogen stabilizes and strengthens the austenitic phase without reducing its ductility.

Molybdenum or, if needed, a high chromium concentration, favors precipitation of intermetallic phases, notably the ferrite. The presence of ferrite is known to decrease pitting resistance. It can also decrease resistance to sensitization when present in grain boundaries. However, isolated ferrite in austenite grains improves resistance to sensitization and stress corrosion cracking. Long-term exposure of ferrite at high temperatures can lead to its transformation to a hard and brittle phase that can reduce ductility and toughness. Nickel and chromium concentrations are balanced to minimize the formation of ferrite rich in chromium. It is for these reasons that austenitic stainless steels usually contain sufficient nickel. However, some ferrite is intentionally added in weld metal where its presence reduces hot tearing, or in special stainless steels in which wear resistance will be improved by intention heat treatments to transform it to a hard phase.

Most of the austenitic stainless steels can undergo martensitic transformations, as a result of cold working, particularly at low temperature. To avoid this precipitation, austenitic steels undergo a quenching process, consisting of heating at 1000°C followed by rapid cooling. The austenite phase formed at high temperature, although thermodynamically unstable, is preserved down to ambient temperature by this process. Under these conditions, preserving purely austenite structure requires a nickel concentration of over 10% if molybdenum is present in stainless steel. The transformation of austenite to the martensite phase can be also induced by surface super saturation in hydrogen isotopes. The high concentration in hydrogen or its isotopes in the lattice results in hydrostatic constraints with very intense compression and favors the generation of embrittled martensite. As a result, the more highly alloyed type 310 stainless steel shows that the austenite phase is nearly stable enough to be used in the furnace for tritiated water cracking.

At high temperature, these steels dissolve carbon, which is very effective in producing the austenite phase. This solubility of carbon decreases at low temperature leading to a carbide precipitation. Time-temperature combinations will be sufficient to precipitate chromium-rich carbide at the grain boundaries, but insufficient to rediffuse chromium back into the austenite near the carbide. This will result in the formation of envelopes of chromium-depleted austenite around the carbide. Since the carbides precipitate along grain boundaries, the net effect is grain boundary corrosion. The remedy to reduce the chromium depletion and carbide precipitation lies in using low carbon grades (types 304L, 316L or N08932 grade). Another possibility is a postweld heat treatment to rediffuse chromium back into the depleted austenite, or titanium additions (type 316Ti) to precipitate carbon as titanium carbide so that little carbon is left to precipitate as the chromium-rich grain boundary carbide on cooling. A stabilizing treatment at 900–925°C is sometimes given to ensure maximum precipitation of carbon as titanium carbide. All these remedies have certain advantages and disadvantages. The low carbon grades have slightly lower strengths, postweld heat treatment is not always practicable in large structures and the stabilized grades can suffer another form of localized corrosion.

In tritium processes, pipes and plates are assembled by welding to ensure perfect gastightness so that there cannot be any leaks from the processing circuit to the environment.

The metal deposited by the welding process should have the same qualities of corrosion resistance as has the bare metal which means that the composition of the welding metal must be close to that of the bare metal. On the other hand, austenitic stainless steels have a high thermal expansion coefficient. Consequently, stresses induced by the solidification and interdendritic segregation result in purely austenitic welding being sensitive to cracks on heating and cooling. The presence of 3–8% of ferrite in the weld reduces sensitivity to embrittlement at high temperature. The interdendritic ferrite should dissolve impurities, thus avoiding precipitation of low melting point elements which causes cracking under the action of solidification stresses. The introduction of ferrite can create another major problem if its percentage is not controlled during welding. The microstructure in a weld bead depends on the mode of solidification and transformation of ferrite to austenite on cooling, and on the dendrite growth rate. These should be controlled. This transformation depends also on the usage temperature. For cyclic utilization at different temperatures, in a furnace, the deposited metal must have very little ferrite in a discontinuous system, because tearing by embrittlement is possible. Less than 8% of ferrite is required to avoid cracking.

Increasing the nitrogen concentration in Duplex steels favors austenitic phase formation, stabilizes it and delays precipitation of intermetallic compounds such as the χ and σ phases. This stabilization effect in the austenitic phase is very important at high temperatures, and plays an essential role in weld properties. The effect of nitrogen on carbides and intermetallic precipitation compounds has another consequence. It delays the loss of ductility during the isothermal annealing process, especially at the critical temperatures. Knowledge and interpretation of phase diagrams make it possible to define the metallurgic state of stainless steels. Addition of iron can lead to four different phase diagrams which show the structural transformations these alloys undergo in thermal processing. Fig. 5.1 obtained from Andrews [48] schematizes these four possible diagram types by addition of:

- gamma elements (Ni, C and N). They can induce eutectoid transformation,
- alpha elements (Cr, Mo and Si).

Recalling the structure of the various steel grades containing α, γ and δ phases provides understanding of the classification of the different stainless steels, namely:

- ferritic steels ($13\% < Cr < 20\%$),
- martensitic steels,
- austenitic steels,
- austenitic-ferritic steels,
- super-ferritic steels having high Cr concentrations ($>20\%$),
- structural hardening steels by second phase precipitation.

Interstitial elements, such as carbon and nitrogen play a determining role as a function of their concentration, by:

- stabilizing the austenitic structure (100% austenite steels),
- increasing mechanical properties (ferritic-martensitic steels or steels with high nitrogen concentrations),

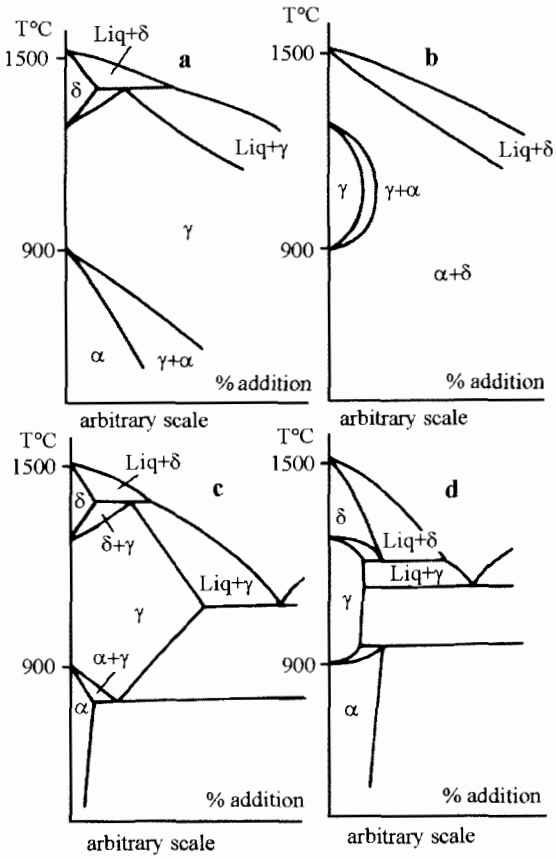

Figure 5.1. Four possibilities of phase diagrams formed with iron and the different added elements, (a): γ field phase, (b): α field phase, (c): limited γ field phase, (d): very limited α, γ and δ field phases, reprinted from ref. [40].

– influencing the corrosion behavior, especially for austenitic steels. On the other hand, the very low concentrations of carbon, nitrogen and oxygen decrease the ductile-brittle transition temperature (case of super-ferritic steels with high chromium concentrations > 20%). In fact, the most important addition justifying the denomination stainless steel is that of chromium. One cannot have a stainless steel if the chromium concentration is above 13%. Austenitic stainless steels are studied in chapters 8–10 and 15, 17, 21.

2. Duplex stainless steel

According to Charles [49,50] and Oltra [51], Duplex stainless steels are regarded as more resistant to stress corrosion, sensitization and pitting than are austenitic grades. These steels

(e.g. S31803 and S32550) with about 28% chromium and 6% nickel contain both austenite and ferrite (~50–50%) phases. They are obtained by work-hardening, followed by annealing at 1050°C and rapid quenching, keeping the temperature at 700–900°C to control the two-phase structure and the element distributions between the austenite and ferrite phases.

The amounts of the γ and α phases are related to the balance between stabilizer elements. These are classed in two families: one made up of elements (Ni, N, Cu) favoring austenitic phase (γ) formation, the others (Cr, Mo) favoring the ferritic phase (α). These stabilizers aid in avoiding localized corrosion of one phase or the other. Hardening precipitates can be produced in the ferrite by precipitation of Cr_2N-type nitrides. The chromium concentration is a fundamental factor for good corrosion resistance but in this steel it is difficult to exceed 23% especially with molybdenum present due to the risks of forming the sigma phase, which can be responsible for embrittlement. The high chromium concentration enables the introduction of the highest nitrogen concentration, since this element increases its solubility in the austenite. Nickel improves the resistance to crevice corrosion and experience shows that optimum improvement is obtained for 50% ferrite concentration. It is difficult to exceed 6% nickel due to the risk of sigma phase formation. Molybdenum additions are very effective in limiting pitting and crevice corrosion. These are limited to 3% in practice due to the risks of sigma phase precipitation. Nitrogen is of greater interest due to its resistance to crevice and pitting corrosion in oxidizing chloride-rich media. This beneficial effect appears to be due to the pH increase resulting from the formation of NH_4^+ at the oxide-alloy interface. Molybdenum and nitrogen are complementary. Molybdenum is segregated in the ferrite while nitrogen is concentrated in the austenite. Combined additions of these two elements simultaneously increase the ferritic and austenitic phases corrosion resistance. Copper improves crevice and pitting resistance by a synergistic effect between it and nitrogen. Duplex stainless steels have been studied in tritium media and results are presented in chapters 18 and 19.

3. Welded Duplex stainless steel

According to Cunat [52], Lippold et al. [53], Van Nassau et al. [54], Bonnefois et al. [55] and Gooch [56], during solidification of welded Duplex, an almost completely ferritic structure is formed (Fig. 5.2).

Further cooling initiates the formation of a secondary austenite phase γ_2, nucleating at the ferritic grain boundaries. The final structure is different from the original pattern due to the transformation and diffusion in the temperature range 300–1300°C. Fusion welding results in significant microstructural alteration in the weld molten and heat-affected zone. The molten zone and region of the heat-affected zone heated above the ferrite solvus temperature transform to ferrite and undergo significant grain growth during welding. Austenite reformation on cooling is a sensitive function of both chemical composition and cooling rate. As a consequence of cooling, the weld molten and heat-affected zones exhibit significantly higher ferrite concentrations than the bare steel. This means also that the element distributions vary. From these considerations, the ferrite-austenite reaction at high temperatures is controlled by nitrogen diffusion, and there may be differences between the nitrogen

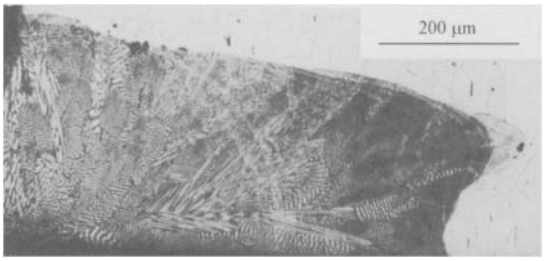

Figure 5.2. Microscopy of weld showing complete ferritic structure.

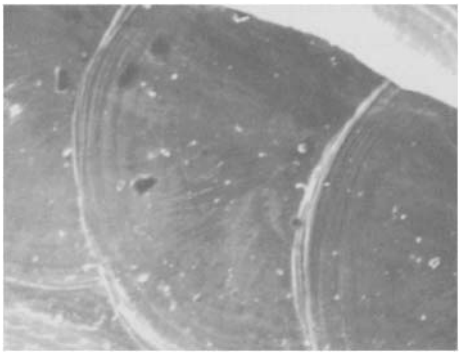

Figure 5.3. Weld made point by point using a laser beam.

concentrations of the two phases on cooling. Nitrogen is an essential alloying element for maximum corrosion resistance and its control during welding is critical. Unfortunately, it is normal with inert gas shielded welding to lose some nitrogen from the weld molten zone. For 0.25% nitrogen in alloy, the proportional nitrogen loss is 22%. To obtain higher nitrogen levels the shielding gas should contain a few percent of nitrogen.

If element distributions and phase balance are respected, weld solidification cracking is not a significant problem. Solidification with ferrite as the primary phase is less susceptible to cracking than are the steels that solidify entirely as austenite. The difference in cracking susceptibility as a function of primary solidification product is generally ascribed to the greater affinity of the ferrite phase for impurity elements. Nevertheless, the corrosion resistance of the weld molten zone frequently tends to be less than that of the Duplex stainless steel due to the modification of phase balance and element distributions. Corrosion has been caused by both general and pitting attack.

For more details for equipment in tritium processing, welds in boilermaking are made using arc welding with 10–20 kJ cm^{-1} energy. Conversely, a laser beam is used for welding expensive parts such as specific valves or flanges (Fig. 5.3). To ensure tritium-tightness in service, these welds must be made taking all precautions to avoid any future leakage of

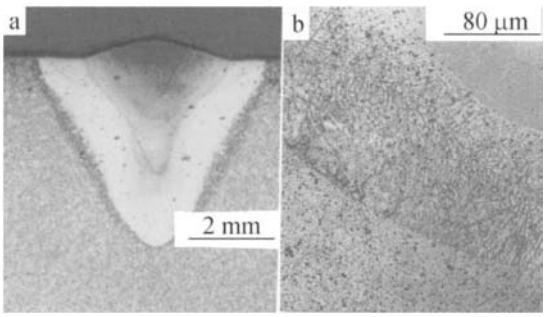

Figure 5.4. (a) Microscopy showing the melted zone, thermally affected zone and sensitized zone, (b) detail of sensitized zone.

tritium to the environment. This is obtained by careful focusing of the beam to ensure good penetration of the flush weld. The parameters include:

- energy deposited, in Joules,
- time of each driving pulse, in milliseconds,
- frequency of each pulse, in Hertz,
- focusing. The beam cross-section is very important and, when chosen well, it allows increasing the specific power which is the quotient of the transported power and the energy deposited on the weld. The greater the diameter of the radiation source, the smaller the diameter of the focused beam impinging on the target,
- focal length. The optical lens must focus the beam on the surface of the steel to be welded. The shorter the focal length, the smaller the diameter of the focused beam impinging on the steel.

These parameters make possible specifying the laser source, in other words, the regular distribution of energy on the target. The object of this section is to indicate optimal values of the beam for obtaining good penetration of the flush weld in depth and width of the welded zone made of stainless steel. The influence of welding parameters is quantified by examining flush welds. For this, polished cross-sections of the weld were prepared and examined microscopically. Such cross-sections showed a major transformation of the microstructure in comparison to the bare metal.

We can see (Fig. 5.4a):

- the central zone corresponding to the melted zone,
- the thermally affected zone,
- the very small width-sensitized zone situated between the thermally affected zone and the bare metal (Fig. 5.4b),
- the bare metal which has not undergone any modification.

In tests, it was observed that the weld penetration decreased and there were more defects with increasing pulse length and frequency. For long pulses, a melted external hemisphere with a furrow is obtained (Fig. 5.5). For short pulses, the thermal inertia favors the weld

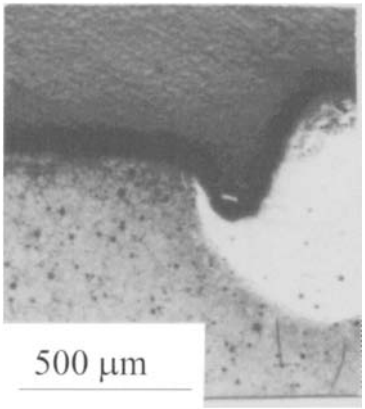

Figure 5.5. Formation of melted external hemisphere with furrow during welding.

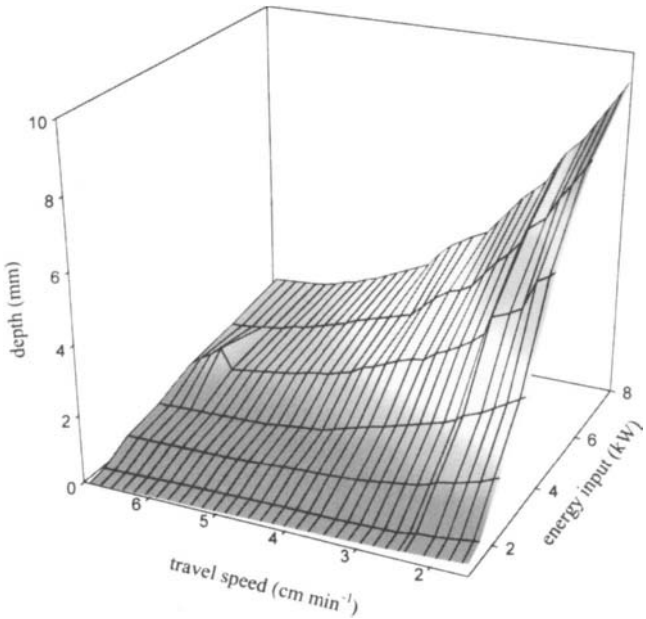

Figure 5.6. Influence of energy and displacement speed of laser on weld depth.

quality. The specific power, depending on time, increases with higher pulse frequencies, which signifies more penetration in the welding process.

The influence of energy is shown in Figs 5.6–5.8. It can be seen from these curves that there is a relationship between the released energy, the beam displacement speed and the

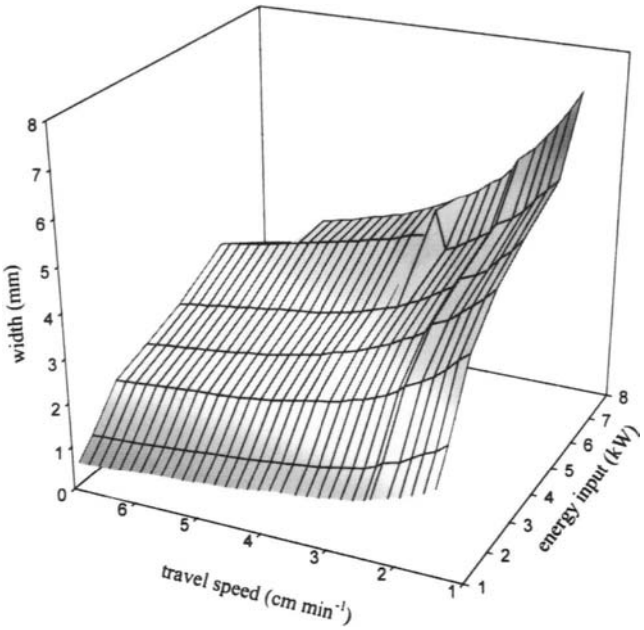

Figure 5.7. Influence of energy and displacement speed of laser on the weld width.

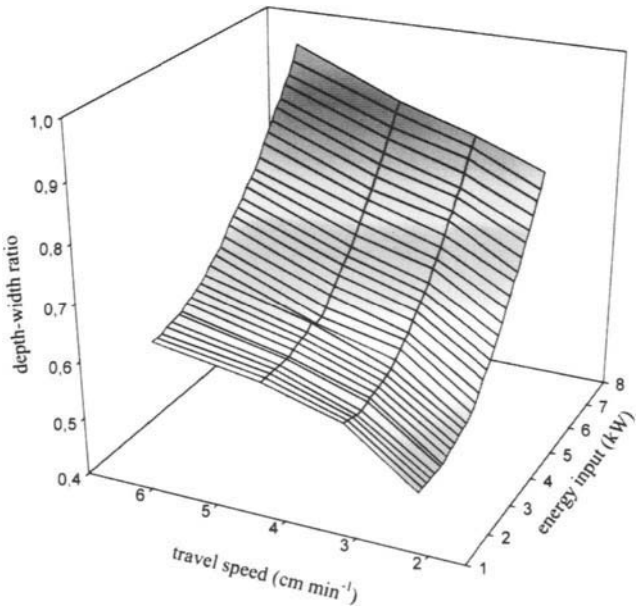

Figure 5.8. Influence of energy and displacement speed of laser on the ratio between weld depth and width.

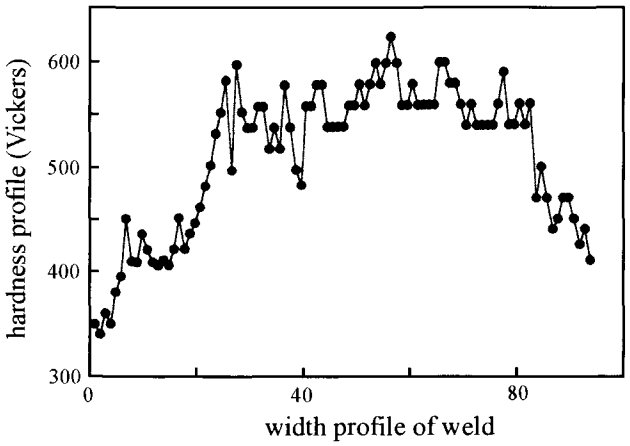

Figure 5.9. Modification of hardness in different zones of a weld.

penetration in welds. Figs 5.6–5.8 can be represented by the relations:

$$\log(d) = 4.6 - 0.5W^{0.5}\log(W) - 57/\bar{v}^{0.5} \tag{5.1}$$

$$\log(w) = 3 - 0.5\log(W) - 22/\bar{v}^{0.5} \tag{5.2}$$

$$d/w = 0.3 + 0.004W^2\log(W) + 0.08\log(\bar{v}) \tag{5.3}$$

where d is the welding depth, w the width, $\bar{v}$ the travel speed and W energy released. The maximum energy, from optimizing the distribution on the welded surface, is 12 J. This good value is obtained by using a nitrogen flow directed to the weld. In this configuration, the maximum penetration is approximately 1.5 mm into bare stainless steel. Beyond this, a flush weld can have surface defects as well as bubbles and cracks. Moreover, the flush weld can be furrowed on its surface over some tenths of millimeters due to the appreciable projections produced during a long pulse (Fig. 5.5). Another advantage of adding nitrogen to the weld is avoiding structural transformation of the thermally affected zone. A decrease in nitrogen contributes to decreasing the hardness. The solution is to use a welding alloy with a higher nitrogen concentration. During welding, this element will diffuse in the weld. The nitrogen distribution in the weld may be inhomogeneous, thus modifying the hardness in the different regions (Fig. 5.9). It is seen that hardness is greater in the melted zone, and lower in the thermally affected and sensitized zones, signifying nitrogen depletion. These curves have enabled specifying an optimal functioning range where the driving pulse time is 5–6 ms, the frequency 4–6 Hz and energy $\leqslant$ 12 J. Any variations of these parameters result in large perturbations. The behavior of welded stainless steels is shown in chapters 9 and 19.

4. Precipitation hardening stainless steels

This subject has been extensively described by Sedriks [28] and Bourrat and Goux [57]. Without going into details, the term hardness in its largest sense evokes four different properties. One sense of the word is the resistance of steel to penetration. The value of this concept of hardness is useful for selecting materials suitable for valves and flanges in vessels for tritium reprocessing. Another definition is that of the elasticity limit of steel. This definition applies to metal assemblies supporting for instance heavy process equipment and piping in the nuclear industry and the metal flanges with valves in tritium processing, that are also important. Corrosion tensile and fatigue resistance tests are interpreted as tests of hardness. These are useful for selecting nuclear facility materials. The precipitation hardening stainless steels are subdivided into martensitic (630 grade and Maraging steels studied in chapters 13 and 14), semi-austenitic and austenitic types. The martensitic types are generally supplied in the martensitic condition and precipitation hardening is achieved by a simple aging treatment. The semi-austenitic types are supplied in the austenitic condition and austenite must be transformed to the martensite phase by heat treatment before precipitation hardening. In the austenitic types, austenite precipitation hardens the phase directly. The precipitation hardening process involves the formation of very fine intermetallic carbides which impede dislocation during deformation, giving rise to higher strength. Precipitation hardening generally results in a slight reduction of corrosion resistance and an increase in susceptibility to hydrogen embrittlement.

In order to obtain a better understanding of the metallurgical changes underlying these heat treatments, it is instructive to refer to the regions of stability of the various phases as a function of carbon concentration (Fig. 4.39). The first step in the heat treatment sequence of precipitation hardening stainless steels is annealing at temperature in the single-phase austenite region. The subsequent step is stabilizing austenite during a relatively rapid cooling. Precipitation hardening is achieved by reheating the austenite to high temperatures at which the fine intermetallic compounds are precipitated. Some minor reversion of the martensite to austenite may also occur. The martensitic precipitation hardening steels are obtained by adjusting the composition. The chromium concentration is in the range of 10–18%, nickel 5–12.5% and carbon plus nitrogen 0.03–0.17%.

Precipitation hardening stainless steels, referred to as semi-austenitic, require an intermediate step to transform the metastable austenite to martensite before precipitation hardening. This can be achieved by tempering at about 750°C to reduce the carbon and chromium concentration of the austenite by the precipitation of carbide. Reduction of dissolved carbon and chromium and cold working can be used to accelerate the transformation of austenite to martensite. Martensite precipitation to high strength levels introduces susceptibility to hydrogen embrittlement.

Precipitation hardening stainless steel surfaces by high pressure is also of interest. Structure can be changed by polygonization as shown in Fig. 5.10 realized with 316 stainless steel exposed to a high force of 10^2 N mm^{-2}. Surface hardening concerns low thicknesses and, austenite is transformed to the martensite phase (Fig. 5.11). Hardening and martensite concentration depend on the shock pressure (Figs 5.12 and 5.13). Laser cladding is also an

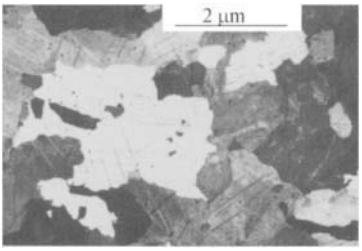

Figure 5.10. Photograph showing polygonization of 316L stainless steel formed by action of a force of 10^2 N mm^{-2}.

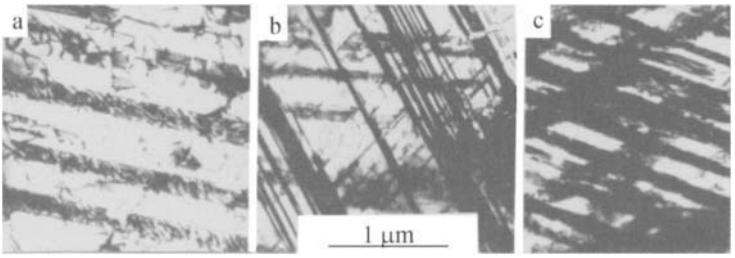

Figure 5.11. Influence of shock pressure in the transformation of austenite to martensite phase at the surface of steel, (a) 1.5×10^7 Pa, (b) 2.5×10^7 Pa, (c) 3.5×10^7 Pa.

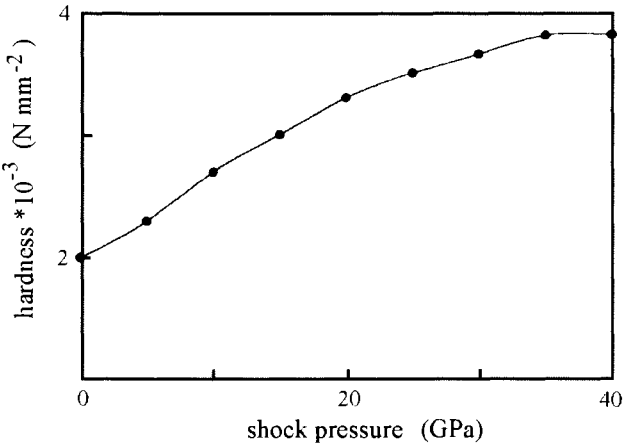

Figure 5.12. Influence of shock pressure on surface hardening of 316L stainless steel.

innovative and attractive manufacturing route for producing a thin hardened surface with martensite (Maraging and 17-4-PH stainless steels). Directly after manufacturing, these

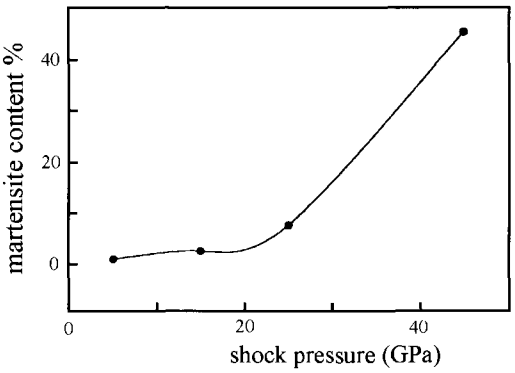

Figure 5.13. Influence of shock on surface martensite concentration of 316L stainless steel.

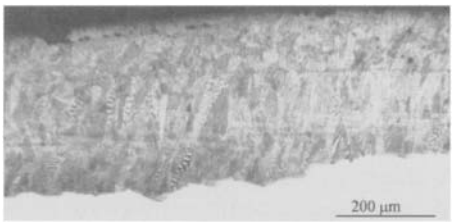

Figure 5.14. Micrograph of a typical coating made using a laser beam.

steels (Fig. 5.14) are sound and metallurgically bonded to the substrate. Their mechanical features are fairly good: hardness: 800 HV, Young's modulus: 210 GPa, yield strength: 1200 MPa. Applications are special valves and tight flanges in tritium processes.

Effects induced by a nanosecond laser pulse on structural changes of Armco-iron were analyzed by Erofeev et al. [58]. Generation of a shock wave with an amplitude of 50–200 GPa in metals is accompanied by a series of phenomena: plasma generation, plastic deformation, phase transitions, martensitic transformation, twinning, spall damage and microcracks formation (Naimark and Belyaev [59]). These processes are the main deformation mechanisms because the plastic relaxation time is sufficiently large compared to the pulse duration. A deformation response to martensitic transformation is linked with the reconstruction of the crystalline lattice. In contrast to martensitic transformation, twinning is a shear process. Statistical thermodynamics were used for the study of characteristic features of the free energy change under martensitic transformation and twinning. A dependence of the free energy on time characterizing the extent of martensitic transformation and of twinning was given by Erofeev et al. [60]. In this publication, macroscopic equations describing the interaction of plastic deformation and structural changes can be obtained in terms of the thermodynamics of irreversible processes. Applications are polymorphic transformations in alloys under high pressure during detonation (Belyaev et al. [61]). The

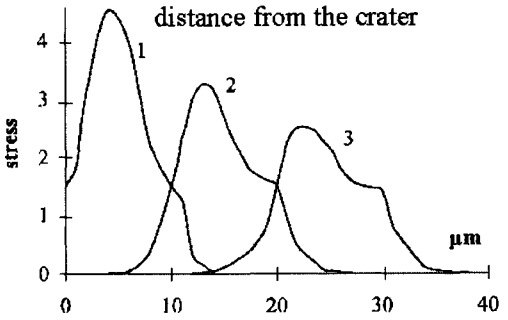

Figure 5.15. Influence of shock wave on kinetics of martensitic transformation, pulse duration: 23 ns, (1): 20 ns, (2): 40 ns, (3): 60 ns, reprinted from ref. [64].

dissipative function has the following form:

$$T,\ P_s = \sigma_{i,k} e^{p}_{i,k} - \frac{\partial F}{\partial s_{i,k}} \frac{\partial s_{i,k}}{\partial t} - \frac{\partial F}{\partial d_{i,k}} \frac{\partial d_{i,k}}{\partial t} \tag{5.4}$$

where T is the temperature, P_s is an entropy production, which is positive for stable phases and negative for unstable phases, $\sigma_{i,k}$ is a macroscopic stress tensor, $e^{p}_{i,k}$ is an irreversible part of a strain rate tensor where the subscript p is used for elastic and plastic parts, F is the free energy correlated to martensitic transformation, $s_{i,k}$ is an independent thermodynamic variable, $d_{k,l}$ describes the deformation reaction of a metal to twinning, and $\frac{\partial F}{\partial s_{i,k}}$ and $\frac{\partial F}{\partial d_{i,k}}$ are thermodynamic forces acting on the system when the values of respective parameters differ from equilibrium values. Equation (5.4) contains a relaxation term for stresses and the parameters of martensitic transformation and twinning. Thus, the changes in the stress state and spatio-temporal evolution of structural changes can be studied for arbitrary loading conditions in terms of boundary values as shown by Silberschmidt et al. [62]. Numerical analysis realized by Silberschmidt [63] shown macroscopic stress develops with shock wave propagation leading to thereby the $\alpha \rightarrow \varepsilon$ transformation. The reverse $\varepsilon \rightarrow \alpha$ transformation in the unloading begins under the lower stress level because of the hysteresis in martensitic transformation.

In Fig. 5.15, the shock wave propagation is accompanied by a sharp decrease in its amplitude and an increase in the distance between the loading and unloading fronts because of the relaxation. These two processes determine specific features of the initiation of structural transformations and their localization. The shock wave propagation is accompanied by the shift of the reversible martensitic transformation. The width of this zone grows with the increase in the distance from the irradiated zone in connection with the change of the shock wave configuration. Results of numerical simulation correlate to experimental data obtained by the microhardness measurements (Romain et al. [65]). A decrease in the wave amplitude to a stress value less than the critical one results in the formation of a localized finite zone of reversible $\alpha \leftrightarrow \varepsilon$ transformation. The initiation of the structural changes

is caused by the overcoming of the threshold stress value in the loading front, and their localization is linked with a rapid decay of the wave amplitude during its propagation.

5. Super alloys

Since all the equipment in the tritium facility is metallic, the selection of super alloys depends not only on their corrosion resistance but also on their hardness: low and high hardness alloys are required. A low hardness component is assembled with a high hardness component to ensure perfect tightness, for example as used in metal seals in valves or flanges where the seal must take the precise shape of the flange surface. It is therefore, important to describe some of the more highly alloyed materials used in this application. These alloys, which are studied in the subsequent chapters, are Inconel, Hastelloy, Elgiloy and Zircaloy. In terms of the Schaeffler diagram, the compositions of Inconel, Hastelloy and Elgiloy alloys lie deep within the region of austenite stability.

Nickel-base alloys (Inconel and Hastelloy) are becoming increasingly important because of their resistance to high temperature and high thermal neutron fluences. More details for materials used in power plants can be obtained in the Reactor Materials Handbook edited by Tipton [66]. These can be manufactured by methods similar to those for stainless steels. The Inconel alloys can be processed by heat-treatment in a vacuum furnace at 1075°C for 24 h followed by a controlled 24 h furnace cooling in argon to ambient temperature. The rate of heating has no appreciable effect; the important factors are the time at temperature and the cooling rate. Proper control of the temperature and the time at temperature to avoid excessive grain growth is necessary. The furnace atmosphere must be free of sulfur and should be slightly reducing. Vacuum melting has proved to be very useful due to the improved metallurgical properties that are obtained. Such a process reduces the loss of hardening elements, reduces the dissolved gas concentration and improves the tensile and rupture strengths, ductility, and fatigue properties. Age hardening increases hardness and strength, and decreases ductility. Relatively low temperature treatment (365–500°C) develops an optimum combination of strength and ductility by dissipating the local stress concentrations. However, if these alloys are subjected to cold work after age hardening, it is advisable to give them a stress-equalizing treatment as a final operation, especially when the intended use involves fatigue or high stresses.

The Inconel alloys have proved to be extremely valuable because of their high tensile strength and high resistance to oxidation and good mechanical properties at elevated temperatures in a radiation field. They have been selected for use in Pressurized Water Reactors (PWR) and other nuclear power plants due to their good stress corrosion cracking and pitting resistance [36,40–47] in pure water at high temperature and pressure. In these reactors, hydrogen gas is added to the primary coolant circuit at a concentration typically between 20 and 50 $cm^3\,kg^{-1}$ water at standard temperature and pressure. This concentration is sufficient to ensure there are no oxidizing species. Consequently, as indicated by Scott [67], corrosion potentials are close to the hydrogen redox potential, as shown by the hydrogen partial pressure and solution pH (Fig. 5.16), avoiding the major problem of intergranular stress corrosion cracking.

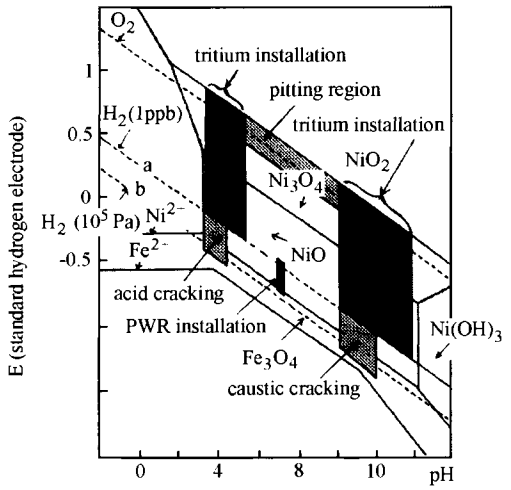

Figure 5.16. Pourbaix diagram showing principal modes of stress cracking corrosion in Inconel 600 for (a): normal water chemistry and (b): the hydrogen-water chemistry, reprinted from ref. [67].

Another additive to the primary circuit of pressurized water reactors is lithium hydroxide for pH control in the range between 7.0 and 7.2. By contrast, in tritium installations, significant concentrations of oxygen and hydrogen peroxide are present as the end products of tritiated water radiolysis and these fix the corrosion potential at significantly more positive values (see chapters 10–12, 17, 19 and 20). More information on cracking corrosion in pressurized water reactors can be obtained in publications of Grabke [68], Kritzer et al. [69], Casales et al. [70], Kritzer et al. [71] and Moshier and Brown [72]. The sensitivity of Inconel 600 to stress corrosion has been clearly shown by slow tensile strength tests, and it has been observed that a diminution of the nickel concentration was beneficial. This lower nickel concentration and a thermal relaxation process result in the easier elimination of residual stresses thus delaying the appearance of cracks and decreasing their propagation. Therefore Inconel 690 has been proposed due to its lower concentration of this element. It is used currently for steam generator tubes and in a number of components in the primary circuit, in particular the bulkhead pipe fitting for nuclear reactors. Inconel alloys are studied in chapters 12 and 16.

The Hastelloy alloys are useful at temperatures up to 1100°C under high stress conditions and in reducing atmospheres. Moreover, these are among the most resistant alloys studied in our laboratory for applications requiring resistance to pitting and crevice corrosion and attack by reducing acids. In fact, the composition of Hastelloy alloys is deep within the region of austenite stability, which ensures freedom from ferrite and strain-induced martensite. However, at elevated temperatures they can precipitate complex intermetallic compounds and carbides at the grain boundaries. Therefore, the concentrations of additives are adjusted to minimize such precipitation during welding or high temperature service. During manufacturing, Hastelloy alloys are subjected to heat-treatment at 1100°C

followed by a full anneal to overcome any hardening or embrittlement that can occur. For critical welds that are exposed to elevated temperatures and corrosive conditions, inert-arc or submerged methods are recommended. After welding, the alloys should be heat treated to develop the best properties. Hastelloy C22 alloy is studied in chapter 22.

Under the severe operating conditions of high-temperature nuclear reactors, cobalt-base alloys are useful [73]. They may be used to contain, protect, and support fissionable material. Their superior elevated-temperature properties compensate to some extent for the high thermal-neutron adsorption of cobalt. At the higher neutron energies in intermediate and fast reactors, the cross-section of cobalt is comparable to that of molybdenum and is a less important consideration. However, a high residual activity is an undesirable characteristic of cobalt-base alloys. At present, cobalt-base alloys are used in reactors in certain wear-resistant components, such as guides for control rods. The melting of cobalt-base alloys is usually done in relatively small batches and induction and electric furnaces are generally used. The melting practices vary with each manufacturer and no descriptions of these practices have been published. Vacuum melting seems to aid the improvement of ductility over that of air-melted materials. Higher ductility is probably a result of the reduction of impurities and closer control of composition. Cobalt-base alloys are strengthened by duplex heat treatment. The material is first given a solution treatment to eliminate work hardening, and to obtain the desired grain structure. This treatment usually consists of heating in the range 1010 to 1320°C followed by rapid cooling. This is followed by age hardening in order to develop the optimal properties. The aging temperatures and times vary with the hardening agent. Carbon and beryllium, which are unintentional impurities, could be responsible for corrosion in grain boundaries, but their low levels cannot lead to any specific localized corrosion. The substances alloyed with molybdenum are hardened in the range from 470 to 560°C. Welding of cobalt-base alloys presents special problems because of the inherent characteristics of these metals. However, with care, these alloys can be successfully welded. The procedure is similar to that for welding austenitic stainless steels. Rapid speed and minimum current consistent with the size of the part should be used to avoid overheating and formation of a large heat-affected zone. Hastelloy electrodes have been successfully used in the welding of cobalt-base alloys. The following methods can be used: resistance welding, submerged arc, metallic arc, hydrogen and inert arc. In this work, we have studied the type R30003 cobalt-base alloy in chapter 6. By cold work hardening, the R30003 face-centered cubic matrix, like that of austenite, is partially transformed to the martensite ε phase. By returning to temperatures between 425 and 650°C, the work-hardened alloy is further greatly hardened by precipitation of the Co_3Mo phase. The mechanical strengths are then sufficiently increased for uses such as membrane valves. The alloys in this family are generally known by their brand name; the alloy studied here is Elgiloy steel.

According to Béranger and Schmuck [75,76], zirconium has two systems of crystallization (α and β phases) depending on temperature treatment (Fig. 5.17). At ambient temperature, the structure is essentially hexagonal alpha. The transition temperature is 920°C. Over this temperature, the structure becomes entirely face-cubic centered beta. The change from the hexagonal α to the face-cubic centered β structure is possible by a simple tem-

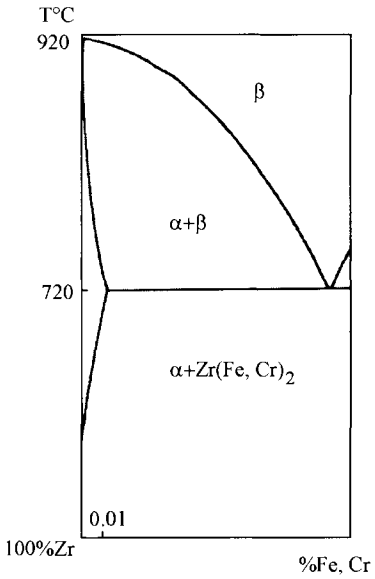

Figure 5.17. Zirconium phase diagram, reprinted from ref. [76].

perature excursion. The presence of iron, chromium and oxygen modifies the transition temperature and produces an intermediate $\alpha + \beta$ phase between 800°C and the transition temperature. Moreover, iron and chromium lead to an eutectoid reaction which decomposes the β phase. On cooling below 800°C, these metals can precipitate in the form of intermetallic grains distributed in zirconium. Their presence and morphology depend on the preliminary thermo-mechanical process and the cooling rate. Dissolution of these elements is necessary and realized during the processing by thermal treatment at 1050°C followed by quenching. In this case, their solubilities are about 100 ppm. Addition of tin is useful for stabilizing the α phase and increasing the temperature of the $\alpha + \beta$ phase. The passage in the $\alpha + \beta$ phase slightly increases the grain size of zirconium and makes possible segregation of intermetallic precipitates which become the grain boundaries in the new structure. α grains are no longer hexagonal but needle-shaped. Moreover, slow cooling in the $\alpha + \beta$ phase leads to formation of α plates while the residual β phase is enriched in iron and chromium. The return to the initial structure can be obtained by post- thermal treatments for recrystallization and relaxation thus limiting deformations and stresses in the α phase. In practice, zirconium is reheated between 500 and 600°C to release stresses, then stepped at 700°C to recrystallize grains- and the last step is at 800°C to redistribute precipitates. Zirconium has a great affinity for oxygen, nitrogen and hydrogen which give not only well-defined compounds, but also interstitial solids. The solubility of hydrogen in the form of hydrides is extremely low at ambient temperature. Rapid cooling leads to finely dispersed globular hydrides. If cooling is very slow, these have higher concentrations and precipitate in the form of plates. Embrittlement is expected and will depend on their quan-

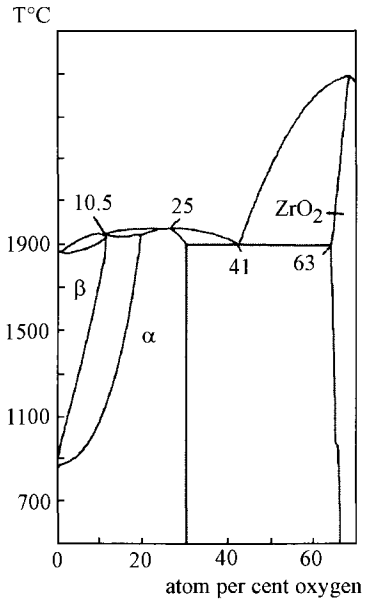

Figure 5.18. Oxygen-zirconium equilibrium diagram showing the different allotropic domains, reprinted from ref. [75].

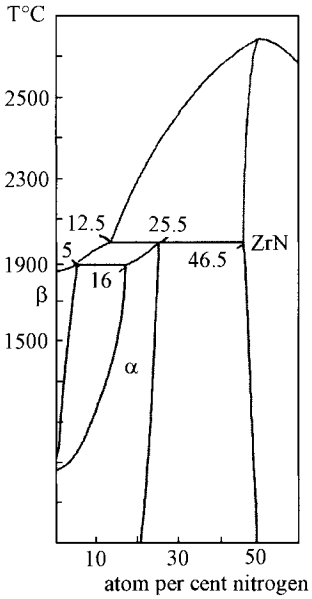

Figure 5.19. Hydrogen-zirconium equilibrium diagram showing the different allotropic domains, reprinted from ref. [75].

tity, morphology and orientation. In examining the two phases of zirconium, it can be seen that the solubilities of oxygen and nitrogen are higher (3.5% and 6.7% wt respectively) for the hexagonal α phase than for the face-centered cubical β phase (Figs 5.18 and 5.19).

The diameters of octahedral and tetrahedral sites are respectively 67 and 37 Å. Therefore, in the hexagonal α structure, octahedral sites will be essentially occupied. Nitrogen and oxygen inserted in zirconium increase the crystalline parameter by deformation of the lattice up to their solubility limits. The hardening and corroding behavior of nitrogen is greater than that of oxygen. To avoid hardening and embrittlement, a low concentration (100 ppm) is introduced during formation of the mechanical characteristics. These different processes are systematically used during the manufacture of zirconium alloys for nuclear applications to guarantee good corrosion resistance. Zirconium and its alloys are used to clad nuclear fuels or to join the nuclear reactor core parts. These applications are possible because zirconium has a low capture cross-section for thermal neutrons. Moreover, these alloys have good mechanical resistance to creep at low temperatures and good corrosion resistance in acidic and chloride media. Consequently, Zircaloy alloys are used in equipment for reprocessing nuclear fuels. Moreover, they emerge as a new material for the chemical industry due to their behavior in corrosive media [74], where usual materials are unusable or have a short lifetime. Zircaloy-4 alloy is studied in chapter 20.

6. Cr-Ni alloy deposit

In water reprocessing, tritiated water can be concentrated by isotopic distillation. To decrease the distillation column height while retaining the same efficiency, the column must be packed. Organic polymer rings cannot, of course, be used because of the risk of producing fluoride or chloride ions from radiolysis by β^- particles. Small, spiral-shaped, 316 stainless steel grids with an irregular surface, to increase the efficiency of the column packing, have replaced these rings. Grids with and without a Ni-Cr deposit are used.

Data on the nickel-chromium alloy can be found in the Reactor Materials Handbook edited by Tipton [77] and in publications of Maykuth [78], Armanet et al. [79] and [80], Moreau and Benard [81], Jallerat et al. [82], Metikos-Hukovic et al. [83], Hampikian [84], Lowell [85], Pivin et al. [86] and Lacombe et al. [87]. From these authors, the corrosion resistance of this alloy depends on its chromium concentration and heat treatment (temperature and time). To understand the composition-structure-temperature relationships governing the precipitation of phases, it is very instructive to refer to the nickel-chromium equilibrium diagram [88] in Fig. 5.20.

According to this diagram, 45–70% Cr concentration leads to formation of the $\beta + \gamma$ phase at higher temperature. Below 1150°C, in the medium range of chromium concentrations, the $\alpha + \gamma$ phase with possible embrittlement is expected. Low and high chromium concentrations are respectively enabled by the growth of γ and β phases with carbide precipitation for the latter. Moreover, studies by Abrahamson and Grant [89] indicate that the γ phase can be stabilized at a lower temperature by the addition of 0.3–0.5 wt% nitrogen, and that addition of this element generally improves the properties of the Cr-Ni alloy.

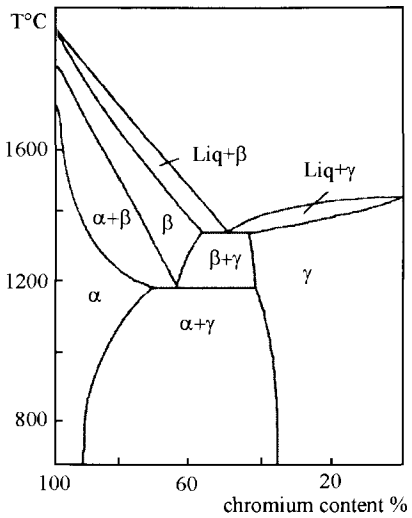

Figure 5.20. Nickel-chromium phase diagram, reprinted from ref. [88].

Therefore, to avoid the phenomena of carbide precipitation, embrittlement and destabilization, an alloy containing about 20% of Cr and 0.4% of nitrogen was selected for packing the isotopic distillation column. Finally, to improve corrosion resistance, during cooling the oxide surface layer is formed in three time-dependent steps. The first step corresponds to the germination of NiO that covers the external surface of alloy grains. Then there is Cr_2O_3 germination under the external NiO surface layer leading to a solid-state reaction to form an intermediate nickel-chromite sublayer ($NiCr_2O_4$) with a spinel structure incorporated in NiO. Finally, there is a third layer enriched in Cr_2O_3 at the base of the alloy. The behavior of Cr-Ni alloy deposits is studied in chapter 15.

7. Titanium nitride deposit

To avoid abrasion corrosion, the equipment must be made of stainless steel covered by hard inorganic materials. This surface may have a titanium nitride deposit to increase hardness. Titanium nitride is a very interesting material, but previous work by Elsener et al. [90] and [91] showed the presence of defects such as pores, pinholes and columnar structures formed during the deposition process, which could favor substrate localized corrosion. Therefore, TiN deposits should be used only with a substrate that passivates easily. TiN can be deposited by sputtering titanium and nitrogen with a magnetron in an argon-nitrogen mixture. These deposition parameters are very critical because they can modify the degree of crystallization and defects. The formation of defects would be more difficult for a dense TiN deposit. Finally, thermodynamic studies indicate that TiN is not very stable in water and can be oxidized to a more stable compound $Ti(OH)_3$ and further to TiO_2, H_2O

with hydrogen evolution. Titanium oxide partially covers the surface up to the transpassive potentials, according to Strehblow et al. [92]. In addition, a noble electrochemical behavior at potentials below the passive potentials has been explained by the presence of a nitrogen-ammonia enriched layer. TiN deposits are used in tritium installations to avoid abrasive corrosion. Their behavior is studied in chapter 14.

8. Palladium and palladium-silver alloy

The hydrogen-palladium system is one of the most studied and best documented metal-hydrogen systems [14] and [93]. This should be attributed mainly to the peculiar characteristics of hydrogen-palladium interactions and to the widespread use of palladium in hydrogen technology. This metal is the only one in the entire periodic system in which all filled electron levels (4s, 4p, 4d) correspond, from the standpoint of the number of electrons, to elements with completely filled shells, while there are no electrons in the 5s and 5p shells. Silver, which is the closest analog of palladium, has one 5s electron. As a result, palladium should show special characteristics in its behavior towards tritium, i.e. a very high sorption capacity combined with a high permeability for triton even at room temperature and relatively low pressures. Evidence exists for the protonized state in palladium. The first step is the chemisorption of hydrogen (or tritium) on the palladium surface. Most authors [94] agree that the chemisorption of hydrogen on palladium involves negligible activation energy. Indeed, palladium is frequently deposited on other metals to serve as a surface film on which surface effects are eliminated, to study the behavior of those metals in hydrogen [95]. The transition of the hydrogen from a chemisorbed to an absorbed state in palladium requires an activation energy that has been variously estimated at between 32 and 42 kJ/mole. As a result of the above transition, the chemisorption of tritium on palladium is irreversible, in particular at high temperatures. The high sorption capacity of palladium for hydrogen (and tritium) and the high diffusion coefficient of hydrogen have led to many practical uses, e.g. palladium (and palladium-alloy) membranes are used to purify the gases by diffusion and palladium is frequently used as a getter for hydrogen and tritium. Also the isotopic effects in the sorption and diffusion of hydrogen have led to the use of palladium in hydrogen isotope separation (see subsections 3.1.2 and 3.1.3).

The maximum amount of tritium in palladium depends on the purity of the metal and hydrogenation conditions. However, it seems that palladium is able to absorb as much as 2800 volumes of tritium per volume of metal, i.e. that the maximum absorption corresponds to the formation of $Pd^3H_{2.2}$. Under normal experimental conditions, the amount of tritium absorbed by palladium upon cathodic charging in electrolytes should correspond to about Pd^3H_2 and the amount absorbed from the gas under high pressures corresponds to Pd^3H. When palladium absorbs tritium at moderate temperatures, a tritium-rich phase, the so-called β phase, is formed at first, near the palladium surface [93]. The surface tritium then diffuses into the metal, forming a solid solution in the α phase. As a result of this diffusion, the β phase reverts to the lower tritium concentration α phase, until the tritium concentration in the bulk increases to a level sufficient for the formation of the β phase in

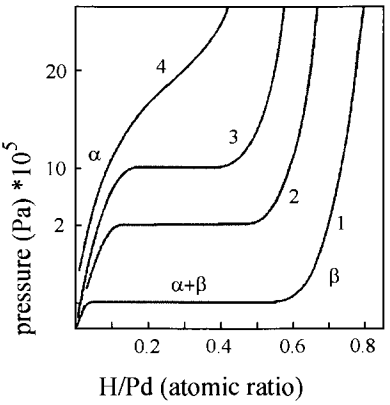

Figure 5.21. Hydrogen–palladium equilibrium diagram, 1: 30°C, 2: 160°C, 3: 230°C, 4: 295°C, reprinted from ref. [93].

the bulk of the metal. At low temperatures, the maximum tritium solubility in the α phase corresponds to $Pd^3H_{0.05}$. At temperatures above the so-called critical temperature (325°C), there is only one phase (Fig. 5.21).

This temperature depends on tritium pressure. Electron microscopy studies [96] of the alpha-to-beta (and reverse) phase transformations in hydrogenated palladium have revealed that at low temperature the formation of the third phase involved incoherent precipitation. Although the α and β phases coexist, they do not mix, i.e. the α phase occupies all the volume in which the tritium concentration is below a certain limit, and the β phase occupies the volume with the higher tritium concentration. The tritium atoms occupy octahedral interstices in the lattice, and completely fill these when a stoichiometric tritium concentration is reached. In the face centered cubic lattice the interstices are of two types, namely, tetrahedral and octahedral in which an interstitial tritium atom would have four and six nearest palladium neighbors, respectively (Fig. 5.22). There is a partial migration of some of the tritium from octahedral into tetrahedral sites. Moreover, the β phase structure should have numerous vacancies in the metal lattice. The face centered cubic structure of palladium remains unchanged on tritium absorption, and the lattice parameter does not change within the range of tritium concentrations corresponding to the existence of the α phase. However, the parameter value increases approximately by 3% at concentrations corresponding to the formation of the β phase. There are local contractions for palladium atoms into vacancies during absorption.

Maeland and Gibb [97] have suggested that the gradual apparent increase of the β phase lattice parameter with increasing hydrogen concentration corresponds to the gradual expansion of the average lattice constant towards a theoretical limit. This limit corresponds to the unit stoichiometric ratio of hydrogen to palladium and which approximately represents the actual bond distances around an occupied interstice at any value of hydrogen concentration. It should be noted that absorption leads to a large expansion of palladium by about 3% in length, and 10% in volume. This leads to the embrittlement of the palladium in the course

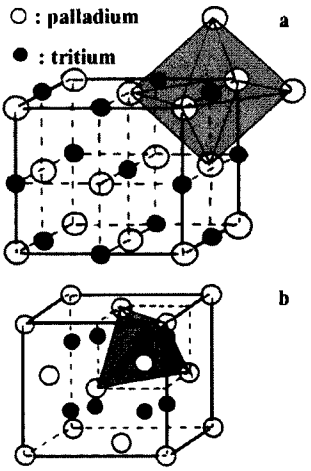

Figure 5.22. Face centered cubic structure of palladium, (a): octahedral site for tritium, (b): tetrahedral site for tritium.

of cycles of hydrogen charging and can result in linear transgranular cracks. On reversing the sequence and removing tritium from the specimen, there is an apparent reversibility of the lattice constant for the pure β phase. It has been argued by Lewis [93] that with hydrogen the nearest neighbor palladium atoms are likely to retract to the previous position which should be little different. Prolonged discharge of tritium on a palladium electrode has been shown to produce unusual features that are different from those obtained in a single absorption run. Such features should be attributed to the irreversible phase changes and to inhomogeneous plastic deformation during the tritium absorption and desorption runs.

Since repeated tritium absorption followed by desorption might result in an accumulation of mechanical stresses generating miscellaneous structural defects, measurements of the electrode potential, expansion, and electrical resistance under well-controlled absorption should be of interest to evaluate the influence of absorption/desorption repetitions on the solid-state properties of palladium. A good understanding of these can be found in the study by Numata and Ohno [98]. Electrochemical behavior, expansion and resistance of palladium electrodes have been measured using hydrogen charging. The measurements were made with respect to the microstructural changes induced by hydrogen ingress in the palladium electrode. It was concluded that in the single α phase the potential obeys the Nernst equation and exhibits a constant value within the $\alpha + \beta$ coexistence region. At the first absorption through the β phase, the electrode potential shifted to a less noble direction accompanied by an increase in expansion which suggests non-equilibrium PdH_{2-x} precipitation followed by conversion to the β phase and void formation. The electrical resistance increased with the H/Pd ratio which was kept constant at 2. The pulse absorption mode showed non-Nernstian behavior. The slopes of the expansion as a function of H/Pd ratio increased progressively, and converged into one line after the fifth pulse corresponding to

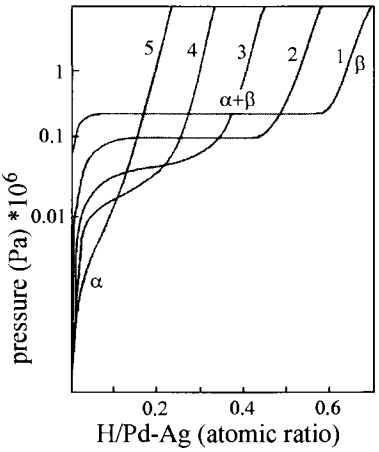

Figure 5.23. Hydrogen–palladium–silver equilibrium diagram, 1: Pd, 2: 10%Ag-Pd, 3: 20%Ag-Pd, 4: 30%Ag-Pd, 5: 40%Ag-Pd, reprinted from ref. [93].

the limit of the expanded lattice before cracks. Moreover, the $\alpha + \beta$ phase coexistence was enlarged corresponding to high-density defect areas surrounding voids.

In the case of palladium powder, the structure upon hydrogenation directly depends on the tritium pressure. The α phase is found at relatively low pressures and the beta phase is formed at higher pressures. Such behavior is observed both when the pressure is gradually increased and when it is decreased with some hysteresis.

The presence of alloying elements in palladium greatly affects both the solubility and diffusion of tritium in the metal. The effects are irregular and depend on the nature of the additive, its concentration and temperature. Silver is widely used as an alloying element. At low concentrations (up to 0.2%) silver has little effect on the diffusion coefficient measured in electrolytic charging. A sharp decrease, however, occurs at higher Ag concentrations, and the diffusion coefficient of tritium in 60% Ag-Pd is only 2×10^{-10} cm^2 s^{-1}, compared with over 10^{-7} cm^2 s^{-1} for pure palladium. Moreover, on increasing the silver concentration [99], the tritium concentration in the β phase exhibits a gradual decrease (Fig. 5.23) which is concurrent with a gradual reduction in the lattice parameters. The difference is that the variation of the lattice constant is much smaller in the phase transitions. The palladium-silver alloy should therefore be less sensitive to embrittlement. Palladium and palladium-silver alloys are studied in chapter 23.

After having reviewed the situation for nuclear processes, materials and corrosion in other parts of the world and in our installations, let us move on to the next section of the book. The following chapters treat the experimental study of corrosion, carried out in our laboratory by electrochemical methods including the effects of the various chemical species observed in tritiated water. Overall, this study concerns the effects of tritium (chapters 7–9) and the energy released (chapter 7) by the β^- particles, radiolytic hydrogen peroxide (chapters 10–12, 17, 19 and 20), chlorides, fluorides (chapters 13–17, and 19–21),

carbonates (chapters 18 and 19), nitrates (chapter 20) and the pH (chapters 11, 13...) on the different stainless steels and superalloys. These radiolytic species will be considered separately and grouped to ascertain their mutual influence on corrosion.

Part III

SCIENTIFIC ASPECTS OF CORROSION

This Page Intentionally Left Blank

Chapter 6

STABILITY OF TRITIATED OXIDE LAYER

1. Introduction

To understand better the properties of tritiated oxide layers a comparative study was carried out with ^3H_2O and H_2O. There was particular emphasis on the influence of time on the stability of contaminated passive oxide layers. Due to equipment lifetimes, time is an important parameter. As with water, the β^- particle energy ionizes and excites metal oxides. The decomposition reaction can be:

$$Me(O^3H)_2 + \beta^- \rightarrow Me(^3HO_2)_n^* + (2-n)\,{}^3HO_2^* \rightarrow {}^3H_2O_2 + O^* \qquad (6.1)$$

This equation implies that excited $Me(^3HO_2)_n^*$ and $Me(O^3H)_2$ are inserted in the oxide (Fig. 6.1) and diffuse by vacancies with oxidizing radiolytic species formation whose concentration is time dependent.

To suppress any uncertainties, the study was carried out with tritiated metal oxide with a tritium concentration of 0.5 TBq cm^{-3}. At this concentration, the tritiated hydroxide produces sufficient excited radiolytic species diffusing into the oxide. The tests carried out with tritiated water were made after decomposition of the radiolytic hydrogen peroxide and dissolved oxygen in tritiated water to avoid their effects on electrochemical measurements. The R30003 alloy was selected because of its nuclear corrosion resistance and its properties as an elastic membrane in all metal valves. Its composition is given in Table 6.1. This Co based-alloy is produced by melting followed by vacuum arc remelting to provide optimum control of the chemistry and desired ingot solidification.

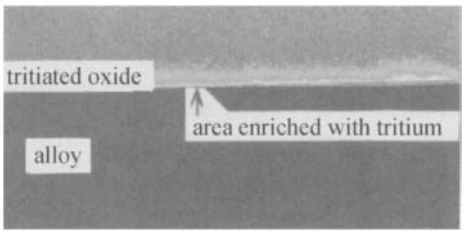

Figure 6.1. Examinations made with autoradiography showing presence of tritium in oxide.

Table 6.1. Composition of Elgiloy

Elements	Co	Ni	Cr	Fe	Mn	Mo
Wt%	40	15	20	16	2	7

2. Experimental results

2.1. Anodic polarization curves

Anodic polarization curves obtained at a low scan rate are shown in Fig. 6.2.

In these curves, the tritium evolution potential is more negative than that of hydrogen. The corrosion potential is shifted towards more negative values with ^3H_2O; this modifies the passive oxide layer potential domain. At the corrosion potential, corrosion should occur at different sites according to the following reactions,
cathodic sites:

$$^3H_2O + e^- \rightarrow O^3H^- + {}^3H_{ads} \tag{6.2}$$

$$2\,{}^3H_{ads} \rightarrow 2^3H \tag{6.3}$$

The cathodic current in the above reactions is:

$$i_c = -k_c F[^3H_2O]^{\nu_{red}} \exp -FE/2RT \tag{6.4}$$

anodic sites:

$$Me + 2O^3H^- \rightarrow Me(O^3H)_{2ads} + 2e^- \tag{6.5}$$

$$Me(O^3H)_{2ads} + O^3H^- \rightarrow MeOO^3H + {}^3H_2O \tag{6.6}$$

These reactions lead to tritiated oxide layer formation. The anodic current is:

$$i_a = 2k_a F[O^3H^-]^{\nu_{ox}} \exp FE/RT \tag{6.7}$$

where the different k are the anodic and cathodic reaction rate constants, ν the electrochemical reaction orders, Me represents the alloy and $MeOO^3H$ is the 'wet' tritiated oxide together with 'dry' Me_2O_3 formed on R30003 alloy. The size and characteristics of the oxide layer change with the potential and with other factors such as time and radioactive medium concentration in the oxide. In these curves, the passive currents are higher with ^3H_2O. The explanation for this could be that tritiated water leads to more ionized 'wet' tritiated metal oxide and less insulating 'dry' oxide. These equations show that O^3H^- are consumed in anodic sites and produced in cathodic sites resulting in local pH modifications as shown in previous work in our laboratories [100].

Equations (6.5) and (6.6) contribute to the passivity by means of $Me(O^3H)_{2ads}$. The corrosion potential of this system is the potential at which both the cathodic and

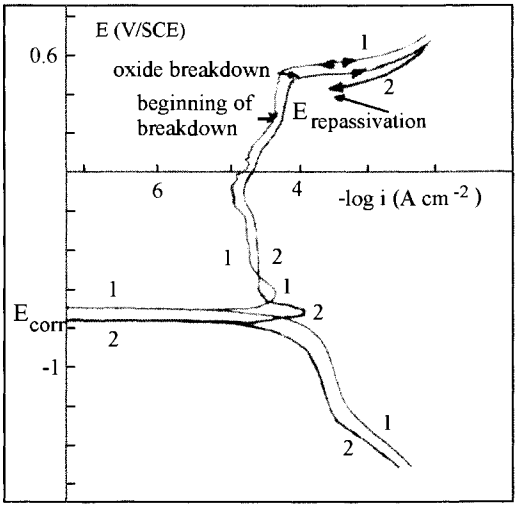

Figure 6.2. Polarization curves with ^3H_2O and H_2O, ω: 2000 rpm, v: 5 mV s^{-1}, pH 10, 1: H_2O, 2: ^3H_2O.

anodic currents are equal. From these equations, E_{corr} is assumed to be in alkaline medium:

$$E_{corr} = \frac{1.5RT}{F}\left(\log \frac{k_c}{k_a}[O^3H^-]\right)_{^3H_2O} \tag{6.8}$$

From eq. (6.8), the logarithm of the rate constants between ^3H_2O and H_2O gives the equation:

$$\partial E_{corr} = \frac{1.5RT}{F}\partial\left(\log \frac{k_c}{k_a}\right)_{H_2O,\,^3H_2O} \tag{6.9}$$

It can be seen from the experimental values that the rate constants and thus the aqueous radioactive medium modify the corrosion potential. The cathodic and anodic experimental Tafel slopes (Fig. 6.3) are, respectively, approximately -110 and 55 mV per decade and are consistent with eqs (6.4) and (6.7).

As in eq. (6.8), the corrosion current is:

$$i_{corr} = \left\{2k_c^{0.66}k_a^{0.33}F(O^3H^-)^{0.5}\right\}_{^3H_2O} \tag{6.10}$$

and:

$$\partial \log i_{corr} = 0.33\left(\partial\left(\log k_a k_c^2\right) + 0.5(\log O^3H^-)_{\Delta pK}\right)_{H_2O,\,^3H_2O} \tag{6.11}$$

The corrosion current, i_{corr}, depends on rate constants and the aqueous medium; it can be seen from Fig. 6.3 that the value of i_{corr} is higher with ^3H_2O. The experimental values

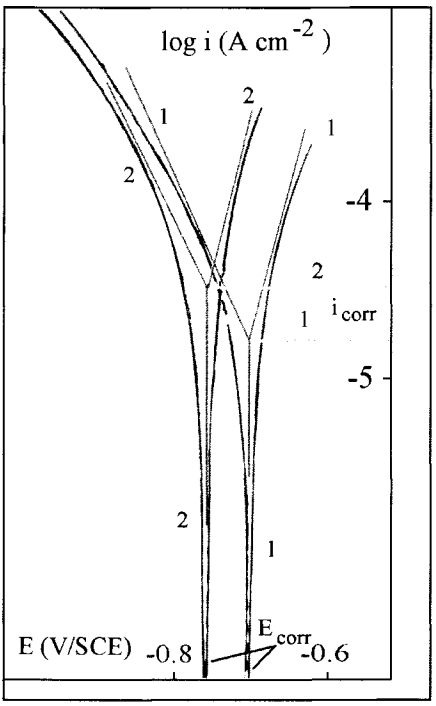

Figure 6.3. Determination of Tafel parameters, $1-\alpha = -110$ mV, $\alpha = 50$ mV, E_{corr}: 1: -0.7 V, 2: -0.75 V/SCE, i_{corr}: 1: 2×10^{-5} A cm^{-2}, 2: 4×10^{-5} A cm^{-2}.

given in Fig. 6.3 are consistent with eqs (6.9) and (6.11) and show smaller protection with tritiated water.

In the transpassivity it is observed that the anodic current increases more with ^3H_2O than with H_2O signifying that localized corrosion is easier. In the backward scans, it is seen that the anodic current increases and is higher than that in the forward scan for ^3H_2O, and returns to ~ 100 mV below the breakdown potential. According to the hysteresis shape, localized corrosion continues to initiate and grow after the scan reversal. As shown by the positive hysteresis shape in the backward scan, with ^3H_2O, the repassivity potential decreases more rapidly than it does with H_2O, which makes it easier for sublayer corrosion to occur. These different results imply that tritiated water does not provide better protection under these conditions, and the locally corroded area must increase. In the current–time curves (Fig. 6.4) for different potentials, the anodic current fluctuations obtained with tritiated water result from the occurrence of breakdowns and repassivity alternatively in potentials close to localized corrosion.

Tracing polarization curves reveals the active behavior modifications. At the corrosion potential and in the active region, the net current is equal to the sum of two currents with

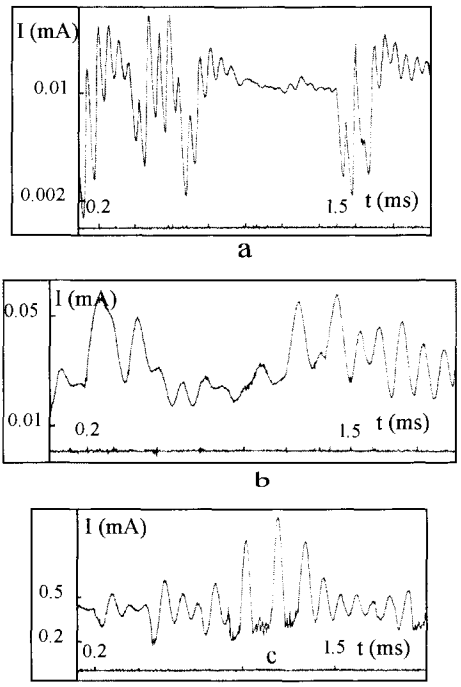

Figure 6.4. Current–time curves at different potentials, ω: 2000 rpm, pH 10, (a): −0.4 V, (b): 0.2 V, (c): 0.5 V/SCE, basis line: current fluctuations in prepassivity and passivity with H_2O.

opposite signs: that due to R30003 alloy oxidation and that due to ^3H_2O reduction. The explanation of active behavior modifications between H_2O and ^3H_2O is helped by using the diagrams in Fig. 6.5 which show several characteristic changes depending on tritiated and light water in the potential–pH equilibrium relationship [101]. The straight line for tritium evolution is below that of hydrogen, the corrosion potential of ^3H_2O should be lower than that of H_2O. A higher active peak in the alkaline corrosion region for ^3H_2O with the formation of $^3HMeO_2^-$ is seen. Part of this region can be hidden by the light water reduction current which is at a more positive potential. Higher potentials than that of active corrosion correspond to the passive region with the formation of passive oxide corresponding to Me_2O_3 and Me_3O_4. The explanation of time-dependent current instabilities obtained in Fig. 6.4 is helped by using the diagram which shows several characteristic changes depending on ^3H_2O and H_2O in the potential–pH equilibrium relationship. With H_2O, complete passivity for R30003 alloy is obtained, whereas with ^3H_2O, there is incomplete passivity and the alloy is more corroded.

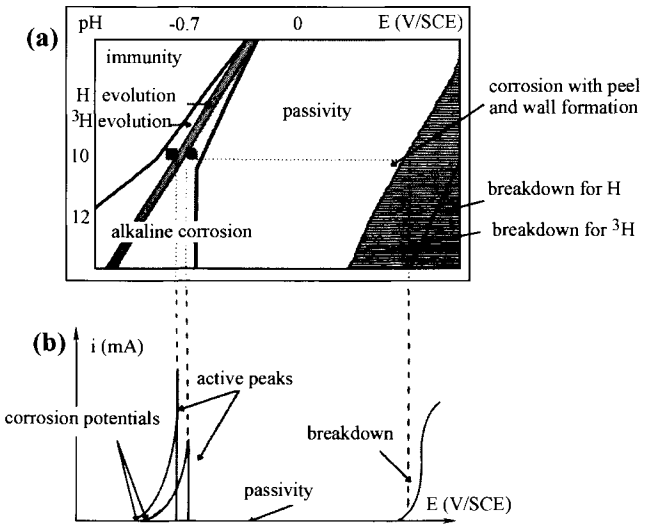

Figure 6.5. Diagram showing R30003 alloy behavior in tritiated water (a), and polarization curve (b), experimental conditions for alkaline corrosion (oxide instability), complete and incomplete passivity (breakdown).

2.2. *Cyclic voltammetry*

The use of relatively fast scan rates is unusual in corrosion testing, and the justification for this technique is given by Morris and Scarberry [102]. With the rapid-scan curves, it is easier to find current fluctuations and therefore oxide layer modifications where the slow-scan curves suggest they might exist. The voltammograms obtained with tritiated water and for high scan rate after applying a passive-transpassive potential for different times are shown in Fig. 6.6.

Evidently the time and therefore the presence of ^3H_2O and O^3H^- diffusion into oxide significantly affect the R30003 alloy oxidation process. On increasing the potential in the forward scan, a prepassive peak is seen. The current values change depending on the time when the passive-transpassive potential is applied. It should be noted that the passive region is followed by a transpassive peak corresponding to oxide layer breakdown and dissolution. The current increases quickly in this region. The breakdown reaction is:

$$MeO^3H + 2\,^3H_2O \rightarrow MeO_4^{2-} + 5\,^3H^+ + 3e^- \qquad (6.12)$$

In this equation, clearly the passive oxide participates in the production of MeO_4^{2-}. Evidently, the presence of ^3H_2O significantly affects R30003 alloy oxidation processes and leads to surface acidification whose effect on corrosion can be inhibited by stirring [100].

The voltammograms exhibit the following characteristics: (a) in the forward scan, the anodic curves intersect the potential axis at more negative potentials due to the lack of

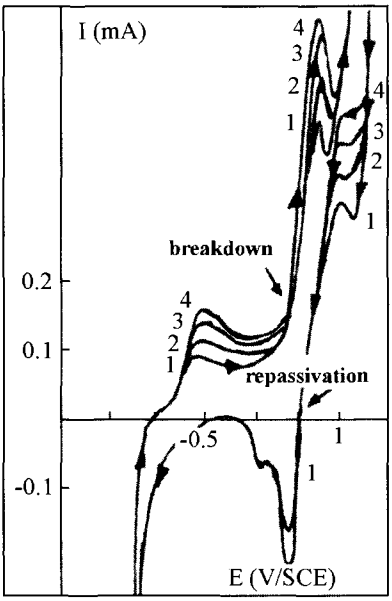

Figure 6.6. Voltammetric curves with ^3H_2O at different times for a passive-transpassive potential of 0.5 V/SCE before the scans, ω: 2000 rpm, v: 200 mV s^{-1}, pH 10, 1: 1 min, 2: 2 min, 3: 3 min, 4: 4 min.

$^3H_2O_2$, as shown in the next chapters, (b) a higher active peak is obtained for a longer pre-polarization time with ^3H_2O, (c) in the passive region, the anodic current increases with the pre-polarization time. It would appear that the passive oxide layer is less protective, (d) in the transpassive region, the anodic peak is higher on applying a long pre-polarization time. The interpretation could be that the oxide breakdown current increases with time. The propensity for localized corrosion by sublayer corrosion can be determined from the difference between the breakdown potential and the repassivation potential and the hysteresis shape in the voltammograms. As the current in the backward scan is greater than that of the forward portion at a low scan rate (Fig. 6.2) and smaller at a high scan rate (Fig. 6.7), R30003 alloy is predicted to be susceptible to localized corrosion. Thus, voltammograms and polarization curves show that there is modification of the passive oxide layer by ^3H_2O.

An increase in the scan rate leads to increasing the passive and active currents in the forward scan (Fig. 6.7) signifying these are related to the ionic species present at the oxide layer surface. In the reverse scan, an increase in the scan rate decreases the transpassive currents signifying these are related to oxide sublayers. At a low scan rate, tritiated water has the time to be adsorbed, then tritium diffuses in the wet oxide layer by O^3H^- and vacancies leading to corrosion in the sublayer as shown subsequently by electrochemical impedance spectroscopy and Scanning Electron Microscopy. The repassivating potential is lower at a low scan rate signifying a greater possibility of sublayer oxide corrosion. On plotting the active peak current vs. scan rate, a straight line is obtained which fits the Levich

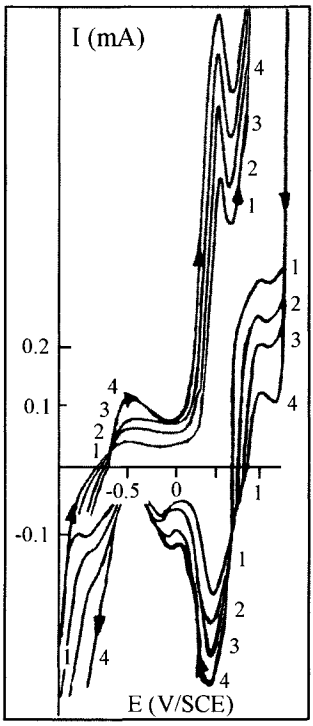

Figure 6.7. Voltammetric curves with ^3H_2O at different scan rates, ω: 2000 rpm, pH 10, 1: 200 mV, 2: 300 mV, 3: 400 mV, 4: 500 mV s^{-1}.

equation:

$$i_p = 1.24FD^{2/3}\Upsilon v^{0.5}A\omega^{0.5}C_{sp} \tag{6.13}$$

where v is the scan rate, D the diffusion coefficient, A the electrode surface, Υ the dynamic viscosity, F the Faraday constant and C_{sp} the species concentration. An experimental diffusion coefficient value of 5×10^{-5} cm^2 s^{-1} is then obtained, which is close to the usual values found for aqueous media [103].

2.3. Impedance spectra

2.3.1. Results This section is concerned with the analysis of impedance data for R30003 alloy passivated at different potentials and with ^3H_2O. Comparative measurements of the Bode plots (Fig. 6.8) made at the different passive potentials near the corrosion potential and in the passivity show changes in $\log|Z|$ and phase angle. In this figure, f is the frequency and $|Z|$ the impedance modulus. The Bode plots are characterized essentially by a linear slope of about -1 in $\log|Z|$ as $\log(f)$ decreases, while phase angle values approach

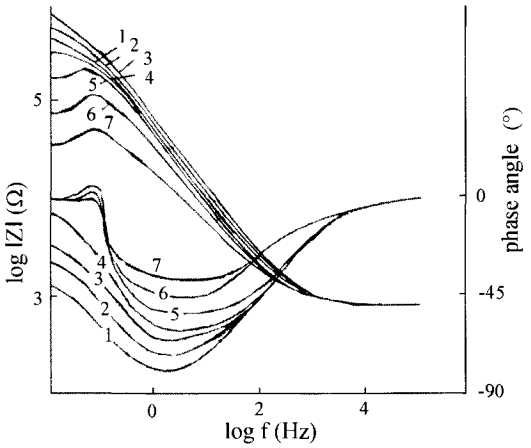

Figure 6.8. Experimental Bode spectra with ^3H_2O, ω: 2000 rpm, pH 10, 1: −0.72 V, 2: −0.7 V, 3: −0.68 V, 4: −0.66 V, 5: −0.2 V, 6: 0.3 V, 7: 0.4 V/SCE.

−90° in the broad low and middle frequency range. This is the characteristic response of a passive oxide capacitance (C_{ox}) in the purely capacitive region. At frequencies below 0.1 Hz, a dip can be seen in the phase angle plots which corresponds to an inductive effect.

According to different studies [104] and [105], the reciprocal oxide capacitance ($1/C_{ox}$) is directly proportional to the oxide layer thickness. To calculate the thickness, the reciprocal capacitance value is taken after passivation using the equations given by Kerrec et al. [106].

$$1/C_{ox} = 2\pi f |Z|_{f=0.16} \tag{6.14}$$

$$d = \varepsilon\varepsilon_0 r/C_{ox} \tag{6.15}$$

where d is the oxide layer thickness, r the roughness factor, ε the relative dielectric constant of oxide, ε_0 the permittivity of free space (8.9×10^{-14} F cm^{-1}). Calculations show that the surface roughness factor is between 1 and 1.6.

In eq. (6.15), as the relative dielectric constant for passive oxide layer was not found in the literature, we measured the current dependence on time during potentiostatic oxide formation at 0.2 V above the corrosion potential and with ^3H_2O (Fig. 6.9).

The total charge obtained by integrating the current–time curve corresponds to oxide layer formation. From Faraday's law, the oxide layer thickness, d, is calculated by another method:

$$d = QM/nF\rho r \tag{6.16}$$

where M is the oxide mean molecular weight (assumed to be 159), n the mean number of electrons required to form the passive oxide and ρ the oxide density, equal to 5.2 g cm^{-3}, according to Schmuki and Böhni [107]. Substitution of eq. (6.16) into eq. (6.15) there-

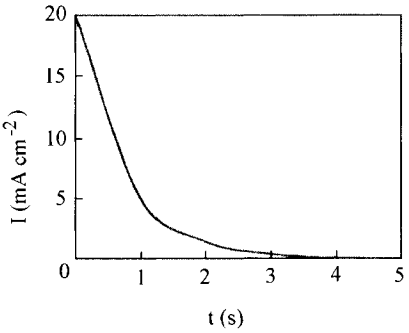

Figure 6.9. Current as a function of time in passivity.

Table 6.2. Dependence of oxide capacitance on passive potentials for ^3H_2O

E (V/SCE)	−0.72	−0.7	−0.68	−0.66	−0.2	0.3	0.4
C_{ox} (μF cm^{-2})	4.2	3.45	3	4.5	6	10	17

fore yields the average value of ε and gives 12. The oxide layer thickness estimated from eq. (6.15) is about 3.6 nm. This corresponds to the value of the passive oxide layer thickness given in the literature [106] without making allowance for the diffusion time of the excited radiolytic oxidizing species in the oxide. The passive oxide capacitance values were calculated for different passive potentials by eq. (6.14) (Table 6.2). In this table, the variation of C_{ox} indicates that the oxide layer formation obeys a growth law depending on the passive potentials as indicated by Schmuki and Böhni [107]. A 'critical capacitance' corresponding to its lower value denotes the perfect oxide layer. Moreover, the Bode plots make it possible to calculate the flatband potential and donor concentration over a sufficient potential range following the simplified Mott-Schottky equation:

$$C_{ox}^{-2} = (2/\varepsilon\varepsilon_0 n_d re)(V_m - V_{fb} - kT/e) \tag{6.17}$$

where e is the charge of the electron, n_d the donor density, k the Boltzmann constant, and V_m, V_{fb} the potentials at which the impedance measurements are carried out and the flatband potential, respectively. Linearity is observed between −0.72 and −0.68 V/SCE. A break was observed indicating that a second donor level is activated as the potential is more anodic. Using eq. (6.17), the average donor density is 2×10^{19} carriers cm^{-3}. The carrier concentration obtained with ^3H_2O is slightly higher than the value for a passive layer in light water, given by Castro and Vilche [108], Simoes et al. [109], Oriani et al. [110] and Barral et al. [111]. The flat-band extrapolated potential appears to be 30 mV above the corrosion potential.

In the passive-transpassive region, the Bode plots show a change of slope in the impedance modulus at frequencies below 0.1 Hz, and a dip at 0.1 Hz in the phase angle

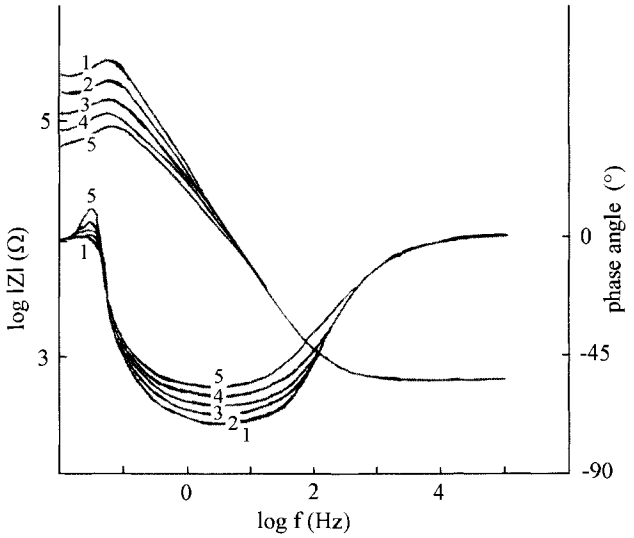

Figure 6.10. Bode plots as a function of time, ω: 2000 rpm, E: 0.3 V/SCE, pH 10, 1: immediately, 2: 5 min, 3: 10 min, 4: 15 min, 5: 20 min.

which tends to 0° at lower frequencies indicating that the oxide becomes inductive. These reflect the formation of a more defective oxide layer and breakdowns at these potentials.

As can be seen in Fig. 6.10, the obtained spectra at different intervals for a passive-transpassive potential show that the R30003 alloy impedance changes with time in the passive-transpassive region which can be considered as an indication of oxide layer modification. This behavior has been observed by Al Kharafi and Badawy [112] and Erné et al. [113] in non-radioactive media where the attack of the oxide sublayer is time-dependent. No definitive results, such as donor density, from the impedance data are possible before stability is reached, due to the changes in the system. Also, the changes with time during exposure of the various components of the equivalent circuit can be used to check the proposed model. The dip observed in the impedance modulus and phase angle at 0.1 Hz is associated with relaxation processes in the oxide layer. Under pre-polarization conditions at the potential limit in passivity-transpassivity domain, the dependence of R30003 alloy attack on time has also been previously confirmed by cyclic voltammetry experiments. This attack is due to the absorption of tritiated species, and it is always localized, leading to corrosion. Tritiated species absorption and R30003 alloy attack change the surface morphology which is confirmed by Scanning Electron Micrography. The variation of C_{ox}^{-1} or actually the oxide layer thickness with time can be formulated as:

$$C_{ox}^{-1} = C_0^{-1} - Bt^{0.5} \tag{6.18}$$

$$d = d_0 - B't^{0.5} \tag{6.19}$$

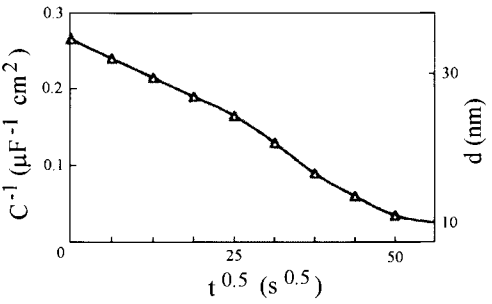

Figure 6.11. Capacitance and thickness as functions of time.

where C_{ox}^{-1} or d and C_0^{-1} or d_0 represent the capacitance or oxide layer thickness at time t and zero time, respectively, after passive oxide layer formation. B and B' are the rate coefficients for oxide layer corrosion. The variation of C_{ox}^{-1} or d vs. $t^{0.5}$ is shown in Fig. 6.11. In this figure, the oxide layer thickness decreases from 3.6 to 1.0 nm. This behavior has been observed for another medium by Al Kharafi and Badawy [112]. As can also be seen, the value of C_{ox}^{-1} or d decreases linearly with $t^{0.5}$, and the rate coefficient changes at a certain time, i.e. there are two linear dependencies with different slopes before obtaining a constant capacitance for 50 $s^{0.5}$. The slope of the first linear section is always lower than that of the second. This means that the rate of oxide layer corrosion changes after a certain time. This change is attributed to a change in the mechanism and indicates that corrosion operates at two levels. These levels are believed to correspond to the absorption of tritiated species in oxide with outer oxide corrosion followed by diffusion and then a gradual removal with void formation in the oxide sublayer and continuous corrosion by inner oxide ionization. Cracking starts at the surface of oxide, when diffusion is high enough, then cracking becomes more important in the oxide bulk (Fig. 6.12). This process leads to inner oxide layer thinning with acid pH and increasing concentrations of excited radiolytic species in a small internal volume. The outer layer is less susceptible to corrosion than the inner one due first to diffusion of O^3H^- into oxide and then higher concentrations of excited radiolytic species in a small volume between oxide and alloy. The variation of the polarization resistance with $t^{0.5}$ is consistent with the variation of C_{ox}^{-1} (Fig. 6.11). The modification of slope, in the linear section, observed with time, indicates the change in the oxide layer corrosion rate. The polarization resistance (R_p) decreases and the R30003 alloy becomes less passive. Such behavior can be also interpreted on the basis that the oxide layer becomes too thin to impart complete passivity, and the extent of attack increases and rapidly spreads laterally beneath the oxide layer leading to the loss of its protective action. At any instant, the rate of change of the thickness can be determined by the difference in the rates of oxide layer growth and layer corrosion.

When excited radiolytic species have reached the alloy-oxide layer interface, they may react producing ionic species and vacancies leading to void formation. According to Strehblow [114] and Macdonald [115,116], metal vacancies ($V_{Me^{n+}}$) diffuse from the tritiated water–oxide to alloy–oxide interfaces, such as O^3H^-, or equal numbers of metal cations

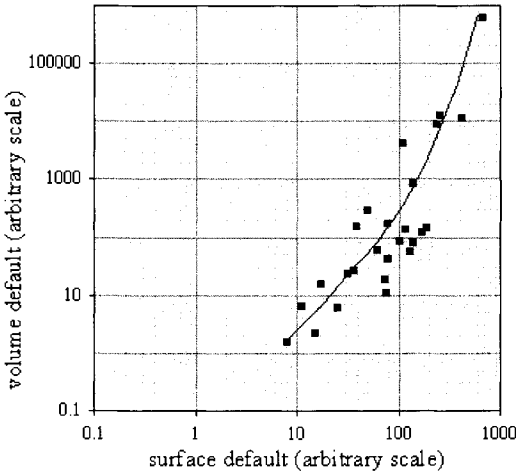

Figure 6.12. Surface and bulk defaults as functions of time.

diffuse in the opposite direction. If the metal vacancies penetrate the alloy at a slower rate than their diffusion through the oxide layer, they accumulate at the alloy-oxide layer interface and finally lead to a local concentration and hence will form a void. When the void grows to a certain critical size, the passive oxide layer is subsequently subject to breakdown with local thin blister formation then delamination that mark the breakdown period. The delaminated site dissolves much faster than any other location on the layer. This implies that the diffusion of metal vacancies is affected by the insertion of O^3H^- ions at the oxide–^3H_2O interface as shown in the following equations.

$$\text{null} \leftrightarrow V_{Me^{n+}} + \frac{n}{2} V_{O^{2-}} \tag{6.20}$$

$$C_{V_{Me^{n+}}} = k(C_{V_{O^{2-}}})^{-0.5n} \tag{6.21}$$

$$V_{O^{2-}} + 2O^3H^-_{\text{aqueous}} \leftrightarrow 2\{O^3H^{-*}\} \tag{6.22}$$

Equation (6.20) represents the Schottky-pair reaction at the oxide–^3H_2O interface. In eq. (6.22), $\{O^3H^{-*}\}$ is a radiolytic excited anion occupying O^{2-} vacancies ($V_{O^{2-}}$). It can be seen that the number of $V_{O^{2-}}$ vacancies that are free decrease. Due to the interdependence of the concentration of cation and anion vacancies ($C_{V_{Me^{n+}}}$, $C_{V_{O^{2-}}}$) and diffusion of O^3H^{-*} into the oxide layer, the number of metal vacancies increases in the oxide layer up to a critical concentration leading to voids (eqs (6.21), (6.22), thin blisters, then delamination with localized corrosion. From these considerations, the criterion for breakdown in

presence of ^3H_2O can be expressed by:

$$\frac{\partial V_{Me^{n+}}}{\partial t} = J_0\left[C_{V_{O^{2-}}}\{\text{oxide-}^3H_2O\}\right]^{-0.5n} \tag{6.23}$$

J_0 depends on thermodynamic constants and $C_{V_{O^{2-}}}\{\text{oxide-}^3H_2O\}$ is the concentration of O^{2-} vacancies at the oxide layer-^3H_2O interface. Equation (6.23) shows that the metal vacancies diffusion is enhanced by decreasing the concentration of O^{2-} vacancies by the O^3H^{-*} present. This enhancement can effectively lead to an accumulation of metal vacancies at the alloy-oxide layer interface. From eqs (6.21) and (6.23) and applying a calculation procedure similar to that given by Strehblow [114] and Macdonald et al. [115] and [116], we can write the simplified equation for the ^3H_2O present:

$$E_{\text{breakdown}} = \frac{2.3\alpha RT}{F}\left(\log\left(\frac{2J_m}{nJ_0\frac{M}{\rho}\exp\{\frac{\text{pH}}{RT}\}^{-0.5n}}\right) - \log O^3H^{-*}\right) \tag{6.24}$$

where J_m is the rate of submergence of the metal vacancies in the alloy. It can be seen that low submergence rates and higher tritium concentrations coming from tritiated water at constant pH decrease the breakdown potential.

2.3.2. Equivalent circuits and value determinations Spectra give a perfect fit with the experimental data if the total impedance is modeled according to the simplified equivalent circuit in Fig. 6.13.

Constant phase element (CPE) is used instead of 'ideal' capacitor for oxide to account for the slight deviations observed, such as a capacitive slope lower than -1. For a constant phase element, the impedance, Z_{CPE} is defined as [117] and [118]:

$$Z_{CPE} = A(j2\pi f)^{-a} \tag{6.25}$$

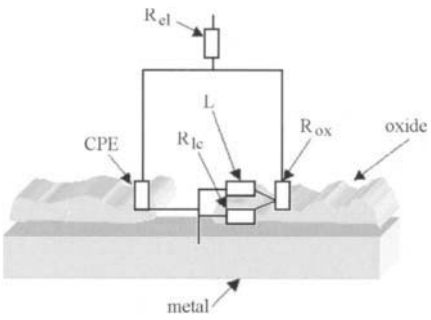

Figure 6.13. Simplified equivalent circuit for impedance simulation, R_{el}: electrolyte resistance, R_{ox}: oxide resistance, R_{lc}: localized corrosion resistance, CPE: constant phase element, L: inductance.

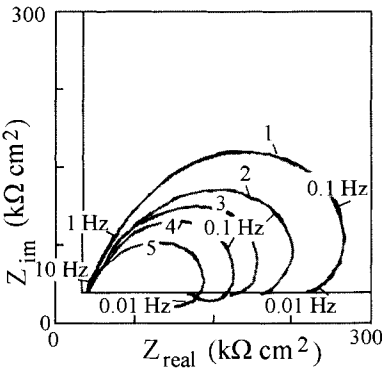

Figure 6.14. Nyquist plots according to Fig. 6.10.

Table 6.3. Dependence of oxide capacitance and resistance on time at the passive-transpassive potential for ^3H_2O

t (min)	0	5	10	15	20
C_{ox} (μF cm^{-2})	4	5	6	7	9
R_{ox} (kΩ cm^2)	250	200	150	100	80

in which a slope of $0 < a < 1$ for the experimental or simulated diagrams and a complex value of $j = \sqrt{-1}$ are taken, while A is a frequency-independent constant considered as the reciprocal capacitance only if $a \approx 1$. The exponent a is related to the constant phase angle of the CPE in the complex plane: $\theta = (1 - a)\pi/2$.

Data in Fig. 6.2 indicate that oxide capacitance decreases then increases with the passive potentials. Inversely, the oxide resistance increases then decreases. This signifies a dependence of oxide layer characteristics on the passive potentials. Using the Nyquist plots (Fig. 6.14), it can be seen that the inductive loop coincides effectively with the dip in the impedance modulus and the phase angle.

Moreover, the values of the oxide resistance and capacitance (Table 6.3) show that the oxide resistance and capacitance change with time signifying more corrosion and localized corrosion. At higher potentials in the Nyquist plots (Fig. 6.14), negative localized corrosion resistance and capacitance are obtained. They do not physically correspond to passive electrochemical components but to a mathematical representation of impedance when instabilities are met. To confirm this, the following Kramers-Kronig equations have been applied to determine whether the impedance data are effectively influenced by time-dependent phenomena [119–123].

$$Z_{i(\omega)} = -\left(\frac{2\omega}{\pi}\right)\int_0^\infty \frac{Z_{r(x)} - Z_{r(\omega)}}{x^2 - \omega^2}\,dx \tag{6.26}$$

$$Z_{r(\omega)} = Z_{r(\infty)} - \left(\frac{2}{\pi}\right)\int_0^\infty \frac{xZ_{i(x)} - \omega Z_{i(\omega)}}{x^2 - \omega^2}\,dx \tag{6.27}$$

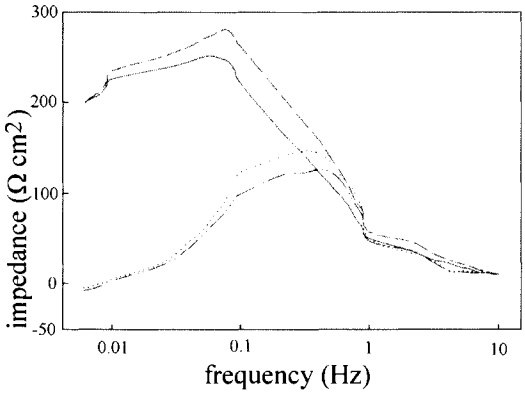

Figure 6.15. Comparison of experimental impedance and impedance calculated using Kramers-Kronig relations, (—): experimental real impedance, (- - -): calculated real impedance, (···): experimental imaginary impedance, (— · —): calculated imaginary impedance.

$$Z_{r(\omega)} = Z_{r(0)} + \left(\frac{2\omega}{\pi}\right) \int_0^{\infty} \frac{\left(\frac{\omega}{x}\right) Z_{i(x)} - Z_{i(\omega)}}{x^2 - \omega^2} \, dx \tag{6.28}$$

where x is an angular frequency determined by a constant increment added to ω, $Z_{r(\omega)}$ the real part, $Z_{i(\omega)}$ the imaginary part and $Z_{r(0)}$, $Z_{r(\infty)}$ the real parts at the frequencies equal to zero and infinity respectively. In these equations, the impedance must have a finite value and be continuous over the frequency range. In particular, it can be noted that the impedance must tend to a constant value as $\omega \to 0$ and $\omega \to \infty$. From the experimental results, the numerical integration was performed applying a constant increment on the higher potentials data. The transformed data are displayed in Fig. 6.15. This diagram is typical of corrosion at the oxide surface and in the sublayer by aggressive species after their adsorption. In this figure, the real and imaginary transforms are compared with the experimental impedances. A poor fit between the experimental and calculated data has been obtained. This does not satisfy Kramers-Kronig transforms signifying instabilities and relaxation processes for the tritiated oxide. The system can be considered a time-variant model with changes between the inner and outer oxide surfaces [124].

2.4. Scanning Electron Microscopy, Atomic Absorption Spectroscopy and X-ray analysis

It can be seen from the scanning micrographs (Fig. 6.16) that the polarization of R30003 alloy near the passive-transpassive potentials and for lengthy immersion in tritiated water leads to peel formation due to the β^- energy range. Depending on time, an appreciable fraction of the oxide layer is removed. Passive oxide peels flake off in thin layers that are the preliminary stage of exfoliation and are a consequence of radiation damage. As a result, at the early stage of polarization, voids and thin blisters appear, forming spaces between the alloy and the oxide layer that are the result of radiation and ionization in the oxide.

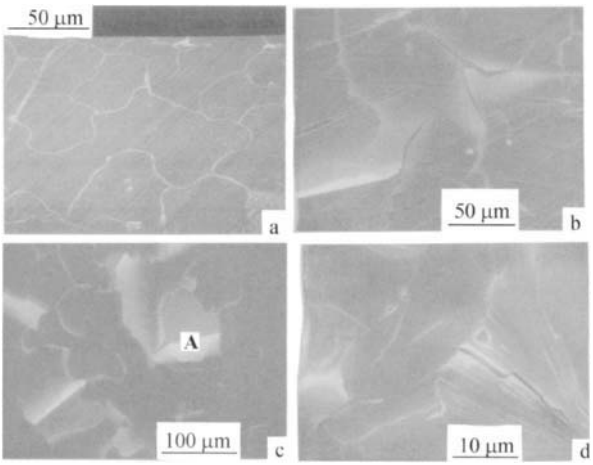

Figure 6.16. Scanning Electron Microscopy photographs of R30003 alloy corroded with peels in presence of tritiated water at 0.5 V/SCE for 20 min, (a): surface in reference condition, (b): adhering oxide, (c): peeled oxides (A: next exfoliation of the oxide layer), (d): detail of (c).

Diffusing excited radiolytic species penetrate the oxide and are accumulated in the oxide-alloy interface with a significant matrix extension towards the outer oxide surface due to internal stresses. In the second stage, the peels no longer adhere. Finally, the oxide peels flake off the surface (delamination) as observed by Erné et al. [113] for non-radioactive media. The voids are below each ionized peel where a few micropits emerge. The oxide peel thicknesses were measured by observing their non-adhering edges using Scanning Electron Microscopy. Expanding ionized flat peels reach each other and no longer grow laterally.

Electron microscopy also reveals a cellular pattern of peels due to a large compressive stress along the surface which is the precursor of exfoliation induced by implanted excited radiolytic species, initially leading to voids from which peels radiate to thin walls. Ionization corrosion causes the surface of the oxide layer to be crumpled, for this reason it should be stressed. Radiation effects should be more effective in a void than in outer oxide layers. Ionization corrosion at the radial fronts of peels proceeds at the same time in all directions and expands until the fronts of neighboring peels meet, at which time the peels no longer adhere and leave adjacent walls. Fig. 6.17 shows walls after peel disappearance; the observed morphology resembles fine lines.

Energy Dispersive X-ray Analysis of the outer oxide of R30003 alloy before and after corrosion gives strong signals (Fig. 6.18). To determine the origin of each peak, a calibration was made to locate the position of element atomic numbers on the x-axis. In this figure, comparison of the signals for Fe, Ni, Cr and Co indicates that the corroded outer oxide has the same composition as does that before tests in tritiated water. After corrosion, the dissolved alloying components were also analyzed by Atomic Absorption Spectroscopy and results are given in Table 6.4. In comparison with Fig. 6.1, these show essentially a weight

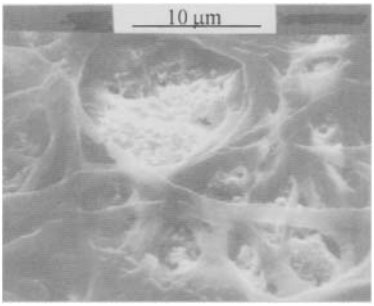

Figure 6.17. Scanning Electron Microscopy photographs of R30003 alloy corroded with wall amasses in presence of tritiated water at 0.5 V/SCE for 40 min.

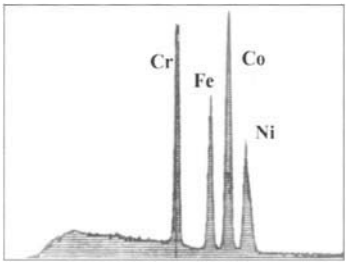

Figure 6.18. X-Ray Microanalysis of R30003 alloy passive oxide before corrosion and surface oxide peeling after corrosion in $^{3}H_2O$.

Table 6.4. Composition of tritiated water after corrosion of R30003 alloy

Elements	Co	Ni	Cr	Fe	Mo
Wt%	44	17	16	18	5

loss for cobalt, iron and nickel for R30003 alloy; these different results signify selective corrosion in inner oxide layers. It is seen in Table 6.4 that cobalt is preferentially corroded and chromium is least attacked.

3. Discussion

Observed oxide peels may develop as follows: corrosion starts by excited radiolytic oxidizing species at a point corresponding to a higher β^- energy concentration pathway and localized excited electron density. From this point, these species grow radially below the oxide layer; this leads to void formation, thin blisters, then delamination with peeling and walls separating each blister and peel. At corrosion initiation in the oxide sublayer, excitation sites on the alloy are randomly distributed over the oxide surface. After this stage, the blisters may grow out of the oxide surface due to the forces in combination with propa-

gation mechanisms such as delamination and undermining leading to peels. Similarly, due to the presence of nuclear ionization, the charge density distribution may be different in the peels compared with that in the walls; a higher charge density leads to enhancement of the electric field strengths at such sites, thus also facilitating void generation and exfoliation. Once voids have been initiated, the electric field can be subsequently enhanced by curvature of the oxide surface: such spots represent serious disruptions of the crystal lattice facilitating localized charge density increases and the value of the field increases with increasing radius of curvature. As a result, voids propagate radially away from this field. The location of the different voids is such that the distance between them is approximately the same everywhere. In the last stage, the delamination occurs because the driving forces consist of reactions taking place at the interface. These may be reduction of excited radiolytic oxygen (cathodic area):

$$O^* + 2e^- \rightarrow 2O^{2-*} \tag{6.29}$$

and hydroxide radical oxidation in sublayers (anodic area) forming blisters:

$$O^3H^- + O^* \rightarrow {}^3HO_2^* + e^- \cdots \rightarrow {}^3H_2O_2^* + 2O \tag{6.30}$$

leading to:

$${}^3HO_2^* + MeOO^3H \rightarrow MeO_4^{2-} + 2\,{}^3H^+ \tag{6.31}$$

Also, depending on the actual oxide layer, O, $^3HO_2^*$ and $^3H_2O_2^*$ concentrations in a small volume in the interface may cause delamination as a result of chemical disintegration of the oxide at the alloy-oxide interface. The propagation of a thin blister leading to anodic delamination under an undamaged oxide layer is schematically illustrated in Fig. 6.19.

After local corrosion initiation, a complex peroxide such as $Me(^3HO_2)_n^*$ can be also formed, by reaction of Me_2O_3 or $Me(O^3H)_n$ with O^3H^-, O^*, $^3HO_2^*$ and $^3H_2O_2^*$. High values for excited radiolytic species in the oxide ensure a decrease of O^{2-} vacancies and sufficient O^3H^{-*} at short diffusion distances in the oxide layer. A high value for diffusion in a radioactive oxide allows void and blister formation and radiolytic compounds formation in a small volume leading to delamination. Also, the excited corrosion products causing highly acid pH and oxidizing media stimulate blister growth. Metal oxide is also formed, as illustrated in Fig. 6.19, where the charge density distribution is reduced due to the smaller curvature at the blister circumference. In this limiting region, metal oxide also acts as a diffusing medium: it allows diffusion of O^3H^- and O^{2-*}, but here the ionic diffusion is lower due to the smaller curvature, consequently corrosion is lower than in void generation where higher electric field strengths are obtained corresponding to the curvature at the top of the peel. The wall areas correspond to the region of smaller curvature after the blister leading to peels is formed. There should be walls around the blister which in the first stage contains a central void. In this initial situation a large anodic area (blister or peel) is adjacent to a small area (walls) formed of more insulating oxide and having higher

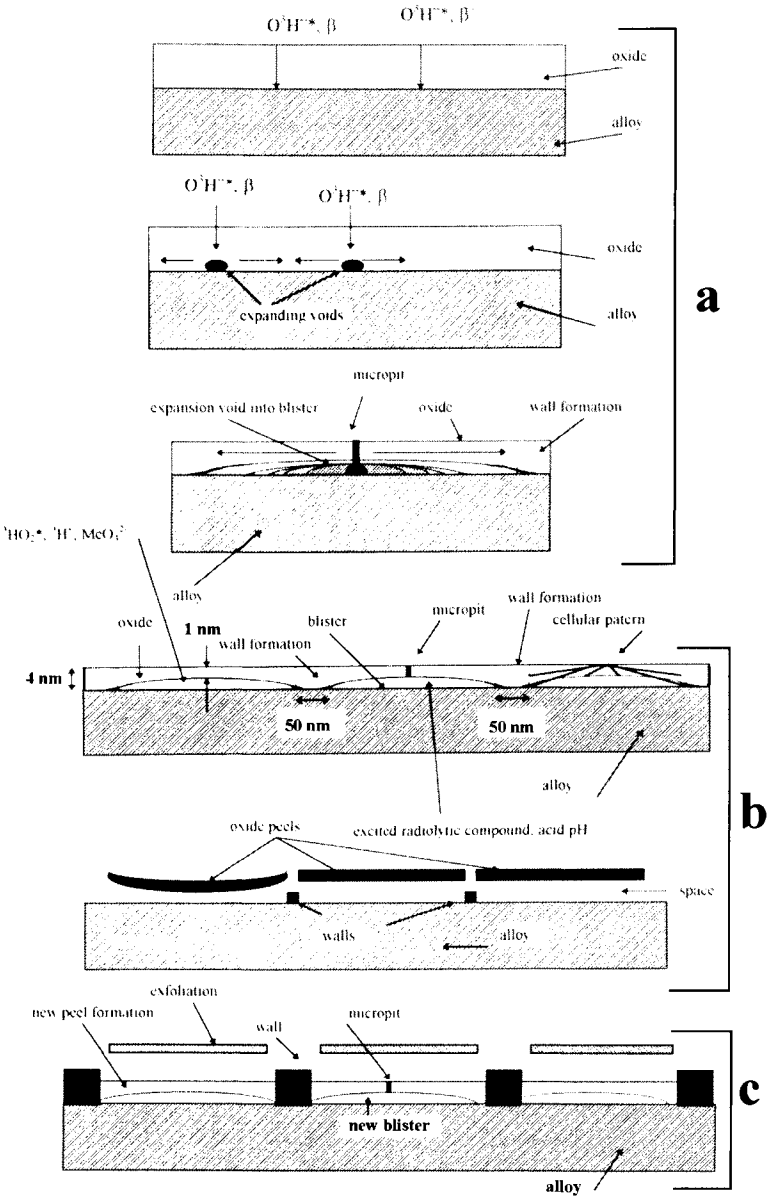

Figure 6.19. Schematic illustration of various stages of corrosion, (a): anodic delamination process, (b): separation of anodic and cathodic regions with wall formation and peeling, (c): schematic illustration of stages for successive exfoliations, thinning-out of peels, and wall thickening.

ionic resistance. This means that capacitive measurements represent the values corresponding to peels, and $^3H_2O_2$ and $^3HO_2^*$ will reach very high values only in blisters. Because delamination is controlled by O^3H^- and $^3HO_2^*$, it is related to:

- the anodic reaction rate, which is limited by the tritium diffusion rate into oxide by O^3H^-,
- void formation,
- blister curvature,
- consumption of O^3H^- and oxide sublayer by reactions.

According to Scanning Electron Micrograph examination, corrosion occurs radially at the same rate in all directions away from the void, so that this is aligned in such a way as to create a widening void front (blister). When fronts of several blisters meet, the curvature is low and corrosion by delamination stops, leaving the domain wall as seen in Fig. 6.19b. After this lateral expansion stops, there is a second stage: new voids grow vertically below the first peeling by excited radiolytic oxidizing species in the bulk of the oxide layer attached to the alloy. This leads to multi-terraced void levels with the generated blisters which cause successive limited peeling (peel A in Fig. 6.16c) along the initial walls as a thinning-out of peels. The reason for this thinning-out is that the excited radiolytic oxidizing species penetrates deep within the oxide layer. After the initial exfoliation of the surface, new exfoliation appears (peel A in Fig. 6.16c). As a result, in the present case, secondary exfoliation originates below the primary exfoliation and propagates vertically away from it in the initial direction. Since it is very likely that the exfoliations are always identically placed at the same location in the top of the oxide layer, it is probable that the walls thicken during these successive exfoliations. Fig. 6.19c shows a view in a cross-section of the superposed exfoliation along the vertical propagation direction leaving a pile of collapsed walls (Fig. 6.19c), which is evidence that delamination and corrosion occur at the same rate in the radial and vertical directions and that the corrosion rate is the same for all expanding blister domains. To our knowledge, the only other published paper on the process and morphology of thinning-out of peels and walls is given by Erné [113]. The simplest way to account for these observations, as indicated above, is to assume that voids occur exclusively where more excited radiolytic species are formed. The observed morphology suggests that the void branches in such a way that the distance between neighboring voids is the same everywhere; consequently, since the voids are aligned in fronts, the local anodic currents are proportional to the respective surface areas of each peel. Lateral expansion of an anodic blister stops when it arrives in contact with the area where more insulating oxide forms walls. Also, halfway between two neighboring blisters or peels, the field is somewhat lower due to lower curvature facilitating wall formation. Electron microscopy shows that the wall width is $\sim$ 50 nm as in the results of Erné [113], and thickness is much greater than that of peels ($\sim$ 1.0 nm). The greater thickness of the walls can be explained by the fact that these are present on the steel surface for a longer time than the peels and due to this they are thickened in successive exfoliations. The thicknesses of different peels are uniform and well-defined and this is supported by the capacitance measurements before delamination. According to eqs (6.15) to (6.19), the thickness d of a

future peel layer is after reduction of the oxide layer (initially 3.6 nm):

$$d = \sqrt{\frac{2\varepsilon\varepsilon_0 r}{e n_d}\left(V_m - V_{fb} - \frac{kT}{e}\right)} \tag{6.32}$$

From eq. (6.32) it follows that for $d = 1.0$ nm according to the time as shown in eq. (6.17), n_d is 3.7×10^{21} carriers cm^{-3}. Charge density in the oxide peels, where corrosion takes place, plays a role in putting a higher limit on the field strength than that in the walls. Complete delamination is therefore expected when the oxide layer is thinner. Furthermore, as the field strength with respect to thickness is proportional to the charge density, the charge density of peels is equal to the product en_d. The result is that the strength of the field directed at the peel is approximately equal to the integral of $en_d/\varepsilon\varepsilon_0$. On this basis, the thickness of the peels should depend mainly on the donor density and on the critical field strength.

4. Conclusions

It is shown experimentally that tritiated water modifies the corrosion potential due to the rate constants in this medium. Contaminated oxide is more corroded in the active and corrosion potential regions with ^3H_2O. The oxide layer capacitance, thickness, donor density and flatband potential were determined at different passive and passive-transpassive potentials. The capacitance and donor density are higher at the passive-transpassive potentials and depend on time due to O^3H^- diffusion into oxide occurring with excited radiolytic species and released low energy. These values indicate the formation of a less perfect passive oxide and less protection in presence of ^3H_2O. Contaminated oxide is locally corroded at passive-transpassive potentials by oxide flaking and internal voids that radiate from the initiation point forming anodic blisters, peels and walls when adjacent blisters or peels meet. Analysis shows a weight loss for cobalt, iron and nickel resulting from oxide sublayer corrosion. These different results imply that tritiated water, rather than providing better protection, increases corrosion of R30003 alloy.

Chapter 7

EFFECT OF ENERGY ON THE OXIDE LAYER

1. Introduction

This study was realized using austenitic stainless steel 316L, whose composition is given in Table 7.1. Compared with other steels, it has good corrosion resistance. Nevertheless, several cases of corrosion have occurred in the nuclear installations. A possible explanation of this corrosion is that both the tritium present and the decay energy on the steel surface react with the oxide layers. To verify these two factors, non-contaminated stainless steels were first tested at different pH with hydrogen dissolved in light water. In tritiated water, pH depends on the radiolysis and can be acid, neutral or alkaline. The following tests were carried out following immersion in tritiated water in order to involve dissolved tritium at 0.05 mmol dm^{-3}, which is adsorbed, and the surface energy of the β^- particles. To apply this low energy, allowance was made for the average path of the particle in tritiated water which is a few μm. At this distance and for tritium introduced, the energy received from the decay is 1.5×10^5 MeV $\mu m^{-1}\, s^{-1}\, cm^{-2}$. This comparative study showed the effective influence of these two factors following the immersion of the steel in tritiated water.

2. Results obtained with non-tritiated water

2.1. Effect of pH

The voltammetric curves in Fig. 7.1 show that in the forward scan the active peak (A) of the steel at −0.4 V/SCE increases with the H^+ ion concentration. The same is true of the current in the passive region (around 0.1 to 0.7 V/SCE). At the end of the backward scan, it is observed that the water reduction current is shifted towards more positive potentials when the H^+ concentration increases. The presence of the reduction peak (C) of the corrosion products (−0.9 V/SCE) is observed only at pH between 5 and 7 (curve 5). At these pH values, the reduction current of the water is at more negative potentials and they no

Table 7.1. Composition of 316L stainless steel

Elements	Fe	Cr	Ni	Mo	Mn	C
Wt%	69	16.8	10.3	2.1	1.4	< 0.03

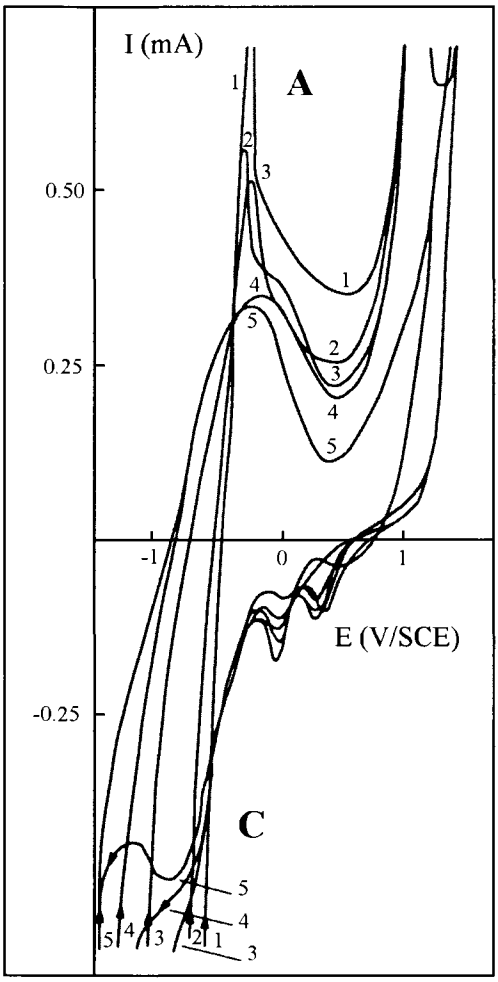

Figure 7.1. Voltammograms—effect of pH for values from 1 to 7, v: 200 mV s^{-1}, ω: 2000 rpm, 1: pH 1, 2: pH 2, 3: pH 3, 4: pH 4, 5: pH 5.6–7.

longer hide the reduction peak. The active peak becomes narrower with increasing H^+ ion concentration. For this condition, there is concomitance of the superimposed currents with opposite signs, that corresponding to the oxidation of the steel and that due to the reduction of the water. The overall or net current is the difference between the two currents.

The voltammetric curves in Fig. 7.2 were obtained at alkaline pH. It can be seen in these curves that, at potentials at around −0.8 V/SCE, the two peaks (A, C) corresponding to steel oxidation and corrosion products reduction increase with the OH^- ion concentration.

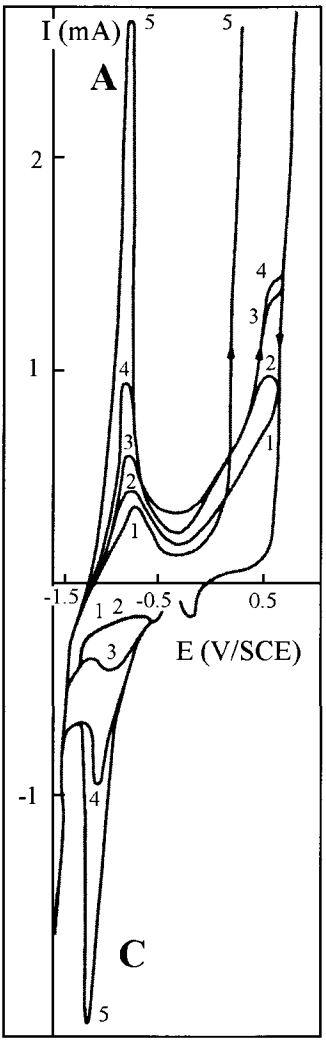

Figure 7.2. Voltammograms—effect of pH for values between 8 and 12, v: 200 mV s^{-1}, ω: 2000 rpm, 1: pH 8, 2: pH 9, 3: pH 10.5, 4: pH 11, 5: pH 12.

It is observed that the current for the release of hydrogen is at more negative potentials than that obtained in acid solutions.

The curves in Figs 7.1 and 7.2 correspond to the variations in the potential–pH equilibrium relationships [101] for water, and for nickel, chromium and iron which are the essential components of the stainless steel.

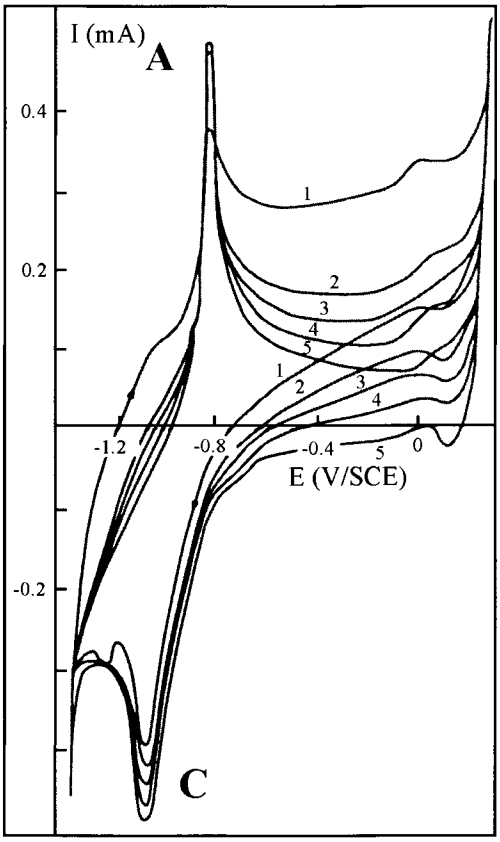

Figure 7.3. Voltammograms—effect of the adsorbed hydrogen, v: 200 mV s^{-1}, ω: 2000 rpm, pH 13, time for addition of H: 4 min, continuous voltammetry cycles after addition of H (the number of the scan is given on each curve).

2.2. *Effect of hydrogen adsorption*

It is known that tritiated water contains dissolved tritium which can be adsorbed on the surface of the steel. To determine its effect by comparison, we have, therefore, added hydrogen formed by electrolysis to the surface and immediately after plotted the voltammetric curves (Fig. 7.3). The difference in current with and without hydrogen charging corresponds to the oxidation of the hydrogen adsorbed and back-diffusing. This current is superimposed on that due to the oxidation of the stainless steel. The hydrogen oxidation current decreases with the number of cycles as there is less and less adsorbed hydrogen to oxidize. It is observed in the curves in Fig. 7.3 that the hydrogen adsorbed on the steel does not hinder the oxidation of the alloy as seen by presence of the active peak (A) and passivity. No

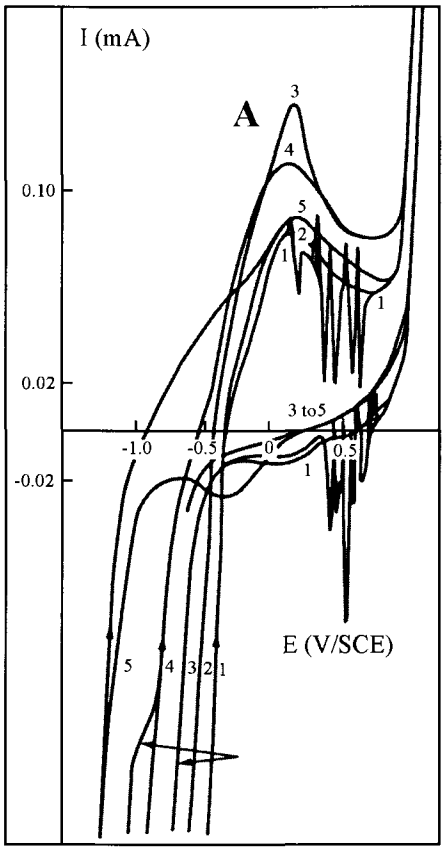

Figure 7.4. Voltammograms—effect of dissolved tritium, 0.05 mmol dm^{-3} $^3H_2$, energy released: 2×10^5 MeV μm^{-1} cm^{-2} s^{-1}, v: 200 mV s^{-1}, ω: 2000 rpm, 1: pH 1, 2: pH 2, 3: pH 3, 4: pH 4, 5: pH 6.

current instabilities originating from the breakdown of the passive oxide layer due to the adsorption and oxidation of hydrogen are observed.

3. Results obtained with tritiated water

3.1. Shape of the curves at slightly acid and alkaline pH

The voltammetric curves in Fig. 7.4 were obtained at acid pH and in the presence of dissolved tritium. From pH 6 to pH 3 (curves 3 to 5), the active peaks (A) increase with the $^3H^+$ ion concentration. This was previously observed in Fig. 7.1, obtained with H_2O. In Fig. 7.4, from pH 3 to pH 1 (curves 1 to 3), the active peak decreases, which is different from Fig. 7.1 (curves 1 to 3). The tritium evolution current results in greater masking of

the active peak due to the difference of evolution potential between these two isotopes. Since the active peak increases or decreases with pH, the corrosion potential must be in this peak. In fact, it has been found experimentally that the free potential at pH 4 is stabilized at around −0.02 V/SCE, i.e. in the active peak. This signifies the possibility of more oxide instability by conjunction with other factors. From the curves, the dissolved tritium would appear to be oxidized at the contact with the oxide surface.

In curve 1 in Fig. 7.4, current instabilities are seen in each cycle and always at the same potentials. They are at the limit of the active peak and the prepassivity region while this had not been the case with H_2O (Fig. 7.1). According to Ford [125], this involves the prepassivity region where the passivating oxide layer is not yet stable. Moreover, the energy of the particles at the oxide surface is 1.5×10^5 MeV $\mu m^{-1}\, s^{-1}\, cm^{-2}$. Consequently, the oxide layer would most certainly be damaged not only by the free potential in the active region but also by dissolved tritium adsorbing and energy of the β^- particles. This type of behavior in the curves corresponds to localized stress corrosion of the oxide layer.

The voltammetric curves in Fig. 7.5 were also obtained with dissolved tritium in tritiated water at pH 13. In this figure, the large variations in current in passivity are obtained. At the onset of the passivity, the current peaked at −0.50 V/SCE, then decreased below the passivating value, and then increased again and maintained a cyclic behavior for potentials from about −0.5 to 0.4 V/SCE. These current instabilities are obtained at different alkaline pH values. At these values the free potential of the steel is −0.25 V/SCE, in the prepassive-passive region. As these current instabilities start approximately in the prepassive region, there is a risk of damaging the protective oxide layer during its formation at the free potential. It is interesting to note that the oscillations in current reproduce themselves during the positive and negative scan. They are cyclic and repetitive and they continue to have the same potential position from one scan to another. The oxide layer is dissolved each time at potentials between −1.5 and −1 V/SCE, and starting with a new peak, a renewed protective oxide layer is formed to be again destabilized. Moreover, from voltammetric experiments where the scan rate was varied, the oscillations are dependent upon potential and time in a complicated manner. Since voltammetric experiments involve the variation of potential and time simultaneously, chronoamperometry was used to determine the dependence of the current oscillations on potential and time on tritium.

Plotting chronoamperometric curves as realized by Vitt and Ma [126], the oscillations are erratic for potentials placed between the Flade potential and −0.55 V/SCE signifying the start of oxide instabilities for a new oxide. For passive potentials greater than −0.55 V/SCE, remarkable bi-periodic oscillations in current are more easily observed (Fig. 7.6) after an induction time of about 30 s–1 min according to the applied potential (Fig. 7.7). These oscillations should be regarded as the superposition of a large number of elementary transient events composed of oxide stabilization and oxide breakdowns depending on time. The induction time decreases, increases then decreases again with the potential applied signifying oxide destabilization, followed by stabilization then its disinvolvement in the passivity-transpassivity limit. It may be noted that the induction time is a measure of the rate of the tritium action on the oxide layer and establishment of critical conditions for the cyclic destabilization. These oscillations are bi-periodic in nature, and

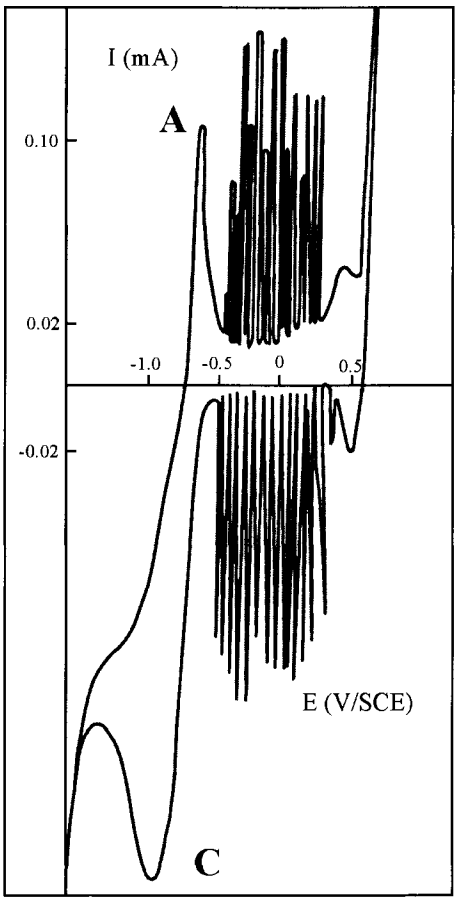

Figure 7.5. Voltammograms—effect of dissolved tritium, 0.05 mmol dm^{-3} $^3H_2$, energy released: 2×10^5 MeV μm^{-1} cm^{-2} s^{-1}, v: 200 mV s^{-1}, pH: 13, ω: 2000 rpm.

as expected, the peak-to-peak amplitude and frequency increase then decrease increasingly becoming periodic with a growth in the passive potential. These oscillations are reproducible and sustained for a few minutes before they stop. Experiments of long duration show that the oscillations restart after a new induction time. The first conclusion is that oscillations seem to be related the position of the free potential leading to alternation of passivity and destabilization in the oxide. However, at the better passive potential where the oscillation amplitude is the lower, a high oscillating current can be again obtained after the potential is stepped back to -1 V/SCE to reform tritium on steel. The onset of complex periodic oscillations should be associated with the low energy released from decaying adsorbed tritium on the passive and prepassive oxide layer. Tritium influences the amplitude and the period of the current oscillations but not the oscillation type. The oscillations

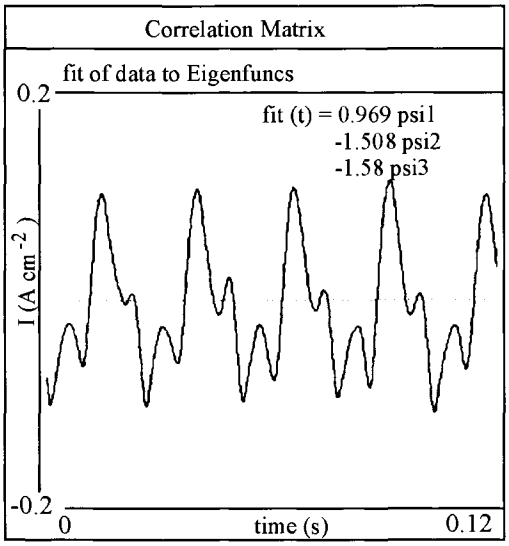

Figure 7.6. Experimental graph and fitting data to eigenfunctions by correlation matrix.

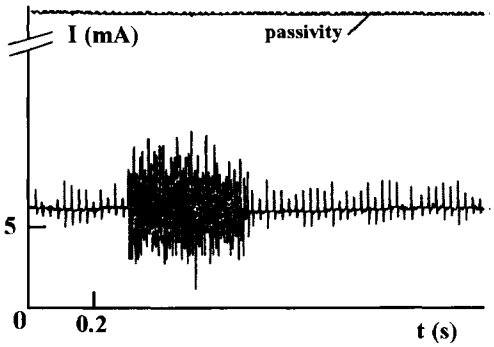

Figure 7.7. Erratic oscillations.

remain always bi-periodic. This is also due to modification of the ionic and electronic properties of the oxide layer and electron transfer in presence of tritium. Clearly, reforming of the oxide with tritium at the surface is important in restoring the bi-periodic oscillations. Mixed-mode oscillations should be interpreted by simulation using a chaos data analyzer program for the best understanding of the system [127]. The route to chaos is the path of bifurcations that the system undergoes from a steady state to a chaotic state as a control parameter is varied. One remarkable feature of chaos is that it occurs in low-dimensional non-linear equations. In this sense, Lorenz [128] published a seminal paper in which he showed that it operates in systems of autonomous first-order differential equations with as

few as three-dimensional variables and two quadratic non-linearities. Although the Lorenz system is often taken as the prototypical chaotic flow, it is not the algebraically simplest example of it. Rössler [129] has previously formulated a toroidal chaotic system of differential equations as a model of chemical reaction. Later, Sprott [130] also found a variety of chaotic jerk functions with cubic non-linearities. A general model can be formulated as:

$$\dddot{i}_{(t)} = a_1\ddot{i}_{(t)} - a_2\varphi(\ddot{i}_{(t)}) + a_3\dot{i}_{(t)} + a_4\varphi(\dot{i}_{(t)}) \ldots \tag{7.1}$$

where t is the time and $\dddot{i}_{(t)} \ldots$ are the derivates of variable (current), and $\varphi(\ddot{i}_{(t)} \ldots)$ is a simple function chosen to permit electronic implementation in our system. Guided by the argument that simple non-linear functions are sufficient to produce chaotic behavior [129], we assume the form:

$$F_m(\Psi_n) = a_{m0} + \sum_{q=1}^{d} a_{mq}\Psi_q + \sum_{q,e}^{d} b_{mqe}\Psi_q\Psi_e \tag{7.2}$$

that is a quadratic polynomial characterized by the constants a and b and where the functions in Ψ form a complete orthogonal set. Equation (7.2) is used to analyze Fig. 7.6. With such complex systems, the easiest and most transparent method for finding approximate solutions to differential equations is to use Euler's hyperbolic functions. In fact, although these equations are not easy to solve, they are of mathematical and practical interest, for example, in that they give the solution of complex equations, or determine the components of chaotic electrical circuits. Another important application is the study of magnetic field lines in a turbulent conducting fluid such as the plasma of electrically charged particles used in controlled nuclear fusion. Various mathematical alternatives are available for interpreting and analyzing chaos. Graphs of data plotted as a function of $i'^{n}_{(t)}$ produce a plot with a discernible structure in the form of closed loops signifying a periodic system (Fig. 7.8).

A simple chaotic system would produce a plot with a discernible structure. A useful tool for distinguishing between a quasi-periodic and a chaotic attractor is the power spectrum of the time series, which will have a few dominant peaks in the spectrum at discrete frequencies for quasi-periodic trajectories but a broad spectrum for random or chaotic trajectories. In Fig. 7.9, the frequency is in units of the Nyquist critical frequency, whereas the power is in arbitrary logarithmic units. The criterion for dynamic chaos orbits is the existence of at least one positive Lyapunov exponent, and in our case, the higher value is 0.175 ± 0.093 (Fig. 7.10).

In general, there are as many exponents as there are dynamical equations. The number of significant eigenvalues is a measure of the complexity of the system, and if the data consist of chaotic and random components, the measure of the Lyapunov exponent should help to extract the randomness. The eigenfunctions obtained for our system are displayed in Figs 7.6 and 7.11, sorted from largest to smallest. The data are then fitted to a set of non-linear model equations. In the procedure for calculating the eigenvalues for the system, it

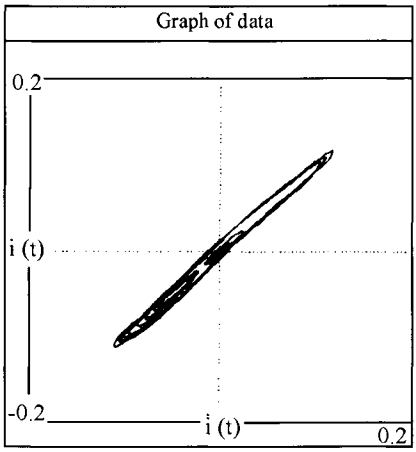

Figure 7.8. Graph of data in $i_{(t)}$ versus $\dot{i}_{(t)}$.

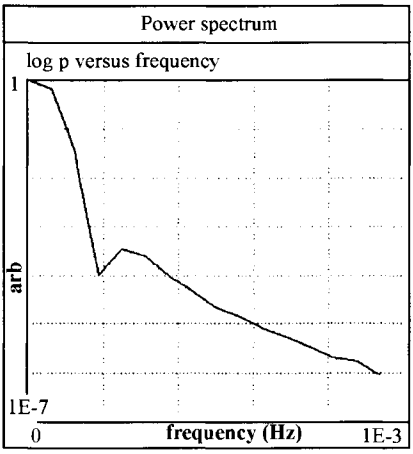

Figure 7.9. Power spectrum obtained by fast Fourier transform.

was necessary to create a Jacobian matrix containing the numerical values of parameters a and b (Table 7.2) characterizing the quadratic polynomial. For these values the dynamic is quasi-periodic, with a trajectory that lies on double-lobed invariant torus in the correlation matrix (Fig. 7.12).

The Rössler attractor in its phase space is topologically simpler than the Lorenz double-lobed attractor, but the two are roughly equivalent in that they both tend to resemble the single folded-band structure. The view of the phase space consists of a two or three-dimensional plot in which the first or second derivative is plotted versus time at each data

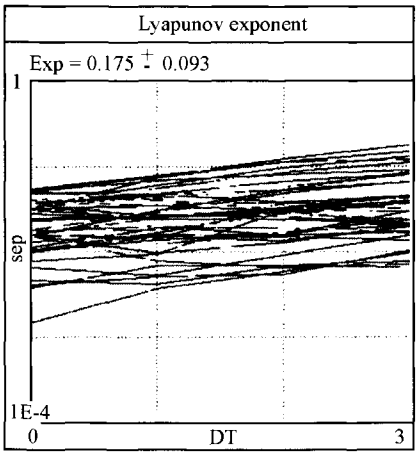

Figure 7.10. Most positive Lyapunov exponent. The plot shows the separation in units of the diameter of the smallest D-dimensional hyper-sphere enclosing the attractor at n successive time steps.

Table 7.2. Coefficients of model equations calculated from the last 32 data points

	psi_1	psi_2	psi_3
a_0	0.000004	−0.000015	−0.000014
a_1	0.991667	0.037877	0.016647
a_2	−0.417497	0.951311	−0.047384
a_3	0.033459	−0.036234	0.002128
b_{11}	0.000016	0.000925	−0.000038
b_{12}	−0.000401	0.000618	−0.000033
b_{22}	0.000039	−0.000099	0.000005
b_{13}	0.000006	0.000013	0.000001
b_{23}	−0.000002	0.000000	−0.000000
b_{33}	−0.000000	0.000000	−0.000000

point. Some cases that are not obviously periodic in two dimensions may reveal their periodicity in three dimensions. Periodic data should appear as a closed curve on such plots. In Fig. 7.13, the system shows that the double-lobed phase-space volume occupied by a set of points will be conserved as the system evolves in time. Then the orbit will eventually return close to the initial data. The solution is semi-chaotic with two periods, but not as an attractor.

In such a system, we can put forward the following interpretation. The oxide layer containing tritium is energetically active by β^- particles and is a powerful source of electrons emitted during decay into oxide, so that it may be called an 'oxide-layer network'. It operates with electron diffusion in a random process in which excited species move from one region to another by attraction or repulsion, depending on the trajectory of the β^- particle. Such a system leads to a deterministic model. Considering the work of Sprott, the dynamical system can be formulated by eqs (7.1) and (7.2), and can be represented by a particular

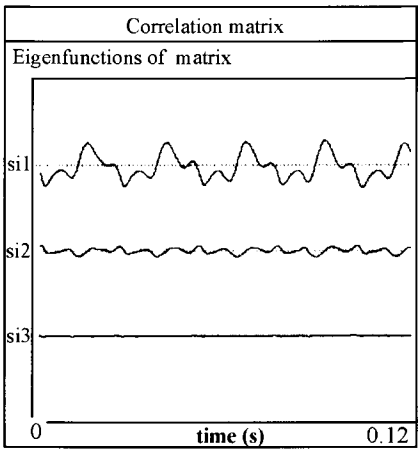

Figure 7.11. Eigenfunctions of the correlation matrix plotted versus time.

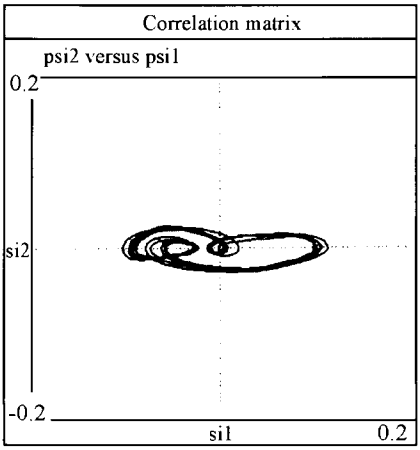

Figure 7.12. Correlation matrix drawn from the two largest eigenfunctions.

electrical circuit as shown in Fig. 7.14. It is equivalent to an oscillator with three phase shifts and non-linear positive feedback. This system was chosen to optimize factors such as robustness to errors in the parameters of chaos. In this case, the low-energy electrical circuit uses resistors, capacitors, diodes with electrical generator brought by decay electrons, which makes the bifurcations occur (Fig. 7.15). Three reactive components are required for chaos in such a system with continuous flows, so that the Kirchhoff representation obeys the differential equations.

When the forward potential drop of the diodes is taken into account, the circuit should permit a bifurcation. This easily constructed oscillator circuit solves the previous equations

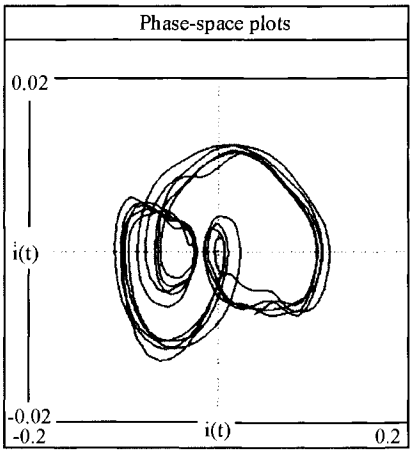

Figure 7.13. Phase space portrait obtained from Fig. 7.6.

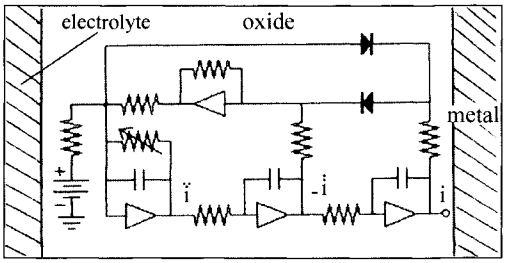

Figure 7.14. Equivalent circuit for chaos simulation with resistors, capacitors, diodes and electrical generator.

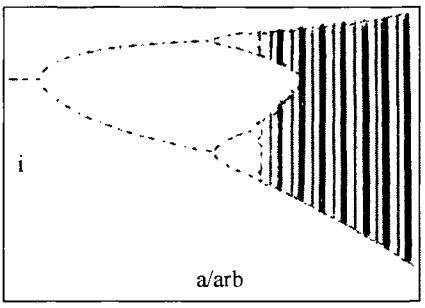

Figure 7.15. Bifurcation diagram as damping is reduced.

over a wide range of frequencies in units of the Nyquist critical frequency, and exhibits a variety of dynamical behaviors. Random and chaotic data give rise to broad spectra.

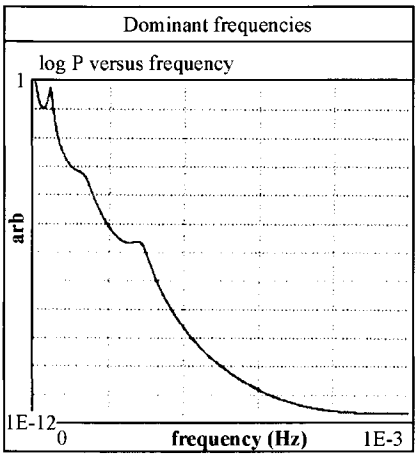

Figure 7.16. Dominant frequencies obtained by the waveform Fourier transform.

Periodic and quasi-periodic data will produce a few dominant peaks in the spectrum. In this electrical circuit, the most straightforward implementation involves three active integrators to generate the ordinary differential equations with bifurcation. Equations (7.1) and (7.2) are well suited for a solution using the weighted sum of the three signals (Fig. 7.14) and the constant terms generated by the electrical source. In Fig. 7.13, one clearly recognizes the phases with two orbits that cause the two amplitudes. The system spirals into an orbit of either large or small radius. The transition to the orbit of large radius occurs abruptly, and is governed by the existence of a bifurcation in phase space from which the system can be attracted to either the small or the large radius orbit, depending on the side from which the separator is approached. In Fig. 7.15, the bifurcation diagram of maximum current versus time $i(t)$ verifies the appearance of chaotic behavior mixed with the periodic network. In this figure, the local maximum of $i(t)$ is plotted as the depressing constant parameters are gradually decreased. Note that the scales are plotted backwards to emphasize the similarity to the logistic map. The Feigenbaum diagram clearly shows a period-doubling route to chaos in the higher values of the constant parameters. Otherwise, the diagram resembles the quadratic chaotic jerk function. Indeed, there is a typical chaotic band structure disrupted by the occurrence of periodic windows. Also interesting is the waveform Fourier transform shown in Fig. 7.16, which exhibits three distinct primary frequencies. The peak denoted f_1 corresponds to the long period of the entire oscillations, f_2 to the period of the small amplitude oscillations, and f_3 to the slightly faster large amplitude oscillations than f_2.

We can model the system by two successive events leading to depassivation and repassivation processes, thereby showing the existence of a chaos law and a cyclic phenomenon. This bifurcation indicates that it should be easy to knock off balance from the passive state to depassivation and vice versa, depending on the tritiated oxide. Since the preceding experiments were all performed in the presence of dissolved and absorbed tritium in oxide, we checked whether its presence was responsible for such behavior, eliminating it

by degassing. After elimination, periodic oscillations are not observed. To conclude, tritium absorbed in steel clearly leads to a modification of the oxide layer characteristics and destabilization.

In greater detail, wide fluctuations in current originate in the energy deposited (ΔE) by the β^- particle in the oxide layer, which is divided for excitation and ionization [131]:

$$\Delta E = \Delta E_e + \Delta E_i \tag{7.3}$$

ΔE_e and ΔE_i represent each part, and it would be interesting to determine their contribution. To do this, fluctuations by ionization are characterized by the significance parameter κ, which is proportional to the ratio of mean absorbed energy to the potential maximum energy generated during radioactive decay of tritium.

$$\kappa = \frac{\Delta E}{E_{max}} \tag{7.4}$$

κ depends on the charge and mass (m) of the β^- particle (electron), and the density and thickness of oxide layer. If the thickness is large, κ tends towards higher values, while if the thickness is small, κ tends towards lower values. In our case, let us consider a particle absorbed in thin oxide layer. The absorbed low energy can therefore be evaluated by the Urban and Monte Carlo methods [131]. In these methods, the atoms forming the oxide are assumed to have only two binding energy levels, E_1 and E_2. The β^- particle-atom interaction is accordingly an excitation with E_1 or E_2, or an ionization with an energy distributed according to the function:

$$g_{(E_i)} = \frac{(E_{max} + I)I}{E_{max} E_n^2} \tag{7.5}$$

where I is the mean ionization energy of oxide which can be expressed as a current. The macroscopic cross-section for excitation is:

$$\Sigma_e = C \frac{f_e \log\left(\frac{2m\varsigma^2\upsilon^2}{E_i}\right) - \varsigma^2}{E_a \log\left(\frac{2m\varsigma^2\upsilon^2}{I}\right) - \varsigma^2}(1 - r) \tag{7.6}$$

and the macroscopic cross-section for ionization is:

$$\Sigma_i = C \frac{E_{max}}{I(E_{max} + I)\log\left(\frac{E_{max}+I}{I}\right)} \tag{7.7}$$

where r and C are the parameters of the model, E_a the atomic energy levels, υ the ratio of the energy concerned to the mass of the β^- particle, ς^2 is equal to $(1 - 1/\upsilon^2)$ and f_e the

oscillator strengths. The oscillator strengths and the atomic level energies should satisfy the constraints:

$$f_1 + f_2 = 1 \tag{7.8}$$

$$f_1 \log E_1 + f_2 \log E_2 = \log I \tag{7.9}$$

Parameter C can be defined as the derivative of absorbed energy as a function of time. The number of impacts in the oxide follow the Poisson distribution with a mean number (n_i). In a step Δt, the mean number of impacts in the oxide is:

$$n_i = \Sigma_i \Delta t \tag{7.10}$$

The derivative of the absorbed energy is the sum of the excitation and ionization contributions:

$$\Delta t \frac{dE}{dt} = \left[\Sigma_1 E_1 + \Sigma_2 E_2 + \Sigma_3 \int_I^{E_{max}+I} E g_{(E_i)} \, dE \right] \Delta t \tag{7.11}$$

Hence using eqs (7.6) to (7.9), one can define parameter C as:

$$C = \frac{dE}{dt} \tag{7.12}$$

The following values have been selected by computation for the parameters:

$$E_2 = 10Z^2 \quad (\text{eV}) \quad \Rightarrow \quad E_1 = \left(\frac{I}{E_2^{f_2}} \right)^{\frac{1}{f_1}} \quad r = 0.4 \tag{7.13}$$

Z is the atomic number of an element in the oxide shelled by a β^- particle. With these values, the atomic level E_2 corresponds approximately to the K-shell energy of the atoms and Zf_2 the number of K-shell electrons. r is the only variable which can be tuned freely. It conditions the relative contributions of ionization and excitation to energy absorption. Each energy quantum is computed with the assumption that this is small, and in consequence, the cross-section can be considered constant along the path length. The energy for excitation is:

$$\Delta E_e = n_1 E_1 + n_2 E_2 \tag{7.14}$$

where n_1 and n_2 are sampled from the Poisson distribution. The part leading to ionization can be generated from the distribution $g_{(E_i)}$ by the inverse transformation method:

$$u = F(E) = \int_I^E g_{(t)} \, dt \tag{7.15}$$

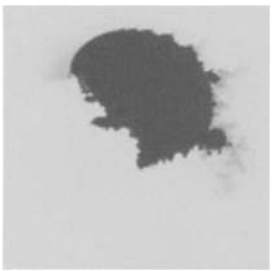

Figure 7.17. Generalized two Phoenix section for the conservative chaotic case.

$$E = F_{(u)}^{-1} = \frac{I}{1 - u\frac{E_{\max}}{E_{\max}+I}} \tag{7.16}$$

where u is a uniform random number between $F_{(I)} = 0$ and $F_{(E_{\max}+I)} = 1$. The contribution leading to ionization will be:

$$\Delta E_{\mathrm{i}} = \sum_{j=1}^{n_3} \frac{I}{1 - u_j\frac{E_{\max}}{E_{\max}+I}} \tag{7.17}$$

where n_3 is the number of ionizations sampled from the Poisson distribution. From eqs (7.3), (7.14) and (7.17) the energy absorbed in the oxide, leading to excitation and ionization effects, becomes:

$$\Delta E = n_1 E_1 + n_2 E_2 + \sum_{j=1}^{n_3} \frac{I}{1 - u_j\frac{E_{\max}}{E_{\max}+I}} \tag{7.18}$$

This energy is responsible for oxide breakdown. Three terms can be observed, with a respective frequency for each. The three frequencies correspond to the peaks obtained in Fig. 7.16.

We have plotted the variation of eq. (7.18) with fractal representation (Figs 7.17 and 7.18). Fig. 7.17 shows a generalized two Phoenix section in which the experimental points are plotted where the trajectory punctures in 2D plane. The quasi-periodic orbit is surrounded by a chaotic region leading to the above conclusions. Considering the work of Sprott [130], correlation can be obtained between the Fig. 26.1 and Fig. 26.9 (chapter 26) which represent the mutual effect of current and energy on the oxide layer in the fractal dimension. These figures are representative of the local over-concentration of tritium in traps: voids, blisters (chapter 6) and around the crystals and cracks (chapter 8) present in the oxide layer. This over-concentration is responsible for excess energy released during decay. Oxide breakdown is appreciable in the presence of tritium.

As known by conventional studies, oxide layers are sensitive both to electrons and to light photons (2 eV), but the similarities end there. While β^- particles are different from

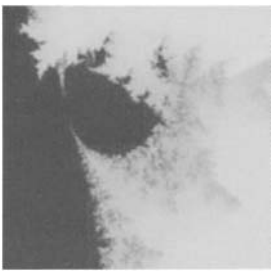

Figure 7.18. Detail showing a chaotic region adjacent to orbit.

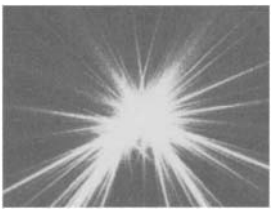

Figure 7.19. Trajectory of radiation obtained by fractal analyzer.

photons, the excited electrons that make up radiation behave differently simply because they are 10^4 times more energetic, and the pictures representing radiation in oxide are therefore different. Moreover, we have no instrument capable of monitoring continuously the entire observation in the keV energy regime over time. However, the software computing the fractal-trajectory in time is ideally suited to monitor the variable energy in the oxide layers and discover sources of a few keV. They serve to simulate the interactions of low energy particles in oxide. Fractal trajectory analyzers have been developed by dynamic mathematics. In the following we will explain the trajectory of radiation and what it can tell us about oxide behavior. These β^- particles move at 1/6 the speed of light in oxide. During displacement, excited species are produced, and these species soon decay, giving rise to radiolysis and, finally, to stable oxidizing species. The excited species have an average half-life of 10^{-15} seconds; this is a challenge when working with them before they decay. In addition, the excited electrons are known to display variable energy: 11.4 to 18.6 keV, and to flare at time scales in femtoseconds. The excited electron could go on to catalyze over 100 reactions in oxide, creating enough energy for this process to be used as a power source. Since the excited electrons are more reactive than conventional electrons, the atoms are bound together far more tightly, so that the nuclide can break down molecules in oxide to form special excited molecules or molecular ions. Moreover, the length of the β^- particle trajectory depends on the energy released (11.4 to 18.6 keV).

Time, trajectory length and volume were aligned using a programmable fractal trajectory analyzer. Figs 7.19 and 7.20 are self explanatory; they show in white the simulated interactions of radiation in absorbent oxide in a volume of 10^{-5} cm^3. In the Fig. 7.19, the

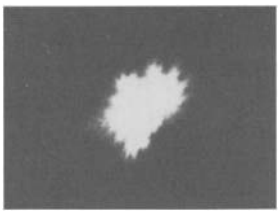

Figure 7.20. Aspect total of radiation obtained after a longer time.

intense region is the tritium decaying in oxide layer. The radiations are charged with negative currents, producing artificial tomography and events. The length of the β^- particle trajectory gives unambiguously the velocity distribution in oxide. It may be observed that radiations are stopped in the oxide layers, and do not cross over. It is evident that electron oscillations are produced in the current; they depend on the two parameters: excitation and ionization (eqs (7.14) and (7.17)).

3.2. *Measuring the tritium adsorbed on the steel surface*

The voltammetric curves in Fig. 7.21 were obtained under the same conditions as those in Fig. 7.3. Electrolytic tritium was added to the surface of the steel and immediately afterward the voltammetric curves were plotted. The currents of the steel curve superimposed on this correspond to the oxidation of the tritium adsorbed and back-diffusion. It can be seen that in the first forward scan, after the production of ^3H by electrolysis, there are current instabilities that start in the prepassivity phase and continue in the passivity.

There are still some instabilities at the beginning of the passive region in the backward scan. These instabilities disappear in the following sweeps. This means that they are present when there is the greatest amount of tritium adsorbed, and also they are not observed when there is only hydrogen (Fig. 7.3). They definitely result from fractures of the passive oxide layer by the combined effect of the energy of the β^- particles [132] and the adsorption of tritium accompanied by diffusion or back-diffusion in the first layers of the steel [133] and [134]. This makes possible embrittlement and stress corrosion of the passive oxide layers. From these curves, we tried to apply Chevalet's equation [135]:

$$i = nFA\pi^{-0.5} D^{0.5} C t^{-0.5} f(\theta) \tag{7.19}$$

$$\text{with:} \quad f(\theta) = \theta^{-1} - (1+\theta^2)^{-0.5} \tag{7.20}$$

$$\text{where:} \quad \theta = (t/T)^{0.5} \tag{7.21}$$

In these equations, D is the coefficient of diffusion of ^3H in the steel, C the amount of ^3H introduced or adsorbed at the steel surface, T the addition time for ^3H and t the time

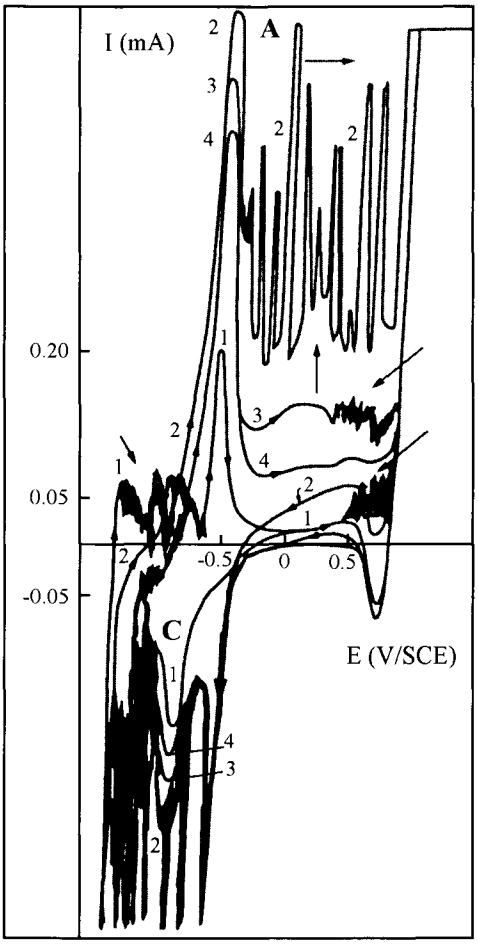

Figure 7.21. Voltammograms—effect of adsorbed tritium, 6×10^{-8} atom cm^{-2} $^3H_2$, energy released: 4×10^3 MeV cm^{-2} s^{-1}, v: 200 mV s^{-1}, ω: 2000, pH: 13, addition of electrolytic $^3H_2$: 3 min at -1.5 V/SCE, 1: before addition to $^3H_2$, 2: 1st cycle after addition, 3: 2nd cycle, 4: 3rd cycle.

following the addition. From these equations, the following is given in [136]:

$$D^{0.5}C = 6 \times 10^{-7} \text{ atom cm}^{-2}\text{ s}^{-1} \tag{7.22}$$

Taking the average value of D as 2.3×10^{-12} cm^2 s^{-1} [136], a volume concentration close to the surface of $C = 10^{-1}$ atom cm^{-3} was derived. The thickness of the diffusion layer is [137]:

$$\delta = (\pi Dt)^{0.5} \tag{7.23}$$

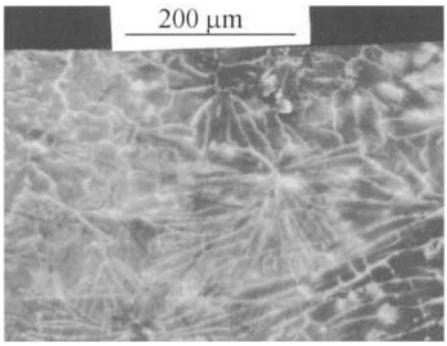

Figure 7.22. Small cracks in the oxidized surface.

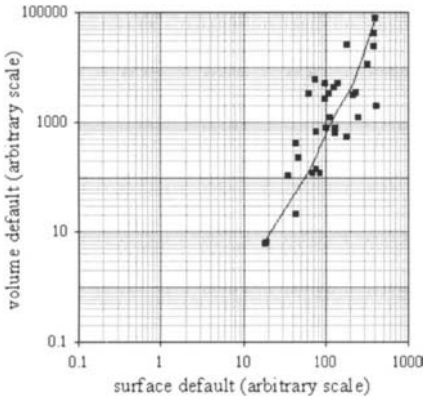

Figure 7.23. Defaults concentration at the oxidized surface and in the bulk.

for $T = 3$ min, $\delta = 400$ nm. Oxide thickness is generally a few tens of nm. This signifies that for this depth, tritium diffuses into oxide and the first layers of alloy. The amount of tritium at this depth and at the surface of the steel is significant. This process must be facilitated by a martensitic transformation which considerably increases the solubility and adsorption of the tritium [138] and [139].

3.3. Appearance of the steel surface after corrosion of tritiated oxide

After having imposed these operating conditions for 30 min and a pH of 6 in tritiated water, the surface of the stainless steel was examined with a Scanning Electron Microscope. The surface was seen to be locally corroded and the photographs in Fig. 7.22 show small cracks in the oxidized surface. These must, in effect, result from stress corrosion of the oxide layer by addition of the free potential position, dissolved tritium adsorption and the energy of the

β^- particles. This corrosion was assured to be due to diffusing tritium in this area. During charging, enrichment is produced: firstly at the surface, then in the oxide layer leading to defaults as seen in the Fig. 7.23. This type of corrosion is not negligible since it can lead to the destruction of the oxide layer.

4. Conclusions

Tritium dissolved in tritiated water adsorbs at the steel surface and when it decays the energy of the β^- particles is released on this surface. The free potential, like the corrosion potential, is located in the active peak of the steel. These phenomena lead to the destabilization of the passive oxide layer and to local surface fractures. Photographs show the presence of small local surface cracks, which definitely result from destabilization and stress corrosion of oxide layers.

Chapter 8

STRESS CORROSION CRACKING BY TRITIUM

1. Introduction

Research on stress corrosion due to tritium and helium trapped in stainless steel has been carried out by different authors to provide better knowledge and understanding of the embrittlement effects. For this, Louthan et al. [139] showed, by autoradiographic examination (sensitization of a photographic plate by β^- particles), the zones where the tritium penetrated the steel. Hirabayashi and Saeki [140] showed that non-negligible concentrations of ^3H_2O, $^3H_2$, and O^3H^- are absorbed by oxide. Moreover, Burns and Moore [141] noted a modification of the corrosion potential indicating that the oxide layers are subjected to stresses and local breakdowns by the β^- particle energy, which is estimated to be 5×10^3 MeV/cm^2 s^{-1}. Oxide subjected internally to β^- particles is progressively degraded [142]. Austin et al. [143] gave higher tritium and helium concentrations at the interface between oxide layer and alloy. These greater concentrations can be explained by the considerable difference in the diffusion coefficients between the alloy and oxide as determined by Tison and Fidelle [144] and [145]. Moreover, Braun et al. [133] showed, by autoradiography, the fixation of tritium at this interface along the grain boundaries. The grain boundaries are diffusion short-circuits, but on desorption, the tritium is trapped at the interface between the grain boundaries and the oxide layer, which results in an internal oxide zone that is particularly sensitive to tritium, helium and release energy. Trapped tritium leads to formation of martensite, which is more corroded than austenite. For this, dislocations in the neighborhood of the grain boundaries, such as the formation of surface cracks on the alloy, were shown by Louthan et al. [146]. For the present study, we used 316L stainless steel that had been internally exposed to gaseous helium and tritium for several years. Using tritiated steel, the voltammetric curves behave differently from those of a non-tritiated steel.

2. Results

To determine the distribution of the tritium on the steel surface into oxide and in the first layers of the alloy, we performed electrolyzes at three different potentials following the technique described in the literature [137] and [147]. According to this, at -0.3 V/SCE, the tritium adsorbed on the oxide is oxidized to ^3H_2O; this tritiated water was recovered

for analysis by liquid-scintillation spectrometry. At −1.3 V/SCE, the oxide layer was practically destroyed, and we again analyzed the tritiated water. The aged oxide thickness was determined to be 50 nm. At −1.5 V/SCE, the tritium present in the first layers ($\leqslant$ 500 nm) of the alloy was displaced by isotopic exchange with the hydrogen generated by electrolysis. Back-diffusing tritium was analyzed by the same method [137] and [147]. The amounts of tritium recovered and the energy released in tritium decay are given in Table 8.1. The energy released in the surface oxide appears to be sufficient to degrade it.

Finally, there is the effect of the trapped helium. Metal embrittlement has to be considered as dependent on the bulk helium concentration. The amounts of helium cannot be negligible since this steel was exposed to tritium for several years. Helium is essentially

Table 8.1. Amounts of tritium at the surface of the steel and energies released

	Oxide		In the alloy	
	At the oxide surface	In the oxide	Tritium back-diffused by H_2 exchange ($\leqslant$ 0.5 μm)	Diffused by H_2 exchange ($\leqslant$ 0.5 μm) and ^3H from deeper layers
^3H atoms cm^{-2}	5×10^{-10}	10^{-10}	5×10^{-11}	10^{-8}
Energies released (MeV cm^{-2} s^{-1})	3×10^3	10^3	5×10^2	10^5

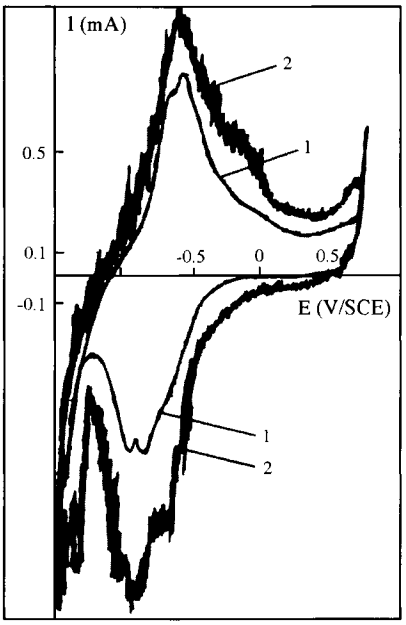

Figure 8.1. Voltammetry curves for stainless steel, v: 200 mV s^{-1}, 1: naturally oxidized non-tritiated steel, 2: naturally oxidized tritiated steel.

trapped in the surface zone of the steel. Its concentration, C, was obtained by melting and analysis by mass spectrometry or by applying the following equation [14]:

$$C(t) = C_0\left[1 - \exp\left(-t \ln(2/\tau_{1/2})\right)\right] \tag{8.1}$$

where C_0 is the initial tritium concentration. The concentrations $(C_0 - C)$ and C are given as the ratio of ^{3}H and ^{3}He atoms to metal atoms at the time t. This means that with eq. (8.1), the concentration of helium-3 trapped in the metal can be easily obtained from the tritium concentration and gives significant concentrations of 10^{-5} atom cm^{-3} ^{3}He in the neighborhood of the steel surface. At these values, tritium and helium with release energy can lead to surface embrittlement of the steel and to breakdowns in the oxide layer.

The voltammetric curves (Fig. 8.1) show higher current at any potential for naturally oxidized tritiated steel (curve 2) than for naturally oxidized non-tritiated steel (curve 1). The Flade potential is shifted by $\sim$ 100 mV toward more positive potentials with respect to the non-tritiated steel and the corrosion current is greater. These differences can be attributed to intergranular corrosion, as Sedriks [28] has done. Confirmation should be given later by Scanning Electron Microscopy examinations.

It can be seen in the curves in Fig. 8.2 obtained with tritiated steel that the current in the second scan is much higher than that in the first for the entire potential range indicating

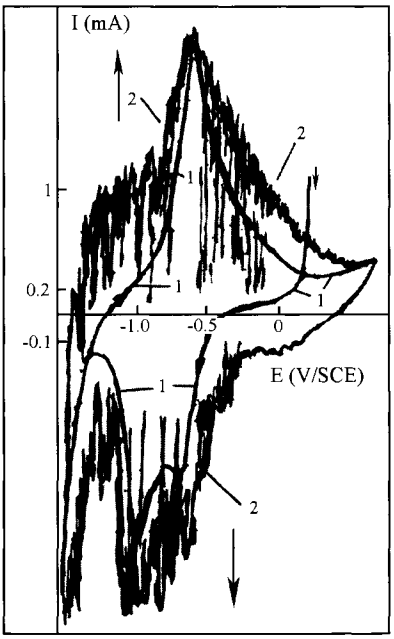

Figure 8.2. Voltammetry curves for naturally oxidized tritiated stainless steel, v: 200 mV s^{-1}, 1: first cycle, 2: second cycle.

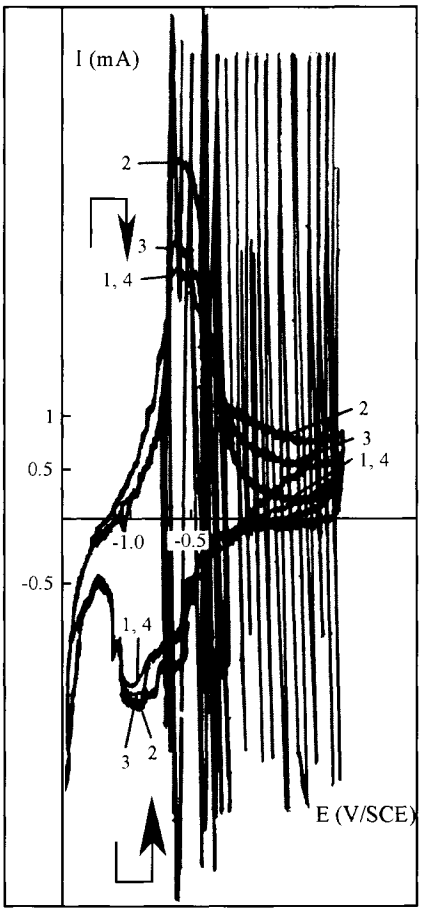

Figure 8.3. Voltammetry curves for naturally oxidized tritiated stainless steel, v: 200 mV s^{-1}, hydrogen charging for 1 min, and continuous voltammetry cycles after the charging, 1: before the hydrogen charging, 2: first cycle after the hydrogen charging, 3: second cycle, and 4: third cycle.

that corrosion is greater. A possible interpretation of the curves is that part of the natural tritiated oxide layer was progressively removed in successive cycles, offering less and less protection, and after some time, a new tritiated oxide layer, which was under the preceding one and had more defects (breakdowns in the oxide layer), was exposed. This results in the current instabilities observed in the curves. This could also involve a fraction of the alloy surface, which could be cracked by embrittlement due to the tritium and the helium.

The curves obtained after charging hydrogen at −1.5 V/SCE are shown in Fig. 8.3. Before hydrogen charging, the curve shows a few current instabilities in the active peak and prepassivity (curve 1). Curve 2 and the following were plotted immediately after the hy-

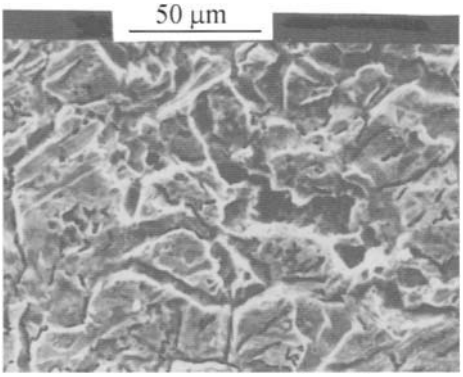

Figure 8.4. Fracture of the oxide layer on stainless steel.

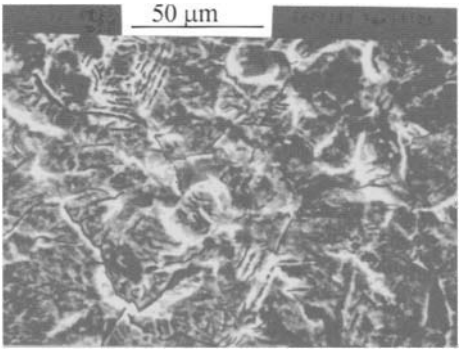

Figure 8.5. Surface embrittlement of the alloy in stainless steel due to tritium.

drogen charging. At the charging potential, it is possible that not all the chromium oxides had been removed [101]. Current instabilities in the prepassivity were again observed in curve 2; these instabilities were extended to the transpassive potential. During the backward scan, the current in the passivity corresponds to the oxidation of the back-diffusing hydrogen increased by that of the steel oxidation. The backward scan did not show any current instabilities. In the second scan after the hydrogen charging (curve 3), the current instabilities were limited to the range of the prepassive potential; these were no longer found in the passive potential range. The current due to the oxidation of back-diffusing hydrogen was again observed. These instabilities can result from defects in the oxide layer (consisting essentially of Cr_2O_3 as indicated by Olefjord et al. [148] among others, who used surface-sensitive techniques such as X-ray photoelectron spectroscopy) or from surface cracks, caused by embrittlement. The defects and the cracks may be due to the tritium and helium present in the oxide and in the surface layers of the alloy.

After these various results were obtained by voltammetry, the surface of the tritiated steel was examined by Scanning Electron Microscopy. The appearance of the oxidized surface of the tritiated steel is shown in Fig. 8.4. It would seem that the microstructure of this steel can be predicted. The grain boundaries have been corroded and surface breakdowns appear to be present that correspond to the oxide layer. The grain boundaries acted as short circuits in the back-diffusion of the tritium, and after this back-diffusion, there could be trapping of the tritium at the interfaces of some of the grain boundaries and in the oxide layer (a high solubility in the oxide [144] and [145]). There is an accumulation of the tritium accompanied by the formation of martensite and helium at this location (Fig. 4.10). Under these conditions, there can be periodic local removal of the unstable oxide layer that was opposite the grain boundaries, subsequently inducing localized stress corrosion. The surface embrittlement of the alloy is shown in Fig. 8.5. The photograph was obtained after removal of the surface tritiated oxide at a potential of -1.3 V/SCE for 1 h. Note that cracks are visible at the surface, and some cleavage planes also appear to be present. Tritiated steel equipment corroded more easily than did that made of non-tritiated steel.

3. Conclusions

It can be concluded that decay helium, tritium, and β^- particle energy hinder good passivity of the tritiated steel and facilitate localized stress corrosion at the oxide layer located below some grain boundaries. Current instabilities observed by voltammetry were shown by very fast variations that successively took on anodic and cathodic polarizations. These variations must depend on the chemical kinetics of the oxide layer during its destruction and its reforming (repassivation) above the involved grain boundaries. These instabilities started to appear in the prepassivity, thus making it more difficult to obtain subsequently a passive layer. They continue to appear for some time and this period can be called successive depassivation and repassivation phases of the steel. Scanning Electron Microscopy examination of the tritiated and oxidized surface of the steel showed breakdowns in the oxide layer. The surface alloy showed some cracks that would appear to be due to the embrittlement by the tritium and helium. Martensite was identified on the surface embedded in austenite.

Chapter 9

STRESS CORROSION CRACKING IN WELDS

1. Introduction

Welded 316L stainless steel is extensively used because of its good mechanical properties and ease of welding. The weldments are made using the tungsten inert gas welding process. The microstructure in the weld is dendritic and thus differs from that of the wrought base steel. Moreover, the ferrite is incorporated, as it must be in the austenitic weld in order to avoid cracking and microfissuring upon cooling. The complex microstructure, thus produced in the weld, can lead to severe corrosive attack in comparison with the base steel. For this reason, an attempt was made to investigate the localized corrosion susceptibility of tritiated oxidized weldments. The tritium and helium concentration profiles are higher near the oxidized surface, as shown by Louthan [139]. This greater concentration is due to the solubility of tritium in the oxide, the difference in the diffusion coefficients between the alloy and oxide, and the low diffusivity in these. On addition of tritium, the energy and helium released may act on oxidized welded stainless steel. The oxidized layers are ionized at low energies (a few keV), or they are broken down at high energies (above 10^4 MeV). The oxide is therefore subjected internally to more energy due to the β^- particles, and more tritium and helium, over a few nm of thickness, and these are liable to degrade it more easily.

2. Results

2.1. Procedure and tritium distribution

The welding parameters are given in Table 9.1. Before and after welding, the samples are chemically cleaned and electrochemically polished, then, the samples were stored in a tritium gas atmosphere for three years at room temperature. After this storage it is necessary to know the distribution of the tritium trapped at the oxidized surface and in the first layer of welded alloy, therefore electrolyzes were performed at three different potentials following the technique described previously [147] and [137]. The amounts of tritium recovered and of energies released in the decay of the tritium are given in Table 9.2. According to the values obtained, the amounts of energy released and of tritium in the oxidized welded

Table 9.1. Welding parameters

Process	Method	Current	Voltage	Welding speed	Inert gas
Tungsten inert gas (TIG)	Negative electrode	50 A	12 V	20 cm min^{-1}	Argon

Table 9.2. Amounts of tritium at the surface of the welded steel and energies released

	On the oxide layer	In the oxide layer	Alloy underlying the oxide
^3H atom cm^{-2}	10^{-10}	4×10^{-11}	6×10^{-9}
Energies released (MeV cm^{-2} s^{-1})	7×10^2	4×10^2	6×10^4

surface and welded alloy near the surface are actually high enough to degrade the tritiated surface.

2.2. *Electrochemical methods*

2.2.1. Polarization curves The anodic curves of tritiated oxidized welds, obtained at pH 11 and low scan rate, are seen in Fig. 9.1. They show an active peak at −0.7 V/SCE, a transpassive peak at 0.3 V/SCE and the corrosion potential at −0.9 V/SCE. The passive region extends from −0.6 to 0.1 V/SCE. No intermediate oxide shoulders are found.

The peak potentials and the passive region are less displaced than voltammetric curves at a high scan rate. This makes it possible to choose accurate potentials in order to draw electrochemical impedance diagrams. It is important to know the corrosion potential of non-tritiated welds. It is equal to −0.6 V/SCE; its value is higher than in tritiated welds. This means that tritiated welds of 316L stainless steel are less 'noble' and the result is that they are more rapidly corroded.

2.2.2. Voltammetric curves The voltammetric curve obtained at a high scan rate is shown in Fig. 9.2 where it is seen that the voltammogram extends between the potential range of the hydrogen and oxygen evolution.

In this figure, on increasing the potential in the forward direction, the active peak appears near −0.5 V/SCE. Before the reverse scan, a major oxidation current is observed from 0.5 V/SCE, this signifies weld oxidation at the transpassivity, and oxidation is again observed at the beginning of the reverse scan. A major reduction peak is seen at −1.2 V/SCE; it is the conjugate of the active peak. With tritiated oxidized welds, there is less passivity and the corrosion is higher than in non-tritiated oxidized welds.

2.2.3. Electrochemical impedance spectroscopy The data in Fig. 9.3 were obtained with tritiated oxidized welds. The Nyquist spectra tend towards infinity at low frequencies for prepassive and passive potentials. Electron diffusion within the oxide may control the kinetics whereas ionic diffusion within the oxide layer would be less limiting. Nevertheless, near the transpassive region, a Warburg straight line is clearly seen. At these frequencies, the ionic diffusion within the oxide layer is slightly greater due to breakdown of the oxide

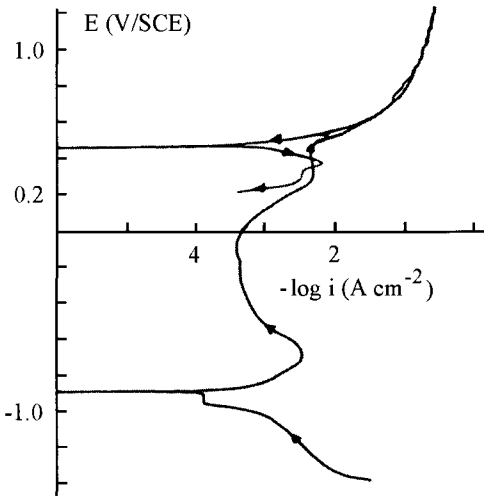

Figure 9.1. Polarization curve of tritiated oxidized weld, v: 5 mV s^{-1}, pH 11.

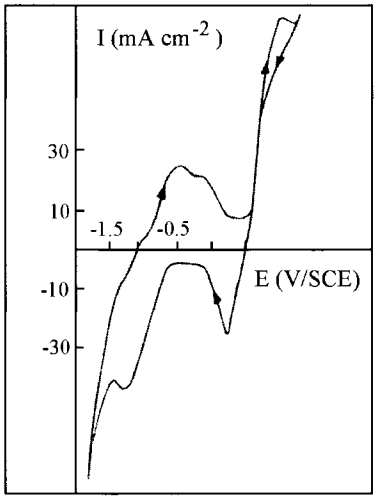

Figure 9.2. Voltammetric curves of tritiated oxidized weld, v: 200 mV s^{-1}, pH 11.

layer [149] and [150]. At high frequencies, the overlapped semi circle depends on the oxide layer characteristics.

The diagrams in Fig. 9.4 were obtained with non-tritiated oxidized welds. For the same potentials located in the passivity, the impedance values are much higher than those of tritiated samples which means greater passivity in the absence of tritium. In the active and

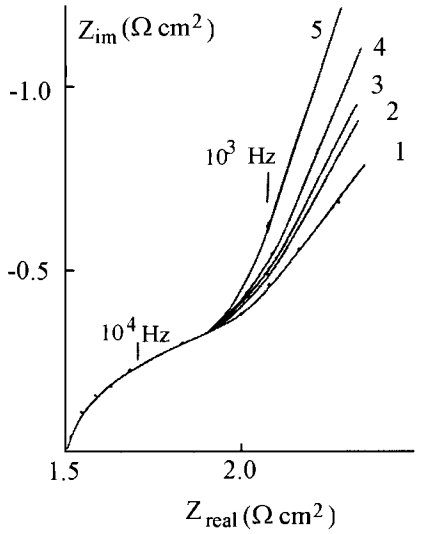

Figure 9.3. Nyquist diagrams—potential effect, pH 11, tritiated oxidized weld, 1: 0.4 V, 2: 0.3 V, 3: 0.2 V, 4: 0 V, 5: −0.2 V to −0.6 V/SCE.

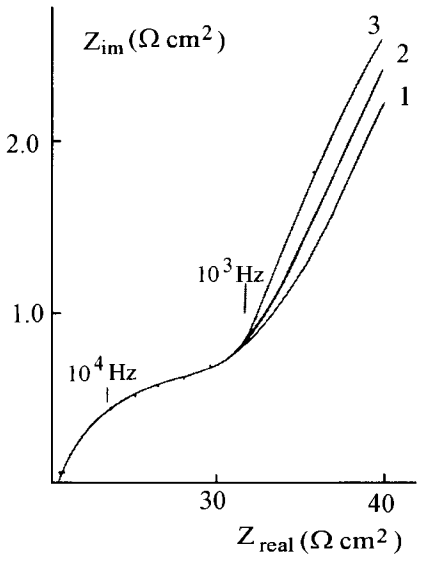

Figure 9.4. Nyquist diagrams—potential effect, pH 11, non-tritiated oxidized weld, 1: 0.4 V, 2: 0.3 V, 3: 0.2 V/SCE.

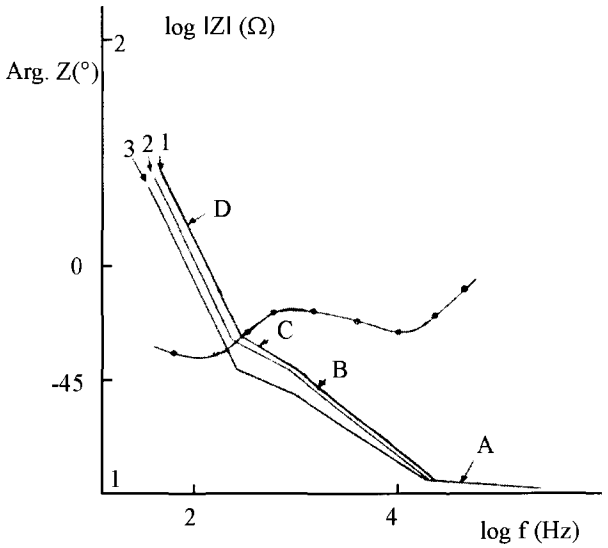

Figure 9.5. Bode diagrams—potential effect, pH 11, non-tritiated oxidized weld, 1: 0.5 V, 2: 0.3 V, 3: 0.2 V/SCE, phase angle: o–o–o.

passive regions, the impedances change less, therefore charge transfer and ionic diffusion have less effect on the kinetics.

Fig. 9.5 shows the phase angle and impedance modulus in Bode plots with three time constants for the passive and transpassive potentials obtained with non-tritiated oxidized welds. The diagrams can be analyzed as follows. Segment A is characterized by the electrolyte resistance. Segment B is the electrical response of oxide marked by non-dissipative characteristics. The slope of segment B must be -1, and in our case the difference may be attributed to superposition of the segments A and C. At lower frequencies, segment C appears and the slope is about -0.2 to -0.3. From this, a highly dissipative part of the oxide can be assumed. Segment D is characterized by a straight line with a slope of about -1, and corresponds to the Warburg straight line in a Nyquist plot.

From the equivalent circuit consisting of an oxide capacitance in parallel with the corresponding resistance and diffusion element, the capacitance value is difficult to determine due to the superposition of the segments A–C impeding the appearance of the slope of -1 in segment B. It is, nevertheless, possible to evaluate the oxide capacitance value taking into account the imaginary part at high frequencies by drawing an equivalent diagram. On this basis, calculations show that the oxide thickness is about a few nm. The thickness of the non-tritiated oxide weld is the lowest and any oxide layer is thus less protective with tritium present.

Fig. 9.6 shows the Bode plots realized with tritiated oxide for the passive and prepassive potentials. From these diagrams, donor densities can be calculated using the simplified Mott-Schottky equation. The value is estimated to be 10^{23} carrier cm^{-3} and the flatband

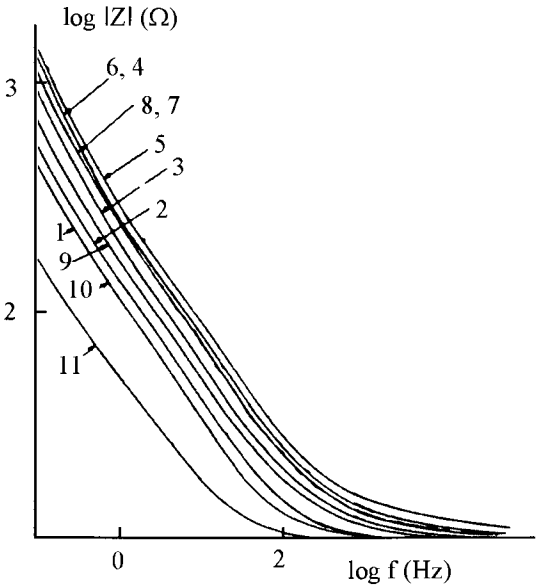

Figure 9.6. Bode diagrams—potential effect, pH 11, tritiated oxidized weld, 1: 0.6 V, 2: 0.4 V, 3: 0.3 V, 4: 0.2 V, 5: 0 V, 6: −0.2 V, 7: −0.4 V, 8: −0.5 V, 9: −0.6 V, 10: −0.65 V, 11: −0.8 V/SCE.

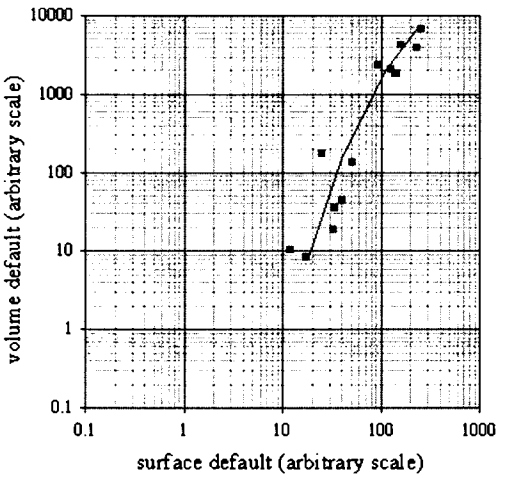

Figure 9.7. Defaults concentration at the oxidized surface and in the bulk of weld.

potential is −0.65 V/SCE at pH 11. Assuming that the density of the passive layer is about 3 g cm^{-3}, the maximum concentration of metal within is estimated to be 2×10^{22} atom cm^{-3}. Since the donor density is higher than the concentration of metal within the

oxide, the concentration of this inner oxide is not entirely Fe_2O_3, Cr_2O_3, NiO... and the tritium may induce the formation of an intermediate oxide with tritium trapped as tritons [110]. If all the trapped tritium reacts with oxide, the donor density would be equal to the sum of the concentration of tritium estimated to be 4×10^{22} atom cm^{-3} and that of metal in the oxide. The sum was found to be 6×10^{22} cm^{-3}, which is less than the donor density value of 10^{23} carrier cm^{-3}. This disagreement could be due to ionization with electrons [151], and destruction of the oxide layer due to the energy of the β^- particles released in tritium decay. The explanation could also be the breakdown of the oxide layer by non-dissolved helium. This would provide electron traps by the formation of O^3H^-, and corrosion. During charging, enrichment is produced in first in the oxide layer, then in the weld as seen in the Fig. 9.7.

In this case of non-tritiated oxidized welded steel, the donor concentration value found is 9×10^{21} carrier cm^{-3}. This value is much lower than that obtained with tritiated oxidized welds and is in much better agreement with the theoretical value. Moreover, the flatband potential decreases on increasing the donor density in the tritiated oxide layer. These results show effectively that the tritium, helium and released energy induce breakdown, ionization and trapped electrons in the oxide layer.

2.3. Microscopy

The Scanning Electron Microscopy examinations were carried out for the tritiated oxidized welded surface (Fig. 9.8). The non-tritiated sample shown for comparison has a more ordered dendritic microstructure (Fig. 9.9).

The more complex microstructure of the tritiated oxidized surface can be attributed to a severe degradation by tritium, helium and energy released from the decay. The tritiated welded alloy surface after removal of the oxide layer by electrolytic dissolution is shown in Fig. 9.10; dendritic microstructure imperfections are more visible. The presence of slip lines on and beneath the oxide suggests deformations by stress on cooling to accommo-

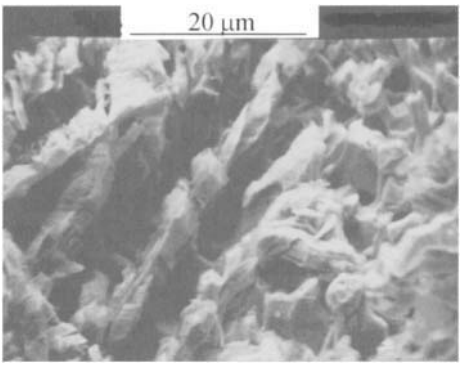

Figure 9.8. Scanning Electron Microscopy, tritiated oxidized surface of weld.

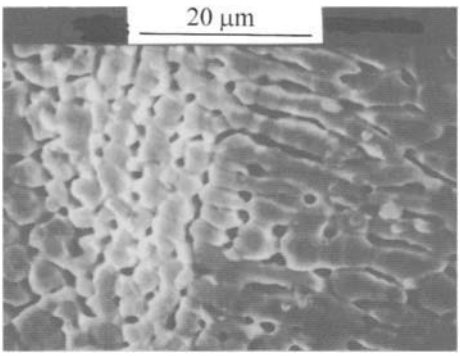

Figure 9.9. Scanning Electron Microscopy, dendrites of non-tritiated oxidized weld.

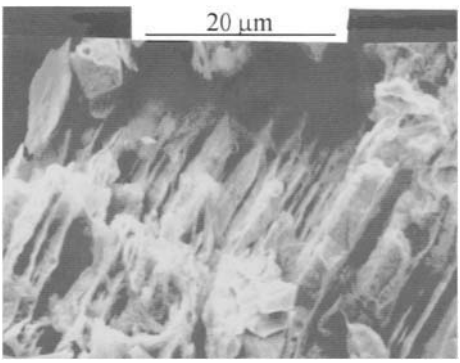

Figure 9.10. Scanning Electron Microscopy, tritiated welded alloy after removal of oxide.

date differential thermal contractions. Intergranular fractures and a few bubbles generated by helium at concentration of 3000 ppm were found. Helium is deeply trapped in damaged areas and the release rate is dependent on its concentration and temperatures as high as 700°C. Bubbles have relieved the large internal pressure. Trapping, fractures and bubbles have a dramatic effect on the stress corrosion.

Fig. 9.11 illustrates the microstructure of alloy without tritium where the vermicular morphology of ferrite is clearly seen. The magnetic measurements of ferrite give a value of 5 FN (ferrite number). During welding, a small quantity of delta ferrite is incorporated into the austenitic phase in order to avoid cracking and microfissuring upon cooling. From a metallurgical viewpoint, heating modifies the microstructure with depletion of the alphagen phase as seen in the Fig. 9.12. The complex microstructures produced in the weld can lead to localized corrosion in the austenite/ferrite border.

Because of the considerably different structures of welded compared to wrought steel, the behavior due to the tritium should differ, as reported by Garcia [152] for hydrogenated welds. According to this author, microcracks nucleate at austenite/ferrite borders.

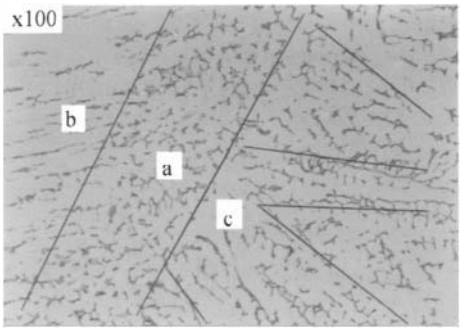

Figure 9.11. Metallographic examination of welded alloy showing the vermicular morphology of ferrite, lines and letters: multipass of welding metal and microstructure.

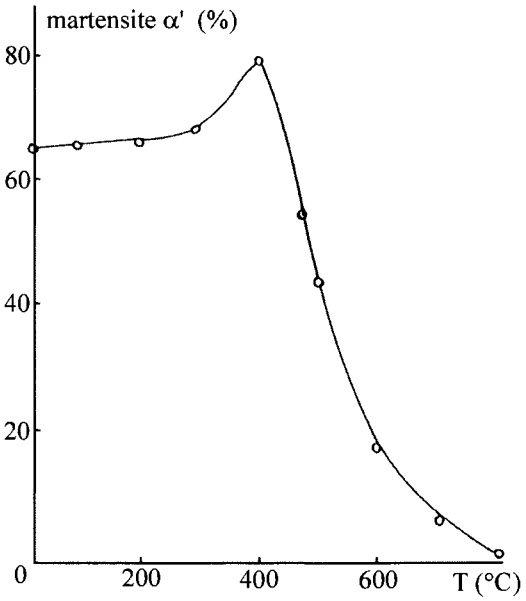

Figure 9.12. Influence of temperature on depletion of alphagen phase for 20 hours.

These results are also in agreement with those of West [153] and Garcia [154], obtained for hydrogenated austenitic stainless steel welds. This is due to differences in hydrogen diffusivity (D) and solubility (S) between austenite (γ) and ferrite (δ), ($D_{H\gamma} \ll D_{H\delta}$; $S\gamma \gg S_\delta$). This is also due to the presence of impurity segregations during welding that would act as traps at the border, helping hydrogen segregation. Because of these facts, borders are the preferential nucleation sites for microcracks. In addition, it is well known that austenitic grain boundaries are preferential sites for hydrogen diffusion. Therefore, in

the fully austenitic structure, tritium segregates preferentially at grain boundaries, where there is structure modification, and thus these become the preferential nucleation sites for microcracks leading to an absence of cohesion of austenite. Therefore, the photographs in Figs 9.8 and 9.10 mean that the tritiated welded 316L stainless steel has locally been preferentially corroded by tritium, helium and released energy. These examinations by Scanning Electron Microscopy would appear to support the above results obtained by electrochemical methods as the oxide becomes deteriorated.

3. Conclusion

The tritiated oxidized welds of type 316L stainless steel deteriorate because of tritium and energy released from the decay. These affected the corrosion potential giving a less 'noble' behavior. A higher concentration of electron carriers is produced by tritium which is trapped as tritons in the oxide resulting in a less insulating oxide. This difference in electron carriers indicates that the tritium and energy released may induce ionization and breakdowns of the oxide layer. Microscopy examinations show complex severe degradations. It is well known that the ferrite is formed in the austenite during welding. It is assumed that the surface austenite/ferrite borders are easily corroded by this radioactive medium.

Chapter 10

PASSIVATION PROCESS BY OXIDIZING SPECIES

1. Introduction

The tritium in tritiated water decays with the formation of dissolved radiolytic products such as $^3H_2O_2$ and O_2 [141,155,156]. The free and corrosion potentials of the stainless steel, as well as the redox potential of the tritiated water taken at high pressure of radiolytic gases, are in the transpassive region. This results from the concentrations of the dissolved radiolytic species. If the pressure decreases, these potentials shift to the prepassive region. This shows the important effects of the concentration of radiolytic $^3H_2O_2$ and dissolved oxygen on the corrosion of 316L stainless steel. The reactions are:

$$^3H_2O \rightarrow 2\,^3He + 0.5O_{2\text{dissolved}} + 2\beta^- \tag{10.1}$$

$$2\,^3H_2O + \beta^- \rightarrow {}^3H^{\bullet}, \quad {}^3HO_2^{\bullet} \cdots \rightarrow {}^3H_2O_2 + 2\,^3H^{\bullet} \tag{10.2}$$

$^3H_2O_2$ can be partially decomposed as follows:

$$^3H_2O_2 \rightleftharpoons O_{2\text{dissolved}} + 2\,^3H^+ + 2e^- \tag{10.3}$$

with the theoretical potential:

$$E = 0.437 - 0.06\text{pH} + 0.03\log[p_{O_2}]/[\,^3H_2O_2]\ (/\text{SCE}) \tag{10.4}$$

where p_{O_2} is the partial pressure of oxygen. This reaction leads to acidification of the tritiated water and the pH is, in general, close to 3 due to the radiolysis. In this work, the behavior of the hydrogen peroxide and oxygen on the 316L stainless steel was studied. To show the presence of these two species, tritiated water was analyzed radiochemically and chemically. Then voltammetric curves were plotted; finally Scanning Electron Microscopy examinations were carried out on the surface of the stainless steel after corrosion in the tritiated water containing $^3H_2O_2$ and oxygen.

2. Results obtained with tritiated water

2.1. Composition of the tritiated water

The hydrogen peroxide and dissolved oxygen concentrations in the tritiated water after degassing and expansion of the gases are given in Table 10.1. Dissolved oxygen can be eliminated by argon bubbling and its concentration is determined by the difference in concentration between that before and that after bubbling. This tritiated water was stored under a pressure of 5×10^5 Pa of radiolytic gas whose composition is given in Table 2.

2.2. Free potentials of the stainless steel and redox potentials of ^3H_2O

The free and corrosion potentials of the stainless steel in tritiated water are given as a function of the pH in Fig. 10.1.

The experimental slope dE/dpH is 0.058. These values relate to the following cathodic reactions:

$$^3H_2O_2 + 2\,^3H^+ + 2e^- \rightarrow 2\,^3H_2O \qquad (10.5)$$

$$0.5O_2 + 2\,^3H^+ + 2e^- \rightarrow {}^3H_2O \qquad (10.6)$$

Table 10.1. Composition of the peroxygenated compounds dissolved in ^3H_2O

Radiolytic products	$^3H_2O_2$ mmol dm^{-3}	O_2 mmol dm^{-3}
Concentration	6	1

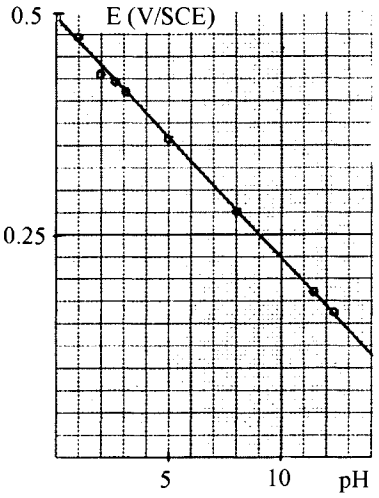

Figure 10.1. Free corrosion potentials of the 316L stainless steel as a function of the pH.

The theoretical potentials related to the reference electrode (SCE) are:

$$E_1 = 1.51 + 0.03 \log[^3H_2O_2][^3H^+]^2 \tag{10.7}$$

$$E_2 = 0.97 + 0.3 \log[p_{O_2}]^{0.5}[^3H^+]^2 \tag{10.8}$$

From eqs (10.7), (10.8), it can be seen that dE/dpH corresponds to the experimental slope in Fig. 10.1. This figure shows that the free and corrosion potentials can be located in the transpassive region; these are confirmed in the experimental voltammetric curves.

The reduction currents of oxygen and hydrogen peroxide can be estimated using refs [157–159]. These give, from eqs (10.5), (10.6),

$$i_1 = -2Fk_1[^3H_2O_2][^3H^+]^{\nu_1} \exp(-\alpha_1 2F\eta_1/RT) \tag{10.9}$$

$$i_2 = -2Fk_2[O_2]^{\nu_2}[^3H^+]^{\nu_3} \exp(-\alpha_2 2F\eta_2/RT) \tag{10.10}$$

where α_n is the transfer coefficient, ν_n the electrochemical orders and η_n is related to the potentials. The sum of the reduction currents is given by combining eqs (10.9), (10.10).

$$i_c = i_1 + i_2 \tag{10.11}$$

This equation gives the theoretical kinetic balance of the reduction half-reactions. The redox potential of the tritiated water obtained by measuring the potential of a platinum electrode related to a saturated calomel electrode is 0.39 V/SCE at pH 11 and 0.68 V/SCE at pH 4. These values are high and as a result the tritiated water is oxidizing. All these potentials are in the transpassive region as can be seen below in the voltammetric curves. These potentials lead to surface breakdowns and localized corrosion of the oxide layer ($E_{breakdown}$).

The value of the free and corrosion potential in tritiated water decreases very rapidly from the start of the voltammetric cycles. For example, at the end of a day of voltammetric scans, the corrosion potential is −0.05 V/SCE for pH 4. The same is true for the redox potential (0.09 V/SCE). At these values, the potentials are within or close to the prepassive region where the passivating oxide layers formed are not yet stable. These results show clearly the instability of the radiolytic products present in the tritiated water and that it is better to carry out tests with high scan rates.

The displacement of the corrosion potential (E_{corr}) in the positive direction has been observed by Glass et al. [160] in the gamma-ray irradiation of oxygenated water. The major species responsible for the observed electrochemical changes has been shown to be radiolytically generated $^3H_2O_2$. Structural modification of the oxide layer, as reflected in corrosion potential changes, would be expected. For practical applications, it is important to know what is the effect of the corrosion potential displacement on the corrosion mechanism. In particular, it would be useful to find out whether the positive potential displacement increases the susceptibility of the oxide to breakdown and localized corrosion.

If the difference, $E_{breakdown} - E_{corr}$, is used as a measure of susceptibility to this corrosion, then the smaller values observed by Glass [160] indicate decreased resistance. However, according to Glass, if $E_{breakdown}$ is still more positive than E_{corr}, localized corrosion would not be spontaneous under irradiation.

2.3. *Effect of the $^3H_2O_2$ and oxygen concentrations*

The voltammetric curves obtained in tritiated water at 20 g dm^{-3}, pH 4 and 10^{-3} to 2×10^{-2} mol dm^{-3} $^3H_2O_2$ are shown in Fig. 10.2. The dissolved oxygen concentration is assumed to be constant and equal to 1 mmol dm^{-3}. A high scan rate was used to draw the voltammetric curves to prevent concentration modifications of the radiolytic hydrogen peroxide and dissolved oxygen. It is easy to control concentration modifications using the successive voltammetric cycles and to compare them with calibrated curves.

The curves exhibit the following characteristics: (a) a higher reduction current during the backward scan, which increases with the concentration of $^3H_2O_2$ obtained by additions, signifying that the latter is reduced, (b) in the forward scan, the active peak at −0.3 V/SCE disappears with the addition of $^3H_2O_2$, (c) the current in the passive region is lower, (d) the peak in the transpassive region decreases and disappears to be progressively replaced by an oxidation current which increases with the $^3H_2O_2$ concentration. The explanation of the behavior of these curves is helped by using the diagram in Fig. 10.3. At low concentrations of $^3H_2O_2$ and of dissolved oxygen, which behaves in the same way, the reduction currents shift towards negative values. The net current is the active peak on the anodic voltammogram. It is equal to the sum of two currents with opposite signs: that due to the oxidation of the steel and that due to the reduction of the $^3H_2O_2$ and oxygen. The corrosion potential will be in the region of potentials of the active peak. For these $^3H_2O_2$ and oxygen concentrations, the corrosion current should be higher (curves 2 and 3, Fig. 10.3) than those achieved in the absence or very low concentrations of these species (curve 1, Fig. 10.3). Their behavior at intermediate concentrations is shown by curve 5 in Fig. 10.3. In this case, the $^3H_2O_2$ and oxygen reduction currents to be considered are in the passive region potentials and are low. The corrosion potential will be in the passive region and the stainless steel is protected against corrosion. It follows that the passive oxide layer should be more difficult to destroy as can be seen in the transpassive oxidation peak which becomes smaller (Fig. 10.2). At high $^3H_2O_2$ and oxygen concentrations, the reduction currents are at still more positive potentials, the passive current is also still lower. It is possible that the two opposing currents are superimposed: that due to the passive oxide layer and that due to the reduction of the $^3H_2O_2$ and oxygen. The passive potential range is smaller at these concentrations. In the transpassive region, the current increases with these higher concentrations. It can be seen in curve 6 of Fig. 10.3 that the corrosion potential will be in the transpassive region and that the steel is corroded at these conditions.

An approach was made by Shoesmith [161], using metal oxide subjected to gamma-ray radiation. With radiolytic hydrogen peroxide, three distinct regions of behavior are apparent. For $H_2O_2 \geqslant 5$ mmol dm^{-3}, the oxidative dissolution rate increases (transpassive region) with peroxide concentration with a first-order dependence. From 0.2 to

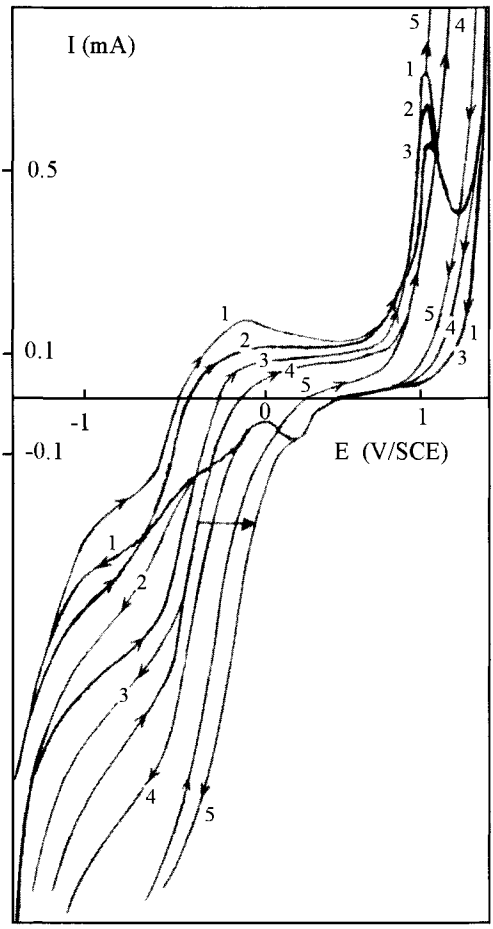

Figure 10.2. Voltammetry curves, $^3H_2O_2$ and oxygen effects, 1: 10^{-3}, 2: 3×10^{-3}, 3: 5×10^{-3}, 4: 8×10^{-3}, 5: 2×10^{-2} mol dm^{-3} $^3H_2O_2$, pH 4, v: 200 mV s^{-1}, ω: 2000 rpm.

5 mmol dm^{-3}, the oxidative dissolution rate is independent of peroxide concentration (passivity). For $H_2O_2 < 0.2$ mmol dm^{-3}, the oxidative dissolution rate is strongly dependent on H_2O_2 concentration (active region). According to this author, the behavior in H_2O_2 solutions is complicated by a strong pH dependence; dissolution is promoted as the pH decreases. These behaviors are in agreement with our results for 316L stainless steel in oxidized tritiated water.

The curves shown in Fig. 10.4 were obtained at pH 11 and at different $^3H_2O_2$ concentrations, as in Fig. 10.2. In the forward scan, immediately after the active peak at −0.8 V/SCE, the current has negative values. This behavior corresponds to curve 4 in Fig. 10.3. The corrosion potential will be either in the prepassive or in active potentials, bringing about in-

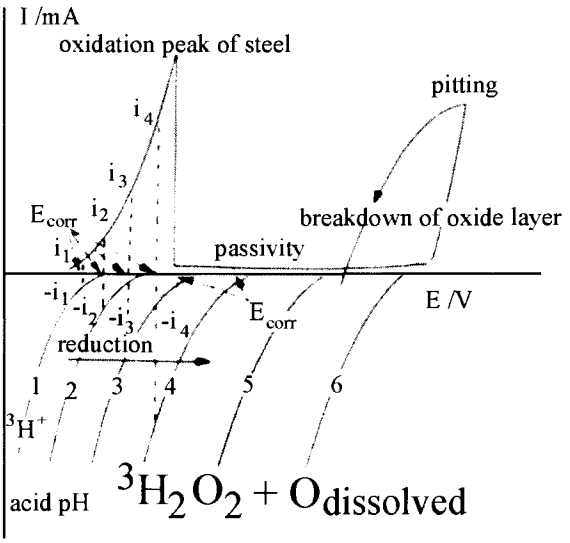

Figure 10.3. Diagram giving the currents, which have opposite signs, for the oxidation of the steel and the reduction of water, hydrogen peroxide and oxygen.

stabilities in the passive oxide layer, which will not be stabilized and passivated. For these reasons we must avoid having these $^3H_2O_2$ concentrations in the tritiated water. Fig. 10.4 also shows that the active current at −0.8 V/SCE is lower when the $^3H_2O_2$ concentration increases. In addition, it can be seen that the current of the corrosion products' reduction peak at −1 V/SCE is shifted towards more negative values. These two types of current behavior result from the $^3H_2O_2$ reduction current, which is superimposed on the corrosion currents and that of the reduction of the corrosion products. This shifts all the currents in this region towards negative values. In the transpassive region, it is observed that the corrosion current increases with the $^3H_2O_2$ concentration. It can also be seen that the oxidation current at the beginning of the backward scan becomes greater than that obtained in the forward scan for the same potential. It seems, at pH 11, that the reduction of $^3H_2O_2$ is possible at potentials preceding those of the prepassive region, and that open-circuit coupling of transpassive dissolution with $^3H_2O_2$ reduction is feasible. As observed, this reduction is made more difficult at passive potentials. The stainless steel should be better protected at these passive potentials. This protection appears to be poorer at pH 4.

The explanations could be as follows. The studies of Olefjord [148] give the duplex structure of the passive layer with an outer layer of hydrated hydroxide and an inner compact oxide layer. The inner is at least two thirds of the complete layer. This means that $^3H_2O_2$ and oxygen reduction on passivated steel requires electrons to transfer across the inner passive barrier layer, according to Sato et al. [162]. The electron transfer may occur by the tunnel mechanism even if the passive layer is an insulator. The reactions took place only when the passive layer was thin enough, or there was appropriate localization of Cr, Fe

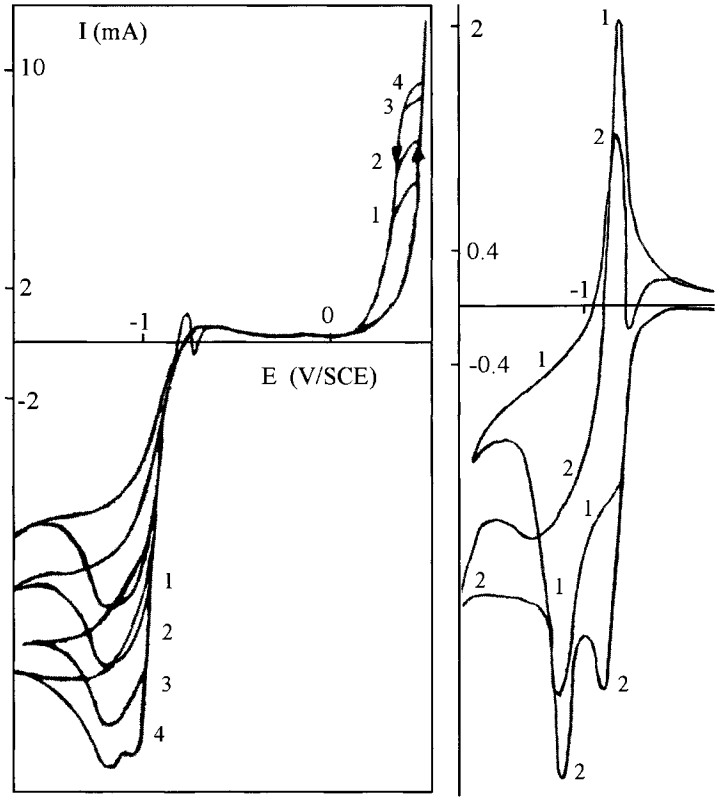

Figure 10.4. Voltammetry curves, $^3H_2O_2$ and oxygen effects, (a): 1: 2×10^{-2}, 2: 2.5×10^{-2}, 3: 3.1×10^{-2}, 4: 3.8×10^{-2} mol dm^{-3} $^3H_2O_2$, 1 mmol dm^{-3} $O_{dissolved}$, pH 11, v: 200 mV s^{-1}, ω: 600 rpm, (b): detail on expanded scale for 6.2×10^{-3} mol dm^{-3} and 1.2×10^{-2} mol dm^{-3} $^3H_2O_2$ and $O_{dissolved}$.

and Mo in the spinel lattice [148], or there were no defects for electron tunneling. According to Simoes [109], the electronic structure of oxide films is reasonably well established and the general formula for the passive layers is: $(Fe^{2+}Fe^{3+}_{1.0-0.9}\ Cr^{3+}_{1.0-1.1})\ O^{2-}_4$.

It seems that the localization of Fe^{2+} in octahedral or tetrahedral positions in the spinel lattice is a determining factor in the electrical conductivity. Nevertheless, the degree of substitution of Fe^{3+} by Cr^{3+} in the cationic sites of the oxide is conversely more important for the internal passive layer closer to the metallic substrate.

According to ref. [162], when the passive layer thickness exceeds a certain value, the current decreases. Once a thick passive layer is well formed, the current no longer appears; the decomposition rate of $^3H_2O_2$ becomes slow. This would explain why the thickness, structure or defects of the passive layer would be different at pH 4 and pH 11, leading to two types of film. Apparently, at pH 11, the current due to the reduction of $^3H_2O_2$ and

oxygen would be limited by electron diffusion within the oxide film at passive potentials. At other potentials, without the passive layer, the current due to the reduction of these would be limited rather by diffusion in the bulk solution [163].

2.4. *Effect of the disk electrode rotation rate*

The effect of the rotation rate of the electrode on the voltammetric curves at pH 4 has been studied. For no rotation, the reduction current that was obtained at potentials below −0.4 V/SCE is lower than at a rotation rate of 2000 rpm (rotations per minute). This results from the depletion of transitory species, $^3H_2O_2$ and dissolved oxygen at the surface of the steel when there is no rotation. With no rotation, an oxidation peak was seen at −0.7 V/SCE; it is possible that this results from the formation of an intermediate oxide which would be hidden by the $^3H_2O_2$ and dissolved oxygen reduction currents. At pH 11, the rotation of the electrode changes the value of the active current. The corresponding peak decreases, to be in the range of the negative currents at the highest rates, and in this latter case the active peak is no longer seen. The electrode rotation rate does not change the current in the passive region. In the transpassive region, the rotation rate has a significant effect on the oxidation current, here, the current in the forward scan decreases with the electrode rotation rate. The same is true for the oxidation current at the beginning of the backward scan, and this current becomes greater than that obtained in the forward scan for the same potential. The supply of $^3H_2O_2$ and oxygen due to electrode rotation increases the corrosion currents. In the backward scan, the corrosion product reduction peaks (at around −1 V/SCE) are shifted towards the more negative range of currents signifying increased hydrogen peroxide and oxygen reduction at higher rotation rates. Such reduction occurs at the same potentials as those of the reduction of the corrosion products. In the backward scan, at potentials below those of the reduction peak (−1 V/SCE), the reduction current has a plateau dependent on the electrode rotation rate; this current again results from the reduction of the $^3H_2O_2$ and oxygen.

2.5. *Ring-disk electrode*

The experimental results obtained at different concentrations of $^3H_2O_2$ and oxygen and different electrode rotation rates show that these species were reduced at pH 11, mainly when the passive oxide layer is not present ($E \leqslant -0.8$ V/SCE and $E \geqslant 0.3$ V/SCE), while this would not be the case at pH 4. We looked for evidence of the corrosion products formed at pH 11 in the transpassive region ($E \geqslant 0.3$ V/SCE) by using a ring-disk electrode. The imposed potentials were 0 and 0.3 V/SCE on the disk for a rotation rate of 3000 rpm. To improve measurements of the formation of the corrosion products, the corrosion rate was increased by raising the temperature to 70°C. The corrosion products formed on the disk are shown by voltammetric scans carried out with the ring. It was seen that the reduction current obtained with the ring is higher by imposing the potential of 0.3 V/SCE on the disk. The shift results from different amounts of corrosion products formed at these two

potentials on the disk, with more corrosion products being formed at 0.3 V/SCE. At this potential the oxide layer is destroyed.

2.6. *Surface appearance*

In the transpassive region and with sufficient $^3H_2O_2$ and oxygen, the steel is corroded (Fig. 10.2). A potential of 0.3 V/SCE was therefore applied at pH 4 for 15 min. The Scanning Electron Microscope examinations showed the presence of numerous small breakdowns with opened cavities. From these examinations, there was plastic bending of oxide which should be the main factor in a surface stress corrosion cracking by breakdowns. Breakdowns and plastic bending can be explained by the free and corrosion potential displaced towards more positive potentials.

3. Discussion

It is useful to clarify the kinetic condition of the reduction of $^3H_2O_2$ and oxygen in tritiated water at the two pH values studied. From ref. [164], the reduction potentials of these two species are the same; this was ascertained by eliminating the dissolved oxygen by argon bubbling. At pH 4, it is observed that the $^3H_2O_2$ and oxygen reduction range extends from the potentials of the active zone of the 316L steel to those including the transpassive region. At pH 11, the potential region concerned extends from the active zone to the prepassive region and subsequently to the transpassivity. From the potential–pH equilibrium diagrams for Fe, Ni and Cr, it can be seen that at pH $\leqslant$ 4, these three metals are in a broad corrosion potential range. In an alkaline medium, their corrosion potential range is at pH $>$ 12. In our case, it is out of the question to take these three metals separately; the stainless steel is protected by the nature of its distinctive protective oxide layer, formed essentially of Cr_2O_3. For the stainless steel, it is possible that this layer is a little thinner, or without defects, or is another structure with (Cr, Fe, Mo)O_n^{2-}, [148] at pH $\leqslant$ 4. On the other hand, it would appear that this would be different at pH 11. The electron transfer into oxide may occur by the tunnel mechanism. Apparently, at pH 11, the currents due to the reduction of $^3H_2O_2$ and oxygen are limited by electron diffusion within the film at passive potentials. At pH 4, the current is less limited by electron diffusion. Outside of the passive potentials (easily observed at pH 11), it can be seen that the reduction of $^3H_2O_2$ and oxygen occurs readily when the oxide layer is not present. The Cr_2O_3 content in this oxide layer also plays a major part as indicated by Berenblit and Guskov [165]. According to these authors, H_2O_2 reduction decreases when the Cr_2O_3 content increases.

Olefjord [148], among other authors, has studied the composition of passive layers formed on stainless steels containing Mo. The thickness of the passive layer increases with the passive potentials up to a few nm and the composition of the oxide and the alloy underneath changes with the passive potential. Alloying elements are enriched on the surface and thereby control the dissolution rate and induce passivation of the alloy. In the oxide and hydroxide, the Cr^{3+} content is about 70%. This does not seem to vary a lot with

the potential. The measured iron oxide (Fe^{2+} and Fe^{3+} with the ratio 0.4) content is in the range 25 at% and slightly higher at higher passive potentials. The higher iron oxide concentration compensates for the lower molybdenum oxide content. The measured molybdenum oxide is 8 at% and 5 at% at higher passive potentials and at small passive potentials, the four-valency state is predominant. The nickel oxide content is low. The contribution of the oxygen corresponds to O^{2-} in the oxide Cr_2O_3, MoO_2 and Fe_2O_3, and OH^- in $Cr(OH)_3$ and Mo-hydroxide.

The X-ray Photoelectron Spectroscopy analyses provided a semi-quantitative identification of the atoms in the tritiated oxide layer (Fig. 4.11). This analysis indicates in the presence of $^3H_2O_2$ and oxygen at alkaline pH and passivity that Cr is markedly enriched, Fe is slightly enriched while Ni is dropped in the oxide. These modifications are caused by selective oxidation in this medium.

Moreover, the dissociation reaction of $^3H_2O_2$ with the formation of $^3HO_2^-$ in an alkaline medium is well known:

$$^3H_2O_2 + O^3H^- \rightleftharpoons {}^3HO_2^- + {}^3H_2O \tag{10.12}$$

The pK is 11.65 [165]. Therefore, at pH 11, it is expected that the $^3H_2O_2$ form still predominates with respect to $^3HO_2^-$ and is the same at pH 4 [101]. The active form to consider during the reduction will be $^3H_2O_2$, and the possible remaining mechanism is then:

$$^3H_2O_2 + e^- \rightarrow O^3H^- + O^3H^{\bullet} \tag{10.13}$$

$$O^3H^{\bullet} + e^- \rightarrow O^3H^- \tag{10.14}$$

with the dissolved oxygen:

$$0.5O_2 + {}^3H_2O + 2e^- \rightarrow 2O^3H^- \tag{10.15}$$

The overall reduction current is given by eq. (10.11). According to this, a log-log plot of current against the $^3H_2O_2$ and oxygen concentrations should be linear with a slope of 1. It is seen that the data points over the entire concentration range at pH 11 are linear in Fig. 10.5 with a slope of 1 as expected. These results agree satisfactorily with the predictions of eq. (10.11).

The reduction currents at potentials below −0.8 V/SCE increase with rotation rate for rates between 0 and 600 rpm (see subsection 2.5). By plotting the curve $i = f(\omega)$, for $E = -0.8$ V/SCE, a straight line is obtained which fits the Levich equation

$$i = 1.24FD^{0.66}\Upsilon\upsilon^{0.5}A\omega^{0.5}(C_{^3H_2O_2} + 2C_{O_2}) \tag{10.16}$$

where Υ is the dynamic viscosity, D the diffusion coefficient of $^3H_2O_2$ and oxygen (these should be close to each other [163] and [166]), ω the electrode angular rotation rate. To obtain the value of the diffusion coefficient, the $^3H_2O_2$ reduction currents considered should

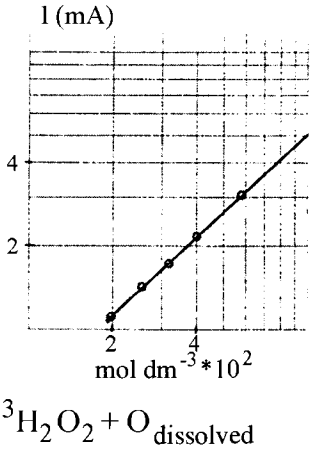

Figure 10.5. Experimental curve giving the reduction current as a function of the $^3H_2O_2$ concentration and $O_{dissolved}$ (1 mmol dm^{-3}) at pH 11, $E = -1$ V/SCE.

be, if possible, high compared with those for the reduction of the corrosion products and oxygen. An experimental value of 4.2×10^{-5} cm^2 s^{-1} is then found for the diffusion coefficient of $^3H_2O_2$ in tritiated water.

The rate of the $^3H_2O_2$ reduction reaction can be determined on the basis of the voltammetric currents measurements applying the equation given by Galus [167].

$$i_{(t+m)}/i_m = \frac{k^{0.5}(C_t)^{0.5}}{0.45a^{0.5}} \tag{10.17}$$

where k is the rate constant, i_m the height of the reduction peak of corrosion products in the absence of $^3H_2O_2$ and oxygen, $i_{(t+m)}$ the height of the reduction peak with essentially $^3H_2O_2$, C_t the concentration of $^3H_2O_2$, a is equal to nFv/RT with $n = 2$ for $^3H_2O_2$. The equation given above is strictly valid if the concentration of reduced $^3H_2O_2$ is sufficiently high to undergo negligible change as a result of corrosion products and oxygen.

The value for the rate constant of reaction (eq. (10.5)) in tritiated water is obtained from Fig. 10.5 and eq. (10.17) and is 5.2×10^{-2} mol dm^{-3} s^{-1} in the active region. The overall reduction of radiolytic $^3H_2O_2$ will take time, but this can be eliminated in tritiated water by applying a potential having the value of the corrosion products reduction peaks. The lack of $^3H_2O_2$ would lead to decreasing the active corrosion.

4. Conclusion

Tritiated water contains radiolytic $^3H_2O_2$ and oxygen; its pH depends on reprocessing conditions and can be slightly acid or alkaline. At high radiolytic pressure, these species shift the redox potential to a value in the transpassivity. The same is true for the free and

corrosion potentials of the stainless steel. At pH 4, $^3H_2O_2$ and oxygen reduction currents are observed at the active potentials where the steel is corroded as well as in passivity up to transpassive regions. This is not the case at pH 11, the reduction of $^3H_2O_2$ and oxygen occurs only in the active zone and in transpassivity. This reduction is practically nil in passivity, owing to slight electron diffusion within the oxide film.

It was possible to clarify the kinetics of the reduction of $^3H_2O_2$ in tritiated water. The values of the diffusion coefficient and rate constant for the reduction of $^3H_2O_2$ are respectively sufficiently low and sufficiently high that the lack of $^3H_2O_2$ would lead to decreasing the active corrosion. Since the redox potential of the tritiated water and the free and corrosion potentials of the stainless steel can be in transpassivity, it is of interest to ascertain the type of corrosion of the 316L stainless steel occurring in tritiated water. Examinations show small cracks and cavities over all of the oxidized surface.

Chapter 11

PASSIVATION BY HYDROGEN PEROXIDE AND pH

1. Introduction

Depending on the tritiated water radiolysis, the pH changes. The objective of this study was to show the combined effects of hydrogen peroxide, having gained electrons and pH on passivity and corrosion of carbon steel. For this, the influence of dissolved radiolytic oxygen had to be eliminated by argon bubbling. The used carbon steel is essentially more than 99% iron and contains traces of carbon and manganese. The latter avoids the metal carbide precipitation responsible for localized corrosion from the carbide grains.

2. Results and discussion

2.1. Voltammograms and polarization curves obtained without $^3H_2O_2$

Representative stabilized voltammograms obtained after multiple and repetitive scans show the behavior of the carbon steel at pH 13, 6, 5.5 and 5 (Figs 11.1 and 11.2).

In general, such voltammograms may yield information on electrochemical mechanisms of oxidation and reduction, particularly at high scan rates where peaks can be easily detected. However, detailed interpretations at high rates are difficult, and complicated by peak potentials that are displaced from their theoretical values. Tacconi et al. [168] have shown that the potentials obtained from the resistance model vary linearly with the square root of the potential scan rate, v.

$$\Delta E = \left[Q R_p / (\partial R_p / \partial \theta) \right]^{0.5} \Delta v^{0.5} \tag{11.1}$$

where θ is the coverage degree, Q the charge required to cover the carbon steel with an oxide layer, and R_p the polarization resistance.

The voltammograms at pH 13 (Fig. 11.1) show that at the most negative potentials, the currents are cathodic, consistent with tritium evolution. On increasing the potential in the forward direction, two minor oxidation peaks (1, 2) appear as shoulders near -1.5 and -1 V/SCE, followed by a major prepassive peak (3) near -0.65 V/SCE. In the backward scan, a major reduction peak (4) occurs near -1.1 V/SCE. Comparison with Schrebler [169] suggests that active peak (3) involves oxidation from $^3HFeO_2^-$ to Fe_3O_4, and Fe_3O_4

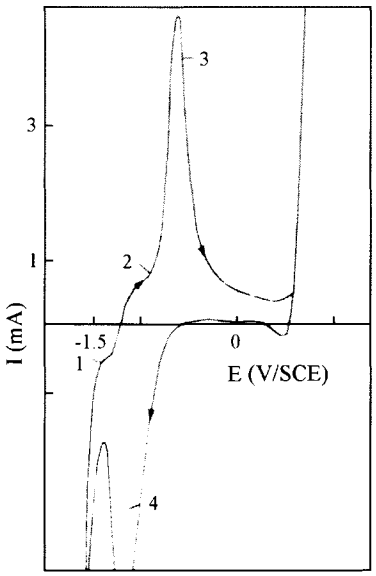

Figure 11.1. Voltammetric curves, v: 350 mV s^{-1}, ω: 2000 rpm, pH 13.

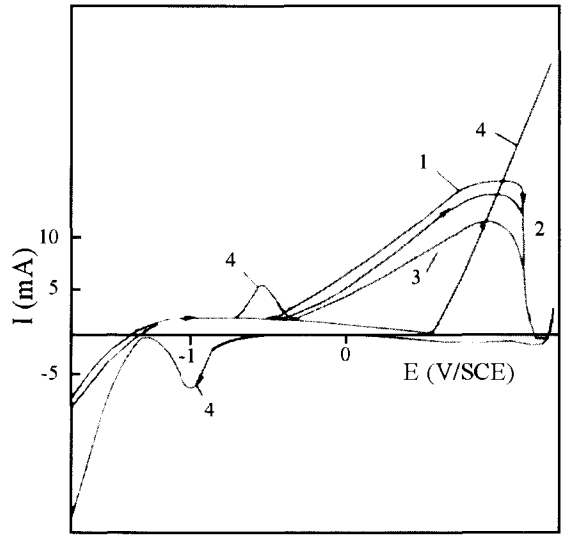

Figure 11.2. Voltammetric curves—pH effect, v: 350 mV s^{-1}, ω: 2000 rpm, 1: pH 5, 2: pH 5.5, 3: pH 6, 4: pH 13.

to Fe_2O_3 leading to the passivity at the higher potentials. Peak (4) is believed to be the conjugate of peak (3). A straight line drawn between the tops of conjugate peaks (3, 4) suggests

this is close to the theoretical potential. Comparison with the potential–pH equilibrium diagram of iron [101] shows that this corresponds reasonably well with the $Fe_3O_4/^3HFeO_2^-$ equilibrium, indicating that the oxide layer related processes in peaks (3, 4) involve formation and reduction of Fe_3O_4, respectively.

The origin of peak (1) is uncertain. It may be associated with the formation of an adsorbed monolayer of FeO^3H, $Fe(O^3H)_2$ or tritium which has the same behavior as hydrogen [147].

In Fig. 11.2, still at pH 13, (curve 4), the transpassive current is detected extending the limit of the forward scan beyond the end of the passive region (potential upon 0.7 V/SCE). According to Beck et al. [170], for iron in NaOH solutions at pH 13, the overall reaction for the transpassive region is formulated as follows:

$$Fe_2O_3 + 10O^3H^- \rightarrow 2FeO_4^{2-} + 5\,^3H_2O + 6e^- \tag{11.2}$$

Clearly part of the O^3H^- ions participate in the production of FeO_4^{2-} from Fe_2O_3. Furthermore, this participation is not only in terms of a bulk effect of the oxide layer, but also in terms of an effect on the resistance associated with the oxide capacitance.

In the case of acid pH, peaks are missing in the voltammetric curves (Fig. 11.2, curves 1 to 3). On the other hand, a much higher anodic current is observed in the potential region where carbon steel is passivated at pH 13. This figure demonstrates that the steel is easily corroded at acid pH, leading to Fe^{2+}, Fe^{3+} ions and the defective oxide layer. These anodic currents increase when the slightly acid pH decreases, and this increase is shifted towards more negative potentials. As a result, cyclic voltammograms using a high scan rate show marked differences at pH 13 and at slightly acid pH, and suggest that there is a more protective oxide layer at alkaline pH.

Anodic polarization curves for pH 13, 6, 5.5 and 5 obtained at a low scan rate are given in Fig. 11.3. Curve 1 shows a prepassive peak at −0.6 V/SCE for alkaline pH. The passive region extends from −0.4 to 0.65 V/SCE. Curves 2 to 4 were obtained at slightly acid pH. The prepassive peaks are not seen; on the other hand, the current increases with the potential and as the slightly acid pH decreases. These currents are higher than at pH 13. The values of the corrosion potential increase with decreasing pH and the experimental slope $\partial E/\partial \mathrm{pH}$ is about 0.05 mV and close to the slope of a reversible tritium electrode. This can be referred to the following cathodic reactions.

$$2\,^3H^+ + 2e^- \rightarrow 2\,^3H \quad \text{in acid medium} \tag{11.3}$$

$$2\,^3H_2O + 2e^- \rightarrow 2O^3H^- + 2\,^3H \quad \text{in alkaline medium} \tag{11.4}$$

In anodic polarization curves using a low scan rate, no intermediate shoulders are found; nevertheless, the peak potential and the passive region are less displaced from their theoretical values. This, as in eq. (11.1), enables us to choose accurate potentials, located for instance in the passive-transpassive region or near the corrosion potential, in order to draw electrochemical impedance diagrams. These diagrams will be used to find the oxide layer characteristics.

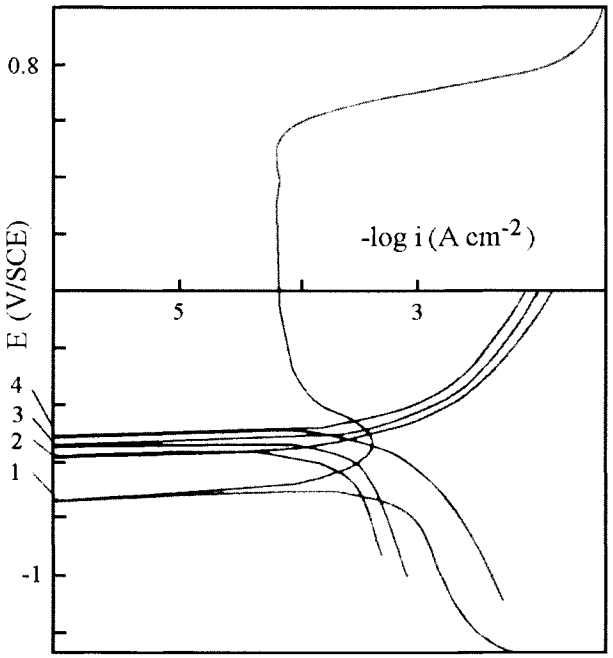

Figure 11.3. Polarization curves—pH effect, v: 5 mV s^{-1}, ω: 2000 rpm, 1: pH 13, 2: pH 6, 3: pH 5.5, 4: pH 5.

2.2. *Voltammograms and polarization curves obtained with* $^3H_2O_2$

Fig. 11.4 illustrates the voltammetric curves obtained with hydrogen peroxide at pH 6 and a high scan rate.

Evidently the presence of hydrogen peroxide significantly affects the oxidation and reduction processes of carbon steel. After the addition of small amounts of hydrogen peroxide, the height of the oxidation current decreases (curves 1 to 5) at the potentials above −0.4 V/SCE. As is shown in curve 6, after several cycles, the curve is again transformed and the current increases. This suggests the thickness of the protective oxide layer is a function of the number of scans; this progressively changes with scans until a limit is reached [171] in the last scan. In the backward scan, the reduction currents increase with the hydrogen peroxide concentration signifying that the latter is reduced following the cathodic reaction:

$$^3H_2O_2 + 2\,^3H^+ + 2e^- \rightarrow 2\,^3H_2O \qquad (11.5)$$

Fig. 11.5 presents several voltammetric curves at a high scan rate illustrating the effect of hydrogen peroxide at alkaline pH.

On increasing hydrogen peroxide concentration peaks 3 and 4 shift towards the more negative currents and active peak 3 is not seen at 8 mmol dm^{-3} of $^3H_2O_2$ (curve 4). On

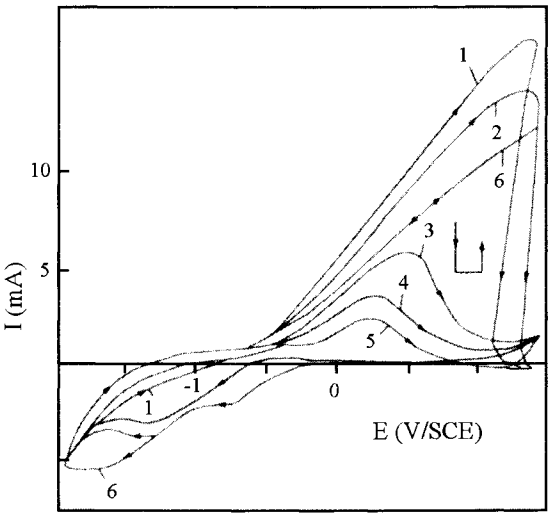

Figure 11.4. Voltammetric curves—$^3H_2O_2$ effect, v: 350 mV s^{-1}, ω: 2000 rpm, pH 6, 1: 10^{-4} mol dm^{-3}, 2: 10^{-3} mol dm^{-3}, 3: 3×10^{-3} mol dm^{-3}, 4: 7×10^{-3} mol dm^{-3}, 5: 10^{-2} mol dm^{-3}, 6: 2×10^{-2} mol dm^{-3} $^3H_2O_2$.

going beyond the passive region, a considerable decrease in anodic current is observed with $^3H_2O_2$ giving place to a well-defined transpassive small peak (curve 4). It would appear that the passive oxide layer is more difficult to break down as can be seen in the passive region where the currents become smaller with hydrogen peroxide.

The explanation of the behavior of these curves with $^3H_2O_2$ is helped, as seen previously, by using the previous diagram in chapter 10 and [172]. At low hydrogen peroxide concentrations, the $^3H_2O_2$ reduction currents shift towards negative values. The net current is the oxidation peak in the anodic voltammograms. It is equal to the sum of two currents with opposite signs: that due to the oxidation of the carbon steel and that due to the $^3H_2O_2$ reduction. The corrosion or rest potential should be in the region of the prepassive peak potentials. For these $^3H_2O_2$ concentrations, the corrosion current should be higher than those obtained in the absence of $^3H_2O_2$. At intermediate hydrogen peroxide concentrations, the $^3H_2O_2$ reduction currents to be considered are in the passive potentials and are low. The corrosion potential will be in the passive region and the carbon steel is protected against corrosion. It follows that the passive oxide layer should be more difficult to destroy as can be seen in the transpassive and passive regions where the currents become smaller. In addition, the characteristics of the oxide layer in slightly acid solution are different from those of the layer formed at pH 13, (Fig. 11.4, curve 6). In such a case, at pH 6, at the same $^3H_2O_2$ concentration, the reduction currents to be considered are shifted towards more positive potentials than at pH 13.

Voltammograms show that the oxide layer is easily and progressively destroyed with successive cycles. The corrosion potential is in transpassivity. These results could be ex-

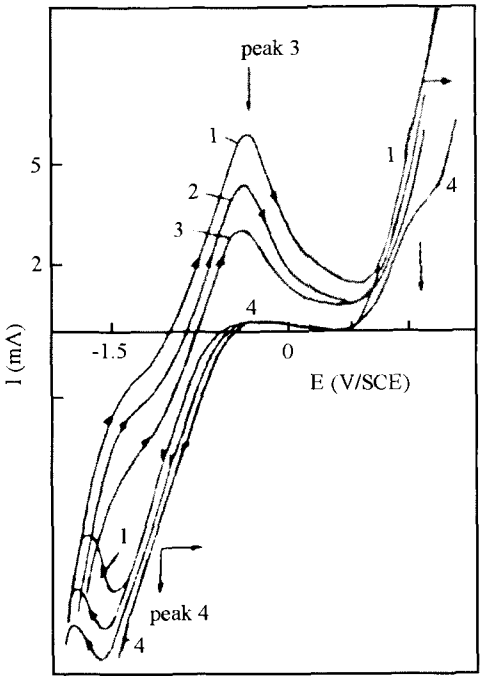

Figure 11.5. Voltammetric curves—$^3H_2O_2$ effect, v: 350 mV s^{-1}, ω: 2000 rpm, pH 13, 1: 2×10^{-3} mol dm^{-3}, 2: 4×10^{-3} mol dm^{-3}, 3: 6×10^{-3} mol dm^{-3}, 4: 8×10^{-3} mol dm^{-3} $^3H_2O_2$.

plained by the pH and the concentration of hydrogen peroxide; the structure or defects of the passive layer should be different with or without $^3H_2O_2$.

Anodic polarization curves, for pH 13 with hydrogen peroxide, are shown in Fig. 11.6. These curves exhibit different characteristics. Following the increase of the hydrogen peroxide concentration, the passive-transpassive currents (located at 0.6 V/SCE) are higher, then subsequently lower and higher. This is due to the displacement of the corrosion or rest potential towards more positive potentials (located first in the active zone, then in passivity, finally near the transpassivity). For example, using a $^3H_2O_2$ concentration from 2 to 20 mmol dm^{-3} the current increases from 0.2 mA cm^{-2} to 0.8 mA cm^{-2}, the carbon steel is more easily corroded with 20 mmol dm^{-3} $^3H_2O_2$.

2.3. Impedance spectroscopy without $^3H_2O_2$

The impedance diagrams obtained at passive-transpassive potentials for pH 13 are shown in Fig. 11.7. The Nyquist response is well represented by the capacitive semi circle with a part below the real axis.

The interpretation could be that the formation of FeO_4^{2-} (eq. (11.2)) is partly limited by adsorbates and charges within the oxide layer leading to breakdowns at higher passive-

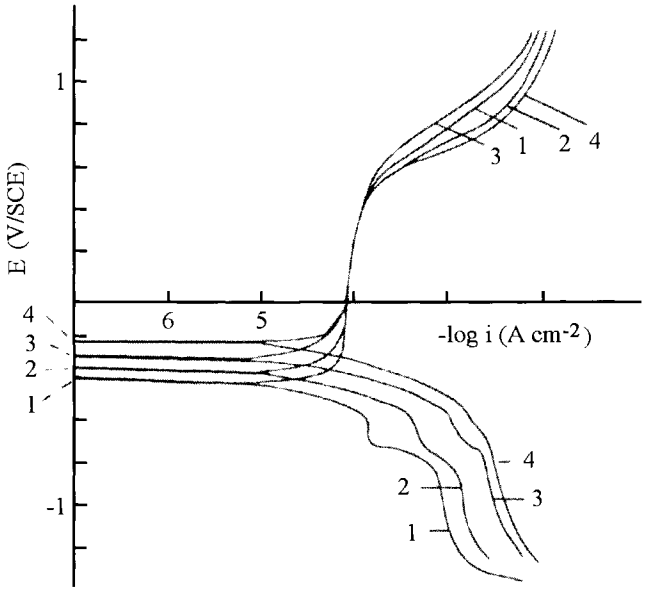

Figure 11.6. Polarization curves—$^3H_2O_2$ effect, v: 5 mV s^{-1}, ω: 2000 rpm, pH 13, 1: 2×10^{-3} mol dm^{-3}, 2: 4×10^{-3} mol dm^{-3}, 3: 6×10^{-3} mol dm^{-3}, 4: 8×10^{-3} mol dm^{-3} $^3H_2O_2$.

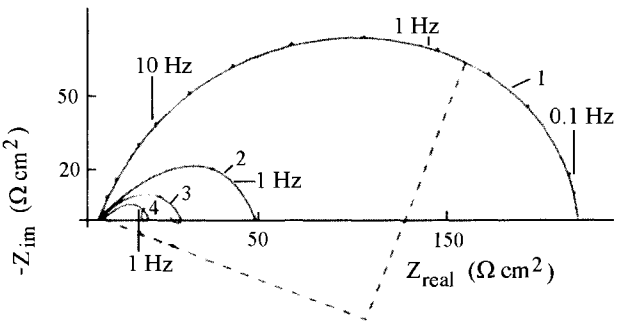

Figure 11.7. Nyquist diagrams—potential effect, ω: 2000 rpm, pH 13, 1: 0.62 V, 2: 0.65 V, 3: 0.675 V, 4: 0.7 V/SCE.

transpassive potentials. As the potentials increase, the transfer resistance decreases considerably; this is the result of the oxidation current increasing.

The values of interfacial capacitance given in Table 11.1 are high. Generally, the Helmholtz capacitance is about 20 $\mu F\,cm^{-2}$. The values found can be interpreted as resulting from capacitive effects of carbon steel subjected to a dissolution process since the potentials selected are located at the boundary of the passive-transpassive region. It would

Table 11.1. Transfer resistance and interfacial capacitance as a function of transpassive potentials

E (V/SCE)	0.62	0.65	0.675	0.7
R_{ct} (Ω cm^2)	227	50	15	8
C_{dl} (F cm^{-2} $\times$ 10^4)	6.4	6.4	6.2	6.6

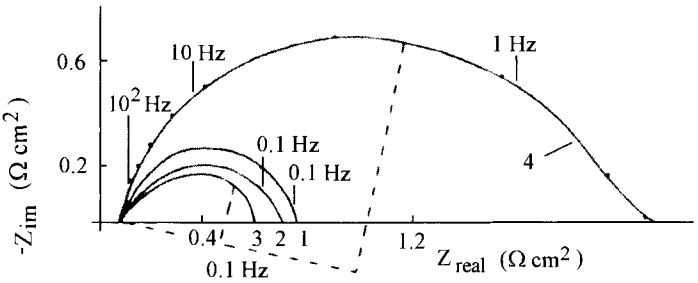

Figure 11.8. Nyquist diagrams—potential effect, ω: 2000 rpm, pH 6, 1: −0.35 V, 2: −0.3 V, 3: −0.25 V, 4: −0.2 V/SCE.

Table 11.2. Interfacial capacitance as a function of active potentials

E (V/SCE)	−0.35	−0.30	−0.25	−0.20
C_{dl} (F cm^{-2} $\times$ 10^4)	1.6	1.2	1.1	1

appear that this not a matter of oxide capacitance for which thickness would decrease with the transpassive potentials.

The Nyquist diagrams of carbon steel at pH 6 are in Fig. 11.8 and the main experimental values obtained by fitting the diagrams are in Table 11.2. The potentials used are near the corrosion potentials. A possible interpretation of the relaxation loop at the low frequencies is that it is due to adsorbates such as FeO^3H or $Fe(O^3H)_2$. As the potential increases, the transfer resistance decreases slightly; this is the result of active corrosion. The interfacial capacitance values are also high. The values found can be interpreted as resulting from capacitive effects of carbon steel being subjected to a corrosion process since the potentials selected are located at the boundary of the corrosion potential. The capacitance values decrease very slightly with more positive potentials. This could show that there is a corrosion mechanism coupled with slight passivity.

2.4. Impedance spectroscopy with $^3H_2O_2$

The Nyquist diagrams obtained at 0.62 V/SCE, pH 13, with hydrogen peroxide at the concentrations from 2 to 8 mmol dm^{-3} are shown in Fig. 11.9.

The chosen potential would appear to be near the rest potential located in the passive-transpassive region. The diagrams show a decreasing impedance. On the other hand, for

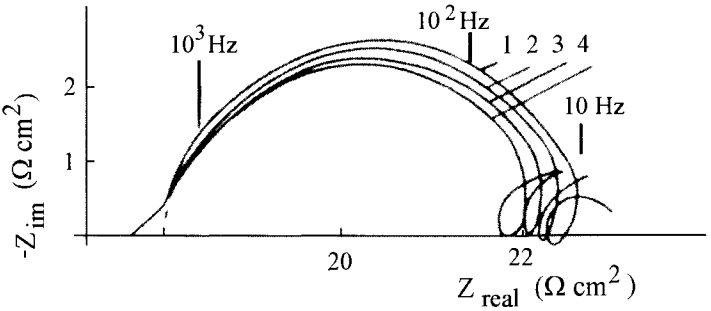

Figure 11.9. Nyquist diagrams—$^3H_2O_2$ effect, ω: 2000 rpm, pH 13, 1: 2×10^{-3} mol dm^{-3}, 2: 4×10^{-3} mol dm^{-3}, 3: 6×10^{-3} mol dm^{-3}, 4: 8×10^{-3} mol dm^{-3} $^3H_2O_2$.

Table 11.3. Interfacial capacitance and resistance as a function of $^3H_2O_2$ concentration

$^3H_2O_2$ (mol dm^{-3} $\times 10^3$)	2	4	6	8
R_{ct} (Ω cm^2)	781	705	629	1857
C_{dl} (F cm^{-2} $\times 10^3$)	2	1.9	0.25	0.05

8 mmol dm^{-3}, the impedance value is much higher. These two types of behavior are confirmed by the voltammograms and polarization curves in the passive-transpassive region (Figs 11.5 and 11.6). As shown in the voltammograms, at 2 to 6 mmol dm^{-3} $^3H_2O_2$, the corrosion current should be higher. At 8 mmol dm^{-3} $^3H_2O_2$, the corrosion potential shifts and will be in the passive region, therefore the carbon steel is protected against corrosion. It follows that the passive oxide layer should be more difficult to destroy, as can be seen in the impedance values with the same concentration of hydrogen peroxide.

Experimental values are given with $^3H_2O_2$ concentrations in Table 11.3. These values show that the interfacial capacitance decreases significantly with the $^3H_2O_2$ concentration. For 2 to 6 mmol dm^{-3} $^3H_2O_2$, it appears that a corrosion mechanism coupled with passivity can be obtained. For 8 mmol dm^{-3} $^3H_2O_2$, the value of the capacitance (50 μF cm^{-2}) would certainly be the oxide and Helmholtz capacitances, this indicates that little passivity would be obtained.

Fig. 11.10 shows the Bode plot of the passive oxide layer at 0.3 V/SCE with different $^3H_2O_2$ concentrations between 0 and 30 mmol dm^{-3}. From the previous interpretation and that of Gebhardt [173], the impedance modulus can be analyzed as follows. Segment A is characterized by the electrolyte resistance at the highest frequencies. Segment B appears when the frequency decreases, and the electrical response is the impedance of the total oxide marked by non-dissipative characteristics. The slope of segment B may be -1, and in this case the very small slope may be attributed to the superposition of the several additive impedances. At a lower frequency, segment C appears and the slope is again negative without hydrogen peroxide or up to 8 mmol dm^{-3} $^3H_2O_2$; the additive impedances may again play a role here. At concentrations up to 8 mmol dm^{-3}, the slope is 0, near the theoretical value, the effect of additive impedances is lower. In segment C, a highly dissipative com-

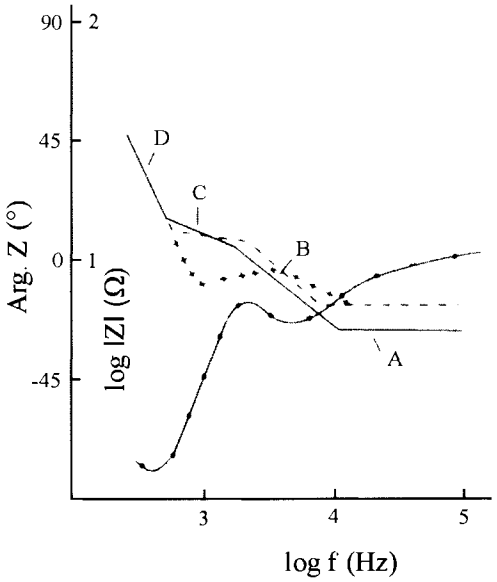

Figure 11.10. Bode diagrams—$^3H_2O_2$ effect, ω: 2000 rpm, pH 11, impedance module: (—) without $^3H_2O_2$, (- - -) 2 to 8 × 10^{-3} mol dm^{-3}, (+ + +) 5 × 10^{-2} mol dm^{-3} $^3H_2O_2$, phase module: (-o-o-).

ponent of the oxide can be assumed. Segment D is characterized by a straight line with a slope of about −1, and would appear to correspond here to more blocking ionic diffusion, a more compact oxide can be assumed. For segment B, it is difficult to calculate the thickness of non-dissipative insulating oxide as shown in [172] and [173], therefore we have drawn the Nyquist diagrams (Fig. 11.11).

The capacitive branches tend towards infinity from the high frequencies down to 10^{-2}. The electron diffusion within the oxide may control the kinetics; the charge transfer and ionic diffusion within the oxide layer are less limiting. The linear part at lower frequencies shifts towards higher real impedance with lower values of hydrogen peroxide meaning less passivity. Furthermore, the electrolyte becomes yellow; the corrosion potential may be near the intermediate peak. At medium values of hydrogen peroxide, the linear part shifts towards negative real impedance (e.g. 10 mmol dm^{-3}) and a loop is seen at the intersection of the semi circle and linear part, these suggest a relaxation; at these concentrations of $^3H_2O_2$, carbon steel is more passivated. At higher values of $^3H_2O_2$, the real linear part tends towards higher positive values meaning more corrosion; the corrosion potential may be in the transpassive region, and the yellow color of electrolyte deepens. The semi-circular arcs overlap the linear parts, and the diameter decreases with the concentration of hydrogen peroxide. The impedance modulus was estimated with respect to the semi circle. From calculating the oxide capacitance, the thickness is about 3 nm and does not really change with $^3H_2O_2$. It is assumed that the ionic diffusion and holes may also play a role, as is seen with the shift of the linear part.

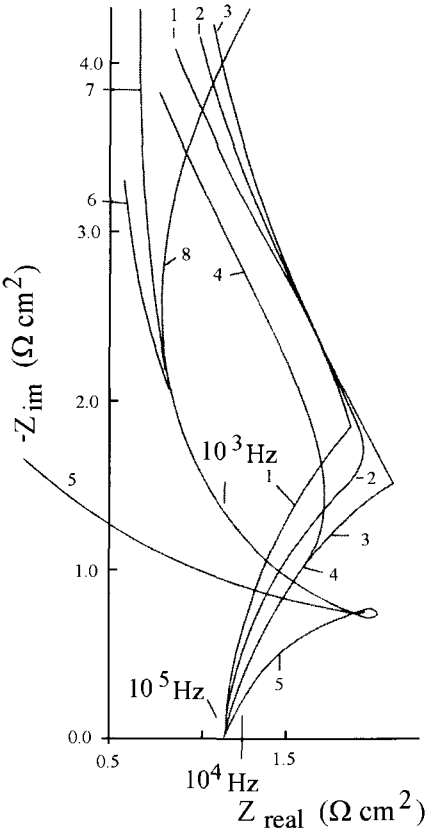

Figure 11.11. Nyquist diagrams—$^3H_2O_2$ effect, ω: 2000 rpm, pH 11, 1: 0 mol dm^{-3}, 2: 10^{-3} mol dm^{-3}, 3: 2 to 4×10^{-3} mol dm^{-3}, 4: 8×10^{-3} mol dm^{-3}, 5: 10^{-2} mol dm^{-3}, 6: 2×10^{-2} mol dm^{-3}, 7: 3×10^{-2} mol dm^{-3}, 8: 4×10^{-2} mol dm^{-3} $^3H_2O_2$.

3. Conclusions

In the transpassive-passive region, the oxide layer formed on carbon steel at slightly acid pH, with or without hydrogen peroxide, would not appear to be a semiconductor. The passivity occurs mainly at pH 13, while at slightly acid pH an oxidation current is observed at higher potentials. The observed dependence of the current associated with hydrogen peroxide reduction on the oxide layer would seem to suggest a better passivity at a medium concentration of $^3H_2O_2$. The corrosion potential may be located in the passive region. The thickness is calculated at the passivity potential; this should provide more protection of the carbon steel.

This Page Intentionally Left Blank

Chapter 12

GROWTH OF OXIDE BY HYDROGEN PEROXIDE

1. Introduction

Inconel alloys are selected for use in nuclear power plant materials such as steam generator tubes due to their good stress corrosion cracking [174,175] and pitting resistance [176] in pure water at high temperatures and pressures. Inconel 690, whose composition is given in Table 12.1, is one of these Ni-based alloys. In this work, the passivity of Inconel 690 in the presence of tritiated water is studied. During tritium decay, non-negligible concentrations of hydrogen peroxide and ionized peroxide radical at a rate of 10^{-3} mol dm^{-3} h^{-1} are produced if the tritiated water is concentrated and stored at a high pressure of radiolytic gases. At low radiolytic gases pressure, concentrations of dissolved species are smaller due to degassing which changes the radiolytic equilibrium in tritiated water and it is important to know this. In more detail, the tritiated water molecules are ionized for short periods (Fig. 12.1) leading to the chemical reaction stage with finally stable $^3H_2O_2$ and $^3HO_2^-$ formation in equilibrium (Fig. 12.2).

These two species act on the passive oxide layer. The ionized peroxide radical, $^3HO_2^-$, is in equilibrium with $^3H_2O_2$ and OH^- with an equilibrium constant of 12 [164]. Therefore, in this study realized at pH < 12, it can be expected that this radiolytic radical does not exist and only hydrogen peroxide is present. The passive oxide layer should then change as a function of its concentration and so the present study is designed to examine its contribution with passive potentials after having observed the effects of dissolved oxygen and pH.

2. Experimental results

Dissolved oxygen was eliminated by argon bubbling. The tests were realized at a pH of 11 taking into account the difference between the dissociation constant of tritiated and light water ($\Delta pK = 1.21$). Measurements were made immediately after polarization pretreatment for 1 min at -1 V/SCE until the oxides were removed.

2.1. Anodic polarization curves

Anodic polarization curves drawn at a low scan rate are shown in Fig. 12.3.

Table 12.1. Composition of Inconel 690

Elements	C	Ni	Cr	Fe	Mn	Si	Ti
Wt%	0.02	59.9	30	9	0.34	0.23	0.24

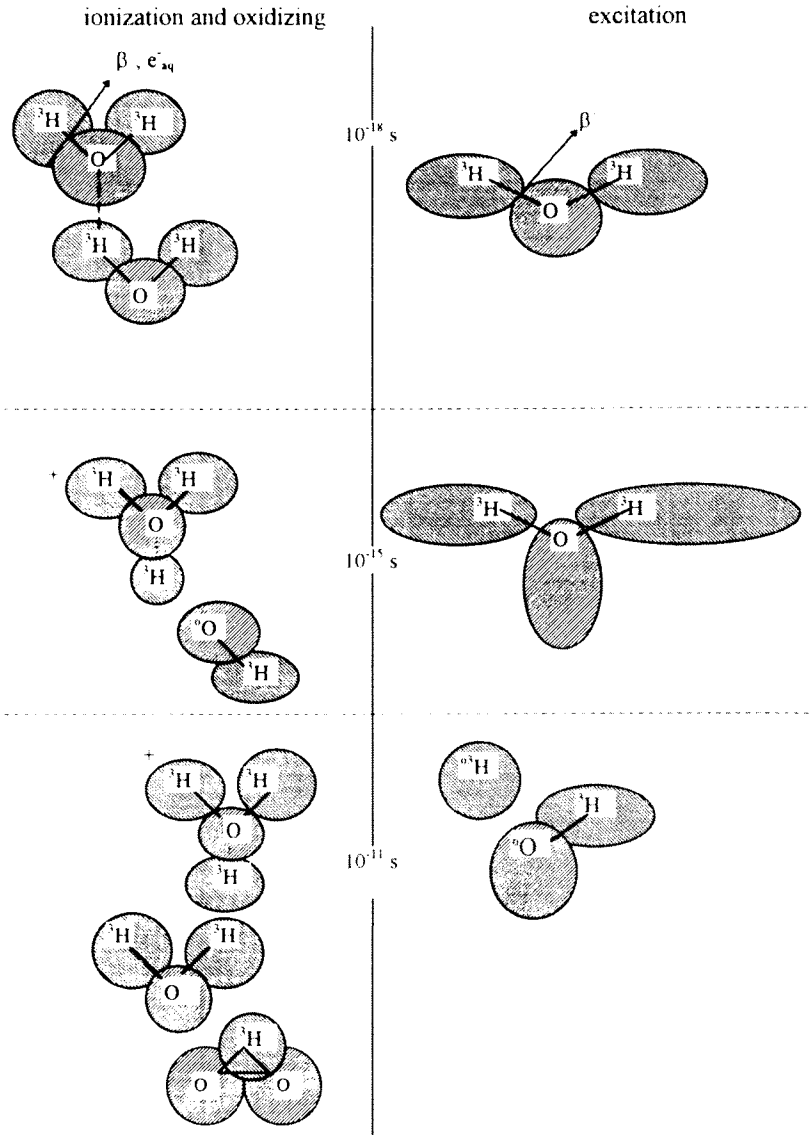

Figure 12.1. Excitation and ionization of tritiated water molecules.

chemical stage 10^{-7} s

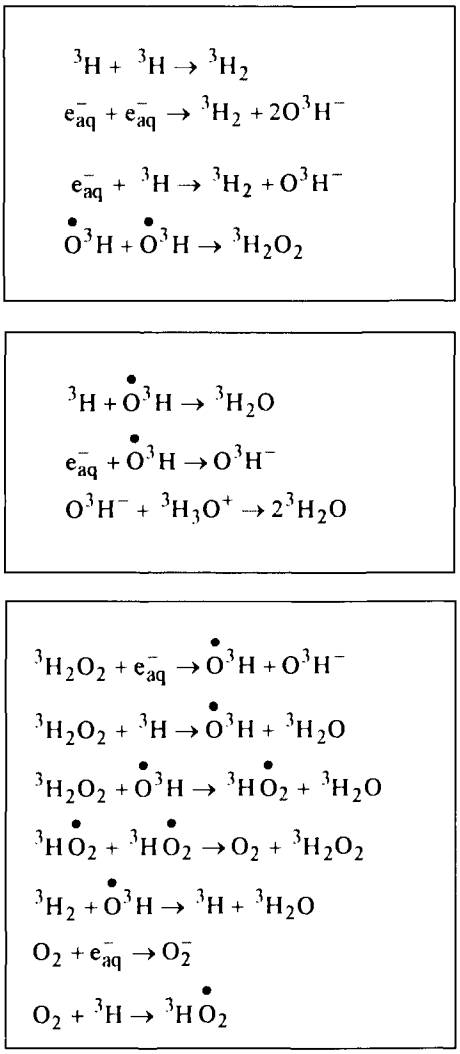

Figure 12.2. Radiolytic chemical transient species stage.

These curves exhibiting different characteristics were obtained starting from the greatest cathodic potentials and the first scan to avoid $^3H_2O_2$ concentration modification. The curve at the lowest $^3H_2O_2$ concentration shows a prepassive peak at −0.3 V/SCE. The passive region extends from −0.2 to 0.4 V/SCE. With increasing hydrogen peroxide concentration,

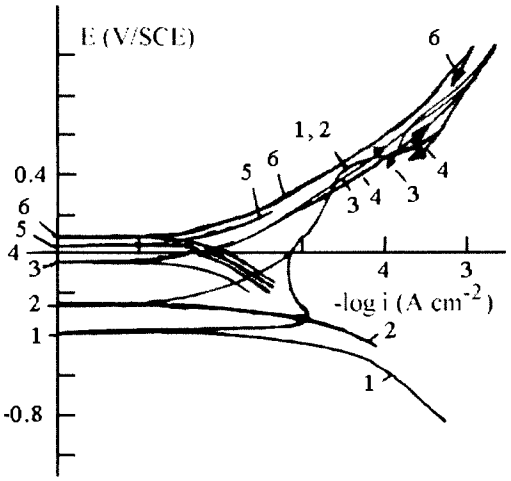

Figure 12.3. Polarization curves with $^3H_2O_2$, ω: 3000 rpm, v: 5 mV s^{-1}, pH 11, 1: 0 mol dm^{-3}, 2: 10^{-3} mol dm^{-3}, 3: 3×10^{-3} mol dm^{-3}, 4: 7×10^{-3} mol dm^{-3}, 5: 10^{-2} mol dm^{-3}, 6: 2×10^{-2} mol dm^{-3} $^3H_2O_2$.

the transpassive currents (located at 0.6 V/SCE) are low then become higher. This is due to the displacement of the corrosion and rest potentials towards more positive potentials (located first in the active zone, then in passivity, finally near the transpassivity). At the corrosion potential, Inconel 690 corrosion takes place at the cathodic and anodic sites and therefore active corrosion is due to the following reactions.

Cathodic reactions:

$$^3H_2O + e^- \rightarrow O^3H^- + \frac{1}{2}\,^3H_2 \tag{12.1}$$

With $^3H_2O_2$, the reaction is:

$$^3H_2O_2 + 2e^- \rightarrow 2O\,^3H^- \tag{12.2}$$

There is, in addition, the reduction of minor transient species which behave in the same way, such as:

$$^3HO_2 + {}^3H_2O + 3e^- \rightarrow 3O\,^3H^- \tag{12.3}$$

The overall cathodic current in the above reactions is:

$$i_c = -F \exp -\frac{FE}{2RT}\{k_c[^3H_2O] + k_d[^3HO_2]^{\nu'_{red}} + 15k_b[^3H_2O_2]^{\nu_{red}}\} \tag{12.4}$$

where k_c, k_b and k_d are the cathodic reaction rate constants and different ν_{red} the electrochemical reaction orders.

Table 12.2. Dependence of E_{corr} on $^3H_2O_2$

$^3H_2O_2$ mol dm^{-3} $\times 10^{-2}$	0	0.1	0.3	0.7	1	2
E_{corr} (V/SCE)	−0.4	−0.25	−0.18	0	0.05	0.1

For the anodic sites, Inconel 690 forms $Me(O^3H)_2$ in the corrosion potential, accordingly the anodic reaction is:

$$Me + 2O^3H^- \rightarrow Me(O^3H)_{2ads} + 2e^- \tag{12.5}$$

Equation (12.5) contributes to the passivity by means of $Me(O^3H)_{2ads}$ and Me_2O_3. Equations (12.1), (12.2) and (12.5) are pH dependent and to avoid any surface pH effects pH was kept constant by measurements at a high rotation rate.

The anodic reaction current determined at the corrosion potential is:

$$i_a = 2k_a F[O^3H^-]^{\nu_{ox}} \exp FE/RT \tag{12.6}$$

where k_a is the anodic reaction rate constant and ν_{ox} the electrochemical reaction order.

The corrosion potential of this system is the potential at which both the cathodic and anodic currents are equal. From these equations, E_{corr} is assumed to be:

$$E_{corr} = \frac{1.15RT}{F}\left(\log \frac{k_c k_b k_d}{k_a[OH^-]^{\nu_{ox}}} + \log[^3H_2O_2]^{\nu_{red}}[HO_2]^{\nu'_{red}}\right) \tag{12.7}$$

According to eq. (12.7), plotting E_{corr} against $\log {}^3H_2O_2$ by addition should give a straight line:

$$\frac{\partial E_{corr}}{\partial \log\left[[^3H_2O_2]^{\nu_{red}}[^3HO_2]^{\nu'_{red}}\right]} = \frac{1.15RT}{F} \tag{12.8}$$

It can be seen that hydrogen peroxide addition modifies the corrosion potential as shown in Table 12.2 and gives experimental curves where the slope is about 200 mV per decade. The value of reaction order expected for $^3H_2O_2$ is negative; this negative sign clearly indicates the cathodic electrochemical reaction [159].

It should be noted that the passive region is followed by a transpassive peak preceding the oxide layer dissolution. The current increases quickly in this region. According to Muralidharan [177], the overall reaction concerning the transpassive region is:

$$MeOO^3H + 5O^3H^- \rightarrow MeO_4^{2-} + 3\,{}^3H_2O + 3e^- \tag{12.9}$$

where $MeOO^3H$ is the hydrated oxide of Me_2O_3 on the surface. In this equation, clearly O^3H^- ions participate in the production of MeO_4^{2-} from Me_2O_3.

2.2. *Voltammetric curves*

In Fig. 12.4, representative cyclic voltammograms of potential versus current are given which show the behavior of Inconel 690 for different $^3H_2O_2$ concentrations.

The voltammograms indicate that at the most negative potentials, the currents are cathodic and consistent with $^3H_2O_2$ and corrosion products reduction and tritium evolution. At the lowest $^3H_2O_2$ concentration, on increasing the potential in the forward direction, there is a major prepassive peak near −0.5 V/SCE. Comparison with Muralidharan et al. [177] suggests that this peak involves formation of $^3HMeO_2^-$ and $Me(O^3H)_2$ leading to the passivity at the higher potentials.

The curves exhibit the following characteristics: (a) in the forward scan, the anodic curves intersect the potential axis at more positive potentials in the presence of $^3H_2O_2$. The corrosion potential is in the active peak bringing about instabilities in the passive oxide layer, which is then more difficult to stabilize and passivate, (b) a higher reduction current (corrosion product reduction peak) accompanied by a $^3H_2O_2$ reduction peak (−1 V/SCE) during the backward scan, which increases with $^3H_2O_2$ concentration signifying that the latter is reduced following the cathodic reaction (eq. (12.2)). This shifts all the currents in this region towards negative values, (c) in the forward scan, the active peak at −0.3 V/SCE

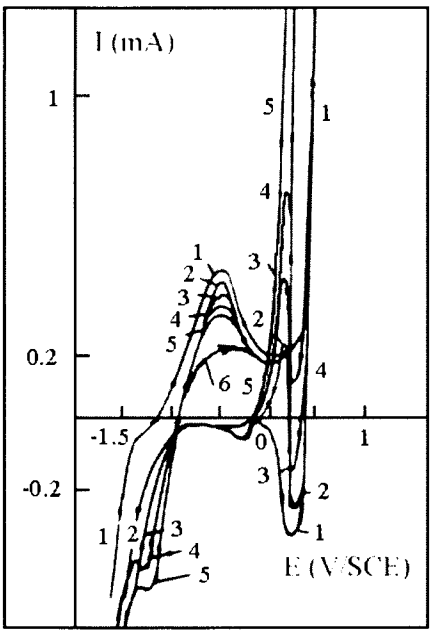

Figure 12.4. Voltammetric curves with $^3H_2O_2$, ω: 3000 rpm, v: 200 mV s^{-1}, pH 11, 1: 0 mol dm^{-3}, 2: 10^{-3} mol dm^{-3}, 3: 3×10^{-3} mol dm^{-3}, 4: 7×10^{-3} mol dm^{-3}, 5: 10^{-2} mol dm^{-3}, 6: 2×10^{-2} mol dm^{-3} $^3H_2O_2$.

decreases when the $^3H_2O_2$ concentration increases. These three types of current behavior result from the $^3H_2O_2$ reduction current, which is superimposed on the corrosion currents and that of the reduction of the corrosion products, (d) the peak in the transpassive-passive region disappears to be progressively replaced by a higher oxidation current which increases with $^3H_2O_2$ concentration, (e) in the reverse scan, a very fast reduction current increase immediately followed by a steep oxidation current increase. The interpretation could be the oxide breakdown potential shifts with this high scan rate. From these results, it seems that at pH 11 $^3H_2O_2$ reduction is easily possible, and that open-circuit coupling of transpassive dissolution with $^3H_2O_2$ reduction is feasible. As a result, cyclic voltammograms using a high scan rate suggest that there is a modification of the protective oxide layer.

The explanation of the behavior of these curves is similar to those given in the previous sections concerning additive effects of dissolved oxygen and pH with $^3H_2O_2$ on 316L stainless steel and 1018 carbon steel. It is deduced that lower and higher $^3H_2O_2$ concentrations in the tritiated water must be avoided. At medium concentrations, Inconel 690 is protected against corrosion, but the passive potential range is smaller at these $^3H_2O_2$ concentrations. In this case, $^3H_2O_2$ reduction on passivated Inconel 690 aids the formation of the inner passive oxide layer. Once a thick passive layer is well formed, the $^3H_2O_2$ reduction rate is slow. This would explain that the thickness and electron transfer in the passive layer is different at different $^3H_2O_2$ concentrations. Apparently, the current due to the reduction of $^3H_2O_2$ is limited by electron diffusion within the oxide layer at the passive potentials. At other potentials, without the passive layer, the current due to the reduction of $^3H_2O_2$ is limited rather by diffusion in the bulk solution [178].

2.3. *Impedance diagrams*

This section is concerned with the analysis of impedance data for Inconel 690 passivated at different passive potentials up to transpassivity and different $^3H_2O_2$ concentrations. The impedance data will be compared in order to evaluate the influence of $^3H_2O_2$ on the passive oxide characteristics. In the passive domain, the semi-circles in the Nyquist diagram are too incomplete over all the frequency range to be easily interpreted, therefore the Bode spectra were drawn for Inconel 690. In Fig. 12.5, the Bode plots were obtained at −0.6 V/SCE for 10^{-3} mol dm^{-3} $^3H_2O_2$ at pH 11 and for different electrode rotation rates. The electrode impedance reciprocal values at the low frequencies are proportional to the rotation rate square root showing that these represent a classical convective diffusion process corresponding to $^3H_2O_2$ and transitory species reduction (Fig. 12.2) at the Inconel 690 surface.

Hydrogen peroxide then reacts inducing passive oxide growth. According to the results in [172] and those of Cox and Jaworski [163] and the correlation coefficient determination using Figs 12.3 and 12.5, the diffusion coefficient for $^3H_2O_2$ is 4.2×10^{-5} cm^2 s^{-1}. Obtaining a diffusion coefficient for an unionized molecule is surprising in classic electrochemistry. In reality this means that hydrogen peroxide molecule is modified and electrically charged by free electrons (Fig. 12.1). The diffusion layer (Nernst layer) is estimated

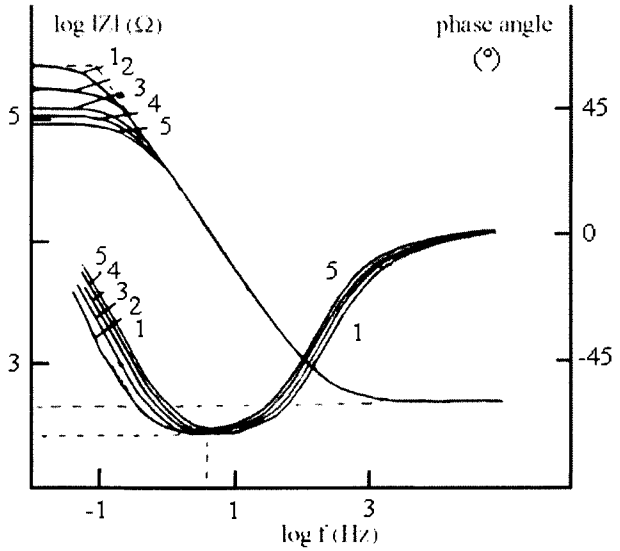

Figure 12.5. Effect of electrode rotation rate on electrode impedance, pH 11, E: −0.6 V/SCE, $^3H_2O_2$: 10^{-3} mol dm^{-3}, ω: 1: 0 rpm, 2: 300 rpm, 3: 600 rpm, 4: 1000 rpm, 5: 1500 rpm.

to be 65 μm from the equation:

$$\delta = 1.6\frac{D^{0.33}\Upsilon^{0.17}}{\omega^{0.5}} \tag{12.10}$$

where Υ is the electrolyte kinematic viscosity, ω the electrode disk rotation speed and D the diffusion coefficient. The diffusion layer calculated from eq. (12.10), is in agreement with the usual value for the diffusion process according to Bard and Faulkner [103].

Comparative measurements realized at pH 11, for different $^3H_2O_2$ concentrations and passive potentials (Fig. 12.6a–d), show changes in the fitted Bode diagrams for $\log|Z|$ and θ versus $\log(f)$, which are due to oxide layer characteristic and thickness modifications. The Bode plots are characterized by two distinct regions:

(a) In the broad low and middle frequency range, the diagrams display a linear slope of about −1 in $\log|Z|$ as $\log(f)$ decreases, while phase angle values approach −90°. This is the characteristic response of a compact passive oxide capacitance (C_{ox}) for Inconel 690 in the purely capacitive region. This capacitive behavior is observed over nearly the whole measurement frequency range.

(b) In the higher frequency range, a dip in the $\theta/\log(f)$ curve and an inflection in the $\log|Z|/\log(f)$ plots were obtained by subtracting the electrolyte resistance (10^3 Ω cm^2). This indicates the presence of a hardly identifiable parallel resistance and a non-dissipative passive oxide capacitance being the result of its formation. The

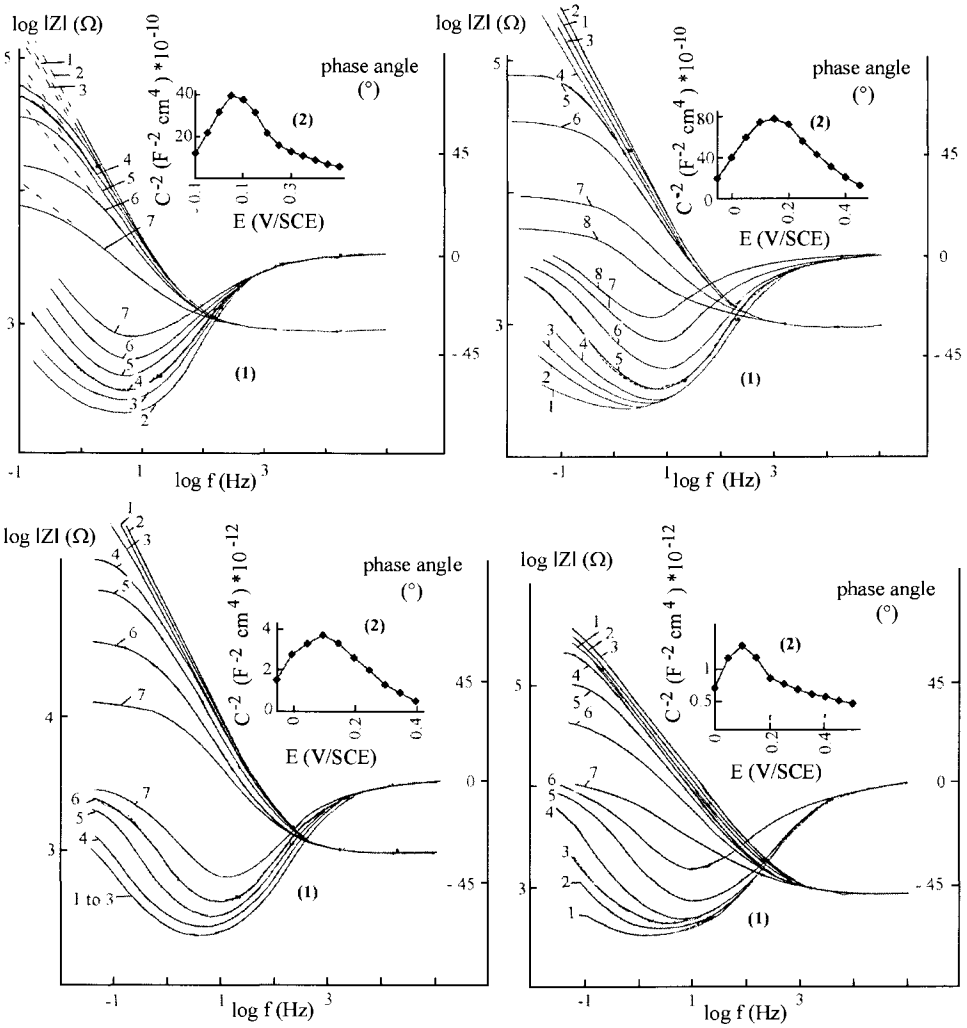

Figure 12.6. Bode diagrams with $^3H_2O_2$ and Mott-Schottky plots, pH 11, ω: 3000 rpm, (a): 1: $^3H_2O_2$: 5×10^{-3} mol dm^{-3}, 1: 0.02 V, 2: 0.1 V, 3: 0.2 V, 4: 0.3 and 0.4 V, 5: 0.5 V, 6: 0.6 V, 7: 0.7 V/SCE, (2): Mott-Schottky curve, (b): 1: $^3H_2O_2$: 10^{-2} mol dm^{-3}, 1: 0 V, 2: 0.1 and 0.2 V, 3: 0.3 V, 4: 0.4 V, 5: 0.5 V, 6: 0.6 V, 7: 0.7 V, 8: 0.8 V/SCE, (2): Mott-Schottky curve, (c): 1: $^3H_2O_2$: 1.5×10^{-2} mol dm^{-3}, 1: 0.06 and 0.2 V, 2: 0.1 V, 3: 0.3 V, 4: 0.4 V, 5: 0.5 V, 6: 0.6 V, 7: 0.7 V/SCE, (2): Mott-Schottky curve, (d): 1: $^3H_2O_2$: 2×10^{-2} mol dm^{-3}, 1: 0.06 and 0.3 V, 2: 0.1 V, 3: 0.2 V, 4: 0.4 V, 5: 0.5 V, 6: 0.6 V, 7: 0.7 V/SCE, (2): Mott-Schottky curve.

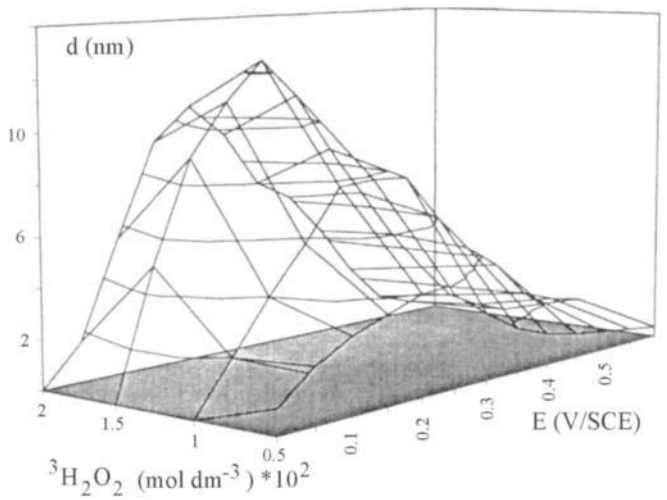

Figure 12.7. Oxide layer thickness as a function of passive potentials and $^3H_2O_2$.

effects appear less pronounced at sufficiently high passive potentials. The measurements effected at these different passive potentials show that the inflection point and the straight line in the $\log|Z|$ and the dip in the θ curves shift slightly from 7 to 9 kHz with a passive potential increase. These indicate a characteristic modification in the oxide layer [179]. Also, the deviation of the phase angle maximum, θ_{max}, from $-90°$ indicates that the passive layer thus formed on Inconel 690 approaches ideal capacitor behavior.

To calculate the thickness, the reciprocal capacitance value can be taken either from the Bode plot at the frequency of 0.16 Hz where the impedance data give a straight line with a slope of ≈ -1, or from the value of the imaginary impedance. In Fig. 12.6, at potentials between 0.3 and 0.7 V/SCE and for 0.16 Hz, the impedance modulus value increases then decreases with increasing passive potential. The higher impedance value signifies greater passivation. From these potentials, the oxide thickness variation is calculated using the oxide dielectric constant. As the relative dielectric constant for Inconel 690 was not found in the literature, passive current vs. time was measured during potentiodynamic oxide formation. The quantity of the total charge obtained by integrating the current-time curve corresponds to oxide layer formation using Faraday's law. The value of the relative dielectric constant is then 20. The values of oxide capacitance and thickness were calculated for different passive potentials and $^3H_2O_2$ concentrations (Tables 12.3–12.7). In Fig. 12.7, the variation of thickness indicates that the oxide layer increase obeys a growth law depending on these two studied parameters: potentials [180] and hydrogen peroxide.

The Bode diagrams (Fig. 12.6), enable us to calculate the donor concentration (n_d) following the simplified Mott-Schottky equation. Linearity is observed between 0 and 0.3 V/SCE, and using the Mott-Schottky equation, the donor density is given in Table 12.8.

Table 12.3. Dependence of oxide capacitance ($\mu F cm^{-2}$) on passive potentials at 5×10^{-3} mol dm^{-3} $^3H_2O_2$

E (V/SCE)	−0.1	−0.05	0	0.05	0.1	0.15	0.2	0.25	0.3
C_{ox}	3.2	2.2	1.8	1.6	1.7	1.8	2.1	2.6	3.2

Table 12.4. Dependence of oxide capacitance ($\mu F cm^{-2}$) on passive potentials at 10^{-2} mol dm^{-3} $^3H_2O_2$

E (V/SCE)	−0.05	0	0.05	0.1	0.15	0.2	0.25	0.3
C_{ox}	2.2	1.6	1.3	1.2	1.1	1.25	1.35	1.54

Table 12.5. Dependence of oxide capacitance ($\mu F cm^{-2}$) on passive potentials at 1.5×10^{-2} mol dm^{-3} $^3H_2O_2$

E (V/SCE)	−0.05	0	0.05	0.1	0.2	0.3	0.4
$C_{ox} \times 10$	8.2	6.2	5.6	5.3	5.6	6.2	7.1

Table 12.6. Dependence of oxide capacitance ($\mu F cm^{-2}$) on passive potentials at 2×10^{-2} mol dm^{-3} $^3H_2O_2$

E (V/SCE)	0	0.05	0.1	0.15	0.2	0.25	0.3	0.35
$C_{ox} \times 10$	12	9	8.6	9.1	11	11.5	13	13.5

Table 12.7. Oxide layer thickness (nm) dependence on $^3H_2O_2$ concentration

E (V/SCE)	0	0.05	0.1	0.15	0.2	0.25	0.3	0.35	0.4	0.45	0.5	0.55	0.6
5×10^{-3} mol dm^{-3}	1	2.2	3	3.5	4	3.7	2.7	1.8	1.3	1	0.8	0.6	0.4
10^{-2} mol dm^{-3}		2	4	5.8	7.8	7.9	7.8	6	4.5	3.5	2	1.5	1.2
1.5×10^{-2} mol dm^{-3}		5	9	11	12.5	11	8.7	6.7	4.7	3	1.5	0.8	0.3
2×10^{-2} mol dm^{-3}		1.6	5.5	9.2	10.5	9	7	6	5	3	1	0.5	

Table 12.8. Donor density dependence on $^3H_2O_2$ concentration

$^3H_2O_2$ mol $dm^{-3} \times 10^2$	0.5	1	1.5	2
$n_d \times 10^{19}$	4	2	1.3	1.7

The carrier concentration is in agreement with the theoretical value for a passive layer given by Castro and Vilche [108], Simoes et al. [109] and Oriani et al. [110]. The flat-band extrapolated potential is close to −0.15 V/SCE for the different $^3H_2O_2$ concentrations.

The greater deviation of the phase angle maximum, θ_{max}, from −90° for 1.5×10^{-2} mol dm^{-3} $^3H_2O_2$ in Bode spectra (Fig. 12.6c), indicates that the passive layer thus formed on Inconel 690 approaches more ideal capacitor behavior. Also, consideration of the electrode impedance values shows that the higher value obtained for this concentration should favor passivating. The thickness and donor density are higher and lower, respectively, for 1.5×10^{-2} mol dm^{-3} $^3H_2O_2$ (Tables 12.7 and 12.8). These values at this $^3H_2O_2$ concentration indicate less electron transfer and higher corrosion resistance. The oxide layer formed for 1.5×10^{-2} mol dm^{-3} $^3H_2O_2$ would then be thicker and slightly more

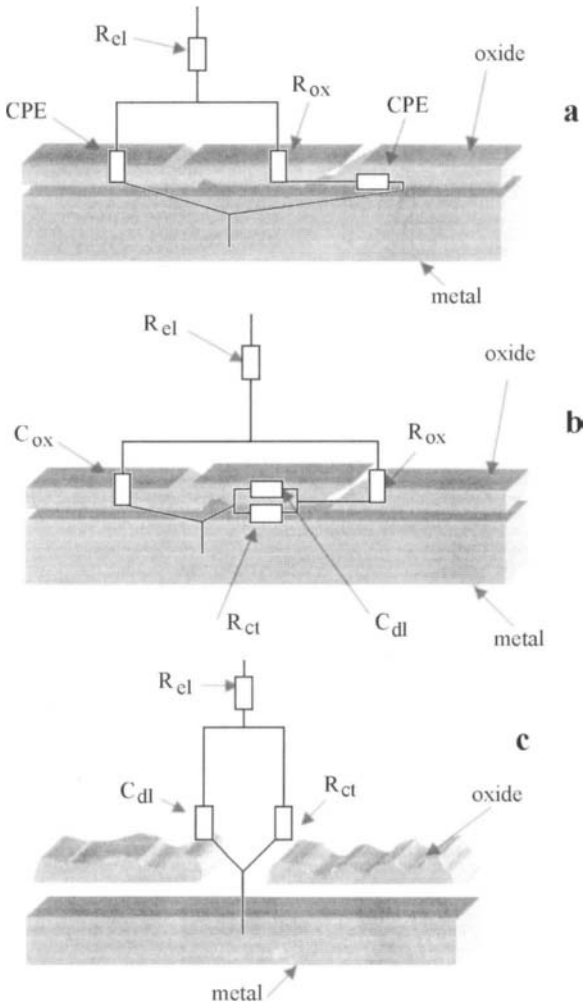

Figure 12.8. Equivalent circuits for impedance simulation (a–c): R_{el}: electrolyte resistance, R_{ox}: oxide resistance, R_{ct}: charge transfer resistance, CPE: constant phase elements, C_{ox}: oxide capacitance, C_{dl}: double layer capacitance.

insulating than that at lower or higher $^{3}H_2O_2$ concentrations. These reflect the formation of a highly ordered and less defective oxide layer.

In the passive-transpassive region, the total impedance for Inconel 690 again becomes predominantly resistive (Fig. 12.6a–d) over a broad frequency range, while the capacitive part is predominant only at higher frequencies. These findings indicate passive layer breakdown at these potentials.

2.4. *Equivalent circuits and value determinations*

Diagnostic criteria for the choice of equivalent circuits for modeling impedance data may be summarized by visual observation of the shifts in experimental Bode plots with changing passive potential and $^3H_2O_2$ concentration. It seems that at potentials in the passive region (mainly purely capacitive impedance), Bode plots give a perfect fit if the total impedance is modeled according to the first circuit in Fig. 12.8a.

Constant phase elements (CPE) are used instead of capacitors to account for the slight deviations observed at a capacitive slope lower than -1.

The perfect fit of Bode plots is also obtained according to the circuit shown in Fig. 12.8b. In this circuit, resistances and capacitances are used to account for the different deviations observed at low and high frequencies.

Either circuit can be used in passivity. The first was taken for different $^3H_2O_2$ concentrations where the slope 'a' should be controlled, and the second was used where the experimental capacitive slope is definitely 1. From Table 12.3 to Table 12.6, the oxide capacitance value, which varies from 0.5 to 3.2 $\mu F\,cm^{-2}$, indicates the passivity of Inconel 690 in the presence of $^3H_2O_2$.

In the passivity-transpassivity limit, the Bode plots obtained in Fig. 12.6 can be explained by the equivalent circuit shown in Fig. 12.8c. From this it was observed that the charge transfer resistance decreases when the potentials increase, signifying more corrosion. In the same way, the charge transfer resistance increases up to 1.5×10^{-2} mol dm^{-3} $^3H_2O_2$, then decreases for 2×10^{-2} mol dm^{-3} $^3H_2O_2$ signifying the improvement of passive oxide characteristics up to 1.5×10^{-2} mol dm^{-3} $^3H_2O_2$.

3. Conclusions

Tritiated water stored at high radiolytic gas pressure contains non-negligible amounts of hydrogen peroxide. This species changes the redox potential of tritiated water, which is shifted to a value in the passive or transpassive region. The same is true for the corrosion potentials of Inconel 690. The reduction of hydrogen peroxide occurs in the active region, passivity and in transpassivity at pH 11. This reduction should be more difficult to obtain in passivity when the corrosion potential is located in this region. Consequently, the observed dependence of the electrochemical parameters associated with this reduction on the oxide layer would seem to suggest better passivity at a medium concentration of hydrogen peroxide.

This Page Intentionally Left Blank

Chapter 13

GROWTH OF PITS AND CREVICES BY CHLORIDE

1. Introduction

Selection of steel alloys depends not only their corrosion resistance but also on their hardness: both low and high hardness alloys are required. A low hardness component is assembled with a high hardness component to ensure that the joints are perfectly tight. Maraging steel, whose composition is given in Table 13.1, is usually selected for special applications requiring the hardness resulting from $Ni_3(Al, Ti)$ precipitation, although precipitation hardening generally leads to a slight reduction in corrosion resistance.

Another problem is that relatively concentrated chloride solutions are formed by decomposition of chlorinated organic polymers by the low energy released in the decay of tritiated water which is in contact with these compounds.

$$R\text{–}Cl + \beta^- \rightarrow Cl^- + CO_2 + R'\text{–} \tag{13.1}$$

An acid medium was selected since relatively concentrated nitric acid solutions are produced. This can be explained by the effect of β^- particles on nitrogen. The reactions are:

$$N_2 + \beta^- \rightarrow 2N^\bullet \tag{13.2}$$

$$N^\bullet + 3\,{}^3HO_2^- \rightarrow {}^3HNO_3 + {}^3H_2O + 2O^\bullet \tag{13.3}$$

The corrosion depends on these parameters; therefore the behavior of Maraging steel was studied at the corrosion, active and passive-transpassive potentials and at acid pH, both in the presence and absence of Cl^-.

Table 13.1. Composition of martensitic Maraging steel

Elements	C	Cr	Ni	Mo	Ti	Al	Fe
Wt%	$\leqslant 0.02$	12	9	2	0.3	0.7	bal.

2. Results and discussion

Before giving the results, it must be specified that the measurements were made immediately after bubbling argon and a prepolarization at −1.3 V/SCE to eliminate dissolved oxygen and hydrogen peroxide. The voltammograms were swept cyclically at a high scan rate until reproducibility was obtained.

2.1. Results without chloride

2.1.1. Polarization curves Polarization curves (Fig. 13.1) were recorded at a low scan rate, at various pH readings for comparison and with electrode rotation to avoid modification of the curve shape by local pH variations. In these polarization curves it is difficult to determine the lower passive potential limit, since no clear active to passive transition is observed. The instabilities obtained in the passive region before a slight smoothing illustrate breakdown or porosity initiations of the oxide layer. Increasing the pH leads to shifting the transpassive and corrosion potentials towards more negative potentials.

It is of interest to comment on the corrosion potential values (E_{corr}), before passivity where the rate is limited by diffusion within the passive oxide as indicated by Pleskow [181], and Randin [182]. At E_{corr}, the corrosion should be caused by the cathodic and

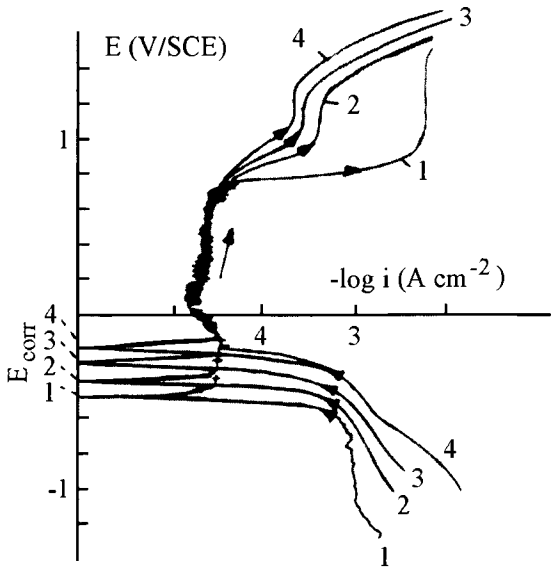

Figure 13.1. Polarization curves without chloride and with electrode rotation—pH effect, v: 5 mV s^{-1}, ω: 2000 rpm, 1: pH 11, 2: pH 7, 3: pH 4, 4: pH 2.

anodic sites due for instance to the following reactions at acid pH, cathodic sites:

$$^3H^+ + e^- \rightarrow {}^3H_{ads} \tag{13.4}$$

$$2\,{}^3H_{ads} \rightarrow 2\,{}^3H \tag{13.5}$$

The current of the above cathodic reaction is:

$$i_c = -k_c F[^3H^+]^{\nu} \exp -FE/2RT \tag{13.6}$$

where k_c is the reaction rate constant, E the electrode potential (e.g., E_{corr}), T the absolute temperature, and F and R are the Faraday and gas constants respectively. The cathodic reaction has an electrochemical reaction order of ν with respect to $^3H^+$.

For the anodic reactions, Maraging steel may be assumed to form intermediates; processes at acid pH are discussed by Bessone et al. [183] and Lorbeer and Lorenz [166]. From the investigations of these authors, realized at low scan rates, the reactions are at acid pH and up to the passive region, anodic sites:

- active range ($0 < \theta < 1$, where θ is the surface coverage)

$$Me + {}^3H_2O \leftrightarrow Me(^3H_2O)_{ads} \tag{13.7}$$

$$Me(^3H_2O)_{ads} + {}^3H_2O \leftrightarrow Me(O^3H,\ {}^3H_2O)_{ads} + {}^3H^+ + e^- \tag{13.8}$$

$$Me(O^3H,\ {}^3H_2O)_{ads} \leftrightarrow Me(O^3H)_{ads} + {}^3H_2O \tag{13.9}$$

$$Me(O^3H)_{ads} \rightarrow MeO^3H^+_{ads} + e^- \tag{13.10}$$

$$MeO^3H^+_{ads} + {}^3H^+ \leftrightarrow Me^{2+}_{ads} + {}^3H_2O \tag{13.11}$$

It has been shown by Muralidharan et al. [184], that eq. (13.11) is the rate determining step at the corrosion potential.

- transition range ($\theta_{Me(O^3H)_{2ads}} \rightarrow 1$)

$$Me^{2+}_{ads} + 2\,{}^3H_2O \leftrightarrow Me(O^3H)_{2ads} + 2\,{}^3H^+ \tag{13.12}$$

- prepassive range ($\theta_{Me(O^3H)_{3ads}} \rightarrow 1$)

$$Me(O^3H)_{2ads} \rightarrow MeO^3H^+ + Me(O^3H)_{ads} + e^- \tag{13.13}$$

$$Me(O^3H)_{2ads} \leftrightarrow MeOO^3H + {}^3H^+ + e^- \tag{13.14}$$

- passive layer formation range (porous → non-porous layer, $\theta_{Me(O^3H)_{3ads}} = 1$)

$$3Me(O^3H)_{2ads},\ x\,{}^3H_2O \leftrightarrow Me_3O_2(O^3H)_4,\ x\,{}^3H_2O + 2\,{}^3H^+ + 2e^- \tag{13.15}$$

$$Me_3O_2(O^3H)_4,\ x\,{}^3H_2O \leftrightarrow 3MeOO^3H + x\,{}^3H_2O + {}^3H^+ + e^- \tag{13.16}$$

Triton diffusion at the electrochemical interface is assisted by the local electrical field. The partially hydrated intermediate undergoes a structural rearrangement along with an electron transfer.

$$2MeOO^3H \leftrightarrow Me_2O_3 + {}^3H_2O \tag{13.17}$$

$$Me(O^3H)_{2ads} + Me_2O_3 \leftrightarrow Me_3O_4 + {}^3H_2O \tag{13.18}$$

The reaction mechanism in the active region indicates that the reactions should be limited by surface coverage. Assuming a symmetry factor of 0.5 at the corrosion potential as indicated by Titz et al. [185] and the formation of Me^{2+}_{ads} with $n = 2$, the anodic current equation for the corrosion potential is:

$$i_a = 2k_aF[Me]\exp FE/RT \tag{13.19}$$

where k_a is the anodic rate constant. The corrosion potential of this system is the potential at which both the cathodic and anodic currents are equal. From eqs (13.6) and (13.19), and applying the same calculation procedure as that given by Jin-Yun Zou and Der-Tau Chin [186,187] in this case:

$$E_{corr} = \frac{4.6RT}{3F}\left[\log\frac{k_c}{k_a} - \nu\,pH\right] \tag{13.20}$$

According to eq. (13.20), a plot of $\log E_{corr}$ against $\log pH$ should give a straight line with a slope of:

$$\frac{\partial \log E_{corr}}{\partial\, pH} = \frac{1.51\nu RT}{F} \tag{13.21}$$

The corrosion current behavior determined from eqs (13.6) and (13.19) is:

$$i_{corr} = 1.26k_a^{0.33}k_c^{0.66}F[{}^3H^+]^{0.66\nu} \tag{13.22}$$

Using eq. (13.22), a log-log plot of the corrosion current against $^3H^+$ should be linear with a slope of:

$$\frac{\partial \log i_{corr}}{\partial\, pH} = -0.66\nu \tag{13.23}$$

The effect of $^3H^+$ on eqs (13.21) and (13.23) has been experimentally checked over the pH range 1 to 7. Table 13.2 gives the values of E_{corr} as a function of pH. The value of $\partial E_{corr}/\partial \log[^3H^+]$ is about 35 mV. The values of i_{corr} were determined from the curves and

Table 13.2. Values of E_{corr} as a function of pH

pH	1	2	3	4	7	11
E_{corr} (V/SCE)	−0.17	−0.2	−0.23	−0.25	−0.4	−0.5

Table 13.3. Values of i_{corr} as a function of pH

pH	1	2	3	4
i_{corr} (μA cm^{-2})	7	2.5	0.7	0.2

are listed in Table 13.3 as a function of acid pH. They yield $\partial \log i_{corr}/\partial \log[^3H^+] = 0.5$. From the experimental values of E_{corr} and i_{corr}, the reaction order (ν) for $^3H^+$ is 1. The cathodic and anodic Tafel slopes are about -115 and 65 mV per decade and they are consistent with eqs (13.6) and (13.19).

2.1.2. Voltammograms Using rapid-scan curves should reveal peaks where inflections in the slow-scan curves suggest they might exist. Therefore the cyclic voltammograms at a high scan rate with and without electrode rotation should demonstrate different behaviors including the modification of local pH on Maraging steel. In the forward scan (Figs 13.2 and 13.3), the potential is swept over the range of activity, then in passivity and up to transpassivity; under this condition, there are adsorbed intermediates, then active peak formation and finally, a passivating oxide layer spreads across the surface until porosity and breakdowns at the higher potentials are obtained.

In the backward scan, the passive oxide layer is reformed and then the corrosion products are reduced in the cathodic peak. Increasing the scan rate very slightly shifts the active peak to more positive values while cathodic peak potentials shift to more negative values. This is partly due to the kinetics of adsorbates formation. At the passive-transpassive limit in the forward scan, the anodic current increases and corresponds to breakdown and porosity formation. The diffusion in the pore openings should become rate controlling.

In Fig. 13.2, curves 1 to 5 were obtained before the stabilized scan (curve 6) and without electrode rotation. On repeated cycling, the anodic and cathodic peak currents in active and transpassive regions increase in the same proportion, indicating they are consecutive. The stabilized scan (curve 6) depends on scan number, e.g. on the species kinetics and oxidation-reduction mechanisms in the active, prepassive and transpassive regions. The active peak potential does not change while the cathodic peak potential becomes slightly more positive with increase in scan number. During the forward scan, the active peak corresponds to the passive layer formation of $Me_3O_2(O^3H)_4$, $x\ ^3H_2O$; its charge increases on subsequent cycling showing the increasing formation of adsorbates and oxide. In the backward scan, the charge under the cathodic peak due to the formation of $Me_3O_2(O^3H)_4$, $x\ ^3H_2O$, increases on subsequent scanning, keeping the ratio of anodic and cathodic charges nearly constant. In Fig. 13.2, the passive oxide repairing current is seen in the beginning of the backward scan for the first cycle (1 V/SCE), and at 0.7 V/SCE for the subsequent cycles. An anodic peak is observed in transpassivity; its current increases with cycle number. A cathodic peak appears at 0.6 V/SCE from the second cycle. This shows that during the initial oxidation stage, the oxide formed is different from that observed in subsequent cycles. The aged oxide favors further transpassive and active oxidation and porosity.

The stabilized cycles obtained with or without electrode rotation and for different acid pH values are shown in Fig. 13.3. Their interpretations, like those concerning the follow-

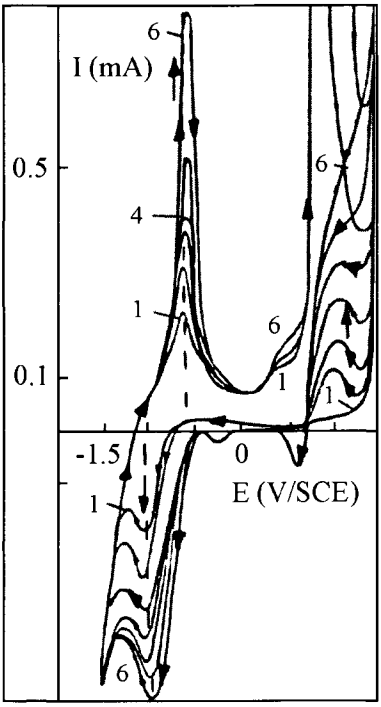

Figure 13.2. Voltammetric curves without chloride and without electrode rotation, v: 350 mV s^{-1}, ω: 0 rpm, pH: 3, cathodic potential limit: −1.5 V/SCE, cycle stabilization (the cycles were performed continuously from the first).

ing voltammetric curves, are not simple but will contribute to our knowledge of local pH modifications, transient formation and surface coverage in the active peak, passivity and transpassive regions. At the most negative potentials, the currents are cathodic; they are consistent with the active region. On increasing the potential in the forward direction, the active peak appears around −0.75 V/SCE without electrode rotation, and 0 V/SCE with rotation; it is followed by the passive region which is anodic and corresponds to the formation of Me_3O_4 or Me_2O_3 from $MeOO^3H$ and $Me(O^3H)_{2ads}$. The peak is the result of intermediates in the active region (eqs (13.8)–(13.11)). It is higher at more acid pH values and the charge is greater for such values. The active peak potentials become slightly more positive at more acid pH in agreement with eqs (13.8), (13.12) and (13.14). If the reactions in eqs (13.7)–(13.18) are reversible and constitute simple conjugated electrochemical systems with an oxide layer formation, the corresponding active and cathodic peaks must occur at the same potentials. Since there is no cathodic peak corresponding to the active peak in the same potential region, the above conjugated reactions are complicated. Without electrode rotation (Fig. 13.3, curves 5 to 7), the active peak is found at more negative potentials. Its potential corresponds to the position of a shoulder with stirring (curves 1 and 2). Bessone

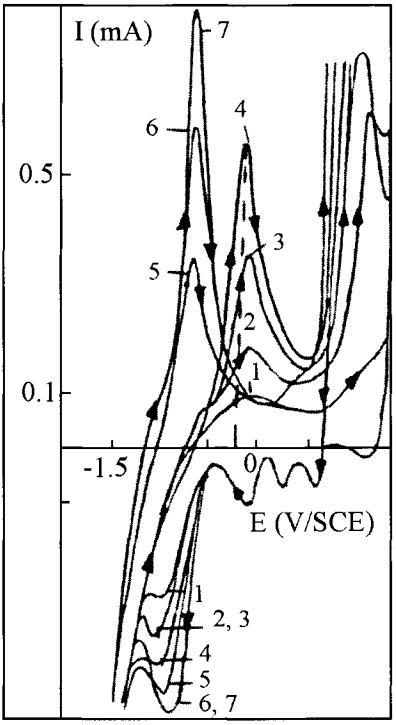

Figure 13.3. Voltammetric curves after stabilization of cycles and without chloride—pH effect, v: 350 mV s^{-1}, cathodic potential limit: −1.5 V/SCE, with electrode rotation: ω: 2000 rpm, 1: pH 7.3, 2: pH 4.6, 3: pH 2.6, 4: pH 1.2, without electrode rotation: ω: 0 rpm, 5: pH 3.5, 6: pH 2.6, 7: pH 1.2.

et al. [183] have shown that the active peak potential shifts towards a negative direction with decreasing rotation rate or less acid pH, which leads to a smaller potential interval between the active and cathodic peaks. According to the discussion of Bessone et al. [183] and also to the shifts in the corrosion and peak potentials with pH, obtained experimentally in Figs 13.1 and 13.3 respectively, curves 5 to 7 in Fig. 13.3 indicate an increase in the pH in the electrolyte–electrode interface without electrode rotation modifying the peak position, as in the potential–pH equilibrium diagrams of Fe, Ni and Cr. However, as claimed by Bessone et al. [183], such behavior cannot be explained by the proposed mechanism alone because the tritons consumed for the formation of soluble Me^{2+} species in eq. (13.11) are produced in eqs (13.8) and (13.12). Therefore, an additional parallel reaction consuming tritons takes place. Such a reaction could be the chemical dissolution of the adsorbed intermediates $Me(O^3H)_{2ads}$ and $MeOO^3H$. Alternatively, it could be the discharge of $^3H^+$ as in eq. (13.4) which decreases the superficial $^3H^+$ concentration in the corrosion potential and active peak. This indicates that the corrosion rate and passivity are dependent on the species remaining on the surface of the steel and also on either a decrease or an increase

in $^3H^+$ concentration. This also indicates that either the diffusion layer thickness is significantly dependent on the hydrodynamic layer or, more probably, that the rate determining processes at the surface are highly dependent upon diffusion through the solution. The $^3H^+$ concentration gradient, intermediate formation and hydrated oxide are responsible for the passive oxide electrochemical activity and characteristics.

No instabilities are seen in the passive region; the kinetics of breakdown of the oxide layers are so slow that at this scan rate they are not observable here. In Fig. 13.3, with or without electrode rotation, the transpassive peak is always obtained at the same potential. It increases with $^3H^+$ concentration in the aqueous bulk, either with or without stirring. A $^3H^+$ concentration increase enhances the corrosion kinetics in the transpassive region. This behavior is related to the oxidation of Me_2O_3 to MeO_4^{2-}. For the same pH, the transpassive peak is higher without stirring as was the active peak (curves 5 to 7). This shows that the transpassive peak depends on the species concentrations on the surface of Maraging steel in the active region: intermediates and the superficial pH modify the electrochemical activity in the electrolyte-Maraging steel interface for passivity, and thereby for transpassivity. On scan reversal, the anodic current decrease appears at 1 V/SCE; it is followed by the cathodic peak at 0.6 V/SCE. Some oxygen atoms from the oxide may be absorbed as in eq. (13.24), thus altering the most cathodic region in the polarization curves (Fig. 13.1, curve 1), where the diffusion limited current of about 1 mA cm^{-2} indicates reduction of trace amounts of adsorbed oxygen to form ^3H_2O.

$$O^{2-} \rightarrow O_{ads} + 2e^- \tag{13.24}$$

In Fig. 13.3, during the backward scan, one or more reduction peaks (0.2 and 0 V/SCE) are seen, depending on the stirring. The corrosion products formed in an intermediate oxidation state of (III) and (IV) such as Me_3O_4, $x\,^3H_2O$ and Me_3O_2 $(O^3H)_4$ would not be removed from the steel surface without stirring, causing the successive reduction peaks. At -1 V/SCE, the major reduction peak appears to be the conjugate of the active peak. It has the same behavior as that of the transpassive peak: it also depends on stirring and the active peak local pH. With or without electrode rotation (Fig. 13.3), the cathodic peak is always at the same potential, whereas the active peak position depends on electrode rotation. This indicates that the superficial pH is the same with or without electrode rotation in the cathodic and transpassive peaks. The electrolyte-Maraging interface should be re-acidified during the scan from passivity as shown in eqs (13.14)–(13.16) and later in eq. (13.26). The cathodic peak is smaller with stirring; this shows that the reduction of corrosion products is dependent on the species remaining on the steel surface. The sum of anodic charges in the forward scan is larger than the sum of cathodic charges in the backward scan, showing that some of the species produced in the scans are not entirely reduced in the backward scan and tritium evolution would take place over the partially reduced oxide. This also means that species are removed by stirring. Entire results for active and reduction peaks and modification of passive layer (waves on right curve) are presented in Fig. 13.4.

The currents observed in the active and passive regions are attributed to double layer and oxide capacitive charging and faradaic current. The double layer capacitance obtained by

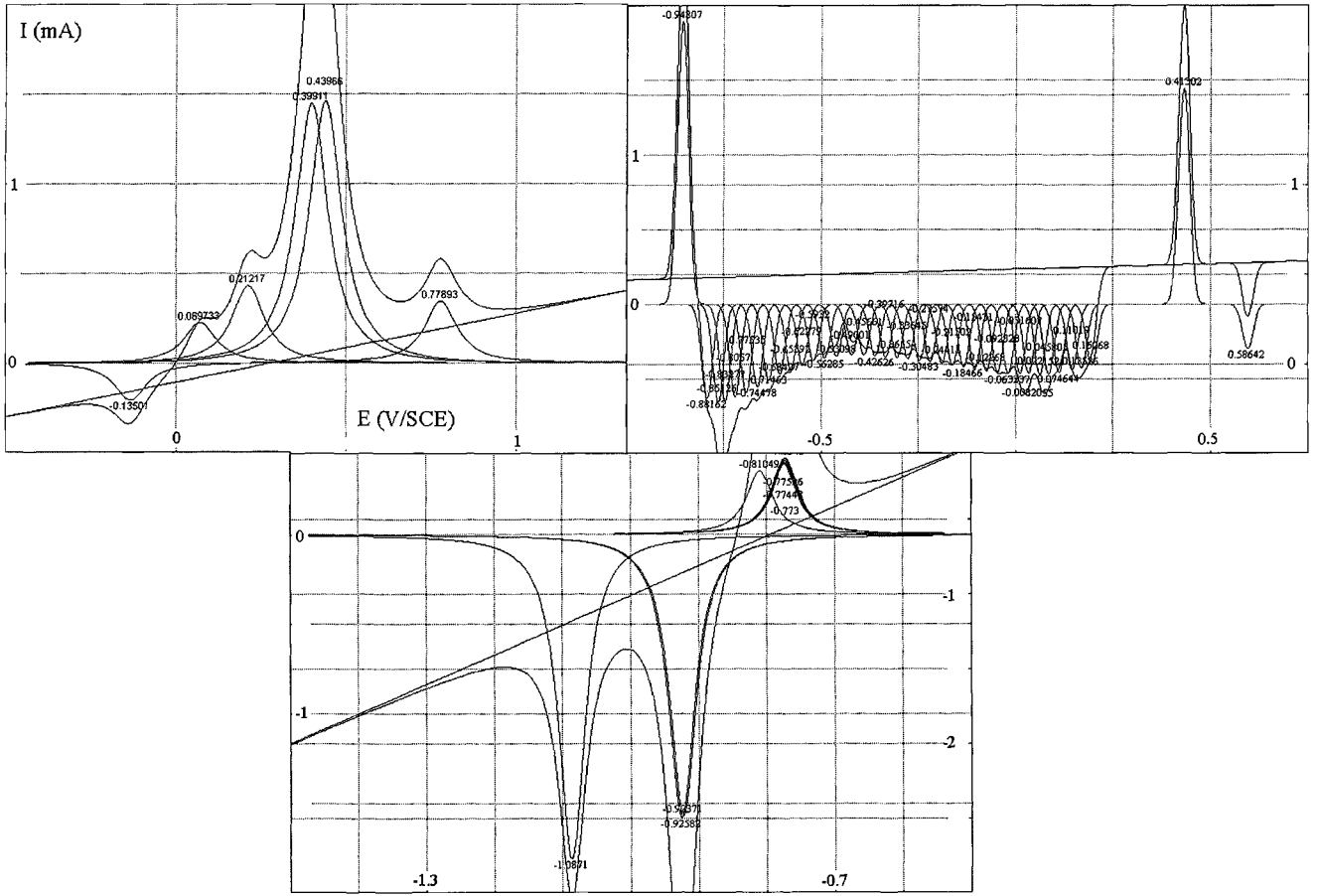

Figure 13.4. Entire active and reduction peaks and moving wave peaks formed during passivity.

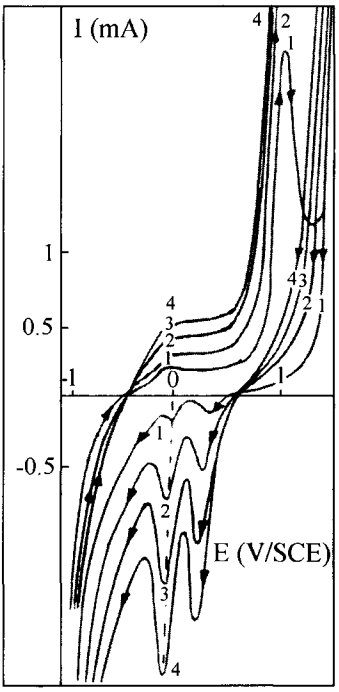

Figure 13.5. Voltammetric curves—scan rate effect, ω: 0 rpm, cathodic potential limit: −1 V/SCE, 1: 270, 2: 1100, 3: 2700, 4: 3900 mV s^{-1}.

impedance measurements in the subsequent section is less than 100 μF cm^{-2} over the potential range, therefore the double layer charging current should be no greater than 15 μA at this high scan rate. The observed currents in the voltammetric curves are thus principally due to the intermediates and passive oxide formation.

In Fig. 13.5, the curves are drawn for different scan rates and a cathodic potential limit more positive than that in Figs 13.2 and 13.3 (−1 instead of −1.5 V/SCE), located in the cathodic peak increase. In these curves, the active peak is replaced by a passive current due to the fact that all oxide and intermediates are not entirely reduced during the backward scan (cathodic potential limit of −1 V/SCE). This current varies linearly with the square root of the scan rate with a constant slope about 0.35, and was found to pass through the origin (Fig. 13.6). This signifies that the same partly free oxide surface is formed for each backward scan; this surface depends on the cathodic potential limit.

The active peak equation given by MacDonald and Roberts [188] and Calandra et al. [189] is:

$$i_p = (nF\rho\kappa/M)^{0.5} A(1-\theta)v^{0.5} \tag{13.25}$$

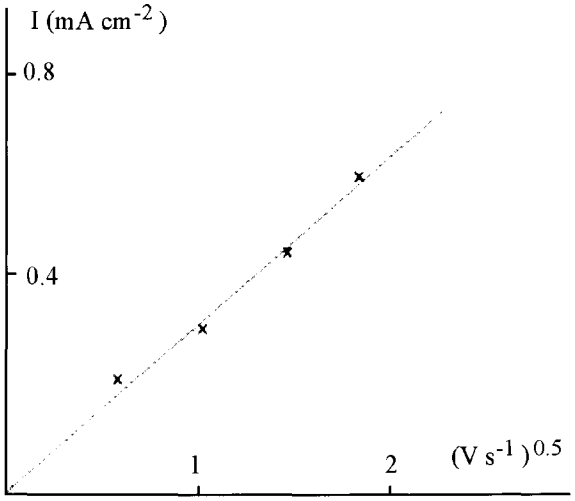

Figure 13.6. Active peak current as a function of the square root of scan rate.

in which ρ is the density of the oxide assumed to be $MeOO^3H$, κ the specific conductance of the solution, M the considered oxide molecular weight and θ the surface coverage. MacDonald and Roberts [188] proposed that $n = 3$, $M = 90$, $\rho \approx 5\ g\,cm^{-3}$, $\kappa = 0.17$, which yield $\theta = 0.95$ without electrode rotation and only at the more acid pH (Fig. 13.3, curve 7). Equations (13.7)–(13.13), related to adsorption, are in agreement with complete surface coverage if there is sufficient $^3H^+$, if any species is not removed by stirring or if the cathodic potential limit is sufficiently negative to reduce the previous oxide.

2.1.3. Impedance diagrams The impedance diagrams, obtained at pH 3 without electrode rotation, are shown with a well-defined capacitive semi circle in Fig. 13.7.

They correspond to the upper transpassive potentials in Figs 13.2 and 13.3. The passive oxide and Maraging steel are assumed to dissolve progressively (porous layer → dissolution), accordingly the reaction is:

$$MeOO^3H + 2\,^3H_2O \rightarrow MeO_4^{2-} + 5\,^3H^+ + 3e^- \qquad (13.26)$$

where $MeOO^3H$ is the hydrated passive oxide of Me_2O_3 on the surface.

Figure 13.8 shows the impedance diagrams obtained for the transpassive peak in Figs 13.2 and 13.3. These are made up of a semi circle which degenerates to a linear section at low frequency. The interpretation of the linear section is not simple, and in this work an original explanation is proposed. This linear section is not due to a Warburg impedance since it does not have a unity slope and varies from a line extended approximately on the Z_{real} axis to a slope of 1.3. Since the impedance was measured at the base and in the transpassive peak, the semi circle and linear section may be an indication of porosity

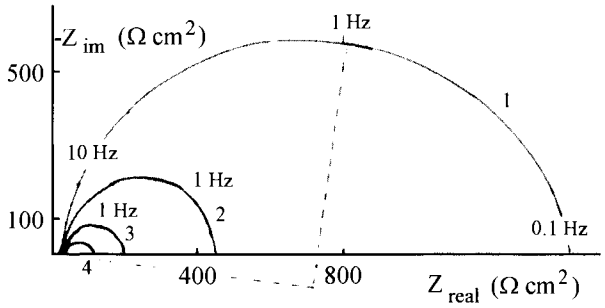

Figure 13.7. Nyquist diagrams without chloride—potential effect, ω: 0 rpm, pH: 3, 1: 1.42 V, 2: 1.45 V, 3: 1.47 V, 4: 1.50 V/SCE.

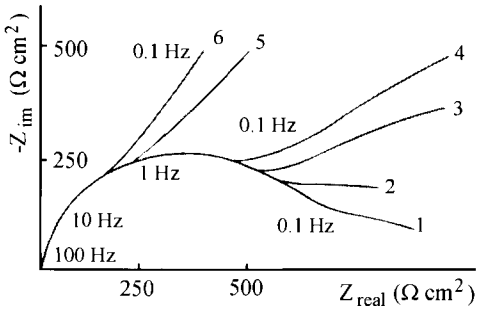

Figure 13.8. Nyquist diagrams without chloride—potential effect, ω: 0 rpm, pH: 3, 1: 0.8 V, 2: 0.82 V, 3: 0.85 V, 4: 0.9 V, 5: 0.95 V, 6: 1.0 V/SCE.

formation and reaction within a porous layer (non-porous layer → porous layer). This is likely since the transpassive peak indicates a pitting process at potentials between 0.7 and 0.8 V/SCE. On the basis of these data, the porous oxide should be invoked as a part of the dissolution mechanism. At the higher potentials in the transpassive peak, the linear section is obtained with a greater slope. These characteristics would appear to be related to the resistance in the porous layer.

The equivalent circuit widely used by many authors such as Mansfeld [190], Aubay and Lojou [191], Armstrong and Wright [192] and Deflorian et al. [193] to study porous layers is shown in Fig. 13.9a. It applies to potentials in the transpassive peak and gives two semi circles corresponding to the ionic conduction in the porous layer and in the compact layer. In agreement with the Deflorian et al. [194], Griffin et al. [195] and Haruyama et al. [196] results for porous layers, the second equivalent circuit proposed in Fig. 13.9b is similar to the previous one, but a constant phase element (CPE) replaces the double layer capacitance. This is to take into account the phenomena related to the processes limiting diffusion into pores accompanied by diffusion into electrolyte, as indicated by the straight line (linearized second semi circle) having different slopes in the Nyquist plots and

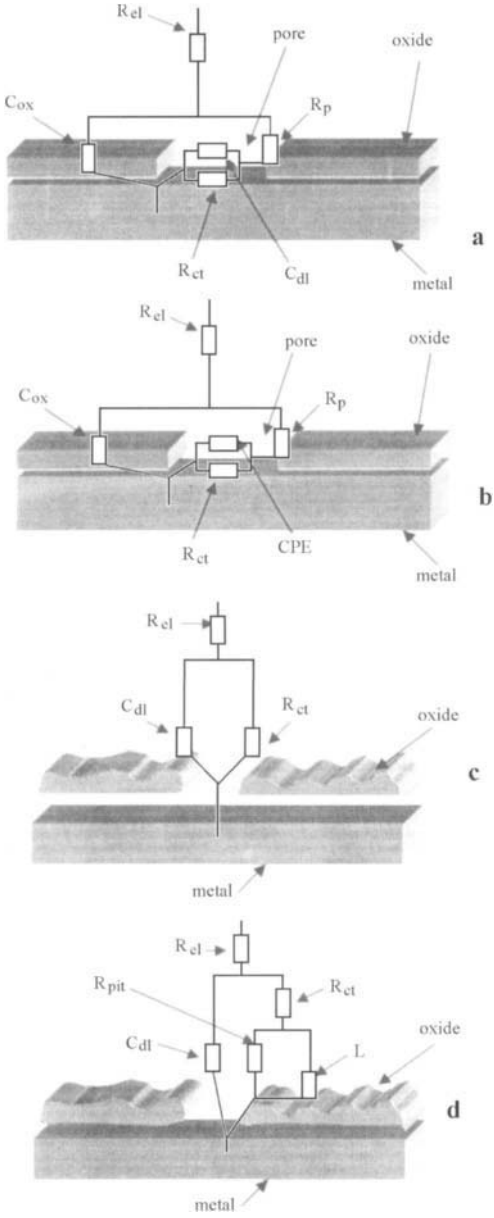

Figure 13.9. Equivalent circuits, (a–d): R_{el}: electrolyte resistance, R_{ct}: charge transfer resistance, R_p: pore resistance, R_{pit}: pitting resistance, C_{dl}: double layer capacitance, C_{ox}: oxide capacitance, CPE: constant phase element, L: inductance.

corresponding to the transpassive peak (Figs 13.2 and 13.3). This equivalent circuit takes into account the Nyquist plots in Fig. 13.8.

At the upper transpassive potentials, the Maraging steel is corroded, and the CPE, C_{ox} and R_p are deleted to be replaced only by the double layer capacitance and the charge transfer and electrolyte resistances as shown in Fig. 13.9c, which takes into account the Nyquist plots in Fig. 13.7. The appropriate values of the equivalent circuit and a kinetic value were obtained fitting Nyquist plots given without electrode rotation and at the upper transpassive potentials. On this basis, the values of R_{ct} and C_{dl} are calculated. At the higher potential (1.5 V/SCE), the charge transfer resistance and double layer capacitance values are 80 $\Omega\,cm^2$ and 70 $\mu F\,cm^{-2}$, respectively, whereas at the lower potential (1.42 V/SCE), the resistance value is about 1440 $\Omega\,cm^2$. As the transpassive potential increases, the charge transfer resistance decreases; this is the result of the oxidation current increasing with dissolution, porosity and breakdown of the oxide layer according to eq. (13.26). The usual value for a double layer capacitance is about 20 $\mu F\,cm^{-2}$ as given by Bard and Faulker [103] and the experimental values located between 30 and 70 $\mu F\,cm^{-2}$ indicate that there is a double layer capacitance without stirring. The rate constants can be determined from a fitting program. Taking the value of 70 $\mu F\,cm^{-2}$, the oxidation reaction rate constant is 0.1 $mol\,cm^2\,s^{-1}$ without stirring. This value is not negligible and shows, as for the low R_{ct} value, that Maraging steel is easily corroded.

According to the equivalent circuit in Fig. 13.9b, the impedance diagrams in the transpassive peak are composed of a capacitive semi circle accompanied by a linearized second semi circle. These diagrams are characteristic of processes limiting diffusion into the porous layer. On this basis, the values of R_p and C_{ox} are practically constant, and R_{ct} and CPE increase and decrease, respectively, as the transpassive potentials increase. These mean the formation of a transpassive region, while porous areas are formed at the base of transpassive peak, then the rate of porosity formation should become nearly constant in the peak. These behaviors observed at the transpassive (Fig. 13.7) and passive-transpassive potentials (Fig. 13.8) clearly show changes in the passive oxide layer: porosity formation, resistance increase in the porous layer and finally oxide dissolution at higher potentials.

2.2. *Results with chloride present*

2.2.1. Polarization curves obtained with chloride The features and comparison of the polarization and voltammetric curves can be used to determine the propensity for localized corrosion (e.g. pitting and crevice corrosion). The difference between the pitting potential and the corrosion potential, and between the repassivation potential and the corrosion potential, and finally the hysteresis shape are shown to be dependent on three variables used to characterize the localized corrosion. If the current in the backward scan is greater than that of the forward scan, the Maraging steel is predicted to be susceptible to corrosion by pitting, and if also the repassive potentials and pitting potentials are close to the corrosion potential, the steel is predicted to be susceptible to crevice corrosion.

To show the specific features obtained in curves during the localized corrosion of Maraging steel by chloride ions more clearly, the curves have not been drawn at zero rota-

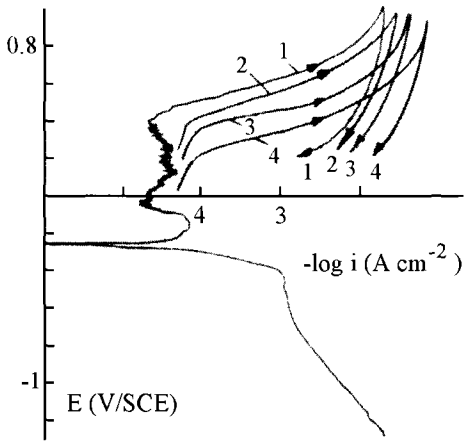

Figure 13.10. Polarization curves—chloride effect, v: 5 mV s^{-1}, ω: 2000 rpm, pH: 3, 1: 0.05 mol dm^{-3}, 2: 0.1 mol dm^{-3}, 3: 0.2 mol dm^{-3}, 4: 0.5 mol dm^{-3} Cl^-.

tion rate, but at 2000 rpm to limit the range of pitting currents as shown in [197]. In the first measurements, the effects of chloride ion concentration on pitting potentials are seen in the polarization curves in Fig. 13.10. At potentials above the pitting potential, pits are expected to grow. In the forward scans, the breakdown potential decreases with increasing chloride ion concentration. In the backward scans, it is seen that the anodic current increases with chloride concentration. The current is greater than that of the forward scan, and returns to the normal values near the corrosion potential. According to the hysteresis shape, pits continue to initiate and grow after the scan reversal. The corrosion potential value does not change with increasing Cl^-. These behaviors, decreasing intervals between E_{corr} and $E_{repassivation}$, suggest pitting followed by crevice corrosion.

2.2.2. Voltammograms In the second set of measurements, the effects of chloride concentration on pitting potentials are seen in the voltammetric curves in Fig. 13.11.

The active peak increases with Cl^- indicating that an intermediate is formed with this ion (e.g., MeO^3HCl^-) after adsorption of Cl^- as indicated by Farvaque-Béra and Leistikow [198]. In the transpassive region, with Cl^- addition, and immediately after scan reversal, the current decreases then increases, showing another unusual hysteresis shape obtained at high scan rate which corresponds to metastable pitting events as indicated in the forward scan realized at low scan rates by Kinlen and Silverman [199]. The photograph in Fig. 13.12 shows that pits are formed on the surface of the Maraging steel.

At lower potentials, the currents return to the corrosion potential favoring crevice corrosion as seen in Fig. 13.13, realized for a longer time of corrosion. This participation of Cl^- depends on the pitting kinetics which, in turn, depend on the scan rate. In Fig. 13.10 the pitting potential can be seen in the course of the forward scan at low scan rate, whereas at high scan rate (Fig. 13.11), it is seen in the backward scan.

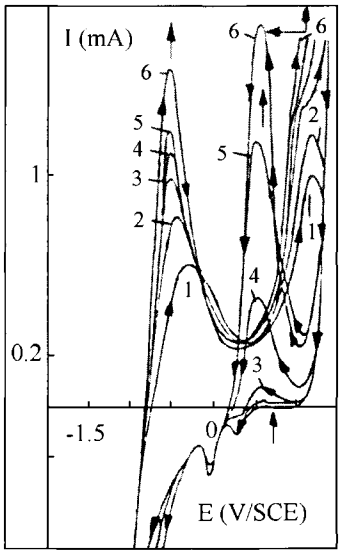

Figure 13.11. Voltammetric curves—chloride effect, v: 350 mV s^{-1}, ω: 2000 rpm, pH: 3, 1: 0 mol dm^{-3}, 2: 0.2 mol dm^{-3}, 3: 0.4 mol dm^{-3}, 4: 0.6 mol dm^{-3}, 5: 0.7 mol dm^{-3}, 6: 0.8 mol dm^{-3} Cl^-.

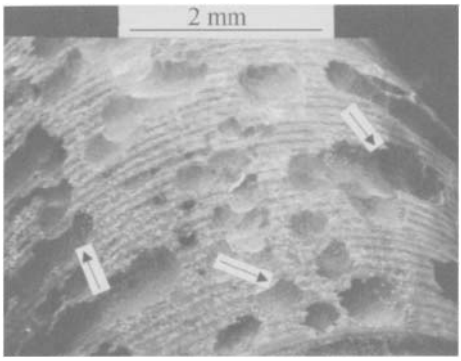

Figure 13.12. Photograph showing pits on Maraging steel.

2.2.3. Impedance diagrams Figure 13.14 shows the impedance diagrams of Maraging steel with 5×10^{-2} mol dm^{-3} Cl^- at different potentials. They correspond to the passive-pitting region border in the polarization curves (Fig. 13.10). Impedance measurements were also carried out at a passive-pitting potential for different chloride concentrations (Fig. 13.15).

The curves in Figs 13.14 and 13.15 show either a well-defined capacitive semi circle or a semi circle with an inductive loop. These curves can be satisfactorily explained on the

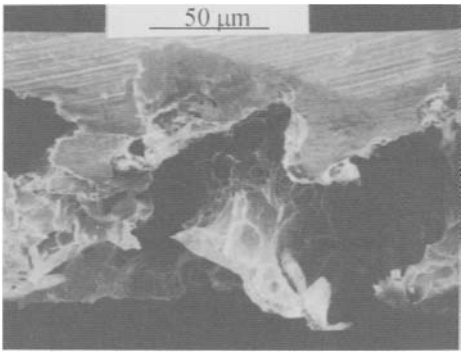

Figure 13.13. Photograph showing crevices in Maraging steel (cross-section).

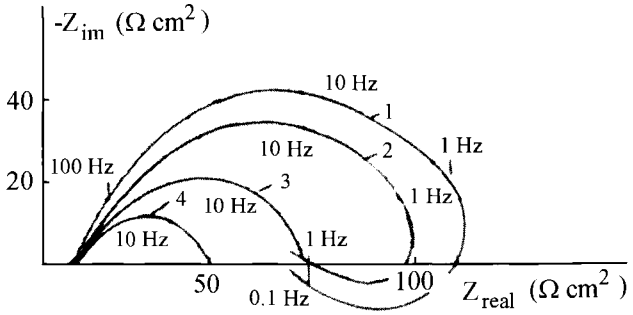

Figure 13.14. Nyquist diagrams with chloride—potential effect, ω: 2000 rpm, pH: 3, Cl^-: 5×10^{-2} mol dm^{-3}, 1: 0.40 V, 2: 0.415 V, 3: 0.43 V, 4: 0.445 V/SCE.

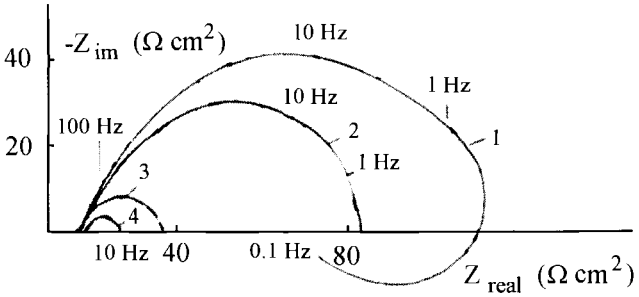

Figure 13.15. Nyquist diagrams with chloride—Cl^- effect, ω: 2000 rpm, pH: 3, E: 0.4 V/SCE, 1: 0.05 mol dm^{-3}, 2: 0.1 mol dm^{-3}, 3: 0.2 mol dm^{-3}, 4: 0.5 mol dm^{-3} Cl^-.

basis of the two equivalent circuit approaches presented in Fig. 13.9c, d. In Fig. 13.9d, the faradaic impedance includes the pitting resistance (R_{pit}) and the inductance (L) due to the

adsorption phenomena during the pitting process. As indicated by Bessone et al. [183], the faradaic impedance is:

$$Z_F = R_{ct} + \frac{j\omega L R_{pit}}{R_{pit} + j\omega L} \tag{13.27}$$

The appropriate values of the equivalent circuit and a kinetic value were obtained by fitting spectra. On this basis, the value of pitting resistance is approximately equal to 40 $\Omega\,cm^2$. Taking the value of 50 $\mu F\,cm^{-2}$ for the double layer capacitance (corresponding to Fig. 13.14, curve 4), the average rate constant is 1.8 mol $cm^2\,s^{-1}$. This value is much higher than that obtained without Cl^- and shows that Maraging steel is easily corroded in the passive-pitting region.

2.3. Scanning Reference Electrode Technique examination

For the direct examination in situ of local currents, the sample was polarized at 0.15 V/SCE for 0.3 mol dm^{-3} Cl^-. The Scanning Reference Electrode Technique (SRET) was used to characterize the anodic or cathodic zones as shown by Isaacs [200] and therefore the areas of microscopic and active sites. In Fig. 13.16, the current changes gradually site by site (0 to ± 50 mA cm^{-2}), and the size of the active sites varies considerably from site to site. Their position can easily be determined by visual inspection (Fig. 13.12). The SRET provides the direct image giving the local corrosion rates by means of coupling currents and nucleation in anodic and cathodic sites. From observation of the current at this passive potential located near the corrosion potential, the corrosion is lower than that at higher potentials.

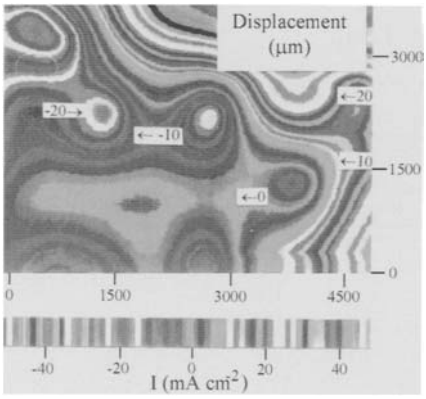

Figure 13.16. Scanning Reference Electrode Technique (SRET), area examined: 0.25 cm^2, E: 0.15 V/SCE, ω: 150 rpm, Cl^-: 0.3 mol dm^{-3}.

3. Conclusion

The corrosion behavior of Maraging steel depends on pH and intermediates remaining on the Maraging steel surface favoring the passivity or corrosion. The corrosion potential does not change with addition of Cl^-, and the repassivation potential is near the corrosion potential signifying localized corrosion by pitting followed by crevice corrosion. Values of localized anodic and cathodic currents are high indicating that Maraging steel is easily corroded. The corrosion rate constants are appreciable in the transpassive region and increase in the presence of chloride.

This Page Intentionally Left Blank

Chapter 14

LOCALIZED CORROSION UNDER TIN DEPOSIT

1. Introduction

To avoid erosion corrosion in the nuclear environment, the equipment must be constructed of hardened special alloys and/or high strength inorganic materials. For example, the surface may have a titanium nitride deposit to increase the hardness. Due to its properties, titanium nitride is of great interest, but work carried out by Elsener et al. [90,91] showed the presence of defects such as pinholes formed during the deposition process that favor steel substrate localized corrosion. Therefore a TiN deposit can be used only with a stainless steel that passivates easily. For this purpose hardened martensitic 630 stainless steel (17-4-PH steel), whose composition is given in Table 14.1 and which has good corrosion resistance can be used. TiN can be oxidized to the stable and protective compound TiO_2 as shown by Elsener et al. [91] and Strehblow et al. [201]. Finally, the noble electrochemical behavior of TiN has been explained by the formation of a monolayer of free nitrogen-ammonia and TiO_2. Ammonia can prevent local acidification on the surface and thereby delay pitting. In this application, the TiN was deposited by 0.2 μm thick multilayer sputtering with a magnetron in an argon-nitrogen mixture. These deposition parameters are very important because they can modify the degree of crystallization and generate microdefects, such as microvoids along grain boundaries in TiN deposits according to In et al. [202]. The formation of pinholes would be more difficult for a dense TiN deposit and easier with microvoids [203]. A TiN deposit was thus applied to provide better protective conditions in tritiated media.

2. Results and discussion

2.1. Results without chloride

2.1.1. Polarization and voltammetric curves The potentiodynamic curves obtained with electrode rotation and at low scan rates are shown in Fig. 14.1, with and without a titanium nitride layer.

These curves were obtained starting from the most negative potentials where tritium evolution is the dominant reaction. With nitride, the corrosion potential is at more positive values than that of 630 stainless steel, showing the noble state of the TiN deposit, but this

can lead to sublayer corrosion between the substrate and the deposit. The cathodic currents are higher between E_{corr} and -1.1 V/SCE with a TiN deposit, which results in a thin oxide layer being formed on TiN at negative potentials, and the surface acts as described in the following equation:

$$2TiN + 4\,^3H_2O \rightarrow 2TiO_2 + N_2 + 4\,^3H_2 \qquad (14.1)$$

Nitrogen and ammonia formation have been identified at the TiO_2-TiN interface by Siemensmeyer [203] using X-ray photoelectron spectroscopy. At the more negative potentials, TiN is not oxidized, and this is in the active state and the cathodic current is lower than without a deposit. Therefore, TiN is not very stable in aqueous media and it can be easily oxidized with tritium and nitrogen formation. In these curves, the passive currents are identical with or without TiN, but the passive potential domain is larger and the transpassive currents are lower with nitride. The explanation for the lower currents could be that the deposit reduces the oxidation rate of the underlying stainless steel and oxygen formation. Noble electrochemical behavior can also be caused by the presence of a remaining trapped nitrogen-enriched oxidized sublayer according to Elsener et al. [91]. At the corrosion potential, the current i_{corr} is lower with a deposit (10^{-5} instead of 7×10^{-5} A cm^{-2} with and without a deposit, respectively). These values show better protection and are in agreement with results obtained by Massiani et al. [204]. The cathodic Tafel slope is around 0.12 V/decade and corresponds to Tafel behavior [205]. This suggests that the TiN deposit

Table 14.1. 630 stainless steel (17-4-PH steel)—composition

Elements	C	Mn	Si	Cr	Ni	Cu	Fe
Wt%	0.04	0.6	0.2	16	4.2	3.2	Balance

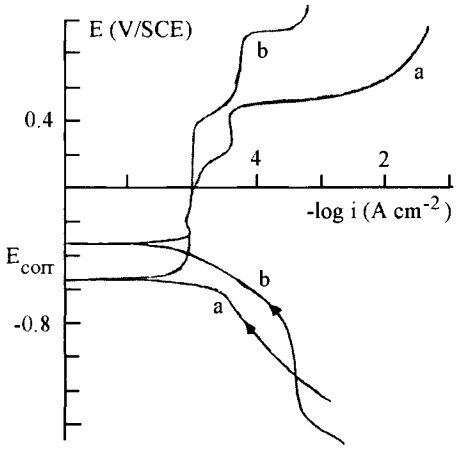

Figure 14.1. Polarization curves pH 11, ω: 3000 rpm, v: 5 mV s^{-1}, a: 630 stainless steel without deposit, b: 630 stainless steel with TiN deposit.

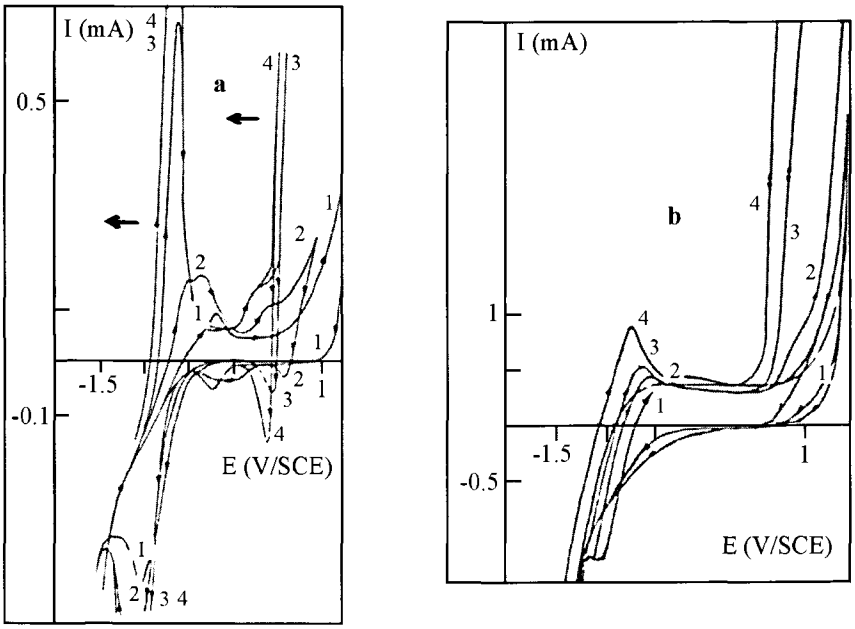

Figure 14.2. Voltammetric curves—pH effect, ω: 2000 rpm, v: 200 mV s^{-1}, a: 630 stainless steel without deposit, 1: pH 6, 2: pH 10, 3: pH 11, 4: pH 13, b: 630 stainless steel with TiN deposit, 1: pH 6, 2: pH 10, 3: pH 11, 4: pH 13.

partly protects the 630 stainless steel at the corrosion potential due to the fact that the layers are porous.

The cyclic voltammetry curves at high scan rates and different alkaline pH values are given in Fig. 14.2. They show the presence of transient currents with and without the titanium nitride deposit. In the forward scan, there is a peak with TiN at −1.3 V/SCE, (Fig. 14.2b) during the gradual increase of tritium evolution current at the most negative potentials. This peak corresponds to the formation of TiO_2 from TiN with tritium evolution. At the most negative potentials, the oxide layer from the TiN deposit is reduced, and TiN is directly exposed to the solution. A second oxidation peak is obtained in the prepassive region; its potential has the same value with or without the deposit for identical pH, and corresponds to the active peak of 630 stainless steel (Fig. 14.2a). The 630 stainless steel peak increases with increasingly alkaline pH indicating a corrosion increase with such pH values for prepassive potentials. The size of the active peak changes depending on whether or not there is a deposit. The small active peak with the deposit shows that it does not provide complete protection and there is a partial path for stainless steel oxidation. With titanium nitride, the transient peak current is 50 $\mu A\,cm^{-2}$ at pH 11, while without this layer it is 0.65 $mA\,cm^{-2}$. The charges under the peak are, respectively, 40 and 300 $\mu C\,cm^{-2}$ and correspond to an amount of alloy subjected to corrosion. The active peak is followed by an abrupt current drop for the more alkaline pH, indicating passiv-

ity at these potentials. The most positive potentials in the curves correspond to steel and deposit transpassive oxidation. A larger current scale shows a wave which is proportional to the degree of alkalinity and thus to hydroxide concentration. In the backward scan, the oxide reduction peak is observed only without the deposit. With titanium nitride, the amount of corrosion products must be smaller and their reduction current is masked by the tritium evolution current. In both cases, the cathodic charge would not cover that obtained in the forward scan, which suggests that the corrosion products were removed by the porous TiN layer during the rotation, or that the hydroxides formed are very difficult to reduce.

2.1.2. Electrochemical impedance spectroscopy Theoretical analysis of the impedance spectra can yield a complicated response due to the possibility of several time constants depending on the oxide layer characteristics. In the simplest case, it behaves as a pure capacitance, corresponding to a compact insulating layer. For a simple circuit, the current can be expressed by the sum of currents due to electron transfer during steel oxidation, and by the interfacial capacitance charging process. As the relative contribution of each current is independent, the total admittance should be the sum of each admittance. With no corrosion, this admittance would be negligible. The corresponding equation is simplified and the total capacitance becomes:

$$1/C = 1/C_{ox} + 1/C_{hl} \tag{14.2}$$

where C_{hl} is the Helmholtz layer capacitance and C_{ox} the oxide layer capacitance. Curves 1 to 9 in Fig. 14.3, which were realized with 630 stainless steel in the Bode plot, are characterized at very high frequencies by pure electrolyte resistance.

At lower frequencies, a straight line with a slope of -1 is observed and corresponds to the oxide layer impedance, which is non-dissipative, and to the Helmholtz layer. At medium frequencies, a straight line with a slope slightly less than -1 is seen and charge transport by the ions can occur in the oxide. The charges carried by the ions into the oxide would lead to Warburg behavior in the Nyquist plot. The electrical characteristics of the oxide depend on its compactness and defects, which can be determined by impedance measurements. In eq. (14.2), the C_{hl} value must be estimated without oxide, this can be done, for example, at the corrosion potential E_{corr} and the value obtained using eq. (14.3) is 16 μF cm^{-2}.

$$C_{hl} = (2\pi f z)^{-1} \tag{14.3}$$

In the same way, but at different potentials taken in the prepassive and passive regions, the oxide layer capacitance was determined and is close to 8 μF cm^{-2}. This value decreases slightly down to the passivity potential of 0.3 V/SCE, indicating a more compact oxide. For potentials above this value, the capacitance increases very slightly indicating defect formation in the passive oxide. In the case of passivity, curves 1 to 9 in Fig. 14.3 can be explained on the basis of the equivalent circuit in Fig. 14.4.

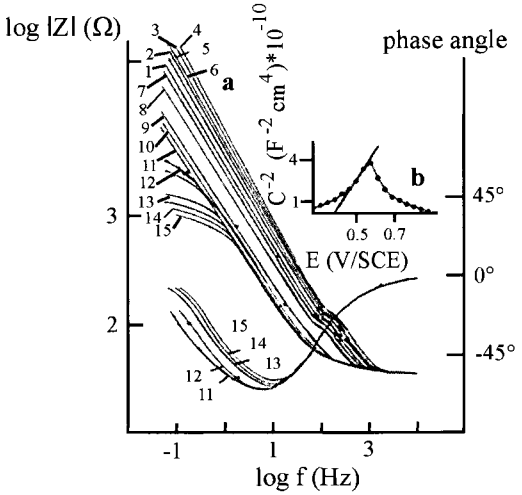

Figure 14.3. 630 stainless steel—bode diagrams (a) and Mott-Schottky plots (b), potential effect, pH 11, ω: 3000 rpm, 1: −0.5 and 0.8 V, 2: −0.2 V, 3: 0/0.1/0.4 and 0.5 V, 4: 0.2 V, 5: 0.3 V, 6: 0.6 and 0.7 V, 7: 0.9 V, 8: 1 V, 9: 1.1 V, 10: 1.15 V, 11: 1.2 V, 12: 1.25 V, 13: 1.26 V, 14: 1.27 V, 15: 1.28 V/SCE.

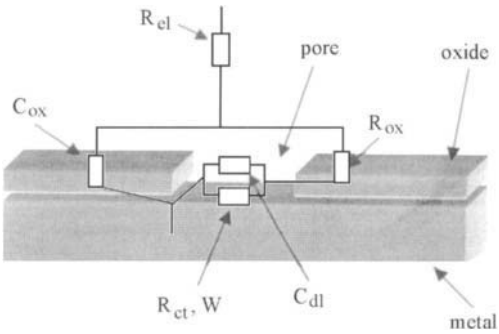

Figure 14.4. 630 stainless steel—equivalent circuit, R_{ct}, and R_{ox} charge transfer and oxide resistances, W: diffusion impedance, R_{el}: electrolyte resistance, C_{dl} and C_{ox}: double layer and oxide capacitances.

Fitting diagrams gives the kinetic constant for the passivity process which is 10^5 mol^{-1} cm^2 s^{-1}. In Fig. 14.3, above 1.15 V/SCE (curves 10 to 15), the Bode plots show, at low frequencies, a change in the capacitive character by a resistive effect indicating corrosion. In this case, the equivalent circuit is formed only by R_{el} and C_{dl} with R_{ct} in parallel. The charge transfer resistance values decrease with the potential indicating corrosion increases. At passive potentials, between 0 and 0.6 V/SCE, the thickness of the passive oxide layer that behaves like a pure capacitance is a few nm. The oxide layer

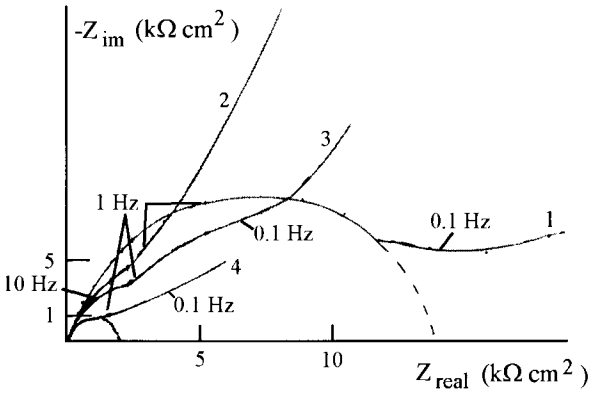

Figure 14.5. 630 stainless steel with TiN deposit—Nyquist diagrams, potential effect, pH 11, ω: 0 rpm, 1: 0.8 V, 2: 1 V, 3: 1.3 V, 4: 1.4 V/SCE.

thickness would increase progressively from the prepassive potentials up to 0.3 V/SCE. This result has already been obtained for passive layers according to Moffat [206]. By using the Mott-Schottky equation explained in detail by Randin [182], the charge carrier concentration is estimated to be 2×10^{22} carriers cm^{-3}, which is close to the theoretical value obtained by Castro and Vilche [108].

The Nyquist plots obtained at the transpassive potentials with a TiN deposit are shown in Fig. 14.5. These diagrams are completely different from those obtained for the stainless steel. They show several time constants corresponding to two overlapped capacitive semi circles at high and medium frequencies and a Warburg straight line at medium and low frequencies. The overlapped capacitive semi circles are more easily observed at 1.4 V/SCE (curve 3). Their presence should be given by the equivalent circuit (according to Elsener et al. [90]) in Fig. 14.6.

In electrical terms, the equivalent circuit shows the impedance of the passivated area short-circuited by the impedance of the spot in localized corrosion. Effectively, in this circuit, the passive area and the corroding spots can be coupled, which shows the characteristic feature of the localized corrosion on very corrosion-resistant materials such as TiN deposits and passive films on stainless steel. The parameter values are given in Table 14.2 for the different potentials. The measured resistance at low frequencies is the apparent resistance (R_p) of the substrate that is exposed to the electrolyte coming from the pores. The part of the medium frequencies spectra corresponds to the electrical characteristics of deposit and passive oxide (denoted $_{TiN}$ and $_{oxide}$). In Table 14.2, typical values indicate the presence of corrosion by the pores and ionic diffusion into two layers. The two layers are considered as excellent protective barriers up to the transpassive potential. Comparison of results shows that the transfer resistance values are much higher with the deposit, and the capacitance values correspond to the usual values of double layer and oxide capacitances given by Bard and Faulkner [103], these indicate an appreciable passivity.

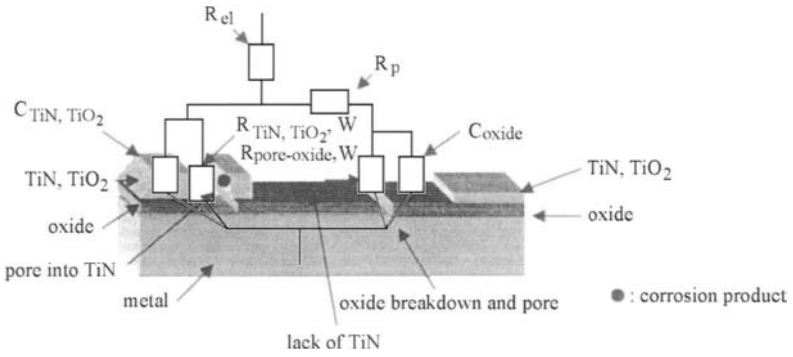

Figure 14.6. 630 stainless steel with TiN deposit—equivalent circuit, R_{TiN,TiO_2}, $R_{pore-oxide}$ and R_p: charge transfer on TiN and oxide and polarization resistances, W: TiN-oxide diffusion impedances, R_{el}: electrolyte resistance, C_{TiN,TiO_2} and C_{oxide}: TiN and substrate capacitances.

Table 14.2. Dependence of electrical components at the electrode surface on potentials

E (V/SCE)	0.8	1	1.3	1.4
R_p ($\Omega\,cm^2 \times 10^3$)	10	8	6	4
R_{TiN} ($\Omega\,cm^2 \times 10^3$)	20	20	15	10
C_{TiN} ($\mu F\,cm^{-2}$)	1	150	200	300
W_{TiN} ($\Omega\,cm^{-0.5} \times 10^3$)	10	15	4	1
R_{ox} ($\Omega\,cm^2 \times 10^3$)	20	20	15	10
C_{ox} ($\mu F\,cm^{-2}$)	1	20	30	40
W_{ox} ($\Omega\,cm^{-0.5} \times 10^3$)	20	20	5	1

2.2. *Results with chloride present*

2.2.1. Polarization and voltammetric curves The potentiodynamic polarization curves obtained with or without TiN and electrode rotation are shown in Fig. 14.7.

Two different regions can be clearly identified: the passive region, which decreases with chloride concentration, and the pitting region. The transition region, that is also called the pitting induction period, is characterized by current fluctuations whose amplitudes and frequencies increase with potential up to the point where pitting propagation occurs. This clearly defines the pitting initiation potential for a given chloride concentration. The critical pitting potential is lower and the passive region is smaller with titanium nitride indicating that 630 stainless steel suffers localized corrosion. However, pitting currents are lower, which can signify that surface pH is buffered by the presence of ammonia. Buffered pH decreases pitting corrosion rate, but does not stop it. This implies that the TiN provides partial protection of 630 stainless steel and thus the number of pits or the pitting active area must increase by pinholes, pores or defects in the TiN. It can be seen that the corrosion potential (−0.3 V/SCE) is the same with or without TiN, signifying a porous deposit, as also seen in the prepassive region with a TiN deposit, there is a pseudo active peak followed immediately by an abrupt current drop. The smaller difference between the cor-

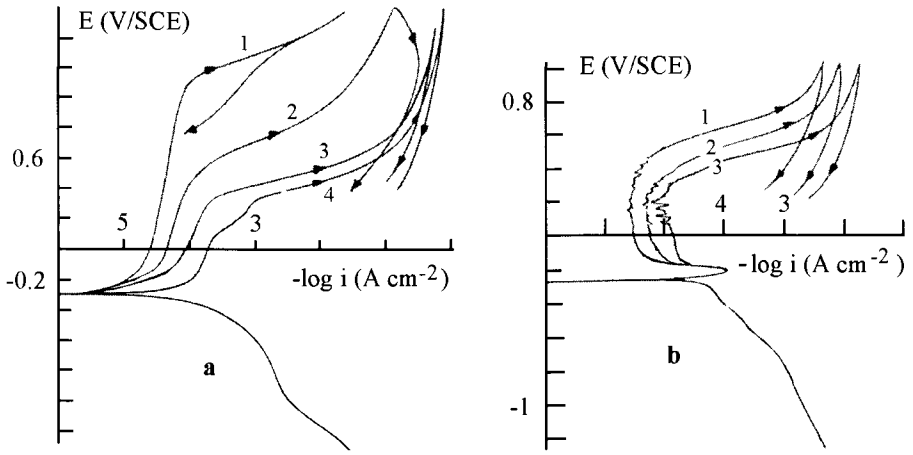

Figure 14.7. Polarization curves—chloride effect, pH 11, ω: 3000 rpm, v: 5 mV s^{-1}, a: 630 stainless steel without deposit, 1: 0.2 mol dm^{-3}, 2: 0.5 mol dm^{-3}, 3: 0.75 mol dm^{-3}, 4: 1 mol dm^{-3} Cl^-, b: 630 stainless steel with TiN deposit, 1: 0.1 mol dm^{-3}, 2: 0.2 mol dm^{-3}, 3: 0.5 mol dm^{-3} Cl^-.

rosion potential and pitting potential shows more susceptibility to sublayer corrosion by stagnant aggressive solution. The pseudo-Flade current just after the active peak (passivity with deposit) is below that for passivity without TiN, showing that the TiN partly improves passivity.

The cyclic voltammetry curves obtained at high scan rates without TiN and at different chloride concentrations are shown in Fig. 14.8.

The height of the transient peak in these curves increases very rapidly with Cl^- concentration signifying Cl^- adsorption followed by corrosion. In the transpassive and passive potential domains, the current due to pitting is essentially located at the beginning of the backward scan, while at a low scan rate (Fig. 14.7), these currents are clearly visible at the end of the forward scan, pitting depends on scan rates and therefore on kinetics. It can also be seen that the repassivity potential is near the cathodic peak conjugated with the transient peak. This indicates formation of deep tips (in side and in depth) during pitting as shown in Fig. 14.9 which can lead to crevice corrosion.

The dependence of the current and pitting propagation potentials on the electrode rotation speed is given in Fig. 14.10. In these curves, the transient peak current increases with this speed. A possible explanation is that the hydroxide transients formed at these potentials are moved away from the steel surface and thus this delays prepassivity, and active corrosion continues. The transient peak potential in these curves is displaced towards more negative potentials at higher rotation rates. The explanation could be the same, i.e. the surface is less protected by a prepassive oxide layer at higher rates. It can also be seen in these curves that the pitting current varies in the opposite direction to that of the transient peak with the electrode rotation rate. This can be explained by oxide film behavior. Without stirring, the chloride ions are adsorbed, then diffuse in the oxide layer by vacancies or by

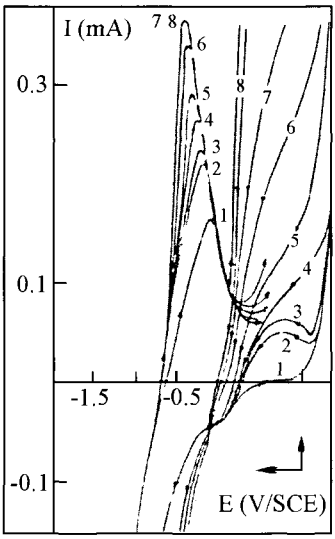

Figure 14.8. 630 stainless steel—voltammetric curves, chloride effect, pH 11, ω: 2000 rpm, v: 200 mV s^{-1}, 1: 0 mol dm^{-3}, 2: 2×10^{-2} mol dm^{-3}, 3: 2.2×10^{-2} mol dm^{-3}, 4: 2.5×10^{-2} mol dm^{-3}, 5: 3×10^{-2} mol dm^{-3}, 6: 6×10^{-2} mol dm^{-3}, 7: 8×10^{-2} mol dm^{-3}, 8: 0.1 mol dm^{-3} Cl^-.

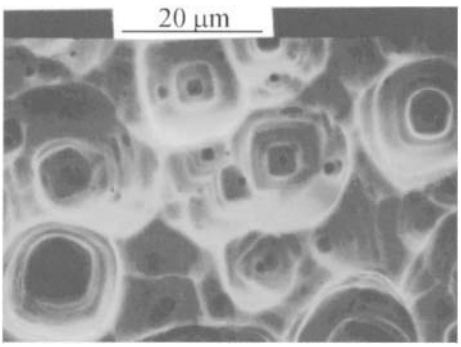

Figure 14.9. Scanning Electron Microscopy showing pits.

the O^{2-} lattice according to Pou et al. [207]. The result is that soluble complex hydroxide-chlorides would be formed and locally dissolve the oxide up to the alloy which is corroded according to:

$$Me + x\,{}^3H_2O \rightarrow Me({}^3OH)_x + x\,{}^3H^+ + xe^- \qquad (14.4)$$

This reaction leads both to local acidification in the pit with ^3HCl formation and possible formation of micro potentials as indicated by Chang and Yu [208]. These would accelerate corrosion by pitting.

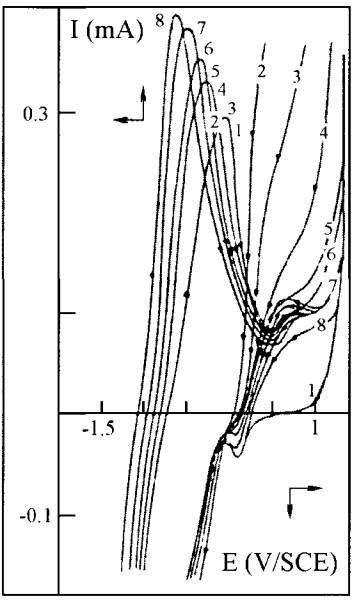

Figure 14.10. 630 stainless steel—voltammetric curves, electrode rotation speed effect, pH 11, v: 200 mV s^{-1}, 3×10^{-2} mol dm^{-3} Cl^-, 1: no Cl^- and 2000 rpm, 2: 0 rpm, 3: 250 rpm, 4: 500 rpm, 5: 2000 rpm, 6: 2500 rpm, 7: 5000 rpm, 8: 10000 rpm, curves 2 to 8 with Cl^-.

From the results with and without electrode rotation, the corrosion rate and passivity are dependent on the intermediate species remaining at the surface of the steel. It is thought that chloride surface adsorption and diffusion into oxide would be slowed down due to the complex hydroxide-chlorides removed by stirring, which subsequently limits pitting corrosion. Similarly, the ^{3}HCl formed can be removed from sufficiently open pits and in this case the pits are passive. The dependence of experimental repassivating potentials on electrode rotation rate is shown in Fig. 14.11, and would explain the previous interpretation in another way.

In Fig. 14.12, obtained at different scan rates, it can be seen at lower rates that the repassivation potential has more negative values and the pitting current is higher; consequently, there would be a risk of deep pits appearing at low scan rates. If the repassivation potential is plotted as a function of the scan rate, a curve is obtained giving its right potential in potentiostatic mode where there is no interaction caused by the scan. In Fig. 14.12, it can be seen that the height of the transient peak at prepassivity potentials increases with scan rate. Thus, this peak could well correspond to the faradaic and capacitance current. At low scan rates, chloride ions could be more readily adsorbed and subsequently diffuse in the oxide film following adsorption and diffusion kinetics. Local dissolution of the oxide layer by complex hydroxide-chlorides, localized attack of the underlying alloy by acid formation in the pits and local micro-potentials would also be involved here. At high scan rates, due to

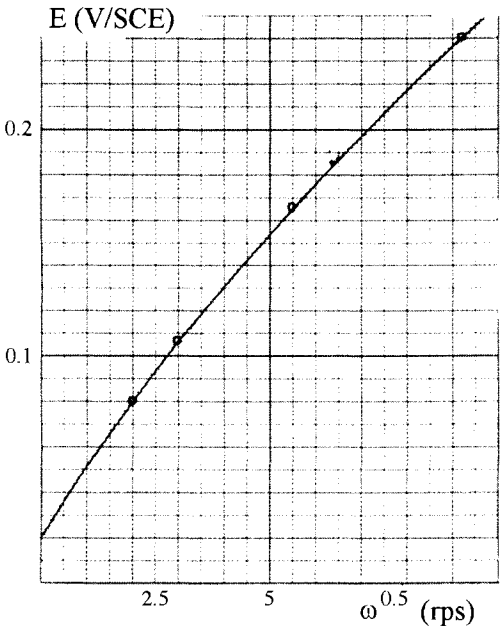

Figure 14.11. Dependence of repassivation potentials on the electrode rotation speed.

their kinetics, these processes do not have the time to develop sufficiently to induce deep enough pits.

The corresponding curves with titanium nitride on the 630 stainless steel are shown in Fig. 14.13. The transient peak current is 0.12 mA cm^{-2} at pH 11 and there is a little increase with Cl^-, while without TiN its value is definitely higher and increases rapidly with Cl^-. Comparison of Figs 14.8 and 14.13 shows that with TiN, the pitting currents are lower in using much more concentrated chloride solutions. These two behaviors, size of transient peak and pitting current, signify lower localized corrosion with a TiN deposit. The presence of ammonia should neutralize acidity in pits at high scan rates. However, for long exposure times, the Scanning Electron Microscopy photographs (Fig. 14.14) show that the deposit no longer covers the steel surface. It consists of a detached TiN deposit and the underlying alloy has undergone pitting corrosion. In the detached TiN surface layer, 'clouds' are seen with holes consisting of plane crystallized TiN grains (formed during production of the deposit) and whiskers showing a columnar structure (Fig. 14.15) as also shown by Massiani et al. [204]. The detached grains could be formed by microvoids along grain boundaries, affecting the pitting resistance [202]. The whiskers crossing through these 'clouds' would appear to be uniaxially grown single crystals.

2.2.2. Electrochemical impedance spectroscopy Electrochemical impedance spectroscopy is often limited in pitting corrosion cases due to the fact that the pitting rate is not,

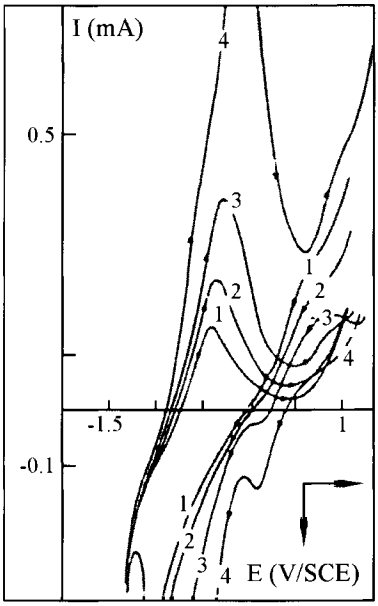

Figure 14.12. 630 stainless steel without deposit—voltammetric curves, pH 11, 3×10^{-2} mol dm^{-3} Cl^-, 1: 50 mV s^{-1}, 2: 100 mV s^{-1}, 3: 200 mV s^{-1}, 4: 600 mV s^{-1}.

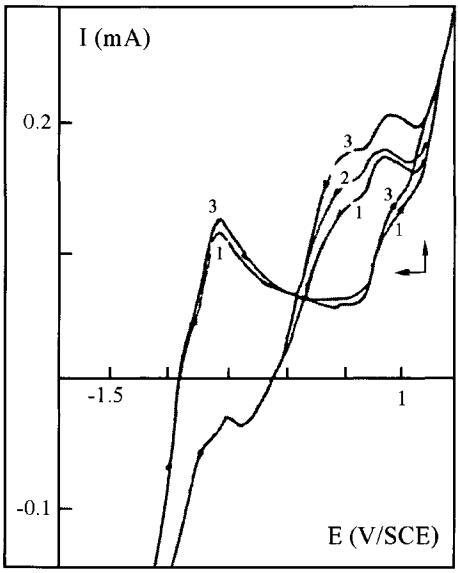

Figure 14.13. 630 stainless steel with TiN deposit—voltammetric curves, chloride effect, ω: 2000 rpm, pH 11, v: 350 mV s^{-1}, 1: 0.25 mol dm^{-3}, 2: 0.3 mol dm^{-3}, 3: 0.35 mol dm^{-3} Cl^-.

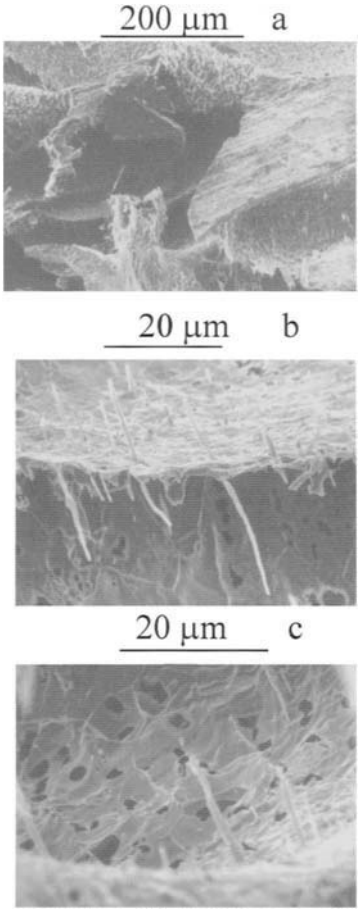

Figure 14.14. Scanning Electron Microscopy of corroded TiN deposit with Cl^-, (a): general appearance, detached TiN deposit, (b, c): detail showing a 'cloud' of plane crystallized TiN grains with holes and uniaxial single crystals growth columnar structure.

in general, constant. The pits can be open or closed and there is also a pitting incubation period. It should be possible, however, to use this method to obtain successfully stable pits. The impedance diagrams obtained for 630 stainless steel subjected to pitting for different passive potentials at the limit of pitting initiation are shown in Fig. 14.16.

At the lowest potential, i.e. just next to the passive region, there is only one time constant (curve 1) while at potentials near pitting initiation, three time constants are observed, one of which is inductive at medium frequencies and is the result of chloride adsorption. To provide physical significance for these diagrams, an equivalent circuit is proposed in Fig. 14.17. In this equivalent circuit, an inductance is introduced indicating Cl^- adsorp-

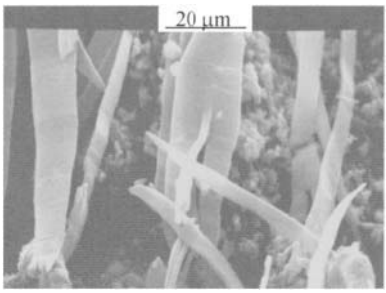

Figure 14.15. 630 stainless steel with TiN deposit—details showing column crystals.

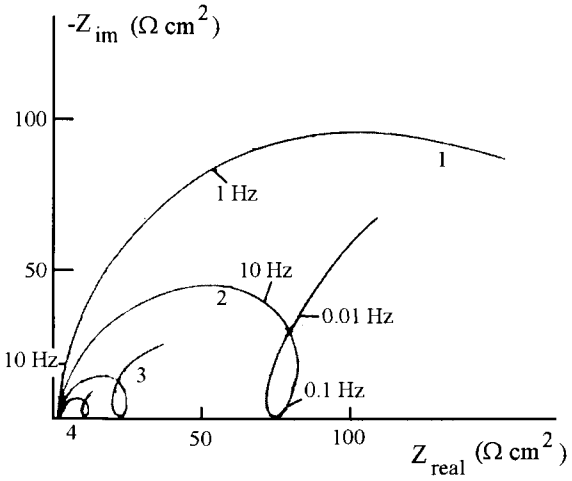

Figure 14.16. 630 stainless steel—Nyquist diagrams, potential effect, ω: 3000 rpm, pH 11, Cl^-: 1 mol dm^{-3}, 1: 0.2 V, 2: 0.25 V, 3: 0.3 V, 4: 0.35 V/SCE.

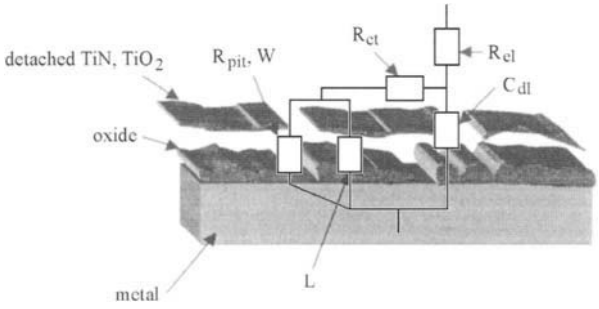

Figure 14.17. Equivalent circuit, R_{ct}: charge transfer resistance, R_{pit}: pitting resistance, W: diffusion impedance, L: inductance, C_{dl}: double layer capacitance, R_{el}: electrolytic resistance.

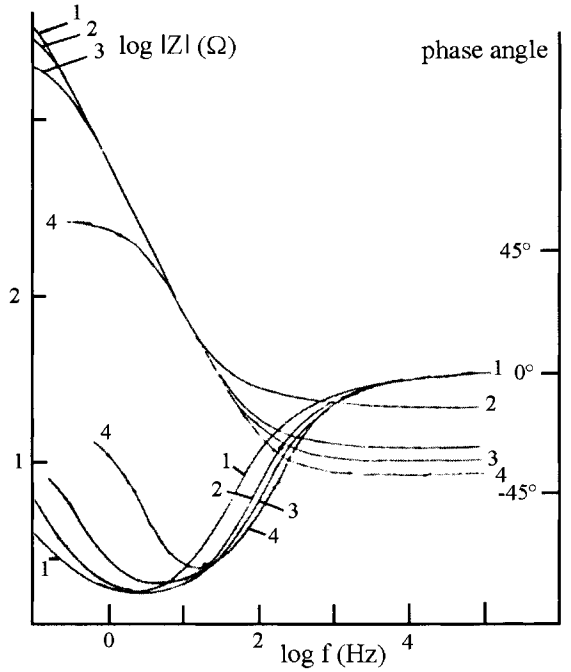

Figure 14.18. 630 stainless steel—bode diagrams, chloride effect, ω: 3000 rpm, pH 11, E: 0.4 V/SCE, 1: 0 mol dm^{-3}, 2: 0.25 mol dm^{-3}, 3: 0.5 mol dm^{-3}, 4: 0.75 mol dm^{-3} Cl^-.

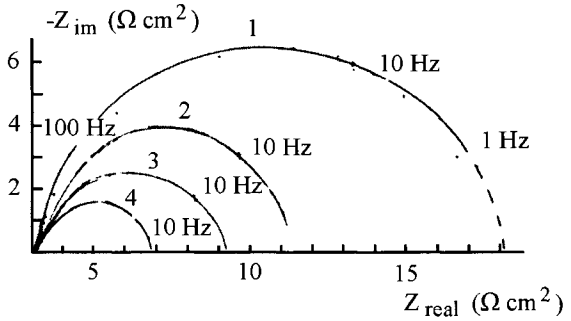

Figure 14.19. 630 stainless steel with TiN deposit—Nyquist diagrams, potential effect, ω: 2000 rpm, pH 11, Cl^-: 1 mol dm^{-3}, 1: 0.4 V, 2: 0.45 V, 3: 0.5 V, 4: 0.55 V/SCE.

tion. From the Nyquist plot in these spectra, the break point at medium frequencies should depend on the pitting resistance and the capacitance of the surrounding passive oxide layer according to Oltra and Keddam [209]. It was seen that the break point frequency changes

Table 14.3. 630 stainless steel—dependence of pitting resistance on Cl^- concentration at 0.4 V/SCE

Cl^- (mol dm^{-3})	0	0.25	0.5	0.75
R_{pit} (Ω cm^2)	–	100	30	5

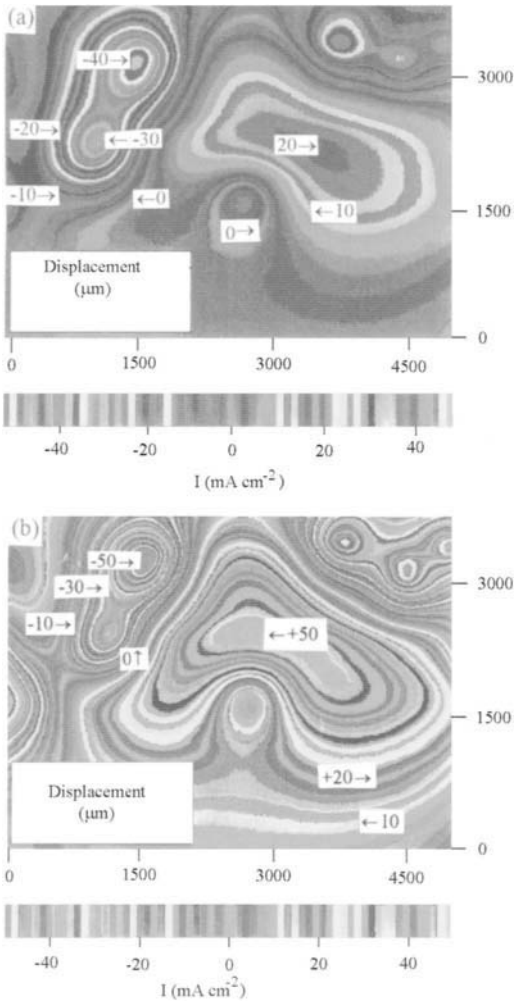

Figure 14.20. 630 stainless steel with TiN deposit—Scanning Reference Electrode Technique examinations showing anodic and cathodic zones, A: 0.2 cm^2, E: 0.45 V/SCE for 30 min, ω: 150 rpm, Cl^-: 0.3 mol dm^{-3}, (a): pitting initiation sites, (b): pitting micro-cells induced by Cl^-.

with the applied potentials. The pit formation rate can be determined from the pitting resistance value (R_{pit}) according to Mansfeld [190].

The impedance diagrams for different Cl^- concentrations are shown in Fig. 14.18.

It can be seen that the frequency phase angle varies with the Cl^- concentration, showing that chloride ions play a role in the oxide layer breakdown and pitting mechanism. At high frequencies, the ohmic drop decreases on adding Cl^-, this results from the increase in electrical conductivity of the aqueous medium. The electrode impedance behaves in the same way at low frequencies, and its dependence on Cl^- concentration was determined as seen in Table 14.3. From the R_{pit} values, localized pitting corrosion increases in the passive-transpassive region on addition of Cl^-.

The curves in Fig. 14.19 were obtained with TiN on 630 stainless steel with 1 mol dm^{-3} Cl^- and for different potentials at pitting initiation values. It is observed in these curves that the size of capacitive semi circles decreases when these potentials increase; the semi circles are related to electrode impedance. The values are lower than those obtained without chloride indicating that pitting corrosion would increase with potential and Cl^-. The charge transfer resistance value is slightly higher than that obtained without TiN showing a slight improvement in resistance to corrosion. Scanning Reference Electrode Technique examinations (Fig. 14.20) show, however, that the steel and the deposit have anodic and cathodic micro-cells due to localized corrosion by pitting increasing with time.

3. Conclusions

It is shown that without chloride, the corrosion would concentrate on TiN defects, and the corrosion rate of underlying stainless steel can be extremely high at these areas by ion diffusion through the pores. However, the TiN deposit shows better protection for stainless steel. With chloride, the critical pitting potential is lower with the TiN deposit which could lead to easier localized corrosion. Pitting and incubation kinetics depend on the chloride adsorption rate, its diffusion in the oxide layer and the $^3H^+$ enrichment in the pores (the pH decrease is an accepted phenomenon in pitting and sublayer corrosion). The TiN deposit detaches at the grain boundaries which confirms the possibility of sublayer corrosion under detached plane crystals. Corrosion can be extremely high in the defects by formation of anodic and cathodic micro-cells during pitting.

This Page Intentionally Left Blank

Chapter 15

SELECTIVE CORROSION OF Ni-Cr ALLOY

1. Introduction

As with chlorine-bonded organic polymers, the β^- particle energy can decompose these materials bonded with fluorine when these are in contact with tritiated water. In this case the decomposition reaction becomes:

$$\text{R–F} + \beta^- \rightarrow \text{F}^- + \text{CO}_2 + \text{R}'- \tag{15.1}$$

It has been observed, for example, that the decomposition of organic polymers is visible after a few months and the tritiated water becomes brown and contains appreciable concentrations of fluoride. If the organic polymers are subsequently removed from the tritiated water, the solution becomes colorless. The products formed have been 'digested' by the tritiated water.

In reprocessing, the tritiated water can be concentrated by isotopic distillation. The tritiated water is introduced without purification in half-height of the distillation column; consequently it can contain impurities such as fluoride and can be slightly acid. The distillation column must be packed using small spiral-shaped 316 stainless steel grids with rough Ni-Cr deposit to increase efficiency compared with that obtained with glass rings. The nickel-chromium deposits, about 10 μm thick, on 316L stainless steel were prepared by the laser cladding technique. The alloy used here contains 20% chromium; it was annealed at 800°C in air for 24 h, and the grain size is a few μm. According to Armanet et al. [79,80], Moreau and Benard [81], Jallerat et al. [82], Metikos-Hukovic et al. [83], Hampikian [84], Lowell [85], Pivin et al. [86] and Lacombe et al. [87], under these conditions the oxide surface layer is formed in three steps. The first corresponds to the germination of NiO that covers the external surface of alloy grains while Cr_2O_3 appears only at the grain boundaries, which can lead to Ni enrichment and Cr depletion in the border. Then there is Cr_2O_3 germination under the NiO surface layer leading to a solid-state reaction between these two oxides to form an intermediate nickel-chromite sublayer ($NiCr_2O_4$) with a spinel structure incorporated in NiO. The growth rate of the spinel layer depends on the temperature and the annealing time. If these are high enough and long enough, this growth can lead to the disappearance of the external NiO layer. Finally, there is a third layer enriched in Cr_2O_3 at the base of the alloy which gives a complex duplex structure.

The sublayer enriched in Cr_2O_3 is liable to be a detached oxide layer. For these different reasons, corrosion of 316L stainless steel with and without the nickel-chromium deposit was studied in this medium.

2. Experimental results

2.1. Substrate oxidation without fluoride

2.1.1. Polarization and voltammetric curves The polarization curves obtained at low scan rate are shown without (Fig. 15.1, curve 1) and with (Fig. 15.2, curve 1) the nickel-chromium deposit. With Ni-Cr, the corrosion potential ($E_{corr} = -0.3$ V/SCE) is identical to that of 316L stainless steel. At the corrosion potential, the corrosion current (i_{corr}) is higher with a deposit (4 and 1 μA cm^{-2} for deposit and 316L stainless steel, respectively). These values show that the deposit is less protective. At E_{corr}, corrosion by transients should result from the partial cathodic and anodic reactions as given previously (eqs (13.4)–(13.18)) for Maraging steel.

Curves 1 in Figs 15.1 and 15.2 show that the passive currents are identical with or without the deposit, but the passive potential domain is smaller and the transpassive currents are higher with deposit. The explanation for the smaller passive potential domain and higher corrosion and transpassive currents would appear to be that the deposit is less protective at the transpassive and active regions, and seems to be sensitive to metastable porosity and then transpassive attack. The identical passive current for 316L stainless steel and NiCr deposit would be related to the rates of formation of the passive layer which are identical for each alloy in passivity.

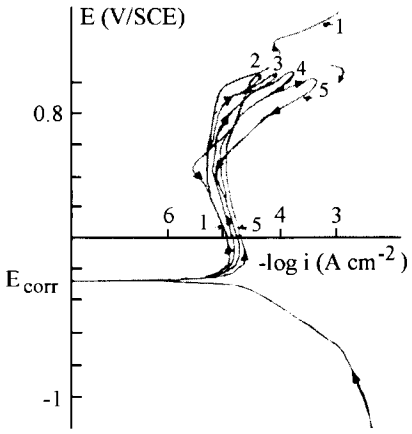

Figure 15.1. 316L stainless steel—polarization curves, fluoride effect, pH 4, v: 5 mV s^{-1}, 1: 0 mol dm^{-3}, 2: 0.08 mol dm^{-3}, 3: 0.1 mol dm^{-3}, 4: 0.12 mol dm^{-3}, 5: 0.15 mol dm^{-3} F^-.

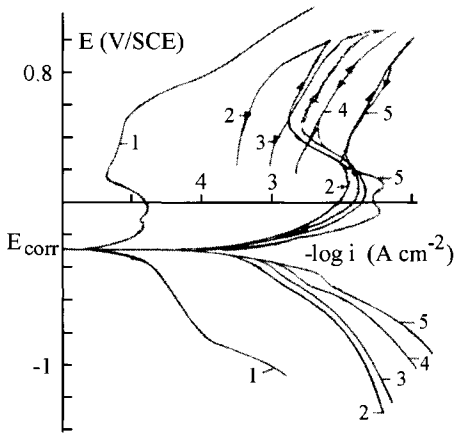

Figure 15.2. 316L stainless steel with Ni-Cr deposit—polarization curves, fluoride effect, pH 4, v: 5 mV s^{-1}, 1: 0 mol dm^{-3}, 2: 0.08 mol dm^{-3}, 3: 0.1 mol dm^{-3}, 4: 0.12 mol dm^{-3}, 5: 0.15 mol dm^{-3} F^-.

In acquiring the cyclic voltammograms, the potentials were swept cyclically at a high scan rate until reproducible voltammograms were obtained. The voltammetric curves realized without and with Ni-Cr are given in Figs 15.3 and 15.4 (curves 1) respectively.

In the backward scan, a reduction peak occurs with Ni-Cr at −0.7 V/SCE. This peak corresponds to the reduction of the protective oxide layer. With 316L stainless steel, the amounts of corrosion products must be smaller as the reduction peak is hidden by the reduction current of $^3H^+$ ions. In both cases, the cathodic charges should not cover that obtained in the forward scan, which suggests that the corrosion products were removed from the surface or that the oxide formed is difficult to reduce. In the forward scan, a poorly defined active oxidation shoulder is obtained at −0.5 V/SCE for the deposit; this corresponds to the prepassive region. Then, the active peak is obtained at −0.3/SCE where the current is 200 μA cm^{-2}. From this, the charge under the peak is 350 μC cm^{-2} and corresponds to amounts of nickel-chromium that are subjected to protection then corrosion. This active peak is followed by an abrupt current drop, indicating passivity above the potential of −0.3 V/SCE. At the most positive potentials, a larger current scale shows a second anodic peak that corresponds to transpassive corrosion and dissolution of Ni-Cr and 316L stainless steel.

2.1.2. Electrochemical impedance spectroscopy From the experimental Nyquist plot drawn for the stainless steel (Fig. 15.5, curve 1), the Helmholtz layer capacitance is 30 μF cm^{-2} at the corrosion potential.

This value corresponds to the usual double layer values as given by Bard and Faulkner [103]. In the prepassive and passive regions, the capacitance value decreases slightly down to the passive potential of 0.25 V/SCE (curves 2 to 4) indicating formation of the protective oxide. At the passivity-transpassivity limit (curve 5), the capacitance increases again whereas the impedance decreases. The interpretation given by Hassel and

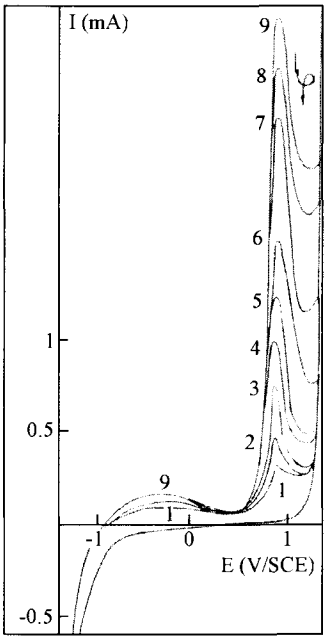

Figure 15.3. 316L stainless steel—voltammetric curves, fluoride effect, pH 4, v: 200 mV s^{-1}, 1: 0 mol dm^{-3}, 2: 0.01 mol dm^{-3}, 3: 0.02 mol dm^{-3}, 4: 0.04 mol dm^{-3}, 5: 0.06 mol dm^{-3}, 6: 0.08 mol dm^{-3}, 7: 0.1 mol dm^{-3}, 8: 0.12 mol dm^{-3}, 9: 0.15 mol dm^{-3} F^-.

Lohrengel [210] indicates dielectric relaxation leading to a non-protective oxide layer. Moreover, decreasing impedance signifies a large increase in charge transfer after breakdown and porosity formation through a thinner metastable oxide layer. Charge transfers from 10 μC cm^{-2} to some mC cm^{-2} are attributed to reactions in these places. The breakdown starts at 'weak' spots which may be given by local defects or by very small thickness fluctuations or roughness. Thickness variations cause large local current increases (e.g. tunnelling processes) leading to $^3H^+$ formation and corrosion.

In the passivity, the Nyquist plot can be explained on the basis of the equivalent circuit presented in Fig. 15.6. From the equivalent circuit, the rate constant for the passivity process is 0.7 mol^{-1} cm^2 s^{-1}. At the transpassivity limit (Fig. 15.5, curve 4), the Nyquist plot obeys the simplified equivalent circuit formed of C_{dl} and R_{ct} in parallel. In this case, the charge transfer resistance decreases indicating corrosion increases.

The Nyquist plots obtained at the transpassivity with a nickel-chromium deposit are shown in Fig. 15.7. These diagrams are completely different from those obtained for stainless steel. They show several time constants corresponding to two capacitive semi circles at high and low frequencies. Their presence should be given by the equivalent circuit in Fig. 15.8. The new parameters (C_{lc}, R_{lc}) of this equivalent circuit correspond to localized corrosion, as will be seen later by Scanning Electron Microscopy. The measured resistance

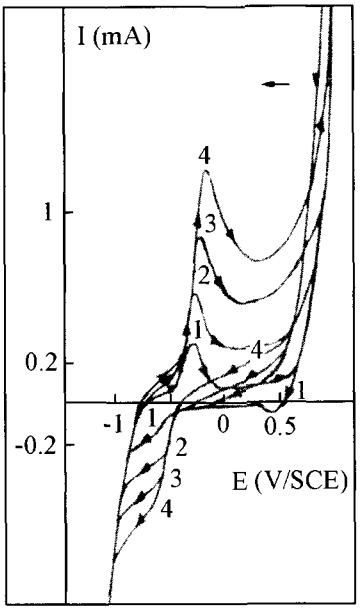

Figure 15.4. 316L stainless steel with Ni-Cr deposit—voltammetric curves, fluoride effect, pH 4, v: 200 mV s^{-1}, 1: 0 mol dm^{-3}, 2: 0.1 mol dm^{-3}, 3: 0.12 mol dm^{-3}, 4: 0.15 mol dm^{-3} F^-.

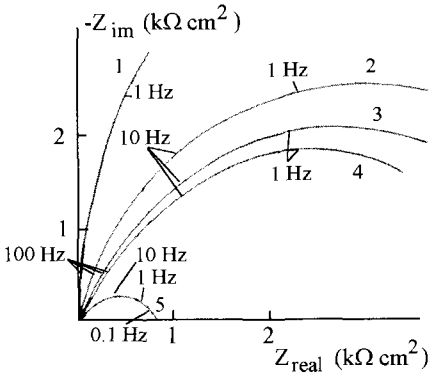

Figure 15.5. 316L stainless steel—Nyquist diagrams, potential effect, pH 4, 1: −0.3 V, 2: −0.2 V, 3: −0.1 V, 4: 0.25 V, 5: 1.2 V/SCE.

at low frequencies is related to localized corrosion whereas in the high frequency section it corresponds to charge transfer for the deposit. Because of the resistance and capacitance values, this oxide layer is not considered as an insulating barrier at these potentials. Com-

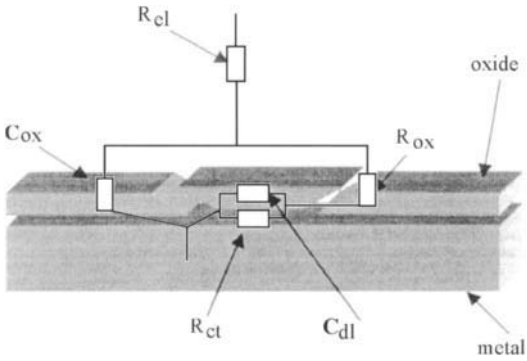

Figure 15.6. 316L stainless steel—equivalent circuit, R_{ct}, and R_{ox}: charge transfer and oxide resistances, C_{dl} and C_{ox}: double layer and oxide capacitances, R_{el}: electrolyte resistance.

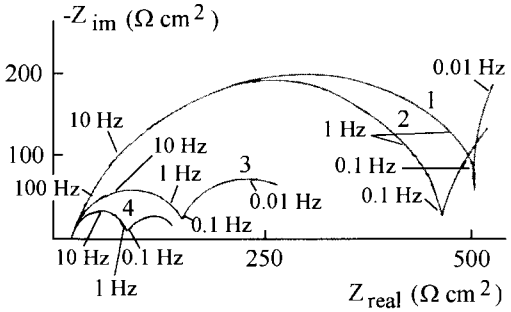

Figure 15.7. 316L stainless steel with Ni-Cr deposit—Nyquist diagrams, potential effect, pH 4, 1: 1 V, 2: 1.1 V, 3: 1.2 V, 4: 1.4 V/SCE.

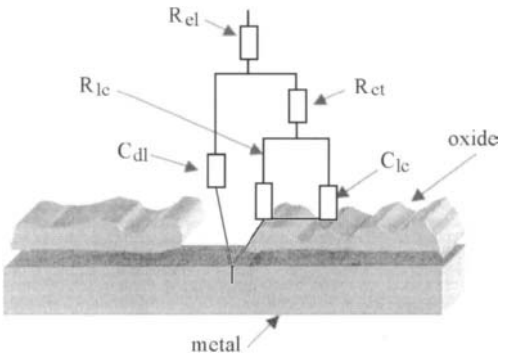

Figure 15.8. 316L stainless steel with Ni-Cr deposit—equivalent circuit, R_{ct}, R_{lc}: charge transfer and localized corrosion resistances, C_{dl} and C_{lc}: double layer and localized corrosion capacitances, R_{el}: electrolyte resistance.

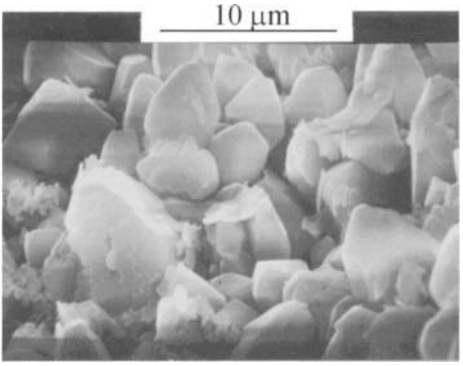

Figure 15.9. SEM photographs showing spinel of oxidized Ni-Cr deposit at the transpassive potentials.

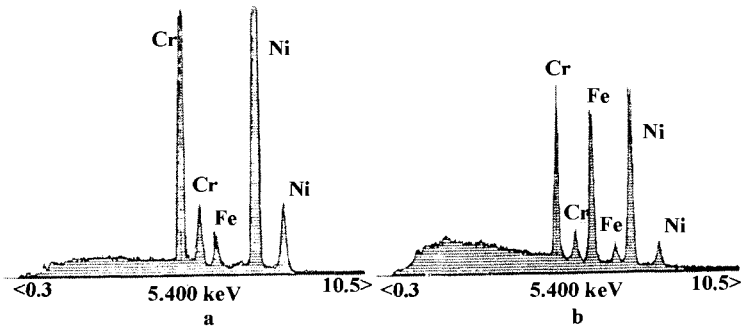

Figure 15.10. X-Ray Microanalysis realized at the transpassive potentials, (a): on oxidized Ni-Cr deposit without F^-, (b): on a crystal of corrosion products with F^-.

parison of spectra shows that the deposit is more corroded than in the case of stainless steel.

2.1.3. Microscopy The Scanning Electron Microscopy examinations were carried out for the deposit corroded at the passive-transpassive potentials. Fig. 15.9 illustrates the microstructure of the spinel sublayer after elimination of the surface oxide. Spinel is incorporated in NiO, as a result the NiO matrix would be the preferential nucleation site for localized corrosion leading to non-cohesion of spinel grains. Therefore, the photographs would appear to indicate that the deposit has been locally and preferentially corroded in agreement with the above results obtained by electrochemical methods.

X-ray microanalysis examinations of the oxide after corrosion show an intense ray for nickel and chromium energies respectively (Fig. 15.10a). Comparison of the energy related to each element with respect to the results of Armanet et al. [211], indicates this is a mixed oxide of NiO and Cr_2O_3 in the same proportions that spreads depending on thermal con-

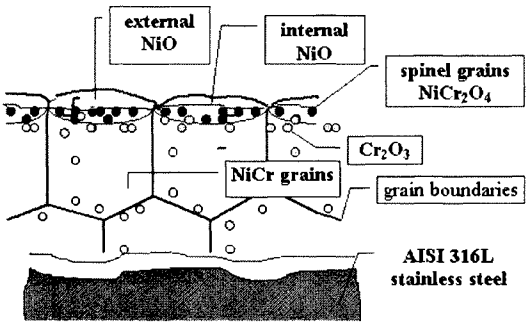

Figure 15.11. Chemical structure of NiCr oxidized layers.

ditions to give the spinel structure ($NiCr_2O_4$). In regard to the results of Armanet [211] for the Cr-Ni alloy superficial oxidation the chemical structure of oxidized layers is given in Fig. 15.11. From this the Scanning Electron Microscopy examination and microanalysis spectrum indicate that NiO formed on the external layer and as spinel grains (internal NiO) are respectively dissolved and locally corroded thus resulting in the spinel structure in the photograph.

2.2. *Substrate oxidation with fluoride present*

2.2.1. Polarization and voltammetric curves The polarization curves obtained with fluoride present and without or with Ni-Cr are shown in Figs 15.1 and 15.2 (curves 2 to 5) respectively. Two different regions can be clearly identified: the passive region, which decreases with fluoride concentration and the pitting region. The transition point, that is also called the pitting induction, shifts to a lower potential. This should define the pitting initiation potential for a given fluoride concentration. The critical pitting potential is not well defined and the passive region is smaller with the nickel-chromium deposit indicating that the deposit is more rapidly corroded locally than is 316L stainless steel. This implies that the deposit does not provide the best protection. It can be seen that the corrosion potential (−0.3 V/SCE) is the same with or without Ni-Cr and with or without fluoride, signifying that it is difficult for galvanic corrosion to occur. In the prepassive region for a nickel-chromium deposit, there is an active peak followed immediately by a current drop. The current just after the active peak (passivity for deposit) is higher than that of passivity for 316L stainless steel, showing the deposit does not improve the best passivity as indicated by Damborenea [212]. It can also be seen that the repassivity potential in the backward scan is near the prepassive oxidation peak. This indicates a corrosion risk by crevices from filling the pit opening, as shown in the photograph (Fig. 15.12). The result is that complex hydroxide-fluorides are formed and locally dissolve the oxide down to the alloy surface with local acidification and ^3HF formation in the pit that accelerates corrosion.

The cyclic voltammetry curves obtained at high scan rates without NiCr and at different fluoride concentrations are shown in Fig. 15.3. The height of the active peak and the

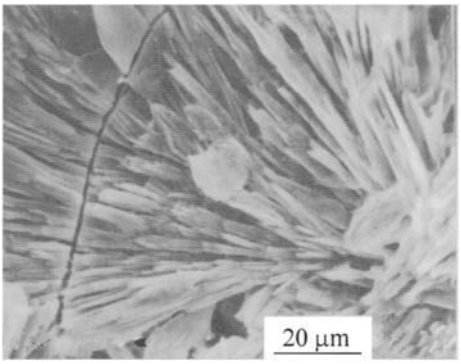

Figure 15.12. Scanning Electron Micrographs of Ni-Cr deposit corroded by F^-, detail showing crystallized corrosion products on pits.

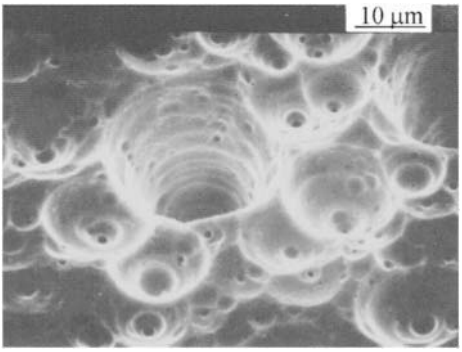

Figure 15.13. Scanning Electron Micrographs of corroded 316L stainless steel by F^-.

passive current in these curves do not increase significantly with F^- concentration. The transpassive peak increases very rapidly with fluoride concentration and the current due to pitting is essentially located at the beginning of the backward scan, while at a low scan rate (Fig. 15.1), these currents are clearly visible at the end of the forward scan; pitting depends on scan rates and therefore on kinetics. Using Scanning Electron Microscopy, pits can be seen on the 316L stainless steel surface (Fig. 15.13).

The voltammetric curves with a nickel-chromium deposit on the 316L stainless steel are shown in Fig. 15.4. The active peak is at −0.3 V/SCE and increases rapidly with F^- concentration, while without Ni-Cr its value is lower with F^-. The pitting currents are higher with Ni-Cr on using the same fluoride solutions. These two behaviors: size of active peak and higher pitting currents signify increased localized corrosion with a nickel-chromium deposit. In Fig. 15.2, realized at low scan rates, fluoride ions could be more easily adsorbed and subsequently diffuse in the oxide film according to adsorption and diffusion kinetics. Local dissolution of the deposit leads to localized attack of the underlying steel by acid for-

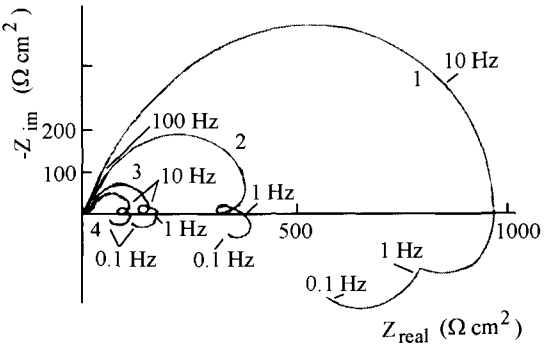

Figure 15.14. 316L stainless steel—Nyquist diagrams, fluoride effect, pH 4, E: 0.9 V/SCE, 1: 0.08 mol dm^{-3}, 2: 0.1 mol dm^{-3}, 3: 0.12 mol dm^{-3}, 4: 0.15 mol dm^{-3} F^-.

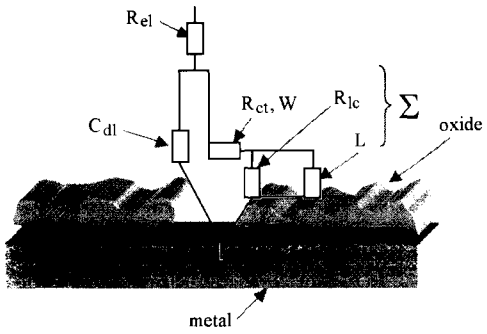

Figure 15.15. 316L stainless steel—equivalent circuit, R_{ct}, and R_{lc}: charge transfer and localized corrosion resistances, W: diffusion impedance, R_{el}: electrolyte resistance, C_{dl} and L: double layer capacitance and inductance.

mation in the pits. At high scan rates, due to their kinetics, these processes do not have the time to develop sufficiently to induce deep enough pits. In the Ni-Cr deposit, crystals can be seen (Fig. 15.12) and X-ray microanalysis (Fig. 15.10b) indicates a significant amount of iron in the corrosion product crystals, indicating that the underlying 316L stainless steel is corroded in the sublayer.

2.2.2. Electrochemical impedance spectroscopy The experimental impedance diagrams obtained for 316L stainless steel subjected to pitting for different fluoride concentrations at the limit of pitting initiation and the passive region are shown in Fig. 15.14.

At different fluoride concentrations, three time constants are observed, two of which are inductive at lower frequencies and should be the result of fluoride and hydroxide competitive adsorption as indicated by Keddam et al. [213]. To provide physical significance for these diagrams, an equivalent circuit is proposed in Fig. 15.15.

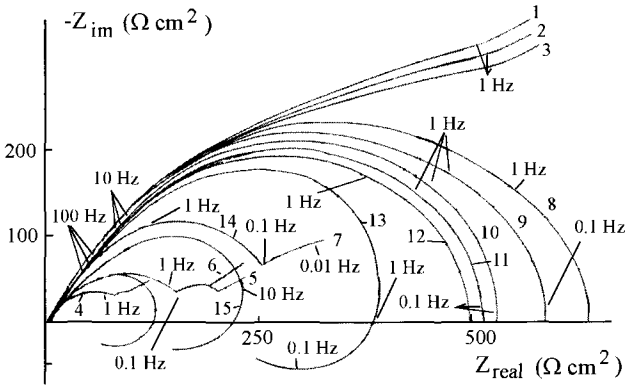

Figure 15.16. 316L stainless steel with Ni-Cr deposit—Nyquist diagrams, potential effect, pH 4, F^-: 0.12 mol dm^{-3}, 1: −0.25 V, 2: −0.2 V, 3: −0.15 V, 4: 0 V, 5: 0.05 V, 6: 0.12 V, 7: 0.2 V, 8: 0.3 V, 9: 0.4 to 0.7 V, 10: 0.73 V, 11: 0.74 V, 12: 0.75 V, 13: 0.77 V, 14: 0.78 V, 15: 0.8 V/SCE.

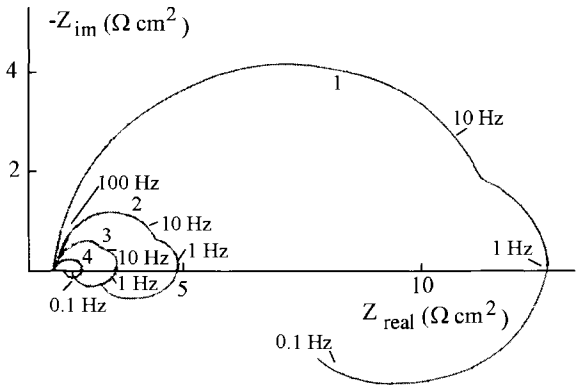

Figure 15.17. 316L stainless steel with Ni-Cr deposit—Nyquist diagrams, potential effect, pH 4, F^-: 0.12 mol dm^{-3}, 1: 0.9 V, 2: 1 V, 3: 1.05 V, 4: 1.1 V/SCE.

In this equivalent circuit, a diffusion impedance and two inductances (L) are introduced indicating F^- adsorption. From the Nyquist plot in these diagrams, the break point at medium frequencies should depend on the pitting resistance and the capacitance of the oxide layer, according to Oltra and Keddam [209]. It has been observed that the break point frequency changes with the fluoride concentration indicating oxide surface evolution.

The experimental diagrams in Figs 15.16 and 15.17 were obtained with Ni-Cr deposit on 316L stainless steel for 0.12 mol dm^{-3} F^- and from the corrosion potential to pitting initiation potential. These diagrams differ from those obtained for the stainless steel without Ni-Cr. In Fig. 15.16, curves 1 to 3, realized in the corrosion potential region, degenerate to a portion of the Warburg straight line. According to the Warburg straight line, ion diffu-

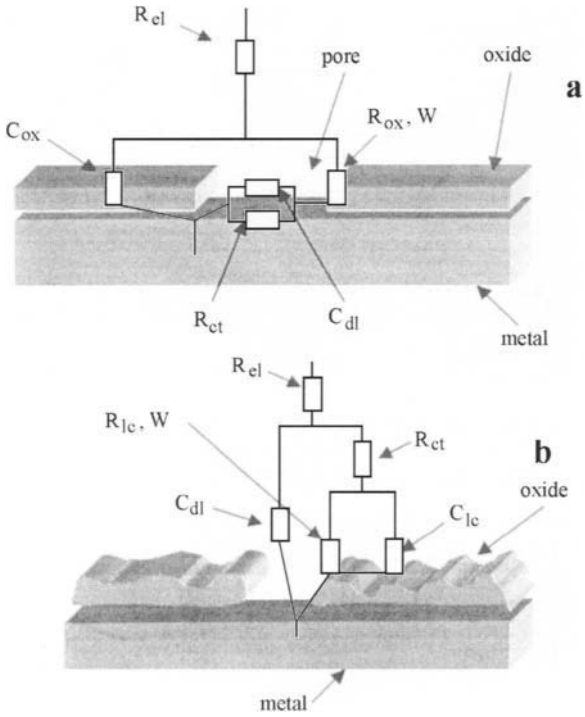

Figure 15.18. 316L stainless steel with Ni-Cr deposit—equivalent circuit, (a, b): R_{el}: electrolyte resistance, R_{ct}: charge transfer resistance, R_{ox}: oxide resistance, R_{lc}: localized corrosion resistance, W: diffusion impedance, C_{dl}: double layer capacitance, C_{ox}: oxide capacitance, C_{lc}: localized corrosion capacitance.

Table 15.1. 316L stainless steel with a Ni-Cr deposit—dependence of electrical components at the electrode surface on potentials for 0.12 mol dm^{-3} F^- active region-oxide diffusion

E (V/SCE)	−0.25	−0.2	−0.15
R_{ox} ($\Omega\,cm^2$)	5	5	5
R_{ct} ($\Omega\,cm^2$)	360	350	345
C_{ox} ($\mu F\,cm^{-2}$)	4.5	5	5
C_{dl} ($\mu F\,cm^{-2}$)	65	70	75
W ($\Omega\,cm\,s^{-0.5}$)	800	700	600

sion in the oxide layer occurs for the prepassive region. Curves 1 to 3 can be satisfactorily explained on the basis of the equivalent circuit approach presented in Fig. 15.18a.

Diffusion impedance depends on the Warburg diffusion coefficient (σ). On the equivalent circuit basis, the parameter values are given as a function of prepassive potentials (Tables 15.1–15.4). The double layer capacitance value is 70 $\mu F\,cm^{-2}$. This low capacitance value appears to correspond to passivity initiation. The ion diffusion coefficient (D) through the oxide layer can be determined exploiting the Warburg straight line. For this,

Table 15.2. 316L stainless steel with a Ni-Cr deposit—dependence of electrical components at the electrode surface on potentials for 0.12 mol dm^{-3} F^- prepassivity-localized corrosion

E (V/SCE)	0	0.05	0.12	0.2
R_{ct} ($\Omega\,cm^2$)	70	140	145	250
R_{lc} ($\Omega\,cm^2$)	70	70	70	100
C_{dl} ($\mu F\,cm^{-2}$)	–	400	420	430
W ($\Omega\,cm\,s^{-0.5}$)	10	9	8	8

Table 15.3. 316L stainless steel with a Ni-Cr deposit—dependence of electrical components at the electrode surface on potentials for 0.12 mol dm^{-3} F^- passivity

E (V/SCE)	0.3	0.4 to 0.7	0.73	0.74	0.75
R_{ox} ($\Omega\,cm^2$)	5	5	4.5	4	3.5
R_{ct} ($\Omega\,cm^2$)	580	550	520	500	480
C_{ox} ($\mu F\,cm^{-2}$)	5	5.5	5.5	6	6.2
C_{dl} ($\mu F\,cm^{-2}$)	70	75	75	80	85

Table 15.4. 316L stainless steel with a Ni-Cr deposit—dependence of electrical components at the electrode surface on potentials for 0.12 mol dm^{-3} F^- passivity-transpassivity

E (V/SCE)	0.77	0.78	0.8	0.9	1	1.05	1.1
R_{ct} ($\Omega\,cm^2$)	50	25	12.5	1.5	0.5	0.25	0.12
C_{dl} ($\mu F\,cm^{-2}$)	25	50	100	–	–	–	–
R_{lc_1} ($\Omega\,cm^2$)	1660	830	415	50	16.7	8.3	4.15
L_{lc_1} ($H\,cm^2$)	0.8	0.4	0.2	0.025	0.008	0.004	0.001
R_{lc_2} ($\Omega\,cm^2$)	328	164	82	10	3.3	1.65	0.82
L_{lc_2} ($H\,cm^2$)	248	124	62	7.5	2.5	1.25	0.62

Table 15.5. 316L stainless steel with a Ni-Cr deposit—dependence of electrical components at the electrode surface on F^- concentration for 1.05 V/SCE

F^- (mol dm^{-3})	0.08	0.1	0.12	0.14
R_{ct} ($\Omega\,cm^2$)	0.6	0.35	0.25	0.12
C_{dl} ($\mu F\,cm^{-2}$)	210	360	500	—
R_{lc_1} ($\Omega\,cm^2$)	19.7	11.6	8.3	4.15
R_{lc_2} ($\Omega\,cm^2$)	3.9	2.3	1.64	0.82

Huggins et al. [214] have shown following the Randles plot, that Z_{real} as a function of the reciprocal of the square root of the angular frequency varies linearly for low frequencies and its slope σ is equal to:

$$\sigma = \frac{RT}{n^2F^2A\sqrt{2}}\left(\frac{1}{D^{0.5}C^{0.5}}\right) \tag{15.2}$$

The experimental value of σ is 800 $\Omega\,cm^2\,s^{-0.5}$ for curve 1 (Fig. 15.16) which agrees with the values in Tables 15.1–15.4. From these, D was calculated to be 2×10^{-14} $cm^2\,s^{-1}$.

The ion diffusion coefficient appears much lower inside the porous prepassive oxide layer than in bulk solution, which is usually 10^{-5} cm^2 s^{-1} [215].

The Nyquist diagrams obtained in the active peak and with fluoride are shown in curves 4 to 7 (Fig. 15.16). Two capacitive semi circles at high and medium frequencies and a Warburg straight line portion at the low frequency are observed between 0 and 0.12 V/SCE. At 0.2 V/SCE, the straight line would disappear to be replaced by capacitive and inductive loops. At low frequencies, the capacitive branch tends to a limit on the real axis defined by the relation $R_{ct}(1 + \delta\sigma D^{-0.5})$. This branch is linked to the process of transport and is called a diffusion loop. It is characterized by two particular frequencies: one is capacitive, and the other is subjected to diffusion. If the characteristic capacitive frequency is too high, the loop becomes unobservable by the fact that this is placed in the high frequency. On the other hand, the same behavior arises for the diffusion straight line if its frequency is too low. Furthermore, values too neighboring for the two characteristic frequencies lead to a coalescence of the capacitive loop with the Warburg straight line, which become no longer separable and thus unexploitable. The amplitude of the diffusion loop is approximately equal to $R_{ct}\delta\sigma D^{-0.5}$, depending on the presence of inductive process at very low frequencies. This value is larger if the charge transfer resistance or the diffusion layer is high (e.g. $\delta \rightarrow \infty$). The straight line tends to a slope of 45° when the diffusion layer is sufficiently thick. It can also be noted that the frequency area corresponding to the loop is moving to the low values when its amplitude increases, signifying that δ or R_{ct} increases. The capacitive current is thus decreased. The inductive loop confirms the hypothesis of adsorbed species formed at the surface of the electrode in the active potentials. The production of this species can be expressed by the relationship:

$$\frac{d\Gamma}{dt} = \frac{1}{F}\left(|i_c| - |i_a|\right) = \Gamma_0 \frac{d\theta}{dt} \tag{15.3}$$

where Γ is the concentration of adsorbed species and the subscript $_0$ indicates the possible maximal concentration. As indicated by Tremillon [216], it is possible thus to obtain the expression of the faradic impedance in function of electrochemical kinetic:

$$Z_F = \frac{\frac{k_c C + k_a}{F k_c k_a C}}{\frac{b_c + b_a(b_a - b_c)(k_c C - k_a)}{(k_c C + k_a) + j\omega\Gamma_0}} \tag{15.4}$$

In this equation, a positive value of product $(b_a - b_c)(k_c C - k_a)$ corresponds to the inductive adsorption loop. A negative value corresponds to the capacitive adsorption loop. The diagrams should be given by the equivalent circuit in Fig. 15.18b. The parameter values (Tables 15.1–15.4) of this circuit shows the characteristic feature of Ni-Cr deposit corrosion by fluoride and diffusion in the active peak. The measured resistance at low frequencies is the apparent resistance (R_{lc}) of the localized corrosion. The medium and high frequency sections of the diagrams correspond to the deposit electrical characteristics (marked $_{ct}$ and W). In Tables 15.1–15.4, typical values indicate, respectively, localized corrosion and ionic diffusion. According to the resistance and capacitance values, this layer is

not considered as an insulating barrier in the active peak. Comparison of results with the steel shows that the resistance values are much lower with the deposit; these indicate more corrosion.

It is observed in the experimental diagrams (curves 8 to 12, Fig. 15.16), realized at the passive potentials, that these are completely different from those obtained for the prepassivity, and they are formed only of a large capacitive semi circle. The capacitive semi circle size increases then decreases when these passive potentials increase; the semi circle is related to oxide characteristics, i.e. formation of more compact oxide then the beginning of oxide breakdowns. These diagrams can be explained on the basis of the equivalent circuit presented in Fig. 15.6 and the parameter values given in Tables 15.1–15.4.

The Nyquist plots (Fig. 15.16) make it possible to calculate the donor concentration following the simplified Mott-Schottky equation. Donor density is 3.5×10^{21} carrier cm^{-3}. The flat-band extrapolated potential is close to −0.05 V/SCE. The carrier concentration is in agreement with the theoretical value for a passive layer given by Castro and Vilche [108], Simoes et al. [109] and Oriani et al. [110]. The oxide layer thickness is a few nm; this experimental value corresponds to usual passive oxide thickness values.

The curves 13 to 15 in Fig. 15.16 and the curves in Fig. 15.17 realized at the passive-transpassive and transpassive potentials show a capacitive semi circle with one or two inductive loops. These curves can be satisfactorily explained on the basis of the equivalent circuit approaches presented in Fig. 15.15. Suitable values of the circuit elements are given as a function of potentials (Tables 15.1–15.4). The resistance values are very low and show that the Ni-Cr deposit is easily corroded in the passive-pitting region and indicate that pitting is more important with Ni-Cr than with stainless steel. It can be seen that the frequency varies with the potentials (Figs 15.16 and 15.17), showing that fluoride ions and potentials play a role in the adsorption, oxide layer breakdown and pitting. At high frequencies, the electrolyte resistance decreases when transpassive potentials increase; this results from an increase in electrical conductivity of the solution inducing corrosion.

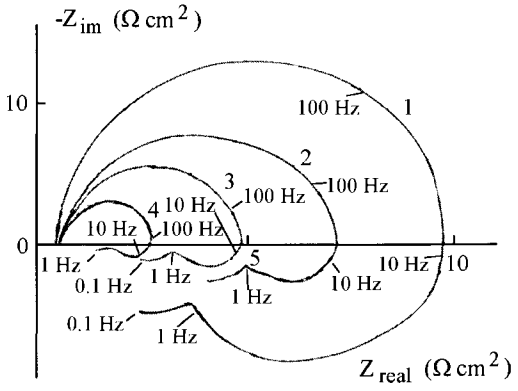

Figure 15.19. 316L stainless steel with Ni-Cr deposit—Nyquist diagrams, fluoride effect, pH 4, E: 1.05 V/SCE, 1: 0.08 mol dm^{-3}, 2: 0.1 mol dm^{-3}, 3: 0.12 mol dm^{-3}, 4: 0.15 mol dm^{-3} F^-.

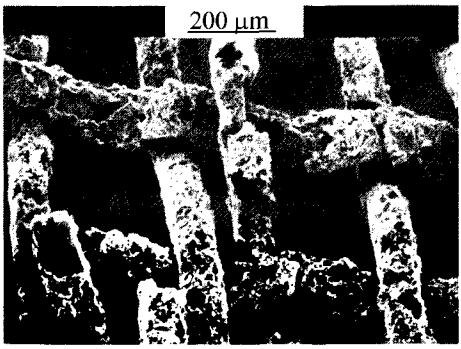

Figure 15.20. Grids after corrosion at the transpassive potentials and in presence of fluoride.

The experimental impedance diagrams realized for different F^- concentrations and at 1.05 V/SCE are shown in Fig. 15.19. A capacitive semi circle and two inductive loops are observed up to 0.1 Hz, and between 0.08 and 0.15 mol dm^{-3} F^-. To provide physical significance for these diagrams, an equivalent circuit is proposed in Fig. 15.15 with numerical values (Table 15.5) for each electrical component so that the results coincide with the experimental diagrams. From the R_{lc} values, pitting corrosion increases in the passive-transpassive region on F^- addition. Grids are rapidly destroyed (Fig. 15.20).

3. Conclusions

It is shown that without fluoride the corrosion potential is the same for 316L stainless steel and Ni-Cr deposits indicating non-galvanic corrosion. Non-cohesion of spinel grains for transpassive potentials is observed for the deposit in transpassivity.

With fluoride, the pitting potential is lower with the Ni-Cr deposit. Pitting depends on fluoride adsorption. The repassive potential indicates that corrosion due to crevices is possible by filling pits. In the active region, ion diffusion through the oxide occurs.

Chapter 16

SUBCRITICAL PIT GROWTH IN ALLOYS

1. Introduction

Nickel-based alloys are extensively used in the nuclear industry for their localized corrosion resistance. The major part of this resistance results from the composition of these alloys and their treatment. One of the most widely used alloys and the one studied here is Inconel 600 whose composition is given in Table 16.1. Nickel has a positive effect with respect to pitting, crevice and cracking corrosion. According to Rouby [217], Houlle [218] and Dupoiron and Verneau [219], incorporating copper improves resistance to pitting and crevice corrosion by displacing the pitting corrosion potential to higher values. Chromium increases the passivity domain by forming a mixed passive oxide layer. Titanium and aluminum are essential for precipitation in the alloy contributing to less pitting and intergranular corrosion. Titanium reacts easily with carbon forming titanium carbides avoiding the depletion in chromium around the grain boundaries (Fig. 4.38). Although Inconel 600 contains titanium, this alloy is liable to undergo intergranular attack. This attack is linked to chromium depletion around the grain boundary following the formation of chromium-rich carbides. This local chromium depletion is such that its concentration is below the stable passivity threshold. The solutions proposed are identical to those recommended for the stainless steels:

- limit the carbon concentration to a low level to prevent chromium carbide formation,
- add elements in order to form more stable carbides than $Cr_{23}C_6$ in grain boundaries.

Silicon is added to improve the corrosion resistance in an oxidizing medium when its concentration is appreciable (0.8–2 wt%). Inconel 600 was heat treated at 1150°C and rapidly air cooled (hyperquenching) in order to homogenize the face cubic centered austenitic structure. The Inconel 600 used was characterized by grain sizes between 5 and 20 μm (Fig. 16.1). The roughness factor is estimated to be in the range 1–1.2.

An acid medium was selected since relatively concentrated acid solutions are produced by radiolysis. The β^- particle energy decomposes organic polymers when these are in

Table 16.1. Inconel 600 composition

Elements	Cr	Fe	C	Mn	Si	Cu	Al	Ti	Ni
Wt%	16	8.7	0.04	0.2	0.2	0.2	0.2	0.2	bal.

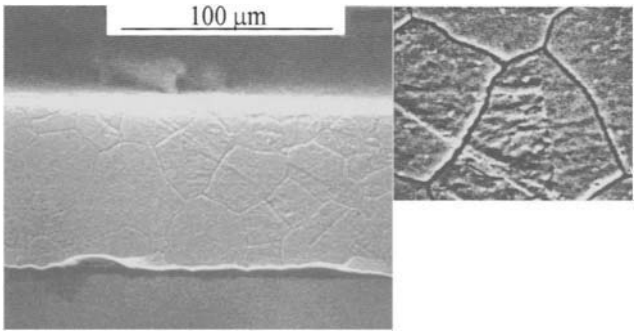

Figure 16.1. Scanning Electron Microscopy (a): photograph of electropolished Inconel 600 showing grains, (b): detail of photograph.

contact with gaseous tritium or tritiated water. If these polymers have R–F or R–Cl bonds the tritiated water contains an appreciable concentration of Cl^- and F^-. Consequently, the effects of F^- and Cl^- at acid pH were studied, first separately, then together, keeping a constant Cl^- concentration and controlling the pH and fluoride concentration for the range of localized corrosion potentials in the active peak. In the tests, the measurements were made in tritiated water deoxygenated by bubbling argon for 10 min and after decomposition of the radiolytic hydrogen peroxide at −1.1 V/SCE. pH was measured taking into account the difference between the pK (dissociation constant) of light and tritiated water ($pK_{^3H_2O} = 15.21$).

2. Experimental results

2.1. Cyclic voltammetry

2.1.1. Voltammograms obtained with chloride present The experimental voltammograms given in Fig. 16.2 were obtained with chloride concentration kept constant at 5×10^{-2} mol dm^{-3} while the pH varied between 1 and 3.5 (curves 2 to 5).

For comparison, a curve was also drawn without chloride (curve 1). In this curve, the active peak is seen at 0.2 V/SCE and the passive region extends from 0.2 to 0.8 V/SCE. When the potential sweep is reversed at 1 V/SCE, the presence of a cathodic peak shows that the passive oxide layer can be reduced to around −0.5 V/SCE. The large potential difference between cathodic and anodic peaks signifies that the passive oxide is difficult to reduce. In curves 2 to 5 obtained with Cl^-, the anodic peak is observed in the localized corrosion current, which increases at lower pH. This continues to be produced during the backward scan to reach the corrosion products' reduction peak, whose height slightly decreases with increasing pH. In the forward and backward scans, the respective currents depend on pH. In these curves, the difference between anodic and cathodic charges is greater than that in curve 1. This difference is not due to any difficulty in reducing the passive oxide layer

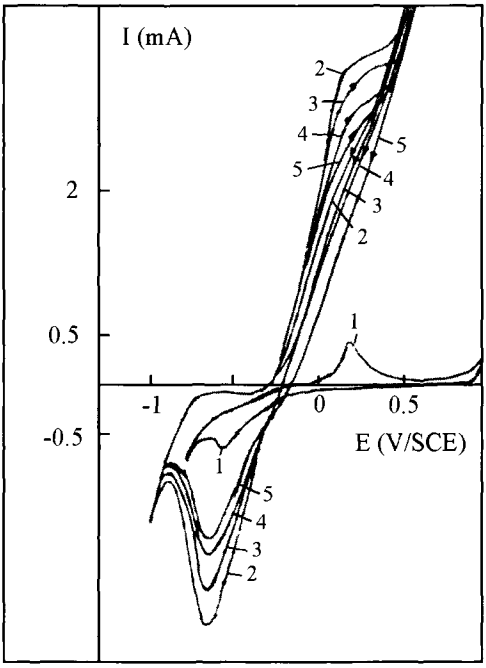

Figure 16.2. Voltammetric curves—pH effect, v: 0.2 V s^{-1}, ω: 2000 rpm, curve 1: polished Inconel 600, without Cl^-, pH 2, curves 2 to 5: with Cl^-: 5×10^{-2} mol dm^{-3}, 2: pH 1, 3: pH 2, 4: pH 2.7, 5: pH 3.5.

under the localized corrosion conditions, since it does not form. Stirring would contribute to sweeping away corrosion products from the tritiated water-oxide interface and consequently an anodic reaction accompanied by ion diffusion occurs in the oxide layer. After these results were obtained by voltammetry, the alloy surface was examined by Scanning Electron Microscopy by applying a potential in the active peak. The surface aspect is shown in Fig. 16.3.

Note that shallow, broad and numerous cavities as widespread pits, about 10 μm diameter and some crusts are visible at this surface and correspond to localized corrosion in the active region as shown by voltammetry.

2.1.2. Voltammograms obtained with fluoride present The effect of fluoride and pH variations on localized corrosion currents are given in Fig. 16.4.

In these curves, pH increases with the selected fluoride concentrations between 10^{-2} and 0.1 mol dm^{-3}, to reach pH 3.5 (Table 16.2) corresponding to the pK_a of the fluoride-hydrofluoric acid buffer. In contrast to chloride, the anodic currents are higher when the pH increases; this results from the fluoride concentration increase with pH. As with chlorides, the anodic peak is observed in the localized corrosion region. In the backward scan, the corrosion products' reduction peak current increases with fluoride concentration like that

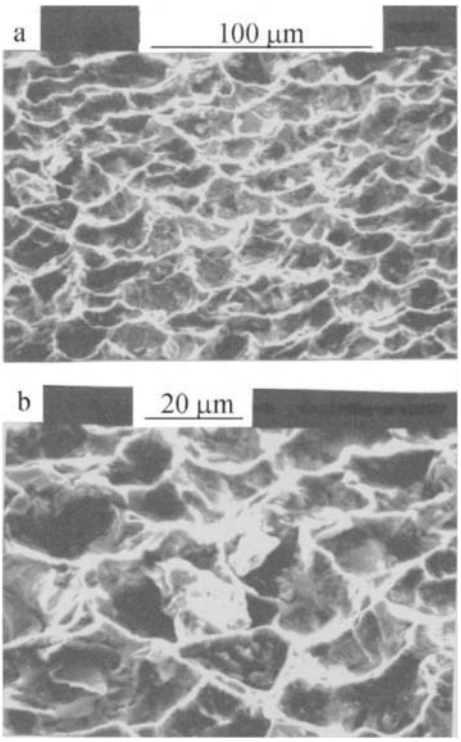

Figure 16.3. Scanning Electron Microscopy of Inconel 600 showing numerous cavities as widespread pits, (a): magnification of 500, (b): magnification of 1000, E: 0.1 V/SCE, Cl^-: 5×10^{-2} mol dm^{-3}, pH 3.5.

in the anodic peak. Scanning Electron Microscopy examinations were carried out at the active-localized corrosion potentials applying a potential of 0.1 V/SCE (Fig. 16.5).

Some pits and microcracking are observed that result from fluoride at acid pH. Microcracking and pits are induced by $^3H^+$ reduction with formation of gaseous tritium in tips of pits and in grain boundaries (Fig. 16.6) for the active region; these lead to embrittlement as shown by Wieckowski [220] and Ford et al. [24] in radioactive media. To explain this attack, Pickering et al. [221] show that hydrogen is generated within the grain boundary even though the alloy surface is about 200 mV more noble than the equilibrium potential of the hydrogen evolution reaction in the bulk electrolyte. As indicated by Ballinger et al. [222], the near grain boundary chromium concentration of Inconel 600 exhibits a degree of variability but in general is lower with respect to the matrix and the grain boundary. Pinard-Legry et al. [223] showed that the intergranular microcracking linked to hydride formation obtained by electrolysis is observed on Inconel 600. As in the ferritic steels, hydrogen preferentially accumulates and diffuses in the perturbed regions such as the carbide-grain boundary interfaces leading to intergranular corrosion. To show the morphology of the microcracking induced directly by tritium, the surface of Inconel 600 was examined by

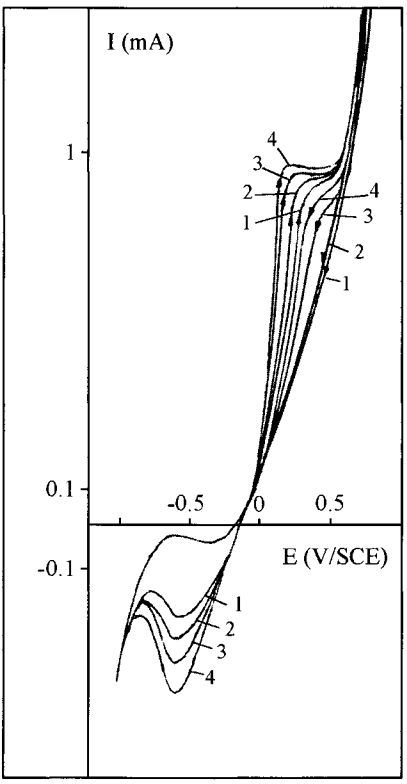

Figure 16.4. Voltammetric curves—pH and fluoride effects, v: 0.2 V s^{-1}, ω: 2000 rpm, 1: 10^{-2} mol dm^{-3}, pH 1, 2: 6×10^{-2} mol dm^{-3}, pH 1.9, 3: 8×10^{-2} mol dm^{-3}, pH 2.3, 4: 0.1 mol dm^{-3} F^-, pH 3.5.

Table 16.2. Effect of F^- on pH

F^- (mol dm^{-3})	10^{-2}	4×10^{-2}	6×10^{-2}	8×10^{-2}	9×10^{-2}	10^{-1}
pH	1	1.3	1.9	2.3	3.1	3.5

Scanning Electron Microscopy. Figs 16.1 and 16.7 show the cross-sectional photographs of two Inconel 600 membranes, one without (Fig. 16.1) and the other charged with tritium (Fig. 16.7a, b).

Without tritium charging, there is no loosening along grain boundaries. The intergranular grooves in Fig. 16.7a, obtained after tritium charging, are clearly more visible in-depth, which shows deeper localized corrosion by stress cracking of grain boundaries induced by tritium diffusion and absorption. Small cavities, about 0.2 μm diameter, are evident within the grains, with their population density dependent on the particular grain selected. Furthermore, cavities are preferentially located adjacent to the grain boundaries. They can correspond to heterogeneities; for example, carbide precipitates, most probably Cr-rich

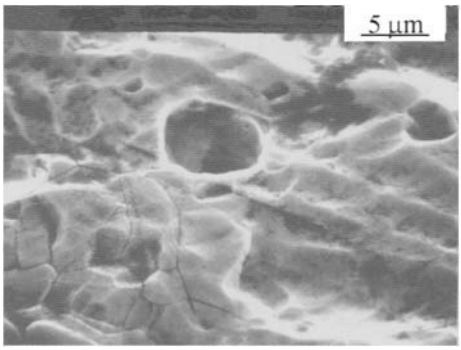

Figure 16.5. Scanning Electron Microscopy of Inconel 600, E: 0.1 V/SCE, F^-: 0.1 mol dm^{-3}, pH 3.5.

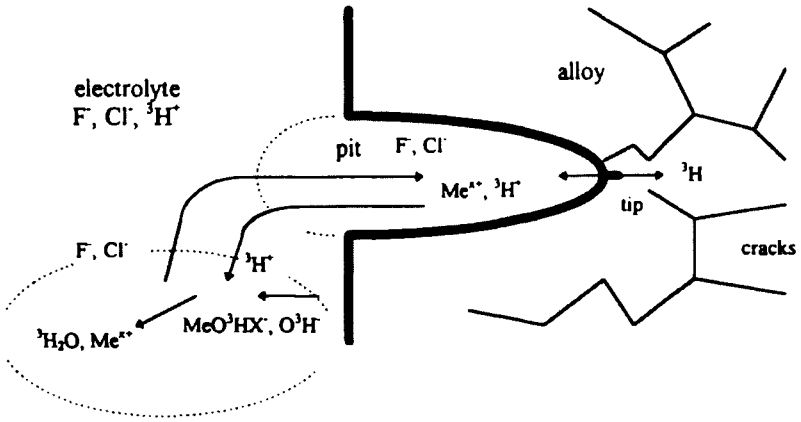

Figure 16.6. Schematic of various species in pits associated with tritium embrittlement in aqueous environment, X^- represents Cl^- and F^-.

carbides, depleted around and inside the grains. More detailed examination in photograph b (Fig. 16.7) shows that locally there is a broader attack of the intergranular groove in some grain boundaries. This must be due to weakening of the boundary by preferential tritium diffusion. From these examinations of the Inconel 600 and discussions in the literature, it is clear that tritium penetrates Inconel 600 by grain boundaries inducing intergranular microcracking. Thus Scanning Electron Microscopy examinations in Fig. 16.5 support the formation of localized corrosion and cracks under these conditions.

2.1.3. Voltammograms obtained with chloride and fluoride present

2.1.3.1. Fluoride and pH effects These specific cases of localized corrosion by Cl^- or F^- with two converse behaviors for the same pH variation will help understand the change

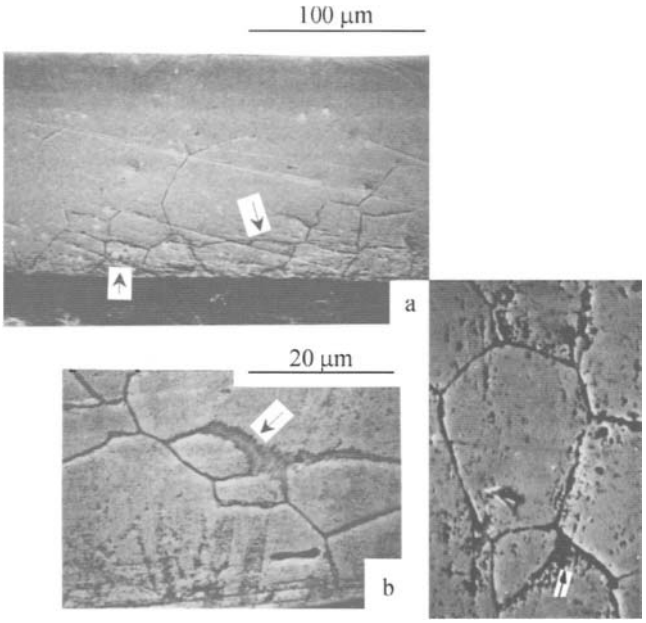

Figure 16.7. Scanning Electron Microscopy, localized corrosion in grain boundaries induced by tritium in cross-section of Inconel 600 membrane, (a): arrows showing grain boundary loosening and highly localized grain attack, (b): detail of photograph a showing broader attack of the intergranular groove by tritium diffusion (arrow).

in the voltammograms for a $^3H^+$, Cl^- and F^- mixture where Cl^- is kept constant (5×10^{-2} mol dm^{-3}) while F^- varies (10^{-2} to 0.1 mol dm^{-3}) with pH up to the value of pK_a, i.e. 3.5. In Fig. 16.8a, the anodic peak decreases then increases when the F^- concentration and pH increase.

This suggests firstly that there are two influences: a slight limitation of Inconel 600 localized corrosion due to the fact that the pH increases and the F^- and Cl^- concentrations must be high enough to produce more localized corrosion. In addition, the gradual increase then decrease of localized corrosion current, as the fluoride concentration increases, corresponds to the same variation of the cathodic peak (−0.5 V/SCE) attributed to the reduction of corrosion products. This experimental observation also indicates clearly that the electrode process is controlled by the surface mechanisms. In the second set of measurements, the effects of fluoride and pH are seen in the voltammograms realized at a higher current scale in order to obtain better observation of pitting currents in the passive and transpassive regions (Fig. 16.8b). Before the reversal scan, the pitting current obtained with chloride decreases then increases when fluoride concentration increases showing an unusual hysteresis shape in the presence of pitting. The fluoride ions are expected to form products adsorbed on the oxide layer that initiate pitting with respect to pH (as chloride ions do) in agreement

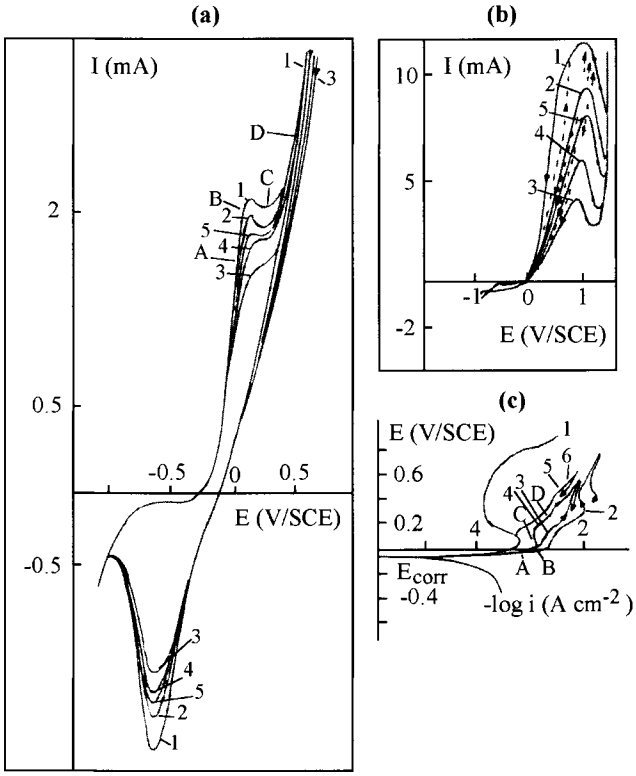

Figure 16.8. Voltammetric and polarization curves in presence of Cl^-—pH and fluoride effects, (a, b): voltammetric curves: v: 0.2 V s^{-1}, ω: 2000 rpm, Cl^-: 5×10^{-2} mol dm^{-3}, 1: 10^{-2} mol dm^{-3}, pH 1, 2: 6×10^{-2} mol dm^{-3}, pH 2.3, 3: 8×10^{-2} mol dm^{-3}, pH 2.9, 4: 0.1 mol dm^{-3}, pH 3.5, 5: 0.12 mol dm^{-3} F^-, pH 3.6, (b): (---) forward scan, (—) backward scan, (c): polarization curves: v: 5 mV s^{-1}, ω: 2000 rpm, initial pH: 1, curve 1: pH 1, without Cl^- and F^-, curves 2 to 6: with 5×10^{-2} mol dm^{-3} Cl^-, 2: 10^{-2} mol dm^{-3} F^-, pH 1, 3: 6×10^2 mol dm^{-3} F^-, pH 2.3, 4: 8×10^2 mol dm^{-3} F^-, pH 2.9, 5: 0.1 mol dm^{-3} F^-, pH 3.5, 6: 0.12 mol dm^{-3} F^-, pH 3.6.

with the reaction given by Farvaque-Béra and Leistikow [198]:

$$Me(O^3H)_2 + X^- \rightarrow MeO^3H\,X_{ads} + O^3H^- \qquad (16.1)$$

where X^- is Cl^- or F^-. Increasing pH and F^- concentration may modify the surface in two ways; this will be examined later by Scanning Electron Microscopy and impedance spectroscopy.

To facilitate the selection of the anodic peak potentials (A, B, C, D) for obtaining impedance diagrams, polarization curves were plotted using a lower scan rate (Fig. 16.8c) and for the same F^-, Cl^- concentrations and pH (curves 2 to 6) as those in Fig. 16.8a, b, and also without Cl^- and F^- (Fig. 16.8, curve 1). These curves can be used to justify

earlier statements. The anodic peak is found more precisely at 0.05 V/SCE, and the slight difference with voltammograms would appear to result from the scan rates, therefore due to reaction kinetics. In these curves, a high localized corrosion current is maintained even at a low scan rate. At low scan rates, chloride and fluoride are more easily adsorbed and subsequently diffuse in the oxide layer leading to localized corrosion in conformity with adsorption and diffusion kinetics. In the anodic peak and pitting region, it is seen that the current decreases, then increases when the F^- concentration and pH increase; the interpretation is the same as that given for the voltammograms (Fig. 16.8a, b). It can be seen that the corrosion potential ($E_{corr} = -0.075$ V/SCE) is the same at different F^- concentrations. Polarization curves (Fig. 16.8) show a well-defined localized corrosion region over a wide range of potentials going from the corrosion potential up to the transpassivity in the forward scan. The repassivity potential in the backward scan is near the corrosion potential. This indicates a corrosion risk by crevices with pitting.

2.1.3.2. Effect of varying stirring and scan rate In Fig. 16.9, stirring increases the anodic peak and shifts the negative current in the shoulder toward positive values, whereas the corrosion product reduction peak does not change indicating that a superficial oxide layer would favor crevice corrosion.

Evidently the anodic peak is affected by active behavior, and the cathodic peak is essentially related to the oxide layer. On plotting the anodic peak current versus stirring, a straight line is obtained which fits the Levich equation. An experimental value for the diffusion coefficient of 5×10^{-5} $cm^2\,s^{-1}$ is then found. This value depends in particular on the absence or the presence of oxide, but it is close to the usual values obtained for aqueous media [224]. The integrated charge (Q_c) for the cathodic peak is higher than those (Q_a) obtained for the active peak and the ratio, Q_c/Q_a decreases when the stirring increases. As the volume of tritiated water is small, it is also deduced that a few species would be trapped below the surface oxide layer and could favor crevice corrosion. It can also be seen that the localized corrosion current varies in the opposite direction to that of the anodic peak with stirring. Adsorption of Cl^- and F^- followed by diffusion in the oxide layer by ion vacancies or the O^{2-} lattice [207] would be slowed down due to the soluble hydroxide-Cl^-, F^- complex removed by stirring, which subsequently limits localized corrosion. Consequently, the localized corrosion rate is dependent on the intermediate species (e.g. MeO^3HX^-, local $^3H^+$) remaining at the surface of the Inconel 600, i.e. on the species kinetics. The soluble hydroxide-Cl^- or F^- complex formed locally dissolves the oxide layer up to the alloy that is corroded according to:

$$Me + x\,{}^3H_2O \rightarrow Me(O^3H)_x + x\,{}^3H^+ + xe^- \qquad (16.2)$$

This reaction leads to increasing the acidity in pits which dissolves the hydroxide and accelerates localized corrosion in absence of stirring.

In Fig. 16.10, the scan rate was varied from 20 to 100 $mV\,s^{-1}$. An increase in the scan rate leads to increasing anodic and cathodic peaks, decreasing pitting currents and does not significantly change the current in the shoulder which can be the result of adsorbed tritium.

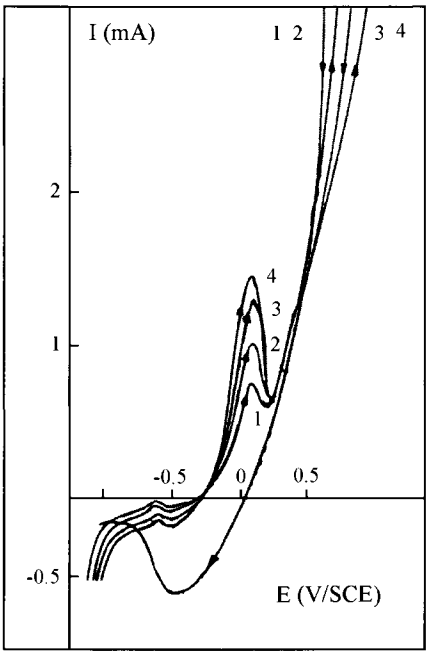

Figure 16.9. Voltammetric curves—electrode rotation speed effect, Cl^-: 5×10^{-2} mol dm^{-3}, F^-: 5×10^{-2} mol dm^{-3}, pH 1.7, v: 20 mV s^{-1}, ω: 1: 500, 2: 1000, 3: 2000, 4: 3000 rpm.

With increasing scan rates, the two peaks are displaced in positive and negative potential directions respectively. Plots of the logarithm of current in the anodic peak vs. logarithm of scan rate give a straight line with a slope close to 0.5. Plots of peak current vs. the square root of scan rate have also been performed. For the anodic peak, a good straight line was obtained; the slope is about 4.5 mA cm^{-2} V$^{-0.5}$ s$^{0.5}$ and corresponds to the value calculated from Delahay's equation for a reaction controlled by ion diffusion [224]. Thus, these peaks correspond well to the classical faradaic and capacitance current equations given in voltammetry, i.e. an active behavior. The value calculated from the active peak is about 2.5 mC cm^{-2} and consequently indicates the formation of a multi-oxide layer. Effectively, X-ray photoelectron spectroscopy examinations made by Moffat and Latanision [206] indicate that the monolayer equivalent charge is about 0.6 mC cm^{-2}. In localized corrosion, at low scan rates, chloride and fluoride ions are more readily adsorbed and subsequently diffuse in the oxide layer following adsorption and diffusion kinetics. Local dissolution of the oxide layer by complex hydroxide-chloride and fluoride and localized attack of the underlying alloy by acid formation are also involved here.

Interpretation of the previous voltammograms is not easy. On increasing the fluoride concentration in presence of chloride, the pitting current should increase; in fact this decreases then increases. This surprising result requires Scanning Electron Microscopy ex-

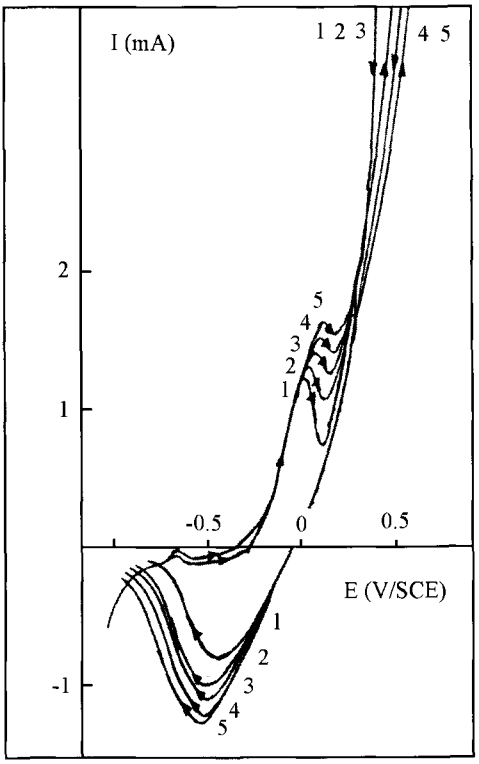

Figure 16.10. Voltammetric curves—scan rate effect, ω: 2000 rpm, Cl^-: 5×10^{-2} mol dm^{-3}, F^-: 5×10^{-2} mol dm^{-3}, pH 1.7, v: 1: 20, 2: 40, 3: 60, 4: 80, 5: 100 mV s^{-1}.

aminations. Inconel 600 potentiostated at 0.1 V/SCE shows localized corrosion in the active peak, with the formation of cracks or crevices as indicated by Pickering [225] and Cho and Pickering [226], and oxide crusts and grain decohesion of the oxide layer (Fig. 16.11) that can lead to porosity and the resulting ion diffusion in the oxide layer then sublayer corrosion. Finally, the results obtained by voltammetry and Scanning Electron Microscopy examinations show that Inconel 600 is corroded at the same time by active corrosion and localized corrosion in the anodic peak.

2.2. *Electrochemical impedance spectroscopy*

2.2.1. Spectra obtained with chloride present The impedance diagrams obtained with 5×10^{-2} mol dm^{-3} Cl^- are shown for different potentials (Fig. 16.12) in the overlapping active and localized corrosion regions, more exactly at the pitting beginning potentials, and different chloride concentrations between 5×10^{-3} and 5×10^{-2} mol dm^{-3} for pH 1 (Fig. 16.13).

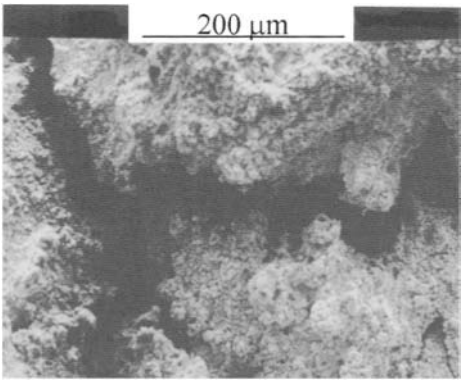

Figure 16.11. Scanning Electron Microscopy of Inconel 600, E: 0.1 V/SCE, Cl^-: 5×10^{-2} mol dm^{-3}, F^-: 0.1 mol dm^{-3}, pH 3.5.

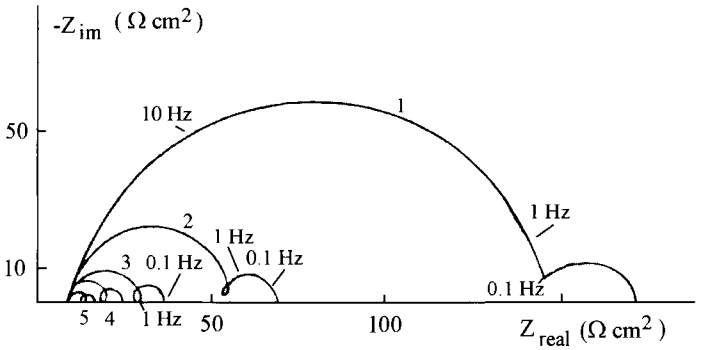

Figure 16.12. Nyquist diagrams—potential effect, ω: 2000 rpm, pH: 1, Cl^-: 5×10^{-2} mol dm^{-3}, 1: 0 V, 2: 0.025 V, 3: 0.065 V, 4: 0.08 V, 5: 0.1 V/SCE.

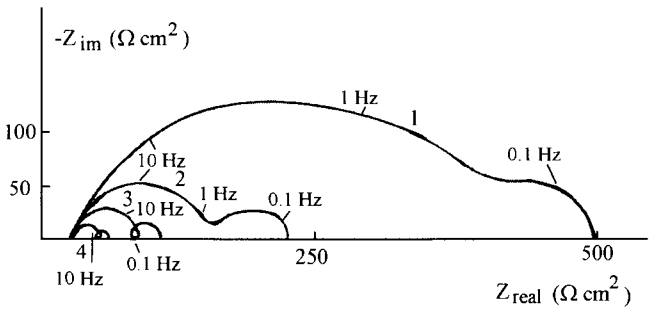

Figure 16.13. Nyquist diagrams—chloride effect, ω: 2000 rpm, pH: 1, E: 0.05 V/SCE, 1: 5×10^{-3}, 2: 10^{-2}, 3: 2×10^{-2}, 4: 5×10^{-2} mol dm^{-3} Cl^-.

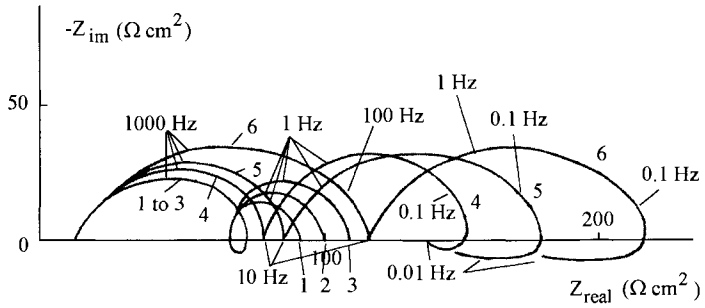

Figure 16.14. Nyquist diagrams—pH effect, ω: 2000 rpm, E: 0.15 V/SCE, Cl^-: 5×10^{-2} mol dm^{-3}, 1: pH 1, 2: pH 1.5, 3: pH 2, 4: pH 3, 5: pH 3.5, 6: pH 4.

The diagrams show two capacitive semi circles at high and low frequencies; these are separated by a loop for higher potentials or Cl^- concentrations. These semi circles indicate two mechanisms as mentioned in subsection 2.2.3. The loop can be ascribed to adsorption phenomena. As shown in Figs 16.12 and 16.13, each capacitive semi circle decreases when the potentials are slightly shifted to more positive values or when the chloride concentration increases.

The impedance diagrams in Fig. 16.14 were obtained at different pH values between 1 and 3.5 for a constant Cl^- concentration (5×10^{-2} mol dm^{-3}) and a potential located in the anodic peak. In these spectra, two capacitive semi circles are obtained. Their size increases with pH, suggesting that corrosion decreases at higher pH. The capacitive semi circle obtained at a low frequency can be followed or preceded by an inductive loop. Its origin is the same as that for Fig. 16.12.

2.2.2. Spectra obtained with fluoride present The impedance diagrams in Fig. 16.15 were obtained at different concentrations of fluoride between 10^{-2} and 0.1 mol dm^{-3} and for 0.05 V/SCE. At this potential chosen in the anodic peak, it is seen that the size of the two capacitive semi circles decreases when the fluoride concentration increases. The last semi circle is terminated by an inductive loop at low frequencies that very definitely signifies the presence of adsorbed species.

2.2.3. Spectra obtained with chloride and fluoride present

2.2.3.1. Potential effects The impedance diagrams in Fig. 16.16 were obtained at constant Cl^- and F^- (5×10^{-2} mol dm^{-3}) concentrations and pH 1.7 but at different potentials in the localized corrosion region corresponding to each side of the anodic peak (Fig. 16.8c).

Two capacitive semi circles are seen at 0.03 V/SCE (spectrum 1). These semi circles are characteristic of reactions in a porous oxide layer and an oxide sublayer [227] as shown in Fig. 16.17. At the potentials corresponding to the maximum height and negative slope in the anodic peak, only a capacitive semi circle (spectra 2 and 3) is observed at high

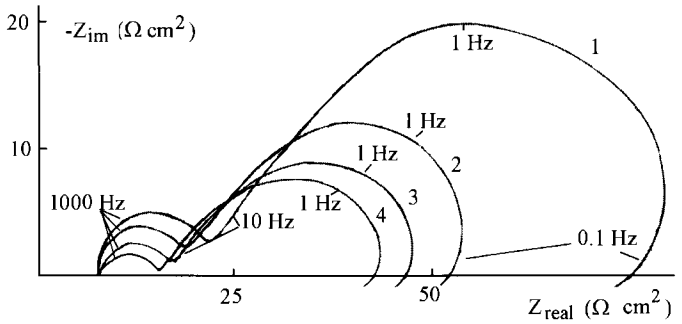

Figure 16.15. Nyquist diagrams—pH and fluoride effects, ω: 2000 rpm, E: 0.05 V/SCE, 1: 10^{-2}, pH 1, 2: 6×10^{-2}, pH 1.9, 3: 8×10^{-2}, pH 2.3, 4: 10^{-1} mol dm^{-3} F^-, pH 3.5.

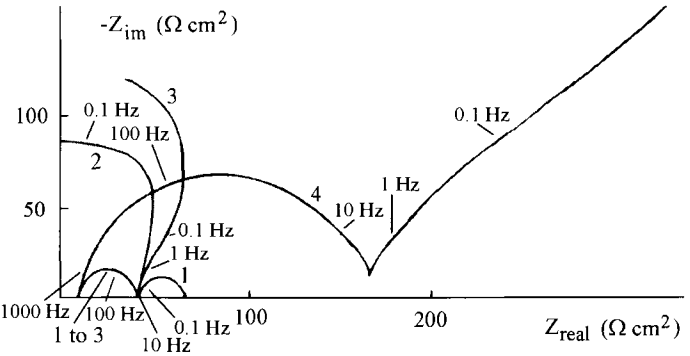

Figure 16.16. Nyquist diagrams—potential effect, ω: 2000 rpm, Cl^-: 5×10^{-2} mol dm^{-3}, F^-: 5×10^{-2} mol dm^{-3}, pH 1.7, 1: 0.03 V, 2: 0.05 V, 3: 0.07 V, 4: 0.1 V/SCE.

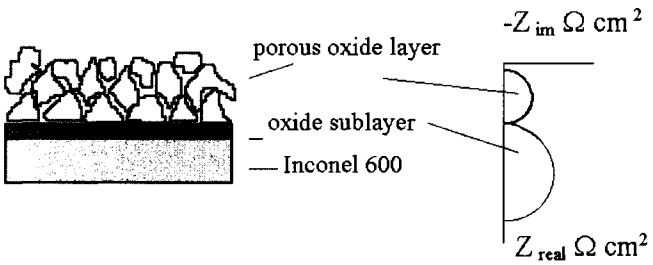

Figure 16.17. Schematic view of oxide layer system and corresponding impedance diagram in the complex plane.

frequencies, then the capacitive branch tends towards a high imaginary impedance value at medium frequencies, and at low frequencies, this bends to negative real impedance values. In spectrum 4 obtained at 0.1 V/SCE, a capacitive semi circle is seen at high frequencies.

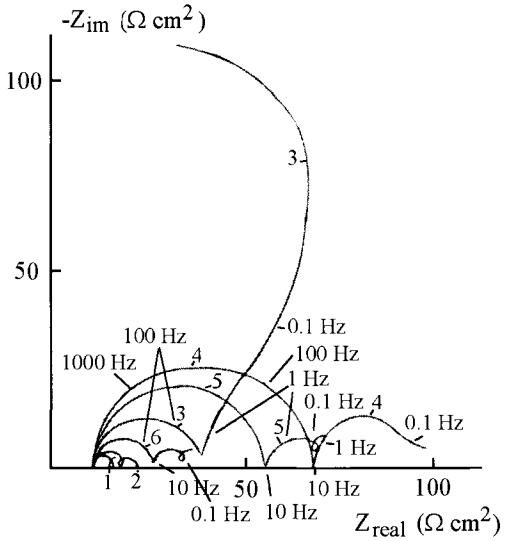

Figure 16.18. Nyquist diagrams—pH and fluoride effects, E: 0.07 V/SCE, ω: 2000 rpm, Cl^-: 5×10^{-2} mol dm^{-3}, 1: 10^{-2} mol dm^{-3}, pH: 1, 2: 2×10^{-2} mol dm^{-3}, pH: 1.2, 3: 5×10^{-2} mol dm^{-3}, pH: 1.7, 4: 7×10^{-2} mol dm^{-3}, pH: 2.1, 5: 0.1 mol dm^{-3}, pH: 3.5, 6: 0.12 mol dm^{-3} F^-, pH: 3.6.

The semi circle diameter increased with respect to the preceding diagrams (spectra 1 to 3) definitely signifying corrosion products accumulation partially protecting Inconel 600. This semi circle is followed by a straight line at low frequencies. It may be a Warburg straight line corresponding to ion diffusion in oxide, and also, signifying that for these experimental conditions, the passive oxide layer does not form. The straight line would appear to signify an anodic reaction accompanied by diffusion through the oxide layer as suggested by Scanning Electron Microscopy examinations (Fig. 16.11).

2.2.3.2. Fluoride and pH effects The impedance diagrams in Fig. 16.18 were obtained at constant potential (0.07 V/SCE) and Cl^- (5×10^{-2} mol dm^{-3}), but at different F^- concentrations and pH in the localized corrosion region corresponding to the anodic peak (Fig. 16.8c).

The impedance diagrams obtained with 10^{-2} and 2×10^{-2} mol dm^{-3} F^- are shown in spectra 1 and 2. Two capacitive semi circles at high and low frequencies separated by a loop are observed. Their origin is likely to be the same as that for Figs 16.12 and 16.13. The impedance diagrams are different for 5 and 7×10^{-2} mol dm^{-3} F^- (spectra 3 and 4). For spectrum 3, the capacitive branch tends rapidly to high imaginary impedance values at low frequencies. Finally, for still lower frequencies, this approaches negative real impedance values. According to Laihonen et al. [227], Rouquette-Sanchez et al. [228] and Keddam [229], these diagrams would result from adsorption, reactions with diffusion through the oxide layer, active dissolution and dissolution with localized corrosion. For a fluoride con-

centration of 7×10^{-2} mol dm^{-3} (spectrum 4), the impedance diagram consists of two capacitive semi circles; the second semi circle lies along the real impedance axis at the low frequencies. Finally, for spectra 5 and 6, obtained at 0.1 and 0.12 mol dm^{-3} F^-, the second capacitive semi circle is terminated at low frequencies by an inductive loop. In spectra 1 to 4, the semi circle size increases at high frequencies whereas in spectra 4 to 6, it decreases when the fluoride concentration increases. These different diagrams show the dependence of modifications of Inconel 600 behavior on the fluoride concentration. Depending on the pH and oxide layer, the localized corrosion by Cl^- and F^- ions must decrease or increase slightly as noted previously in the anodic peak region (Fig. 16.8).

3. Discussion, equivalent circuits and value determination

3.1. Discussions

These experimental diagrams can be interpreted following the explanations given by Keddam [229], Epelboin et al. [230] and Jouanneau and Keddam [213]. Equivalent circuit models were proposed by Epelboin [230] and by Chu-Nan Cao [231], [232]. In the interpretation, the current (i) is a function of the chosen potentials in the anodic peak and a parameter (x) depending on adsorbed species and oxide layer [227]:

$$i = f(E, x) \tag{16.3}$$

With adsorbed species, the faradaic impedance is:

$$1/Z_F = 1/R_{ct} + f'_E b/(j\omega - a) \tag{16.4}$$

where $Z_F = R_{ct} + \frac{j\omega L R_{pit}}{R_{pit} + j\omega L}$ is the ratio of the current to potential variations, R_{ct} the charge transfer resistance, ω angular frequency and a and b are dependent on:

$$a = \left(\partial(dx/dt)/\partial x\right)_E = \tau_x^{-1} \tag{16.5}$$

$$b = \left(\partial(dx/dt)/\partial E\right)_x \tag{16.6}$$

where τ_x is the time constant for a given value of x. From these equations, for a sufficiently high frequency with $\omega \gg \tau_x^{-1}$, the expression $f'_E b/(j\omega - a)$ tends to zero, and we have:

$$(1/Z_F)_{f\to\infty} = 1/R_{ct} \tag{16.7}$$

At very low frequencies, with $\omega \ll \tau_x^{-1}$ the current varies with the potential, and we obtain:

$$(1/Z_F)_{f\to 0} = 1/R_{ct} - 1/\varphi = 1/R_p \tag{16.8}$$

where R_p is the polarization resistance and $1/\varphi$ depends on $f'_E b/a$. At the high-frequency limit, the impedance is equal to the electrolyte resistance. At the low-frequency limit, the faradaic impedance, i.e. R_p, can be considered equal to the slope of the polarization curve $(\partial i/\partial E)$ at the steady state.

From the previous equations (eqs (16.3) and (16.6)), the adsorbed species also play a role in these spectra. For this, Jouanneau and Keddam [213] showed that the OH^- ions adsorb on metal forming an Me–OH dipole allowing electron transfer at the reactive interface. According to these authors, the oxide layer would provide adsorbed OH^- ions. For another adsorbed species, e.g. an X^- anion which could be F^- or Cl^-, there is competitive adsorption with OH^- ions and this can lead to oxide layer modification, depassivation, active dissolution and dissolution with localized corrosion. On the basis of the interpretation given by Jouanneau and Keddam [213], a reaction scheme can be written for competitive adsorption, oxide layer modification and depassivation.

$$\begin{array}{lllll} \mathrm{Me} \overset{O^3H^-}{\rightarrow} & \mathrm{Me{-}O^3H_{ads}} \overset{O^3H^-}{\underset{of}{\rightarrow}} & \mathrm{O^3H\ {-}Me{-}O^3H} & & \mathrm{Me^{2+}} \\ & \mathrm{om}\downarrow \mathrm{X^-} & \mathrm{pd}\downarrow \mathrm{X^-} & & \uparrow \mathrm{disso.} \\ & \mathrm{X{-}Me_{ads}} \overset{O^3H^-}{\underset{pd}{\rightarrow}} & \mathrm{O^3H_x{-}Me-X_y} & \overset{sd}{\rightarrow} & \mathrm{Me{-}O^3H} \\ & \mathrm{O^3H} & & & \end{array} \qquad (16.9)$$

In this scheme, $_{of}$ is the oxide layer formation, $_{om}$ the oxide layer characteristic modification, $_{pd}$ the primary depassivation and $_{sd}$ the secondary depassivation leading to the dissolution reaction ($_{disso.}$) of Inconel 600 by active and localized corrosion. This reaction scheme would involve several steps beginning with adsorption and where pH, oxide layer and potential may also have an effect.

3.2. *Spectra obtained with chloride present*

The general simplified equation (for instance, according to for instance, Bessone et al. [233]) corresponding to an oxide layer is:

$$Z = R_{el} + \left(jC_{dl}\omega + Z_F^{-1}\right)^{-1} \qquad (16.10)$$

where the angular frequency is $\omega = 2\pi f$, f being frequency, and Z_F the faradaic impedance including several electrical components. In Fig. 16.19a, the faradaic impedance consists of charge transfer and localized corrosion resistances (R_1) with a small diffusion term, an inductance (L) depending on $f''_E b$, and finally the resistive term, φ, in addition to the inductance. The resistive term, φ, will have little effect on simulated diagrams. According to these, the faradaic impedance is:

$$Z_F = R_{ct} + \frac{j\omega L R_1}{R_1 + j\omega L} \qquad (16.11)$$

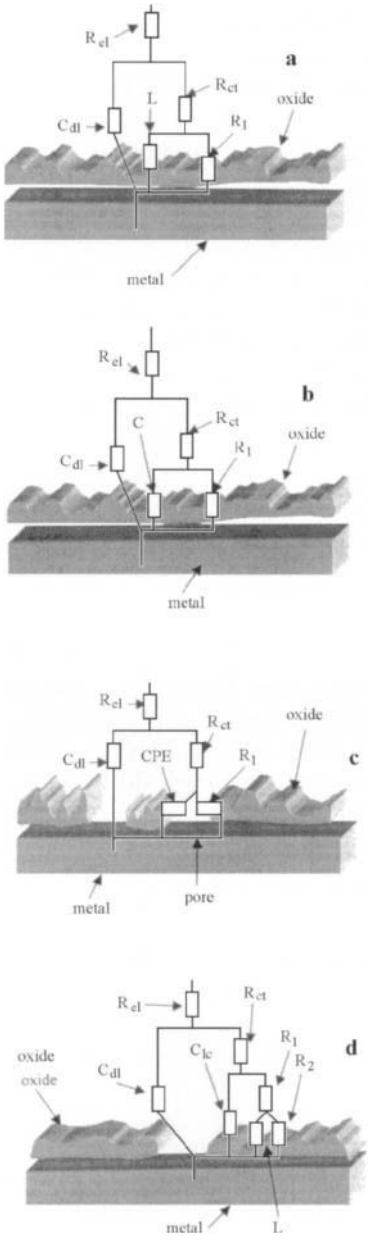

Figure 16.19. Equivalent circuits, (a): following Figs 16.12, 16.13, 16.16, curve: 1, Fig. 16.18, curves: 1 and 2, (b): following Fig. 16.16, curves 2 and 3, Fig. 16.18, curves 3 and 4, (c): following Fig. 16.16, curve 4, (d): following Fig. 16.18, curves 5 and 6, R_{el}, R_{ct} and R_n: electrolyte, charge transfer and corrosion resistances, C_{dl} and C: double layer capacitance and capacitance, CPE: constant phase element, L: inductance.

Table 16.3. Effect of potential for 5×10^{-2} mol dm^{-3} Cl^-

E (V/SCE)	0	0.025	0.05	0.065	0.08	0.1
R_{ct} (Ω cm^2)	140	60	12	21	11	6
R_1 (Ω cm^2)	90	17	7	9	7	6

Table 16.4. Effect of Cl^- at 0.05 V/SCE

$Cl^- \times 10^{-2}$ (mol dm^{-3})	0.5	1	2	5
R_{ct} (Ω cm^2)	300	140	20	9
R_1 (Ω cm^2)	250	90	45	7

Table 16.5. Effect of F^- at 0.05 V/SCE

$F^- \times 10^{-2}$ (mol dm^{-3})	1	6	8	10
R_{ct} (Ω cm^2)	15	11	7	5
R_1 (Ω cm^2)	60	45	41	39

The frequency of the top of the first capacitive semi circle increases with a higher Cl^- concentration (e.g. curves 1 and 2 in Fig. 16.13) and depends on pH. The values of the main equivalent circuit elements are given in Tables 16.3 and 16.4. As the potentials or Cl^- concentration increase, the values of resistances decrease; this is the result of the corrosion increasing. Also, according to Fig. 16.14, the corrosion is lower at higher pH.

3.3. *Spectra obtained with fluoride present*

The curves obtained with different fluoride concentrations and for 0.05 V/SCE (Fig. 16.15) can be satisfactorily explained on the basis of the same equivalent circuit approach presented in Fig. 16.19a.

The values of the equivalent circuit elements are given in Table 16.5. The charge transfer resistance decreases at higher fluoride concentration; this is the result of corrosion increasing. From the general equations giving the relation between the diffusion coefficient and the diffusion thickness [234], the expression for the diffusion coefficient is:

$$D/\delta^2 = 0.1 \tag{16.12}$$

where δ is the diffusion layer thickness. If we take the previous value of D, the thickness is a few μm.

3.4. *Spectra obtained with chloride and fluoride present*

3.4.1. Potential effects As indicated by Al-Kharafi [235], the main advantage of electrochemical impedance spectroscopy is the use of an electrical model to represent the metal-electrolyte interface. An interface undergoing electrochemical reactions is typically analogous to an electrical circuit consisting of a specific combination of resistors, capacitors

and inductors; hence an electrochemical system can be characterized in terms of its equivalent circuit. For a given electrochemical system, impedance plots can be correlated with one or more equivalent circuits. The correlation is used to verify models for the system. Once a particular model is chosen, physical and/or chemical properties can be correlated with circuit elements and numerical values are obtained by fitting experimental data to the equivalent circuit. Simple equivalent circuits generate relatively straightforward results to present metal-oxide-electrolyte systems. It is essential to subject simple equivalent circuit models, that are found to represent a good approach to electrochemical systems, to obtain reasonable matching of data. The experimental diagrams (Fig. 16.16), obtained at different potentials in the anodic peak and with constant Cl^- and F^- concentrations and pH 1.7, can be satisfactorily explained on the basis of equivalent circuits (Fig. 16.19a–c) according to the explanations given by Epelboin et al. [230] and Jouanneau and Keddam [213]. In Fig. 16.19b, the faradaic impedance implies resistances and a capacitance linked to $a\tau_x/bR_1^2 f'_E$. From this, the faradaic impedance is given in eq. (16.13).

$$Z_F = R_{ct} + \frac{R_1}{1 + j\omega R_1 C} \tag{16.13}$$

where R_1 is equal to $R_{ct}^2/\{(a/bf'_E) - R_{ct}\}$. In Fig. 16.16, spectrum 1 corresponds to resistances and an inductance (L) in the equivalent circuit (Fig. 16.19a). Spectra 2 and 3 correspond to a resistance in parallel with a capacitance (Fig. 16.19b). Spectrum 4 shows a capacitive semi circle followed by a straight line at low frequencies. The straight line is a depressed semi circle with a very long time constant represented by a constant phase element (CPE). It is due to a partial ion transfer and indicates a reaction in porous and duplex layers that do not guarantee good corrosion protection. The diffusion of the dissolving species through the layer limits the corrosion rate. The equivalent circuit (Fig. 16.19c) corresponds to the double layer capacitance, localized corrosion and charge transfer resistances and constant phase element, defined as:

$$Z_{CPE} = A(j2\pi f)^{-a} \tag{16.14}$$

in which a is a slope between 0 and 1, $j = \sqrt{-1}$, and A is a frequency-independent constant considered as the reciprocal capacitance only if $a \approx 1$. These different diagrams show the complexity of the system studied and the evolution in the equivalent circuit with potential. One of the aims of plotting the diagrams was to find the values of the main electrical elements and, if possible, to interpret them as a function of potentials. These are given in Table 16.6; the value of the double layer capacitance corresponds to a normal value according to Bard and Faulkner [103]. Its variation signifies lower corrosion and then corrosion enhancement. The charge transfer resistance is small and slightly increases with the potentials signifying then a very slight oxide layer improvement. From the simulation programs and according to eqs (16.3) to (16.8), the lowest frequency branch which bends towards the negative real impedance value corresponds to the negative $\partial i/\partial E$ slope obtained at point C in voltammetry (Fig. 16.8a, c); this appears to agree with the theoretical interpretation proposed by Keddam [229] and Epelboin et al. [230] for a negative polarization resistance.

Table 16.6. Effect of potential for 5×10^{-2} mol dm^{-3} Cl^- and 5×10^{-2} mol dm^{-3} F^-

E (V/SCE)	0.03	0.05	0.07	0.1
R_{ct} (Ω cm^2)	15	40	40	120
C_{dl} (μF cm^{-2})	50	25	30	45

Table 16.7. Effect of fluoride concentration, for 5×10^{-2} mol dm^{-3} Cl^-, at 0.07 V/SCE

$F^- \times 10^{-1}$ (mol dm^{-3})	0.1	0.2	0.5	0.7	1	1.2
pH	1	1.2	1.7	2.1	3.5	3.6
R_{ct} (Ω cm^2)	8	3	20	60	50	15
C_{dl} (μF cm^{-2})	100	70	10	10	20	50

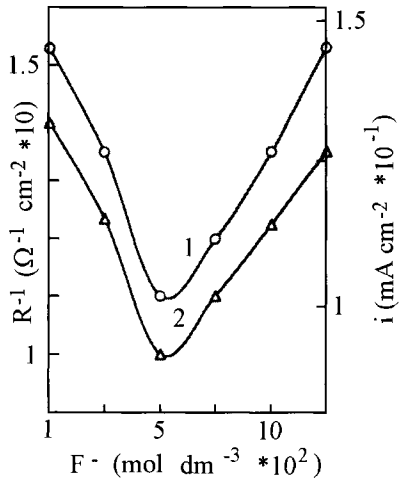

Figure 16.20. i and R_{ct}^{-1} vs. F^- from Fig. 16.8a, c and Table 16.7, 1: impedance Ω^{-1} cm^{-2}, 2: current mA cm^{-2}.

3.4.2. Medium effects The experimental diagrams (Fig. 16.18) obtained in presence of Cl^- and at different F^- concentrations and pH can be satisfactorily explained on the basis of equivalent circuits (Fig. 16.19a, b and d). The values of the equivalent circuit elements are given in Table 16.7. It can be seen that the charge transfer resistance increases then decreases when F^- concentration and pH increase. It can also be seen that the value of the double layer capacitance varies inversely. Fig. 16.20 presents the variation of R_{ct}^{-1} and i vs. fluoride concentration from impedance and voltammetry measurements (Fig. 16.8a, c).

As shown in this figure, the values R_{ct}^{-1} and i decrease at lower F^- concentration, and then these increase starting with the same F^- concentration. This mean that the rate of oxide layer corrosion changes as predicted with the F^- concentration and pH ($\approx 5 \times 10^{-2}$ mol dm^{-3}). This change indicates that pH and adsorbates, F^-, Cl^- concentrations modify the nature of the oxide layer and corrosion mode in overlapping active and pitting regions.

4. Conclusions

Localized corrosion occurs from the active potentials up to the passivity and transpassivity. Results indicate that there are definitely reactions with the oxide layer and that there are several processes occurring simultaneously: adsorption of Cl^- and F^-, localized and active corrosion, oxide layer dissolution and ion diffusion. Two influences are observed in the overlapped regions during the pH increase which gives a slight decrease in corrosion, whereas the F^- and Cl^- concentrations must be high enough to produce more corrosion. It can be thought also that the adsorbed species such as O^3H^-, Cl^-, F^- lead to active and localized corrosion. The characteristics of the oxide layer were found to depend on the concentration of studied species. The oxide layer has a complex structure.

Chapter 17

DETRIMENTAL EFFECTS OF OXIDIZERS

1. Introduction

The energy released by tritium decay decomposes tritiated water molecules with the production of non-negligible concentrations of hydrogen peroxide and ionized peroxide radical if the water is stored for long periods in closed containers with a pressure of radiolytic gases. In this case, it is shown that the corrosion potential is in the passive-transpassive region. With decreasing pressure, the concentrations of peroxides and the corrosion potential decrease. The same is true for the redox potential of the tritiated water which shifts towards the passive or active regions. These modifications lead to corrosion or passivation.

The composition of the austenitic N08932 stainless steel is given in Table 17.1. During production, this steel was heat treated at 1170°C at high nitrogen pressure followed by quenching in water in order to homogenize the face centered cubic austenitic structure (γ). The size of grains is approximately 40 μm. The incorporated nitrogen is highly effective in generating the γ solid solution and can replace carbon in forming metal nitrides. Depending on the heat treatment, nitrogen can be found in grain boundaries, and manganese is added to increase its solubility. Incorporating nitrogen stabilizes and strengthens the austenite phase without reducing its ductility, which is interesting for tightness of process. According to Rouby [217] and Dupoiron and Verneau [219], copper, like nitrogen, has a beneficial effect on the resistance to pitting and crevice corrosion by displacing the pitting potential to higher values. Silicon is present due to the fact that it improves the corrosion resistance in an oxidizing medium.

The equilibrium constant for $^3H_2O_2$ and $^3HO_2^-$ is 12 as shown in [164]. Therefore, at pH 13, the oxidizing ionized peroxide radical predominates. Moreover, tritium absorbs and diffuses easily in organic polymers by forming bonds, e.g., $-(Cl–R–^3H)_n–$. There is chloride formation by decomposition of these and we have thus studied the effects of Cl^- and $^3HO_2^-$, first separately, then together, for the range of the corrosion, passive and localized corrosion potentials.

Table 17.1. N08932 stainless steel—composition

Elements	Ni	Cr	C	Mn	Si	Mo	Cu	N	Fe
Wt%	25.9	25.1	0.01	0.94	0.25	4.73	1.45	0.21	bal.

2. Experimental results

2.1. Results obtained with ionized peroxide radical

2.1.1. Anodic polarization curves Anodic polarization curves obtained at a low scan rate are presented in Fig. 17.1.

The corrosion potential is shifted towards the passivity and transpassivity with increasing $^3HO_2^-$ concentrations. At the corrosion potential, corrosion should occur at the cathodic and anodic sites e.g., by the following reactions at alkaline pH.

Cathodic sites:

$$^3HO_2^- + {}^3H_2O + 2e^- \rightarrow 3O^3H^- \tag{17.1}$$

The cathodic current in the above reaction is:

$$i_c = -2k_c F[^3HO_2^-]^{\nu_{red}} \exp -FE/RT \tag{17.2}$$

Anodic sites:

$$Me + 2O^3H^- \rightarrow Me(O^3H)_{2ads} + 2e^- \tag{17.3}$$

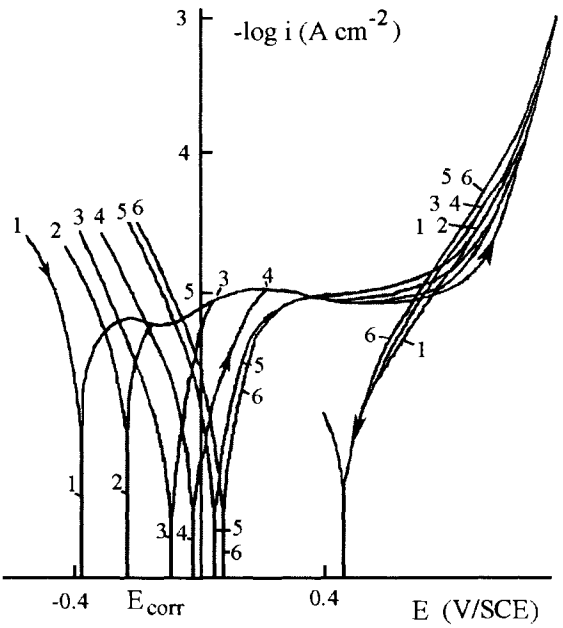

Figure 17.1. Polarization curves with $^3HO_2^-$, ω: 3000 rpm, v: 5 mV s^{-1}, pH 13, 1: 10^{-4} mol dm^{-3}, 2: 10^{-3} mol dm^{-3}, 3: 3×10^{-3} mol dm^{-3}, 4: 7×10^{-3} mol dm^{-3}, 5: 10^{-2} mol dm^{-3}, 6: 2×10^{-2} mol dm^{-3} $^3HO_2^-$.

$$Me(O^3H)_{2ads} + O^3H^- \rightarrow MeOO^3H + {}^3H_2O \tag{17.4}$$

$$i_a = 2k_a F[O^3H^-]^{\nu_{ox}} \exp FE/RT \tag{17.5}$$

where $MeOO^3H$ is the 'wet' oxide together with 'dry' Me_2O_3 formed on N08932 steel. The passive layer has a complicated chemical structure which is described by a multilayer or bilayer model as hydroxyl-oxide. The size and structure of the related layers change with the potential and with other factors such as aqueous composition. The above equations show that O^3H^- are consumed in anodic sites and produced in cathodic sites resulting in local pH modifications.

The corrosion potential of this system is the potential at which both the cathodic and anodic currents are equal. From these equations, E_{corr} is assumed to be:

$$E_{corr} = \frac{1.15RT}{F} \log\left(\frac{k_c[{}^3HO_2^-]^{\nu_{red}}}{2k_a[O^3H^-]^{\nu_{ox}}}\right) \tag{17.6}$$

According to eq. (17.6), plotting E_{corr} against $\log HO_2^-$ should give a straight line:

$$\frac{\partial E_{corr}}{\partial \log[{}^3HO_2^-]^{\nu_{red}}} = \frac{1.15RT}{F} \tag{17.7}$$

It can be seen that the ionized peroxide radical modifies the corrosion potential as shown in Table 17.2 where the slope is about 200 mV per decade. The reaction order sign expected for $^3HO_2^-$ is consequently negative which clearly indicates the cathodic electrochemical reaction [159]. The cathodic and anodic experimental Tafel slopes are about −120 and 74 mV per decade. The cathodic slope value indicates that another reaction limiting the electron transfer takes place as shown by Nogami and Shiratsuchi [236]. This reaction will be discussed in subsection 2.1.3.

As in eq. (17.6), the corrosion current is:

$$i_{corr} = 2F[k_a k_c]^{0.5}[O^3H^-]^{0.7}[{}^3HO_2^-]^{0.5\nu_{red}} \tag{17.8}$$

The corrosion current, i_{corr}, is given in Table 17.2 as a function of ionized peroxide radical concentration. In this table, it can be seen that the value of i_{corr} is greater in the active region without $^3HO_2^-$ or high $^3HO_2^-$ concentration than at medium $^3HO_2^-$ concentration (10^{-3} mol dm^{-3} $^3HO_2^-$).

In the transpassivity, it is observed that the anodic current increases with $^3HO_2^-$ concentration. It can also be seen in Fig. 17.1 that the positive current in the reverse scan becomes

Table 17.2. Dependence of E_{corr} and i_{corr} on $^3HO_2^-$

$^3HO_2^-$ (mol dm^{-3} × 10^2)	0.01	0.1	0.3	0.7	1	2
E_{corr} (V/SCE)	−0.4	−0.2	−0.13	0	0.05	0.1
i_{corr} (μA cm^{-2})	1	0.8	1	1.5	2	4

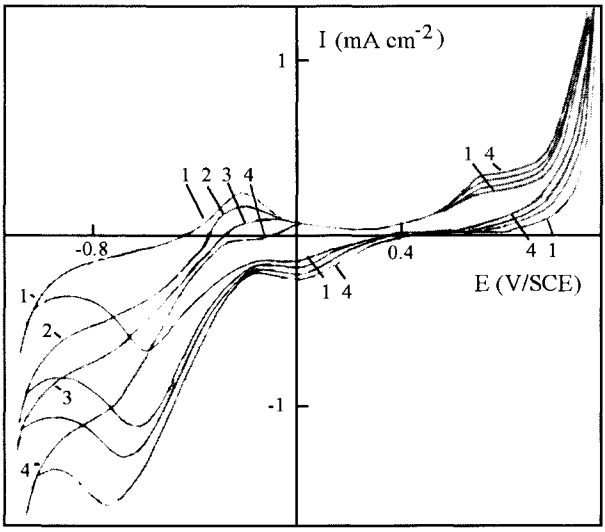

Figure 17.2. Voltammetric curves with $^3HO_2^-$, ω: 3000 rpm, v: 100 mV s^{-1}, pH 13, 1: 10^{-4} mol dm^{-3}, 2: 10^{-3} mol dm^{-3}, 3: 3×10^{-3} mol dm^{-3}, 4: 5×10^{-3} mol dm^{-3} $^3HO_2^-$.

greater than that in the forward scan for the same potential. It appears that $^3HO_2^-$ reduction is possible and that open-circuit coupling of transpassive corrosion with ionized peroxide radicals is feasible.

2.1.2. Voltammetric curves Fig. 17.2 illustrates the voltammograms obtained with different $^3HO_2^-$ concentrations.

Evidently the presence of ionized peroxide radical significantly affects N08932 steel oxidation and reduction processes. On increasing the potential in the forward scan, a prepassive peak is seen at −0.2 V/SCE. In the backward scan, a major reduction peak occurs near −0.75 V/SCE. It should be noted that the passive region is followed by a small transpassive peak preceding the oxide layer dissolution potential. The current increases quickly in this region. The reaction concerning the transpassive region is:

$$2MeOO^3H + 3\,^3HO_2^- \rightarrow 2MeO_4^{2-} + {}^3H^+ + 2\,^3H_2O \qquad (17.9)$$

In this equation, it is clear that $^3HO_2^-$ ions participate in the production of $^3H^+$ and MeO_4^{2-} from passive oxide. Evidently the presence of ionized peroxide radicals significantly affects the oxidation and reduction processes of N08932 steel and leads to a local acidification. Moreover, the curves exhibit the following characteristics:

(a) in the forward scan, the anodic curves intersect the potential axis at more positive potentials with $^3HO_2^-$ present. At lower $^3HO_2^-$ concentrations, the corrosion potential

will be in the active peak bringing about instabilities in the prepassive oxide layer, which will be more difficult to stabilize and passivate,

(b) a higher reduction peak which increases with $^3HO_2^-$ concentration, signifying that the latter is reduced following the cathodic reaction (eq. (17.1)). This shifts all the currents in this region towards negative values. By plotting the cathodic peak current vs. $^3HO_2^-$, a straight line is obtained that fits the Levich equation. From this, an experimental diffusion coefficient value of 5×10^{-5} cm^2 s^{-1} is found and is close to the usual values obtained for aqueous media [103],

(c) in the forward scan, the N08932 steel oxidation peak at −0.2 V/SCE disappears and the current takes a negative value when the $^3HO_2^-$ concentration increases,

(d) in the passive region, the anodic current does not change significantly for the different $^3HO_2^-$ concentrations. It would appear that the passive oxide layer is more difficult to break down at high scan rates. Effectively, its mechanism depends on kinetics which in turn depend on the scan rate,

(e) in the transpassive region, the anodic peak increases slightly with $^3HO_2^-$ concentration. The interpretation could be that the oxide breakdown current increases with the presence of the ionized peroxide radical. From these results, $^3HO_2^-$ reduction is easily possible in prepassivity and transpassive dissolution with $^3HO_2^-$ reduction is feasible. As a result, voltammograms and polarization curves suggest that there is modification of the passive oxide layer.

The explanation of the behavior of these curves is identical to that for the chapter concerning the effects of oxygen and hydrogen peroxide on 316L stainless steel. Thus, lower and higher $^3HO_2^-$ concentrations must be avoided in the tritiated water. At intermediate ionized peroxide radical concentrations, the $^3HO_2^-$ reduction current to be considered is in the passive potentials, consequently the corrosion and free potentials are in this region and steel is protected.

2.1.3. *Impedance spectra*

2.1.3.1. Results This section is concerned with the analysis of impedance data for N08932 steel passivated at different passive potentials up to the passive-transpassive limit and at different $^3HO_2^-$ concentrations. The impedance data will be compared to evaluate the effect of $^3HO_2^-$ on the passive oxide characteristics. In the passive domain, the semi circles in the Nyquist plots are too incomplete over all the frequency range to be easily interpreted, therefore the Bode plots were drawn for N08932 steel.

Comparative measurements made at pH 13, for different $^3HO_2^-$ concentrations and passive potentials (Fig. 17.3a–e), show changes in $\log|Z|$ and phase angle vs. $\log(f)$. The Bode plots are characterized essentially by two distinct regions:

(a) In the broad low and middle frequency range, the diagrams display a linear slope of about −1 in $\log|Z|$ as $\log(f)$ decreases, while phase angle values approach −90°. This is the characteristic response of a passive oxide capacitance (C_{ox}) in the purely capacitive region. This capacitive behavior is observed over a large frequency range.

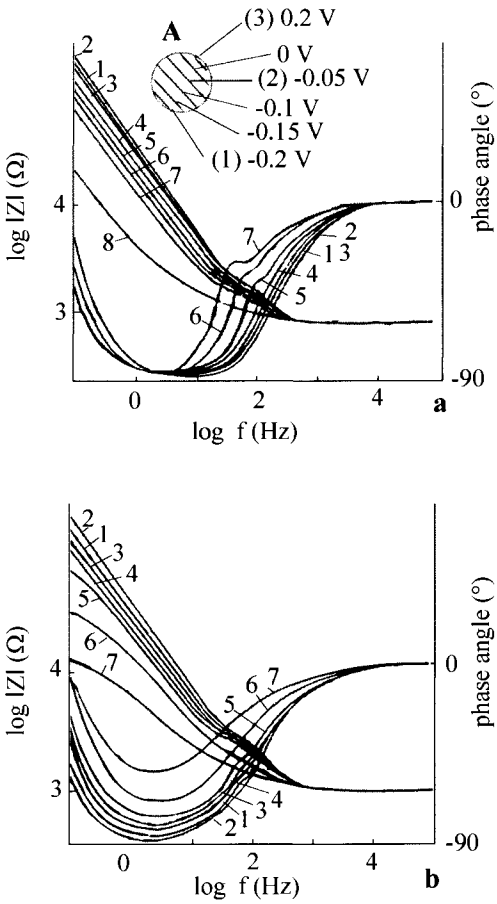

Figure 17.3. Bode diagrams with $^3HO_2^-$, pH 13, ω: 3000 rpm, (a): $^3HO_2^-$: 10^{-4} mol dm^{-3}, 1–8: −0.2 to 0.8 V/SCE, (A): on expanded scale, (b): $^3HO_2^-$: 10^{-3} mol dm^{-3}, 1–7: −0.05 to 0.8 V/SCE, (c): $^3HO_2^-$: 5×10^{-3} mol dm^{-3}, 1–11: 0 to 0.65 V/SCE, (d): $^3HO_2^-$: 10^{-2} mol dm^{-3}, 1–9: 0.1 to 0.62 V/SCE (e): $^3HO_2^-$: 2×10^{-2} mol dm^{-3}, 1–9: 0.25 to 0.65 V/SCE.

(b) In the higher frequency range of (a), a dip in the phase angle curve and an inflection in the log $|Z|$ plots are seen; these can be more easily obtained by subtracting the electrolyte resistance. They indicate the presence of a hardly identifiable parallel resistance and a non-dissipative passive oxide capacitance due to its formation. Also, the deviation of the phase angle maximum, near −90°, signifies that the passive layer thus formed on N08932 steel approaches more ideal capacitor behavior.

The values of C_{ox} are given for different passive potentials and $^3HO_2^-$ concentrations (Table 17.3). In Fig. 17.4 plotted in 3 dimensions, the variation of C_{ox} shows two inverted

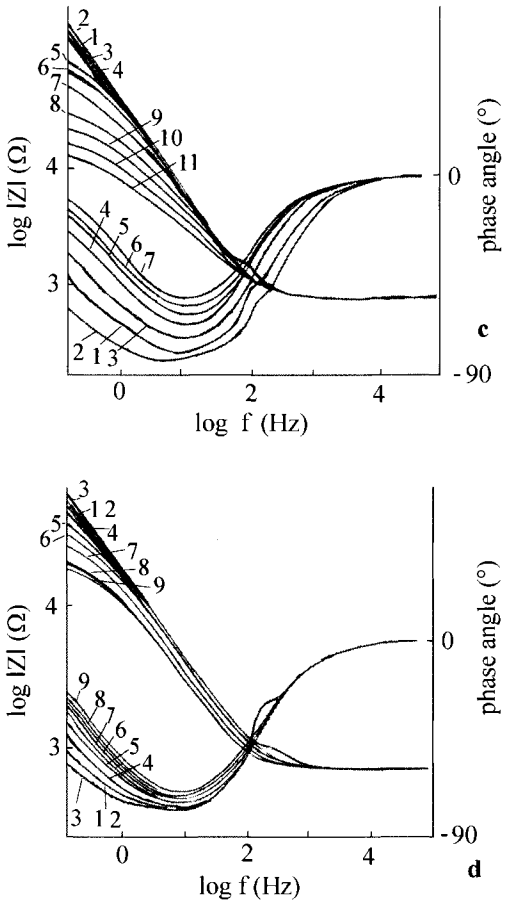

Figure 17.3. (Continued).

Table 17.3. Dependence of oxide capacitance (μF cm^{-2}) on passive potentials at different $^3HO_2^-$ concentrations (mol dm^{-3}), underlined numbers: characteristic oxide layer zone

$^3HO_2^-$	E (V/SCE)												
	−0.2	−0.15	−0.1	−0.05	0	0.05	0.1	0.15	0.2	0.3	0.4	0.5	0.6
10^{-4}	27	13	10.5	10	10	8.3	8	9	10.5	13	19		
10^{-3}	11	9	8	8	6.5	5.5	6	7.5	8.5	10.5	14	15	20
5×10^{-3}	40	32	25	17	12	10	8.4	9.6	10	11	15	40	80
10^{-2}	72	61	50	34	19	14.5	11	9	10	14	20	20	30
2×10^{-2}	130	112	92	70	50	30	20	14	10	25	60	180	240

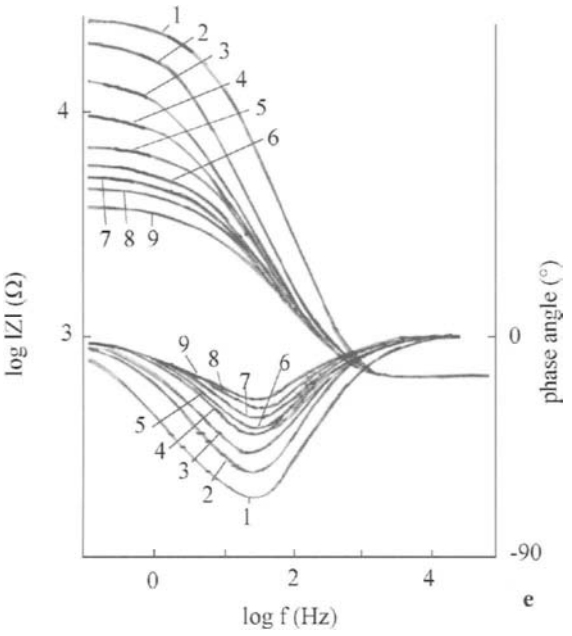

Figure 17.3. (Continued).

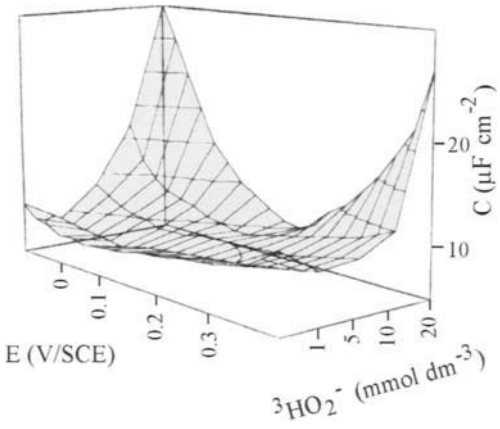

Figure 17.4. Oxide layer capacitance as a function of passive potentials and $^{3}HO_2^-$.

slopes and indicates that the oxide layer formation obeys a growth law depending on these two studied parameters: potentials as indicated by Schmuki and Böhni [237] and the ionized peroxide radical. A 'critical capacitance' corresponding to its lower value denotes the

perfect oxide layer. The Bode plots enable us to calculate the donor concentration (n_d) over a sufficient potential range following the simplified Mott-Schottky equation. Assuming that additional capacitive elements such as the Helmholtz layer capacitance can be neglected, the donor density is between 0.4 and 2.9×10^{20} carrier cm^{-3}. The obtained carrier concentration agrees with the theoretical value for a passive layer given by Castro and Vilche [108], Simoes et al. [109] and Oriani et al. [110]. The flat-band extrapolated potential is close to −0.2 V/SCE at 10^{-3} mol dm^{-3} $^3HO_2^-$. The oxide layer thickness estimated is 8 nm; this experimental value corresponds to a thicker oxide value for these conditions. The smaller deviation of the phase angle maximum from −90° for 10^{-3} mol dm^{-3} $^3HO_2^-$ would indicate that the passive layer thus formed on N08932 steel approaches ideal capacitor behavior. The thickness and donor density are higher and lower, respectively, for 10^{-3} mol dm^{-3} $^3HO_2^-$. These values indicate less electron transfer and higher corrosion resistance. The passive oxide layer formed is more insulating than that at higher $^3HO_2^-$ concentrations. These reflect the formation of a highly ordered and less defective oxide layer.

At higher ionized peroxide radical concentrations, the Bode plots (Fig. 17.3e) show a horizontal line at low frequencies that corresponds to the charge transfer resistance, indicating that N08932 steel becomes predominantly more resistive in the shorter concerned passive region. The passive layer thus formed on N08932 steel approaches less ideal capacitor behavior at higher ionized peroxide radical concentrations or potentials. The oxide layer formed for higher $^3HO_2^-$ concentrations would then be less stable. These reflect the formation of a more defective oxide layer and breakdowns.

In the passive-transpassive region, the total impedance for N08932 steel again becomes predominantly resistive (Fig. 17.3b–e) over a broad frequency range, while the capacitive part is predominant only at higher frequencies. The value of the charge transfer resistance decreases when the passive potentials shift towards the transpassive region. This indicates passive layer breakdown and oxide dissolution at these potentials.

2.1.3.2. Equivalent circuits and value determinations Diagnostic criteria for the choice of equivalent circuits for modeling impedance data may be summarized by visual observation of the shifts in experimental Bode plots with changing passive potentials and $^3HO_2^-$ concentrations. It seems that at potentials in the passive region (mainly purely capacitive impedance), spectra give a perfect fit with the experimental data if the total impedance is modeled according to the circuit in Fig. 17.5a.

Constant phase elements (CPE) are used instead of 'ideal' capacitors to account for the slight deviations observed such as a capacitive slope lower than −1. The perfect fitting of Bode plots is also obtained according to the second circuit in Fig. 17.5b. In this circuit, resistances and capacitances are used to account for the different deviations observed at low and medium frequencies. Either circuit can be used in passivity. The first was taken for different $^3HO_2^-$ concentrations where the capacitive slope 'a' should be checked, and the second was used where the slope is definitely 1 (eq. (6.25)).

One of the aims of plotting the experimental diagrams is to find the values of the main electrical elements. The major values obtained for these are given in Table 17.4. It can be

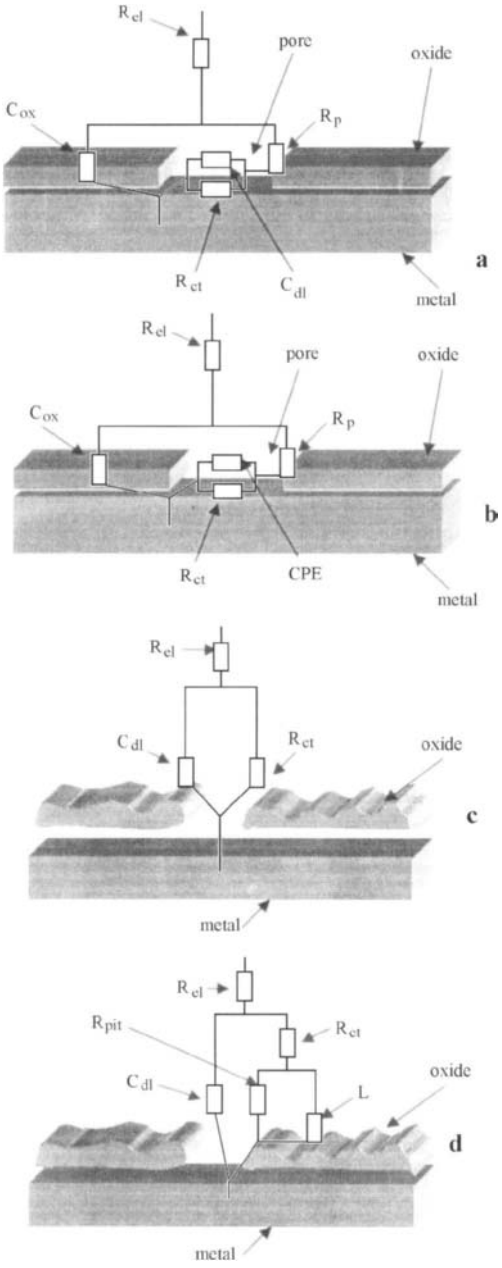

Figure 17.5. Equivalent circuits, (a, b, c, d): R_{el}: electrolyte resistance, R_{ox}: oxide resistance, R_{ct}: charge transfer resistance, R_{lc}: localized corrosion resistance, CPE_n: constant phase elements, C_{ox}: oxide capacitance, C_{dl}: double layer capacitance, L: inductance.

Table 17.4. Dependence of electrode resistance ($\times 10^2$ kΩ cm^2) on passive and passive-transpassive potentials at different $^3HO_2^-$ concentrations (mol dm^{-3})

$^3HO_2^-$	E (V/SCE)													
	−0.2	−0.15	−0.1	−0.05	0	0.05	0.1	0.15	0.2	0.3	0.4	0.5	0.6	0.7
10^{-4}	0.37	0.77	0.95	1.0	1.0	1.20	1.25	1.11	0.95	0.77	0.53			
10^{-3}	0.91	1.11	1.25	1.25	1.54	1.82	1.67	1.33	1.18	0.95	0.71	0.67	0.50	0.33
5×10^{-3}	0.25	0.31	0.40	0.59	0.83	1.0	1.19	1.04	1.0	0.91	0.67	0.25	0.13	0.08
10^{-2}	0.14	0.16	0.20	0.29	0.53	0.69	0.91	1.11	1.0	0.71	0.50	0.50	0.33	0.30
2×10^{-2}	0.08	0.09	0.11	0.11	0.14	0.33	0.50	0.71	1.0	0.40	0.17	0.06	0.04	0.03

seen that the charge transfer resistance varies from 1.8 to 0.8×10^2 kΩ cm^2. Also, consideration of these values shows that the higher value (180 kΩ cm^2) obtained for 10^{-3} mol dm^{-3} $^3HO_2^-$ would favor passivating. It is observed that the charge transfer resistance decreases when the potentials or ionized peroxide radicals increase, signifying more corrosion.

In the passivity-transpassivity limit, the experimental diagrams obtained in Fig. 17.3e can be explained by the equivalent circuit shown in Fig. 17.5c. The values of the charge transfer resistance are given in Table 17.4. It is seen that the charge transfer resistance decreases when the potential and $^3HO_2^-$ increase, signifying more corrosion.

2.1.3.3. Discussion As indicated by Macdonald et al. [115] and Lorenz et al. [233], it is possible to explain the presence of a diffusion-controlled process within the passive oxide layer. The model contains these basic features:

- the oxide layer contains vacancies ($V_{Me^{n+}}$ and $V_{O^{2-}}$),
- the vacancies are in equilibrium at the ionized peroxide radical–oxide and oxide–alloy interfaces,
- the passive oxide layer kinetics are governed by vacancies across the oxide layer.

Based on these considerations, the following reactions, besides eqs (17.1), (17.3) and (17.4), are in equilibrium at each interface:

- alloy–oxide interface:

$$Me \leftrightarrow \{oxide\} + V_{O^{2-}} \tag{17.10}$$

$$Me + V_{Me^{n+}} \leftrightarrow \{oxide\} \tag{17.11}$$

- oxide–$^3HO_2^-$:

$$V_{O^{2-}} + {}^3HO_2^- + 2e^- \leftrightarrow O^3H^- + O^{2-} \tag{17.12}$$

$$\{oxide\} + nO^3H^- \leftrightarrow V_{Me^{n+}} + Me(O^3H)_n + ne^- \tag{17.13}$$

where {oxide} represents metal cations in the passive oxide layer that are in equilibrium with the metal vacancies. Apparently, $V_{O^{2-}}$ are produced at the oxide–alloy interface and consumed at the oxide-ionized peroxide radical interface. As a result, $V_{O^{2-}}$ diffuses from the oxide–alloy to oxide-ionized peroxide radical interfaces, or equivalently,

O^{2-} diffuses from oxide-$^3HO_2^-$ to oxide–alloy interfaces. Similar arguments show that $V_{Me^{n+}}$ diffuses from the oxide-ionized peroxide radical to alloy–oxide interfaces, and equivalently, {oxide} diffuses in the opposite direction. The net results of $V_{O^{2-}}$ migration can be seen by combining eqs (17.10) and (17.12):

$$Me + {}^3HO_2^- + 2e^- \leftrightarrow \{oxide\} + O\,{}^3H^- + O^{2-} \tag{17.14}$$

Similarly, combining eqs (17.11) and (17.13) shows that the net result of $V_{Me^{n+}}$ migration can be expressed as:

$$Me + nO^3H^- \leftrightarrow Me(O^3H)_n + ne^- \tag{17.15}$$

From the set of previous reactions, it is clear that the diffusion of $V_{O^{2-}}$ (or equivalently O^{2-}) results in oxide growth, depends on flatband potential, and is produced with consumption of $^3HO_2^-$ at the oxide-ionized peroxide radical interface, whereas the diffusion of $V_{Me^{n+}}$ (or equivalently {oxide}) is accompanied by $Me(O^3H)_n$ formation, as in eqs (17.3) and (17.4). The reactions occurring on passive oxide are influenced by the different potential drops in the alloy-oxide and oxide-ionized peroxide radical interfaces and within the oxide layer, where the latter is $\Delta\Phi$. Therefore, these require in addition field-assisted ion transport through the passive layer. Within the passive layer of a few nm, the electrical field strength is of the order of a few hundreds of mV [114], which enables the migration of ions through the oxide layer at a measurable level in currents of a few μA or less. The physical model proposed to interpret the diffusion processes is shown schematically in Fig. 17.6.

The oxide-ionized peroxide radical interface is polarizable, therefore it is expected that the total potential drop is a function of surface $^3HO_2^-$ concentration.

$$\partial\Delta E = \partial\Delta E_{\text{oxide–alloy}} + 2.3\frac{RT}{2F}\left[\partial\log[{}^3HO_2^-]\right] + \partial\Delta\Phi \tag{17.16}$$

where ΔE represents the potential drop between the interfaces and within the oxide layer. It is expected that:

$$\partial\left(C_{ox}^{-1}\right) = \partial\Delta E - 2.3\frac{RT}{2F}\left[\partial\log[{}^3HO_2^-]\right] \tag{17.17}$$

The thickness is given by:

$$\partial d = b\left(\partial\Delta E - 2.3\frac{RT}{2F}\left[\partial\log[{}^3HO_2^-]\right]\right) \tag{17.18}$$

where b is a constant obtained by considering the oxide layer as a plane capacitor. Thus eqs (17.17) and (17.18) represent the functional dependence of the passive layer growth law on $\partial\Delta E$ and $\partial\log{}^3HO_2^-$ up to a determined size preceding the stress and breakdown formation at higher potentials than that corresponding to the 'critical capacitance' in Fig. 17.4.

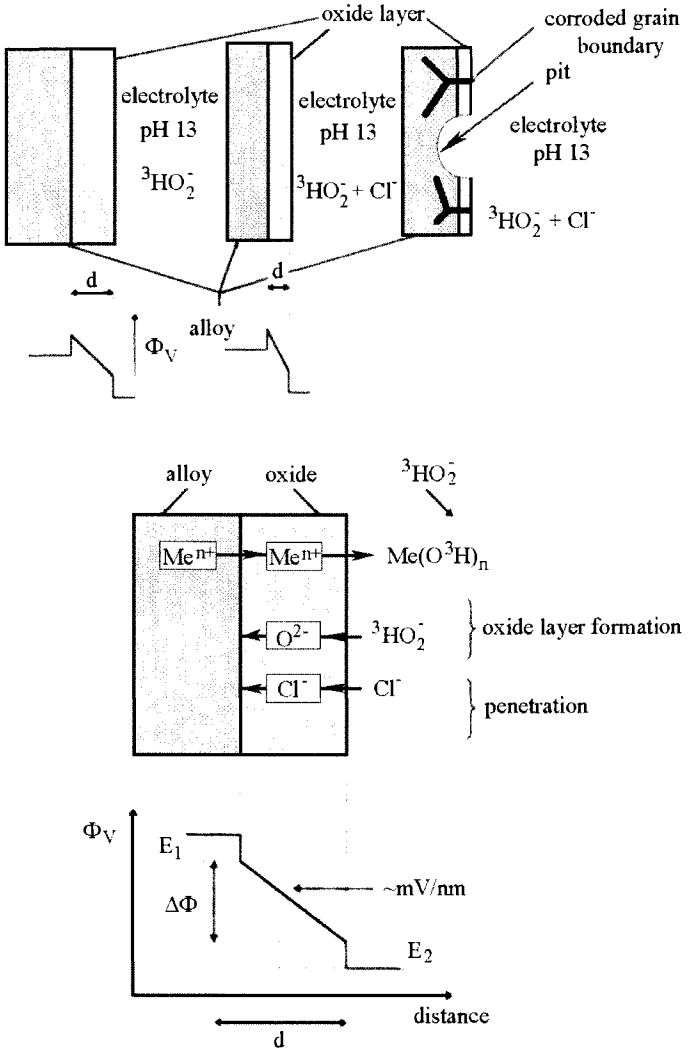

Figure 17.6. Physical model proposed to interpret the diffusion processes, E_1, E_2: potential drops.

2.2. *Results obtained with chloride*

2.2.1. Polarization and voltammetric curves The polarization curves obtained with chloride are shown in Fig. 17.7.

Two regions can be identified: the passive region and a sharply defined pitting region. N08932 steel remains passivated over a large potential domain. The transition potential

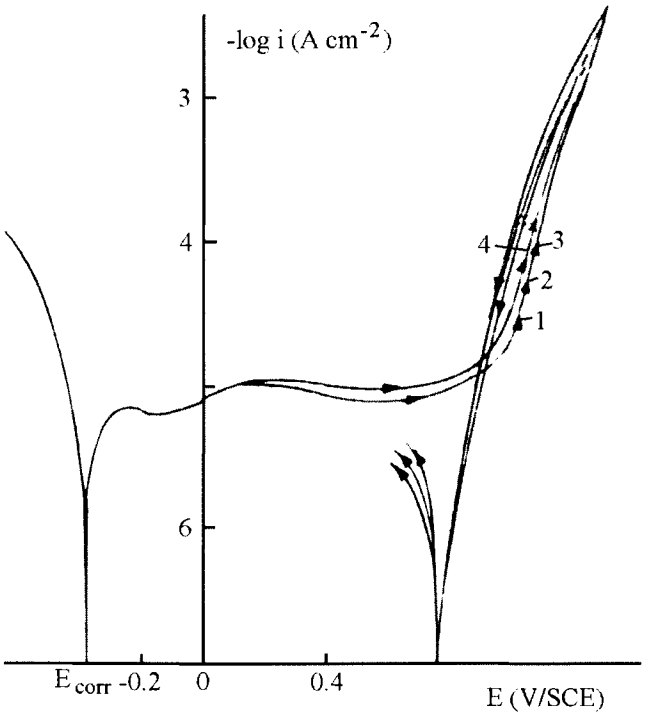

Figure 17.7. Polarization curves with Cl^-, ω: 3000 rpm, v: 5 mV s^{-1}, pH 13, 1: 0.1, 2: 0.2, 3: 0.5, 4: 0.7 mol dm^{-3} Cl^-.

(E_{pit}) decreases slightly with chloride concentration increase. This defines the pitting critical potential for a given chloride concentration. As suggested by the shape of the positive and negative hysteresis, a few pits would continue to initiate and grow but only in the beginning of the backward scan. This clearly defines a very small pitting potential region and shows that the passive oxide provides protection over a large potential domain. It can be seen that the corrosion potential ($E_{corr} = -0.4$ V/SCE) is the same with or without chloride, and the large deviation between E_{corr} and E_{pit} indicates no risk of crevice corrosion. Tests realized by cyclic voltammetry (Fig. 17.8) which is more sensitive than analysis using polarization curves, do not show any modification of pitting current on varying stirring from 50 to 3000 rpm and scan rates from 5 to 100 mV/s. Fig. 17.9 shows the surface morphology obtained by Scanning Electron Micrography. The surface is corroded in places as a result of having had imposed the pitting potential of 1.05 V/SCE with 0.7 mol dm^{-3} Cl^-. A few pits are seen in examinations and these can be repassivated by filling, therefore there is no pitting propagation. This localized corrosion is not seen with light water; it is credible that pitting is facilitated by this medium.

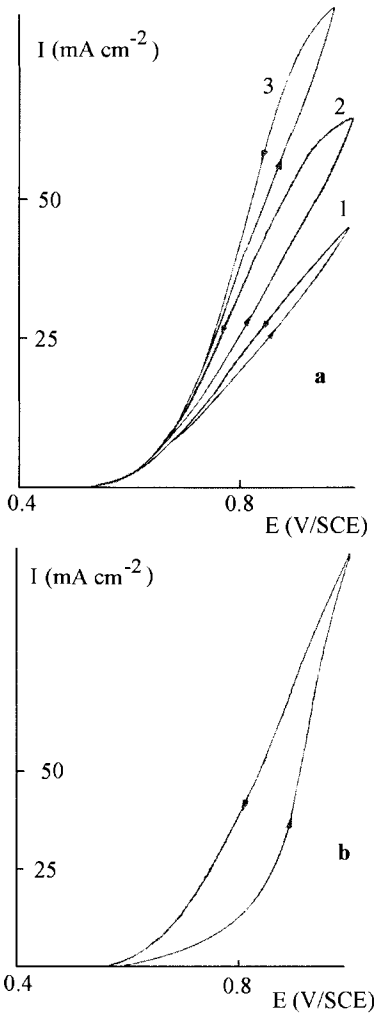

Figure 17.8. Voltammetric curves with Cl^-—electrode rotation and scan rate effects, pH 13, 0.7 mol dm^{-3} Cl^-, (a): ω: 1: 100, 2: 250, 3: 500 rpm, (b): v: 5–100 mV s^{-1}.

2.2.2. Impedance diagrams The experimental Nyquist plots obtained for N08932 steel subjected to different chloride concentrations and high pitting potentials are shown in Fig. 17.10.

A linear region with a slope of 1 is observed in the spectra at higher frequencies. This is characteristic of ion diffusion impedance. Alteration of the angular velocity shifts the frequency in the straight line very slightly and has no effect on the spectra, suggesting that mass transport occurs in the filled pits without changes in pitting. Three time constants are

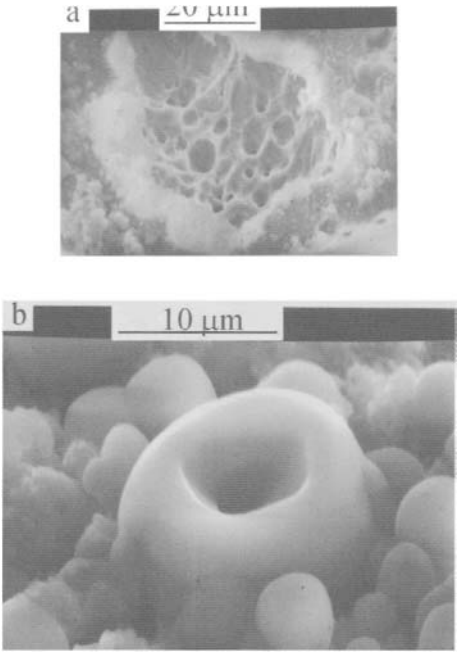

Figure 17.9. Scanning Electron Microscopy of N08932 steel, (a): pits, (b): filling of pits by corrosion products (nipples) in presence of 0.7 mol dm^{-3} Cl^- at 1.05 V/SCE.

observed, two of which are inductive at lower frequencies and should be associated with relaxation processes in the oxide layer as indicated by Keddam et al. [229]. The diameter of the capacitive semi circle depends on the chloride concentration. To provide physical significance for these spectra, an equivalent circuit is proposed in Fig. 17.5d so that the simulated spectra coincide with the experimental diagrams. In this circuit, the total impedance (Z) is given by:

$$1/Z = 1/R_{el} + j\omega C_{dl} + 1/Z_F \tag{17.19}$$

$$Z_F = R_{lc_1} + \frac{j\omega L_n R_{lc_2}}{j\omega L_n + R_{lc_2}} \tag{17.20}$$

where inductances represent the adsorption phenomenon and R_{lc_n} are the resistances implied in the process. In eq. (17.20), R_{lc_1} also includes a time constant given as D/δ^2 where δ is the diffusion layer thickness. Suitable values of the circuit elements were obtained for the pitting potentials (Tables 17.5 and 17.6). It can be seen that the impedance value is reduced as the spectrum passes from the passive-pitting limit range to the pitting range. Also, the onset of pitting can be clearly determined by considering the spectra. They show

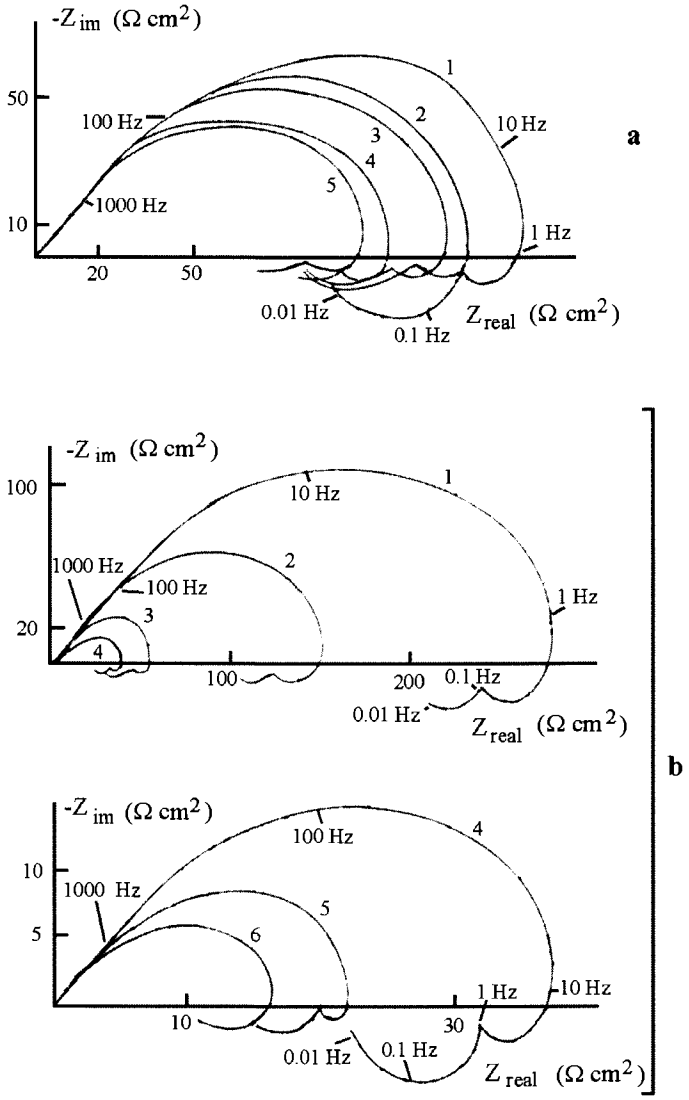

Figure 17.10. Nyquist spectra—Cl^- concentration and potentials effects, pH 13, ω: 3000 rpm, (a): 1: 0.05, 2: 0.1, 3: 0.2, 4: 0.3, 5: 0.5 mol dm^{-3} Cl^-, 1.05 V/SCE, (b): 1: 1.02, 2: 1.05, 3: 1.1, 4: 1.12, 5: 1.15, 6: 1.17 V/SCE, 0.5 mol dm^{-3} Cl^-.

capacitive and inductive behaviors when pitting propagates and repassivates under the applied potential and corresponding Cl^- concentration. Note that according to eqs (17.19) and (17.20), the limiting value of Z_F for $j\omega \rightarrow 0$ should be equal to the repassivation resistance, which also corresponds to the polarization resistance for polarization curves

Table 17.5. Dependence of localized corrosion resistances on different transpassive potentials

Cl^- (mol dm^{-3})	0	0.1	0.2	0.35	0.5
R_{lc_1} ($\Omega\,cm^2$)	160	150	130	120	80
R_{lc_2} ($\Omega\,cm^2$)	19	18	16	15	12

Table 17.6. Dependence of localized corrosion resistances on Cl^- concentrations

E (V/SCE)	1.02	1.05	1.1	1.12	1.15	1.17
R_{lc_1} ($\Omega\,cm^2$)	240	160	80	60	25	19
R_{lc_2} ($\Omega\,cm^2$)	30	19	12	10	10	10

obtained at a steady state. The electrolyte resistance, like R_{lc} decreases when chloride and potentials increase; this results from an increase in solution electrical conductivity induced by corrosion.

2.3. Results obtained with chloride and ionized peroxide radical

2.3.1. Polarization curves According to Strehblow [114] and Macdonald [115,116], if the metal vacancies penetrate the alloy at a slower rate than their diffusion through the oxide layer, they accumulate at the alloy–oxide layer interface and finally lead to a local concentration and hence will form a void. When the void grows to a certain critical size, the passive oxide layer suffers local collapse which then marks the end of the pit incubation period. The collapsed site dissolves much faster than any other location on the layer thereby leading to pit growth. From this, the diffusion of metal vacancies is affected by the incorporation of Cl^- ions at the oxide–$^3HO_2^-$ interface as shown in Fig. 17.6 and in the following equations:

$$V_{Me^{n+}} - \frac{n}{2} V_{O^{2-}} = 0 \tag{17.21}$$

$$C_{V_{Me^{n+}}} = k(C_{V_{O^{2-}}})^{-0.5n} \tag{17.22}$$

$$V_{O^{2-}} + Cl^-_{aqueous} \leftrightarrow \{Cl^-\} \tag{17.23}$$

Equation (17.21) represents the Schottky-pair reaction at the oxide–$^3HO_2^-$ interface. In eqs (17.22) and (17.23), $\{Cl^-\}$ is a chloride anion occupying O^{2-} vacancies and C the vacancies concentrations with an inverse dependence on $V_{Me^{n+}}$ and $V_{O^{2-}}$. It can be seen that the number of free $V_{O^{2-}}$ vacancies decreases. Due to interdependence of the concentration of metal and O^{2-} vacancies and the penetration of Cl^- within the oxide layer as shown by ellipsometry [238], the number of metal vacancies increases in the oxide layer up to a critical concentration leading to breakdown at the pitting potential. From these

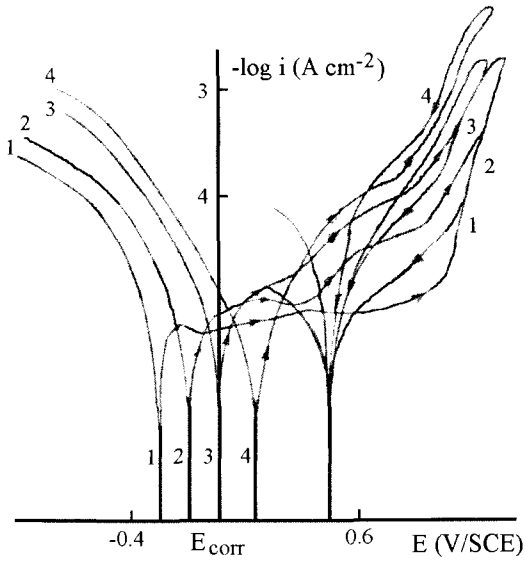

Figure 17.11. Polarization curves with $^3HO_2^-$ and Cl^-, ω: 3000 rpm, v: 5 mV s^{-1}, pH 13, 0.7 mol dm^{-3} Cl^-, 1: 10^{-3} mol dm^{-3}, 2: 5×10^{-3} mol dm^{-3}, 3: 10^{-2} mol dm^{-3}, 4: 2×10^{-2} mol dm^{-3} $^3HO_2^-$.

considerations, the criterion for pit initiation in the presence of $^3HO_2^-$ can be expressed by:

$$\frac{\partial V_{Me^{n+}}}{\partial t} = J_0\left[C_{V_{O^{2-}}}\{\text{oxide}-^3HO_2^-\}\right]^{-0.5n} \tag{17.24}$$

where J_0 depends on thermodynamic constants and $C_{V_{O^{2-}}}\{\text{oxide}-^3HO_2^-\}$ is the concentration of O^{2-} vacancies at the oxide layer–$^3HO_2^-$ interface. Equation (17.24) shows that the diffusion of metal vacancies is enhanced by decreasing the concentration of O^{2-} vacancies, e.g. with chloride present. This enhancement can effectively lead to an accumulation of metal vacancies at the alloy–oxide layer interface. From eqs (17.21) and (17.24), and applying a calculation procedure similar to that given by Strenblow [114] and Macdonald et al. [115,116], we can write the simplified equation in the presence of $^3HO_2^-$:

$$E_{pit} = \frac{4.6RT}{\alpha Fn}\log\left(\frac{J_m}{J_0\frac{M}{\rho}\exp\left\{\frac{^3HO_2^-}{RT}\right\}^{0.5n}}\right) - \frac{2.3RT}{\alpha F}\log Cl^- \tag{17.25}$$

where J_m is the rate of submergence of the metal vacancies in the alloy. It can be seen that low submergence rates and the presence of $^3HO_2^-$ facilitate pitting by Cl^-.

The polarization curves obtained with $^3HO_2^-$ are shown in Fig. 17.11. The passive potential domain decreases rapidly as the pitting potential shifts towards negative values, and

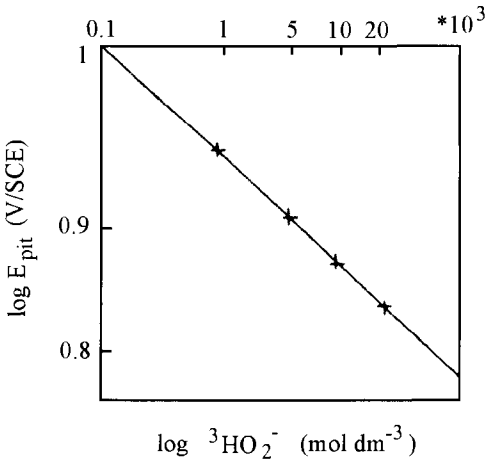

Figure 17.12. Pitting initiation potentials logarithm as a function of Cl^- and $^3HO_2^-$ logarithm.

the corrosion potential shifts towards more positive values. As shown by the negative hysteresis shape, the repassivity potential does not change at different $^3HO_2^-$ concentrations, which makes it a little more difficult to obtain crevice corrosion at the lower $^3HO_2^-$ concentration. The smaller difference between the corrosion potential and pitting potential shows more susceptibility to crevice corrosion at high ionized peroxide radical concentration. The current in passivity is higher than that obtained in Fig. 17.1. These different results imply that the ionized peroxide radical does not provide better protection under these conditions and the number of pits or the locally corroded area must increase.

In Fig. 17.12, the pitting potential logarithm is plotted as a function of the logarithm of the ionized peroxide radical concentration. It can be seen that E_{pit} decreases with $^3HO_2^-$ which confirms the validity of eq. (17.25) indicating a linear variation with $^3HO_2^-$. From scanning micrographs (Fig. 17.13), it is seen that the N08932 steel is highly corroded over all the surface with localized corrosion: this takes the form of pitting and grain boundary dissolution (Fig. 17.6).

This local corrosion would appear to be due to an element-depleted zone along the grain boundary by the Cl^- and $^3HO_2^-$ mixture. It is accepted that a depletion in chromium concentration on both sides of the grain boundaries is the origin of susceptibility to intergranular corrosion. This chromium depletion can be minimized by carrying out a suitable annealing or by adding stabilizing elements (Ti, Nb) which tend, by diffusion, to homogenize the chromium content in this zone. Also, examinations of the bottom of a small number of shallow pits show corrosion product deposits which could lead to crevice formation in the area.

There are several explanations in the literature concerning the corrosion mechanisms for steels containing nitrogen that provide better understanding of these experimental results for localized corrosion based on electrochemical methods. These different explanations are

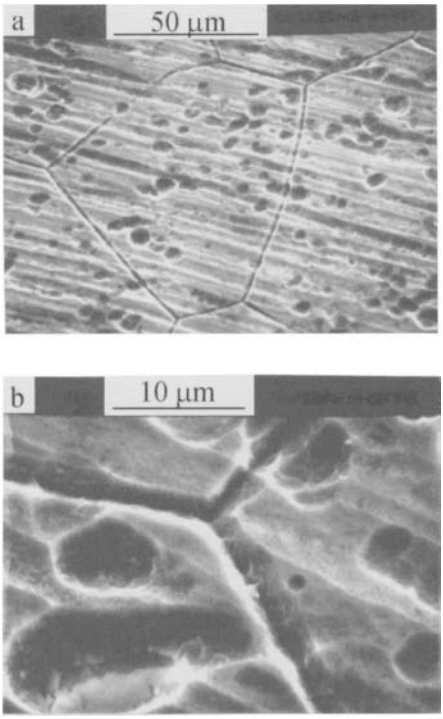

Figure 17.13. Scanning Electron Microscopy photographs of N08932 steel corroded locally by pitting and in grain boundaries in presence of Cl^- and $^3HO_2^-$ at 1.05 V/SCE, (a): magnification of 600, (b): magnification of 3000.

provided by surface examinations at acid pH and in the presence of chloride. On the other hand, details of mechanisms in the passive-transpassive region have not yet been published for chloride and oxidizing species such as ionized peroxide radicals at slightly alkaline pH. Previous work has shown, by X-ray photo-electron spectrometry and Auger electron spectroscopy analysis with a focus on the lateral and depth distributions, that nitrogen modifies the surface composition and changes corrosion mechanisms. For example, according to Pagetti et al. [239], there are higher chromium and nitrogen concentrations at grain boundaries. These can lead to element depletion around these boundaries and to passive oxide layer transformations and variation in the face centered cubic austenite lattice when the nitrogen concentration increases. Depletion around the grain boundaries of passivating elements would tend to modify the corrosion behavior of N08932 stainless steel in the case of oxidizing $^3HO_2^-$ and Cl^- at alkaline pH. Pagetti et al. [239], Olsson [240], Olefjord and Wegrelius [241], Clayton et al. [242] and Huang et al. [243] agree that with polarization in the cathodic-active and passive regions, nitrogen seems to be transformed to NH_3 which is retained at the surface and in aqueous solution. According to Olsson [240] and Clayton et al. [242], in the passive-transpassive region there is a possibility of the formation of sol-

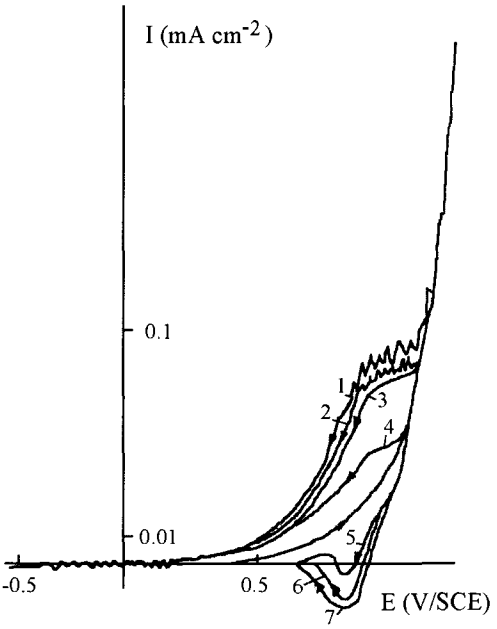

Figure 17.14. Voltammetric curves with Cl^- and $^3HO_2^-$ for different scan rates, ω: 1000 rpm, pH 13, 0.7 mol dm^{-3} Cl^-, 2×10^{-2} mol dm^{-3} $^3HO_2^-$, v: 1: 5, 2: 10, 3: 25, 4: 50, 5: 70, 6: 80, 7: 100 mV s^{-1}.

uble oxidized species, for example NO_2^- via a reaction suggested by the potential-pH equilibrium diagram [244]. Nitrogen depletion occurs at passive-transpassive potentials when the passive oxide layer becomes locally broken. Clayton et al. [242] suggest that in passivity, nitrogen segregates at the oxide–alloy interface. The surface becomes enriched with nitrogen as a surface nitride. The composition of the alloy under the passive oxide layer changes markedly as indicated by Olefjord and Wegrelius [241]. Nickel is enriched while Fe, Cr and Mo are depleted at the interface to produce a passive layer with more Cr and Mo which enhance repassivation of initiated pits as seen in our micrographs (Fig. 17.13). Auger spectroscopy shows that pits are covered by Fe chloride corrosion products.

2.3.2. Voltammetric curves In Fig. 17.14, a decrease in the scan rate leads to increasing the pitting currents in the backward scan which are higher than those obtained in the forward scan up to 50 mV/s.

In localized corrosion, using low scan rates, chlorides, in presence of $^3HO_2^-$, are more readily adsorbed and subsequently diffuse in the oxide layer following their respective kinetics. The existence of anodic current fluctuations results from the occurrence of metastable pits (prepitting events) in potentials close to pitting with competitive adsorption between the Cl^- and $^3HO_2^-$ ions, or oxide breakdowns due to displacement of the corrosion potential in the active-passive transition region by $^3HO_2^-$ as indicated in section 2.1.1.

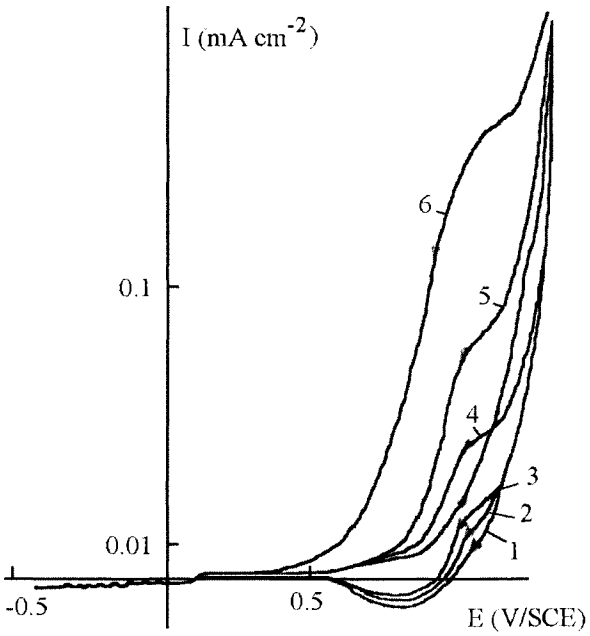

Figure 17.15. Voltammetric curves with Cl^- and $^3HO_2^-$ for different electrode rotation rate, v: 50 mV s^{-1}, pH 13, 0.7 mol dm^{-3} Cl^-, 2×10^{-2} mol dm^{-3} $^3HO_2^-$, ω: 1: 50, 2: 100, 3: 200, 4: 500, 5: 1000, 6: 2000 rpm.

The fluctuation frequency, the maximum fluctuation intensity, and the fluctuation potential increase with low and disappear at high scan rates. It can be deduced that at low scan rates the breakdowns and prepitting events have the time to develop, therefore these depend on kinetics. Note that the lower fluctuations occur near the passivity corresponding to the more compact oxide, and in the active-passive transition region where these, in some cases, have negative current values signifying repassivity and breakdowns alternatively.

In Fig. 17.15, stirring increases the pitting current in the backward scan which is higher than those in the forward scan above 500 rpm. This behavior is surprising in pitting corrosion. On increasing stirring, the pitting current should decrease, but in fact it changes in the opposite direction. This result is explained by the presence of $^3HO_2^-$ and transitory oxidizing species. Stirring favors the convective diffusion of such species as in the Levich equation which increases the amount of reducible ionized peroxide radical at the N08932 steel surface. This shows that pitting by Cl^- is significantly dependent on the hydrodynamic layer formed of $^3HO_2^-$, and the rate determining processes depend more on the quantity of this layer at the surface than on chloride adsorption. No current fluctuations are seen, the kinetics of oxide layer breakdowns are so slow that at this high scan rate they are not observable.

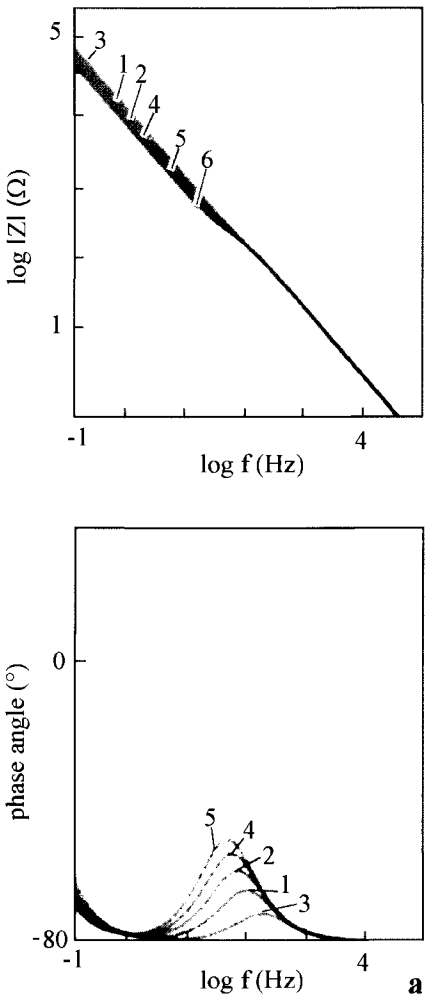

Figure 17.16. Bode diagrams in passivity with $^3HO_2^-$ and 0.7 mol dm^{-3} Cl^-, (a): $^3HO_2^-$: 10^{-3} mol dm^{-3}, 1: −0.05 V, 2: 0 V, 3: 0.05 V, 4: 0.1 V, 5: 0.15 V, 6: 0.2 V/SCE, (b): $^3HO_2^-$: 10^{-2} mol dm^{-3}, 1: 0 V, 2: 0.25 V, 3: 0.05 V, 4: 0.075 V, 5: 0.1 V, 6: 0.2 V/SCE, (c): $^3HO_2^-$: 2×10^{-2} mol dm^{-3}, 1: 0.15 V, 2: 0.2 V, 3: 0.25 V, 4: 0.3 V, 5: 0.4 V/SCE.

2.3.3. Electrochemical impedance spectroscopy The experimental Bode plots obtained for N08932 steel subjected to a constant Cl^- and different $^3HO_2^-$ concentrations and for different passive potentials are shown in Fig. 17.16.

The Bode plots are characterized as previously (see subsection 2.1.3) by the same distinct regions. However, in this section we discuss a different behavior in that the electrolyte resistance is clearly negligible with respect to the interfacial impedance in the oxide forma-

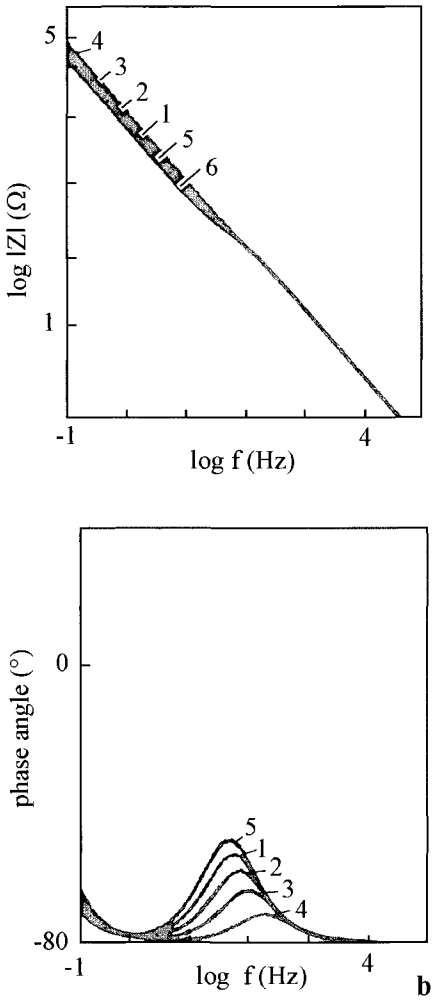

Figure 17.16. (Continued).

Table 17.7. Dependence of oxide capacitance (μF cm^{-2}) on passive potentials with Cl^- and different $^3HO_2^-$ concentrations (mol dm^{-3}), underlined numbers: characteristic oxide layer zone

$^3HO_2^-$	E (V/SCE)											
	−0.05	−0.01	0	0.02	0.05	0.07	0.1	0.15	0.2	0.25	0.3	0.4
10^{-3}	16	15	12	11	10	9	10	11	11	12	14	26
5×10^{-3}	20	17	14	13	12	11	10	10	11	15	20	70
10^{-2}	40	35	30	25	20	15	13	11	11.5	12	30	90
2×10^{-2}	90	80	70	60	50	42	33	15	13	25	59	120

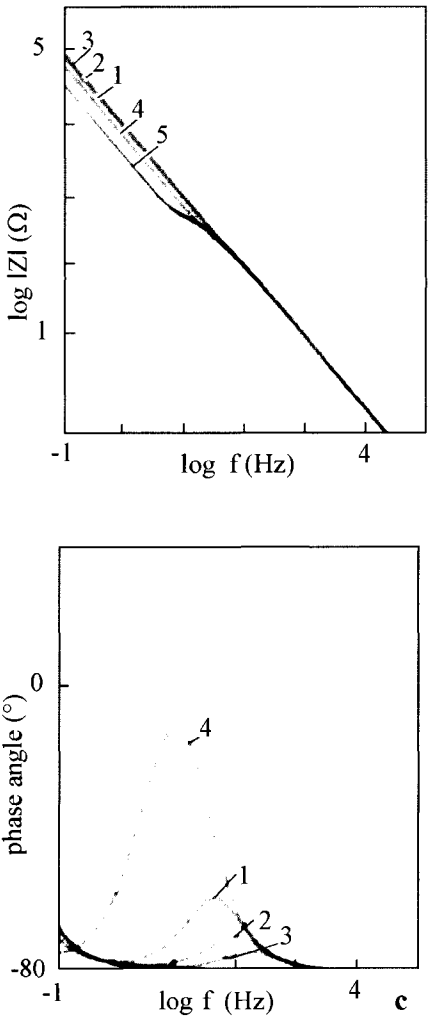

Figure 17.16. (Continued).

Table 17.8. Dependence of electrode resistance (10^2 kΩ cm^2) on passive potentials with Cl^- and different $^3HO_2^-$ concentrations (mol dm^{-3})

$^3HO_2^-$	*E* (V/SCE)											
	−0.05	−0.01	0	0.02	0.05	0.07	0.1	0.15	0.2	0.25	0.3	0.4
10^{-3}	0.62	0.67	0.83	0.91	1.0	1.11	1.0	0.91	0.91	0.83	0.71	0.39
5×10^{-3}	0.50	0.59	0.71	0.77	0.83	0.91	1.0	1.0	0.91	0.67	0.50	0.14
10^{-2}	0.25	0.29	0.33	0.40	0.50	0.67	0.77	0.91	0.87	0.83	0.33	0.11
2×10^{-2}	0.11	0.13	0.14	0.17	0.20	0.14	0.30	0.67	0.77	0.40	0.17	0.08

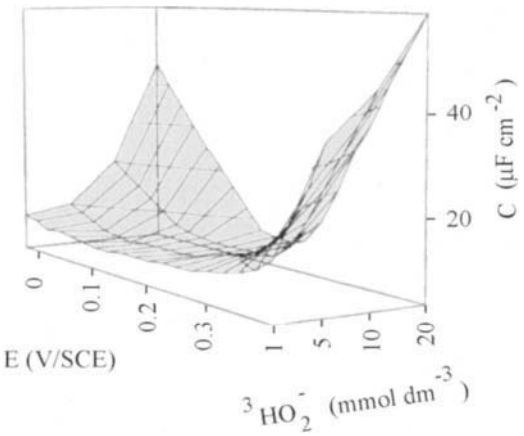

Figure 17.17. Oxide layer capacitance as a function of passive potentials and $^3HO_2^-$ and Cl^-.

tion region and provides direct observation of the inflection in the $\log|Z|$ plots. Neglecting the electrolyte resistance, the values of different elements are obtained more easily in spectra allowing observation of the oxide layer changes with the Cl^- and $^3HO_2^-$ mixture. Data in Tables 17.7, 17.8 and Fig. 17.17 indicate that oxide capacitance increases.

Effectively, comparison with Tables 17.3 and 17.4 and Fig. 17.4 shows that the passive oxide layer is less insulating; this signifies adsorption and diffusion of Cl^- within the oxide. This interpretation can be verified by determining the charge donor density. The values obtained are between 0.9 and 4×10^{20} carrier cm^{-3}. These values, that are higher than without Cl^- indicate, from eqs (17.22) to (17.24), that the O^{2-} vacancies decrease and Me^{n+} vacancies in equilibrium with metal cation increase with chloride, improving the diffusion. It thus appears that chloride ions adsorb and diffuse corresponding to the incubation period. The oxide thickness is also determined, its value is about 2 nm, and is lower than without Cl^-, which gives a higher electrical field strength, reducing corrosion resistance (Fig. 17.6).

The Nyquist plots obtained for N08932 steel subjected to different $^3HO_2^-$ concentrations are shown in Fig. 17.18a. Along the capacitive semi circle, a linear unit slope region at high frequencies is observed (Fig. 17.18b). This is a characteristic of a mass transport process. Changes in $^3HO_2^-$ concentration affect the frequency shift in the straight line and capacitive semi circle suggesting mass transport is dependent on $^3HO_2^-$ concentration and transitory oxidizing species. The capacitance value obtained from $C = (\pi f R_{real})^{-1}$, f being the frequency at the top of semi circle, does not correspond to a passive layer capacitance ($\sim 5\ \mu F\,cm^{-2}$) indicating that an electrochemical process implying corrosion with $^3HO_2^-$ occurs. Fig. 17.19 shows the effect of the disk rotation rate in the impedance diagrams.

Alteration of the disk rotation rate slightly affects the frequency shift in the straight line and capacitive semi circle. Moreover, on increasing stirring, there is a decrease in size of the capacitive semi circle obtained at high frequency. These behaviors suggest, in this

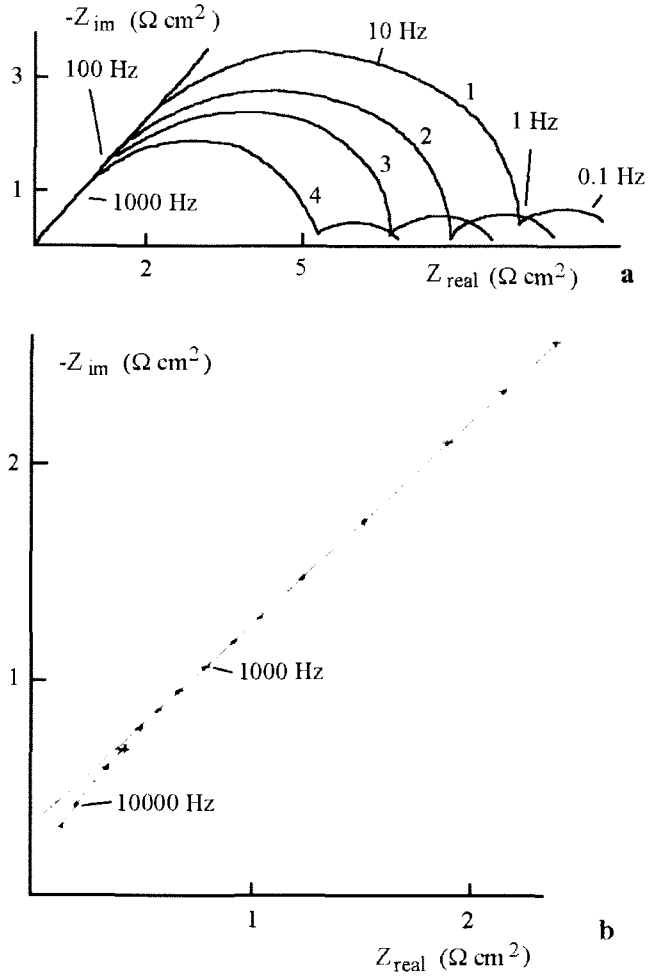

Figure 17.18. Nyquist spectra with $^3HO_2^-$ and Cl^-, pH 13, ω: 2000 rpm, E: 1.05 V/SCE, 0.7 mol dm^{-3} Cl^-, 1: 2×10^{-3}, 2: 4×10^{-3}, 3: 8×10^{-3}, 4: 1.2×10^{-2} mol dm^{-3} $^3HO_2$, (a): full spectra, (b): spectra showing the straight line at higher frequencies.

situation, that mass transport occurs in the tritiated water. The spectra are affected by rotation rate at long hold times signifying active surface modification by aggressive ions. The presence of $^3HO_2^-$ and Cl^- modifies the spectra with the exposure time which can lead to a decrease in corrosion resistance. It should also be noted that the entire loop is observed at low frequencies as rotation rate decreases, which is in agreement with an adsorbate and pitting processes by the appearance of the inductive effect. In order to account for these observations, $^3HO_2^-$ reduction and pitting processes take place simultaneously. From these

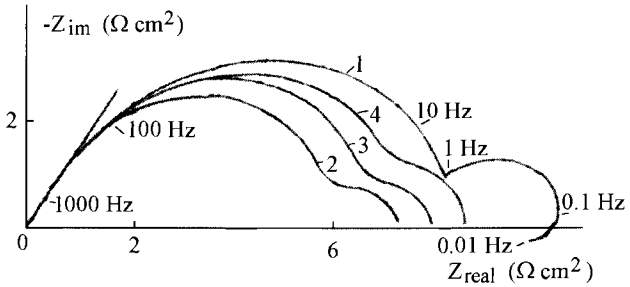

Figure 17.19. Nyquist spectra with $^3HO_2^-$ and Cl^-, pH 13, 0.7 mol dm^{-3} Cl^-, 1.2 × 10^{-2} mol dm^{-3} $^3HO_2^-$, E: 1.05 V/SCE, 1: 500 rpm, 2: 750 rpm, 3: 1000 rpm, 4: 500 rpm after holding N08932 steel for 15 min.

observations, and those in voltammetry, it can be seen that $^3HO_2^-$ reduction and pitting initiation vary inversely with rotation rate. $^3HO_2^-$ reduction is enhanced whereas pitting decreases with stirring. The experimental diagrams can be satisfactorily explained on the basis of the equivalent circuit approach presented in Fig. 17.5d, which includes the Randles diffusion impedance. From this, the electrode impedance decreases at higher $^3HO_2^-$ concentration or potentials; this is the result of increasing corrosion. From the general equations giving the relation between the diffusion coefficient and the diffusion thickness [103] and the experimental results, the diffusion layer thickness is a few tens of μm.

3. Conclusions

The observed dependence between the oxide layer and ionized peroxide radical suggest better passivity at a low $^3HO_2^-$ concentration and for free and corrosion potentials outside the active and passive-transpassive ranges. In this medium, the passive potential domain becomes narrower: the transpassive potential shifts slightly towards negative values, and the corrosion potential towards more positive values. At high $^3HO_2^-$ concentrations and with Cl^-, N08932 steel is locally corroded by pitting and grain boundary dissolution. Oxidizing radiolytic media favor highly the localized corrosion of stainless steel by chloride.

This Page Intentionally Left Blank

Chapter 18

PASSIVATION BY RADIOLYTIC CARBONATE

1. Introduction

The presence of carbonate is explained by the fact that organic polymers are decomposed by reactions induced by the low energy released from β^- particles:

$$-(^3\text{H–R–}^3\text{H})_n- + 3\text{O}^* + \beta^- \rightarrow \text{CO}_3^{2-} + -(^3\text{H–R}'-^3\text{H})_{n'}- \qquad (18.1)$$

Data on metal oxide-carbonate layers can be found in publications by Abdelmoula et al., Drissi et al. and Blengino et al. [245–247]. According to these authors, the corrosion resistance of stainless steels depends on their carbonate content and therefore, the behavior of oxide layers was studied from the corrosion potential to the passive and transpassive potentials. Also, the formation of transient oxides and their modification at the electrode surface have not been studied extensively. One of the aims of this work is to have a better understanding of the effects of the transient oxide layer.

2. Materials and preparation

The composition of the S31803 stainless steel is given in Table 18.1. This steel is characterized by a two-phase structure comprising a mixture of austenite, γ, and ferrite, α, grains. This sample contains 45.8% ferrite, and the average grain size is 20μm for the austenite and 7μm for the ferrite. This alloy can be considered as a standard Duplex stainless steel, and whose nitrogen content (0.16%) has been increased to improve further its pitting corrosion resistance in oxidizing chloride-rich media. The corrosion resistance is equivalent to that of the super-austenite steels containing 5–6% Mo. Fig. 18.1 shows the etched surface microstructure where the ferrite phase appears as light filiform grains, the austenite is in gray for comparison and the sigma phase as black aggregates inside γ and α grains.

This specimen obtained from an as-rolled plate shows the orientation grains in the longitudinal section (photograph (a)) and the cross-section (photograph (b)). S31803 steel was

Table 18.1. S31803 stainless steel—composition

Elements	Cr	Ni	Mo	N	Si	Mn	P	Cu	S	C	Fe
Wt%	22.5	5.5	3	0.16	0.57	1.5	0.02	0.18	< 0.002	0.02	bal.

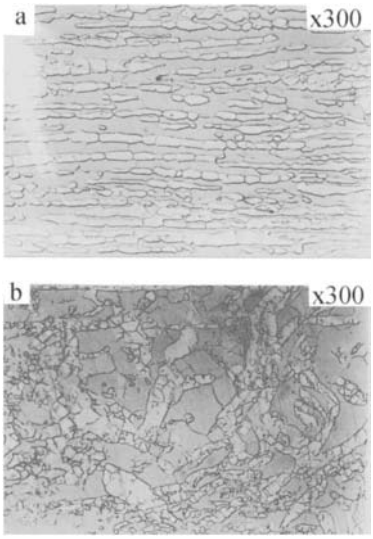

Figure 18.1. Metallographic examinations in longitudinal (photograph (a)) and cross-sections (photograph (b)) showing austenite and ferrite grains.

Table 18.2. Partition coefficient α/γ between ferrite and austenite phases

Cr	Ni	Mo	Si	Cu	Mn
1.1	0.6	1.65	1.15	0.67	0.86

obtained by work-hardening, followed by annealing and quenching with control of the two phase structure $\sim 50\gamma/50\alpha$ and the element partition coefficient between the austenite and ferrite phases (Table 18.2). The quenching conditions are very critical and must be rigorously respected to obtain the desired precipitation of the austenite and ferrite phases. For example, rapid quenching starting at 1050°C while keeping the temperature at 700–900°C leads to formation of a fine intergranular austenite precipitate in the ferrite grains. According to Charles [49], Desestret and Charles [50] and Ravindranath and Malhotra [248], numerous structural changes can occur in the Duplex stainless steel during heat treatments and quenching, leading to precipitation of intermetallic phases (σ, χ and ε) that affect the corrosion resistance. The austenitic-structure, copper-rich ε phase does not appear to be responsible for the very marked localized corrosion. Formation of the σ phase with or without intermediate χ phase formation deserves greater attention due to its rapid formation and the effects on corrosion. Experience has shown that only splat cooling completely avoids any precipitation in S31803 steel. The added elements contribute to equilibrating the grade. These are classed in two families: one made up of gamma phase-producing elements (Ni, N, Cu), the other of alpha phase-producing elements (Cr, Mo). Hardening precipitates, such as Cr_2N-type nitrides, can be produced in the γ/α or α/α grain boundaries. It is also observed that σ precipitation starts at either γ/α or α/α boundaries and grows into the

two matrix phases. In practice, the annealing temperature chosen is as low as possible, but sufficient to take any precipitate phases into solution. The amounts of the γ and α phases are related to the balance between γ-stabilizers and α-stabilizers. These stabilizers aid in avoiding localized corrosion of one phase or another. In practice, increasing the nitrogen content will lead to a marked enrichment of this element in the austenite without changing its level in the ferrite.

3. Experimental results

The tests were made immediately after decomposition of the radiolytic hydrogen peroxide and dissolved oxygen in tritiated water by electrolytic reduction to avoid their effects on measurements.

3.1. Anodic polarization curves

Plotting polarization curves at a low scan rate shows the active behavior modifications (Fig. 18.2a).

It can be seen that the corrosion potential decreases when the CO_3^{2-} concentration increases. At this potential, corrosion should occur at the cathodic and anodic sites. The cathodic reactions and the formulae of the corresponding currents are given in the previous chapters. For the anodic sites, the reactions are:

$$\mathrm{Me} + \mathrm{O^3H^-} \rightarrow \mathrm{MeO^3H_{ads}} + \mathrm{e^-} \tag{18.2}$$

$$\mathrm{MeO^3H_{ads}} \rightarrow \{\mathrm{MeO^3H^+}\} + \mathrm{e^-} + \cdots + \mathrm{O^3H^-} \rightarrow \{\mathrm{Me(O^3H)_2\text{-oxide phase}}\} \tag{18.3}$$

$$\begin{aligned}(x+y)\{\mathrm{Me(O^3H)_2\text{-oxide phase}}\} + \mathrm{CO_3^{2-}} + 2\,{}^3\mathrm{H_2O} \\ \rightarrow \{\mathrm{Me_x^{(II)}Me_y^{(III)}(O^3H)_{2(x+y)}}\}\mathrm{CO_{3hydrated}} + n\mathrm{e^-}\end{aligned} \tag{18.4}$$

$$\begin{aligned}\{\mathrm{Me_x^{(II)}Me_y^{(III)}(O^3H)_{2(x+y)}}\}\mathrm{CO_{3hydrated}} \\ \rightarrow (x+y)\mathrm{MeOO^3H} + 2\,{}^3\mathrm{H_2O} + \mathrm{CO_3^{2-}} + (x+y)\,{}^3\mathrm{H^+} + m\mathrm{e^-}\end{aligned} \tag{18.5}$$

$$2\mathrm{MeOO^3H} \rightarrow \mathrm{Me_2O_3} + {}^3\mathrm{H_2O} \tag{18.6}$$

The exact formula of the oxy-carbonated complex for iron was established by Abdemoula et al., Drissi et al. and Blengino et al. [245–247]. In our case, as the different constituents of the Duplex steel will also be involved in the oxide surface composition,

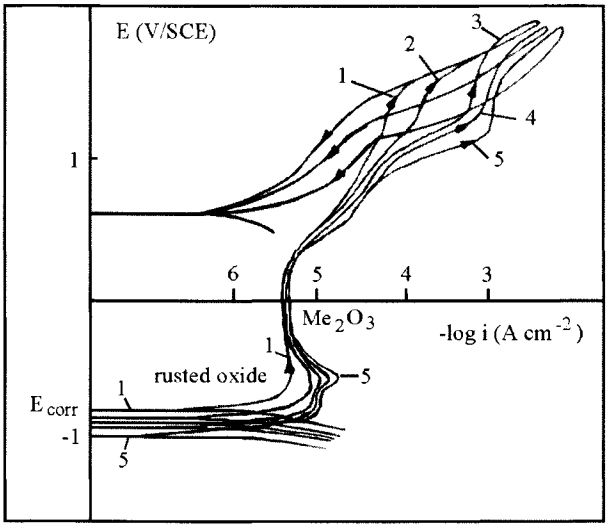

a

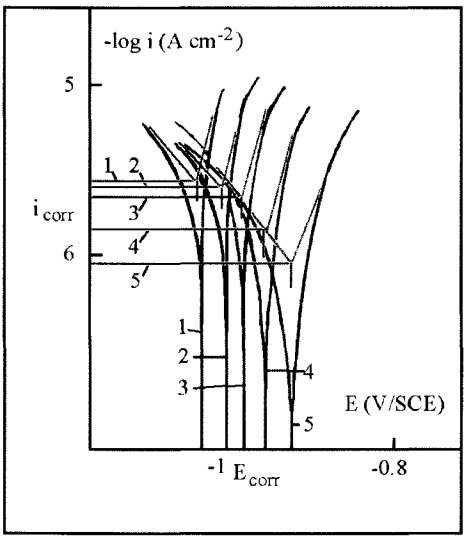

b

Figure 18.2. Polarization curves with and without carbonate, (a): ω: 2000 rpm, v: 5 mV s^{-1}, pH 10, 1: 0, 2: 10^{-3}, 3: 10^{-2}, 4: 2×10^{-2}, 5: 5×10^{-2} mol dm^{-3} CO_3^{2-}, (b): corrosion potential region, 1: 0, 2: 10^{-3}, 3: 10^{-2}, 4: 2×10^{-2}, 5: 5×10^{-2} mol dm^{-3} CO_3^{2-}.

we cannot directly apply these authors' formula. In addition, it is very difficult to implement these surface analysis techniques in a highly contaminated glove box. Consequently, we introduce the subscripts x and y in the oxy-carbonated complex formula without giving their values. Equations (18.2) to (18.5) correspond to transient formation, and eq. (18.6) contributes to the passivity by means of {$Me(O^3H)_2$-oxide phase} and Me_2O_3. $\{Me_x^{(II)}Me_y^{(III)}(O^3H)_2(x+y)\}CO_{3hydrated}$ must be understood as the formula of a passivated hydroxide-carbonated oxide layer studied previously by Abdelmoula et al., Drissi et al. and Blengino et al. [245–247], and $MeOO^3H$ is the 'wet' tritiated oxide together with 'dry' Me_2O_3 passive oxide formed on S31803 steel. From these equations, if this alloy is left in tritiated water, the rusted layer should oxidize into $MeOO^3H$. This layer therefore plays an important role in the corrosion processes and passivity of steels in general, since it is involved in the oxidation of divalent hydroxide, as the transient intermediate compound between initial MeO^3H^+ and the final trivalent oxyhydroxide. As above, the anodic current is:

$$i_a = 2k_a F\left[O^3H^-\right]^{\nu_{ox}}\left[CO_3^{2-}\right]^{\nu'_{ox}} \exp FE/RT \tag{18.7}$$

These equations indicate that carbonate and hydroxide ions present in tritiated water play an active role in the S31803 steel corrosion processes. There is experimental evidence that CO_3^{2-} is selectively present in the rusted layer, $\sim 4\%$, according to Abdelmoula et al. [245,246]. In this work, the authors examined the surface oxide by X-ray diffraction and conversion electron Mössbauer spectroscopy. It can be seen from the results that the rusted layer is formed and covers the surface with a homogeneous layer corresponding to the approximate formula $\{Me_x^{(II)}Me_y^{(III)}(O^3H)_{2(x+y)}\}CO_{3hydrated}$.

In the polarization curves, the passive currents are higher with carbonate ions. The explanation for this could be that carbonates are incorporated into the oxide and lead to a defective layer and less insulating 'dry' oxide. Equation (18.5) shows that lower pH is produced resulting in local corrosion and acidity. From these equations, it can be seen that carbonate ions interact in the strata forming a passive layer. According to Bohnsack et al. [249], Raman spectroscopy shows that the carbonated layer is associated with corrosion inhibition and has been identified as actively participating in the formation of a protective layer. Sontheimer et al. [250] assumed that the solid carbonate layer acts as a transformation agent to the final oxyhydrate protective layer. If this is true, the carbonate layer should be observed. Castro et al. [251] and Rubim and Dunnwald [252] using X-ray photoemission spectroscopy and Raman spectroscopy showed that carbonate is present in the layer before passivity by Me_2O_3. Therefore, a carbonate-oxide layer is a precursor to Me_2O_3 formation. An oxycarbonate layer may aid in the chemical processes associated with a passive layer.

The corrosion potential of this system is the active potential at which both the cathodic and anodic currents with respect to CO_3^{2-} are equal. From these equations, E_{corr} is assumed to be:

$$E_{corr} = \frac{1.5RT}{F}\left(\log \frac{k_c}{k_a}\left[O^3H^-\right]^{\nu_{ox}}\left[CO_3^{2-}\right]^{\nu'_{ox}}\right)_{^3H_2O} \tag{18.8}$$

Table 18.3. Corrosion potential and current as a function of carbonate concentration

CO_3^{2-} (mol dm^{-3})	0	10^{-3}	10^{-2}	2×10^{-2}	5×10^{-2}
E_{corr} (V/SCE)	−0.90	−0.95	−0.98	−1.005	−1.03
i_{corr} (μA cm^{-2})	1	1.7	2	2.3	3

This equation effectively shows that the corrosion potential depends on the carbonate concentration (Table 18.3). As in eq. (18.8), the corrosion current is:

$$i_{corr} = \left\{2k_c^{0.66}k_a^{0.33}F\left(O^3H^-\right)^{\nu_{ox}}\left(CO_3^{2-}\right)^{\nu'_{ox}}\right\}_{^3H_2O} \tag{18.9}$$

The corrosion current, i_{corr}, depends on anodic and cathodic rate constants. Moreover, it also depends on the nature of oxide as $\{Me_x^{(II)}Me_y^{(III)}(O^3H)_{2(x+y)}\}CO_{3hydrated}$ and the aqueous medium because it can be seen from Fig. 18.2b that the value of i_{corr} is higher with CO_3^{2-} (Table 18.3). The experimental values show less protection with carbonate.

Higher potentials than that of $\{Me_x^{(II)}Me_y^{(III)}(O^3H)_{2(x+y)}\}CO_{3hydrated}$ formation correspond to the passive region with the formation of Me_2O_3. With CO_3^{2-}, there is incomplete passivity, whereas with Me_2O_3, complete passivity for S31803 steel is obtained.

It should be noted that the passive region is followed by the transpassive peak preceding the transpassive plateau and the oxide layer dissolution at higher potentials. The current increases quickly. The oxide reactions would appear to involve the 'wet' passive oxide as indicated in previous chapters.

Clearly the results presented in the polarization curves demonstrate that CO_3^{2-}, by the definite participation of intermediate adsorbates and the passive oxide, markedly leads to the production of MeO_4^{2-} and surface acid pH. As shown in Fig. 18.2a, the effect of carbonate ion leads to shifting the beginning of the transpassive peak to lower potentials and to reducing the passive region. This change is related to modification of the structure of the passive layer with the involvement of CO_3^{2-}. In the transpassivity it is observed that the anodic current increases more with CO_3^{2-}, signifying greater corrosion of S31803 steel. At potentials above that of breakdown, localized corrosion is expected to grow. In the backward scans, it is seen that the anodic current increases and is higher than that in the forward scan with CO_3^{2-}, and returns to near the breakdown potential. According to the hysteresis shape, layer dissolution continues to initiate and grow after the scan reversal. These different results imply that carbonate does not provide protection under these conditions and the corroded area must increase.

3.2. Voltammetric curves

The voltammograms obtained with carbonate and a high scan rate are shown in Fig. 18.3.

A higher active peak in the alkaline corrosion region with CO_3^{2-} is seen showing an active-passive transition for the high scan rates. This depends on the transitory species formed at the electrode surface and their kinetics [100]. There is also a second active peak

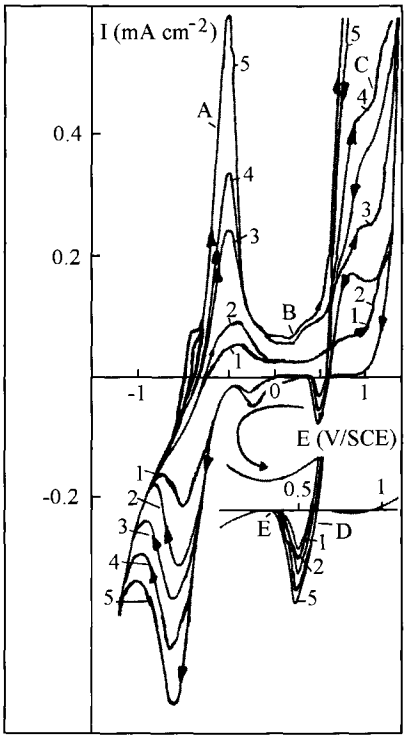

Figure 18.3. Voltammetric curves with and without carbonate, ω: 2000 rpm, v: 200 mV s^{-1}, pH 10, 1: 0, 2: 10^{-3}, 3: 10^{-2}, 4: 2×10^{-2}, 5: 5×10^{-2} mol dm^{-3} CO_3^{2-}, A: active peak, B: breakdown potential, C: transpassive peak, on extended scale: D: ending of breakdown, E: repassive potential.

preceding the first whose presence and size depend on carbonate concentration. It corresponds to a specific corrosion product leading to $\{Me_x^{(II)}Me_y^{(III)}(O^3H)_{2(x+y)}\}CO_{3hydrated}$ formation. Evidently the presence of CO_3^{2-} ions significantly affects S31803 steel oxidation processes. With carbonate present, the higher active peak observed probably indicates the electrochemical reaction coupled to chemical processes with this ion and a greater extent of species growth. Moreover, the potential of the smaller active peak slightly decreases with CO_3^{2-}, and the displacement cannot be attributed to the uncompensated potential drop, but to species formed by electrochemical reactions and their kinetics as indicated in eq. (18.3). The active region can be ideally divided into two domains, one of which is observed without carbonate, and one which depends on its presence. Consequently, they do not involve two distinct oxides related to ferrite and austenite respectively, but to an oxide related to the $\{Me(O^3H)_2$-oxide phase$\}$ and carbonate rust layers. The passive oxide layers should exhibit their intrinsic nature in the prepassivity-passivity ranges where there is $\{Me(O^3H)_2$-oxide phase$\}$ then $\{Me_x^{(II)}Me_y^{(III)}(O^3H)_{2(x+y)}\}CO_{3hydrated}$ and Me_2O_3 formation depending on the passive potentials. Therefore carbonate leads to a less protective

layer, and certainly the nature of the formed layer and corrosion products may be different at these prepassive-passive potentials.

Beyond the passive region, a considerable increase in current is observed producing a peak and a plateau in the transpassive region. This peak is observed with or without carbonate ions. The initial transpassive peak potential shifts towards less positive values when the CO_3^{2-} concentration increases. It is also noted that the transpassive peak increases with the carbonate concentration.

In the course of the reverse scan, dissolution stops and the ending of breakdown leads to repassivity. A reduction peak appears at −1 V/SCE; this is conjugated to the active peak. Its negative charge is slightly higher, but on the other hand, the total sum of anodic charges is larger showing that some of the species produced in the forward scan are not entirely reduced in the reverse scan. This means that soluble species are removed by the rotating electrode. From these different results, voltammograms and polarization curves show that there is modification of the passive oxide layer induced by CO_3^{2-}.

3.3. Impedance spectra

3.3.1. Results without carbonate This section is concerned with the analysis of impedance data for S31803 steel passivated at different potentials. Comparative measurements (Fig. 18.4) made at the different passive potentials near the corrosion potential and in the prepassivity-passivity show changes in $\log|Z|$ and phase angle/$\log(f)$. The diagrams display, essentially in the broad low and middle frequency range, a linear slope of

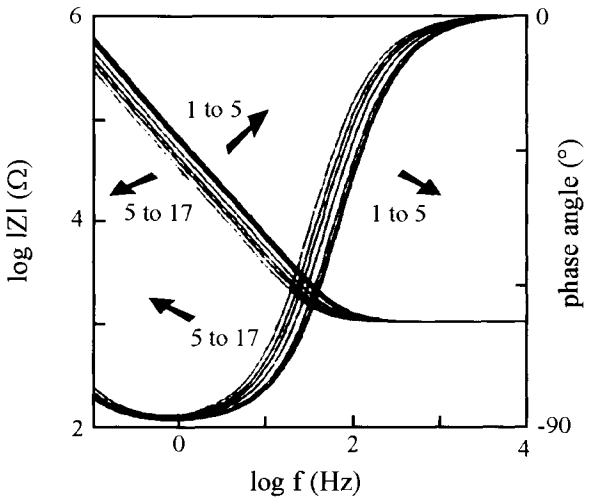

Figure 18.4. Bode spectra without carbonate, ω: 2000 rpm, pH 10, 1: −0.8 V, 2: −0.79 V, 3: −0.78 V, 4: −0.77 V, 5: −0.76 V, 6: −0.75 V, 7: −0.74 V, 8: −0.73 V, 9: −0.72 V, 10: −0.71 V, 11: −0.7 V, 12: −0.65 V, 13: −0.6 V, 14: −0.55 V, 15: −0.5 V, 16: −0.45 V, 17: −0.4 V/SCE.

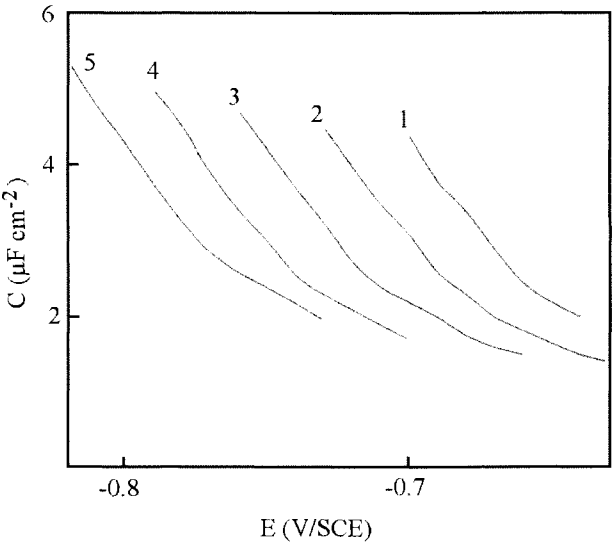

Figure 18.5. Oxide capacitance as a function of passive potentials and carbonate concentration, 1: 0, 2: 10^{-3}, 3: 10^{-2}, 4: 2×10^{-2}, 5: 5×10^{-2} mol dm^{-3} CO_3^{2-}.

about -1 in $\log|Z|$ as $\log(f)$ decreases, while phase angle values approach $-90°$. This is the characteristic response of a passive oxide capacitance in the purely capacitive region corresponding to a single oxide layer. This capacitive behavior is observed over a broad measurement frequency range.

Calculation shows that the value of the relative dielectric constant is 12. This value indicates that the passive oxide layer is not porous since the dielectric constant of pure water is far from this value (~ 80). The estimated oxide layer thickness is about 5 nm. The monolayer oxide thickness is about 1.5 nm [230]. Therefore the thickness found corresponds to superposition of thin wafers. The passive oxide capacitance (C_{ox}) values were calculated for different potentials. The 'critical capacitance' corresponding to its lower value denotes the perfect oxide layer (Fig. 18.5, curve 1).

The Bode plots enable us to calculate the donor concentration density (n_d) over a sufficient potential range following the simplified Mott-Schottky equation. To explain the carrier density, Strehblow [114] and Macdonald [116,117] showed that Me^{n+} into oxide must be transported from the alloy/oxide layer interface to the oxide layer/tritiated water interface (Fig. 18.6).

On the other hand, O^{2-} ions are transported in the reverse direction, with the relative fluxes of these species depending upon formation of the respective vacancies. As a result, the model is based on the migration of point defects (oxygen and metal vacancies) under the influence of the electrical field (Φ_V) in the oxide layer. From this, metal vacancies ($V_{Me^{n+}}$) diffuse from the tritiated water-oxide to alloy-oxide interfaces, as Me^{n+} diffuses in the opposite direction. Because the barrier layer is envisaged to grow into the alloy by

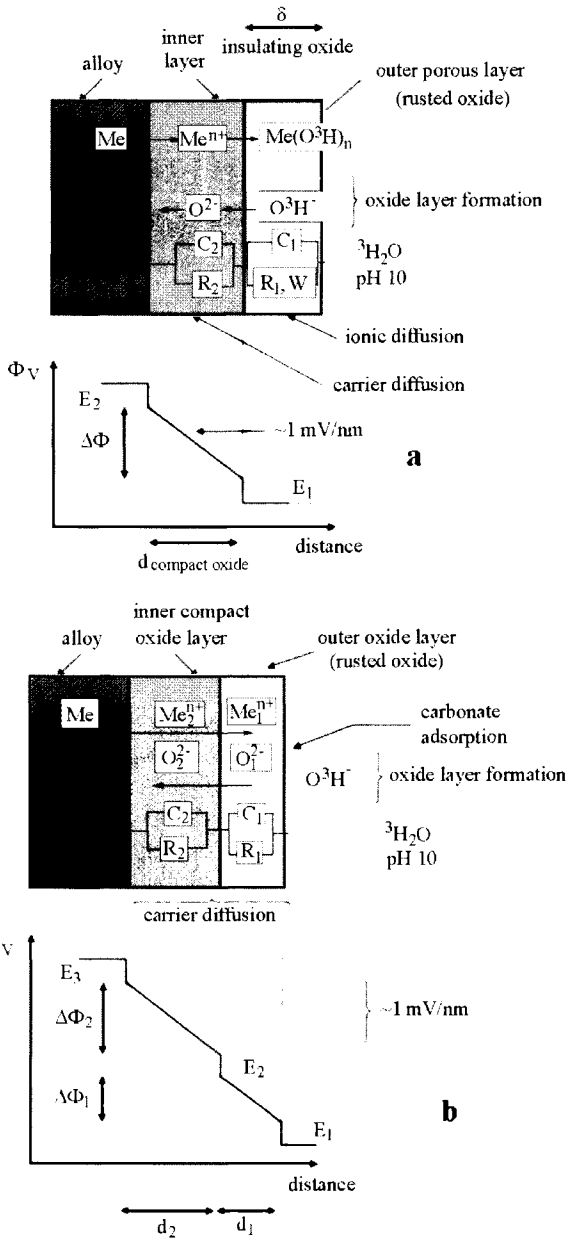

Figure 18.6. Physical model and equivalent circuits proposed to interpret the processes in mixed carbonated oxide, (a): ionic diffusion layer and insulating oxide layer, (b): two insulating oxide layers, R_1: oxide resistance including or not the Warburg impedance, R_2: oxide resistance including the restricted impedance, C_n: constant phase elements.

Table 18.4. Donor density dependence on $CO_3^{2-}{}_1$: {$Me(O^3H)_2$-oxide phase} or without $CO_3^{2-}{}_2$: rusted oxide

CO_3^{2-} (mol dm^{-3} × 10^2)	0	0.1	1	2	5
n_{d_1} (carrier cm^{-3} × 10^{20})	1.37	1.54	1.66	1.98	2.32
n_{d_2} (carrier cm^{-3} × 10^{20})	–	2	2.3	2.6	2.8

the generation of oxygen vacancies at the alloy/oxide layer interface, and by their consumption at the barrier layer/aqueous medium interface, the diffusion properties and distribution of oxygen vacancies within the oxide layer are of great interest. A key parameter in describing the transport properties of oxygen vacancies and hence the kinetics of oxide layer growth is the vacancy diffusibility for the flux and dependence on the vacancy concentration. Analysis has shown that the vacancy concentration is very large (of the order of 10^{19}–10^{20} carriers cm^{-3}). The C_{ox}^{-2} vs. the potential plot has a positive slope implying an n-type semi-conductor behavior. From this slope, the donor density is 1.37 × 10^{20} carriers cm^{-3} (Table 18.4).

3.3.1.1. Equivalent circuits and value determinations It seems that spectra give a perfect fit with the experimental data if the total impedance is modeled according to the equivalent circuit in Fig. 18.7a.

In this case, the transfer function of a homogeneous oxide is given by

$$Z_t = R_{el} + \frac{R_{ox}}{1 + A(j\omega)^a R_{ox}} \tag{18.10}$$

where R_{ox} represents the single oxide layer resistance. One of the aims of plotting the experimental diagrams is to find the values of the main electrical elements (Table 18.5). Data in Table 18.5 indicate that oxide capacitance decreases with the prepassive-passive potentials, and varies inversely as the single oxide layer resistance increases. This signifies a dependence of oxide layer thickness on the passive potentials.

3.3.2. Results with carbonate The characteristic Bode diagrams for the potentials near the corrosion potential are given in Fig. 18.8.

At the low frequency range, a slope of −1 is seen, indicating a blocking (quasi-capacitive) behavior which can be associated with the inner insulating oxide layer contribution. In the higher frequency section, the spectrum changes. It is characterized by a slope of −0.5 which accounts for an ion diffusion-controlled process through a finite region corresponding to the thickness of an outer porous oxide layer. The Warburg impedance is defined according to equation:

$$Z_{ou} = \sigma^{-0.5}(1 - j) \tag{18.11}$$

where σ is the Warburg impedance coefficient. This equation shows that an ideal Bode plot solely of the Warburg impedance, Z_{ou}, will be characterized by a slope of −0.5 and will intercept the impedance modulus-axis for $\log\{\sigma(2\pi^{-0.5})\}$ at 1 Hz. From the Warburg

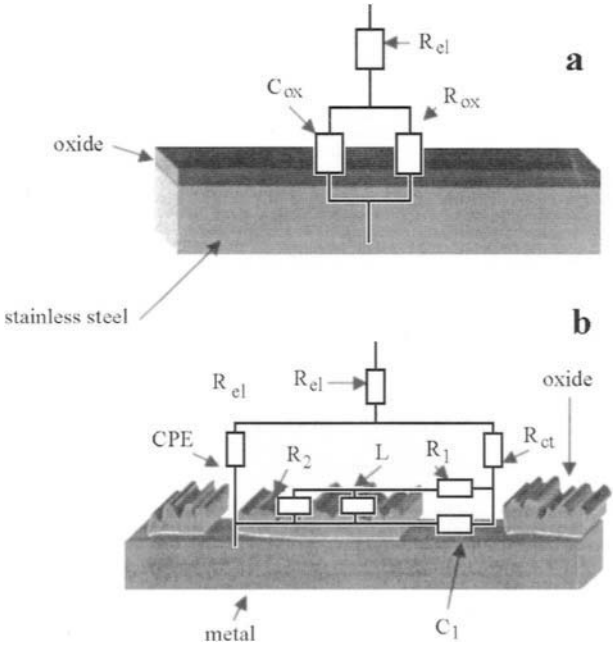

Figure 18.7. Equivalent circuits, (a, b): R_{el}: electrolyte resistance, R_{ox}: oxide resistance, R_{ct}: charge transfer resistance, R_1: thin-walled oxide fracture cleavage resistance, R_2: sublayer oxide resistance, C_{ox}: oxide capacitance, CPE: constant phase element, C_1: capacitance, L: inductance.

coefficient and the characteristic frequency corresponding to the intersection of the two sections, we can calculate the diffusion coefficient of inserted ions and the outer porous oxide layer thickness:

$$\delta = \frac{RT}{2n^2F^2\sigma}\sqrt{\frac{3}{\pi f_c C_{CO_3^{2-}}}} \tag{18.12}$$

and:

$$D = 2\frac{\pi f_c \delta^2}{3} \tag{18.13}$$

where σ is $6 \times 10^3\ \Omega\,s^{-0.5}$. It can be seen in the spectra realized in the Bode representation obtained from the bilayer model in Fig. 18.6a that the characteristic frequencies (marked A) change with the potential; this indicates a modification of the oxide layer thickness. The linear section between 10 and 1000 Hz is characterized by a slope of -0.5 and this is related to ion diffusion. At lower frequencies, when $f \ll 3D/2\pi\delta^2$, where δ is the diffusion layer thickness, the phase angle approaches $-90°$ the restricted diffusion region can be seen at these frequencies. At the frequency in point A, where $f_c \sim 3D/2\pi\delta^2$, the break

Table 18.5. Dependence of oxide capacitance and resistance on prepassive-passive potentials without carbonate

E (V/SCE)	−0.8	−0.79	−0.78	−0.77	−0.76	−0.75	−0.74
R_{ox} ($M\Omega\,cm^2$)	2	2.7	3.4	4.1	4.8	5.2	6
C_{ox} ($\mu F\,cm^{-2}$)	4.4	3.8	3.4	2.9	2.4	2.2	2.1

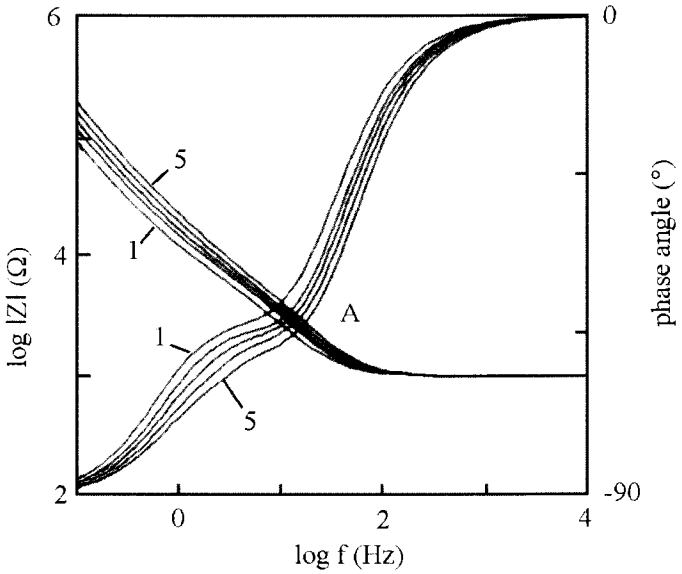

Figure 18.8. Bode spectra in presence of carbonate and for the potentials near the corrosion potentials, ω: 2000 rpm, pH 10, 5×10^{-2} mol dm^{-3} CO_3^{2-}, 1: −1.02 V, 2: −1.01 V, 3: −1 V, 4: −0.99 V, 5: −0.98 V/SCE.

from the semi-infinite diffusion region to the finite diffusion region occurs. Moreover, the experimental impedance spectra can be described by the following transfer function:

$$Z_t = R_{el} + \left\{Z_{in}^{-1} + A_{in}(j\omega)^a\right\}^{-1} + \left\{Z_{ou}^{-1} + A_{ou}(j\omega)^a\right\}^{-1} \qquad (18.14)$$

where Z_{ou} is the specific impedance of the outer oxide layer incorporating a Warburg coefficient and Z_{in} the blocking impedance of the inner oxide layer. In the Bode representation, the respective separation of the characteristic frequency is evident and data analysis presents no problems, whereas if we use the Nyquist representation there is an overlap of the charge transfer and diffusion-controlled regions. Calculation yields $D = 4.2 \times 10^{-15}$ cm^2 s^{-1} and the estimated diffusion layer thickness is 5 nm. These values are consistent with ion diffusion in an external porous oxide layer. The interpretation of this type of diagram is that the Warburg straight line and blocking behaviors are related to the outer porous layer and inner insulating passive layer. Similar impedance spectra have also been observed in several processes implying two thin duplex layers as indicated by Gassa et al. [253]. The difference between the two layers is related to structural differences. For

example, outer layers such as $\{Me_x^{(II)}Me_y^{(III)}(O^3H)_{2(x+y)}\}CO_{3hydrated}$ or $\{Me(O^3H)_2$-oxide phase$\}$ are hydrated as seen in eq. (18.4) while the passive layer corresponds to a less hydrated and more homogeneous structure with a higher number of electronic defects. The electrochemical exchange of charge across the oxide is treated as a bridge between the electronic and the ionic conductivity. The electrical field (Φ_V) leads to the migration of ion species and to a decrease in the carrier number in the passive oxide layer (Fig. 18.6).

Fig. 18.9 displays the impedance spectra of oxide grown at different prepassive and passive potentials with two linear slopes; here there is a break at intermediate frequencies corresponding to time constants in the Bode plots. This provides evidence of two oxide layers depending on carbonate concentration, and changing with the potentials. As the carbonate concentration is further increased, both these effects appear more pronounced (Fig. 18.9c, d). The linear section between 10 and 1000 Hz is characterized by a slope about -1. The high frequency range time constant is related to the conversion oxide layer comparable with a barrier oxide layer. It must be noted that the frequencies at the break increase with the prepassive potentials, as seen more easily in the phase angle (Fig. 18.9c, d point A). Therefore, the approach of describing the oxide layer in terms of insulating properties using the Mott-Schottky equation is valid and provides a better understanding of the properties of passive oxide layers (dependence of vacancies diffusion) as indicated by Mansfield [190]. This validity is applicable up to a maximum potential representing the limit of the semi-conductive region. At higher potentials, the characteristic frequency varies in the opposite direction (Fig. 18.9a point A) signifying the formation of defects in the oxide. According to the modifications in the position of the two linear slopes, the $\{Me(O^3H)_2$-oxide phase$\}$ layer should exhibit its intrinsic nature at the high frequencies, whereas $\{Me_x^{(II)}Me_y^{(III)}(O^3H)_{2(x+y)}\}CO_{3hydrated}$ exhibits its intrinsic nature at the low frequencies. This enables the calculation of the parameters (Table 18.6 to Table 18.11) with respect to the potential for each oxide layer formation in two successive steps (Fig. 18.3) as indicated by Dolata et al. [254]. The capacitance values show the insulating character and the duplex structure of the two oxide layers. The capacitance change of the two oxide layers leads to the characteristic frequency shift in the Bode plot. From the evolutive diagrams, the oxide phase layer predominates at lower prepassive potentials, whereas the rusted oxide layer predominates at the higher potentials. The $\log |Z|$ vs. $\log f$ curve shows the linear variation that is characteristic of capacitive behavior with phase angle which tends to $-90°$ at low and medium frequencies. However, it does not reach this value because the system does not behave exactly as an ideal capacitor, whereas at the higher passive potentials, the transfer function of the oxide layer would be used, probably due to oxide breakdown. In the prepassive potentials, the value of the slope 'a' used in the CPE is close to 1 (eq. (6.25)) for the two oxide layers but it decreases with increasing thickness, indicating the departure from ideal capacitive behavior. The outer oxide layer may be associated with the appearance of some defects because the oxide appears to begin breaking due to the stress at the higher passive potentials, certainly enhanced in this case by a dehydration mechanism. As the oxide grows, it tends to be more compact and consequently the dehydration process could take place, increasing oxide vacancies and further stresses that can finally produce oxide breakdown. The system can be modeled as a function of two successive lay-

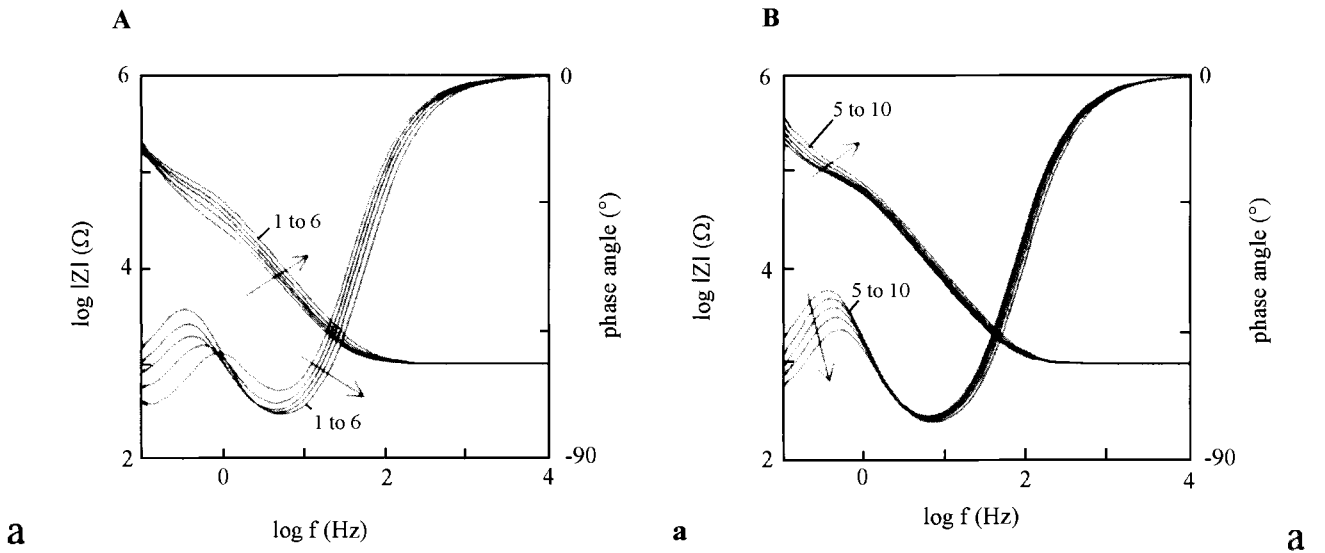

Figure 18.9. Bode spectra with carbonate in prepassivity-passivity and passivity-transpassivity, ω: 2000 rpm, pH 10, (A/B): (a): 10^{-3} mol dm^{-3} CO_3^{2-}, 1–10: −0.83 to −0.74 V/SCE, (b): 10^{-2} mol dm^{-3} CO_3^{2-}, 1–10: −0.86 to −0.77 V/SCE, (c): 2×10^{-2} mol dm^{-3} CO_3^{2-}, 1–10: −0.89 to −0.8 V/SCE, (d): 5×10^{-2} mol dm^{-3} CO_3^{2-}, 1–10: −0.92 to −0.83 V/SCE.

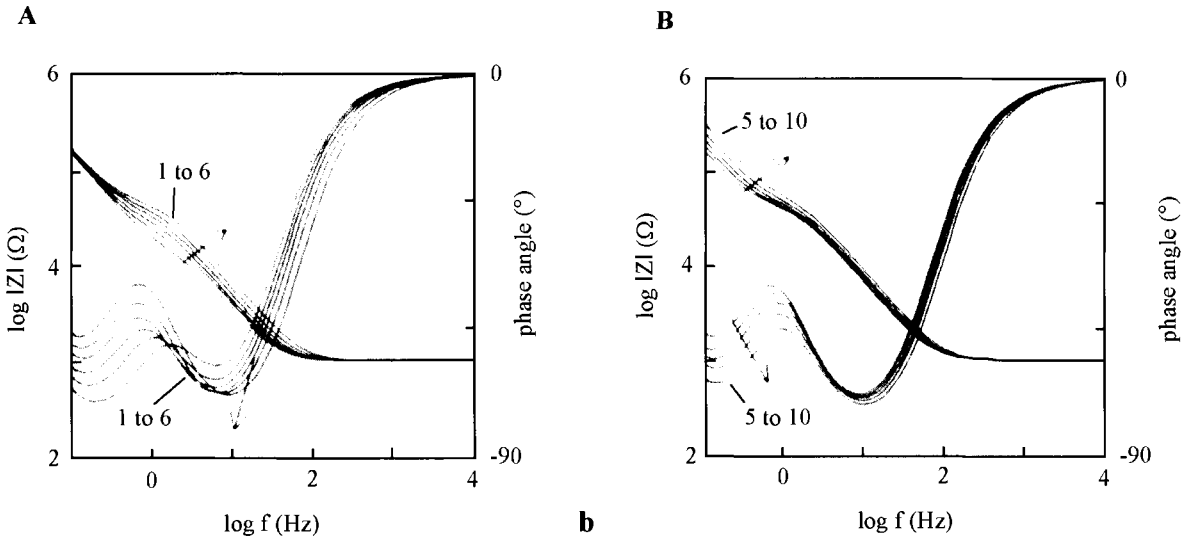

Figure 18.9. (Continued).

Figure 18.9. (Continued).

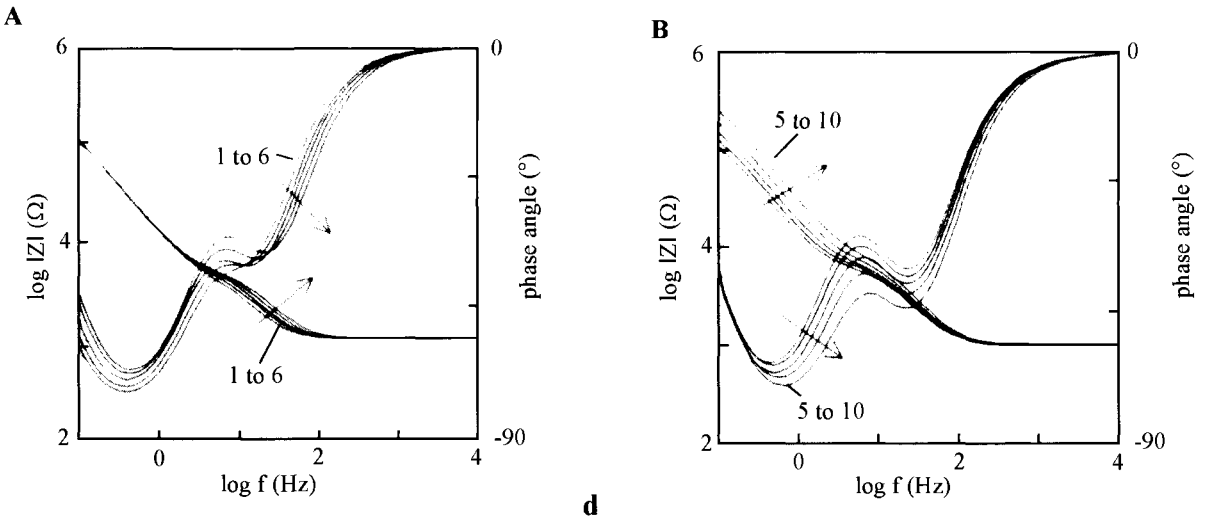

Figure 18.9. (Continued).

Table 18.6. Dependence of oxide capacitances and resistances on prepassive-passive and passive-transpassive potentials in presence of 10^{-3} mol dm^{-3} CO_3^{2-}, underlined results: main evolution of oxide

E (V/SCE)	−0.83	−0.82	−0.81	−0.8	−0.79	−0.78	−0.77	−0.76	−0.75	−0.74	−0.73
R_{ox_1} (kΩ cm^2)	15	26	38	48	60	70	70.1	70.3	70.6	70.7	70.9
R_{ox_2} (MΩ cm^2)	1.15	1.1	1.05	1.05	1	1	1.5	2	2.5	3	4
C_{ox_1} (μF cm^{-2})	8.3	7	6	5	4	3	2.9	2.8	2.7	2.6	2.5
C_{ox_2} (μF cm^{-2})	10.5	10.4	10.3	10.2	10.1	10	8.8	7.6	6.4	5.2	4

Table 18.7. Dependence of oxide capacitances and resistances on prepassive-passive and passive-transpassive potentials in presence of 10^{-2} mol dm^{-3} CO_3^{2-}, underlined results: main evolution of oxide

E (V/SCE)	−0.86	−0.85	−0.84	−0.83	−0.82	−0.81	−0.8	−0.79	−0.78	−0.77	−0.76
R_{ox_1} (kΩ cm^2)	8	13.5	19	25	29.5	35	35.2	35.3	35.5	35.7	35.9
R_{ox_2} (MΩ cm^2)	0.65	0.62	0.6	0.55	0.52	0.5	0.65	0.8	1	1.5	2
C_{ox_1} (μF cm^{-2})	8.5	7	6	5	4	3	2.9	2.8	2.7	2.6	2.5
C_{ox_2} (μF cm^{-2})	10.5	10.4	10.3	10.2	10.1	10	8.7	7.4	6.1	4.8	3.5

Table 18.8. Dependence of oxide capacitances and resistances on prepassive-passive and passive-transpassive potentials in presence of 2×10^{-2} mol dm^{-3} CO_3^{2-}, underlined results: main evolution of oxide

E (V/SCE)	−0.89	−0.88	−0.87	−0.86	−0.85	−0.84	−0.83	−0.82	−0.81	−0.8
R_{ox_1} (kΩ cm^2)	4	7	10	13	16	19	19.2	19.3	19.5	19.7
R_{ox_2} (MΩ cm^2)	0.35	0.33	0.29	0.26	0.23	0.2	0.25	0.3	0.35	0.4
C_{ox_1} (μF cm^{-2})	9	7.8	6.6	5.4	4.3	3	2.9	2.8	2.7	2.6
C_{ox_2} (μF cm^{-2})	11.5	11.4	11.3	11.2	11.1	11	10.3	8.6	6.9	5.1

Table 18.9. Dependence of oxide capacitances and resistances near the corrosion potential and in presence of 5×10^{-2} mol dm^{-3} CO_3^{2-}

E (V/SCE)	−1.02	−1.01	−1.0	−0.99	−0.98
R_{ct} (Ω cm^2)	48	50	55	57	60
R_{ox_2} (kΩ cm^2)	9	10	10.5	12	15
C_{dl} (μF cm^{-2})	48	45	43	41	39
C_{ox_2} (μF cm^{-2})	15	7	4	2	1

ers formed of {Me$(O^3H)_2$-oxide phase} and $\{Me_x^{(II)}Me_y^{(III)}(O^3H)_{2(x+y)}\}CO_{3\text{hydrated}}$. The first oxide layer may be explained by a free-carbonate layer definitely leading to a carbonate contaminated layer at higher potentials. The presence of this foreign ion alters the electrical field (Φ_V) and the chemical oxide properties. Intercalation of such ions would depend upon the growth rate.

The following section shows how to determine the oxide characteristic parameters with carbonate present. A good representation of the transfer function for taking this evolutive structure into account is:

$$Z_t = R_{el} + \sum_{1}^{2} \frac{R_{ox}}{1 + A(j\omega)^a R_{ox}} \tag{18.15}$$

Table 18.10. Dependence of oxide capacitances and resistances in the prepassivity-passivity

E (V/SCE)	−0.92	−0.91	−0.9	−0.89	−0.88	−0.87	−0.86	−0.85	−0.84	−0.83
R_{ox_1} (kΩ cm^2)	2	2.4	2.8	2.9	3	4	4.2	4.3	4.5	4.7
R_{ox_2} (MΩ cm^2)	0.33	0.3	0.26	0.22	0.2	0.18	0.2	0.25	0.3	0.4
C_{ox_1} (μF cm^{-2})	10	7.8	6.6	5.4	4.4	3.5	3.4	3.3	3.2	3.1
C_{ox_2} (μF cm^{-2})	13	12.9	12.8	12.7	12.6	12.5	10.7	8.9	7.1	5.3

Table 18.11. Dependence of oxide capacitances and resistances in the passivity-transpassivity

E (V/SCE)	0.48	0.49	0.5	0.51
R_{ct} (kΩ cm^2)	3	1.5	1	0.8
R_1 (Ω cm^2)	40	20	10	5
R_2 (kΩ cm^2)	0.8	0.4	0.3	0.2
CPE (μF cm^{-2})	50	67	75	80

From the transfer function, the most probable equivalent circuit consists of a series connection of two R/[CPE] elements (Fig. 18.6b) with a residual resistance at high frequencies attributed to the ohmic resistance of the electrolyte. To obtain a connection for determining the characteristic parameters of the two successive oxide layers depending on potentials, the oxide charge (Q) is calculated integrating the derived current-time curves for several prepassive-passive potentials (Fig. 18.3). The corresponding values indicate the formation of a multi-oxide layer. According to Schmuki and Böhni [237], the oxide charge is written as:

$$Q = \frac{\varepsilon_1 \varepsilon_0 n F \rho_1}{C_{ox_1} M_1} + \frac{\varepsilon_2 \varepsilon_0 n F \rho_2}{C_{ox_2} M_2} \tag{18.16}$$

where M_n is the oxide mean molecular weight, assumed to be 90 and 616 for each respective oxide and ρ the oxide density equal to 6. In this equation, $_{ox_1}$ and $_{ox_2}$ correspond to {Me(O^3H)$_2$-oxide phase} and $\{Me_x^{(II)}Me_y^{(III)}(O^3H)_{2(x+y)}\}CO_{3hydrated}$ respectively. The C_{ox_1} and C_{ox_2} values are determined by fitting the spectra using a non-linear least-squares algorithm. From the schematic evolution in the Bode diagram, it is reasonable to assume that the term in $_{ox_1}$ interacts principally for the first prepassive potentials and the term in $_{ox_2}$ for higher prepassive potentials (Fig. 18.3). In order to obtain the unknown parameters, eq. (18.16) is transformed into a matrix equation. For this, the oxide charge values associated with the current are used. Taking this consideration into account, calculations show that each oxide layer thickness varies between 5 and 15 nm. Ion diffusion processes are not observed in this potential region. However, it is suggested that there is a porous oxide situated further out and the corresponding ion diffusion may exist over practically the same frequency range where the 'ox_2' oxide and electrolyte resistance effects are observed. This means so that the impedance contribution due to the primary process (hydrated layer and ion diffusion) cannot be separated in the large dip of the phase angle vs. the frequency. This primary effect should be weak and can be neglected. Therefore, it is reasonable to assume that σ should be close to zero, and the physical model is shown in Fig. 18.6b. At lower potentials, σ essentially appears in Bode plots as shown in Fig. 18.6a.

This means that ion diffusion processes take place especially for the formation of the conversion oxide layer, $\{Me(O^3H)_2$-oxide phase$\}$, leading to rusted oxide. The changes with and without σ depending on the prepassive-passive potentials mean that there are successive reaction processes on passivated S31803 steel. Under this limitation of σ, applying eq. (18.16) for several prepassive-passive potentials and the iterative method, the variations of $\Sigma(1/C_{ox_n}) = f(Q)$ enabled us to determine the relative dielectric constants. Taking the experimental values in Tables 18.6–18.11 and integrating the curves in Fig. 18.3, a linear relationship between $\Sigma(1/C_{ox_n})$ and Q is obtained. This signifies that the amount of oxide is proportional to the reciprocal of the oxide capacitance and depends on its thickness. The value of ε_2 is 15 which corresponds to the formed carbonate-oxide layer as indicated in eq. (18.4) whereas ε_1 is 13. These values and that obtained without CO_3^{2-} (~ 12) are similar and do not interact in the final results. These indicate the two oxide layers are insulating and are consistent with capacitance results given in Tables 18.6–18.11. The latter values (ε_1) concern the oxide layers that are more insulating. In the case of oxides that grow as two successive layers, the total reciprocal capacitance is obtained from the equation:

$$\frac{1}{C_{ox}} = \frac{d_1}{\varepsilon_1 \varepsilon_0 r} + \frac{d_2}{\varepsilon_2 \varepsilon_0 r} \tag{18.17}$$

This equation shows that the capacitance depends on the thickness of the two successive oxide layers. According to impedance measurements, the oxide layer thickness grows with the prepassive-passive potentials. As can be seen in Tables 18.6–18.11, obtained fitting the spectra, the capacitance of the grown $\{Me(O^3H)_2$-oxide phase layer is lower than that for the $\{Me_x^{(II)}Me_y^{(III)}(O^3H)_{2(x+y)}\}CO_{3hydrated}$ oxide. This confirms its compact nature, indicating the higher corrosion resistance, in good agreement with the analysis made in relation with $\{\Sigma(1/C_{ox_n})\}^{-1}$ for the prepassive-passive potentials (Fig. 18.5, curves 2 to 5). Two charge carrier densities can be expressed for the two successive oxide layers:

$$n_{d_n} = \frac{2\varepsilon_n \varepsilon_0 r}{e d_n^2}\left(V_m - V_{fb} - \frac{kT}{e}\right) \tag{18.18}$$

It is possible to determine each value of the charge carrier density as shown by Schmuki et al. [255]. These workers found good agreement between the doping concentrations determined from Mott-Schottky analysis for two passive oxide layers and those obtained by physical-chemistry analysis. The data show that the donor density in the vicinity of the alloy/oxide layer interface changes with the oxide nature.

To interpret the value of the donor density, oxygen vacancies are formed at the alloy/oxide layer interface, but are consumed at the oxide layer/aqueous medium by the injection of oxide ions into the oxide layer from tritiated water. According to this, the diffusion of metal vacancies is affected by the adsorption of CO_3^{2-} ions at the oxide–^3H_2O interface as shown in the following equations.

$$V_{O^{2-}} + 2\{CO_3^{2-}\}_{adsorption} \leftrightarrow 2\{CO_3^{2-}\}_{aqueous} \tag{18.19}$$

$$\mathrm{Me} \leftrightarrow \{\text{carbonated oxide}\} + \mathrm{V}_{\mathrm{O}^{2-}} \qquad \text{(alloy–oxide interface)} \tag{18.20}$$

$$\mathrm{Me} + \mathrm{V}_{\mathrm{Me}^{n+}} \leftrightarrow \{\text{carbonated oxide}\} \qquad \text{(alloy–oxide interface)} \tag{18.21}$$

where {carbonated oxide} represents metal in the oxide layer. If the number of $\mathrm{V}_{\mathrm{O}^{2-}}$ that are free decreases, {oxide}, $\mathrm{V}_{\mathrm{Me}^{n+}}$ and carrier concentration increase. Due to interdependence of the concentration of cation and anion vacancies ($C_{\mathrm{V}_{\mathrm{Me}^{n+}}}$, $C_{\mathrm{V}_{\mathrm{O}^{2-}}}$) in the two oxide layers and the adsorption of CO_3^{2-}, the number of metal vacancies increases in the oxide layer (eq. (18.19)) up to a critical concentration leading to a few defects between the alloy and oxide layer. From these considerations, the following criterion for passivity in presence of carbonate can be derived:

$$\frac{\partial \mathrm{V}_{\mathrm{Me}^{n+}}}{\partial t} = J_{\mathrm{Me}}\left[C_{\mathrm{V}_{\mathrm{O}^{2-}}}\left\{\text{oxide} - {}^3\mathrm{H_2O} - \mathrm{CO}_3^{2-}\right\}\right]^{-0.5n} \tag{18.22}$$

where J_{Me} depends on diffusion of metal vacancies and thermodynamic constants, and $C_{\mathrm{V}_{\mathrm{O}^{2-}}}\{\text{oxide} - {}^3\mathrm{H_2O} - \mathrm{CO}_3^{2-}\}$ is the concentration of O^{2-} vacancies at the oxide layer/tritiated water interface. Equation (18.22) indicates that the diffusion of metal vacancies is enhanced by increasing the adsorption of CO_3^{2-}. This enhancement can lead effectively to an accumulation of metal vacancies and defects at the alloy-oxide layer interface. In the passivity-transpassivity limit, the breakdown potential can be determined from Mott-Schottky's equation and eq. (18.22) as shown by Strenblow [114] and Macdonald et al. [116,117]:

$$E_{\text{breakdown}} = \frac{4.6\alpha RT}{nF}\log\left(\frac{J_{\mathrm{m}}}{J_0\frac{M}{\rho}\exp\left\{\frac{\mathrm{pH}}{RT}\right\}^{-0.5n}}\right) - \frac{2.3\alpha RT}{F}\log \mathrm{CO}_3^{2-} \tag{18.23}$$

where J_{m} is the rate of submergence of the metal and O^{2-} vacancies in the alloy/oxide layer interface. It can be seen that low submergence rates and higher adsorbed CO_3^{2-} concentration at constant pH decrease the breakdown potential. If the metal vacancies in the oxide layer penetrate the alloy at a slower rate than their diffusion, they accumulate at the alloy/oxide layer interface and finally lead to a local concentration and hence will form a void. When the void grows to a certain critical size the passive oxide layer is subsequently subject to breakdown. This behavior arises between oxide layer and alloy. Recognizing this deductive reasoning, it should be emphasized that the experimental curve in Fig. 18.10 is effectively in accordance with eq. (18.23).

In extending this analysis, the diffusion mechanism in passivity should be further elucidated by the theoretical development of vacancies in the oxide layer. The flux of oxygen vacancies, J_0 through the passive layer may be written as

$$J_0 = -D_0\left(\frac{\partial C_{\mathrm{V}_{\mathrm{O}^{2-}}}}{\partial d}\right) - \frac{2F\Phi D_0 C_{\mathrm{V}_{\mathrm{O}^{2-}}}}{RT} \tag{18.24}$$

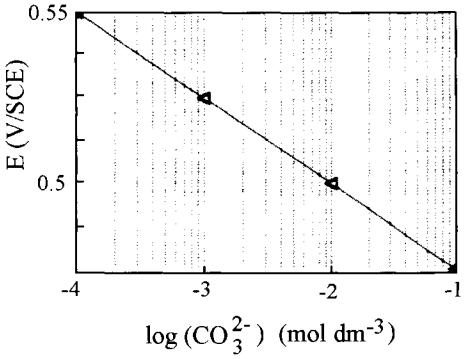

Figure 18.10. Dependence of breakdown potentials on the carbonate concentration.

where D_0 is the diffusion coefficient of oxygen vacancies. The concentration profile for oxygen vacancies is obtained by solving the Nernst-Planck equation:

$$(C_{V_{O^{2-}}})_x = \left[C_{V_{O^{2-}}}\{\text{oxide} - {}^3H_2O - CO_3^{2-}\}\right]\exp\left(-\frac{2\Phi Fx}{RT}\right) - \frac{J_0RT}{2D_0\Phi F}\left[1-\exp\left(-\frac{2\Phi Fx}{RT}\right)\right] \tag{18.25}$$

where Φ is the electrical field related to the respective oxide capacitance and x the considered oxide thickness. The concentration of oxygen vacancies in the two successive oxide layers should result in the two linear Mott-Schottky sections. It is concluded that the donor density, n_d, is the oxygen vacancy concentration in these locations. Thus the previous equation gives for each oxide layer:

$$n_{d_n} = C_{V_{O^{2-}}}\{\text{oxide} - {}^3H_2O\}\exp\left(-\frac{2F\Phi_n d_n}{RT}\right) - \frac{J_0RT}{2F\Phi_n D_{0_n}}\left[1-\exp\left(-\frac{2F\Phi_n d_n}{RT}\right)\right] \tag{18.26}$$

These equations effectively show that the vacancies or charge carrier concentration depend on each diffusion. The oxide capacitance results given in Tables 18.6–18.11 enable the determination of the donor density applying eq. (18.22) (Table 18.4). According to Sikora et al. [256], Φ is estimated to be 100 mV/nm, the first term is negligible in eq. (18.26) and an oxide thickness calculation shows that $d \sim 15$ nm. In order to interpret the results in Table 18.4, the small difference in donor density between the two oxide layers should be attributed to the alteration of the electrical field Φ_2. From these values, it can be noted in the two previous equations that $\exp(-2F\Phi d/RT) \to 0$. In consequence, the

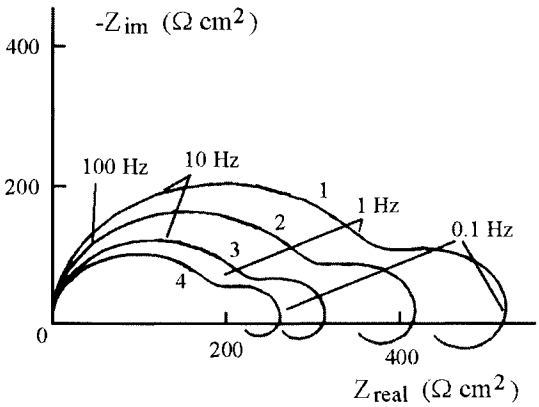

Figure 18.11. Nyquist diagrams in passivity-transpassivity with carbonate—potential effect, ω: 2000 rpm, pH 10, 5×10^{-2} mol dm^{-3} CO_3^{2-}, 1: 0.53 V, 2: 0.54 V, 3: 0.55 V, 4: 0.56 V/SCE.

diffusion coefficient can be determined from the simplified equation:

$$D_0 = \frac{J_0 RT}{2Fn_d\Phi} \tag{18.27}$$

where

$$J_0 = \frac{i_{passive}}{2e} \tag{18.28}$$

In eq. (18.28), the number 2 is the result of the double charged O^{2-} vacancies and the prepassive-passive current measured in steady-state is $2\mu A\,cm^{-2}$, so that the derived value of D_0 is 5×10^{-15} cm^2 s^{-1}.

In the passive-transpassive region, the Nyquist plots (Fig. 18.11) correspond to two capacitive semi circles followed by an inductive loop. The two time constants involved are due to surface property differences. Accurate analysis of the characteristic frequency obtained from the simulated spectra shows this depends on potentials, signifying that corrosion processes depend on these. This kind of spectrum can be explained by an oxide layer relaxation with mass transport by local oxide crusts formed after breakdown as shown by Scanning Electron Microscopy (Fig. 18.12).

The impedance spectra can be fitted according to the following transfer function (eq. (18.29)) corresponding to the equivalent circuit proposed in Fig. 18.7b. From the values in Tables 18.6–18.11, the decrease in R_{ct} representing the charge transfer resistance, with increasing passive-transpassive potential suggests that the surface of the passivated S31803 steel is gradually damaged. There are no passivating processes in this region and

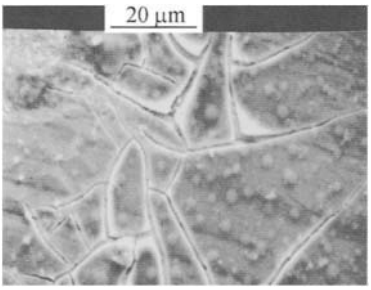

Figure 18.12. Scanning Electron Microscopy photograph showing S31803 steel corroded with carbonated oxide crusts.

the corrosion increases with CO_3^{2-} and the passive-transpassive potentials.

$$Z_t = R_{el} + \left[A(j\omega)^a\right]^{-1} + \left\{R_{ct} + \frac{R_1}{1 + j\omega C_1 R_1} + \frac{j\omega L R_2}{j\omega L + R_2}\right\}^{-1} \tag{18.29}$$

In eq. (18.29), L and R_2 are associated with the inductive contribution at the lowest frequencies which can be interpreted by assuming sublayer oxide corrosion dependence on potential causing oxide relaxation, and R_1 and C_1 can be related to a faradaic contribution of the thin-walled fracture cleavage of oxide crusts as shown in Fig. 18.12.

4. Conclusions

Carbonate addition produces several effects. The first is ion diffusion into the pre-oxide. Following this the prepassivity shows two regions depending on potential: the first is the formation of {$Me(O^3H)_2$-oxide phase}. There is then adsorption of CO_3^{2-} with formation of two successive protective passive oxide layers and passivation with Me_2O_3 formation at the higher passive potentials. This means that the carbonate oxide layer has a complex structure that depends on adsorbed oxyhydroxide and carbonate and the respective prepassive-passive potentials.

This Page Intentionally Left Blank

Chapter 19

PROTECTION BY CARBONATE AND OXIDIZERS

1. Introduction

The austenite stainless steels used in nuclear installations are often corroded in the weld regions and more particularly in the heat-affected zones (Fig. 19.1). Moreover, in this figure, tritiated ice does not prevent corrosion due to the fact that the energy released is high enough to overheat ice locally until it melts. This leads to pockets of tritiated water that is very reactive and causes damage by localized corrosion. Duplex stainless steels are becoming widely accepted as alternatives to austenite steels in applications requiring high resistance to pitting. The desirable properties exhibited by these steels are achieved through the careful balance of austenite and ferrite in the weld pool region and in the heat-affected zone.

We report here a study of the passivity of welded S32550 stainless steel using tritiated water containing alkaline carbonate, chloride and hydrogen peroxide formed by β^- particle radiolysis. Data on oxide-carbonate layers can be found in publications by Abdelmoula et al., Drissi et al. and Blengino et al. [245–247]. As indicated in the previous chapter, the oxide layer is formed in two steps. The first corresponds to the formation of $\{Me(OH)_2$-oxide phase$\}$ followed by carbonate rust ($\{Me_x^{(II)}Me_y^{(III)}(O^3H)_{2(x+y)}\}CO_{3\text{hydrated}}$) that covers the external alloy surface in the prepassive-passive region while Me_2O_3 appears principally at higher passive potentials; these two layers lead to passivity. We have found nothing in the literature for the behavior of the mixture of these three radiolytic aqueous species in presence of S32550 stainless steel. For these reasons, the behavior of oxide layers of welded S32550 stainless steel was studied using electrochemical methods from the corrosion potential to the passive potentials that were easily implemented.

2. Materials and preparation

The composition of the S32550 Duplex stainless steel is given in Table 19.1. As indicated by Lippold et al. [53], van Nassau et al. [54], Bonnefois et al. [55] and Gooch [56], this steel is characterized by a two-phase structure comprising a mixture of austenite, γ, and ferrite, α, grains. The parent Duplex contains 45.8% ferrite, and the average grain size is 20 μm for the austenite and 7 μm for the ferrite. It can be seen in Fig. 19.2 that considerable modification in microstructure is produced across the weld pool zone. It exhibits a large prior ferrite grain size with continuous networks of intragranular austenite, γ_2, in the

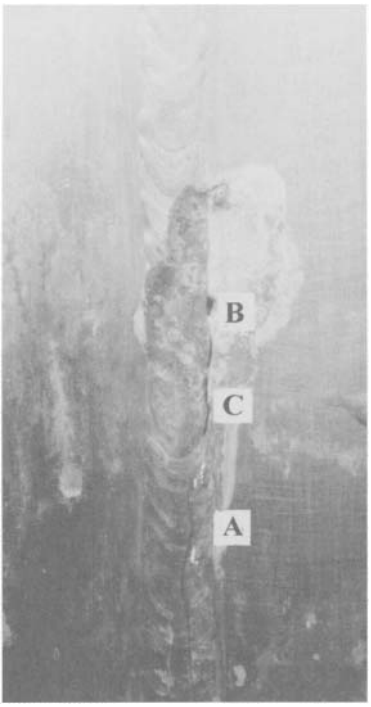

Figure 19.1. Photograph of corroded surface of the weld heat-affected zone taken in an austenitic stainless steel tank for tritiated water, A: tritiated ice, B: pit, C: cracks.

Table 19.1. Composition of S32550 stainless steel

Elements	Cr	Ni	Mo	N	Si	Mn	P	Cu	S	C	Fe
Wt%	24.9	6.02	3.7	0.25	0.33	1.13	0.01	1.65	0.001	0.015	bal.

substructure. During solidification of welded Duplex an almost complete ferrite structure is formed in the weld pool and in the heat-affected zone. The structure is the result of primary solidification of S32550 stainless steel welds as delta ferrite and that are fully ferritic until cooling below the ferrite solvus. The precipitates seen in the austenite substructure (Fig. 19.2) result from the increased affinity of austenite for nitrogen and the segregation of more soluble elements in austenite. Weld solidification cracking does not seem to be a significant problem. However, a few cracks are seen in the austenite substructure shown in Fig. 19.2.

Note that the precipitate-free highly ferritic 'collar' exists at the weld heat-affected zone located between the heat-affected and weld pool zone and the parent S32550 stainless steel (Fig. 19.2). This zone alters the ferrite-austenite balance. This represents the region of the heat-affected zone that has completely transformed to ferrite and undergone grain growth during the welding. The width of this region is of the order of 1–2 grain diameters (about

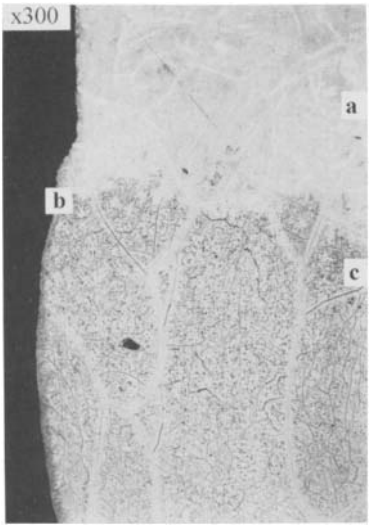

Figure 19.2. Metallographic examinations in the longitudinal section showing austenite and ferrite grains, (a): parent steel, (b): weld pool zone, (c): weld heat-affected zone.

50 μm) and is a function of the time available for dissolution of the austenite at temperatures close to that of solidification. In this zone, the diffusion rates are extremely high, especially for interstitial elements. Effectively, nitrogen can diffuse some 50–100 μm. Therefore, if the weld pool zone has a lower nitrogen activity than the parent S32550 stainless steel, nitrogen will migrate into the fused region out of the heat-affected zone thus forming initiation sites for corrosion. Higher nitrogen concentration into the fused region leads to hardening (Fig. 5.9). The resistance to heat-affected zone liquation cracking probably results from the fact that the S32550 stainless steel typically contains very low impurity levels and that ferrite microstructures are generally resistant to grain boundary liquation due to the high diffusivity of alloying and impurity elements at elevated temperatures.

3. Experimental results

3.1. Polarization curves

Polarization curves obtained for pH 10.2, with chloride and carbonate ions and different hydrogen peroxide concentrations are presented in Fig. 19.3a. This pH corresponds to the pK_b of the $^3HCO_3^-$–NaOH basic buffer. Carbonate ions act to keep the alkaline buffer pH constant at the welded S32550 steel surface. At more negative potentials than the corrosion potential, the current corresponds to the $^3H_2O_2$ reduction. In contrast to the situation without carbonate ions where the surface pH varies (Fig. 19.4), the corrosion potential is not shifted towards the passivity (Fig. 19.3) with increasing $^3H_2O_2$ concentrations. The

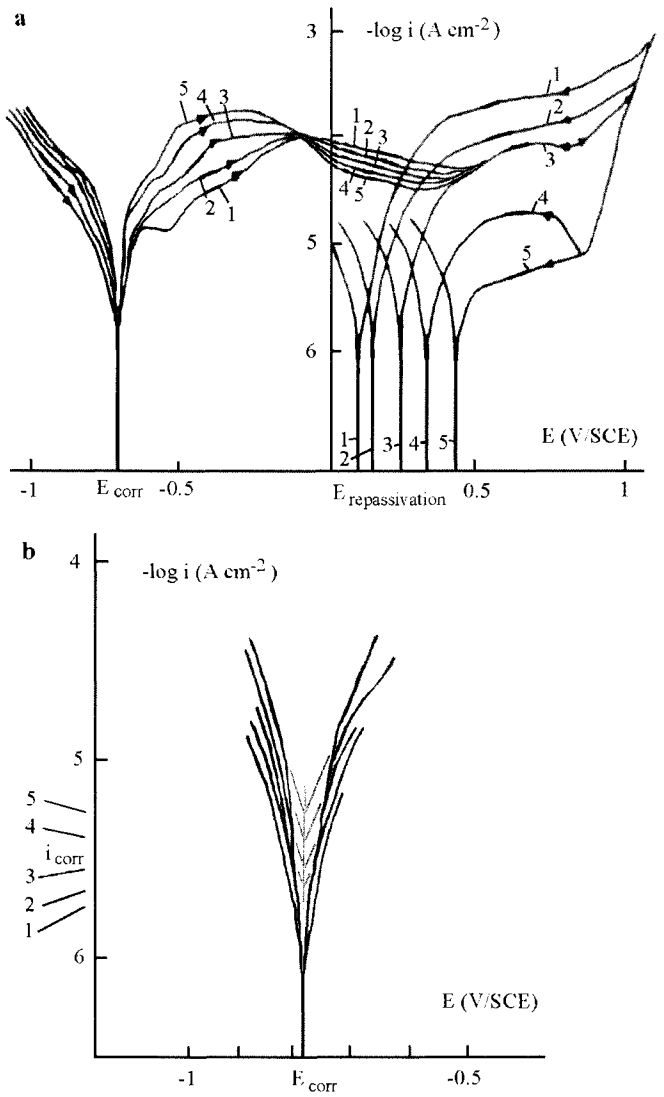

Figure 19.3. Polarization curves with hydrogen peroxide, carbonate and chloride, (a): v: 5 mV s^{-1}, 5×10^{-2} mol dm^{-3} CO_3^{2-}, 0.2 mol dm^{-3} Cl^-, pH 10.2, 1: 10^{-3}, 2: 2×10^{-3}, 3: 10^{-2}, 4: 2×10^{-2}, 5: 5×10^{-2} mol dm^{-3} $^3H_2O_2$, (b): corrosion potential region.

decreasing alkaline pH [100] and increasing $^3H_2O_2$ [257] shift the corrosion potential towards more positive values (Fig. 19.4).

It is also of interest to comment on the corrosion potential in presence of CO_3^{2-} and $^3H_2O_2$ before passivity where the corrosion rate is also limited by surface coverage and

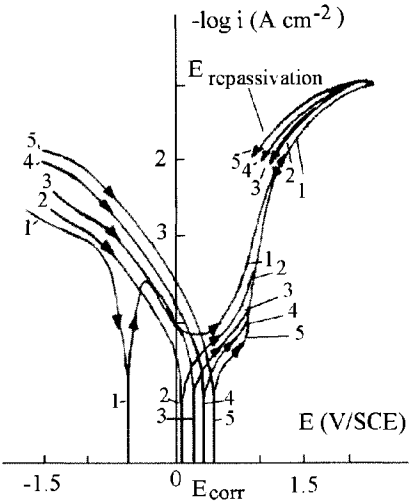

Figure 19.4. Polarization curves with hydrogen peroxide, chloride and without carbonate, v: 5 mV s^{-1}, 0.2 mol dm^{-3} Cl^-, pH 10.2, 1: 10^{-3}, 2: 2×10^{-3}, 3: 10^{-2}, 4: 2×10^{-2}, 5: 5×10^{-2} mol dm^{-3} $^3H_2O_2$.

diffusion within the prepassive oxide. At the corrosion potential, corrosion occurs at the cathodic and anodic sites by the following reactions at alkaline pH.

Cathodic sites:

$$^3H_2O_2 + 2e^- \rightarrow 2O^3H^- \tag{19.1}$$

The cathodic current in the above reaction is:

$$i_c = -2k_c F[^3H_2O_2]^{\nu_{red}}_{pH\ constant} \exp -FE/RT \tag{19.2}$$

anodic sites:

– active range ($\theta < 1$, where θ is the surface coverage)

$$Me + O^3H^- \rightarrow MeO^3H_{ads} + e^- \ldots \rightarrow \{MeO^3H^+\} + e^- \tag{19.3}$$

– transition range (porous layer, $\theta \rightarrow 1$)

$$\{MeO^3H^+\} + O^3H^- \rightarrow \{Me(O^3H)_2\text{-oxide phase}\} \tag{19.4}$$

From the literature, we can write:

$$(x+y)\{Me(O^3H)_2\text{-oxide phase}\} + CO_3^{2-} \rightarrow \{Me_x^{(II)}Me_y^{(III)}(O^3H)_{2(x+y)}\}CO_{3hydrated} + ne^- \tag{19.5}$$

– prepassive range (outer porous oxide layer, inner oxide: $\theta \rightarrow 1$).

$$\{Me_x^{(II)}Me_y^{(III)}(O^3H)_{2(x+y)}\}CO_{3\text{hydrated}} \rightarrow (x+y)MeOO^3H + 2\,{}^3H_2O + CO_3^{2-} + (x+y)\,{}^3H^+ + me^- \quad (19.6)$$

– passive layer formation range (outer porous oxide layer, inner oxide: $\theta = 1$)

$$2MeOO^3H \rightarrow Me_2O_3 + {}^3H_2O \quad (19.7)$$

The surface pH variation will interfere if this is not buffered with $^3H_2O_2$ and carbonate. Also, the partially hydrated-carbonated oxide intermediate undergoes a structural rearrangement along with electron transfer. The reaction mechanism in the active region and corrosion potential indicate that the reactions should be limited by surface coverage, O^3H^-, carbonate and hydrogen peroxide. Equations (19.3) to (19.6) correspond to transient formation, and eq. (19.7) contributes to the passivity by means of $\{Me(O^3H)_2$-oxide phase$\}$ and Me_2O_3. $\{Me_x^{(II)}Me_y^{(III)}(O^3H)_{2(x+y)}\}CO_{3\text{hydrated}}$ must be understood as the formula of a passivated hydroxide-carbonate rust layer, and $MeOO^3H$ is the 'wet' tritiated oxide together with 'dry' Me_2O_3 passive oxide formed on welded S32550 steel. From these equations, if this alloy is left in tritiated water, the rust layer should oxidize into $MeOO^3H$ in an equilibrated reaction. The rusted layer thus plays an important role in the corrosion processes and passivity, since it is involved in the oxidation of divalent hydroxide, as the transient intermediate compound between initial MeO^3H^+ and the final trivalent oxyhydroxide. In these anodic equations, O^3H^- ions are consumed with the formation of $^3H^+$ at the electrode surface. Due to the fact that the carbonate ions buffer the pH, acidification of the surface and in the porosities does not occur and the oxide is formed at a surface pH which remains alkaline. It was previously shown that oxide formed at alkaline pH is definitely more insulating than that obtained at lower pH, and that in an alkaline medium it is more difficult to reduce $^3H_2O_2$ [258,259]. Under such conditions the $^3H_2O_2$ reduction current is very strongly limited by ion and electron diffusion in the oxide. This reduction occurs with a lower current at the oxide surface formed in an alkaline-buffered environment. This means that the oxide formed in a carbonate-alkaline-$^3H_2O_2$ environment offers greater protection than that formed without carbonate at alkaline pH. It is also more protective than the oxide formed on a neutral or acid surface. The result is that for this medium the properties, composition and structure of the oxide are different.

As above, the anodic current is:

$$i_a = 2k_aF[O^3H^-]^{\nu_{ox}}_{\text{pH constant}}\left[CO_3^{2-}\right]^{\nu'_{ox}} \exp FE/RT \quad (19.8)$$

The subscript pH in eq. (19.2) signifies that $^3H_2O_2$ concentration is equilibrated with radiolytic transients depending on surface pH. These equations indicate that the present carbonate buffer, pH and hydrogen peroxide and surface coverage in tritiated water play an active role in the welded S32550 steel corrosion and passivation processes. It thus clearly ap-

pears that rust formed in a second stage leads to $MeOO^3H$ formation at higher potentials indicating two successive oxide layers. The main oxidation sequence is Me → {$Me(O^3H)_2$-oxide phase} → rusted oxide → $MeOO^3H$. The passive layer thus has a complicated chemical structure which is described by a bilayer model. The size and structure of the related layers change with the potential and with other factors such as tritiated water composition, e.g. $^3H_2O_2$ addition.

In the polarization curves, the pre-passive currents are higher with increasing $^3H_2O_2$. The explanation for this could be that $^3H_2O_2$ increases the adsorbates (surface coverage), the carbonated oxide bilayer thickness and interacts in the strata forming the passive layer. The carbonated layer formed under these conditions is associated with corrosion inhibition and has been identified as actively participating in the formation of a protective layer. Also, Sontheimer et al. [250] assumed that the oxycarbonate layer acts as a transformation agent to the Me_2O_3 oxyhydrate protective layer where the passive current is constant. These results signify thickening of the outer porous oxide at lower and medium passive potentials with $^3H_2O_2$ and CO_3^{2-}, whereas at higher passive potentials, the thickness should be constant before de-thickening in the passivity-transpassivity limit. Therefore, a carbonate-oxide layer is a precursor to Me_2O_3 formation. An oxycarbonate layer may aid in the chemical processes associated with a passive layer. From these equations, E_{corr} is assumed to be [178,260]:

$$E_{corr} = \frac{1.15RT}{F}\left(\log\frac{k_c}{k_a}[^3H_2O_2]^{\nu_{red}}[O^3H^-]^{-\nu_{ox}}_{pH\ constant}\left[CO_3^{2-}\right]^{-\nu'_{ox}}\right) \tag{19.9}$$

This equation effectively shows that the corrosion potential should depend on the presence of O^3H^-, carbonate buffer and hydrogen peroxide. In fact, in the polarization curves, it does not change and is related to the pH buffer and formation of the different structure of the insulating passive oxide layer with the joint involvement of CO_3^{2-} and $^3H_2O_2$. As in eq. (19.9), the corrosion current is:

$$i_{corr} = 2(k_c k_a)^{0.5} F\left(^3H_2O_2\right)^{\nu_{red}}[O^3H^-]^{\nu_{ox}}_{pH\ constant}\left(CO_3^{2-}\right)^{\nu'_{ox}} \tag{19.10}$$

The corrosion current, i_{corr}, depends on anodic and cathodic rate constants. It also depends on the nature of carbonated oxide and the aqueous medium; it can be seen from Fig. 19.3b that the value of i_{corr} is higher with $^3H_2O_2$ (Table 19.2).

It is observed in the transpassivity that the pitting current decreases and the repassive potential increases in the reverse scan when the $^3H_2O_2$ concentration increases. This is the opposite case to the behavior without CO_3^{2-}, as shown in Fig. 19.4 and in [258,259]. The buffered surface pH and thicker oxide layer limit pitting corrosion due to the fact

Table 19.2. Corrosion current as a function of $^3H_2O_2$ concentration

$^3H_2O_2$ (mol dm^{-3})	10^{-3}	2×10^{-3}	10^{-2}	2×10^{-2}	5×10^{-2}
i_{corr} (μA cm^{-2})	1	1.7	2	2.3	3

that this localized corrosion depends on the local pH and oxide thickness and chloride diffusion rate across this layer. It can also be seen that the positive current in the reverse scan is greater than that in the forward scan for the same potential, signifying risk of crevice corrosion at lower $^3H_2O_2$ concentrations. It appears that localized corrosion can be avoided at higher $^3H_2O_2$ concentrations and that increasing the passive domain in the passive-transpassive region with hydrogen peroxide is feasible. These different results imply that surface pH buffer, carbonate and $^3H_2O_2$ provide protection under these conditions, and the area corroded by pitting must decrease.

3.2. Voltammetric curves

In the voltammograms, we expect to find the adsorbed intermediate formation in the beginning and in the active peak and a porous and passivating non-porous oxide layer which spreads across the surface from the prepassivity and the Flade potential. In the backward scan produced from the pitting-transpassive region, the pits would be filled by the corrosion products, the passive oxide layer reformed at lower potentials and finally the corrosion products and $^3H_2O_2$ would be reduced in the cathodic peak. In an initial approach, to know the contribution of local non-buffered and buffered pH, CO_3^{2-} and $^3H_2O_2$ at the welded S32550 steel surface and to guarantee the different nature of oxide layers by electrochemical impedance analysis, the voltammograms were drawn in presence of $^3H_2O_2$ and either with hydrogen peroxide and chloride (Fig. 19.5), with hydrogen peroxide, carbonate and chloride (Fig. 19.6) or with carbonate and chloride (Fig. 19.7).

The voltammograms shown in Fig. 19.5 were obtained at pH 10.2, in presence of Cl^-, at different $^3H_2O_2$ concentrations and without CO_3^{2-}. In the forward scan, curve 2 obtained at lower $^3H_2O_2$ concentration shows an active peak. Immediately after the active peak, the current takes on negative values. The corrosion potential is either in prepassivity, passivity or at that of the active peak. This corresponds to mixed electrode behavior bringing about instabilities in the passive oxide layer, which is not stabilized and passivated. Fig. 19.5 also shows that the active peak current is lower when the $^3H_2O_2$ concentration increases. In addition, it can be seen that the cathodic peak current is shifted towards more negative values. These two types of current behavior result from the $^3H_2O_2$ reduction current, which is superimposed on the corrosion currents depending on the oxide surface acidification in the anodic sites, and that of the reduction of the corrosion products. This shifts overall currents in this region towards negative values and the corrosion or rest potentials towards more positive values (located first in the active zone, then in prepassivity and finally in the Flade potential). At higher $^3H_2O_2$ concentrations, the active peak disappears and the corrosion potential shifts again to a more positive potential changing the passive domain. In the passive domain, the anodic current decreases only slightly, signifying that the thickness does not change significantly. The passive potential range is indeed smaller at higher $^3H_2O_2$ concentrations. In the transpassive-passive region, the pitting current increases and the repassive potential shifts toward smaller values with higher $^3H_2O_2$ concentration, whereas with carbonate present, the behavior is inverted (Figs 19.6 and 19.7). The interpretation

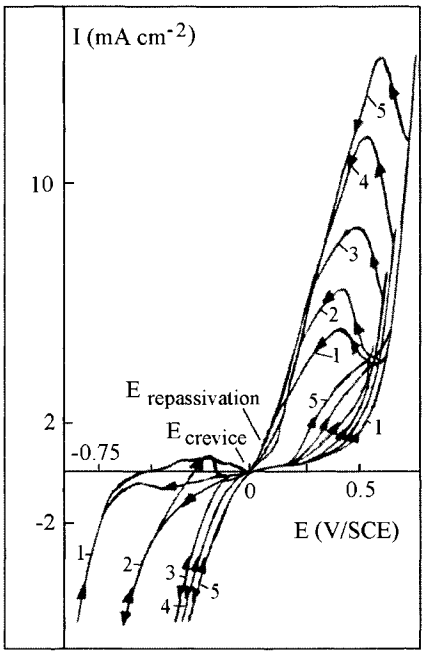

Figure 19.5. Voltammetric curves with hydrogen peroxide, chloride and without carbonate, v: 32 mV s^{-1}, 0.2 mol dm^{-3} Cl^-, pH 10.2, 1: 10^{-3}, 2: 2×10^{-3}, 3: 10^{-2}, 4: 2×10^{-2}, 5: 5×10^{-2} mol dm^{-3} $^3H_2O_2$.

is that carbonate ions with or without hydrogen peroxide favors passivity, and the oxide breakdown current and pitting increase when hydrogen peroxide is on its own. The local pH is not buffered and the local acidification in pits allows their propagation. Also, chloride has the time to cross the thin oxide layer by diffusion with the vacancies. Evidently the presence of hydrogen peroxide and chloride significantly affect welded S32550 steel oxidation-reduction and corrosion processes by pitting and crevice formation in the absence of CO_3^{2-}.

The voltammograms obtained with carbonate and hydrogen peroxide for a constant scan rate are shown in Fig. 19.6. In contrast to Fig. 19.5, the corrosion potential where the current crosses the potential axis does not change significantly when the $^3H_2O_2$ increases. Carbonate ions act to keep the alkaline pH constant at the electrode surface. Also, the oxide formed at an alkaline pH is clearly more insulating than that obtained at another pH and the $^3H_2O_2$ reduction is more difficult to obtain [258,259]. A higher active peak in the alkaline corrosion region with CO_3^{2-} is seen showing more clearly the active-passive transition for the high scan rates. The higher active peak indicates more surface coverage by transients and oxides according to eqs (19.3) to (19.7). This depends on the transient species formed at the electrode surface and their kinetics [100]. Unlike the situation shown in Fig. 19.5, the active peak increases with the $^3H_2O_2$ concentration. There is also a second active peak preceding the first whose appearance depends on carbonate and $^3H_2O_2$

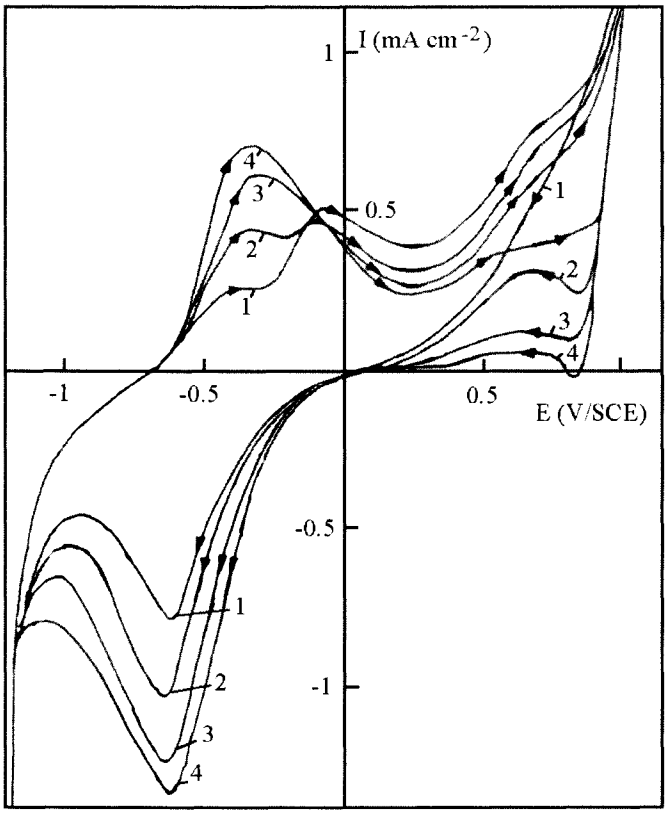

Figure 19.6. Voltammetric curves with hydrogen peroxide, carbonate and chloride, v: 32 mV s^{-1}, 5×10^{-2} mol dm^{-3} CO_3^{2-}, 0.2 mol dm^{-3} Cl^-, pH 10.2, 1: 2×10^{-3}, 2: 10^{-2}, 3: 2×10^{-2}, 4: 5×10^{-2} mol dm^{-3} $^3H_2O_2$.

being present. It is stated [261] to correspond to a specific corrosion product leading to carbonated oxide formation. Evidently the presence of CO_3^{2-} ions and $^3H_2O_2$ together significantly affect welded S32550 steel oxidation processes. With these species, the higher active peak observed probably indicates the electrochemical reaction coupled to chemical processes with both CO_3^{2-} and $^3H_2O_2$ present and a greater extent of oxide growth. The active region should be ideally divided in two domains which involve two distinct oxides related to the {Me(O^3H)$_2$-oxide phase} and carbonate rust layers. The passive oxide layers should exhibit their intrinsic nature in the prepassivity-passivity ranges where, according to eqs (19.4) to (19.7), there is {Me(O^3H)$_2$-oxide phase} then carbonated oxide and Me_2O_3 formation depending on the passive potentials. Therefore carbonate and hydrogen peroxide lead to a more protective layer, and certainly the nature of the formed layer, thickness and corrosion products may be different at these prepassive-passive potentials from that without carbonate ions and with the different hydrogen peroxide concentration.

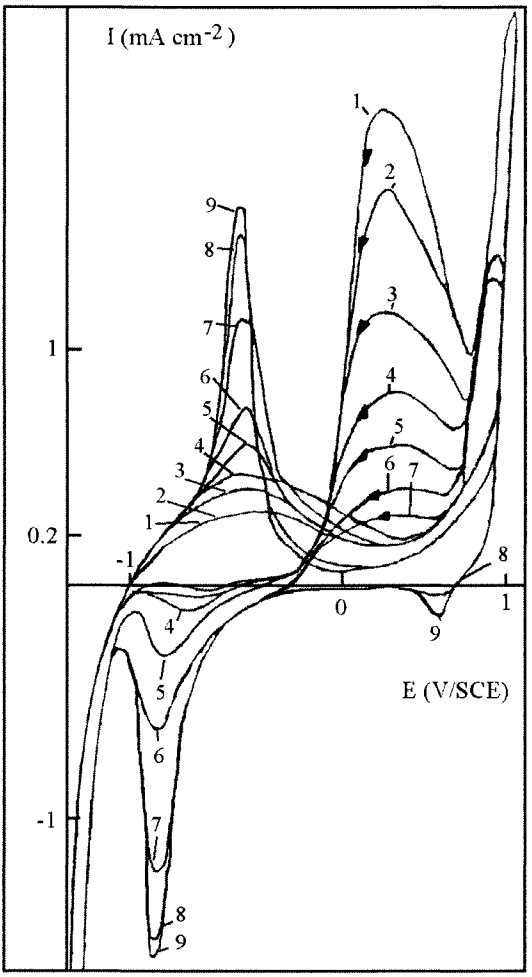

Figure 19.7. Voltammograms in presence of carbonate and chloride, ω: 2000 rpm, v: 200 mV s^{-1}, pH 10.2, 0.5 mol dm^{-3} Cl^-, 5 × 10^{-3} mol dm^{-3} NO_3^-, 1: 0, 2: 10^{-4}, 3: 10^{-3}, 4: 2 × 10^{-3}, 5: 3 × 10^{-3}, 6: 5 × 10^{-3}, 7: 0.01, 8: 0.05, 9: 0.1 mol dm^{-3} CO_3^{2-}.

In the backward scan, the cathodic peak current is shifted to negative values. This behavior is similar to that obtained in Fig. 19.5 and corresponds to hydrogen peroxide and corrosion product reduction.

In the passive region, the anodic current decreases with the $^3H_2O_2$ concentration. The explanation is that hydrogen peroxide and carbonate ions modify the electron diffusion and the global oxide layer thickness forming more protective layers. In this case, the passive potential range is wider at higher $^3H_2O_2$ concentrations and with CO_3^{2-}.

In the transpassive region, the pitting current decreases and the repassive potential shifts toward higher values with increasing $^3H_2O_2$ concentration. The interpretation could be that the oxide breakdown current and pitting decrease with the joint presence of hydrogen peroxide and carbonate. Evidently the presence of hydrogen peroxide with carbonate buffer and the thicker oxide layer formed with these species significantly retain passivity and delay welded S32550 steel pitting nucleation. The pH buffer is also mentioned by Olefjord et al. [262] in the alloy-oxide interface for the nitrogen stainless steel. It is clear that $^3H_2O_2$ and carbonate ions jointly participate in the production of the passive oxide. This indicates that the corrosion rate and passivity are dependent on the carbonate ions remaining on the surface of the welded steel and also on the absence of any superficial alkaline pH modification. The carbonate, hydrogen peroxide and intermediates formed are responsible for the passive oxide electrochemical activity and characteristics. Chloride ions require more time to cross the thicker passive oxide layer by diffusion as seen in Fig. 19.8 where

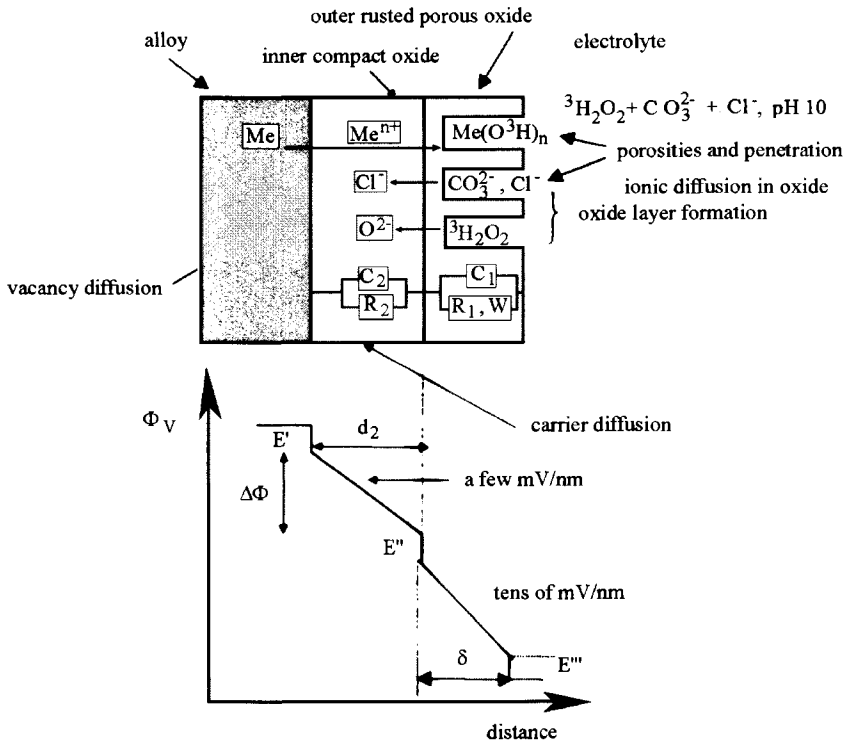

Figure 19.8. Physical model and equivalent circuit proposed to interpret the processes in mixed carbonated oxide with hydrogen peroxide and chloride, R_1: oxide resistance including the diffusion impedance, R_2: oxide resistance, C_n: constant phase elements.

a decrease in the scan rate should lead to facilitating diffusion and increasing the pitting currents in the backward scan.

In Fig. 19.9, an increase in the scan rate leads to increasing the anodic and cathodic peaks. Plots of the logarithm of current in the anodic major peak vs. logarithm of scan rate give a straight line with a slope close to 0.5. Plots of peak current vs. the square root of scan rate have also been made. For the anodic peak, a good straight line was obtained, and corresponds to the Levich equation for a reaction controlled by ion diffusion [224]. These peaks correspond well to the classical faradaic and capacitance current equations given in voltammetry, i.e. an active behavior that fits the Levich equation that in turn depends on surface coverage. The value calculated from the active peak is about 6.4 $mC\,cm^{-2}$, whereas without either CO_3^{2-} or $^3H_2O_2$, the charge is about 2.5 $mC\,cm^{-2}$. Evidently, the joint CO_3^{2-} and $^3H_2O_2$ presence should increase the oxide layer thickness and porosity. Results indicate that the carbonate oxide layer formed with $^3H_2O_2$ is an oxide multilayer. In Fig. 19.9, the repassive and pitting potentials increase with the scan rate. In this case, the effects of diffusion kinetics of Cl^- in oxide thickness and repassivity kinetics on potentials are more clearly shown in the voltammograms obtained at the lower $^3H_2O_2$ concentration as seen in Fig. 19.9a, b.

3.3. Impedance spectra

3.3.1. Results in the prepassive-passive region The characteristic Nyquist and Bode diagrams for the prepassive-passive potentials of the welded S32550 stainless steel, and for different $^3H_2O_2$ concentrations and with CO_3^{2-} and Cl^- present are given in Figs 19.10 and 19.11.

Spectra with the same appearance were obtained by Maximovitch et al. [263] for metals and we have looked for the best possible solution for their interpretation. This was not obvious since the simplest expression for the equivalent circuit has 8 components. This electrical circuit corresponds to an oxide bilayer with diffusion in the outer oxide layer. For this interpretation, it was necessary to draw both the Nyquist and Bode diagrams and the fitting results showed that by attributing the highest resistance to the outer oxide layer we have a high frequency capacitive response, but the resistance value was outside that commonly accepted for the outer barrier oxide. This first hypothesis was therefore dropped. We then tried another solution for interpreting the diagrams. Here, we considered ion diffusion in the outer oxide pores, but the high electrical resistance value was also counter to that commonly accepted. Finally, in attributing a high value to the resistance of the inner layer, we simultaneously obtained a barrier behavior for the internal capacitance with a low frequency capacitive response. This high value of the internal resistance is in better agreement with those commonly accepted. In fact, these values for the two layers agree with the proposal given by Silverman [264] for predicting corrosion by applying circuit models to evaluate the corrosion inhibition. In the following subsections the diagrams are described and interpreted in detail.

At higher frequencies, the Nyquist spectrum (Fig. 19.10) consists of a small capacitive semi-circle. Spectral analysis shows that it really corresponds to corrosion in porosities of

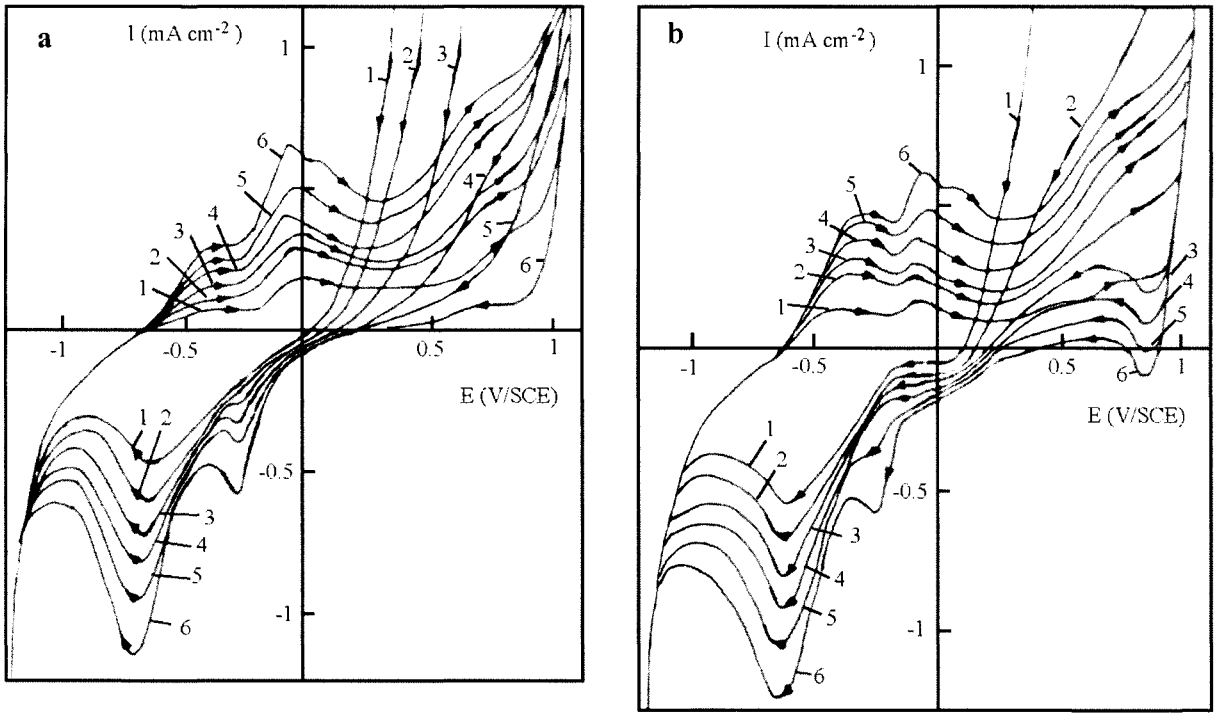

Figure 19.9. Voltammetric curves for different scan rates and $^3H_2O_2$ concentration, 5×10^{-2} mol dm^{-3} CO_3^{2-}, 0.2 mol dm^{-3} Cl^-, pH 10.2, v: 1: 10, 2: 25, 3: 32, 4: 40, 5: 50, 6: 75 mV s^{-1}, (a): 2×10^{-3}, (b): 10^{-2}, (c): 2×10^{-2}, (d) 5×10^{-2} mol dm^{-3} $^3H_2O_2$.

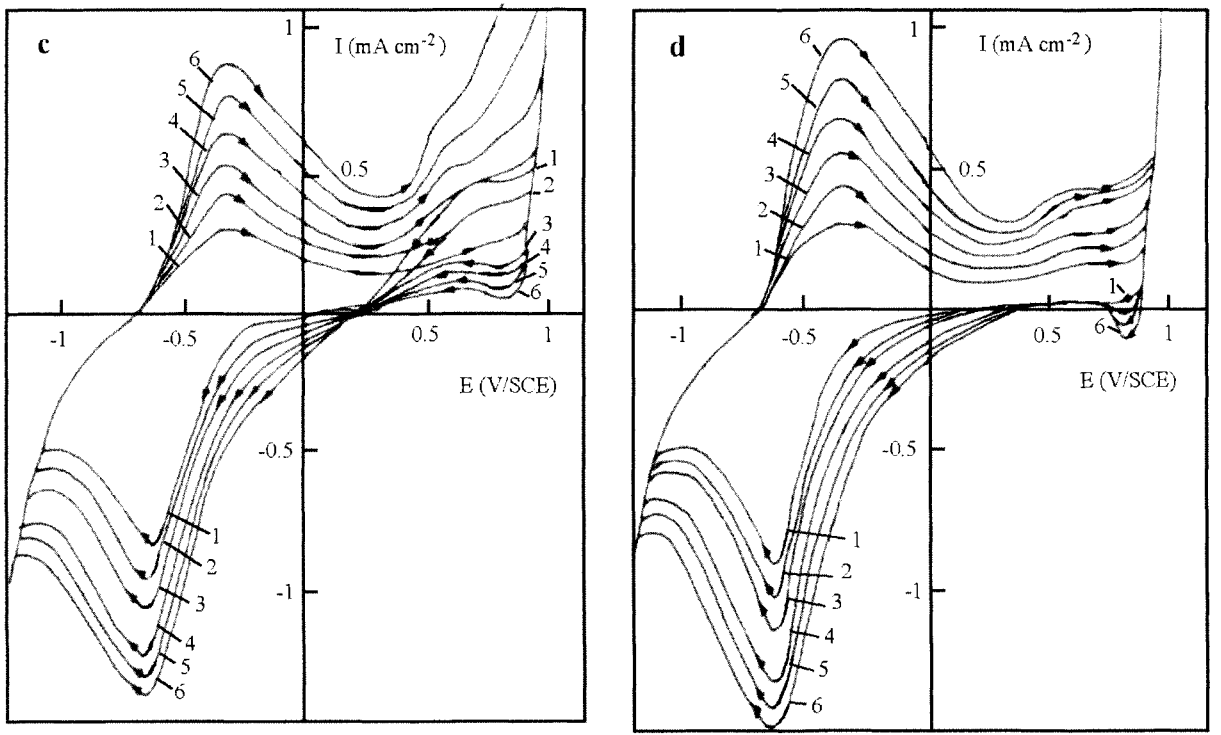

Figure 19.9. (Continued).

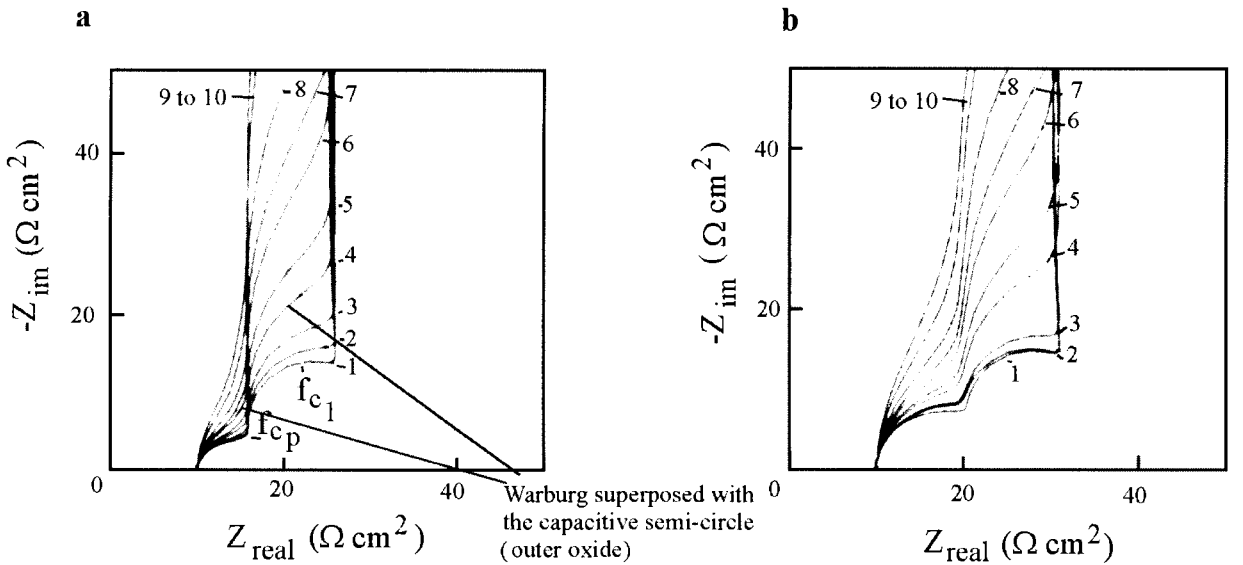

Figure 19.10. Nyquist spectra in presence of CO_3^{2-}, Cl^-, $^3H_2O_2$ in prepassivity-passivity, 5×10^{-2} mol dm^{-3} CO_3^{2-}, 0.2 mol dm^{-3} Cl^-, pH 10.2, (a): 10^{-3} mol dm^{-3}, (b): 2×10^{-3} mol dm^{-3}, (c): 10^{-2} mol dm^{-3}, (d): 2×10^{-2} mol dm^{-3}, (e): 5×10^{-2} mol dm^{-3} $^3H_2O_2$, 1: −0.60 V, 2: −0.58 V, 3: −0.56 V, 4: −0.53 V, 5: −0.50 V, 6: −0.45 V, 7: −0.40 V, 8: −0.35 V, 9: −0.30, 10: −0.25 V/SCE.

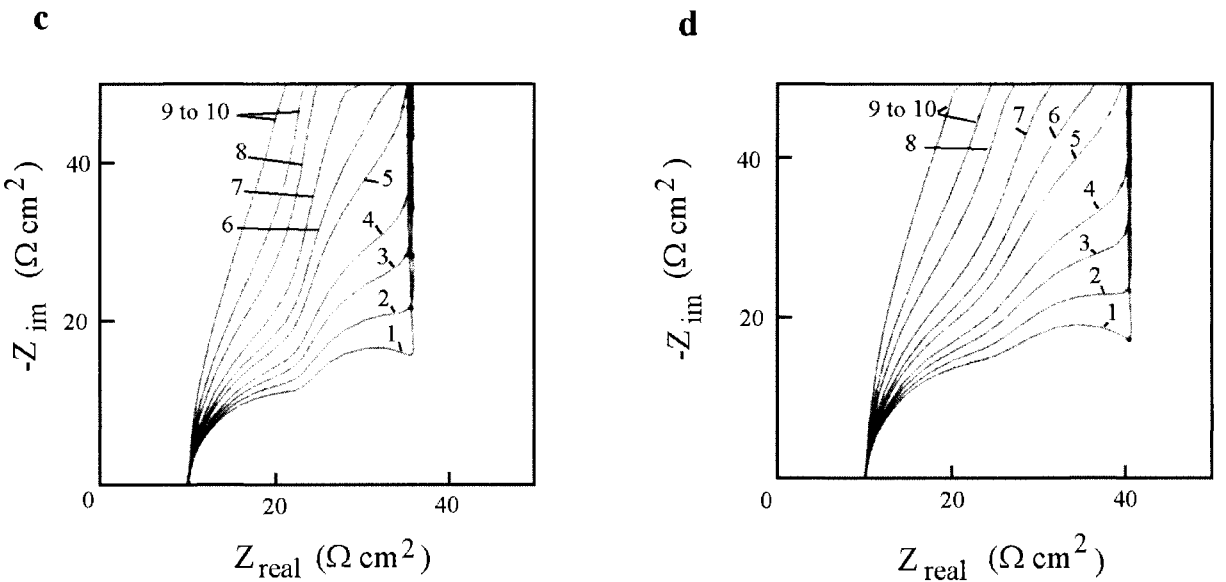

Figure 19.10. (Continued).

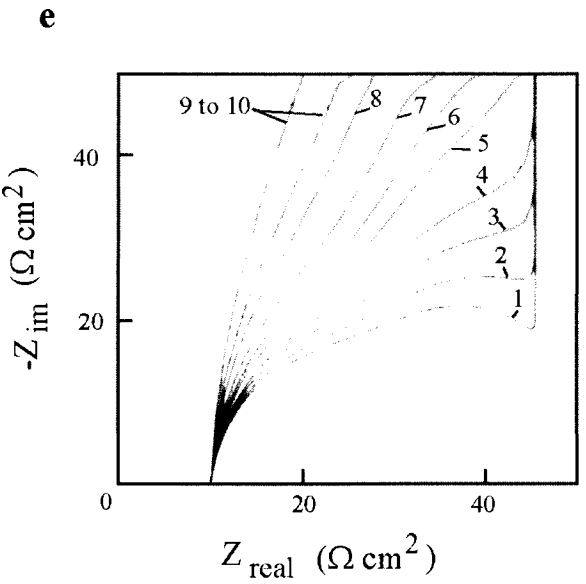

Figure 19.10. (Continued).

the outer oxide layer (ox_1). This indicates that localized corrosion should be possible inside the pores. This semi-circle can be superposed with a Warburg straight line that accounts for an ion diffusion-controlled process through the porosities [261]. The Warburg straight line is essentially seen at the middle prepassive-passive potentials (curve 4). The semi-circle size increases when the $^3H_2O_2$ concentration increases signifying repassivation in porosities. In the middle frequency section, the spectrum is characterized by a second semi-circle corresponding to the outer oxide layer. From the appearance of Fig. 19.10, the values of the two semi-circles would partially hide the diffusion behavior in the porosities. At the lower frequencies, the vertical straight line corresponds to a very large semi-circle (quasi-resistive and capacitive) due to the inner oxide layer (ox_2).

In Fig. 19.11A, the Bode plots display four distinct regions with a break between those in the impedance modulus and three dips in the phase angle, that depend on the grown oxide:

(a) At higher frequency, a dip for the characteristic frequency, f_{c_p}, in the phase angle/$\log(f)$ curve and a linear hump in the $\log|Z|/\log(f)$ plots depending on the $^3H_2O_2$ concentration. The subscript p indicates the reaction in porosities. The dip and hump are represented by the first small semi-circle in the Nyquist spectra (Fig. 19.10). They can be more easily obtained at the higher $^3H_2O_2$ concentrations or by subtracting the electrolyte resistance, as shown in the simulated Bode plots (Fig. 19.11B). These indicate the presence of a parallel resistance and the oxide capacitance (Fig. 19.8). Also, the greater deviation of the phase angle at the higher $^3H_2O_2$ concentrations or prepassive-

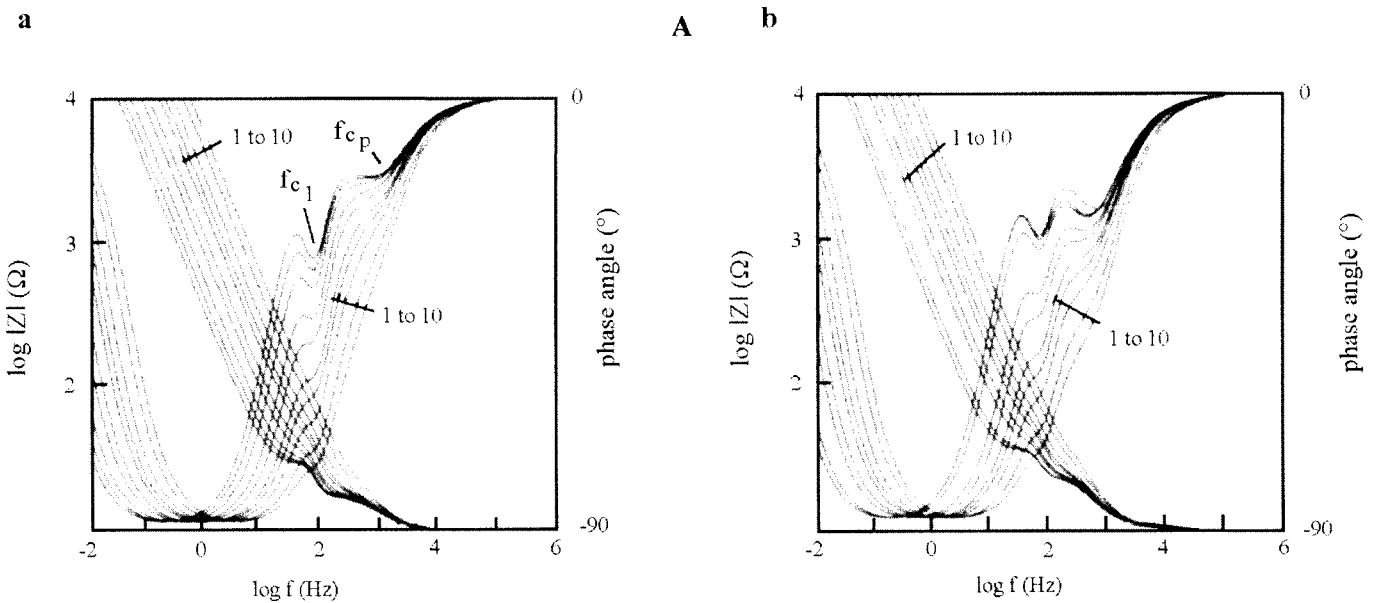

Figure 19.11. Bode spectra in presence of CO_3^{2-}, Cl^-, $^3H_2O_2$ in prepassivity-passivity, 5×10^{-2} mol dm^{-3} CO_3^{2-}, 0.2 mol dm^{-3} Cl^-, pH 10.2, (A): complete spectra, (a): 10^{-3} mol dm^{-3}, (b): 2×10^{-3} mol dm^{-3}, (c): 10^{-2} mol dm^{-3}, (d): 2×10^{-2} mol dm^{-3}, (e): 5×10^{-2} mol dm^{-3} $^3H_2O_2$, 1: −0.60 V, 2: −0.58 V, 3: −0.56 V, 4: −0.53 V, 5: −0.50 V, 6: −0.45 V, 7: −0.40 V, 8: −0.35 V, 9: −0.30, 10: −0.25 V/SCE, (B): simulated spectra by subtracting the electrolyte resistance.

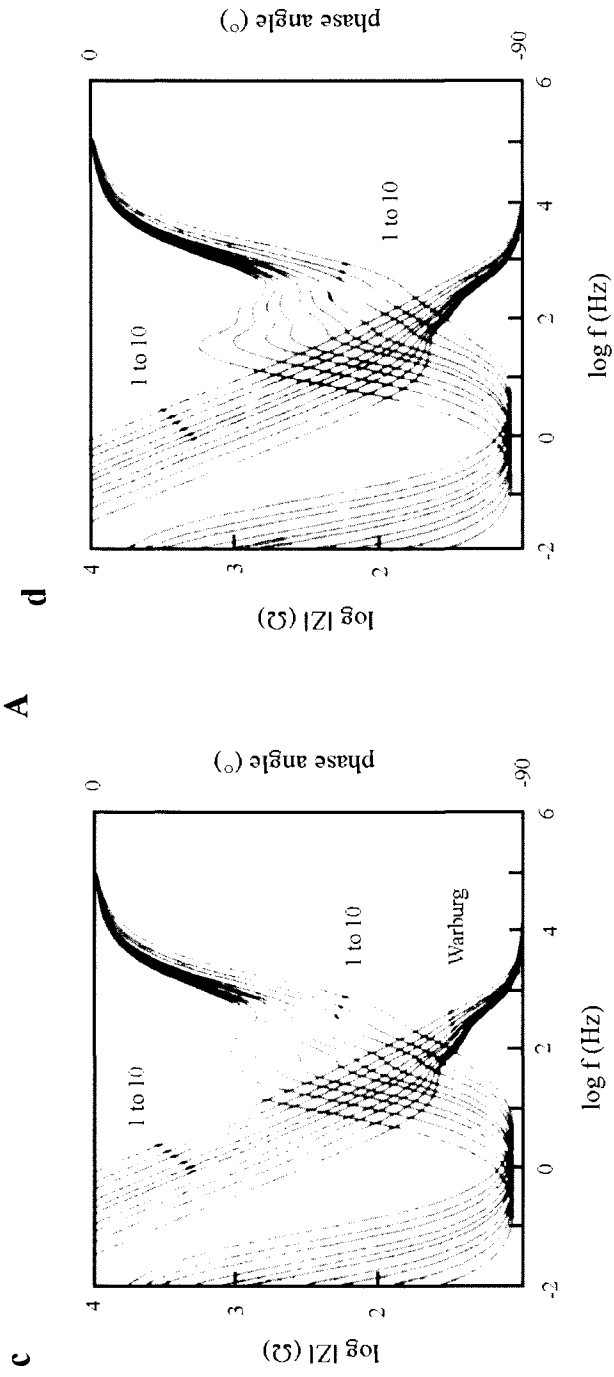

Figure 19.11. (Continued).

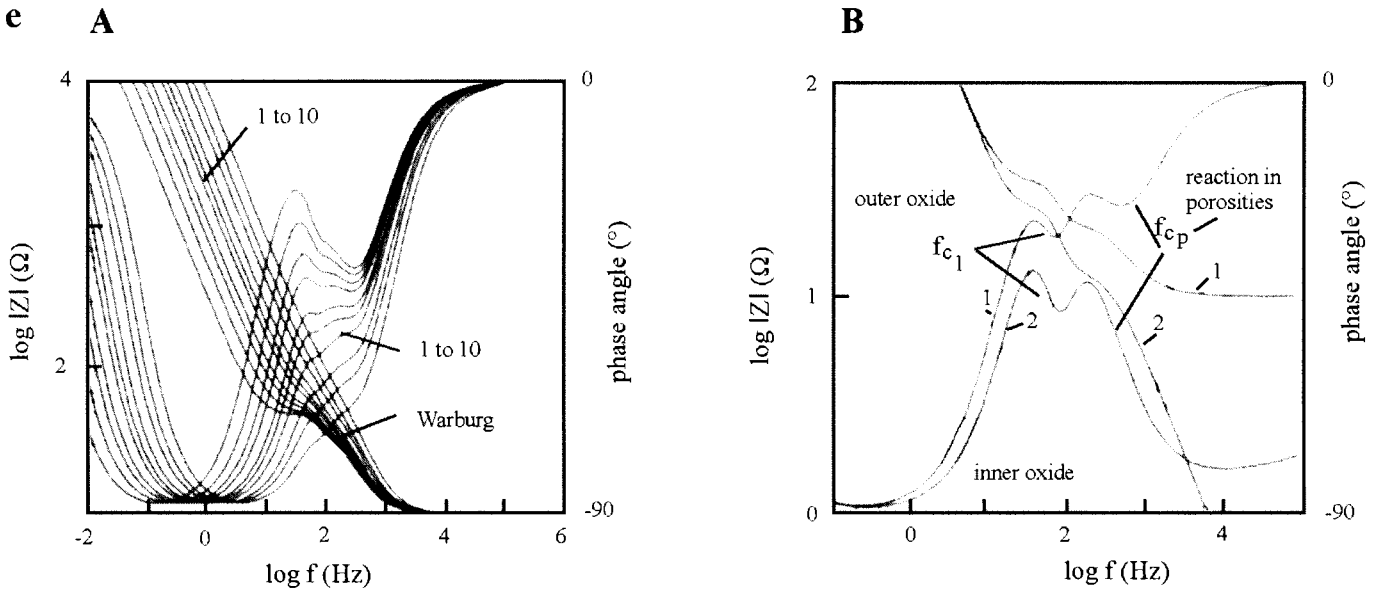

Figure 19.11. (Continued).

passive potentials signifies that the porosities thus formed on welded S32550 steel tend to be repassivated.

(b) Between 200 and 40 Hz, a slope of -0.5 with a time constant of around 5×10^{-3} s taken at the break in the impedance modulus, visible essentially at the middle prepassive-passive potentials, indicating an ion diffusion process in the porosities of the outer porous oxide layer [261].

(c) A second dip in the phase angle/$\log(f)$ curve at the characteristic frequency, f_{c_1}, where the subscript 1 indicates the outer oxide layer, and a second linear hump in the $\log|Z|/\log(f)$ plots. This is represented by the second semi-circle in the Nyquist spectra (Fig. 19.10) which corresponds to the outer oxide layer.

(d) In the broad low frequency range, there is a linear slope of -0.85 in $\log|Z|$ as $\log(f)$ decreases, while phase angle values tend to $-90°$ over the measurement frequency range. This is the characteristic response of the inner barrier layer associated with a high impedance.

To calculate the diffusion coefficient (D) of inserted ions and estimate the outer porous oxide layer thickness, we have analyzed the Warburg impedance. At the characteristic frequency, where $f_{c_p} \sim 2.5D/2\pi\delta^2$, the break between the semi-infinite diffusion and the outer oxide regions occurs in the Bode or Nyquist spectra representations. Calculations yield $D = 2.2 \times 10^{-12}$ cm^2 s^{-1} and the semi-infinite diffusion layer thickness is estimated to be 70 nm. Thus the outer oxide thickness is not negligible. The diffusion coefficient value is fairly low, indicating the porosity effect for ion transport.

According to these results, the difference between the two layers is related to structural changes. For example, the outer layer such as $\{Me_x^{(II)}Me_y^{(III)}(O^3H)_{2(x+y)}\}CO_3$ is hydrated for the prepassivity as seen in eq. (19.5) and the passive layer corresponds to a less hydrated ($MeOO^3H$ or Me_2O_3); in this layer there is also a more homogeneous structure with a higher number of electron defects due to the $^3H_2O_2$ and Cl^- present. This means that ion diffusion processes with temporary oxidizing species, $^3H_2O_2$, CO_3^{2-} and Cl^- take place for the transformation of the outer conversion oxide layer, $\{Me(O^3H)_2$-oxide phase$\}$, leading to rusted oxide. Also, the electrical field (Φ_V) leads to the migration of ionic species and to a decrease in the carrier number in the passive oxide layer (Fig. 19.8). Examination of the impedance spectra is then an appropriate method of studying the evolution of passive layers and ion or electron diffusion that have not been evidenced by other electrochemical methods or surface analysis techniques.

These results indicate that the diffusion is produced at any $^3H_2O_2$ concentration in the presence of temporary oxidizing species and there are fewer barrier layer effects for the inner oxide layer when the $^3H_2O_2$ concentration increases. The explanation can be that electron diffusion by O^{2-} vacancies increases in this oxide layer and the current flows through the layer as seen in the polarization and voltammetric curves. This provides evidence of two oxide layers depending on carbonate and $^3H_2O_2$ concentration changing with the prepassive-passive potentials. As the hydrogen peroxide concentration is further increased, both these effects appear more pronounced (Fig. 19.11A). The time constants in the higher frequency range are related to the reaction in the porosities involving $^3H_2O_2$

and Cl^- and the outer oxide layer. The phase angle of f_{c_p} increases slightly when the prepassive potentials or $^3H_2O_2$ concentration increase signifying that the porosities should repassivate and therefore the description of the oxide layers in terms of barrier properties is valid. This provides a better understanding of the dependence on vacancies diffusion as indicated by Mansfield [190]. A good representation of the transfer function for taking this evolutive structure as having two layers was given in the previous chapter. From the transfer function, the equivalent circuit consists of series connections of Z/[CPE] or capacitance elements (Fig. 19.8) with a resistance at high frequencies attributed to the aqueous medium. To obtain a connection for the characteristic parameters of the two successive oxide layers depending on $^3H_2O_2$ and potentials, the total oxide charge (Q) is calculated by integrating the current-time curves obtained from the voltammograms for different $^3H_2O_2$ concentrations. The corresponding values are related to the formation of the oxide bilayer. According to Schmuki and Böhni [237], the oxide charge is:

$$Q = \frac{nF\delta}{\rho_1} + \frac{\varepsilon_2 \varepsilon_0 nF}{C_{ox_2}\rho_2} \tag{19.11}$$

where δ is the porous oxide layer thickness estimated previously in the characteristic frequency and ρ_n the carbonated oxide concentration in moles per cm^3. The C_{ox_2} value is determined by fitting the measured spectra (Tables 19.3 to 19.7).

From the variation in the Bode diagram (Fig. 19.11A), it is reasonable to assume that the term ox_2 interacts at the different $^3H_2O_2$ concentrations and the prepassive and passive potentials. This indicates that C_{ox_2} depends essentially on $^3H_2O_2$ and C_{ox_1} should vary essentially with the CO_3^{2-} buffer. By applying eq. (19.11) for different $^3H_2O_2$ concentrations, the values obtained by fitting the spectra (Tables 19.3 to 19.7) and integrating the curves give a linear relationship between $(1/C_{ox_2})$ and Q. This signifies that, for different $^3H_2O_2$ concentrations, the amount of oxide formed in prepassivity and passivity is proportional to the reciprocal of the oxide capacitance and depends on its thickness. According to impedance measurements, the inner oxide layer thickness grows with the prepassive-passive potentials and $^3H_2O_2$ concentration with the CO_3^{2-} buffer present.

For these calculations, the oxide capacitance is estimated from [265]:

$$1/A_n = C_{ox_n}^a \left(\frac{1}{R_{ox_n}}\right)^{1-a} \tag{19.12}$$

In these equations, R_{ox_n} is the oxide resistance, C_{ox_n} the oxide layer capacitance, A_n the constant phase element related to the oxide layer capacitance, and 'a' the frequency-independent parameter. When $a = 1$, $1/A_n$ corresponds to the oxide layer capacitance; when $a = 0$, A_n is as a resistance. For the second point, in passivity, the current response may be attributed to two possible processes: passive layer formation and oxide layer dissolution. To investigate this we analyzed quantitatively Fe, Ni, Cr and Mo ions, which could be present in tritiated water, by Atomic Absorption Spectroscopy; before analysis, the potential was kept for 1 h at the selected passive potential. The detection limit by Atomic

Table 19.3. Dependence of oxide capacitances and resistance on prepassive-passive potentials in presence of carbonate, chloride ions and hydrogen peroxide (10^{-3} mol dm^{-3} $^3H_2O_2$)

E (V/SCE)	−0.60	−0.58	−0.56	−0.53	−0.50	−0.45	−0.40	−0.35	−0.30	−0.25
R_{ox_2} (MΩ cm^2)	0.1	0.1	0.1	0.1	0.11	0.11	0.11	0.11	0.11	0.11
C_{ox_1} (μF cm^{-2})	15	14.5	14	13.5	13	12.5	12	11	10.5	10
C_{ox_2} (μF cm^{-2})	32	30	29	28	26	25	24	23	22	20

Table 19.4. Dependence of oxide capacitances and resistance on prepassive-passive potentials in presence of carbonate, chloride ions and hydrogen peroxide (2×10^{-3} mol dm^{-3} $^3H_2O_2$)

E (V/SCE)	−0.60	−0.58	−0.56	−0.53	−0.50	−0.45	−0.40	−0.35	−0.30	−0.25
R_{ox_2} (MΩ cm^2)	0.11	0.11	0.11	0.12	0.12	0.12	0.12	0.13	0.13	0.13
C_{ox_1} (μF cm^{-2})	15	14.5	14	13.5	13	12.5	12	11	10.5	9.5
C_{ox_2} (μF cm^{-2})	25	23	22	21	19	18	17	16	16	15

Table 19.5. Dependence of oxide capacitances and resistance on prepassive-passive potentials in presence of carbonate, chloride ions and hydrogen peroxide (10^{-2} mol dm^{-3} $^3H_2O_2$)

E (V/SCE)	−0.60	−0.58	−0.56	−0.53	−0.50	−0.45	−0.40	−0.35	−0.30	−0.25
R_{ox_2} (MΩ cm^2)	0.12	0.12	0.12	0.13	0.13	0.14	0.14	0.15	0.15	0.15
C_{ox_1} (μF cm^{-2})	12	11.5	11	10.5	10	9.5	9	8.5	8	7.2
C_{ox_2} (μF cm^{-2})	20	18	17	16	14	13	12	12	11	10

Table 19.6. Dependence of oxide capacitances and resistance on prepassive-passive potentials in presence of carbonate, chloride ions and hydrogen peroxide (2×10^{-2} mol dm^{-3} $^3H_2O_2$)

E (V/SCE)	−0.60	−0.58	−0.56	−0.53	−0.50	−0.45	−0.40	−0.35	−0.30	−0.25
R_{ox_2} (MΩ cm^2)	0.14	0.14	0.15	0.15	0.16	0.16	0.16	0.17	0.17	0.17
C_{ox_1} (μF cm^{-2})	12	11.5	11	10.5	10	9.5	9	8.5	7.8	7
C_{ox_2} (μF cm^{-2})	15	14	14	13	12	11	11	10	9	9

Table 19.7. Dependence of oxide capacitances and resistance on prepassive-passive potentials in presence of carbonate, chloride ions and hydrogen peroxide (5×10^{-2} mol dm^{-3} $^3H_2O_2$)

E (V/SCE)	−0.60	−0.58	−0.56	−0.53	−0.50	−0.45	−0.40	−0.35	−0.30	−0.25
R_{ox_2} (MΩ cm^2)	0.17	0.17	0.18	0.18	0.19	0.19	0.19	0.2	0.2	0.2
C_{ox_1} (μF cm^{-2})	11	10	9.5	9.2	9	8.6	8.1	7.6	7	6
C_{ox_2} (μF cm^{-2})	12	12	11	11	10	10	9	9	8	8

Absorption Spectroscopy was found to be 10^{-10} mol cm^{-3}, while the total amount of oxide was 2×10^{-8} mol, taking a surface of 1 cm^2 in the tests. The dissolution current was negligible as were the amounts of iron, nickel, chromium and molybdenum analyzed in the tritiated water. Therefore the quantity of the total charge obtained by integrating the current-time curve from voltammograms corresponds to oxide layer formation.

From the results in Tables 19.3–19.7, the variation of C_{ox_2} indicates that the oxide layer formation obeys a growth law depending on these two studied parameters: potentials as indicated by Schmuki and Böhni [237] and hydrogen peroxide concentration. A 'critical

capacitance' corresponding to its lower value denotes a more perfect inner oxide layer at higher $^3H_2O_2$ concentration. This behavior signifies that the thicker oxide obtained at higher $^3H_2O_2$ concentration is in accordance with the polarization and voltammetric curves. In comparison with previous results [258,259], this behavior would appear also to depend on carbonate buffer. The Bode plots (Fig. 19.11A) enable us to estimate the donor concentration (n_{d_2}) over a sufficient potential range following the simplified Mott-Schottky equation as shown by Schmuki et al. [255]. The charge carrier density can be expressed for the inner oxide layer:

$$n_{d_2} = \frac{2C_{ox_2}^2}{e\varepsilon_2\varepsilon_0 r}\left(V_m - V_{fb} - \frac{kT}{e}\right) \tag{19.13}$$

where e is the charge of the electron, n_{d_2} the donor density, k the Boltzmann constant, and V_m, V_{fb} the potentials at which the impedance measurements are carried out and the flat-band potential, respectively. Assuming that the vacuum permittivity ε_0 is 8.8×10^{-14} F/cm and the value of the oxide layer dielectric constant ε_2 is about 14 for welded stainless steel [266], and additional capacitive elements such as the double layer capacitance ($\sim$40 μF cm^{-2}) can be neglected, linearity is observed between -0.5 and -0.2 V/SCE for the different $^3H_2O_2$ concentrations. Using Mott-Schottky equations, $\Delta C_{ox_2}^{-2}/\Delta E$ is between 1 and 2.6×10^{10} cm^4 F^2 V^{-1} in agreement with Maximovitch et al. [263], and the donor density (that corresponds to Me^{n+} in oxide) varies from 3.1 to 1×10^{20} carrier cm^{-3} signifying protection of the alloy by $^3H_2O_2$. The obtained carrier concentration for the inner oxide layer is slightly higher than the theoretical value for a passive layer given by Castro et al. [251], Simoes et al. [109] and Oriani et al. [110], signifying a slight amount of chloride diffusion. The flat-band extrapolated potential is close to -0.8 V/SCE at 10^{-3} mol dm^{-3} $^3H_2O_2$ and does not change significantly for any conditions indicating that the surface pH is buffered by CO_3^{2-} ions, as shown by Quarto et al. [267] and Horvat-Radoševic and Kvastek [268]. The main values obtained for the equivalent circuit are given in Table 19.3. It can be seen that the inner oxide capacitance varies from 20 to 9 μF cm^{-2}. Also, consideration of these values shows that the lower value obtained for higher $^3H_2O_2$ concentrations would favor passivating.

3.3.1.1. Discussion The model contains these basic features:

- the rusted oxide layer contains vacancies in the inner layer ($V_{Me^{n+}}$ and $V_{O^{2-}}$),
- the vacancies are in equilibrium with the $^3H_2O_2$ and CO_3^{2-}–inner oxide and oxide–alloy interfaces and the ion diffusion,
- the passive oxide layer kinetics are governed by vacancies across the inner complex oxide layer.

Based on these considerations, the following reactions, besides eq. (19.1) and eq. (19.4) to eq. (19.6), are in equilibrium at each interface:

- alloy–inner oxide interface:

$$Me \leftrightarrow \{\text{inner oxide}\} + V_{O^{2-}} \tag{19.14}$$

$$Me + V_{Me^{n+}} \leftrightarrow \{\text{inner oxide}\} \tag{19.15}$$

– $^3H_2O_2$ outer–inner oxide:

$$V_{O^{2-}} + {}^3H_2O_2 + \{CO_3^{2-}, O^3H^-\}_{\text{outer oxide}} + 2e^- \leftrightarrow {}^3H_2O + O^{2-} \tag{19.16}$$

$$\{\text{inner oxide}\} + n\{CO_3^{2-}, O^3H^-\} \leftrightarrow V_{Me^{n+}} + Me(CO_3^{2-}, O^3H^-)_n + ne^- \tag{19.17}$$

where {inner oxide} represents Me^{n+} species in the inner passive oxide layer that are in equilibrium with the metal vacancies, and $_{aqs}$ represents aqueous CO_3^{2-} and $^3H_2O_2$. It can be seen that CO_3^{2-} and O^3H^- imply that the pH is buffered in the porosities of the outer oxide avoiding local acidification according to eqs (19.4) and (19.6). Apparently, $V_{O^{2-}}$ are produced at the inner oxide–alloy interface and consumed in the porosities of outer-inner oxide-hydrogen peroxide interfaces. As a result, $V_{O^{2-}}$ diffuses from the oxide-alloy to the bottom of the porosities of the outer oxide-hydrogen peroxide interfaces. Similar arguments show that $V_{Me^{n+}}$ diffuses from the bottom of the outer porous oxide-hydrogen peroxide to alloy–oxide interfaces. The net results of $V_{O^{2-}}$ migration can be seen by combining eqs (19.14) and (19.16):

$$Me + {}^3H_2O_2 + 2e^- \leftrightarrow \{\text{inner oxide}\} + {}^3H_2O + O^{2-} \tag{19.18}$$

Similarly, combining eqs (19.15) and (19.17) shows that the net result of $V_{Me^{n+}}$ migration can be obtained from the total expression:

$$Me + nCO_3^{2-}, O^3H^- \leftrightarrow Me(CO_3^{2-}, O^3H)_n + ne^- \tag{19.19}$$

From the set of previous reactions, it is clear that the diffusion of $V_{O^{2-}}$ results in oxide growth, depends on flatband potential, and is produced with consumption of $^3H_2O_2$ in the bottom of the porosities of the outer oxide–hydrogen peroxide interface where the pH is buffered throughout, whereas the diffusion of $V_{Me^{n+}}$ is accompanied by $Me(CO_3^{2-}, O^3H)_n$ formation also keeping the pH buffered, as in eq. (19.5). The reactions occurring on passive oxide are influenced by the different potential drops in the oxide and interfaces within the two oxide layers. The physical model proposed to interpret the diffusion processes is shown schematically in Fig. 19.8. Within the passive layer of some tens of nanometers, the electrical field strength for the inner oxide is of the order of some hundreds of mV [256], which enables the migration of ions and electrons through the two oxide layers. The rusted oxide–hydrogen peroxide interface is polarizable, therefore it is expected that the total potential drop capacitance and thickness variations are a function of surface $^3H_2O_2$ concentration as shown in the chapter concerning N089932 stainless steel in contact with ionized peroxide radicals.

3.3.2. Results in the passive-pitting region The experimental Nyquist and Bode plots obtained for welded S32550 steel, subjected to carbonate, chloride and hydrogen peroxide,

for prepitting potentials are shown in Figs 19.12 and 19.13. Initial examination of the Nyquist representation (Fig. 19.12A), along the capacitive region, shows a linear unit slope of Warburg semi-infinite diffusion at high frequencies.

Stirring does not affect its characteristic frequency and this suggests that mass transport occurs in the outer defective porous oxide. Processes in this oxide layer are more clearly shown by tracing the smaller spectra obtained for the lower $^3H_2O_2$ concentration with an expanded scale (Fig. 19.12B). The expanded curve actually shows two capacitive semi-circles overlapped at the marked frequency and the superposed Warburg straight line which account for a reaction in porous oxide implying Cl^- ion diffusion. According to spectral analysis of these two figures, the depressed semi-circle obtained at high frequency should correspond to the outer defective oxide layer whereas the second semi-circle should be attributed to the inner oxide layer.

Also, examination of spectra at the higher frequencies shows a small third capacitive semi-circle (Fig. 19.12C). The impedance is only of the order of a few $\Omega\,cm^2$. Its size increases with the $^3H_2O_2$ concentration and its presence should be related to reactions in the outer oxide layer porosities. According to Fig. 19.12C, pitting resistance increases at higher $^3H_2O_2$ concentrations indicating a possible repassivation in accordance with the polarization and voltammetric curves. In other words this signifies, in agreement with Scanning Electron Microscope examinations, that the outer oxide porosities are corroded thus leading to local nucleated pits, and these had not the time to grow and cross the inner oxide layer when they were formed by buffering pH in the porosities by CO_3^{2-} ions. Electrochemical impedance spectroscopy results suggest also that all the outer carbonated oxide layer would not be transformed entirely into Me_2O_3.

In Fig. 19.13A, the Bode plots are characterized by:

- In the higher frequency region, the dip for the characteristic frequency, f_{c_p}, in the phase angle/$\log(f)$ curve and a linear hump in the $\log|Z|/\log(f)$ plots depend on the $^3H_2O_2$ concentration. This corresponds to the reaction in the porosities of outer defective oxide layer. These characteristics can be more easily obtained at the higher $^3H_2O_2$ concentrations. Also, the greater deviation of the phase angle at the higher $^3H_2O_2$ concentrations signifies that the outer layer thus formed on welded S32550 steel is less defective.
- In the broad low frequency range, it is seen that the linear slope in $\log|Z|$ vs. $\log(f)$ decreases, while phase angle values tend to $-40°$ over the measurement frequency range at lower $^3H_2O_2$ concentrations. This is the response of the outer oxide layer capacitance. This behavior signifies increasing corrosion for the outer layer at lower $^3H_2O_2$ concentration as shown in Fig. 19.13B drawn with the two representations.
- A second overlapped dip in the phase angle/$\log(f)$ curve for the characteristic frequency, f_{c_2} (curve 4). This is represented by the second overlapped semi-circle in the Nyquist representation (Fig. 19.12B), which corresponds to the inner oxide layer. It can be seen in the spectra in Bode and Nyquist representations obtained from the model in Fig. 19.14 that the characteristic frequency (f_{c_2}) changes with the $^3H_2O_2$ concentration and is hidden at lower passive-pitting potentials by the response of the outer oxide capacitance, indicating changes in the oxide layer depending on these two parameters.

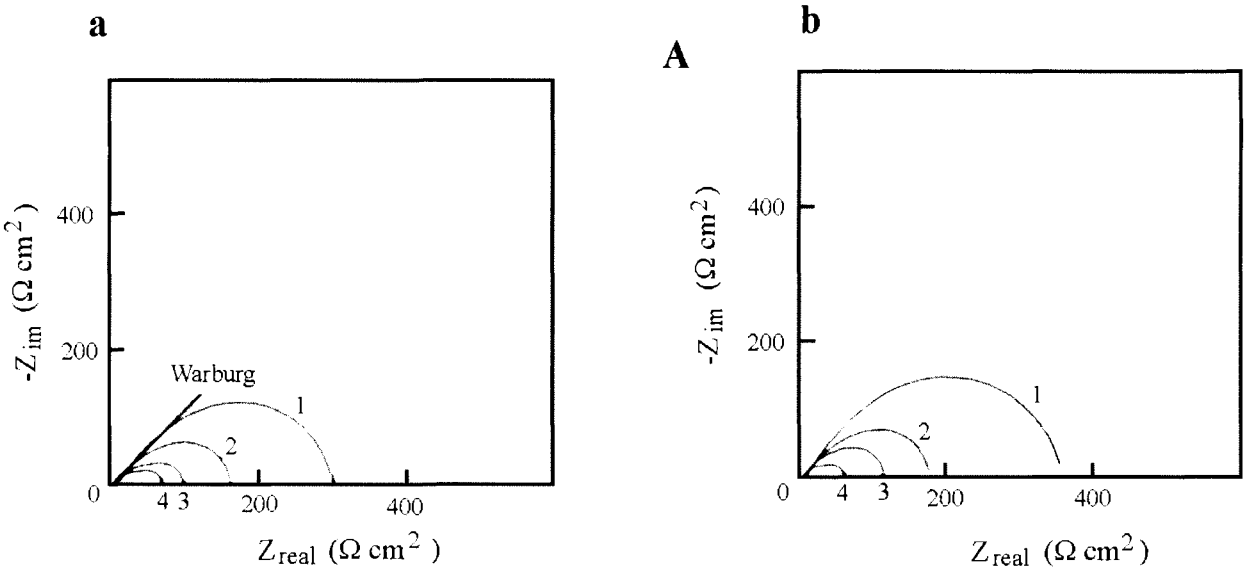

Figure 19.12. Nyquist spectra in presence of CO_3^{2-}, Cl^-, $^3H_2O_2$ in passivity-transpassivity, 5×10^{-2} mol dm^{-3} CO_3^{2-}, 0.2 mol dm^{-3} Cl^-, pH 10.2, (A): complete spectra, (a): 10^{-3} mol dm^{-3}, (b): 2×10^{-3} mol dm^{-3}, (c): 10^{-2} mol dm^{-3}, (d): 2×10^{-2} mol dm^{-3}, (e): 5×10^{-2} mol dm^{-3} $^3H_2O_2$, 1: 0.90 V, 2: 0.95 V, 3: 1.00 V, 4: 1.02 V/SCE, (B): complete spectra realized with an expanded scale, 10^{-3} mol dm^{-3} $^3H_2O_2$, E: 1.02 V/SCE, (C): spectra realized in the high frequency region with an expanded scale.

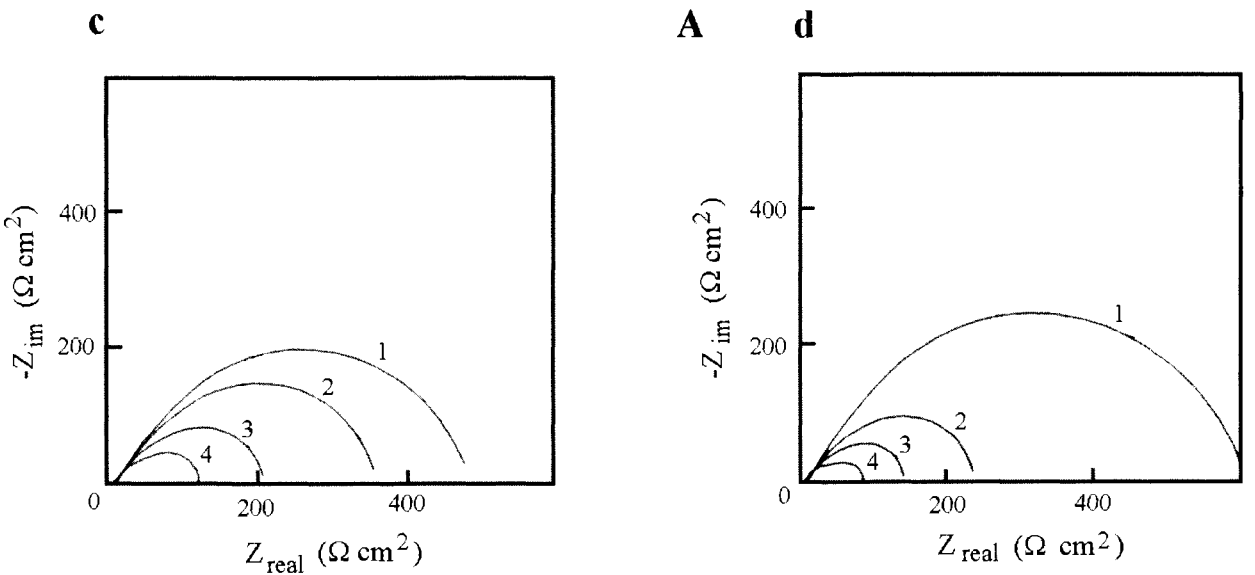

Figure 19.12. (Continued).

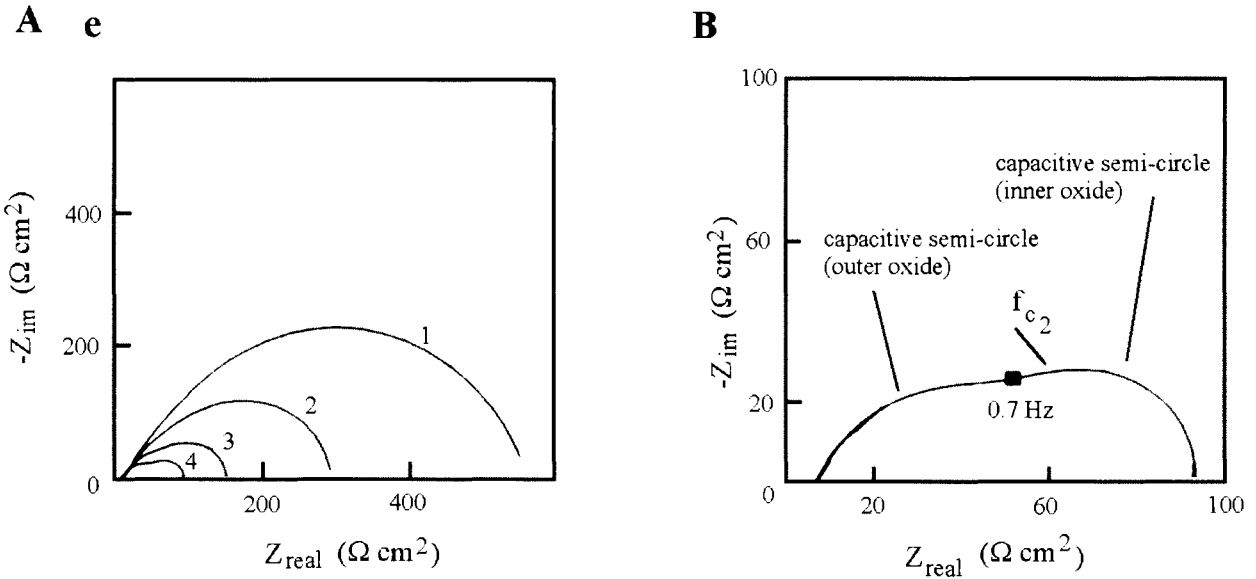

Figure 19.12. (Continued).

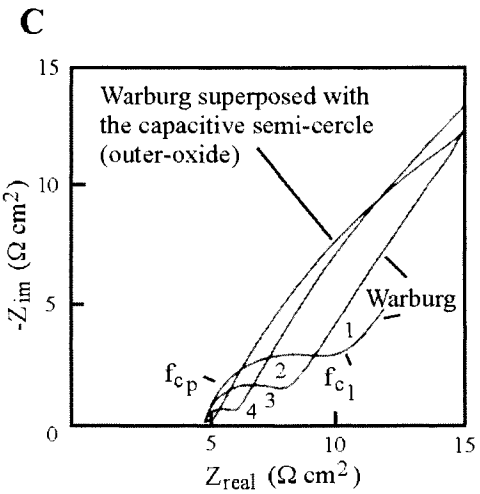

Figure 19.12. (Continued).

Also, the time constant, τ_{c_p}, slightly decreases, signifying enhancement of the inner oxide [190] and filling of metastable pits in the outer layer by higher $^3H_2O_2$ concentrations (Tables 19.8–19.12). It is assumed that the metastable pits are suppressed by low passivation at the nucleation stage, and do not start propagating, as was seen by Scanning Electron Microscopy examination. The nucleation stage continues to survive if the presence of the $^3H_2O_2$ and CO_3^{2-} buffers, provided by diffusion in the porosities, is maintained, i.e. the inner layer is better protected by these species.

3.3.2.1. Equivalent circuit and value determination To provide physical significance for these spectra, an equivalent circuit is proposed in Fig. 19.14 so that the system coincides with the real situation. In this circuit, the impedance for the outer oxide (Z_{outer}) is given by:

$$\frac{1}{Z_{outer}} = j\omega C_p + \frac{1}{R_{p,w} + \frac{R_{ox_1}}{1+j\omega C_{ox_1}}} \tag{19.20}$$

where the subscript p indicates a reaction in porosities. Suitable values of the inner capacitance were obtained from the equivalent circuit and the fitting program for the prepitting potentials (Tables 19.8–19.12). It can be seen that the inner capacitance value is decreased when $^3H_2O_2$ concentration increases in the passive-prepitting range. Also, the onset of metastable pits can be clearly determined by considering the spectra. They show more capacitive behavior when pitting is repassivated (reaction in porosities) under the applied potential and corresponding Cl^- and $^3H_2O_2$ concentrations and surface CO_3^{2-} buffer.

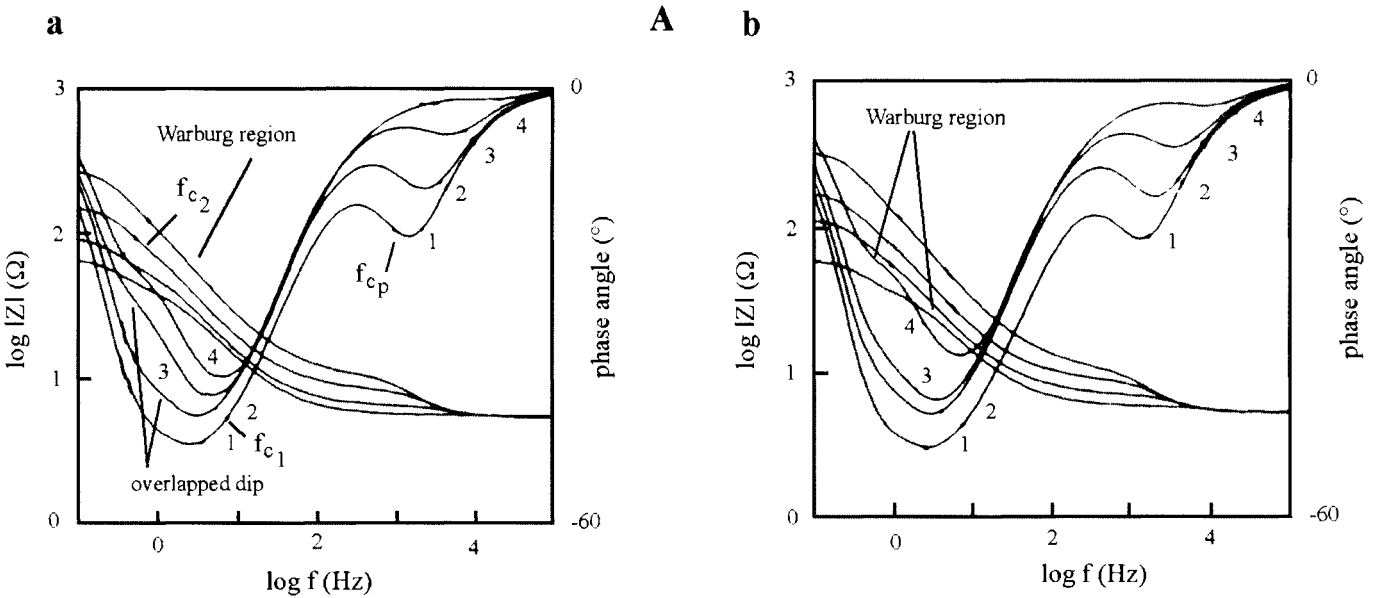

Figure 19.13. Bode spectra in presence of CO_3^{2-}, Cl^-, $^3H_2O_2$ in passivity-transpassivity, 5×10^{-2} mol dm^{-3} CO_3^{2-}, 0.2 mol dm^{-3} Cl^-, pH 10.2, (A): complete spectra, (a): 10^{-3} mol dm^{-3}, (b): 2×10^{-3} mol dm^{-3}, (c): 10^{-2} mol dm^{-3}, (d): 2×10^{-2} mol dm^{-3}, (e): 5×10^{-2} mol dm^{-3} $^3H_2O_2$, 1: 0.90 V, 2: 0.95 V, 3: 1.00 V, 4: 1.02 V/SCE, (B): influence of $^3H_2O_2$ concentration on the two representations, 1: 10^{-3} mol dm^{-3}, 2: 2×10^{-3} mol dm^{-3}, 3: 10^{-2} mol dm^{-3}, 4: 2×10^{-2} mol dm^{-3}, 5: 5×10^{-2} mol dm^{-3} $^3H_2O_2$.

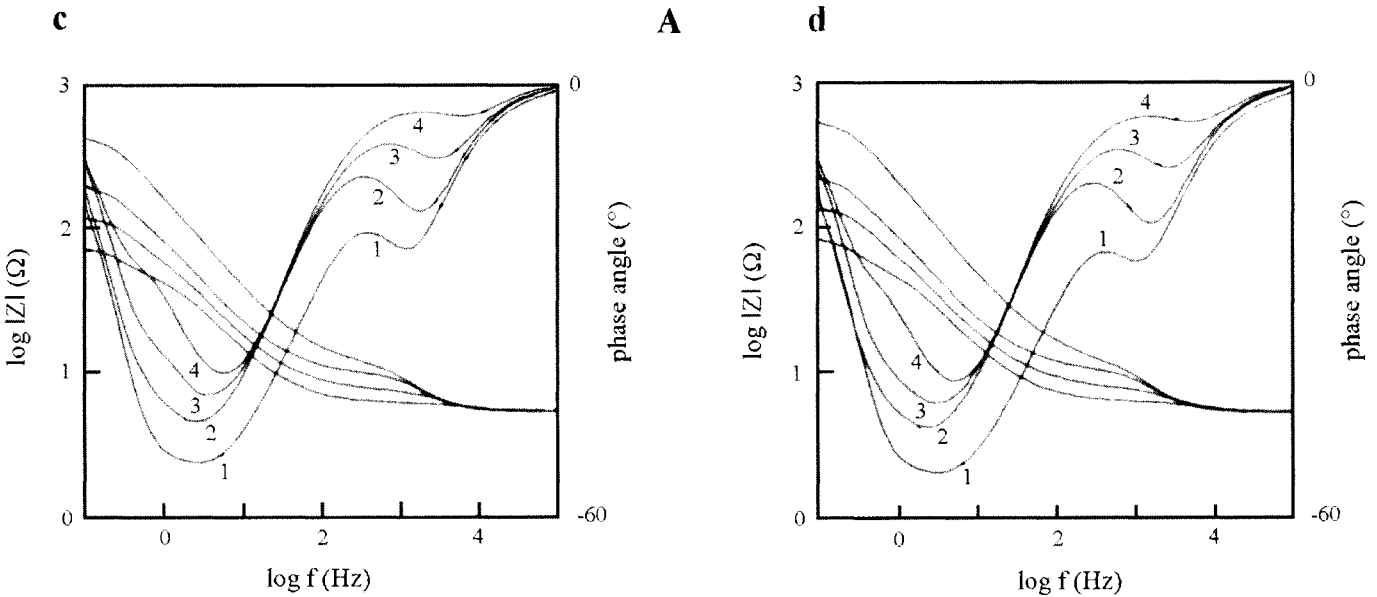

Figure 19.13. (Continued).

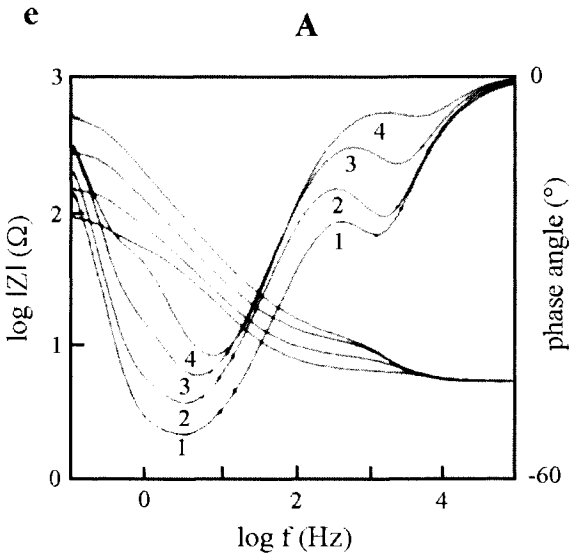

Figure 19.13. (Continued).

3.3.2.2. Discussion For a deactivated or activated pit, there must be a relationship between Cl^-, CO_3^{2-}, O^3H^- and $^3H_2O_2$ depending on diffusion of vacancies and void formation at the oxide-alloy interface. From this, the diffusion of metal vacancies is affected by the incorporation of Cl^- ions at the inner oxide–$^3H_2O_2$ interface as shown in Fig. 19.8 and in the equations given in the chapter concerning corrosion of N08932 stainless steel by chloride. From these considerations, the criterion for pit initiation in presence of $^3H_2O_2$ can be expressed by:

$$E_{pit} = \frac{4.6RT}{\alpha nF} \log\left(\frac{J_m}{J_o \rho \exp\left\{ \frac{([^3H_2O_2]\{CO_3^{2-}, O^3H^-\})^{-1}}{RT} \right\}^{0.5n}} \right) - \frac{2.3RT}{\alpha F} \log Cl^- \qquad (19.21)$$

where J_m is the rate of submergence of the metal vacancies in the alloy. It can be seen that low submergence rates and the presence of $^3H_2O_2$ avoid pitting by Cl^-. Also, CO_3^{2-} should again be incorporated into the outer oxide which modifies the surface alkaline pH by buffering. This analysis should include examinations of the electrode surface to check the results. The absence of marked or localized corrosion for the weld pool zone, the weld heat-affected zone and the parent S32550 Duplex stainless steel in presence of carbonate, chloride ions and the high tritiated hydrogen peroxide concentrations, were observed by Scanning Electron Microscopy. Only a few scarcely observable blisters were noted. They correspond to early stage pitting, e.g. pit nucleation.

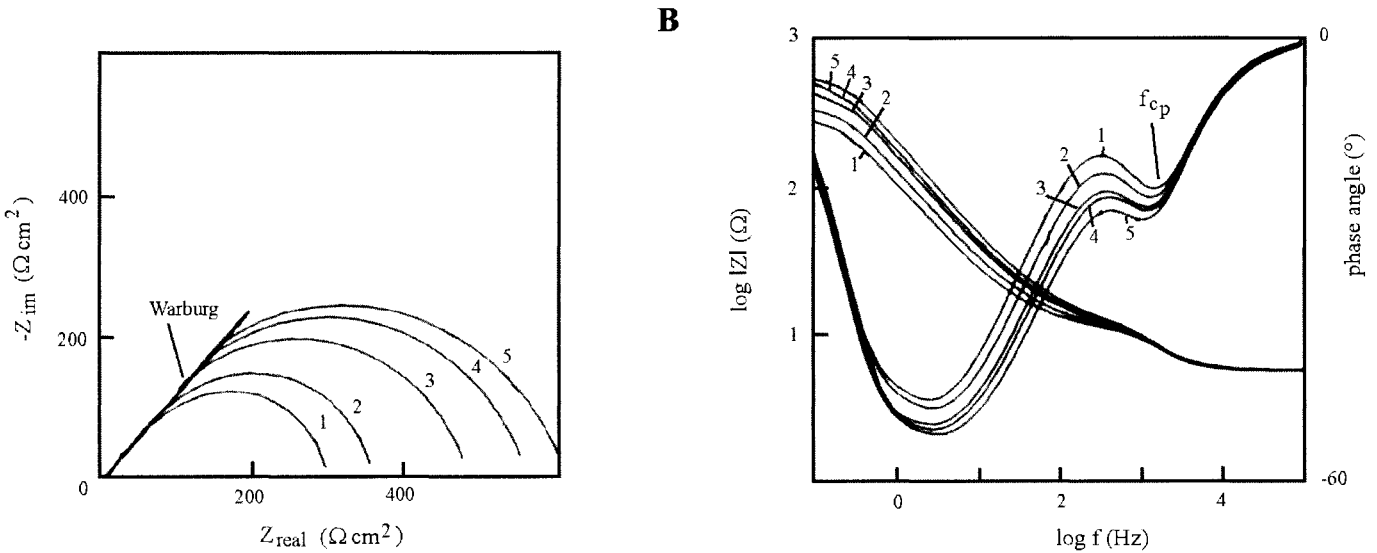

Figure 19.13. (Continued).

Table 19.8. Dependence of oxide capacitance and time constant on passive-transpassive potentials in presence of carbonate, chloride ions and hydrogen peroxide (10^{-3} mol dm^{-3} $^3H_2O_2$)

E (V/SCE)	0.90	0.95	1.00	1.02
C_{ox_2} (μF cm^{-2})	30	30	32	34
τ_{c_p} (s $\times$ 10^4)	1.1	1.25	1.3	1.5

Table 19.9. Dependence of oxide capacitance and time constant on passive-transpassive potentials in presence of carbonate, chloride ions and hydrogen peroxide (2×10^{-3} mol dm^{-3} $^3H_2O_2$)

E (V/SCE)	0.90	0.95	1.00	1.02
C_{ox_2} (μF cm^{-2})	27	30	30	31
τ_{c_p} (s $\times$ 10^4)	1.1	1.2	1.3	1.35

Table 19.10. Dependence of oxide capacitance and time constant on passive-transpassive potentials in presence of carbonate, chloride ions and hydrogen peroxide (10^{-2} mol dm^{-3} $^3H_2O_2$)

E (V/SCE)	0.90	0.95	1.00	1.02
C_{ox_2} (μF cm^{-2})	27	30	30	31
τ_{c_p} (s $\times$ 10^4)	1.1	1.1	1.2	1.3

Table 19.11. Dependence of oxide capacitance and time constant on passive-transpassive potentials in presence of carbonate, chloride ions and hydrogen peroxide (2×10^{-2} mol dm^{-3} $^3H_2O_2$)

E (V/SCE)	0.90	0.95	1.00	1.02
C_{ox_2} (μF cm^{-2})	26	29	29	31
τ_{c_p} (s $\times$ 10^4)	1	1.1	1.1	1.2

Table 19.12. Dependence of oxide capacitance and time constant on passive-transpassive potentials in presence of carbonate, chloride ions and hydrogen peroxide (5×10^{-2} mol dm^{-3} $^3H_2O_2$)

E (V/SCE)	0.90	0.95	1.00	1.02
C_{ox_2} (μF cm^{-2})	25	27	28	30
τ_{c_p} (s $\times$ 10^4)	1	1	1.1	1.1

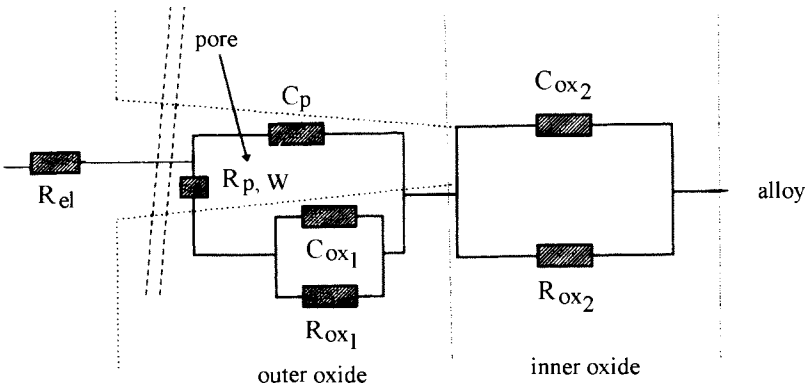

Figure 19.14. Equivalent circuit, R_{el}: electrolyte resistance, R_{ox_1}: outer oxide resistance, R_{ox_2}: inner oxide resistance, $R_{p,W}$: impedance for reaction and diffusion in the pores, C_{ox_n}: oxide capacitance, C_p: capacitance in the pores.

4. Conclusion

Depending on the aqueous medium, two protective successive oxides layers are formed in the prepassive-passive region. Carbonate ions formed by the action of the low energy on polymers keep the alkaline buffer pH constant for the outer porous oxide giving protection from localized corrosion, whereas $^3H_2O_2$ enhances the characteristics of the inner passive oxide layer. Presence of $^3H_2O_2$ at the surface of steel is assisted by diffusion of temporary oxidizing species. As a result, the breakdown potential shifts towards more positive values on increasing $^3H_2O_2$ or carbonate concentration. Due to these two effects: alkaline pH kept constant at the electrode surface and enhancement of the characteristics of the inner oxide layer by $^3H_2O_2$, no pitting is observed in presence of chloride ions. The ability of the nucleation sites to propagate as metastable pits is limited.

This Page Intentionally Left Blank

Chapter 20

PROTECTION BY NITRATE AND OXIDIZERS

1. Introduction

Chloride is produced during decomposition of organic polymers by the β^- particle energy. Similarly, hydrogen peroxide is formed by radiolysis of tritiated water, as explained previously. Relatively concentrated solutions of nitrate are present in tritiated water reprocessing installations. This is explained by the activated nitrogen formation due to the effect of β^- particles on nitrogen in the air used for gaseous tritium oxidation. The reaction is:

$$N^\bullet + 4\,{}^3H_2O_2 \rightarrow NO_3^- + 4\,{}^3H_2O + O^\bullet \qquad (20.1)$$

The choice of Zircaloy-4, whose composition is given in Table 20.1, as alloy in the nuclear plants is justified by the qualities of its passive layer. In this case, the Zircaloy sample was processed by hot rolling followed by recrystallization annealing for 2 hours at 650°C under vacuum. Its surface is characterized by equiaxial 25-μm diameter grains. Passivation of Zircaloy has received a great deal of attention [151,269–271]. It is well known that its corrosion resistance is due to the protective capacity of its passive oxide layer already formed at the more negative potentials, leading to a 'pseudo' behavior near the corrosion potential, but unfortunately with chloride and powerful oxidants, local depassivation by cracking of oxide layers can occur, leading to pitting. However, nitrates act as inhibitors. We have found nothing in the literature for a mixture of these three species. For these reasons, the behavior of Zircaloy-4 was studied using tritiated water containing chloride, nitrate and hydrogen peroxide over a wide range of passive potentials.

2. Experimental results

Before discussing the shape of the curves and their interpretation we must provide details of the development of the experimental study. Initially, we describe the overall effect on the

Table 20.1. Chemical composition of Zircaloy-4

Elements	Sn	Fe	Cr	O	Zr
Wt%	1.45	0.21	0.10	0.01	bal.

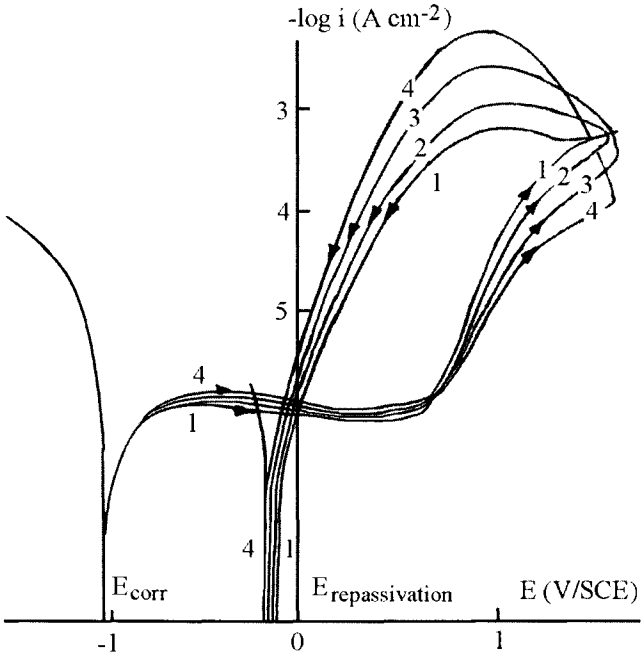

Figure 20.1. Polarization curves with chloride, nitrate and hydrogen peroxide, v: 5 mV s^{-1}, pH 6, 0.1 mol dm^{-3} Cl^-, 0.1 mol dm^{-3} NO_3^-, 1: 3×10^{-2}, 2: 5×10^{-2}, 3: 7×10^{-2}, 4: 0.1 mol dm^{-3} $^3H_2O_2$.

polarization curves when Cl^-, NO_3^- and $^3H_2O_2$ are present together. Next, using voltammetry or electrochemical impedance spectroscopy, we study each of these species alone or in groups of two or three to show the individual and reciprocal influence on pitting corrosion and passivity phenomena. To simplify, Zircaloy-4 is represented by the symbol for zirconium.

2.1. *Anodic polarization curves*

In the polarization curves (Fig. 20.1), the passive currents are higher with increasing $^3H_2O_2$. The 'pseudo' corrosion potential does not change with $^3H_2O_2$ present. In the transpassivity, it is observed that the repassive potential decreases whereas the pitting potential increases and the pitting current increases with $^3H_2O_2$.

2.1.1. Analysis and interpretation of polarization curves The interpretation for higher passive currents could be that $^3H_2O_2$ thickens the oxide layer forming constraints. At more negative potentials than the 'pseudo' corrosion potential, the current should correspond to $^3H_2O_2$ reduction with formation of O^3H^- and oxide layer. It can be seen that $^3H_2O_2$ reduction is not really involved. This results from the ZrO_2 layer which is already present

and partially inhibits $^3H_2O_2$ reduction by greatly limiting the passage of current in the oxide, which behaves as an insulating capacitance. The ZrO_2 presence at these negative potentials is shown in the potential-pH equilibrium diagram [101] for zirconium. The corrosion resistance results from its strong affinity for oxygen resulting in the formation of a thin protective layer of oxide spontaneously formed at the lower potentials. Nevertheless, oxidation of Zircaloy-4 continues to occur by anodic and cathodic reactions throughout the passive oxide layer with a very low oxidation current of a few $\mu A\,cm^{-2}$.

From anodic and cathodic active sites at the surface, acidification and alkalization occur that can locally modify the pH. In fact, nitrate should act to keep the surface pH buffered by means of chemisorbed $N^3H_4^+$ film formation. Also, it will be shown later that oxide formed with NO_3^- present is definitely more protective than that formed in its absence, or in its presence with that of $^3H_2O_2$. $^3H_2O_2$ should certainly be responsible for removal of an adsorbed $N^3H_4^+$ film leading to a repassive potential shift in the negative direction. According to Fig. 20.1, the oxide layer formed under these conditions is associated with localized corrosion by Cl^-, and has been identified as participating in protection depending on all the radiolytic species present. The result is that, for this medium, the properties and composition of the oxide should be different from those obtained in the absence of $^3H_2O_2$ and NO_3^-.

2.2. *Voltammetric curves*

With the rapid-scan voltammograms, we expect to find more easily the variation of pitting and repassivation potentials and the maximum current in pitting, first with only chlorides (Fig. 20.2) then, with both chloride and nitrate (Fig. 20.3) and finally with different $^3H_2O_2$ concentrations and with NO_3^- and chlorides (Fig. 20.4). In these figures, the 'pseudo' active peak for Zircaloy of a few μA indicates oxide rearrangement by thickening.

2.2.1. Analysis of voltammograms obtained with Cl^- In the passive domain (Fig. 20.2), the anodic current increases slightly, signifying a mismatch with Cl^-. Nevertheless, the passive current before pitting is very low. The passive potential range is smaller at higher Cl^- concentrations. In the transpassive-passive region, the pitting and repassive potentials shift dramatically toward smaller values with higher Cl^- concentration. The interpretation is that the pit propagation and pitting increase with chloride present. In fact, Energy Dispersive X-ray analysis reveals the presence of Cl in the passive oxide layer (Fig. 20.5) for the sample used in voltammograms after a cleaning procedure. Also, chloride crosses the oxide layer by diffusion.

2.2.2. Analysis of voltammograms obtained with NO_3^- and with Cl^- In Fig. 20.3, the passive potential range is wider with NO_3^- present. In the transpassive region, the maximum pitting current decreases and the pitting and repassive potentials shift toward higher values with increasing NO_3^- concentration. Evidently, the oxide layer is clearly more protective and in this case pitting is more difficult to obtain, as observed by Olefjord and

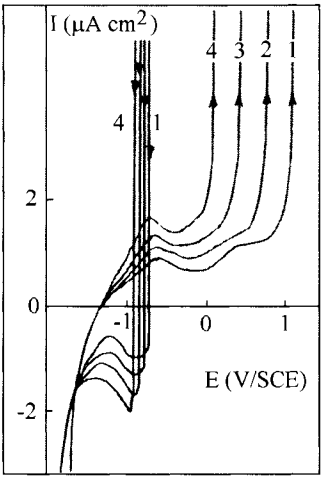

Figure 20.2. Voltammetric curves with chloride, v: 200 mV s^{-1}, pH 6, 1: 4 × 10^{-2}, 2: 6 × 10^{-2}, 3: 8 × 10^{-2}, 4: 0.1 mol dm^{-3} Cl$^-$.

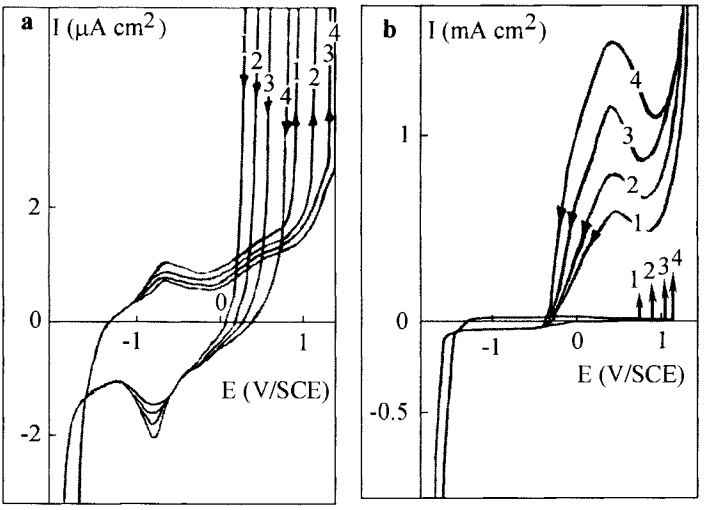

Figure 20.3. Voltammetric curves with chloride, nitrate and without hydrogen peroxide, (a): expanded current scale, (b): higher current scale v: 200 mV s^{-1}, pH 6, 0.1 mol dm^{-3} Cl$^-$, 1: 3 × 10^{-2}, 2: 5 × 10^{-2}, 3: 7 × 10^{-2}, 4: 0.1 mol dm^{-3} NO_3^-.

Clayton [262,272]. To investigate the nature of the passive layer formed under these conditions on the Zircaloy-4 surface, the oxide surface was analyzed by X-ray photoelectron

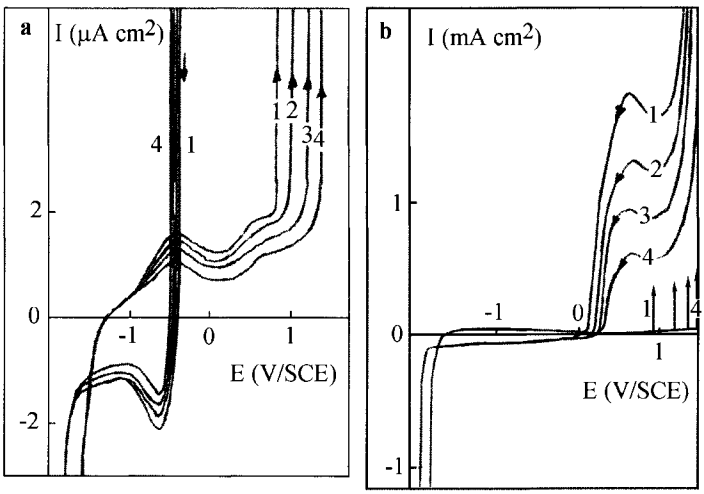

Figure 20.4. Voltammetric curves with hydrogen peroxide, nitrate and chloride, v: 200 mV s^{-1}, pH 6, 0.1 mol dm^{-3} Cl^-, 3×10^{-2} mol dm^{-3} NO_3^-, 1: 3×10^{-2}, 2: 5×10^{-2}, 3: 7×10^{-2}, 4: 0.1 mol dm^{-3} $^3H_2O_2$, (a): expanded current scale, (b): higher current scale.

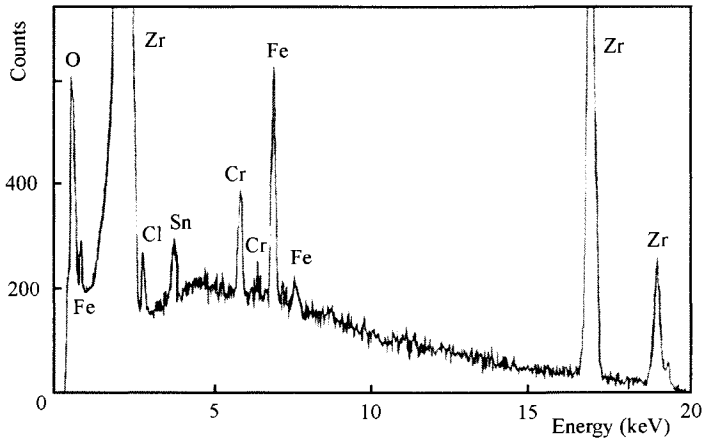

Figure 20.5. Energy Dispersive X-Ray analysis examinations peaks of elements in Zircaloy-4 and peak of Cl showing its presence in the oxide (sample of Fig. 20.2).

spectroscopy (Fig. 20.6) and a small peak is observed at 400 eV indicating the presence of N.

The peak suggests effectively that NO_3^- is reduced to $N^3H_4^+$. This would indicate that $N^3H_4^+$ is present as adsorbate on the surface. $N^3H_4^+$ acts to keep the buffered surface pH constant and to retain passivity and delay pitting nucleation. This indicates that the pitting

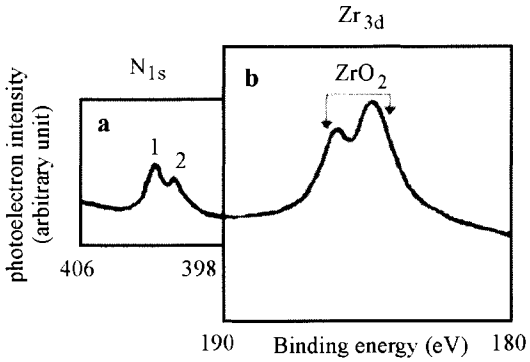

Figure 20.6. X-Ray Photoelectron Spectroscopy of Zircaloy-4 after passivation showing presence of $N^3H_4^+$ on the oxide, (a): XPS spectrum of N_{1s} peak, 1: $N^3H_4^+$, 2: N^3H_3, (b): XPS spectrum of Zr_{3d} peak.

corrosion rate and passivity are dependent on the absence of any superficial pH modification towards acid pH in pits. Chloride ions are less adsorbed and require more time to cross the passive oxide layer under these conditions as seen for instance in Fig. 20.7 where an increase in the scan rate leads to decreasing the pitting currents. These results show, without any doubt, the effectiveness of NO_3^- as corrosion inhibitor in pitting initiation.

2.2.3. Analysis of voltammograms obtained with $^3H_2O_2$, NO_3^- and Cl^- The 'pseudo' corrosion potential does not change (Fig. 20.4) when the $^3H_2O_2$ increases. This behavior results from the difficulty of $^3H_2O_2$ reduction whose current is superimposed on the passivation current. In the passive domain, the anodic current is slightly higher than that obtained in the subsection 2.2.2, signifying a greater thickness and a risk of more defective oxide. The passive potential range is larger when $^3H_2O_2$ concentration increases. In the transpassive-passive region, the pitting potential shifts toward higher values, whereas the repassive potential shifts slightly toward smaller values and the maximum pitting current increases when $^3H_2O_2$ concentration increases. This can be explained by the fact that $^3H_2O_2$, as a powerful oxidizing species, is capable of oxidizing the surface and limits pit initiation whereas it makes repassivation of existing pits more difficult.

2.2.4. Results and discussion This discussion makes use of comments made by Aramaki et al. [273], Al-Kharafi [274] and Ming-Yu Chang and Ge-Ping Yu [176] on other metals and environments.

2.2.4.1. Influence on pitting potential Fig. 20.8 shows the linear variation of pitting potential, E_{pit}, as a function of the logarithm of the inhibitor to chloride concentration ratio. The pitting potential obtained with only chloride ions (E_{pit}^0) is represented by a diamond.

In this figure, the pitting potential shifts towards higher values when the inhibitor-chloride ratio increases. This signifies that addition of inhibitor stops pit initiation for po-

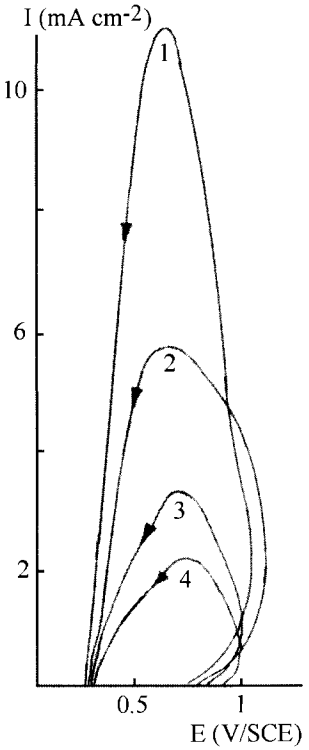

Figure 20.7. Voltammetric curves realized for different scan rates and with chloride and nitrate present, pH 6, 0.1 mol dm^{-3} Cl^-, 0.1 mol dm^{-3} NO_3^-, v: 1: 25, 2: 50, 3: 100, 4: 200 mV s^{-1}.

tentials under the curves as shown by analyzing the local currents (Fig. 20.9, plates (a) and (b)). Effectively, in plate (b) obtained at 0.8 V/SCE and for $NO_3^-/Cl^- = 0.35$, the studied section shows a greater area of zero local current indicating a marked tendency to limit pitting initiation sites. Also, pit initiation is less easily stopped by nitrate and $^3H_2O_2$ as seen in Fig. 20.8. Because these inhibitors provide a more perfect passive layer in the potential region under the straight lines, defects at the passive surface are repassivated.

2.2.4.2. Influence on repassivation potential The values of the repassivation potential, E_{rep}, as a function of the logarithm of the inhibitor to chloride concentration ratio are shown in Fig. 20.10. In this figure, the repassive potential obtained with only chloride ions (E^0_{rep}) is represented by a diamond.

Because NO_3^-, in the absence of $^3H_2O_2$, makes E_{rep} more positive, it is an effective inhibitor for establishing repassivation. NO_3^- plugs the pits by buffering the pH, as shown by Refaey and Rehim [275]. Nevertheless, propagation of existing pits appears to occur at the lower concentration of inhibitors as suggested by the i_{max} values between E_{pit} and

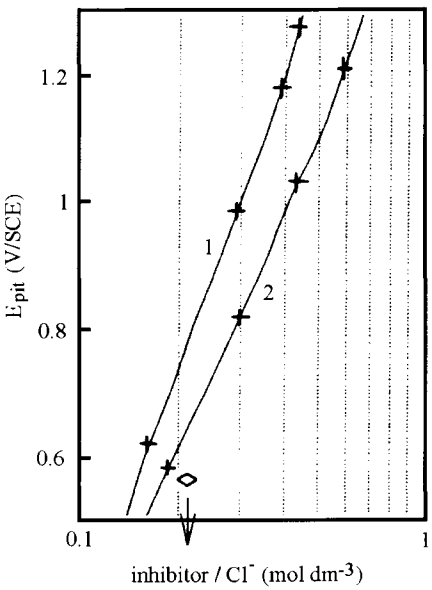

Figure 20.8. Pitting potential as a function of inhibitor concentration, 1: 0.1 mol dm^{-3} Cl^-, variation of NO_3^- concentration according to Fig. 20.3, 2: 0.1 mol dm^{-3} Cl^-, 3×10^{-2} mol dm^{-3} NO_3^-, variation of $^3H_2O_2$ concentration according to Fig. 20.4, ◇: Cl^- without inhibitor (arrow).

E_{rep} in the voltammograms (Figs 20.3b, 20.4b). The curve obtained with NO_3^- and $^3H_2O_2$ present shows a negative slope when hydrogen peroxide concentration increases [176]. Localized corrosion is aided between E_{pit} and E_{rep} within the existing pits by $^3H_2O_2$ addition, and there is less repassivation than with NO_3^- alone. Thus, the inhibitive effects depend really on the inhibitor nature, concentration and potentials.

2.2.4.3. Influence on the gap between pitting and repassivation potentials The graph giving the relationship between E_{pit} and E_{rep} is shown in Fig. 20.11. Two linear curves are obtained: one for NO_3^- with a positive slope, the other for NO_3^- with $^3H_2O_2$ where the slope is slightly negative. Each curve divides the figure into two domains: aggressiveness for points above the considered curve and inhibition below this curve. The NO_3^- inhibitor shifts both E_{pit} and E_{rep} in the positive direction, indicating suppression of both pit nucleation and initiation and slowing propagation of existing pits between E_{pit} and E_{rep}. On the other hand, NO_3^- with $^3H_2O_2$ changes E_{pit} towards a positive potential but E_{rep} shifts slightly towards a negative potential with increasing $^3H_2O_2$ concentration. It is definitely concluded that with $^3H_2O_2$ addition, the propagation of existing pits should be faster than for NO_3^- alone. Nevertheless, NO_3^- and $^3H_2O_2$ result in better repassivation than that for tritiated water containing only chlorides.

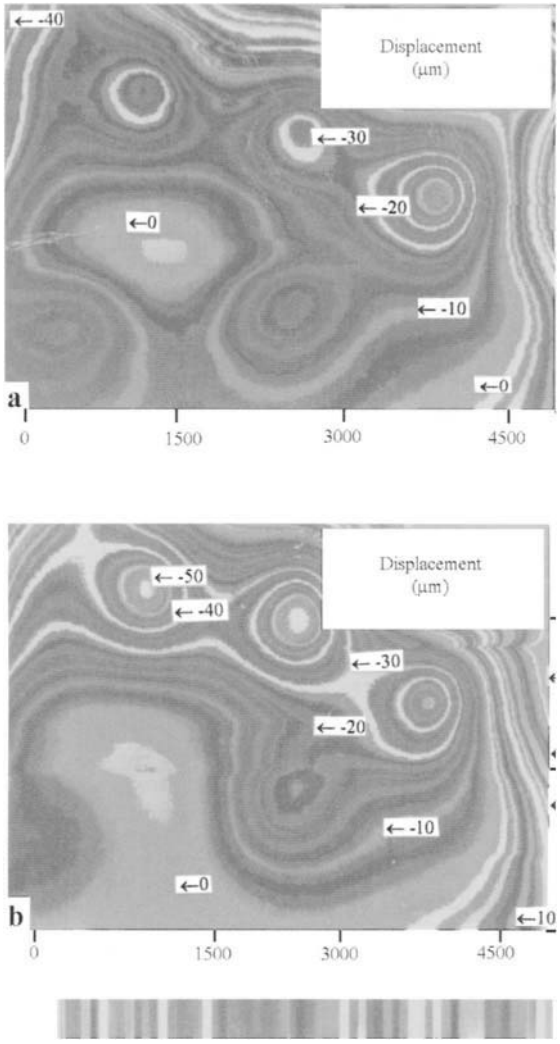

Figure 20.9. Photograph obtained by the Scanning Reference Electrode Technique, (a): pitting micro-cells induced by Cl^-, (b): local repassivation of pitting micro-cell induced by NO_3^-.

2.2.4.4. Influence on maximum current Without these inhibitors, it was observed that the pitting current reaches the higher maximum value (i^0_{max}), as represented by the diamond in Fig. 20.12. On addition of NO_3^-, the maximum current decreases indicating a significant

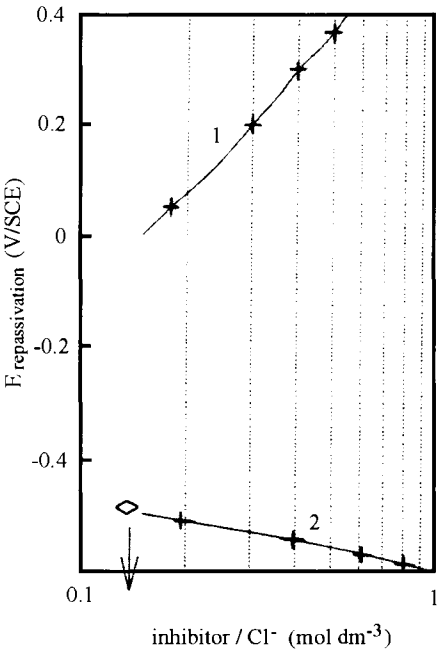

Figure 20.10. Repassivation potential as a function of inhibitor concentration, 1: 0.1 mol dm^{-3} Cl^-, variation of NO_3^- concentration according to Fig. 20.3, 2: 0.1 mol dm^{-3} Cl^-, 3×10^{-2} mol dm^{-3} NO_3^-, variation of $^3H_2O_2$ concentration according to Fig. 20.4, ◇: Cl^- without inhibitor (arrow).

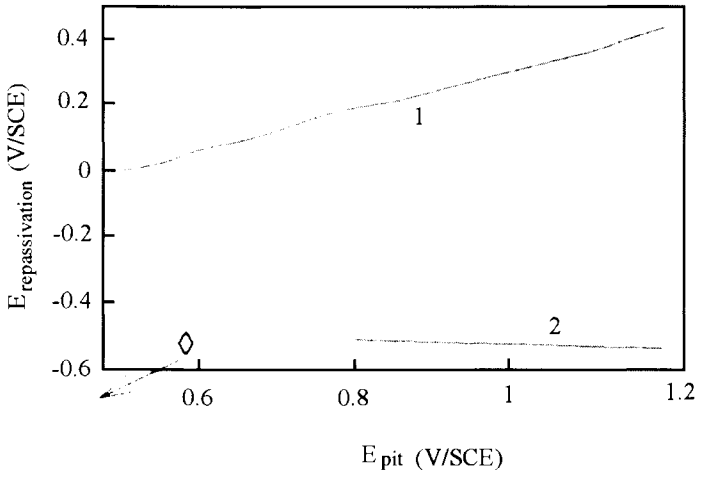

Figure 20.11. Relationship between E_{pit} and E_{rep}, 1: Cl^- and NO_3^-, 2: Cl^-, NO_3^- and $^3H_2O_2$, graph plotted according to Figs 20.8 and 20.10, ◇: Cl^- without inhibitor (arrow).

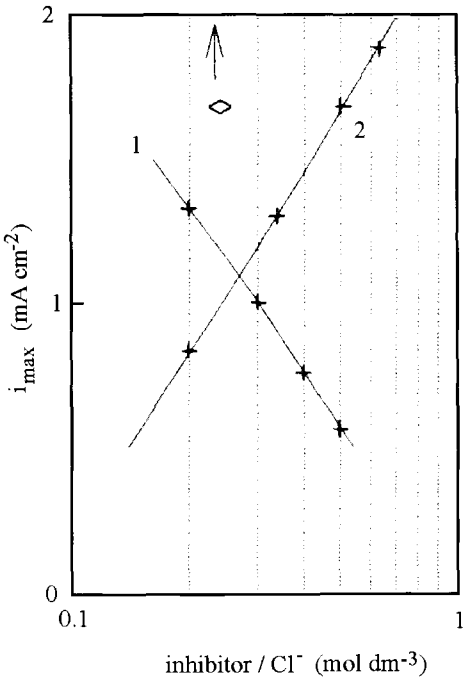

Figure 20.12. Maximum pitting current as a function of inhibitor concentration, 1: 0.1 mol dm^{-3} Cl^-, variation of NO_3^- concentration according to Fig. 20.3, 2: 0.1 mol dm^{-3} Cl^-, 0.1 mol dm^{-3} NO_3^-, variation of $^3H_2O_2$ concentration according to Fig. 20.4, ◇: Cl^- without inhibitor (arrow).

limitation of the propagation of existing pits. Fig. 20.12 also shows higher values of i_{max} for $^3H_2O_2$ addition as compared with only NO_3^-.

$N^3H_4^+$ adsorption should be hindered by $^3H_2O_2$ present and consequently there is less buffering of the surface pH limiting repassivation of the existing pits. In addition, a thicker oxide layer, due to $^3H_2O_2$, should limit the pitting current. From these different curves it appears that propagation of existing pits and the area corroded by pitting can be essentially avoided at higher NO_3^- concentrations.

2.2.4.5. Relation between the gap between E_{pit} and E_{rep} and maximum current In the potentials between E_{rep} and E_{pit} (ΔE), the inhibitors suppress pit nucleation by repairing defects in the passive layer. As a result, the potential difference $\Delta E = E_{pit} - E_{rep}$ can be associated with a remarkable lowering of pitting current (i_{max}) as seen in Fig. 20.13 corresponding to eq. (20.2):

$$\log i_{max} = k_d \Delta E + k_e \tag{20.2}$$

The values of log i_{max} for the plots of NO_3^- are to some extent lower than that obtained with $^3H_2O_2$ indicating the inhibiting effects of NO_3^-. Hence NO_3^- suppresses pit nucle-

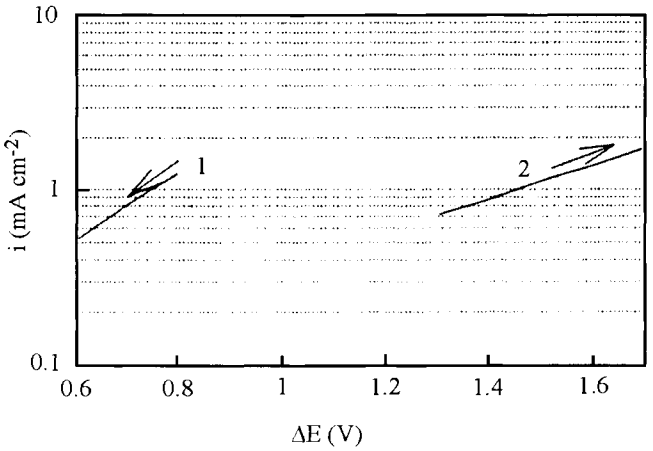

Figure 20.13. Relationship between the maximum pitting current and $\Delta E = (E_{pit} - E_{rep})$, 1: Cl^- and NO_3^-, 2: Cl^-, NO_3^- and $^3H_2O_2$, graph plotted according to Figs 20.8, 20.10 and 20.12, arrows: increasing ratio between inhibitor and chloride.

ation and slows the propagation of existing pits. With $^3H_2O_2$ addition ΔE increases with i_{max}, hence in this case it is difficult to have appreciable repassivation of the existing pits. These results confirm the previous conclusions: inhibition, nucleation or stimulation of pit formation and propagation of existing pits. Partial inhibition of existing pits is attributed to the presence of the inhibitor NO_3^-. In the presence of $^3H_2O_2$, propagation of existing pits is not stopped leading to a slowing down of the repassivation. The presence of $^3H_2O_2$ has provided a partly beneficial effect on the inhibiting action of NO_3^-.

2.3. Impedance spectra

The inhibition of the chloride pitting corrosion processes is studied indirectly by the passive potentials. From this, the Bode plots for:

- Cl^- are summarized in Fig. 20.14,
- Cl^- and NO_3^- are given in Fig. 20.15,
- Cl^-, NO_3^- and $^3H_2O_2$ are given in Fig. 20.16.

In these figures, each Bode plot displays two main regions:

(a) At higher frequency, a dip for the characteristic frequency, f_{c_1}, in the phase angle and a linear hump of slope -1 in the impedance modulus plots which corresponds to the double layer capacitance.

(b) A second dip in the phase angle which tends to $-90°$ at the characteristic frequency, f_{c_2} and a second linear hump of -0.9 to -1 in the impedance modulus depending on the $Cl^-/NO_3^-/^3H_2O_2$ present which corresponds to the passive oxide layer.

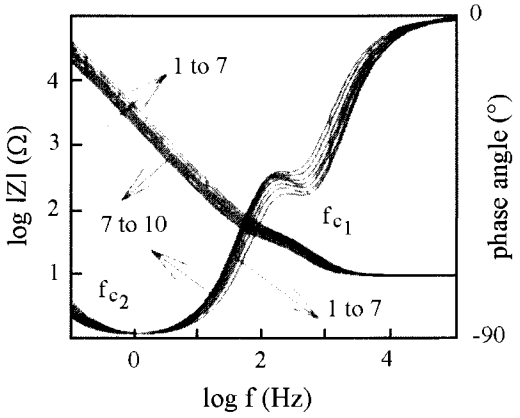

Figure 20.14. Bode spectra in presence of Cl^- in passivity, pH 6, 0.1 mol dm^{-3} Cl^-, 1: −1 V, 2: −0.97 V, 3: −0.95 V, 4: −0.92 V, 5: −0.9 V, 6: −0.87 V, 7: −0.85 V, 8: −0.82 V, 9: −0.8, 10: −0.77 V/SCE.

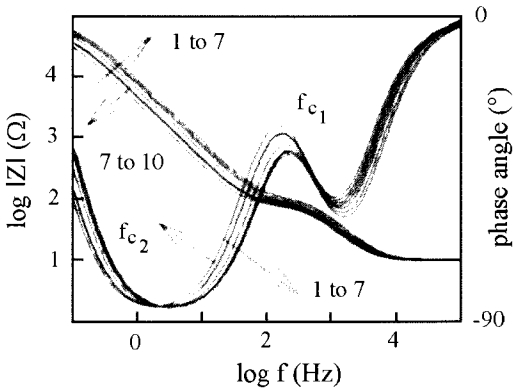

Figure 20.15. Bode spectra in presence of Cl^- and NO_3^- in passivity, pH 6, 0.1 mol dm^{-3} Cl^-, 0.1 mol dm^{-3} NO_3^-, 1: −1 V, 2: −0.97 V, 3: −0.95 V, 4: −0.92 V, 5: −0.9 V, 6: −0.87 V, 7: −0.85 V, 8: −0.82 V, 9: −0.8, 10: −0.77 V/SCE.

2.3.1. Discussion All the spectra have the same appearance, signifying only modification of values of discrete electrical components, which indicates that passivity is essentially dependent on the buffered pH, oxidizing power and oxide thickness. Spectra give a perfect fit with the data (Tables 20.2–20.4) if the total impedance is modeled according to the following transfer function for taking the evolutive structure into account:

$$\frac{1}{Z} = j\omega C_{dl} + \frac{1}{R_{ct} + \frac{R_{ox}}{1+(j\omega)^a A^{-1} R_{ox}}} \tag{20.3}$$

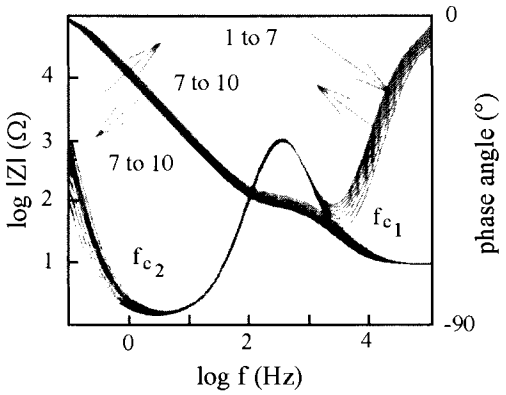

Figure 20.16. Bode spectra in presence of Cl^-, NO_3^- and $^3H_2O_2$ in passivity, pH 6, 0.1 mol dm^{-3} Cl^-, 0.1 mol dm^{-3} NO_3^-, 0.1 mol dm^{-3} $^3H_2O_2$, 1: −1 V, 2: −0.97 V, 3: −0.95 V, 4: −0.92 V, 5: −0.9 V, 6: −0.87 V, 7: −0.85 V, 8: −0.82 V, 9: −0.8, 10: −0.77 V/SCE.

Table 20.2. Dependence of oxide capacitance on passive potentials. Results in presence of 0.1 mol dm^{-3} Cl^- alone

E (V/SCE)	−1	−0.97	−0.95	−0.92	−0.9	−0.87	−0.85	−0.82	−0.8	−0.77
C_{ox} (μF cm^{-2})	25	22	19	17	15.7	14	13	14.2	15.9	17.2

Table 20.3. Dependence of oxide capacitance on passive potentials. Results in presence of 0.1 mol dm^{-3} Cl^- and 0.1 mol dm^{-3} NO_3^-

E (V/SCE)	−1	−0.97	−0.95	−0.92	−0.9	−0.87	−0.85	−0.82	−0.8	−0.77
C_{ox} (μF cm^{-2})	5	4.6	4.3	4	3.7	3.3	3	3.4	3.6	4.2

Table 20.4. Dependence of oxide capacitance on passive potentials. Results in presence of 0.1 mol dm^{-3} Cl^-, 0.1 mol dm^{-3} NO_3^- and 0.1 mol dm^{-3} $^3H_2O_2$

E (V/SCE)	−1	−0.97	−0.95	−0.92	−0.9	−0.87	−0.85	−0.82	−0.8	−0.77
C_{ox} (μF cm^{-2})	2.3	2.1	2	1.8	1.6	1.5	1.3	1.6	1.7	1.9

The transfer function given by eq. (20.3) includes two time constants, $\tau_1 = R_{ct}C_{dl}$ and $\tau_2 = R_{ox}/A$ depending on the phase angle and reciprocal of the characteristic frequencies. Decreasing time constants show enhancement of oxide capacitive characteristics as indicated by Mansfield [190] and filling of metastable pits. The metastable pits must be suppressed by passivation at the early nucleation stage and never start propagating. The greater deviation of the phase angle towards negative values as a function of the radiolytic species and passive potentials signifies that the passive layer increasingly approaches ideal behavior.

From the data (Tables 20.2 to 20.4), it is interesting to note that the capacitance results for Cl^- alone reflect the poorer corrosion resistance. With NO_3^-, the oxide capacitance values indicate effective protection by adsorption of $N^3H_4^+$ and pH buffering. Also, the

Table 20.5. Dependence of oxide thickness on passive potentials for each medium

E (V/SCE)	−0.95	−0.92	−0.9	−0.87	−0.85
Thickness in nm (0.1 mol dm^{-3} Cl^-)	1	1	1.1	1.2	1.3
Thickness in nm (0.1 mol dm^{-3} Cl^-, NO_3^-)	3.5	3.7	4.3	4.8	5.3
Thickness in nm (0.1 mol dm^{-3} Cl^-, NO_3^-, $^3H_2O_2$)	8	8.9	10	10.7	12.3

Table 20.6. Donor concentration and flatband potential as a function of Cl^-, NO_3^- and $^3H_2O_2$ present

Aqueous medium	Cl^-	Cl^-, NO_3^-	Cl^-, NO_3^-, $^3H_2O_2$
n_d (number of carriers per cm^3 × 10^{-19})	20	10	2
V_{fb} (V/SCE)	−0.88	−0.95	−0.91

value of the exponent 'a' of the constant phase element is close to 1 (eq. (6.25)) for the oxide layer obtained with NO_3^-. This value denotes the closer to perfect oxide layer. It can also be seen that the impedance modulus value is reduced as the spectrum passes from the passive range to the repassivation range. In this case, it should be noticed that the test, carried out in displacing the potential in the negative direction shows repassivation. These results confirm strongly that the accumulation of $N^3H_4^+$ on the Zircaloy surface enhances the oxide layer properties by blocking the chloride adsorption sites.

In presence of $^3H_2O_2$, the impedance modulus slope is slightly less than the slopes for NO_3^- alone, thus indicating a few defects. Also, it is seen that the changing characteristic frequencies indicate a modification of the oxide layer thickness depending on the passive potentials and the presence of $^3H_2O_2$, as noted by Schmuki and Böhni [237]. This fact can be associated with the nucleation of existing pits because the oxide begins to be stressed by its thickness and defects. Also, the results emphasize that the presence of $^3H_2O_2$, fed by temporary oxidizing species, stimulates the repair of flawed regions of the passive layer and oxidation of the active sites on the surface. The oxide layer thus formed is more corrosion resistant. As a result a marked delay in the pitting evolution is recorded. This could be explained by reduced chloride incorporation into the oxide layer.

To ascertain the oxide layer characteristics, the thickness is obtained from the usual formula for reciprocal plane capacitance considering the surface roughness and the value of the oxide layer dielectric constant for ZrO_2 to be equal to 14 [269]. According to Table 20.5, the oxide layer thickness grows with the passive potentials and depends on the three media: Cl^-–Cl^-/NO_3^-–$Cl^-/NO_3^-/^3H_2O_2$. From these results, it can be deduced that oxide layer thickening facilitates passivation and constraints to modify electrochemical exchange of charge across this. This means that the electrical field changes modify the carrier number and vacancies diffusion through the oxide layer. Finally, the approach of describing the oxide layer in terms of barrier properties using the Mott-Schotky equation should be valid for calculating the donor concentration as shown by Schmuki et al. [255]. Using this equation, the donor density, n_d, varies from 20 to 2 × 10^{19} carrier cm^{-3} (Table 20.6) signifying protection of the Zircaloy-4 by NO_3^- or $^3H_2O_2$. The higher carrier concentration for the oxide layer obtained for Cl^- alone signifies chloride diffusion. It can also be seen that n_d is lower with $^3H_2O_2$ present, indicating oxide layer thickening as reported by

Quarto et al. [276]. In addition, the influence of surface pH on the oxide properties should be considered through its effect on the overall oxide charge density as shown by Quarto et al. [267] and Horvat-Radoševic and Kvastek [268].

$$V_{fb} = -k - 0.06pH_{surface} \tag{20.4}$$

The flatband extrapolated potential V_{fb} is close to -0.9 V/SCE in the presence of Cl^- and increases toward negative values with NO_3^- present, indicating that the surface pH is buffered by $N^3H_4^+$ formation.

It is important to emphasize the role of NO_3^- and $^3H_2O_2$ in the corrosion inhibition process and to understand the interaction of these radiolytic species with the incorporated chloride throughout the layer thickness. Strehblow [114], emphasizes that the formation of a thin metal-chloride layer was observed between the oxide and the alloy. Since chloride is responsible for the formation of this inner chloride layer, this location leads to the simple conclusion that the incorporated chlorides migrate at a significantly higher rate than that of oxygen ions into oxide. This conclusion, however, leads to the following question. Is the migration of chlorides independent of, or coupled to, nitrate and hydrogen peroxide concentration? We shall try to answer this question by finding a relationship between the corresponding different parameters, i.e. vacancies diffusion, pitting potential and donor density with Cl^-, NO_3^- and $^3H_2O_2$ present.

We first propose a succession of chemical and electrochemical reactions in ZrO_2 and at its interfaces without initially taking account of Cl^-. After an adsorption stage, there is oxygen ion diffusive penetration in the oxide layer by vacancies towards the Zr–ZrO_2 interface. This can be described in the following form, as shown by Macdonald et al. [116] and Lorenz et al. [233]. The vacancies are the limiting parameter for any diffusion. Based on these considerations, the following simplified reactions with NO_3^- alone (eq. (20.5)) or with $^3H_2O_2$ (eq. (20.6)) are in equilibrium at each interface:

– aqueous–ZrO_2 interface:

$$2V_{O^{2-}} + NO_3^- + 2\,{}^3H_2O + 8e^- \leftrightarrow \{N^3H_4^+, O^3H^-\}_{\text{local pH}} + 4O^{2-} \tag{20.5}$$

$$V_{O^{2-}} + 2\,{}^3H_2O_2 + NO_3^- + 12e^- \leftrightarrow \{N^3H_4^+, O^3H^-\}_{\text{local pH}} + 6O^{2-} \tag{20.6}$$

$$\{\text{oxide}^{4+}\} + 2\,{}^3H_2O_2 + 4e^- \leftrightarrow V_{Zr^{4+}} + ZrO_2 + 2\,{}^3H_2O \tag{20.7}$$

– diffusion in ZrO_2:

$$(O^3H^-)_{\text{local pH}}, O^{2-} + V_{O^{2-}} \leftrightarrow V_{O^{2-}} + O^{2-} \tag{20.8}$$

– Zr–ZrO_2 interface:

$$Zr \leftrightarrow \{\text{oxide}^{4+}\} + 2V_{O^{2-}} + 4e^- \tag{20.9}$$

$$Zr + V_{Zr^{4+}} \leftrightarrow \{\text{oxide}^{4+}\} + 4e^- \tag{20.10}$$

{oxide^{4+}} represents Zr ions in the passive oxide layer which are in equilibrium with the corresponding vacancies. In this mechanism, the electron flux in ZrO_2 is in the tritiated water direction for oxide growth. It can be seen that the presence of O^3H^- ions implies that the surface pH is buffered by NO_3^- that avoids local acidification by $N^3H_4^+$ formation. Apparently, $V_{O^{2-}}$ species are produced at the ZrO_2–Zr interface and consumed at the oxide–aqueous interface. As a result, $V_{O^{2-}}$ diffuses from the ZrO_2–Zr to the ZrO_2–aqueous interface. The net results of $V_{O^{2-}}$ migration can be seen by combining eqs (20.5), (20.6) and (20.9). From the set of previous reactions, it is clear that the diffusion of $V_{O^{2-}}$ effectively results in oxide growth, should depend on flatband potential, and is produced with consumption of $^3H_2O/^3H_2O_2$ at the ZrO_2–aqueous interface where the pH is buffered throughout, whereas {oxide^{4+}} keeps the pH buffered with $N^3H_4^+$ and O^3H^- formed in the 'pseudo' active region.

These reactions occurring on passive oxide are influenced by the different potential drops $\Delta\Phi_V$ in the Zr–ZrO_2 and the ZrO_2–aqueous interfaces. Within the passive layer of a few nanometers (Table 20.5), the potential drop into oxide is of the order of some hundreds of mV [114], which enables the migration of electrons through the oxide layer at a measurable level in currents of a few μA (Fig. 20.1). The corresponding physical model to interpret the diffusion processes and the potential drops is shown schematically in Fig. 20.17. Since the ZrO_2–aqueous interface is polarizable, it is expected that the total potential drop is given by:

$$\partial\Delta E = \partial\Delta E_{ZrO_2-Zr} + 2.3\frac{RT}{2F}\left[\partial\log\left[NO_3^-, O^3H^-, {}^3H_2O_2\right]\right] + \partial\Delta\Phi_V \qquad (20.11)$$

where ΔE represents the potential drops between the interfaces and within the oxide layer. It is expected that:

$$\partial\left(C_{ox}^{-1}\right) = \partial\Delta E - 2.3\frac{RT}{2F}\left[\partial\log\left(NO_3^-, O^3H^-, {}^3H_2O_2\right)\right] \qquad (20.12)$$

The oxide thickness is given by:

$$\partial d = b\left(\partial\Delta E - 2.3\frac{RT}{2F}\left[\partial\log\left(NO_3^-, O^3H^-, {}^3H_2O_2\right)\right]\right) \qquad (20.13)$$

where b is a constant resulting from considering the oxide layer as a plane capacitor. Thus eqs (20.11)–(20.13) represent the functional dependence of the passive layer growth law on $\partial\Delta E$ and $\partial\log(NO_3^-, {}^3H_2O_2)$ up to a determined size also aided by the buffered pH. Therefore the formation of the oxide layer, its thickness and its mode of growth are dependent on radiolytic species in tritiated water.

In the presence of Cl^-, for a metastable pit at a given potential, there must be a relationship between Cl^-, NO_3^-, O^3H^- and $^3H_2O_2$ concentrations where the pit can be deactivated or activated. According to Strehblow [114] and Macdonald [116,117], if the Zr vacancies

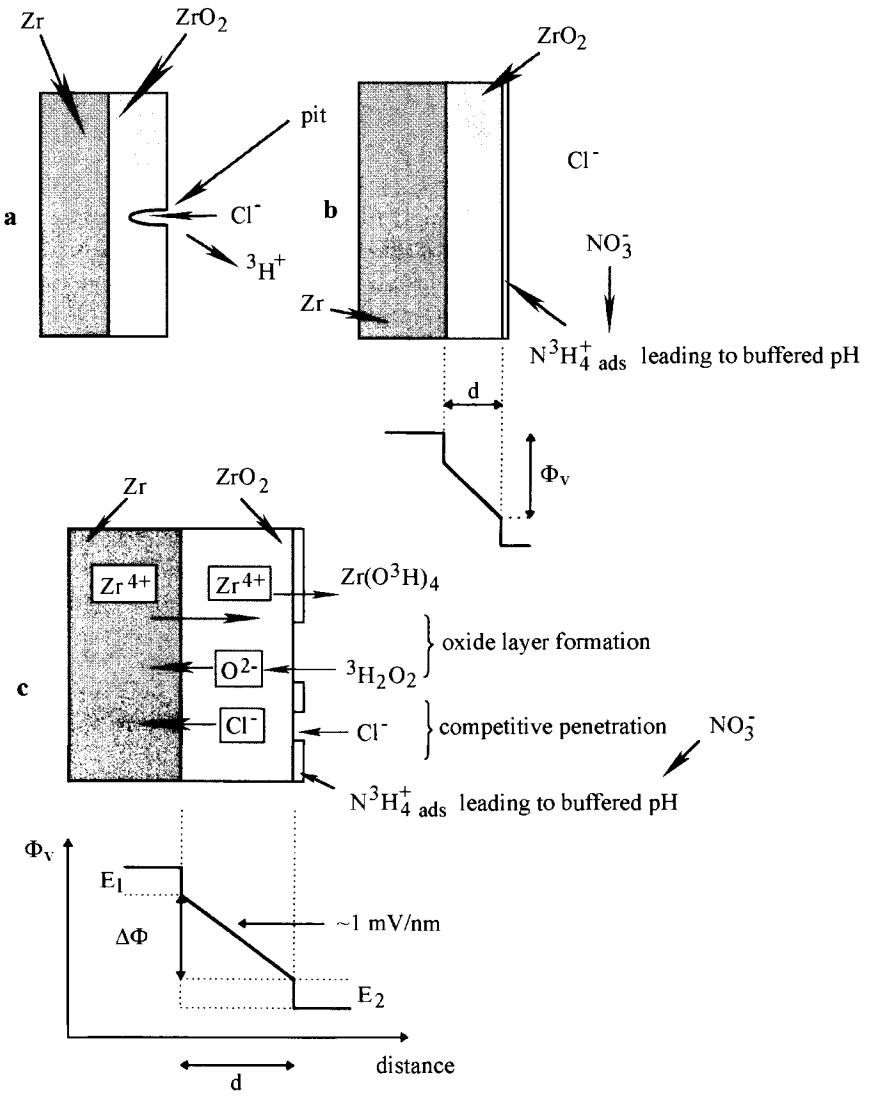

Figure 20.17. Physical model proposed to interpret the processes in oxide with chloride, nitrate and hydrogen peroxide, (a): Cl^-, (b): Cl^- and NO_3^-, (c): Cl^-, NO_3^- and $^3H_2O_2$ present.

penetrate the Zircaloy at a slower rate than their diffusion through the oxide layer, they accumulate at the Zr–ZrO_2 interface and finally lead to a local concentration and hence will form a void. When the void grows to a certain critical size, the passive oxide layer suffers local collapse, which then marks the end of the pit incubation period. The collapsed site

dissolves much faster than any other location on the layer thereby leading to pit growth. From this, the Zr vacancies are affected by the incorporation of Cl^- ions at the ZrO_2–aqueous interface as shown in the physical model (Fig. 20.17) and the equations given by Strehblow [114] and Macdonald [116,117].

From these considerations, the number of $V_{O^{2-}}$ species increases by introducing more NO_3^- and $^3H_2O_2$ and inversely decreases with $\{Cl^-\}$. Due to interdependence of the concentration of Zr and O^{2-} vacancies and the penetration of Cl^- within the oxide layer, the number of Zr vacancies decreases in the oxide layer by the presence of NO_3^- or $^3H_2O_2$ avoiding the critical concentration whose repercussions are shown in Figs 20.3, 20.4 and 20.7. From these considerations, the criterion for pit initiation in the presence of NO_3^- and $^3H_2O_2$ can be expressed by:

$$\frac{\partial V_{Zr^{4+}}}{\partial t} = J_0\left[C_{V_{O^{2-}}}\{ZrO_2\text{–}NO_3^-, {}^3H_2O_2\}\right]^{-2} \tag{20.14}$$

where J_0 depends on thermodynamic constants and $C_{V_{O^{2-}}}$ $(ZrO_2\text{–}NO_3^-, {}^3H_2O_2)$ is the concentration of O^{2-} vacancies at the ZrO_2–aqueous interface. Applying a calculation procedure similar to that given by Strehblow [114] and Macdonald et al. [116,117], we can write the simplified equation in the presence of NO_3^- and $^3H_2O_2$:

$$E_{pit} = \frac{2.3RT}{\alpha F}\log\left(\frac{J_m}{J_0\frac{M}{\rho}\exp\left\{\frac{(\{^3H_2O_2\}\{O^3H^-, NO_3^-\})}{RT}\right\}^{-0.5n}}\right) - \frac{2.3RT}{\alpha F}\log Cl^- \tag{20.15}$$

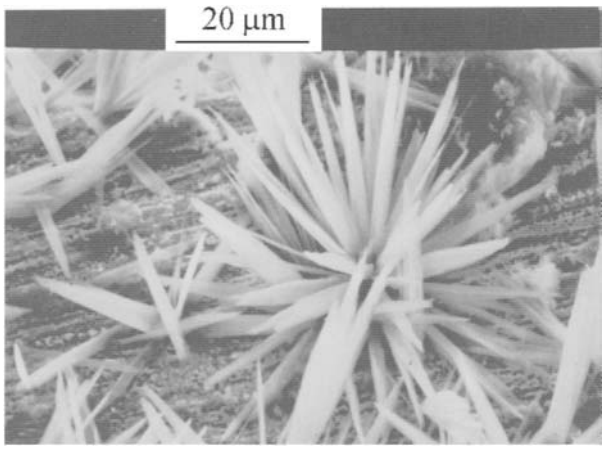

Figure 20.18. Scanning Electron Micrography showing repassivated pits obtained with Cl^-, NO_3^- and $^3H_2O_2$ and covered with zirconium oxide crystals.

where J_m is the rate of submergence of the Zr vacancies in the Zircaloy-4, M the oxide molecular weight and ρ the oxide density. It can be seen effectively that higher concentrations of NO_3^-, O^3H^- and $^3H_2O_2$ would delay and avoid pitting by Cl^-, shifting this potential in the positive direction. This analysis should include examinations of the Zircaloy-4 surface to check the results. The absence of marked or localized corrosion in the presence of NO_3^-, Cl^- and $^3H_2O_2$, was observed by Scanning Electron Microscopy (Fig. 20.18). Only a few observable crystals covering the repassivated pits were noted. They correspond to early stage pitting.

3. Conclusions

From the experimental results, several conclusions arise naturally. The more beneficial effect is due to the radiolytic nitrate presence leading to formation of $N^3H_4^+$ and its adsorption. $N^3H_4^+$ may be considered as a counter-ion for neutralizing acid pH in the pitting process. In this connection, it is of interest to speculate that the pH is buffered on the surface oxide layer and plays a determinant role in avoiding pitting and favoring repassivation. In this case, nucleation pits do not have the possibility of being transformed to metastable or stable pits. Nitrate without hydrogen peroxide shows the greatest effectiveness against pitting corrosion.

The addition of $^3H_2O_2$ by temporary oxidizing species to tritiated water containing Cl^- and NO_3^- significantly increases the thickness and changes the oxide layer characteristics. Results indicate the formation of a more stressed passive oxide than for NO_3^- alone. The pitting potential shifts towards more positive values so that pitting formation ceases; the repassivation potentials shift slightly towards more negative values resulting in a limitation of propagation of existing pits. It is deduced that existing pits are less easily passivated with $^3H_2O_2$ than with NO_3^- alone. However, the combined effects of NO_3^- and $^3H_2O_2$ together show greater resistance to pitting corrosion than those for Cl^- alone.

Chapter 21

CORROSION INHIBITION BY DEUTERIUM OXIDE

1. Introduction

Tritiated water from fusion reactors contains deuterium oxide. Moreover, deuterium oxide is produced as waste in making deuterated-tritiated titanium targets. The quantity of tritium trapped in titanium is between 0.04 and 40 TBq. These targets produce 17.6 and 3.3 MeV fast neutrons with the formation of fluxes between 10^8 and 10^{13} n cm^{-2} s^{-1} when they are bombarded in accelerators. These neutrons are afterwards used to irradiate materials (e.g. to sterilize surgical instruments) or human tissue in the treatment of cancer or to produce fission in military activities. Consequently, tritiated water contains the three hydrogen isotopes.

$$^2H + ^3H \rightarrow ^4He + n + \alpha \qquad 17.6\ MeV \tag{21.1}$$

$$^2H + ^2H \rightarrow ^3He + n + \alpha \qquad 3.3\ MeV \tag{21.2}$$

The dissociation constant (pK_w) for deuterium oxide is 14.8 and therefore the pH in ^2H_2O differs from that of water. This difference leads to a slight pH increase in acid media and a slight decrease in alkaline media for ^2H_2O. This modification should change the characteristics of the oxide layer. Therefore, the effects of deuterium oxide were studied in comparison to light water and with or without Cl^- for the range of corrosion, passive and localized corrosion potentials. The composition of the 316Ti austenite stainless steel is given in Table 21.1. It can be seen that there is a non-negligible carbon content. Titanium, which forms a titanium carbide in the carbon grain boundary, is added to avoid localized corrosion.

Table 21.1. 316Ti steel—composition

Elements	C	Ni	Cr	Fe	Mn	Si	Mo	Cu	Ti
Wt%	0.06	12	16.8	bal.	1.8	0.34	2	0.3	0.44

2. Experimental results

2.1. Results obtained with deuterium oxide or light water without chloride

2.1.1. Anodic polarization curves Anodic polarization curves obtained for different pH values without Cl^- and at a low scan rate are presented in Figs 21.1, 21.2 and 21.3a. In these curves, the deuterium evolution potential is more negative than that of hydrogen. At alkaline and near neutral pH, the corrosion potential is shifted towards more positive values with ^2H_2O, whereas at acid pH this is shifted in the opposite direction. This is probably due to the positive and negative pH differences between ^2H_2O and H_2O (Table 21.2) taking account of the constant kinetics. At the corrosion potential, the corrosion should occur at the cathodic and anodic sites resulting in local pH modifications. It can also be seen in these curves that the passive currents are lower for pH 7.5 and with ^2H_2O.

The explanation for the lower currents could be that deuterium oxide leads to less dissociated 'wet' deuterated metal oxide and more insulating 'dry' oxide. The interpretation of experimental results indicates that the E_{corr} vs. pH derivative is assumed to be:

$$\left\{\frac{\partial E_{corr}}{\partial pH}\right\}_{H_2O,\,^2H_2O} = \frac{1.15\nu RT}{F} - \Delta pK_w \tag{21.3}$$

This equation shows effectively that the pH variation with deuterium oxide and H_2O (Table 21.2) modifies the corrosion potential as shown by the experimental values in Table 21.3 where the slope is about 57 mV per pH decade. The reaction order sign expected for ^2H_2O is consequently negative which clearly indicates the cathodic electrochemical reaction [159]. The cathodic and anodic experimental Tafel slopes are, respectively -110 and 55 mV per decade and are consistent with the detail of eq. (21.3).

The corrosion current derivative is, for example, for alkaline pH:

$$\left\{\frac{\partial \log i_{corr}}{\partial pH}\right\}_{H_2O,\,^2H_2O} = 0.3\nu - \Delta pK_w \tag{21.4}$$

The corrosion current depends on O^2H^- and $^2H^+$ activity and therefore on pH modification by deuterium oxide. The values determined from the experimental data are given in Table 21.3, where it can be seen that the value of i_{corr} is lower with ^2H_2O. These values show better protection with deuterium oxide.

In the transpassivity, it is observed that the anodic current increases with ^2H_2O or H_2O signifying corrosion of 316Ti steel.

Table 21.2. Dependence of pH on aqueous medium

Aliquots added (mmol)		pH	
		^2H_2O	H_2O
H_2SO_4	0.1	4.5	4
NaOH	10^{-3}	7.3	8
	20	12	12.5

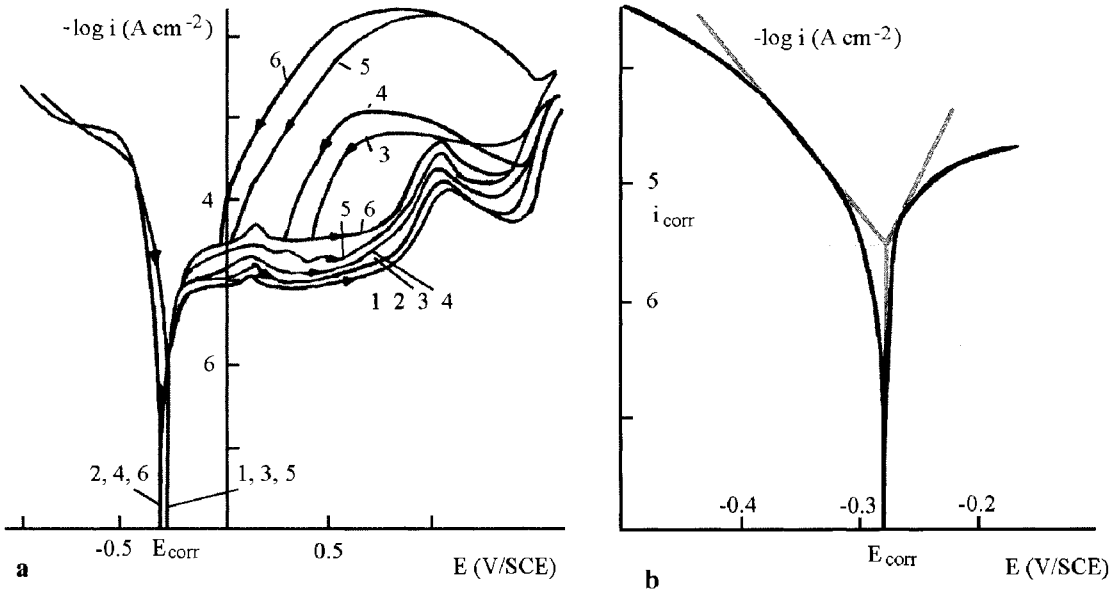

Figure 21.1. (a): Polarization curves with ^2H_2O or H_2O at acid pH, ω: 2000 rpm, v: 5 mV s^{-1}, H_2O at pH 4, ^2H_2O at pH 4.5, 1: H_2O without Cl^-, 2: ^2H_2O without Cl^-, 3: H_2O, 0.02 mol dm^{-3} Cl^-, 4: ^2H_2O, 0.02 mol dm^{-3} Cl^-, 5: H_2O, 0.05 mol dm^{-3} Cl^-, 6: ^2H_2O, 0.05 mol dm^{-3} Cl^-, (b): determination of Tafel parameters with ^2H_2O, $1-\alpha=-110$ mV, $\alpha=50$ mV.

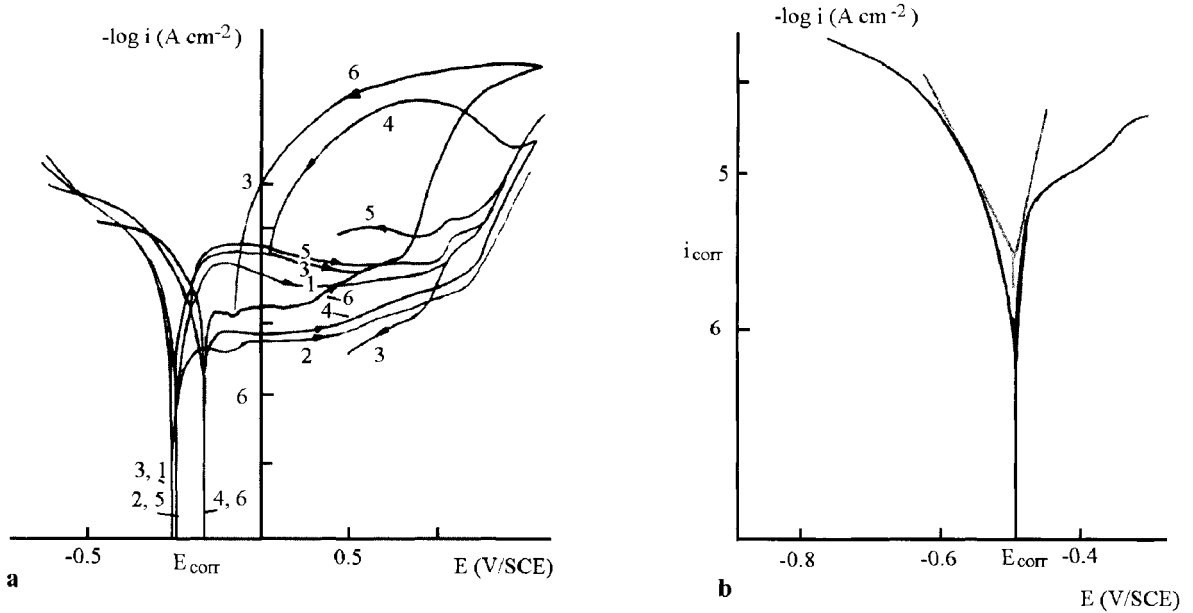

Figure 21.2. (a): Polarization curves with ^2H_2O or H_2O at near neutral pH, ω: 2000 rpm, v: 5 mV s^{-1}, H_2O at pH 8, ^2H_2O at pH 7.5, 1: H_2O without Cl^-, 2: ^2H_2O without Cl^-, 3: H_2O, 0.02 mol dm^{-3} Cl^-, 4: ^2H_2O, 0.02 mol dm^{-3} Cl^-, 5: H_2O, 0.05 mol dm^{-3} Cl^-, 6: ^2H_2O, 0.05 mol dm^{-3} Cl^-, (b): determination of Tafel parameters with ^2H_2O, $1-\alpha=-105$ mV, $\alpha=55$ mV.

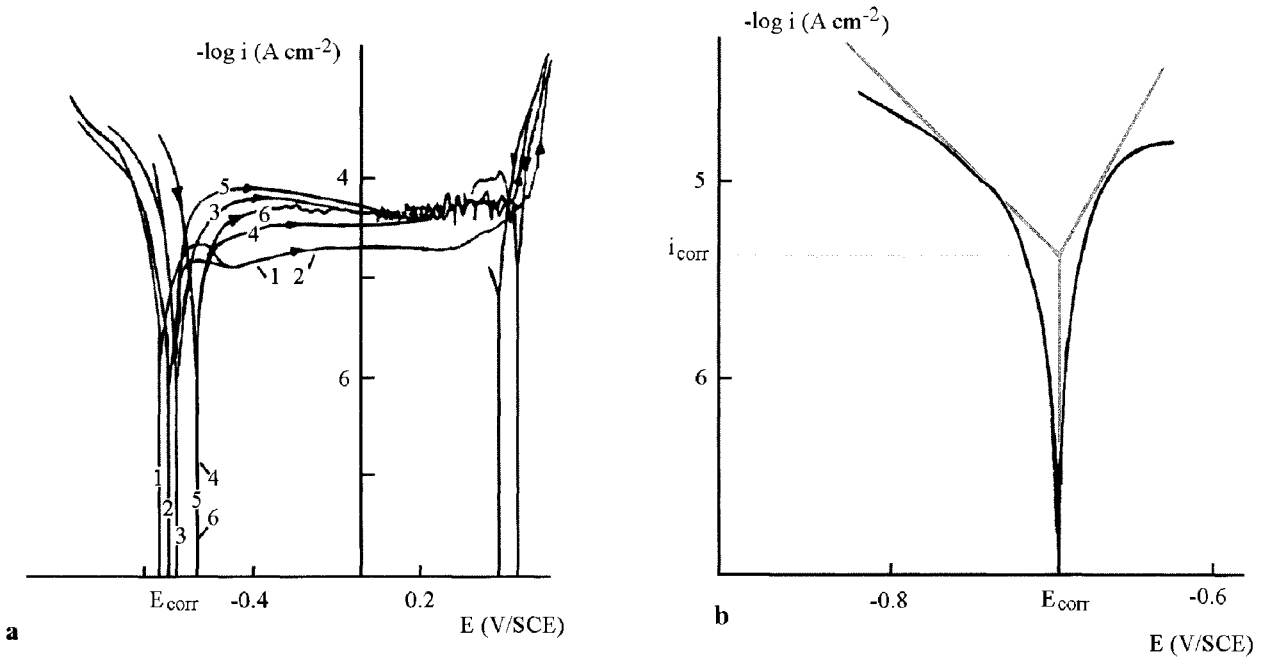

Figure 21.3. (a): Polarization curves with ^2H_2O or H_2O at alkaline pH, ω: 2000 rpm, v: 5 mV s^{-1}, H_2O at pH 12.5, ^2H_2O at pH 12, 1: H_2O without Cl^-, 2: ^2H_2O without Cl^-, 3: H_2O, 0.02 mol dm^{-3} Cl^-, 4: ^2H_2O, 0.02 mol dm^{-3} Cl^-, 5: H_2O, 0.05 mol dm^{-3} Cl^-, 6: ^2H_2O, 0.05 mol dm^{-3} Cl^-, (b): determination of Tafel parameters with ^2H_2O, $1-\alpha=-120$ mV, $\alpha=60$ mV.

Table 21.3. Dependence of E_{corr} and i_{corr} on H_2O or ^2H_2O for different pH

	H_2O			^2H_2O		
pH	4	8	12.5	4.5	7.5	12
E_{corr} (V/SCE)	−0.25	−0.5	−0.75	−0.28	−0.48	−0.7
i_{corr} ($\mu A\,cm^{-2}$)	6	5	7	5	4	6

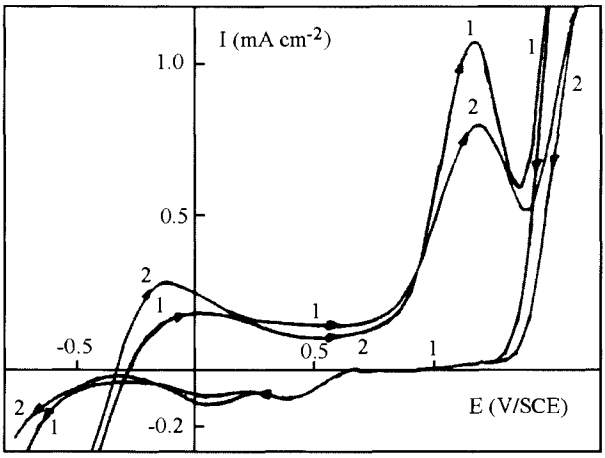

Figure 21.4. Voltammetric curves with ^2H_2O or H_2O at acid pH, ω: 2000 rpm, v: 100 mV s^{-1}, without Cl^-, 1: H_2O at pH 4, 2: ^2H_2O at pH 4.5.

2.1.2. Voltammetric curves Figs 21.4, 21.5 and 21.6 illustrate the voltammograms obtained with deuterium oxide and light water at a high scan rate. Evidently the presence of ^2H_2O significantly affects 316Ti steel oxidation and reduction processes. On increasing the potential in the forward scan, a prepassive peak is seen at alkaline pH. At more acid pH, the prepassive peak is hidden to a greater extent by the deuterium and hydrogen evolution current. The size of the prepassive peak changes or disappears depending on whether or not there is deuterium oxide (Fig. 21.5). In the backward scan, a major reduction peak occurs near −0.8 V/SCE as seen at alkaline or more neutral pH and corresponds to the reduction of corrosion products. Near neutrality and with ^2H_2O, the passive current is fairly low and shows that the oxide layer is an excellent isolating barrier.

It should be noted that the passive region is followed by a transpassive peak preceding the oxide layer dissolution. The current increases quickly in this region and corresponds to MeO_4^{2-} formation. Evidently, the presence of ^2H_2O significantly affects the oxidation and reduction processes of 316Ti steel as with H_2O and leads to a local acidification whose effect on corrosion is inhibited by stirring. Due to less alkaline and acid pH with ^2H_2O, the transpassive peak is smaller in this medium.

Moreover, the curves exhibit the following characteristics: (a) in the forward scan, the anodic curves intersect the potential axis at more positive potentials with ^2H_2O and for alkaline and near neutral pH, (b) a lower reduction peak is obtained with ^2H_2O for these

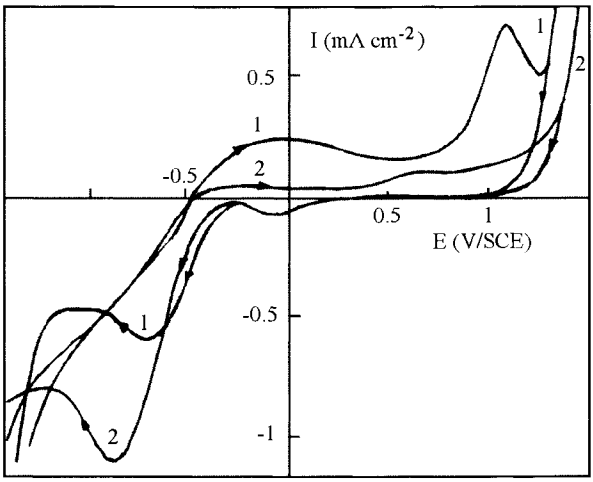

Figure 21.5. Voltammetric curves with ^2H_2O or H_2O at near neutral pH, ω: 2000 rpm, v: 100 mV s^{-1}, without Cl^-, 1: H_2O at pH 8, 2: ^2H_2O at pH 7.5.

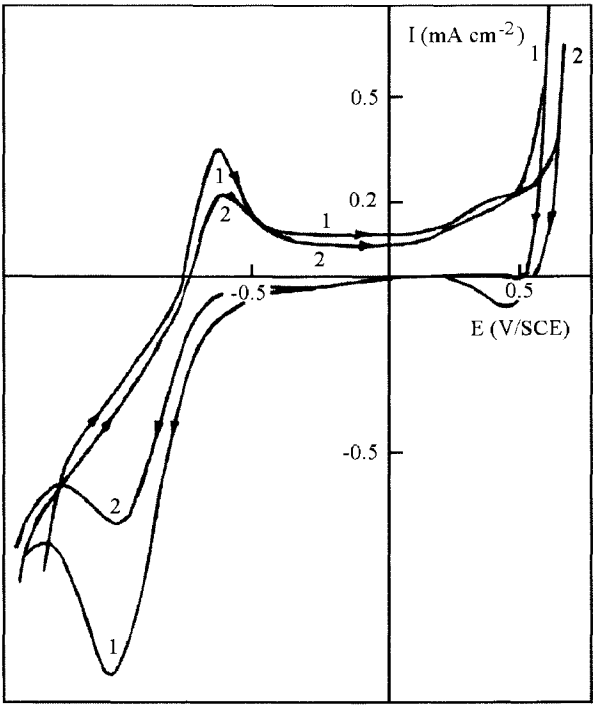

Figure 21.6. Voltammetric curves with ^2H_2O or H_2O at alkaline pH, ω: 2000 rpm, v: 100 mV s^{-1}, without Cl^-, 1: H_2O at pH 12.5, 2: ^2H_2O at pH 12.

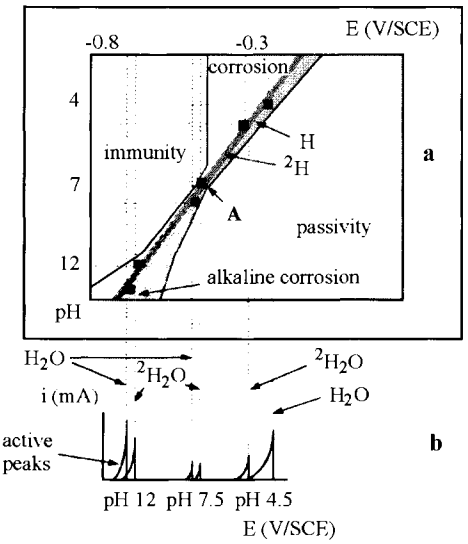

Figure 21.7. Diagram giving the behavior of 316Ti steel in chloride-free solution (a), polarization curves at pH 4–12 (b), experimental circumstances of general corrosion, alkaline corrosion and passivity.

pH values (c) in the forward scan, the 316Ti steel active peak disappears with ^2H_2O at close to neutral pH, (d) in the passive region, the anodic current decreases more with ^2H_2O. It would appear that the passive oxide layer is more protective with ^2H_2O, (e) in the transpassive region, the anodic peak is lower with ^2H_2O. The interpretation could be that the oxide breakdown current decreases. As a result, voltammograms and polarization curves show that there is modification of the passive oxide layer between ^2H_2O and H_2O.

The tracing of voltammograms at different pH values reveals the active behavior modifications. At the corrosion potential and in the active region, the net current is equal to the sum of two currents with opposite signs: that due to 316Ti steel oxidation and that due to ^2H_2O reduction. The explanation of active behavior modifications is helped by using the diagrams in Fig. 21.7 which show several characteristic changes depending on pH in H_2O or ^2H_2O according to the potential–pH equilibrium relationship [277]:

- At pH 12.5 obtained with H_2O, a larger alkaline corrosion region with the formation of $HMeO_2^-$ is seen. 316Ti steel is easily corroded with the formation of a high active peak. Higher potentials than that of alkaline corrosion correspond to the passive region. At pH 12 obtained with ^2H_2O, a narrower alkaline corrosion region is seen with the formation of passive oxide corresponding to Me_2O_3 and Me_3O_4. 316Ti steel is passivated with the formation of a smaller active peak.
- At pH 7.5 obtained with ^2H_2O, the corrosion potential is more easily placed in passivity (contraction point A) than at pH 8 obtained with H_2O, therefore 316Ti steel is passivated without the formation of an active peak. For this pH, the corrosion current should be lower than that obtained at pH 8.

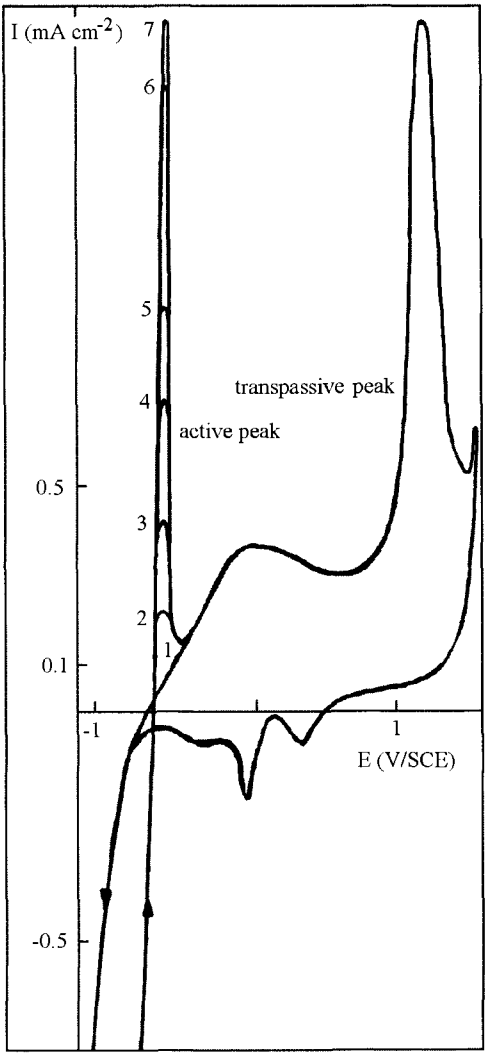

Figure 21.8. Active peak partially hidden by the reduction current of deuterium oxide at acid pH and 3×10^{-2} mol dm^{-3} corrosion products for 316Ti, v: 200 mV s^{-1}, ω: 1: 0, 2: 360, 3: 460, 4: 560, 5: 660, 6: 960, 7: 1200 rpm.

– At pH 4 and 4.5, a wider corrosion region preceding the passivity is seen, with the possible formation of Me^{2+} and Me^{3+}. 316Ti steel is corroded with the formation of an active peak. This peak can be partially hidden and is narrower by the deuterium oxide reduction current (Fig. 21.8) at more acid pH values. In this figure, the active peak

depends on ionic species coming from corrosion of steel in deuterium oxide whereas the transpassive peak does not depend on ionic species.

It is also necessary to compare the straight lines for the evolution of deuterium and of hydrogen (Fig. 21.7). That of deuterium is below that of hydrogen, but due to the positive and negative pH differences between ^2H_2O and H_2O (Table 21.2), at alkaline and near neutral pH, the corrosion potential of ^2H_2O is higher than that of H_2O, and at acid pH the corrosion potential of ^2H_2O is lower than that of H_2O. From the potential–pH equilibrium diagram, it can be seen that:

- At alkaline pH, the corrosion potential will be nearer potentials of the narrow corrosion region for ^2H_2O, while with H_2O, the corrosion potential will be positioned more centrally in the alkaline corrosion region resulting in a higher active peak.
- Near neutrality, H_2O is slightly more dissociated and the pH is 8, whereas the pH of ^2H_2O is 7.5. According to the potential–pH equilibrium diagram, at pH 7.5, the straight line for deuterium is nearer the contraction in point A. This results in more passivity than at pH 8 and a very small passive current without an active transition (Fig. 21.5) and higher corrosion potential as seen also in the voltammograms. Fewer corrosion species are formed since the reduction peak is lower than that obtained at pH 8.
- At acid pH, the corrosion potential of ^2H_2O is lower than that of H_2O in voltammograms which corresponds to the situation given in the potential–pH equilibrium diagram for pH 4.5 and pH 4. In this case the corrosion potential of ^2H_2O will be towards the contraction point whereas that of H_2O will be nearer the corrosion region. The active peak can be hidden by the cathodic current corresponding to hydrogen or deuterium evolution.

2.1.3. Impedance spectra

2.1.3.1. Results This section is concerned with the analysis of impedance data for 316Ti steel passivated at different passive potentials and with ^2H_2O or H_2O. The impedance data will be compared to evaluate the effect of ^2H_2O on the passive oxide characteristics. Comparative Bode diagrams (Figs 21.9 and 21.10) made at the different pH values, with ^2H_2O or H_2O and passive potentials near the corrosion potential (up to +200 mV) show changes in $\log|Z|$ and phase angle/$\log(f)$. The diagrams are characterized essentially by two distinct regions:

(a) In the broad low and middle frequency range, the diagrams display a linear slope of about -1 in $\log|Z|$ as $\log(f)$ decreases, while phase angle values approach $-90°$. This is the characteristic response of a passive oxide capacitance. This capacitive behavior is observed over a broad measurement frequency range.

(b) In the higher frequency range of (a), an inflection in the phase angle/$\log(f)$ curve and the $\log|Z|/\log(f)$ plots. These indicate the presence of a hardly identifiable parallel resistance and a non-dissipative passive oxide capacitance due to its formation. Also, the deviation of the phase angle maximum, near $-90°$, signifies that the passive layer thus

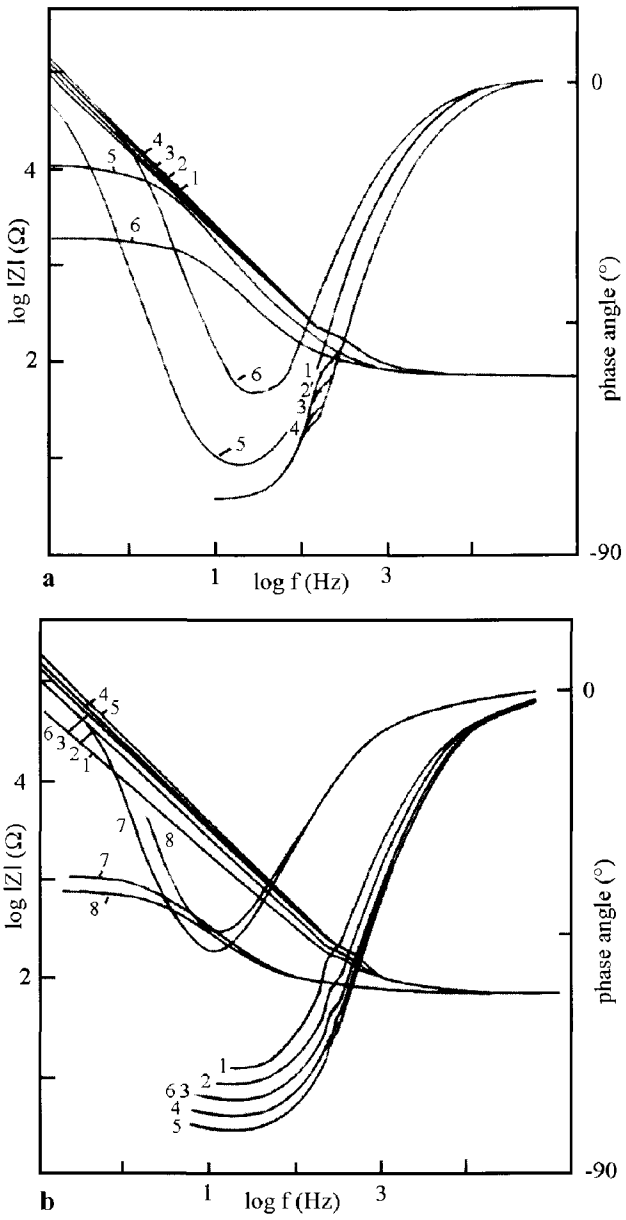

Figure 21.9. Bode spectra with H_2O, ω: 2000 rpm, (a): pH 4, 1: −0.2 V, 2: −0.17 V, 3: −0.15 V, 4: −0.12 V, 5: 1.375 V, 6: 1.425 V/SCE, (b): pH 8, 1: −0.22 V, 2: −0.2 V, 3: −0.17 V, 4: −0.15 V, 5: −0.12 V, 6: −0.1 V, 7: 1.3 V, 8: 1.325 V/SCE, (c): pH 12.5, 1: −0.35 V, 2: −0.32 V, 3: −0.3 V, 4: −0.27 V, 5: −0.25 V, 6: −0.22 V, 7: −0.2 V, 8: −0.17 V, 9: −0.15 V, 10: 0.58 V, 11: 0.6, 12: 0.65 V/SCE.

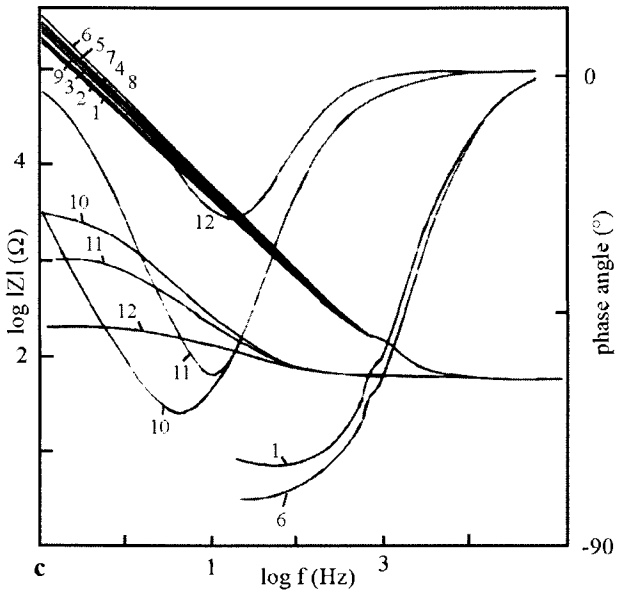

Figure 21.9. (Continued).

Table 21.4. Dependence of oxide capacitance (μF cm^{-2}) on passive potentials for H_2O at different pH

E (V/SCE)	−0.35	−0.32	−0.3	−0.27	−0.25	−0.22	−0.2	−0.17	−0.15	−0.12
pH 4							11	10	9	6.9
pH 8						11	10	9	8.3	6.5
pH 12.5	5.3	4.8	4	3.6	3.2	2.8				

Table 21.5. Dependence of oxide capacitance (μF cm^{-2}) on passive potentials for ^2H_2O at different pH

E (V/SCE)	−0.37	−0.35	−0.32	−0.3	−0.27	−0.25	−0.22	−0.2	−0.17	−0.15	−0.12	−0.1
pH 4.5								8.3	7.7	6.2	5	4
pH 7.5							8.3	6.7	5.3	4.3	3.5	
pH 12	6.2	4.9	4.3	3.8	3.4	2.7	2.3					

formed on 316Ti steel approaches more ideal capacitor behavior. From voltammogram transform and Faraday's law, the oxide layer thickness is:

$$d = QM/nF\rho r \tag{21.5}$$

where M is the mean molar weight of oxide, assumed to be 159, n the mean number of electrons required to form the passive oxide and ρ the oxide density, equal to 5.2 g cm^{-3} according to Schmuki and Böhni [237]. From this equation, the values of passive oxide capacitance are determined for different passive potentials and with

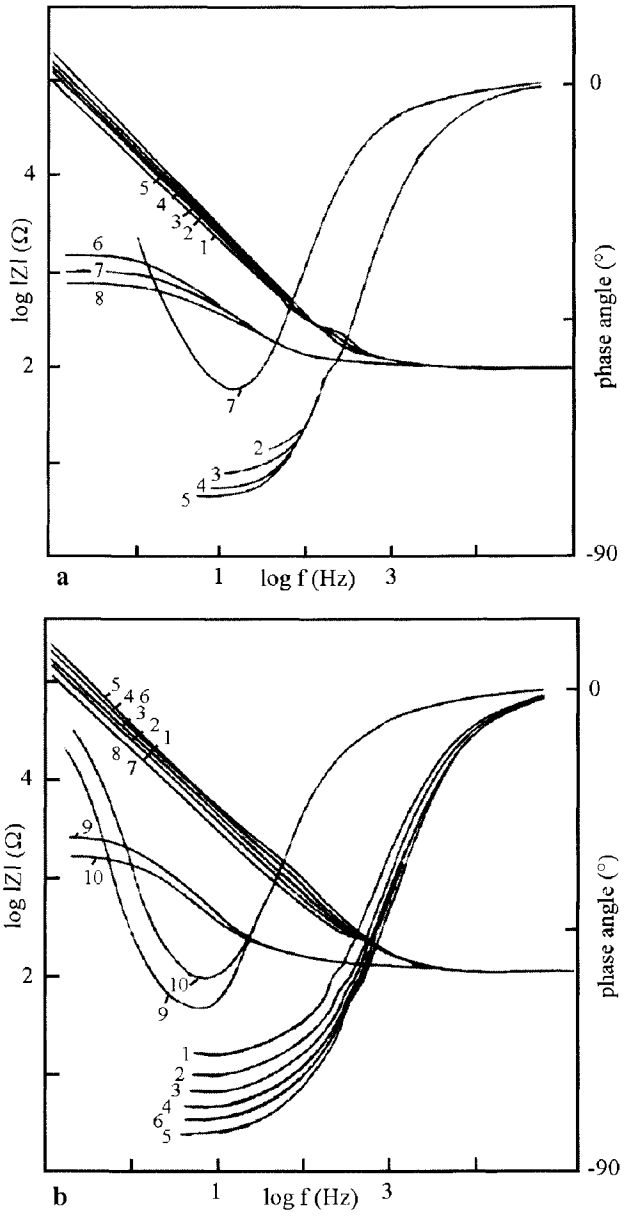

Figure 21.10. Bode spectra with ^2H_2O, ω: 2000 rpm, (a): pH 4.5, 1: −0.2 V, 2: −0.17 V, 3: −0.15 V, 4: −0.12 V, 5: −0.1 V, 6: 1.425 V, 7: 1.3 V, 8: 1.325 V/SCE, (b): pH 7.5, 1: −0.22 V, 2: −0.2 V, 3: −0.17 V, 4: −0.15 V, 5: −0.12 V, 6: −0.1 V, 7: −0.07 V, 8: −0.05, 9: 1.3 V, 10: 1.325 V/SCE, (c): pH 12, 1: −0.37 V, 2: −0.35 V, 3: −0.32 V, 4: −0.3 V, 5: −0.27 V, 6: −0.25 V, 7: −0.22 V, 8: 0.6 V, 9: 0.65 V/SCE.

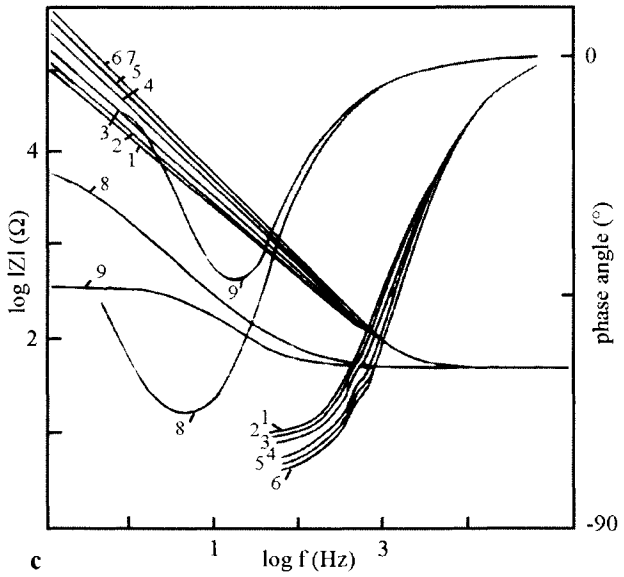

Figure 21.10. (Continued).

Table 21.6. Thickness and donor density dependence on H_2O and ^2H_2O

	Acid pH		pH near neutrality		Alkaline pH	
	H_2O	^2H_2O	H_2O	^2H_2O	H_2O	^2H_2O
d (nm)	19	24	21	28	42	52
$n_d \times 10^{19}$	6	2	3	1	0.5	0.3

^2H_2O or H_2O (Tables 21.4 and 21.5). In these tables, the variation of C_{ox} indicates that the oxide layer formation obeys a law depending on the passive potentials as indicated by Schmuki and Böhni [237]; they are given at different pH values and are different for deuterium oxide and for light water. The lower oxide value denotes the perfect passive layer. The Bode plots (Figs 21.9 and 21.10) enable us to calculate the flatband potential and donor concentration.

The donor density is lower with ^2H_2O for the different pH values (Table 21.6). The carrier concentration obtained with H_2O, agrees with the theoretical value for a passive layer given by Castro and Vilche [108], Simoes et al. [109] and Oriani et al. [110]. The flat-band extrapolated potential depends on pH and ^2H_2O or H_2O (Fig. 21.11). The oxide layer is thicker with ^2H_2O and alkaline pH (Table 21.6). These values indicate less electron transfer and higher corrosion resistance. The passive oxide layer formed is more insulating for ^2H_2O and alkaline pH. These reflect the formation of a highly ordered and less defective oxide layer.

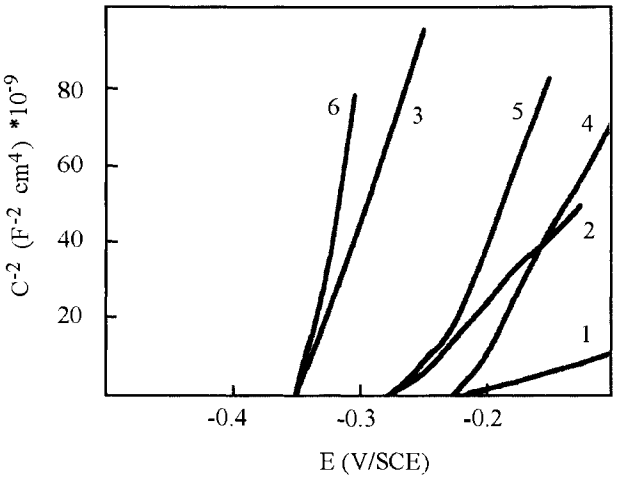

Figure 21.11. Mott-Schottky plots for passive oxide layer, 1: H_2O at pH 4, 2: H_2O at pH 8, 3: H_2O at pH 12.5, 4: ^2H_2O at pH 4.5, 5: ^2H_2O at pH 7.5, 6: ^2H_2O at pH 12.

In the passive-transpassive region, the Bode plots (Figs 21.9 and 21.10) show a horizontal line at low frequencies (1 to 0.1 Hz) which corresponds to the charge transfer resistance indicating that 316Ti steel becomes predominantly more resistive over a broad frequency range while the capacitive part is predominant only at higher frequencies. The value of the charge transfer resistance decreases when the passive potentials shift towards the transpassive region. The oxide layer thus formed on 316Ti steel approaches less ideal capacitor behavior and would then be less stable. These reflect the formation of a more defective oxide layer, breakdowns and oxide dissolution at these potentials.

2.1.3.2. Equivalent circuits and value determinations It seems that at potentials in the passive region (mainly purely capacitive impedance), spectra give a perfect fit with the experimental data if the total impedance is modeled according to the equivalent circuit in Fig. 21.12a.

In fitting spectra it is found that the charge transfer resistance is higher with ^2H_2O (4.4×10^2 kΩ cm^2). Also, consideration of this value shows that the deuterium oxide would favor passivating. In the passivity-transpassivity limit, the experimental diagrams obtained in Figs 21.9 and 21.10 can be explained by the equivalent circuit shown in Fig. 21.12b. In this case, the values of the charge transfer resistance decrease (200 Ω cm^2) when the potential increases, signifying more corrosion.

2.1.3.3. Discussion As indicated by Macdonald et al. [115] and Lorenz et al. [233], the vacancies are in equilibrium between $^2H_2O/H_2O$-oxide and oxide-alloy interfaces, and the passive oxide layer kinetics are governed by vacancy diffusion across the oxide layer.

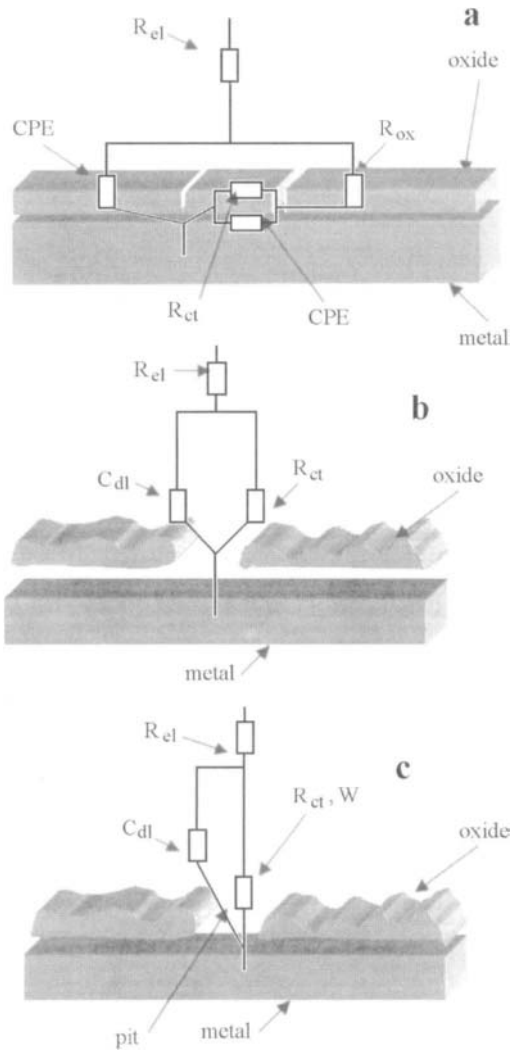

Figure 21.12. Equivalent circuits, (a, b, c): R_{el}: electrolyte resistance, R_{ox}: oxide resistance, R_{ct}: charge transfer resistance, CPE: constant phase elements, C_{dl}: double layer capacitance, W: diffusion impedance.

Based on these considerations, the reactions at oxide–^2H_2O interface are:

$$V_{O^{2-}} + {}^2H_2O \leftrightarrow 2\,{}^2H^+ + O^{2-} \tag{21.6}$$

$$\{\text{oxide}\} + n\,{}^2H_2O \leftrightarrow V_{Me^{n+}} + Me(O^2H)_n + n\,{}^2H^+ + ne^- \tag{21.7}$$

From the set of these equations, it is clear that the oxide potential drop is a function of deuterium oxide or light water taking into account the pH modification:

$$\partial \Delta E = \partial \Delta E_{\text{oxide–alloy}} + 2.3\alpha \frac{RT}{2F} \partial (\text{pH})_{\text{H}_2\text{O},\, {}^2\text{H}_2\text{O}} + \partial \Delta \Phi \tag{21.8}$$

where α is a constant and ΔE represents potential drop between the interfaces and within the oxide layer. It is expected that:

$$\partial \left(C_{\text{ox}}^{-1}\right) = \partial \Delta E + 2.3\alpha \frac{RT}{2F} \partial (\text{pH})_{\text{H}_2\text{O},\, {}^2\text{H}_2\text{O}} \tag{21.9}$$

The thickness variation is given by:

$$\partial d = b\left(\partial \Delta E + 2.3\alpha \frac{RT}{2F} \partial (\text{pH})_{\text{H}_2\text{O},\, {}^2\text{H}_2\text{O}}\right) \tag{21.10}$$

$$C_{\text{V}_{\text{O}^{2-}}} = \frac{M}{\rho} \exp\left[\left(\frac{\Delta G - 2F\Phi}{RT}\right) + 4.6\alpha (\text{pH})_{\text{H}_2\text{O},\, {}^2\text{H}_2\text{O}}\right] \tag{21.11}$$

where C is the vacancies concentration with a dependence on $V_{\text{Me}^{n+}}$ and $V_{\text{O}^{2-}}$ and pH variation, ΔG the standard Gibbs energy, b a constant resulting from considering the oxide layer as a plane capacitor. Thus eqs (21.8)–(21.11) represent the functional dependence of the passive layer growth law on $\partial \Delta E$ and ∂pH between H_2O and ${}^2\text{H}_2\text{O}$.

2.2. *Results obtained with deuterium oxide or light water and chloride*

The different experimental curves were drawn for the same previous pH, with H_2O or ${}^2\text{H}_2\text{O}$ and two Cl^- concentrations.

2.2.1. Polarization curves According to Strehblow [114] and Macdonald [116,117], the critical vacancy concentration leading to oxide breakdown in the presence of ${}^2\text{H}_2\text{O}$ can be expressed by:

$$\frac{\partial V_{\text{Me}^{n+}}}{\partial t} = J_0 \left[C_{\text{V}_{\text{O}^{2-}}} \{\text{oxide-}{}^2\text{H}_2\text{O}\}\right]^{-0.5n} \tag{21.12}$$

where J_0 depends on thermodynamic constants and $C_{\text{V}_{\text{O}^{2-}}} \{\text{oxide-}{}^2\text{H}_2\text{O}\}$ is the concentration of O^{2-} vacancies at the oxide layer–${}^2\text{H}_2\text{O}$ interface. Equation (21.12) shows that the metal vacancies diffusion is enhanced by decreasing the concentration of O^{2-} vacancies, e.g. with chloride present. This enhancement can effectively lead to an accumulation of metal vacancies at the alloy–oxide layer interface. From this equation, we can write the

simplified pitting equation with ^2H_2O present:

$$E_{pit} = \frac{4.6\alpha RT}{nF} \log\left(\frac{J_m}{J_0 \frac{M}{\rho} \exp\left\{\frac{pH}{RT}\right\}^{-0.5n}_{H_2O,\,^2H_2O}}\right) - \frac{2.3\alpha RT}{F} \log Cl^- \qquad (21.13)$$

where J_m is the rate of submergence of the metal vacancies in the alloy. It can be seen that low submergence rates and the pH modification by ^2H_2O and H_2O change pitting by Cl^-.

In the polarization curves, the difference between the pitting potential and corrosion potential, and between the repassive potential and corrosion potential, and the hysteresis shape enable us to determine the propensity for localized corrosion (e.g. pitting and crevice corrosion). If the current in the backward scan is greater than that of the forward portion of the scan, the 316Ti steel is predicted to be susceptible to corrosion by pitting, and if also the repassive potentials and pitting potentials are close to the corrosion potential, the steel is predicted to be susceptible to both crevice corrosion and pitting.

In the first measurements, the effects of chloride at acid pH on pitting potentials are observed in the polarization curves in Fig. 21.1. It can be seen that the corrosion potential is the same with or without Cl^-. The passive currents for ^2H_2O are lower than those obtained with H_2O, and in both cases, the respective currents are higher than that obtained without Cl^-. In the passive region, the anodic peak obtained at 0.15 V/SCE corresponds to the formation of titanium oxide identified by voltammetry in comparison with pure Ti. The critical pitting potential in transpassivity is not well defined and the passive region is the same indicating that pitting is unlikely to occur. At potentials above the pitting potential, pits are expected to grow. In the backward scans, it is seen that the anodic current increases with chloride concentration and is higher with ^2H_2O than it is with H_2O, and returns to $\geqslant 200$ mV above the corrosion potential for ^2H_2O. According to the hysteresis shape, pits continue to initiate and grow after the scan reversal. These behaviors, decreasing intervals between E_{corr} and $E_{repassivation}$, suggest pitting followed by crevice corrosion with deuterium oxide.

The polarization curves obtained at more neutral pH values are shown in Fig. 21.2. As shown above, the passive currents for ^2H_2O are lower than those obtained with H_2O, and in both cases, the respective currents are higher than that obtained without Cl^-. The corrosion potential shifts towards more positive values on increasing the Cl^- concentration. With ^2H_2O, the passive potential domain decreases as the pitting potential shifts towards lower values. As shown by the positive hysteresis shape in the backward scan, with ^2H_2O, the repassive potential decreases more rapidly than that of H_2O when Cl^- concentration increases, which makes it easy for crevice corrosion to occur. These different results imply that deuterium oxide does not provide better protection under these conditions, and the number of pits or the locally corroded area must increase. Metallographic examination (Fig. 21.13) shows rod-shaped ferrite and cubic and pyramidal crystallites of titanium carbide coming from grain boundary decohesion.

Magnetic measurements of ferrite give a concentration of 0.8%. In this case, as carbon is present (0.06%), chromium, molybdenum and titanium-rich carbides precipitate depleting the ferrite and grain boundaries in these elements. Localized corrosion and microcracks

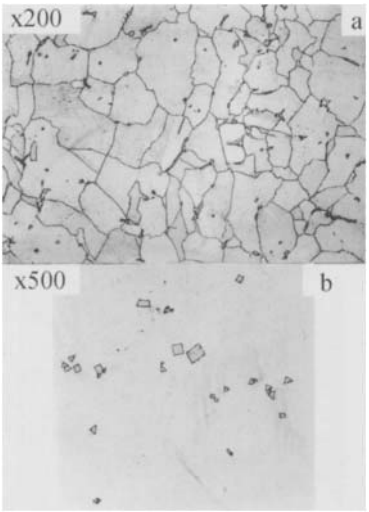

Figure 21.13. Metallographic examination of 316Ti steel, (a): general aspect, (b): titanium carbide crystallites.

Table 21.7. Composition of deuterium oxide after corrosion of 316 Ti

Elements	Ni	Cr	Fe	Mo	Ti
Wt%	19.2	5.5	74.2	0.5	0.6

in the austenite/ferrite and titanium carbide borders of grain boundaries can arise. From scanning micrographs realized in the cross-section (Fig. 21.14), it is seen for 1.5 V/SCE that the 316Ti steel is highly corroded with localized corrosion: pitting, crevices and grain boundary decohesion leading to internal cavities expanding where ferrite is present. The corrosion is also shown by the yellow color of deuterium oxide and the purple-black precipitate (titanium hydroxide), whereas at 1 V/SCE no pitting is seen by Scanning Electron Microscopy. These two potentials correspond to, respectively, initiation and propagation of pits in the transpassive potentials (1.5 V/SCE), and without initiation (1 V/SCE), therefore pits cannot propagate or form. As titanium hydroxide precipitates at pH > 3, the ^2H_2O used was acidified to dissolve the metal cations before analyzing for Fe, Cr, Ni and Ti ions by Atomic Absorption Spectrometry. The analysis results are given in Table 21.7. In comparison with Table 21.1, these show essentially a weight loss for titanium, iron and nickel on the surface of 316Ti steel. Along the grain boundaries there is localized corrosion of ferrite and formation of titanium carbide by Cl^- and ^2H_2O.

The polarization curves obtained with chloride at alkaline pH are shown in Fig. 21.3. Two regions can be identified: the passive region and a sharply defined pitting region. The anodic current fluctuations obtained with deuterium oxide and the higher Cl^- concentration result from the occurrence of metastable pits (prepitting events) signifying breakdowns and repassivity alternatively in potentials close to pitting. 316Ti steel remains passivated

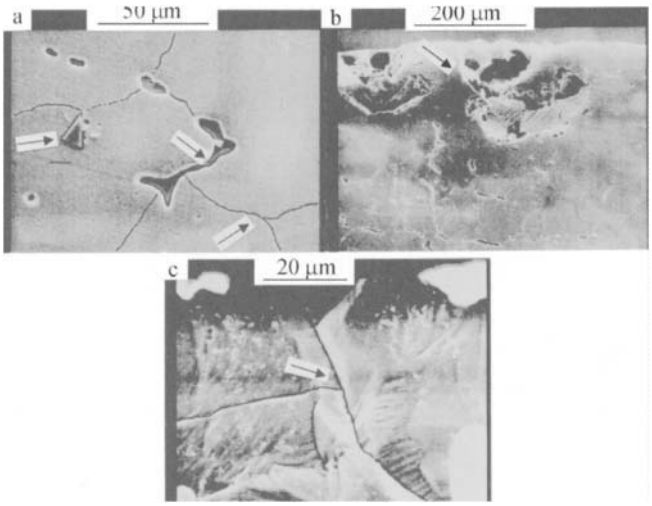

Figure 21.14. Scanning Electron Microscopy photographs of 316Ti steel corroded in presence of 0.02 mol dm^{-3} Cl^- in ^2H_2O at 1.5 V/SCE, (a): internal cavities coming from ferrite corrosion, and titanium carbide crystallite, (b): pits, (c): grain boundary decohesion (arrows).

over a large potential domain. The transition potential (E_{pit}) decreases very slightly with a chloride concentration increase. As suggested by the shape of the positive and negative hysteresis, a few pits continue to initiate and grow only in the beginning of the backward scan. This clearly defines a very small pitting potential region and shows that the passive oxide provides protection over a large potential domain. It can be seen that the corrosion potential increases with chloride, and the large deviation between E_{corr} and E_{pit} indicates no risk of crevice corrosion.

2.2.2. *Voltammetric curves* In Fig. 21.15, realized at acid pH, a decrease in the scan rate leads to decreasing the passive and transpassive currents and the anodic peak of titanium oxide in the forward scan. In the backward scan, a decrease in the scan rate increases the pitting currents (Fig. 21.15b). It can also be seen that the repassive potential is higher at a high scan rate. At a low scan rate, chloride ions have the time to adsorb, then diffuse in the oxide layer by ion vacancies leading to pitting following the kinetics. Using deuterium oxide, the repassivating potential is lower (Fig. 21.15d) than that of H_2O, signifying a greater possibility of crevice formation.

Fig. 21.16, realized at more neutral pH, shows that the pitting current in the backward scan is higher than that obtained at acid pH and with ^2H_2O. In these figures, the anodic current increases with the scan rate and Cl^- concentration. By plotting the cathodic peak current vs. scan rate, a straight line is obtained that fits the Levich equation. An experimental diffusion coefficient value of 5×10^{-5} cm^2 s^{-1} is then found and is close to the usual values found for aqueous media [103].

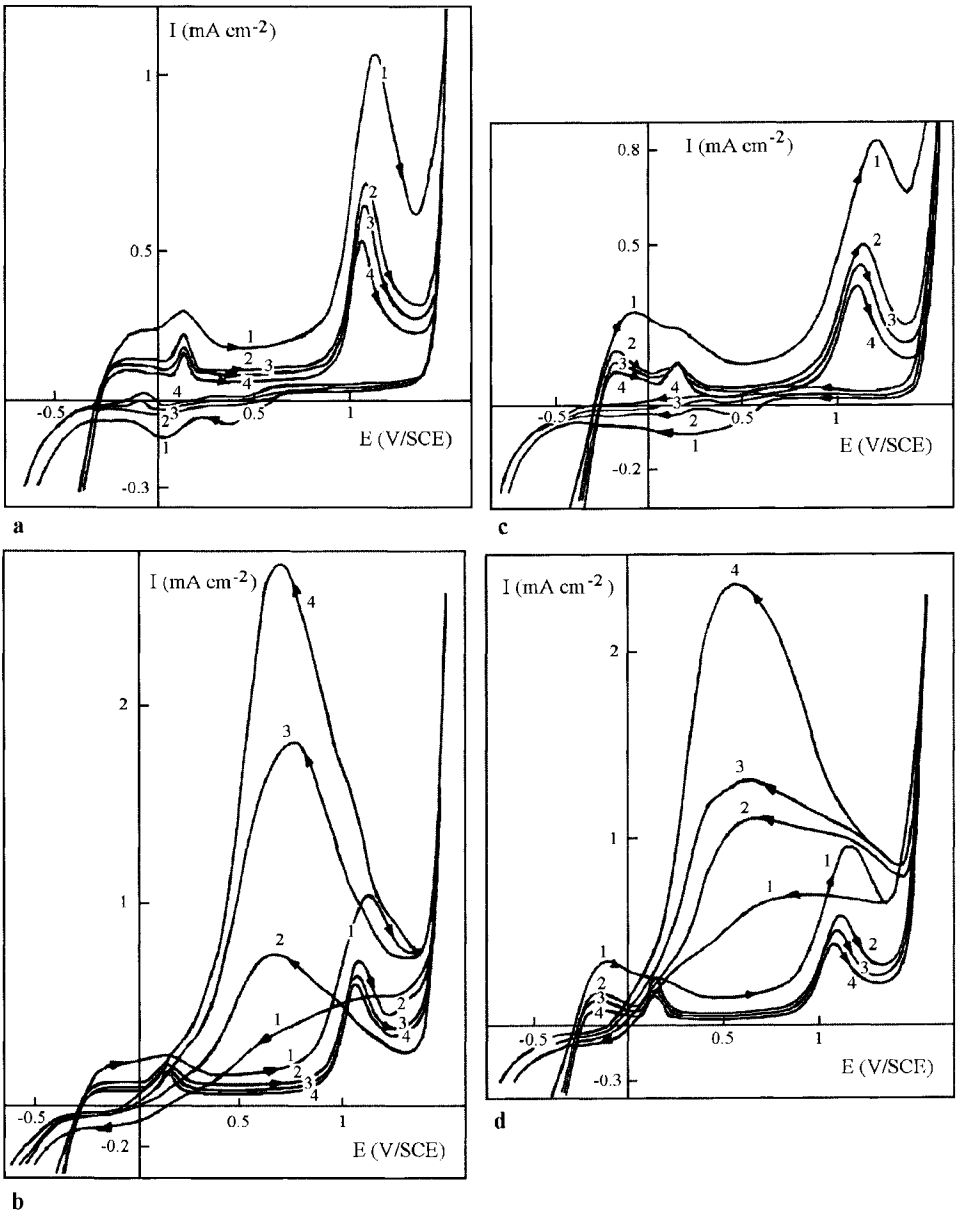

Figure 21.15. Voltammetric curves with Cl^- and ^2H_2O or H_2O at acid pH, ω: 2000 rpm, scan rates: 1: 100, 2: 50, 3: 40, 4: 30 mV s^{-1}, (a): with H_2O, 0.02 mol dm^{-3} Cl^-, (b): with H_2O, 0.05 mol dm^{-3} Cl^-, (c): with ^2H_2O, 0.02 mol dm^{-3} Cl^-, (d): with ^2H_2O, 0.05 mol dm^{-3} Cl^-.

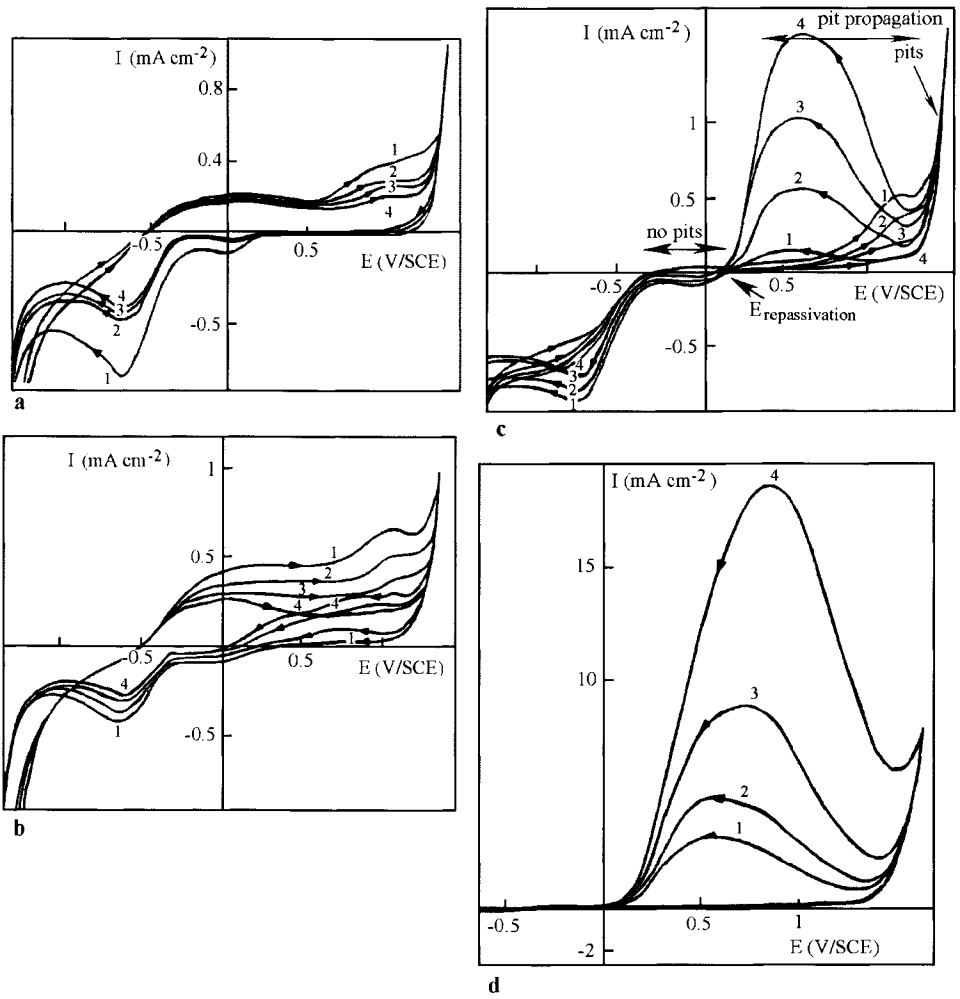

Figure 21.16. Voltammetric curves with Cl^- and ^2H_2O or H_2O at near neutral pH, ω: 2000 rpm, scan rates: 1: 100, 2: 50, 3: 40, 4: 30 $mV\,s^{-1}$, (a): with H_2O, 0.02 $mol\,dm^{-3}$ Cl^-, (b): with H_2O, 0.05 $mol\,dm^{-3}$ Cl^-, (c): with ^2H_2O, 0.02 $mol\,dm^{-3}$ Cl^-, (d): with ^2H_2O, 0.05 $mol\,dm^{-3}$ Cl^-.

Tests realized at alkaline pH (Fig. 21.17) do not show any pitting current on varying the scan rate. No current fluctuations are seen; the kinetics of oxide layer breakdowns are so slow that at these scan rates they are not observable. There is no pitting propagation: pits are easily repassivated.

The explanation of pitting behavior obtained by polarization and voltammetric curves is helped by using the diagrams in Fig. 21.18 that show several characteristic changes depending on pH in the potential-pH equilibrium diagram. At alkaline pH, perfect passivity

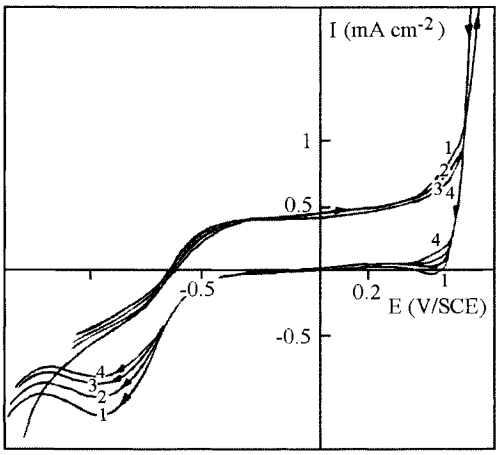

Figure 21.17. Voltammetric curves with Cl^- and ^2H_2O or H_2O at alkaline pH, ω: 2000 rpm, 0.02 or 0.05 mol dm^{-3} Cl^-, scan rates: 1: 100, 2: 50, 3: 40, 4: 30 mV s^{-1}.

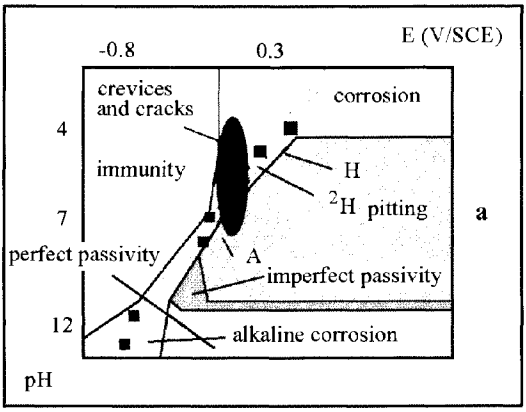

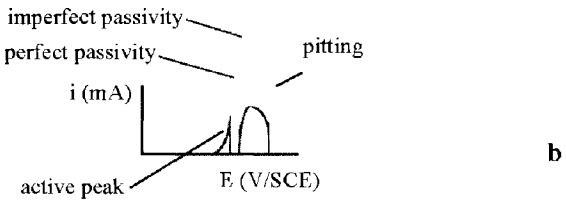

Figure 21.18. Diagram giving the behavior of 316Ti steel in water containing chloride, (a) polarization curves in solution at pH 3–12, (b) experimental circumstances of general corrosion and perfect, non-perfect passivity, crevice corrosion and pitting.

Table 21.8. Dependence of oxide capacitance ($\mu F\,cm^{-2}$) on passive potentials with Cl^- and H_2O

	E (V/SCE)	−0.35	−0.32	−0.3	−0.27	−0.25	−0.22	−0.2	−0.17	−0.15	−0.12
pH 4	0.02 mol dm^{-3} Cl^-							17	14	12	11
	0.05 mol dm^{-3} Cl^-							25	20	19	17
pH 8	0.02 mol dm^{-3} Cl^-			31	27	24	19	16	12	9	
	0.05 mol dm^{-3} Cl^-		42	32	29	25	21	18	14	11	8
pH 12.5	0.02 mol dm^{-3} Cl^-	8	6	5	4	3.7	3.5				
	0.05 mol dm^{-3} Cl^-	10	8	7	5	4.5					

Table 21.9. Dependence of oxide capacitance ($\mu F\,cm^{-2}$) on passive potentials with Cl^- and ^2H_2O

	E (V/SCE)	−0.37	−0.35	−0.32	−0.3	−0.27	−0.25	−0.22	−0.2	−0.17	−0.15	−0.1
pH 4.5	0.02 mol dm^{-3} Cl^-								13	11	8	7
	0.05 mol dm^{-3} Cl^-							17	15	13	10	8
pH 7.5	0.02 mol dm^{-3} Cl^-				27	23	17	14	10	9	7	
	0.05 mol dm^{-3} Cl^-			48	30	25	19	16	13	11	9	
pH 12	0.02 mol dm^{-3} Cl^-	9	6	5	4	3.2						
	0.05 mol dm^{-3} Cl^-	11	7	6	5	4						

for 316Ti steel is seen. At more neutral pH, there is imperfect passivity and pitting with H_2O at pH 8, whereas with ^2H_2O, 316Ti steel is more corroded by pitting and crevice corrosion at pH 7.5. At acid pH, the Cl^- concentration must be too low, and the polarization and voltammetric curves show a mixed behavior: passivity and corrosion with greater possibility of pitting for ^2H_2O as seen in the experimental curves for pH 4.5 and 4.

2.2.3. Impedance diagrams The experimental Bode plots obtained for 316Ti steel subjected to Cl^- in ^2H_2O and H_2O and drawn from about the corrosion potential are shown in Fig. 21.19 and those following.

The Bode plots are characterized as previously (subsection 2.1.3) by the same distinct regions. Data in Tables 21.8 and 21.9 indicate that oxide capacitance increases with Cl^-. The higher value (48 $\mu F\,cm^{-2}$) obtained at pH 7.5 with ^2H_2O and 0.05 mol dm^{-3} Cl^- corresponds to the double layer [103]. Comparison with Tables 21.4 and 21.5 shows that the passive oxide layer is less insulating, signifying adsorption and diffusion of Cl^- within the passive oxide. This interpretation can be verified by determining the charge donor density. The values obtained are between 0.3 and 6×10^{19} carrier cm^{-3} (Table 21.10). These values, which are higher than those without Cl^-, indicate, from eq. (21.12), that the O^{2-} vacancies decrease and Me^{n+} vacancies in equilibrium with metal increase with chloride, improving the diffusion. It thus appears that chloride ions adsorb and diffuse corresponding to the incubation period. Comparison of results shows that the flatband potential decreases with chloride which corresponds to the variation of oxide capacitance with respect to eq. (21.9). The oxide thickness is also determined, its value is lower than without Cl^-. In the tables for ^2H_2O, the oxide layer is more insulating in alkaline pH which corresponds closer to a perfect oxide.

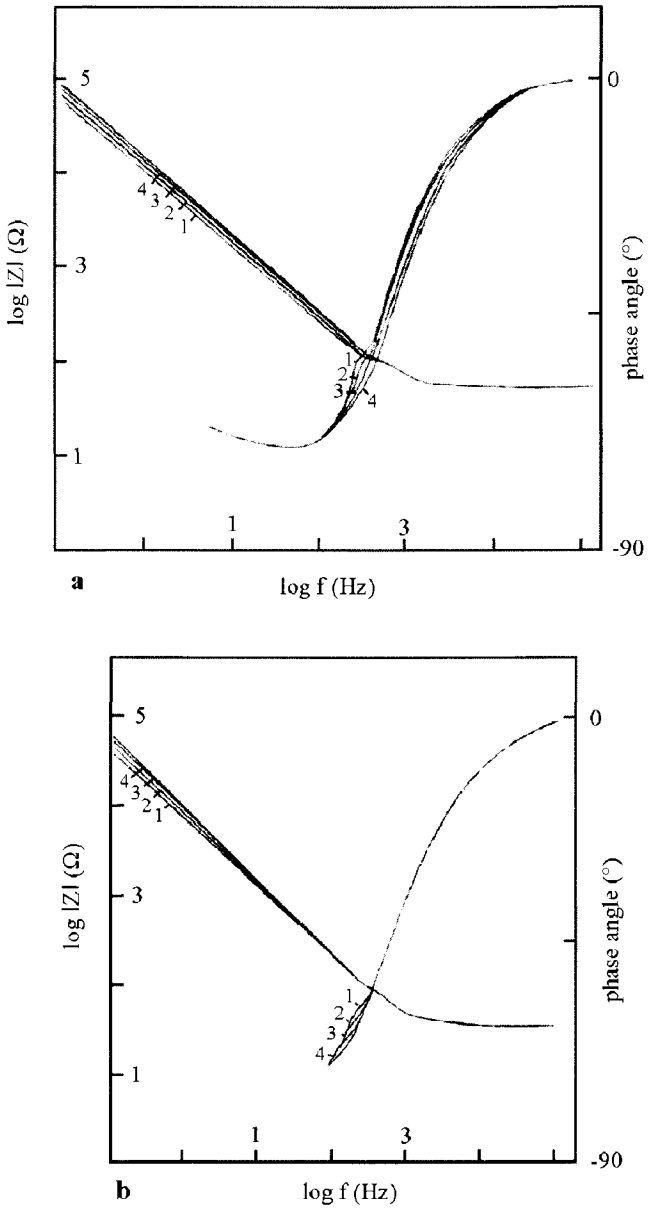

Figure 21.19. Bode spectra in passivity with ^2H_2O or H_2O at acid pH, ω: 2000 rpm, (a): with H_2O, 0.02 mol dm^{-3} Cl^-, 1: −0.2 V, 2: −0.17 V, 3: −0.15 V, 4: −0.12 V/SCE, (b): with H_2O, 0.05 mol dm^{-3} Cl^-, 1: −0.2 V, 2: −0.17 V, 3: −0.15 V, 4: −0.12 V/SCE, (c): with ^2H_2O, 0.02 mol dm^{-3} Cl^-, 1: −0.2 V, 2: −0.17 V, 3: −0.15 V, 4: −0.12 V, 5: −0.1 V/SCE, (d): with ^2H_2O, 0.05 mol dm^{-3} Cl^-, 1: −0.2 V, 2: −0.17 V, 3: −0.15 V, 4: −0.12 V/SCE.

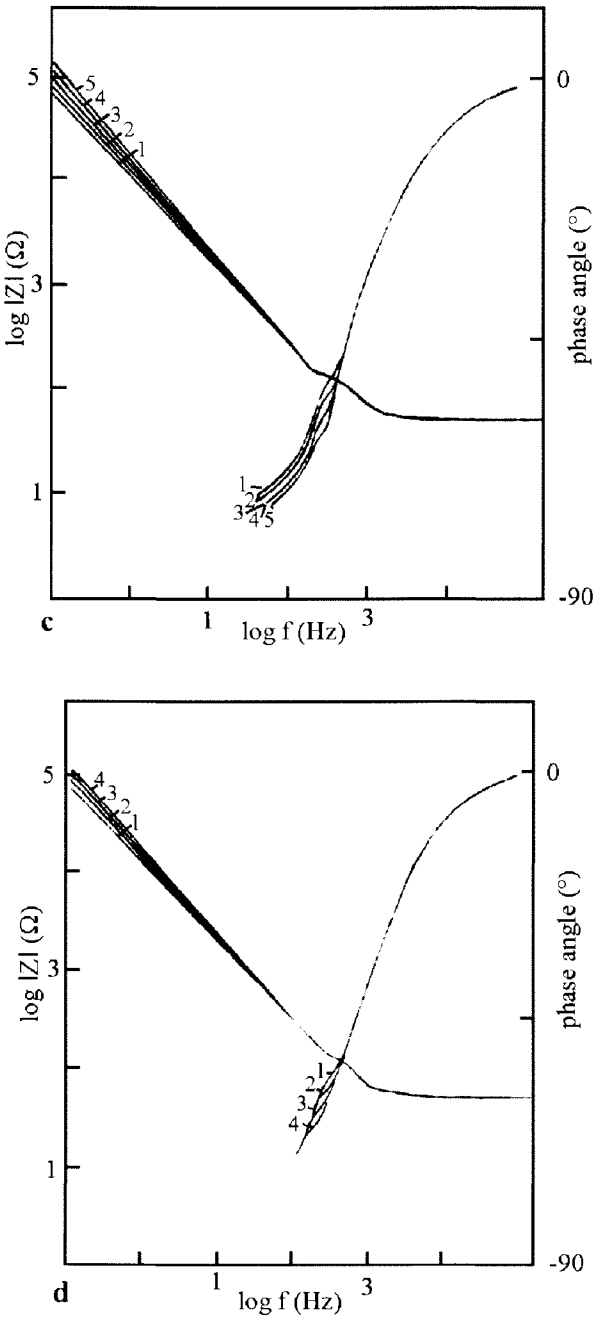

Figure 21.19. (Continued).

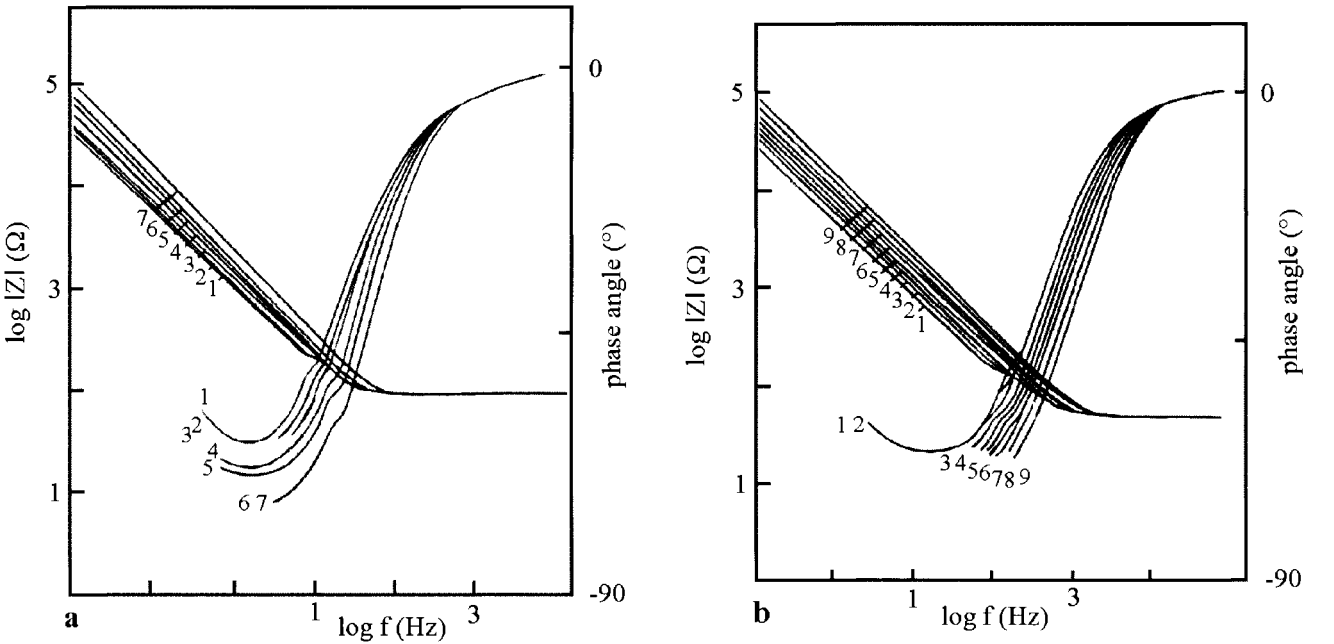

Figure 21.20. Bode spectra in passivity with ^2H_2O or H_2O at near neutral pH, ω: 2000 rpm, (a): with H_2O, 0.02 mol dm^{-3} Cl^-, 1: −0.3 V, 2: −0.27 V, 3: −0.25 V, 4: −0.22 V, 5: −0.2 V, 6: −0.17 V, 7: −0.15 V/SCE, (b): with H_2O, 0.05 mol dm^{-3} Cl^-, 1: −0.32 V, 2: −0.3 V, 3: −0.27 V, 4: −0.25 V, 5: −0.22 V, 6: −0.2 V, 7: −0.17 V, 8: −0.15 V, 9: −0.12 V/SCE, (c): with ^2H_2O, 0.02 mol dm^{-3} Cl^-, 1: −0.27 V, 2: −0.25 V, 3: −0.22 V, 4: −0.2 V, 5: −0.17 V, 6: −0.15 V, 7: −0.12 V, 8: −0.1 V/SCE, (d): with ^2H_2O, 0.05 mol dm^{-3} Cl^-, 1: −0.27 V, 2: −0.25 V, 3: −0.22 V, 4: −0.2 V, 5: −0.17 V, 6: −0.15 V/SCE.

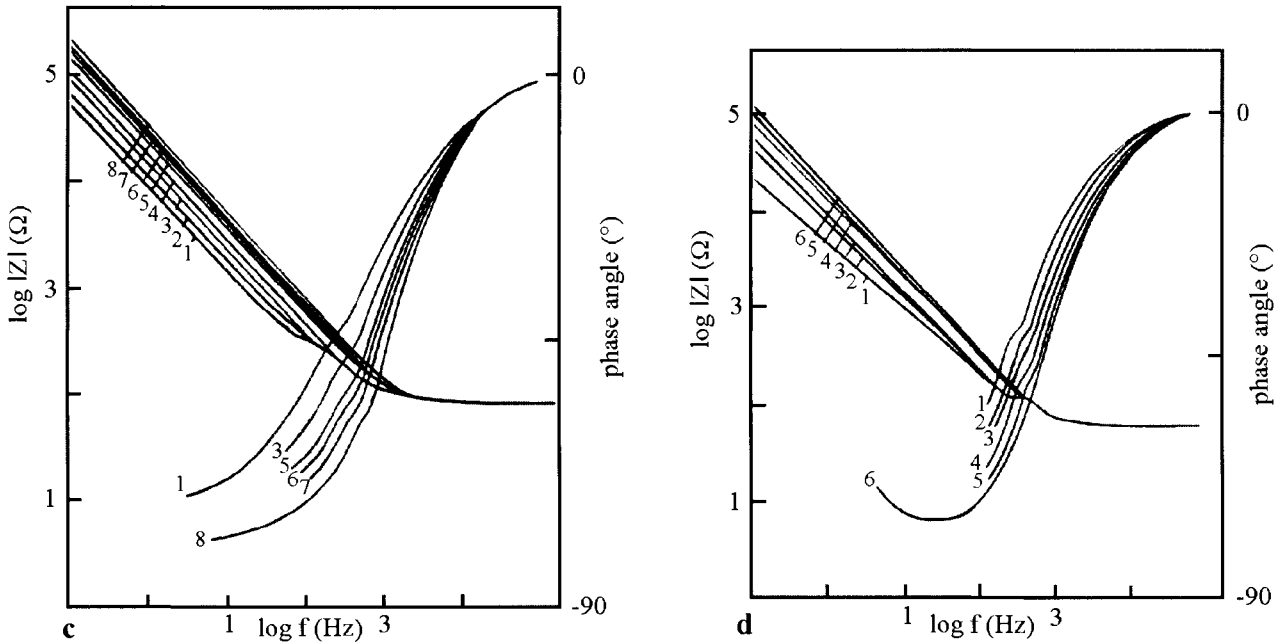

Figure 21.20. (Continued).

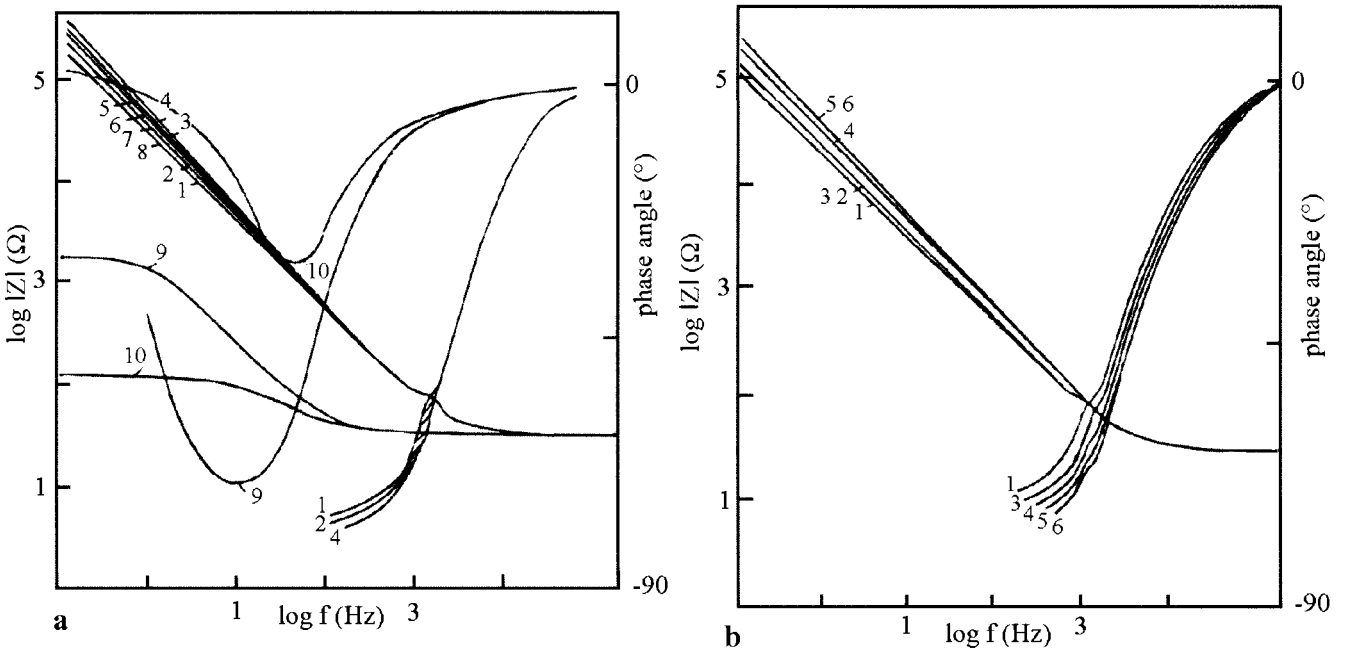

Figure 21.21. Bode spectra in passivity with ^2H_2O or H_2O at alkaline pH, ω: 2000 rpm, (a): with H_2O, 0.02 mol dm^{-3} Cl^-, 1: −0.3 V, 2: −0.27 V, 3: −0.25 V, 4: −0.22 V, 5: −0.2 V, 6: −0.17 V, 7: −0.15 V, 8: −0.12 V, 9: 0.6 V, 10: 0.675 V/SCE, (b): with H_2O, 0.05 mol dm^{-3} Cl^-, 1: −0.35 V, 2: −0.32 V, 3: −0.3 V, 4: −0.27 V, 5: −0.25 V, 6: −0.22 V/SCE, (c): with ^2H_2O, 0.02 mol dm^{-3} Cl^-, 1: −0.45 V, 2: −0.42 V, 3: −0.4 V, 4: −0.37 V, 5: −0.35 V, 6: −0.32 V, 7: −0.3 V, 8: −0.27 V/SCE, (d): with ^2H_2O, 0.05 mol dm^{-3} Cl^-, 1: −0.45 V, 2: −0.42 V, 3: −0.4 V, 4: −0.37 V, 5: −0.35 V, 6: −0.32 V/SCE.

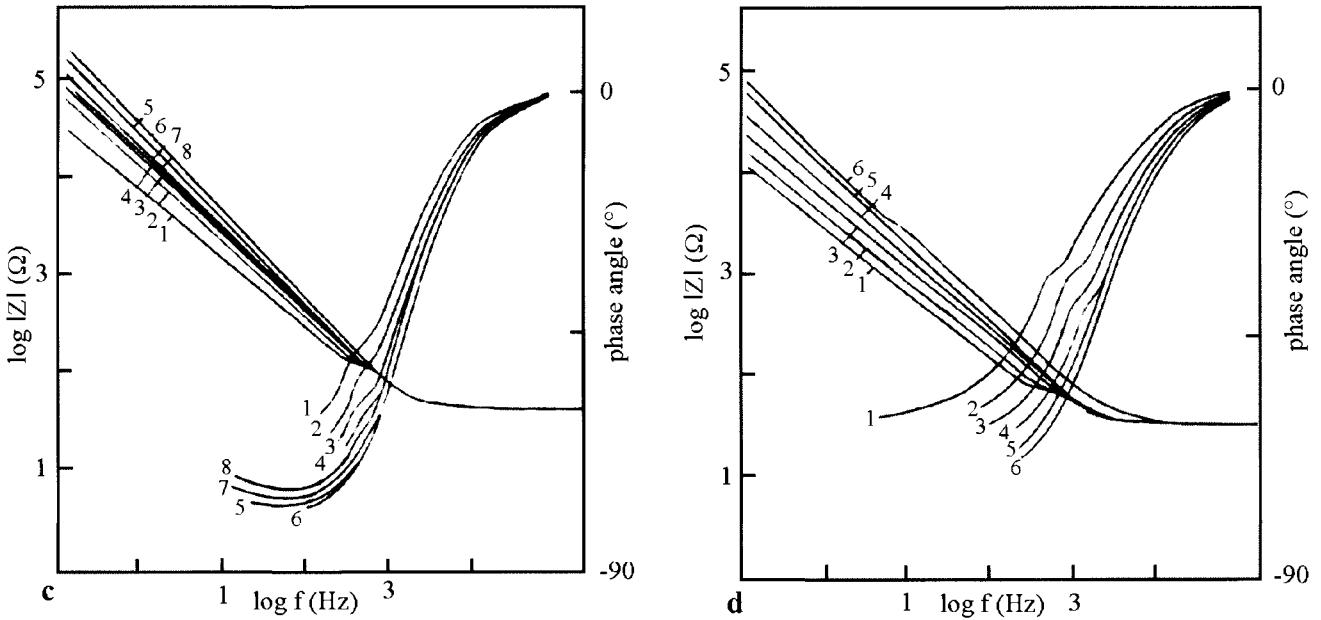

Figure 21.21. (Continued).

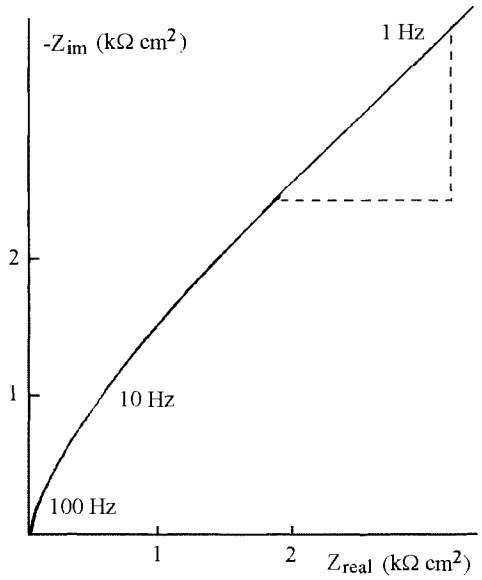

Figure 21.22. Nyquist diagrams with ^2H_2O and Cl^-, pH 7.5, ω: 2000 rpm, 0.05 mol dm^{-3} Cl^-, E: −0.35 V/SCE.

Table 21.10. Thickness and donor density dependence on H_2O and ^2H_2O containing Cl^-

	Acid pH				pH near neutrality				Alkaline pH			
	H_2O		^2H_2O		H_2O		^2H_2O		H_2O		^2H_2O	
Cl^- (mol dm^{-3})	0.02	0.05	0.02	0.05	0.02	0.05	0.02	0.05	0.02	0.05	0.02	0.05
d (nm)	11	7	17	13	18	11	25	13	27	11	48	27
$n_d \times 10^{19}$	7	13	2	6	3	7	2	5	0.7	3	0.3	1

The experimental Nyquist plots obtained for 316Ti steel subjected to chloride in ^2H_2O are shown in Fig. 21.22. Along the capacitive semi circle, a linear unit slope region is observed. This is a characteristic of diffusion impedance. Changes in Cl^- concentration affect the frequency shift in the straight line and capacitive semi circle suggesting mass transport is dependent on Cl^- concentration. The experimental diagrams can be satisfactorily explained on the basis of the equivalent circuit approach presented in Fig. 21.12c including a Randles diffusion impedance. The ion diffusion coefficient (D) through the prepassive oxide layer can be determined using the spectra in the Warburg region. For 0.02 and 0.05 mol dm^{-3} Cl^-, the diffusion coefficient was calculated to be 0.9 and 1.5 × 10^{-18} cm^2 s^{-1}. The ion diffusion coefficient increases slightly with Cl^- concentration and appears to be much lower inside the passive oxide layer than it does in deuterium oxide. These values indicate that the prepassive oxide layer is present at the corrosion potential.

3. Conclusions

Without chloride, deuterium oxide modifies the corrosion potential due to the positive or negative displacement in pH between ^2H_2O and H_2O. The pH modification contributes to changing the size of the activity, transpassivity and passivity of 316Ti steel. Values indicate the formation of a closer to perfect passive oxide and better protection with ^2H_2O.

With Cl^- and acid pH or near neutral pH and with ^2H_2O, the critical pitting potential is in transpassivity indicating that pitting is unlikely to occur for 316Ti steel. Crevice corrosion is produced after pitting and dissolution of ferrite/austenite along grain boundaries. These different results imply that deuterium oxide does not provide better protection with chloride. Nevertheless, the passive oxide layer is more insulating with ^2H_2O than it is with H_2O.

Chapter 22

EFFECTS OF TEMPERATURE

1. Introduction

If the tritiated water radioactivity is very high, e.g. 70 PBq dm^{-3}, the temperature of tritiated water is higher than the ambient due to the energy of β^- particles. Depending on temperature, the corrosion resistance is affected. To avoid corrosion, using very highly radioactive aqueous solutions, the equipment must be constructed completely of stainless steels or super-alloys. Since all the equipment in the nuclear facility is metallic, the selection of alloys depends not only on their corrosion resistance but also on their hardness: low and high hardness alloys are required. A low hardness component (e.g., Hastelloy C22) is assembled with a high hardness component to ensure that the joints are perfectly tight. The composition of Hastelloy C22 is given in Table 22.1. This is a nickel-based alloy that has the particularity that it contains cobalt. It should be noted that Hastelloy C22 is one of the most resistant alloys to localized corrosion [28].

2. Results and discussion

2.1. Anodic polarization curves

Fig. 22.1 shows the anodic and cathodic polarization curves obtained at a low scan rate to study the corrosion of Hastelloy C22 alloy at pH 3, over a temperature range of 20 to 70°C.

There is a slight shift of the corrosion potential, E_{corr}, towards the more positive potentials with increasing temperature. According to Jin Yun Zou and Der Tau Chin [186], plotting E_{corr} against T should give a straight line with a slope of:

$$\frac{\partial E_{corr}}{\partial T} = \frac{2.3R}{2.3F}\left[\log\frac{k_c}{k_a} + \nu \log {}^3H^+\right] \tag{22.1}$$

Table 22.1. Hastelloy C22 alloy—composition

Elements	Co	Cr	Fe	Ni	Mo	W
Wt%	2.5	22	3	bal.	13	3

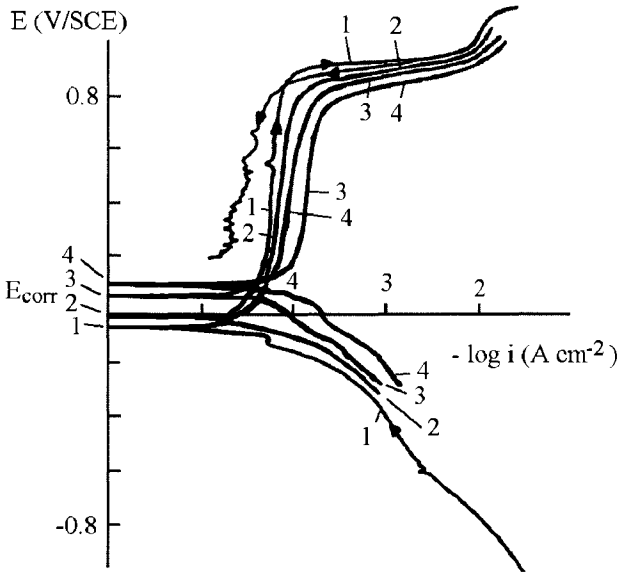

Figure 22.1. Polarization curves, v: 5 mV s^{-1}, ω: 3500 rpm, pH 3, 1: 20°C, 2: 30°C, 3: 50°C, 4: 70°C.

Table 22.2. Dependence of E_{corr} on temperature

T (°C)	20	30	50	70
E_{corr} (V/SCE)	−0.075	−0.05	0.04	0.1

The experimental value found from Table 22.2 is 2 mV/°K, which gives $k_a[^3H^+]^v k_c = 1.5$. This value indicates that the corrosion potential increases with temperature.

The corrosion current is given by:

$$i_{corr} = 1.26 k_a^{0.33} k_c^{0.66} F[A^+]^{0.66} \tag{22.2}$$

where A^+ represents species positively charged and intervening at the surface of electrode. From this equation, it appears that the corrosion current changes with the kinetics depending on temperature. The average experimental value is 0.25 μA cm^{-2}, and these values increase slightly with temperature. As shown in Fig. 22.1, increasing the temperature leads to a shift of the transpassive region towards less positive potentials. The shifts of corrosion potential and the transpassive region lead to a reduction of the passive region, as reported by Duquette et al. [278]. The current instabilities during the backward scan in the passive region increase with lower passive potentials. These instabilities result from the fact that breakdowns of the passive oxide layer occur all throughout this scan. In the transpassive peak, the reverse scan current is higher than those in the forward scan for the same potential (curve 1). This behavior is due to oxide dissolution through breakdowns of the passive layer.

2.2. Voltammetric curves

To elucidate the effect of temperature, it is worth observing the difference between polarization and voltammetric curves. A standard procedure was adopted in acquiring the cyclic voltammograms to obtain good reproducibility of the data. The potentials were swept cyclically from tritium to oxygen formation at a high scan rate until reproducible voltammograms were obtained. Fig. 22.2 shows the curves at pH 3, over a 20 to 80°C temperature range with Hastelloy alloy. A large prepassive peak is observed in this figure.

This, which is set at 0.1 V/SCE for 20°C, systematically increases with temperature. A negative shift of the peak potential as a function of the increase in temperature is observed, and the displacement is the reverse of the corrosion potential. The displacement can be attributed to the uncompensated ohmic drop and the rapid kinetics of transient species formed in the active region. At higher temperatures, the higher peak observed in

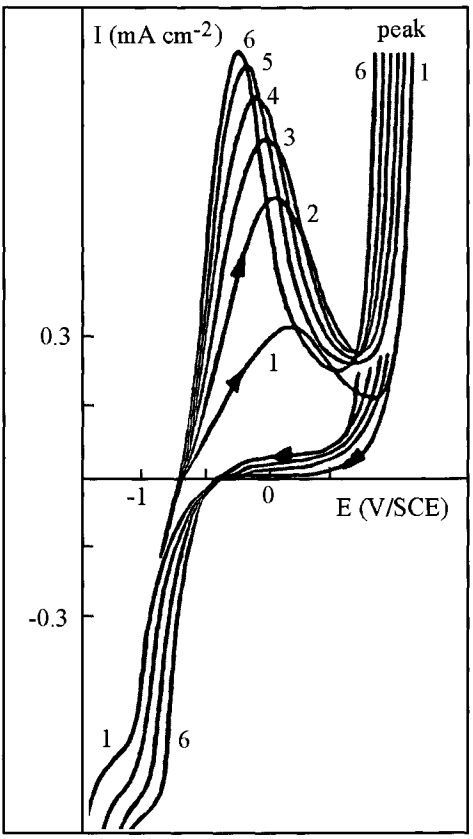

Figure 22.2. Voltammetric curves, v: 200 mV s^{-1}, ω: 2000 rpm, pH 3, 1: 20°C, 2: 30°C, 3: 40°C, 4: 60°C, 5: 70°C, 6: 80°C.

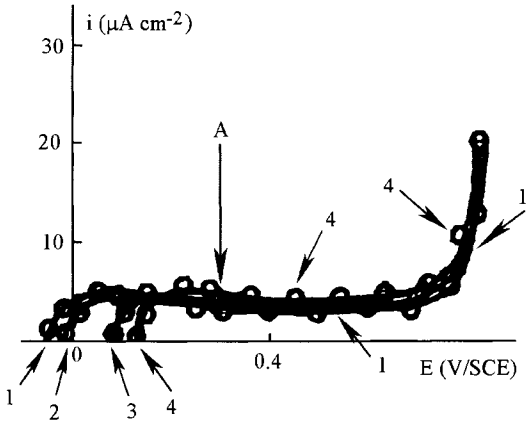

Figure 22.3. Potentiostatic mode polarization curves, ω: 3500 rpm, pH 3, 1: 20°C, 2: 30°C, 3: 50°C, 4: 70°C.

the prepassive region probably indicates a greater extent of related species growth. The present results indicate that Hastelloy alloy is corroded more quickly at higher temperatures for the prepassive peak. At this scan rate, the passive region is not actually seen. Scan rate and temperature have a large effect on the kinetics of the oxide layer growth before and during stabilization in the active-passive region, and certainly the nature of the formed oxide layer may be different at low and high temperatures or scan rates. This dependence reflects the effect of temperature on corrosion, as proposed by Jin You Zou and Der Tan Chim [186]. Beyond the short passive region, a considerable increase in current is observed, giving place to a high transpassive peak with adsorbed hydroxide or oxygen formation [157]. This peak increases with temperature. In the course of the backward scan, a reduction peak appears at -0.8 V/SCE during the gradual increase in tritium evolution current. This reduction peak is conjugated to the prepassive peak.

To facilitate the selection of the active potential in order to obtain more accuracy for the impedance diagrams at different temperatures, the polarization curves with potentiostatic mode were plotted (Fig. 22.3). At 0.3 V/SCE, it is seen that the slope $\partial i/\partial E$ takes a negative value (point A). This potential will be used to draw the impedance diagrams.

2.3. Impedance diagrams

The impedance diagrams were realized in the prepassivity, passivity and passivity-transpassivity limit. The potentials in prepassivity were selected with respect to the polarization curves drawn with the potentiostatic mode (Fig. 22.3), where the current decreases slightly after the active peak.

Moreover, a standard procedure was adopted in acquiring the impedance diagrams in passivity. The Hastelloy C22 was prepassivated at the temperature and measurement potential in steps upwards to higher passive potentials. After reaching stability, the impedance

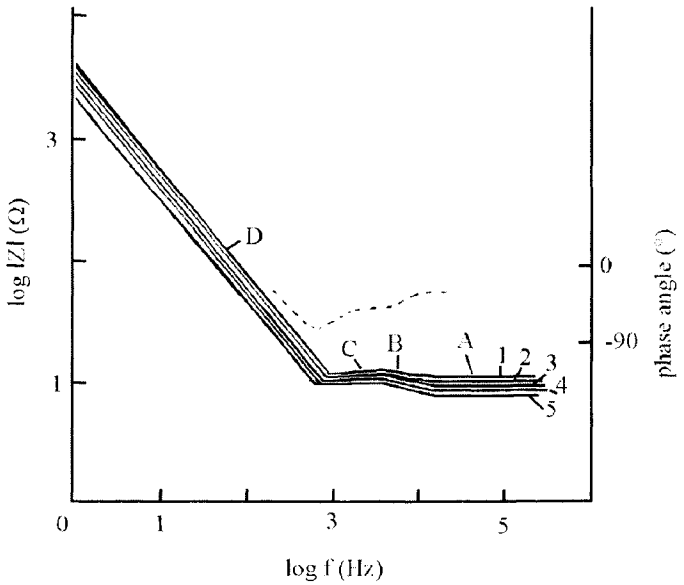

Figure 22.4. Bode diagrams in prepassivity, ω: 0 rpm, pH 3, E: 0.3 V/SCE, 1: 20°C, 2: 30°C, 3: 40°C, 4: 60°C, 5: 70°C, (—): phase angle.

measurements were carried out. In the passive-transpassive region, it was observed following the suggestions of Bessone et al. [233] that the stationary conditions were achieved much faster during change of the potential towards a negative direction. Thus, the impedance measurement sequence was: (1) to apply a given potential, for instance E, to achieve the corresponding stationary conditions, (2) to obtain its impedance spectrum until reaching good reproducibility, (3) to shift the potential and wait to ensure the new stationary condition, (4) to obtain the impedance spectrum at this new potential, and (5) to repeat the sequence from point 3 in the potential range.

Fig. 22.4 shows the Bode plots corresponding to the passive oxide layer formation at 0.3 V/SCE (point A in Fig. 22.3) for different temperatures. From the interpretation of Gebhardt [173], the impedance spectra can be analyzed as follows. Segment A is characterized by the electrolyte resistance at the highest frequencies. Segment B appears when the frequency decreases, and the electrical response is the impedance of the oxide marked by non-dissipative characteristics. The slope of segment B may be -1 and in our case the very small slope may be attributed to the superposition of the several impedances in the same range of frequencies. At lower frequencies, segment C appears and the slope is zero instead of -0.2 to -0.3; the impedance superposition may again play a role here. Segment D is characterized by a long straight line with a slope of about -1, and would appear to correspond here to a capacitive branch which tends towards infinite imaginary impedance in the Nyquist plot; a more compact oxide is formed. With respect to segment B, it is difficult to calculate the thickness of non-dissipative insulating oxide formed, as indicated by

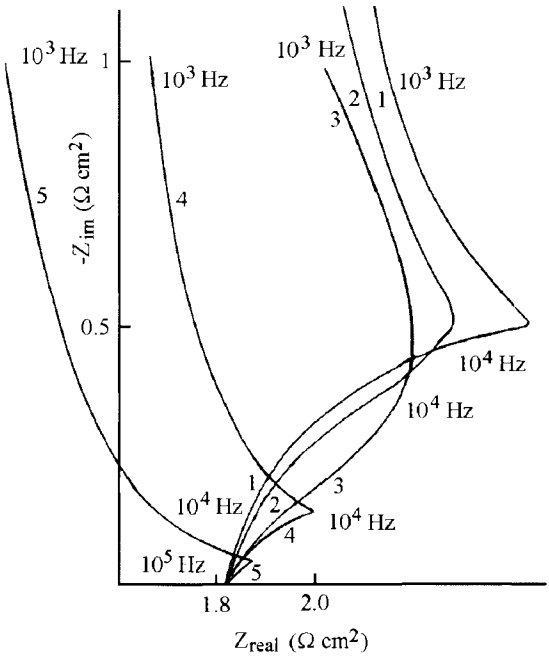

Figure 22.5. Nyquist diagrams in prepassivity, ω: 0 rpm, pH 3, E: 0.3 V/SCE, 1: 20°C, 2: 30°C, 3: 40°C, 4: 60°C, 5: 70°C.

Table 22.3. Dependence of thickness on temperature at 0.3 V/SCE

T (°C)	20	30	40	60	70
d (nm)	5	4	3	2	2

Gebhardt [173] and Castro and Vilche [108]. Therefore we have drawn the experimental Nyquist diagrams (Fig. 22.5) using a lower electrolyte resistance in decreasing the distance between electrodes.

These diagrams are formed of a capacitive semi circle at higher frequencies, followed by capacitive branches that tend towards infinity from the semi circle down to 0.01 Hz, meaning passivity. At higher frequencies, even at 10^4 Hz, the overlapped capacitive semi circle can be interpreted by the growth of the passive layer. With increasing temperature, the semi circles are much smaller, meaning a higher oxide layer growth and these are hidden by the capacitive branch, which is linked to segment B. As regards the semi circle top, we have calculated the oxide thickness (Table 22.3). Apparently this decreases with temperature.

On drawing the Bode diagrams between -0.5 V/SCE and 0.6 V/SCE, segment D is easily obtained as in Fig. 22.4. These diagrams enable us to calculate the donor concentration which is 4.9×10^{20} carrier cm^{-3}. The flat-band extrapolated potential is close to

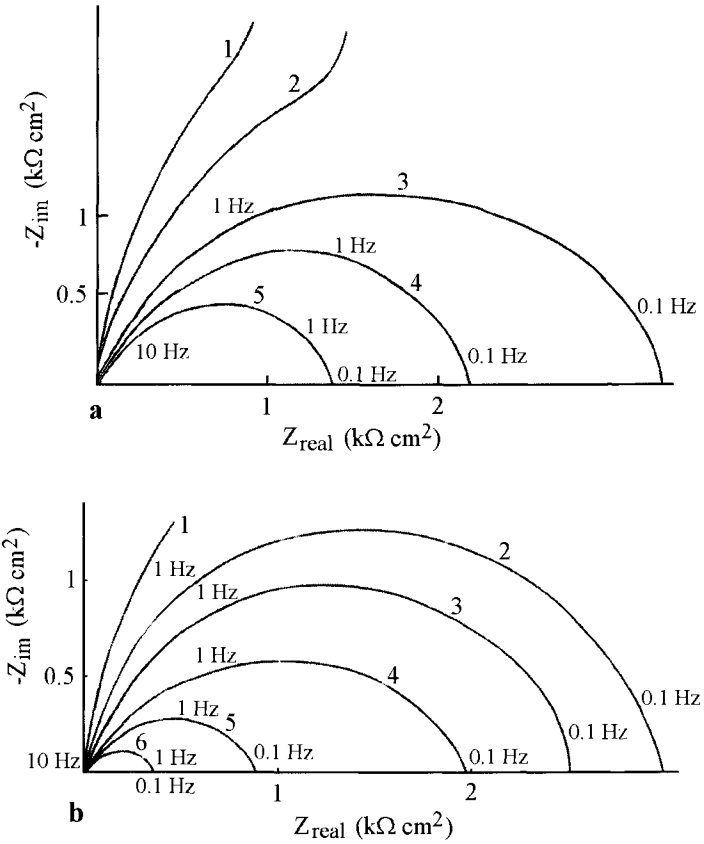

Figure 22.6. Nyquist diagrams in passivity—potential and temperature effects, ω: 0 rpm, pH 3, (a): 20°C, 1: 0.5 V, 2: 0.6 V, 3: 0.7 V, 4: 0.75 V, 5: 0.8 V/SCE, (b): 40°C, 1: 0.4 V, 2: 0.5 V, 3: 0.6 V, 4: 0.7 V, 5: 0.75 V, 6: 0.8 V/SCE, (c): 60°C, 1: 0.4 V, 2: 0.5 V, 3: 0.6 V, 4: 0.62 V, 5: 0.65 V, 6: 0.7 V, 7: 0.75 V, 8: 0.8 V/SCE, (d): 80°C, 1: 0.4 V, 2: 0.5 V, 3: 0.6 V, 4: 0.7 V, 5: 0.75 V, 6: 0.8 V/SCE.

−0.3 V/SCE. The carrier concentration is in agreement with the theoretical value for a passive layer given by Castro and Vilche [108], Simoes et al. [109] and Oriani et al. [110].

The Nyquist plots obtained at higher potentials than those of prepassivity and for different temperatures are shown in Fig. 22.6. These diagrams are completely different from those obtained for the prepassivity and they are formed only of a capacitive semi circle. It is observed that the size of the capacitive semi circle decreases when the potentials or temperature increase, signifying more corrosion.

The impedance diagrams obtained at the passivity-transpassivity limit potentials are shown for different temperatures in Fig. 22.7. The Nyquist response is well represented by a capacitive semi circle and inductive loop which corresponds to adsorption phenomena leading to a secondary passivity in the transpassive peak region, as indicated by Maga-

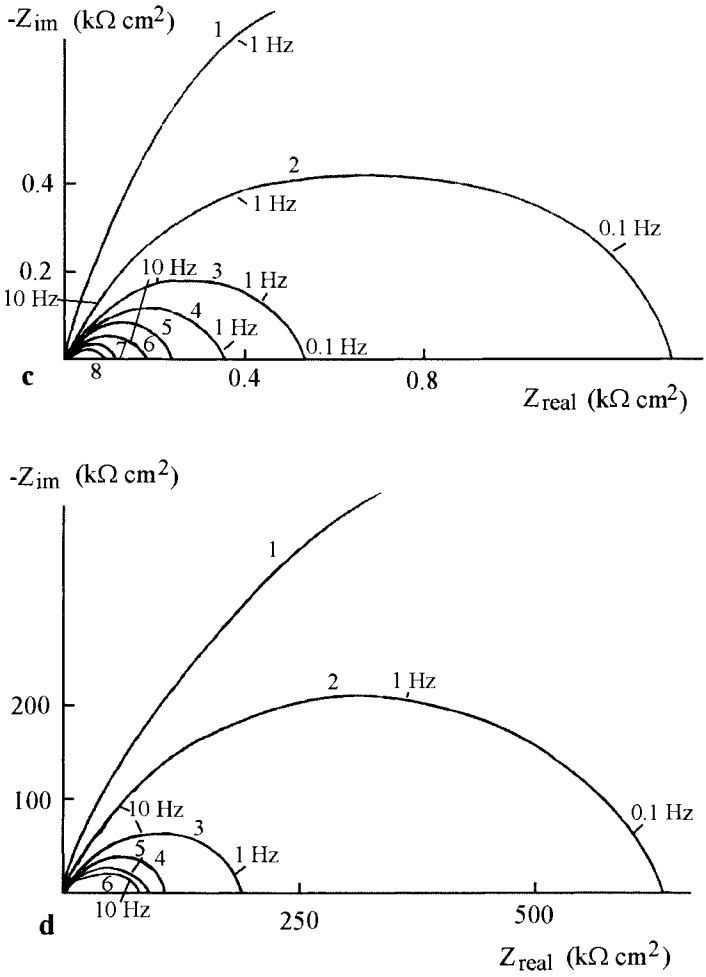

Figure 22.6. (Continued).

ino et al. [279], Epelboin and Keddam [280], Feller et al. [281], Jouanneau and Keddam [213] and Gebhardt [173]. The interpretation of the capacitive semi circle with the center slightly below the real axis could be that the oxide dissolution through its breakdown is limited by the adsorption. As the temperature increases, the size of semi circle decreases; this is the result of corrosion. Moreover, the small size of the semi circle indicates that Hastelloy alloy is easily corroded at the passivity-transpassivity limit potential and this is also shown by the pink color of electrolyte signifying the presence of cobalt ions. Therefore, the tritiated water used was analyzed for Fe, Cr, Ni and Co ions by Atomic Absorption Spectrometry. The electrolyte analysis results are given in Table 22.4. In comparison with

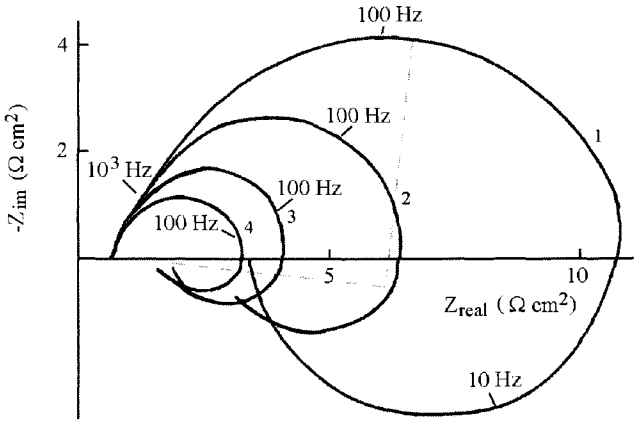

Figure 22.7. Nyquist diagrams in passivity-transpassivity limit, pH 3, E: 0.9 V/SCE, 1: 20°C, 2: 30°C, 3: 40°C, 4: 60°C.

Table 22.4. Composition of electrolyte after corrosion of Hastelloy

Elements	Co	Cr	Fe	Ni	Mo
Wt%	23	12	3	56	6

Table 22.1, these show a selective corrosion of cobalt and an enrichment of chromium and molybdenum on the surface of Hastelloy.

From Pound and Becker's results [282] using the Surface Analysis by Laser Ionization technique for a nickel base super-alloy containing cobalt, the oxide layer is basically $(Ni_{0.3}Co_{0.02}Cr_{0.5}Mo_{0.16}Fe_{0.02})_x O_y^{2-}$. The oxide layer formed is characterized by a higher chromium content due to the marked segregation of this element to the oxide layer which appears to be a general phenomenon for passive oxide layers. This enrichment was accompanied by a depletion in nickel, and it was found that the Mo content of the passive layer is slightly enriched. From Pound and Becker's studies [282], Mo was midway through the oxide layer but not on the surface or in the near surface layer. The combination of a higher Cr and slightly higher Mo concentration in the oxide on nickel base super-alloy containing Co would be expected to render this alloy extremely corrosion resistant, which was in fact observed experimentally in our laboratory. In the same way, the studies of Olefjord [283] give a duplex structure of the passive layer with an outer layer of hydrated hydroxide and an inner layer of oxide. The inner layer, more resistant to corrosion, is at least two-thirds of the total oxide with an appropriate localization of alloying elements in a spinel lattice.

3. Discussion, equivalent circuits and value determination

The experimental impedance diagrams obtained in the active, passive and transpassive regions and for different temperatures are complex and show that the equivalent circuits to be analyzed are evolutive. Before giving the equivalent circuit for the active region, the

Table 22.5. Effect of temperature in the prepassive region ($E = 0.3$ V/SCE)

T (°C)	20	30	40	60	70
C_{ox} (μF cm^{-2})	20	10.7	10.5	10.2	10
C_{dl} (μF cm^{-2})	40.5	40.5	50	50.2	50.5

experimental diagrams with the real and imaginary impedances, which tend towards the negative and infinite values, respectively, are interpreted below following the explanations given by Epelboin et al. [230] and Jouanneau and Keddam [213].

According to Epelboin, the faradaic impedance is dependent on:

$$1/Z_F = 1/R_{ct} + f'_E b/(j\omega - a) \tag{22.3}$$

where $f'_E = (\partial i/\partial E)_x$ is the ratio of the current to potential variations in the prepassive region; x a parameter depending on adsorbates (MeO^3H_{ads} and $Me(O^3H)_{2ads}$) that depend on temperature [284] and a is related to:

$$a = \tau_x^{-1} \tag{22.4}$$

In the previous equation, τ_x is the time constant related to the parameter x. In the same way as a does the term b depends on the active potential's time constant. From eq. (22.3), for a sufficiently high frequency with $\omega \gg \tau_x^{-1}$, the expression $f'_E b/(j\omega - a)$ tends to zero, therefore we have:

$$(1/Z_F)_{f\to\infty} = 1/R_{ct} \tag{22.5}$$

At lower frequencies, with $\omega \ll \tau_x^{-1}$, the current follows the variation of the parameter depending on adsorbates, and eq. (22.3) becomes:

$$(1/Z_F)_{f\to 0} = 1/R_{ct} - f'_E b/a = 1/R_p \tag{22.6}$$

where R_p is the polarization resistance. With respect to the curves in Fig. 22.3, point A gives a slight negative slope of $\partial i/\partial E$, compatible with the polarization resistance variation, which enables us to conclude that the term $f'_E b/a$ in eq. (22.3) tends to increase the impedance value towards infinity, and then to shift the spectrum towards the negative real part at lower frequencies, depending on the temperature. The shape of these impedance diagrams is characteristic of the active region and passivating process in accordance with Jouanneau and Keddam's results [213].

The diagrams obtained for the prepassive region (Figs 22.4 and 22.5) should be satisfactorily explained on the basis of the equivalent circuit presented in Fig. 22.8a. One of the aims of plotting the experimental diagrams is to find the values of the main electrical elements. The values obtained for these are given in Table 22.5; the double layer capacitance value is 25 μF cm^{-2} at the corrosion potential; this value is slightly higher (50 μF cm^{-2}) in the active region. These values of the double layer capacitance correspond to a normal value according to Bard and Faulkner [103]. From Table 22.5, the oxide capacitance value

is 10 $\mu F\,cm^{-2}$ and represents a characteristic oxide. The oxide and double layer capacitance values indicate the passivity of Hastelloy.

In the impedance diagrams realized at different temperatures, for 0.3 V/SCE and from the equivalent circuit results, the overlapped capacitive semi circle at the high frequencies, even at 10^4 Hz, is due to the growth of passive oxide. In addition to the capacitive semi circle, the part at lower frequencies that tends towards the negative real impedance, corresponds to the previous explanations given by Epelboin for the negative $\partial i/\partial E$ slope obtained at point A in Fig. 22.3. This corresponds to the double layer capacitance in parallel with a negative polarization resistance and Warburg impedance in the equivalent circuit. The passive oxide formation resistance values are small and decrease slightly when the temperature increases, signifying a slight enhancement of oxide formation.

In the Bode diagrams (Fig. 22.4), electrolyte and oxide formation resistances are 6 $\Omega\,cm^2$ and 1 $\Omega\,cm^2$, respectively. The accurate measurement of oxide thickness from the diagrams appears to be difficult, due to the low difference between the two resistances impeding the appearance of the phase angle and the second impedance slope of about -1 in region B (Fig. 22.4). It is nevertheless possible to calculate the value of oxide formation taking into account the value of the electrolyte resistance. On this basis, we have drawn the simulated diagrams (Fig. 22.9) with a lower value of R_{el} (1 $\Omega\,cm^2$). The diagrams show the phase angle and two very well defined slopes equal to -0.5 at lower frequencies and -1 at higher frequencies in which it is possible to measure the oxide capacitance and therefore determine the oxide thickness. This is about a few nm, and as in the previous results, the thickness of the passive oxide is lowest for higher temperatures.

In the case of passivity, the experimental diagrams in Fig. 22.6 can be explained by the equivalent circuit presented in Fig. 22.8b. In this circuit, the oxide resistance and capacitance can be neglected in comparison to values of charge transfer resistance (Tables 22.6–22.9). From this, it is observed that the charge transfer resistance decreases (Fig. 22.10) when the potentials or temperature increase, signifying more corrosion.

Taking the average value of 150 $\mu F\,cm^{-2}$ (corresponding to Fig. 22.6), the average rate constant is 10^{-2} $mol^{-1}\,cm^2\,s^{-1}$, and the number of active sites is 10^{-10} $mol\,cm^{-2}$ for a potential near the passivity, and 3×10^{-8} $mol\,cm^{-2}$ for a potential near the passivity-transpassivity limit. The rate constant value is low and shows that Hastelloy is slightly corroded at these potentials. The increase in the number of active sites at the passivity-transpassivity limit indicates that the passive oxide starts to break down.

The experimental diagrams (Fig. 22.7) obtained at the passivity-transpassivity limit and different temperatures can be explained satisfactorily on the basis of an equivalent circuit (Fig. 22.8c). The faradaic impedance implies the charge transfer resistance in series with an inductance, in parallel with localized corrosion resistance. From these, the faradaic impedance is given in eq. (22.7):

$$Z_F = R_{ct} + \frac{j\omega L R_{lc}}{R_{lc} + j\omega L} \tag{22.7}$$

From this equation, the faradaic impedance includes the localized corrosion resistance (R_{lc}) and the adsorption inductance. As the temperature increases, the charge transfer and

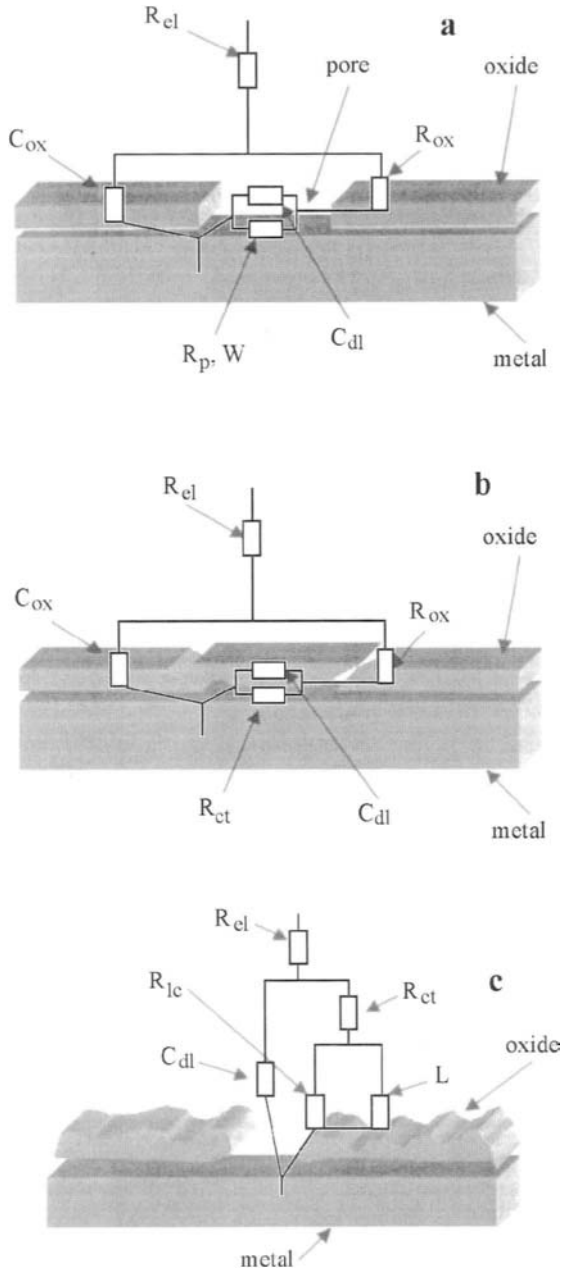

Figure 22.8. Equivalent circuit, (a, b, c): R_{el}: electrolyte resistance, R_{ox}: oxide resistance, R_p: polarization resistance, R_{ct}: charge transfer resistance, R_{lc}: localized corrosion resistance, C_{ox}: oxide capacitance, C_{dl}: double layer capacitance, W: diffusion impedance, L: adsorption inductance.

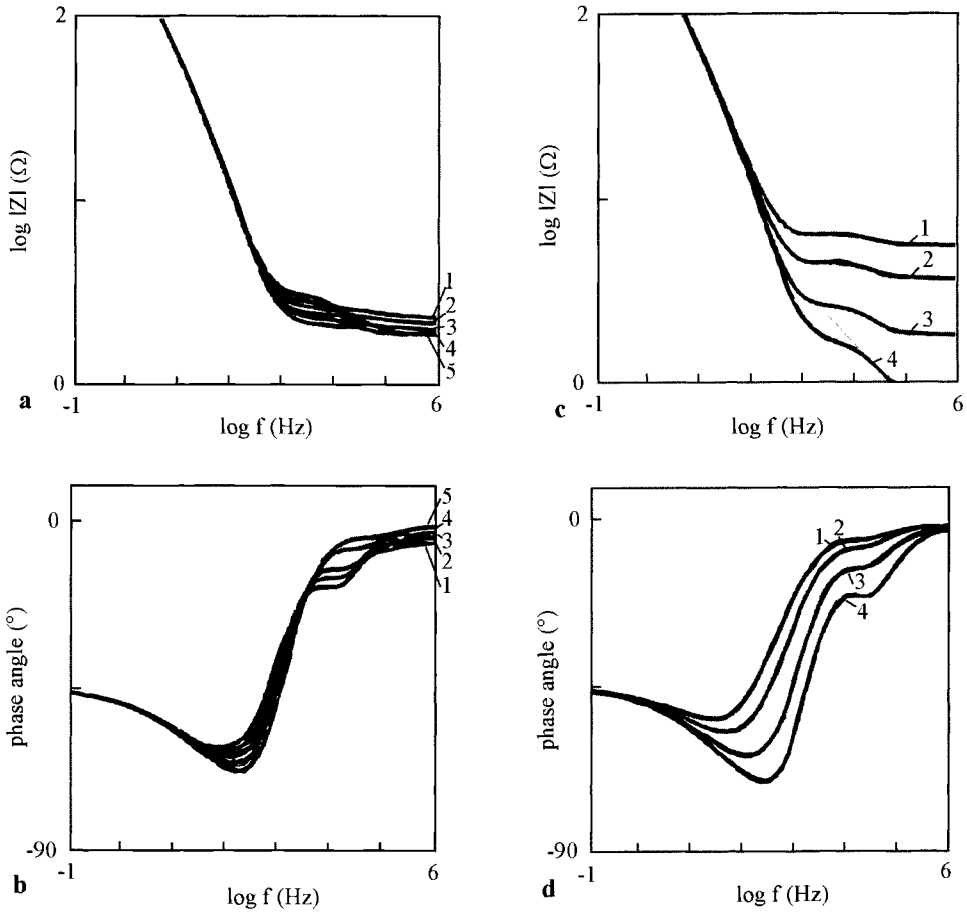

Figure 22.9. Simulated Bode spectra for comparison with Fig. 22.4, ω: 0 rpm, pH 3, E: 0.3 V/SCE, (a, b): R_{el}: 6 $\Omega\,cm^2$, 1: 20°C, 2: 30°C, 3: 40°C, 4: 60°C, 5: 70°C, (c, d): 20°C, 1: R_{el}: 6 $\Omega\,cm^2$, 2: R_{el}: 4 $\Omega\,cm^2$, 3: R_{el}: 2 $\Omega\,cm^2$, 4: R_{el}: 1 $\Omega\,cm^2$.

Table 22.6. Effect of temperature in the passive region and for different potentials. Temperature 20°C

E (V/SCE)	0.7	0.75	0.8
R_{ct} ($\Omega\,cm^2$)	2970	2100	1400

Table 22.7. Effect of temperature in the passive region and for different potentials. Temperature 40°C

E (V/SCE)	0.5	0.6	0.7	0.75	0.8
R_{ct} ($\Omega\,cm^2$)	2750	2450	1700	1050	400

Table 22.8. Effect of temperature in the passive region and for different potentials. Temperature 60°C

E (V/SCE)	0.6	0.62	0.65	0.7	0.75	0.8
R_{ct} (Ω cm^2)	550	420	400	180	100	90

Table 22.9. Effect of temperature in the passive region and for different potentials. Temperature 80°C

E (V/SCE)	0.4	0.5	0.6	0.7	0.75	0.8
R_{ct} (Ω cm^2)	1400	550	300	95	80	75

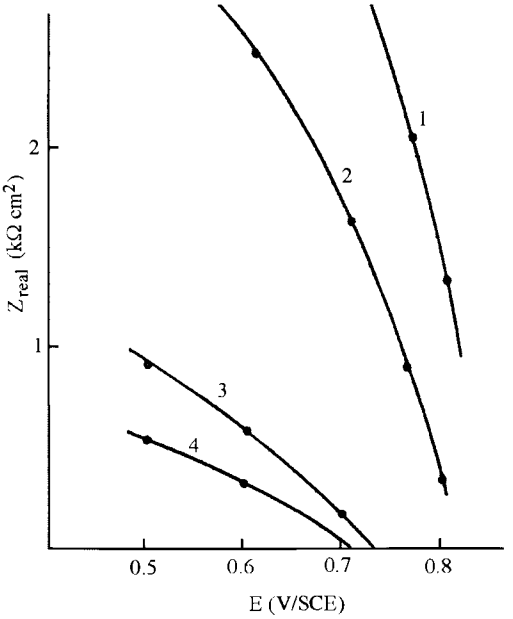

Figure 22.10. Charge transfer resistance as a function of passive potentials and temperature, 1: 20°C, 2: 40°C, 3: 60°C, 4: 80°C.

localized corrosion resistances decrease; this is the result of the oxidation current increasing. Taking the average value of 150 μF cm^{-2} (corresponding to Fig. 22.7), the average rate constant is 0.1 mol^{-1} cm^2 s^{-1} and the number of active sites is between 2 and 9×10^{-6} mol cm^{-2}. These increase with temperature and potentials.

4. Conclusions

Increasing the temperature leads to a reduction of the passive region and a higher current in the passivity. As shown by current instabilities during the backward scan and a higher current than those in the forward transpassivity scan, not all the oxide layer should be destroyed at the breakdown transpassive potentials. Apparently, the thickness of pas-

sive oxide decreases with temperature in the prepassive region. In passivity, the results show an enhancement of corrosion for higher potentials or temperatures. At the passivity-transpassivity limit potentials, it is found that corrosion increases with temperature.

This Page Intentionally Left Blank

Chapter 23

EMBRITTLEMENT OF PALLADIUM BY TRITIUM

1. Introduction

Palladium-silver alloy cathodic membranes are used in tritiated water processing for recycling tritium and its isotopes. During electrolysis, these adsorb on the cathodic surface, diffuse through the alloy and finally are desorbed on the side opposite to the cathodic entry surface. The diffusion is dependent on PdAg thickness, temperature and applied cathodic potential. The objective of this study is to ascertain the embrittlement of cathodic membranes of palladium and a Pd–25%Ag alloy.

2. Experimental results

2.1. Diffusion layer thickness analyzed by stripping voltammetry

To determine the electrochemical behavior of palladium and its alloy in tritiated water, voltammetric curves were plotted. The back-diffusion curves obtained after cathodic charging of palladium with tritium are shown in Fig. 23.1.

Curve 1 indicates values before $^3H_2$ charging, and curves 2 to 5 were obtained continuously after $^3H_2$ charging. An anodic peak is obtained at −0.5 V/SCE. It corresponds to the oxidation of the adsorbed back-diffused tritium. It is followed by a decreasing current showing that the oxidation of tritium continues to occur due to its back-diffusion. The back-diffusion velocity decreases with time measured from the application of the scans. Its current is superposed on the palladium oxidation current. In the cathodic scan, the oxidation of the tritium continues and a reduction peak appears at −0.4 V/SCE. This corresponds to the oxide reduction peak with superposition of the tritium oxidation current. In the curve, the integrated oxide reduction value is 0.7 mC cm^{-2}. This value represents a thickness of a few oxide atoms. The tritium oxidation current continues up to around the reduction potential of tritiated water. As indicated above, the current measured during the anodic scan is due to the superposition of the oxide formation current and that of the tritium oxidation which have the same sign, while in the cathodic scan, they have opposite signs. The oxide layer does not prevent the back-diffusion but slightly slows it down. The reactions at the surface during back-diffusion are:

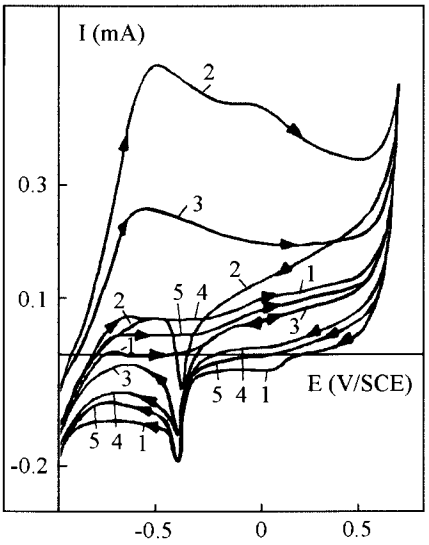

Figure 23.1. Voltammetry curves for Pd after the decomposition of $^3H_2O_2$ temperature: 70°C, electrolyte: pH 12, v: 160 mV s^{-1}, scan limits: −1 and 0.6 V/SCE, ^3H_2O: 1 mol/dm^3, time of $^3H_2$ charging (τ): 5 min at −1 V/SCE, curve 1 was obtained before $^3H_2$ charging, curves 2 to 5 indicate the cycles performed continuously after $^3H_2$ charging.

Anodic scan:

$$Pd + 2O^3H^- \rightarrow PdO + {}^3H_2O + 2e^- \tag{23.1}$$

$$Pd^3H_{ads} \rightarrow Pd + {}^3H^+ + e^- \tag{23.2}$$

Cathodic scan:

$$PdO + {}^3H_2O + 2e^- \rightarrow Pd + 2O^3H^- \tag{23.3}$$

$$Pd^3H_{ads} \rightarrow Pd + {}^3H^+ + e^- \tag{23.4}$$

In the alloy, the diffusion reactions are:

$$\begin{array}{c} {}^3H_2O + r + e^- \overset{k_1}{\longleftrightarrow} O^3H^- + {}^3H, s \overset{k_{-2}}{\longleftrightarrow} {}^3H_{abs} + r \quad \text{(bulk diffusion)} \\ \uparrow\downarrow \\ \text{released in tritiated water: } 1/2\,{}^3H_2 + r \end{array} \tag{23.5}$$

r denoting the adsorption site on the membrane and $_{abs}$ absorption. To suppress any uncertainties, the study of the diffusion parameters was carried out in the potential zone in the

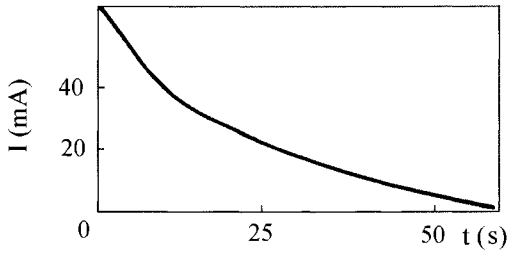

Figure 23.2. Variations of retrodiffusing $^3H_2$ oxidation current with time obtained by double-step potentiostatic method, E: −0.9 V/SCE, T: 70°C, charging time: 1 min.

absence of oxide and after decomposition of the major part of the radiolytic hydrogen peroxide. The retrodiffusion phenomenon was analyzed by the double-step potential method. The potential was first held at −1 V/SCE for 60 seconds (τ), and then stepped up to a value of −0.7 V/SCE. The variation of the current with the time t, measured from the application of the second step, is shown in Fig. 23.2.

The quantity of retrodiffusing tritium is 1.4×10^{-5} mol cm^{-2}. Using Kimmerle and Chevalet's equations [135], the expression for the current for the linear semi-infinite diffusion in palladium–silver is:

$$i = F\pi^{-0.5} D^{-0.5} C_t \tau^{-0.5} f(\theta) \tag{23.6}$$

where τ is the charging time, D the diffusion coefficient in cm^2 s^{-1}, C_t the tritium concentration near the surface of the membrane in mol cm^{-3}, and:

$$f(\theta) = \theta^{-1} - (1 + \theta^2)^{-0.5} \tag{23.7}$$

in which:

$$\theta = (t/\tau)^{0.5} \tag{23.8}$$

The curve $i = f(\theta)$ is linear (Fig. 23.3) and its slope yields for the product $D^{0.5} C_t$,

$$D^{0.5} C_t = 4 \times 10^{-6} \text{ mol cm}^{-2} \text{ s}^{-0.5} \tag{23.9}$$

The diffusion layer thickness, δ, can be estimated from the equation:

$$\delta = (\pi D \tau)^{0.5} \tag{23.10}$$

For a 5-min electrolysis time, δ is 300-μm.

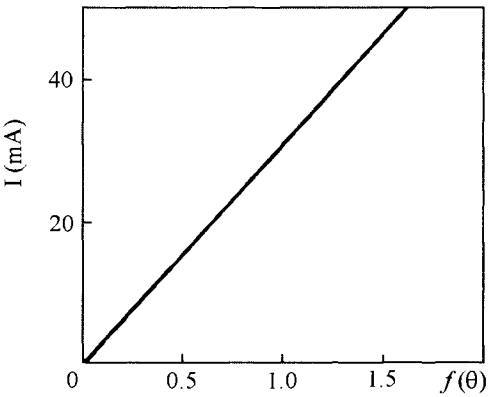

Figure 23.3. Curve $i = f(\theta)$ according to Cottrell's equations.

2.2. *Spectral analysis for determination of diffusion coefficient*

The diffusion phenomenon was quantitatively analyzed using electrochemical impedance spectroscopy. Fig. 23.4 shows the Nyquist and Bode plots obtained for different potentials during tritium charging with an insertion reaction on both faces of the 100 μm thick palladium–silver membrane.

Tritium charging on both faces leads to symmetry of the concentration and diffusion profile with respect to the membrane central axis (Fig. 23.5) as shown by Chen et al. [285] and Durand et al. [286]. The result is that the diffusion profile slope at this axis, midway ($\delta = 50$ μm) between the two entrance faces, would be zero by blockage of tritium diffusion and the system symmetry makes it possible to obtain the impedance of the restricted diffusion. The diagrams are characterized by three distinct regions:

- at high frequencies (10^5–0.1 Hz), the capacitive semi circle characterizes the charge transfer resistance acting in parallel with the double layer. In this region, the impedance modulus increases rapidly (zone B in the spectra), and a dip is seen in the phase angle which corresponds to a characteristic frequency, f_t.
- at intermediate and low frequencies (0.1–0.006 Hz), the Warburg straight line segment with a slope of 1 corresponds to the diffusion resistance defined by eq. (23.11). In the Bode plots, this Warburg straight line is represented by a slight inflection in the impedance modulus (zone D) or a phase angle which tends to $-45°$. This is characteristic of the semi-infinite diffusion over this frequency range. At the lower frequency, there is a break between the Warburg straight line and the vertical line in the Nyquist plot, which is characterized by the changing slope for the zones D and E.

$$R_D = -\frac{\delta}{FD}\frac{\partial E}{\partial C_t} \tag{23.11}$$

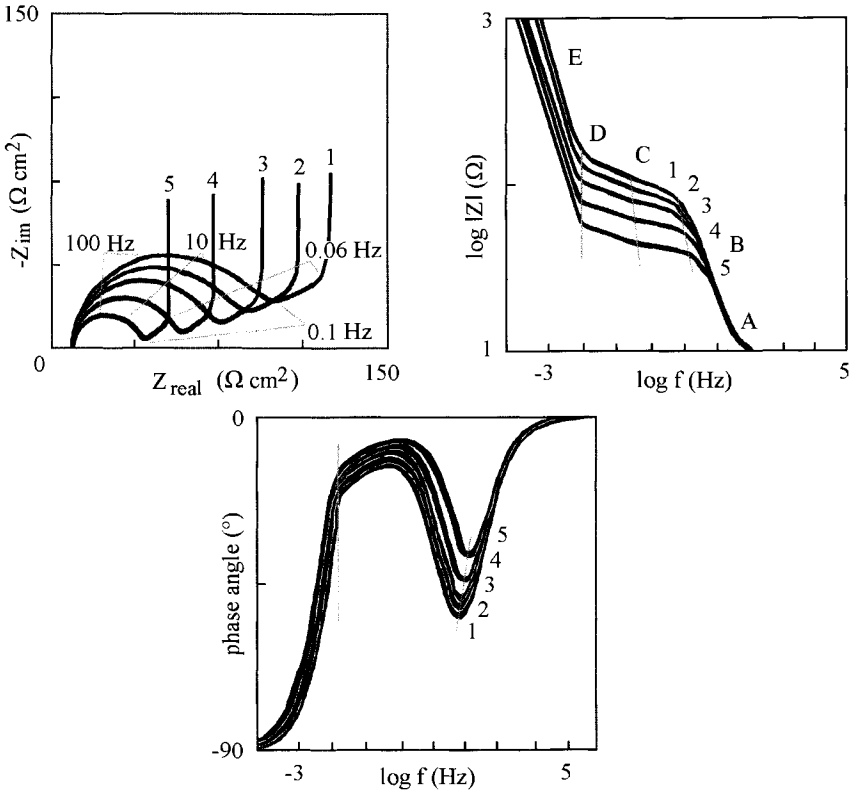

Figure 23.4. Nyquist and Bode diagrams showing the potential effects, 20°C, pH 12, 1: −0.95 V, 2: −1.0 V, 3: −1.2 V, 4: −1.25 V, 5: −1.35 V/SCE.

In eq. (23.11), $F(\partial C_t/\partial E)$ is the differential capacity of tritium insertion related to the permeation. In this part of the spectra, the value of diffusion resistance enables us to derive $\partial C_t/\partial E$.

- at very low frequencies < 0.006 Hz, a vertical straight line corresponding to the restricted diffusion impedance for the finite diffusion process defined by the diffusion impedance:

$$Z_D \approx -\frac{1+\frac{j\omega\delta^2}{3D}}{j\omega\delta F\frac{\partial C_t}{\partial E}} \tag{23.12}$$

This is characterized by a phase angle which tends to −90° in the Bode plot, and a change of slope in the impedance modulus (zone E).

It can be seen that the spectra change with the different potentials. The capacitive semi circle and the Warburg straight line decrease on increasing the cathodic potentials, therefore increasing the diffusion, giving way to the vertical line due to finite length effects. This

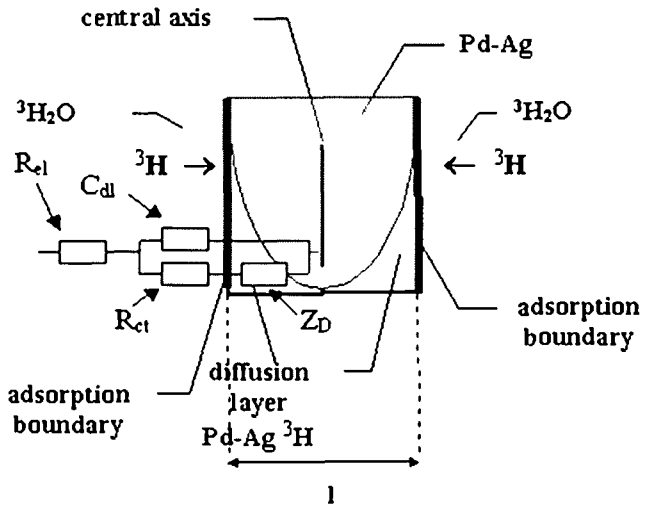

Figure 23.5. Schema and equivalent circuit showing the diffusion profile in a PdAg cathode charged on two faces, R_{el}: electrolyte resistance, R_{ct}: charge transfer resistance, C_{dl}: double layer capacitance, Z_D: diffusion impedance including the restricted diffusion elements.

means that the permeability is accelerated. At potentials closer to the tritium reversible reaction, the respective separations of a semicircular region with the Warburg straight line and vertical line, and the two zones C and D, are more evident in the Nyquist and Bode (zone C) representations, and the diffusion is lower. It can be seen that at these potentials the breaks for semi-infinite and finite diffusion and semicircular region occur readily, and data analysis presents no problems. The diffusion resistance is measured from the point at which the Warburg straight line would intercept the real axis. Whereas if the different breaks are not well-defined, due to overlap of the semi-infinite and finite diffusion and charge transfer-controlled regions (Fig. 23.4, curve 3), an inaccuracy will be introduced in the diffusion coefficient calculation. The separation of semi-infinite and finite diffusion with the semicircular region should be distinct only if the frequency at the top of semi circle is well above that in the break:

$$f_t \gg f_D, f_c \tag{23.13}$$

f_D and f_c are the characteristic frequencies of the Warburg with the semi circle and vertical straight lines respectively. The impedance modulus, given in Fig. 23.4, shows effectively that the frequencies in the zones D and E are far below those which allow an easy determination of the Warburg straight line according to the condition for eq. (23.13). For the spectral analysis, the faradaic impedance can be defined as:

$$Z = \frac{dE}{di} \tag{23.14}$$

The concentration of discharged tritium C_t, is directly related to the current and the current differential can be obtained using the Taylor's series expansion:

$$di = \left(\frac{\partial i}{\partial C_t}\right) dC_t + \left(\frac{\partial i}{\partial E}\right) dE \tag{23.15}$$

To find the expression for the faradaic impedance in the Laplace domain, Z_L, the terms in eq. (23.15) must be divided by dE from eq. (23.14).

$$Z_L = \left[\frac{\partial i}{\partial C_t}\left(\frac{dC_t}{dE}\right) + \frac{\partial i}{\partial E}\right]^{-1} \tag{23.16}$$

The concentration profile of the tritium is obtained by Fick's laws of diffusion.

$$\frac{\partial C_t}{\partial t} = D\frac{\partial^2 C_t}{\partial y^2} \tag{23.17}$$

Semi-infinite diffusion forms the criterion for onset of boundary conditions:

$$t = 0, \quad 0 \leqslant y \leqslant \delta \quad \text{and} \quad C_t = 0, \quad t > 0 \quad \text{and} \quad y = 0, \quad D\frac{\partial C_t}{\partial y} = -\frac{i}{nF},$$

$$\text{and} \quad y \to \infty, \quad \frac{\partial C_t}{\partial y} = 0 \tag{23.18}$$

The Laplace transformation from eqs (23.16)–(23.18) is taken with respect to the time (t) and the resulting differential equation is solved yielding the faradaic impedance in this domain:

$$Z_L = \frac{\partial E}{\partial i} + \frac{\partial E}{\partial C_t}\frac{1}{nF\sqrt{D}} \coth\sqrt{\frac{s\delta^2}{D}} \tag{23.19}$$

where s is the Laplace operator. This equation must be transformed from the Laplace domain into the frequency domain. This can be done by series expansion and introducing the variable complex, j, which governs the response of the electrode in the frequency domain.

$$Z_\omega = \frac{\partial E}{\partial i} + \frac{(1-j)\sigma}{\sqrt{\omega}} \coth(1+j)\sqrt{\frac{\omega\delta^2}{3D}} \tag{23.20}$$

where σ is the Warburg coefficient given by

$$\sigma = \frac{\partial E}{\partial C_t}\frac{1}{nF\sqrt{2D}} \tag{23.21}$$

Table 23.1. Effect of potential on the charge transfer and diffusion resistances

E (V/SCE)	−0.95	−1.0	−1.2	−1.25	−1.35
R_{ct} ($\Omega\,cm^2$)	300	250	130	60	20
R_D ($\Omega\,cm^2$)	140	70	30	20	10

From eq. (23.20), the faradaic impedance of tritium diffusing in palladium-silver or palladium is a linear combination of the charge transfer resistance and modified Warburg diffusion resistance defined by the first and second terms, respectively, on the right hand side of this equation. The electrolyte resistance can be included but does not affect the charge transfer resistance or slope of the Nyquist plot or the impedance modulus (zone A, Fig. 23.4) in the diffusion controlled regime. In eq. (23.20), at high frequencies when $\omega \gg 3D/\delta^2$, the coth term tends to unity, the modified Warburg impedance behaves like the conventional Warburg impedance and the straight line region with a slope of 1 is observed in the Nyquist plot. At lower frequencies, when $\omega \ll 3D/\delta^2$ the phase angle tends to $-90°$ (Fig. 23.4), the vertical line region perpendicular to the real axis is seen on a Nyquist plot. At the intermediate frequencies when $\omega \sim 3D/\delta^2$, the break from the semi-infinite diffusion region to the finite diffusion region is obtained. The break between the semi-infinite diffusion region and the finite diffusion region can provide the restricted diffusion impedance. In this region, the diffusion behavior is limited by the finite length of the palladium-silver alloy and the capacitive effect is observed in the Nyquist plot due to charge saturation. In eq. (23.11), diffusion resistance depends on potential and in this case on permeation which increases at higher cathodic potentials. The time constant, between semi-infinite diffusion and finite diffusion regions, can be obtained from:

$$\tau_c = \delta^2/3D = (2\pi f_c)^{-1} \tag{23.22}$$

where δ (50 μm) is the palladium–silver membrane half-thickness and f_c the characteristic frequency at the intersection between the Warburg and the vertical straight lines. The characteristic frequency position, between the two straight lines, is controlled by the value of the diffusion coefficient and not by the potentials.

The PdAg model can be based on the modified Randles-type equivalent circuit shown in Fig. 23.5. In this circuit, Z_D is the diffusion impedance including the parameter $\delta^2/3D$ given in seconds and the diffusion resistance with its insertion capacitance. It is observed that the double layer capacitance is about 40 $\mu F\,cm^{-2}$ which agrees with the corresponding value given by Bard and Faulkner [103]. The charge transfer and the diffusion resistances decrease (Table 23.1) and the frequency between the semi circle and the Warburg straight line increases slightly keeping the double capacitance constant when the cathodic potentials increase towards higher potentials. This indicates more tritium absorption as well as diffusion. At these potentials, the diffusion coefficient, $3 \times 10^{-7}\ cm^2\ s^{-1}$ at 20°C, is calculated from the frequency between the two straight lines in Fig. 23.4 and from eq. (23.22). This value is close to that obtained by permeation measurements for the same temperature. The thickness of the diffusion layer and the time constant were calculated and are approximately 50 μm and 26 seconds. Taking into account the membrane thickness of 100 μm, the

Table 23.2. Effect of temperature on the charge transfer, diffusion resistances and the time constant

T (°C)	20	40	70
R_{ct} ($\Omega\,cm^2$)	75	50	30
R_D ($\Omega\,cm^2$)	75	40	20
τ_c (s)	26	16	10

Table 23.3. Diffusion coefficient dependence on temperature

T (°C)	20	40	70
D ($cm^2\,s^{-1} \times 10^7$)	2.4	4	6.5

value of the diffusion layer indicates that the tritium diffusion is restricted. We derive from eq. (23.9) that C_t, the tritium concentration near the surface, is $\sim 7 \times 10^{-3}$ mol cm^{-3}. It is therefore possible to use these experimental methods for determining the diffusion coefficient, diffusion layer and surface solubility of tritium in a palladium-silver cathode responsible for stress corrosion. In the Bode representation in Fig. 23.4, it is also seen that the characteristic frequency between the zones E and D does not change. This corresponds to the break between the Warburg straight line and the vertical lines in the Nyquist plot. According to eq. (23.22), this signifies that the diffusion coefficient does not vary with potential. In the same figure, the frequency in zone C changes with the potential. Its position corresponds to the break between the capacitive semi circle and the Warburg straight line in the Nyquist plot. The interpretation is that the tritium permeation value increases with the potential.

The diagrams in Fig. 23.6 were obtained for different temperatures. We can see that the Nyquist plots exhibit each of the three characteristic regions and the breaks observed earlier. When the temperature increases the frequency in the break placed between the two straight lines increases and the time constant decreases. This signifies, according to eq. (23.22), that the diffusion coefficient increases (Table 23.2) whereas tritium solubility and cracking corrosion decrease. In this figure, the frequency in zone C changes with the temperature. The interpretation is that the tritium permeation increases with the latter. The values of the diffusion coefficient as a function of temperature obtained with eq. (23.23) are given in Table 23.3. Plotting the curve $D = f(T^{-1})$, where T is the absolute temperature, yields an equation that gives the diffusion coefficient and the relation between the characteristic frequency and the temperature.

$$D = 3 \times 10^{-3} \exp -23.2 \times 10^3 / RT \tag{23.23}$$

$$f_c = \frac{1.9 \times 10^{-3}}{\delta^2} \exp\left(-\frac{2.8 \times 10^3}{T}\right) \tag{23.24}$$

3. Scanning electron microscope results

Palladium is a transition metal that crystallizes in the face-centered cubic system. The edge of the cube is 3.89 Å at 20°C [93]. Tritium, on insertion in the lattice as tritons [14],

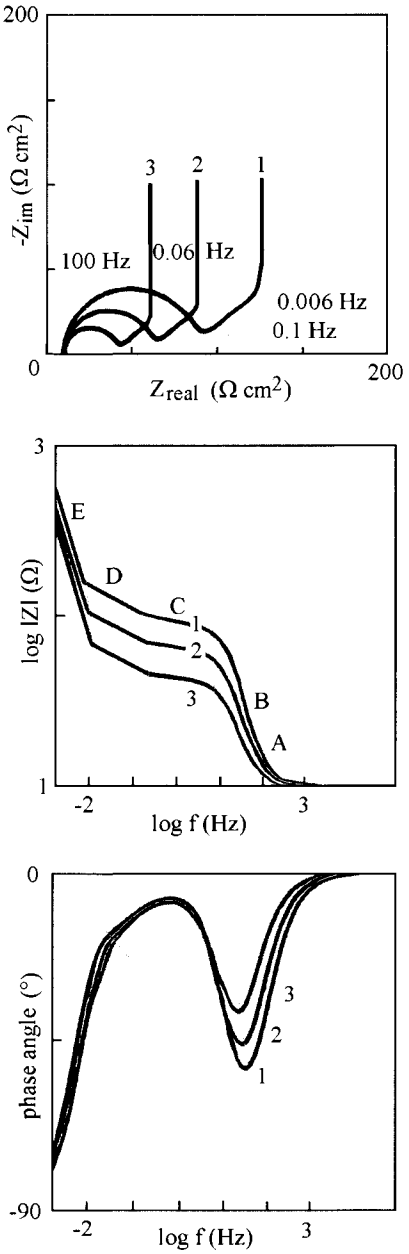

Figure 23.6. Nyquist and Bode diagrams showing the temperature effects, 1: 20°C, 2: 40°C, 3: 70°C.

gives two types of solid solutions (phases) depending on their concentration (dissolved and non-dissolved in diffusion) at temperatures below the critical temperature of 200°C, above which there is only one phase:

- α phase: low concentrations,
- β phase: high concentrations.

These two phases have a face-centered cubic structure analogous to that of palladium. The edge length varies little with the tritium concentration in each phase, the change occurs essentially on going from one phase to another. This leads to the embrittlement in the case of palladium in the course of successive cycles of tritiation and can result in linear transgranular cracks (see Fig. 23.7, which shows a cross-section of the membrane).

The cracks go through the thickness of the membrane after about 300 hours of operation of the cathode at 80°C at a current density of 75 mA cm^{-2}. Both phases are formed in the membrane: the β phase on the cathodic face where the tritium enters, and the α phase on the desorption face. At the beginning of the cathodic charging, a 'swelling' of the entry face is observed with the formation of hillocks (Fig. 23.8). Subsequently, cracks appear on both faces (see Fig. 23.9). The stresses due to the inserted tritium lead first to a creased membrane (Fig. 23.10), and subsequently during the course of its cathodic charging to a change in the dimensions of the membrane with time (Fig. 23.11). Its length decreases while its thickness increases (Fig. 23.12).

The insertion of tritium in the palladium–silver alloy takes place at the same type of site as that of the face-centered cubic metal lattice. There are also two types of solid solutions. The only difference is that the variation of the length of the edge is much smaller in the phase transitions when the silver concentration increases. This critical temperature is lower for palladium–silver alloy ($\sim$ 100°C). The palladium–silver alloy is therefore less sensitive to embrittlement. The tritium diffusion coefficient in palladium–silver alloy is approximately the same as that of palladium. This was shown in this work using a palladium alloy cathode and the same operating conditions as those for palladium, i.e. a temperature of 80°C, a cathode current density of 75 mA cm^{-2} and 300 hours of operation. A loss of cohesion in the alloy occurs with the formation of cracks in the bordering zone between the

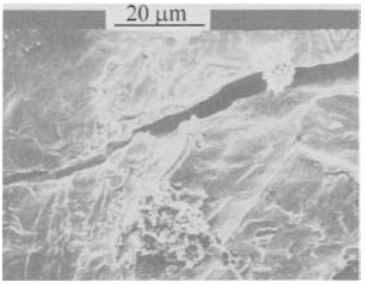

Figure 23.7. Scanning Electron Micrographs of the cross-section of a Pd membrane showing the transgranular cracks due to $^3H_2$.

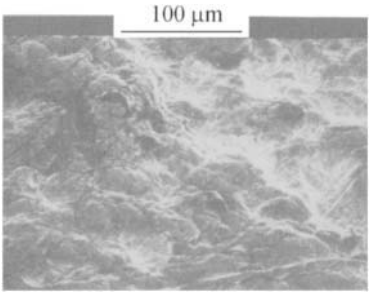

Figure 23.8. Scanning Electron Micrograph of the cathodic face of a Pd membrane showing the hillocks due to $^3H_2$ before cracking.

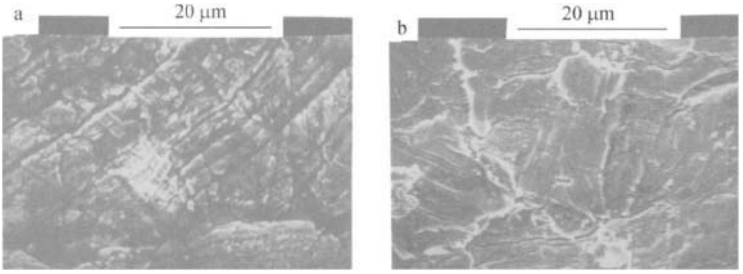

Figure 23.9. Scanning Electron Micrographs of the cathodic (a) and desorption faces (b) of a Pd membrane. The transgranular cracks are due to $^3H_2$.

Figure 23.10. Photograph of the Pd membrane creased immediately after $^3H_2$ charging.

electrolyte and the gas atmosphere from the electrolyzer (Fig. 23.13), proving the existence of two tritiated phases in this zone. The examination of the cross-section of the thickness of the PdAg membrane shows the presence of cracks (Fig. 23.14). In this case, they appear

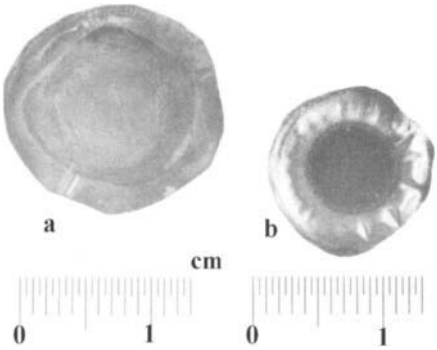

Figure 23.11. Visual examination, (a): palladium before $^3H_2$ charging, (b): palladium after 300 h of $^3H_2$ charging. Note changes in the membrane dimensions.

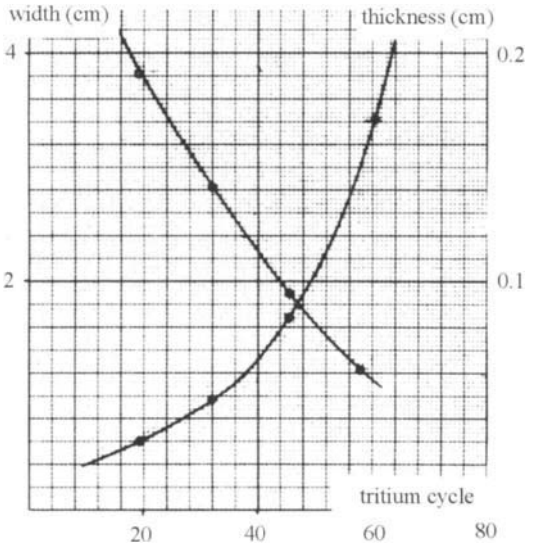

Figure 23.12. Changes in the diameter and thickness of the Pd.

to be intergranular, which would give rise to diffusion and back-diffusion loops following the tritium charging cycles.

4. Conclusions

Scanning Electron Microscopy examinations show that the cracking is transgranular in the case of palladium, while it appears to be intergranular for the PdAg alloy. With palladium, this cracking involves all the surface subjected to charging, whereas for the alloy only

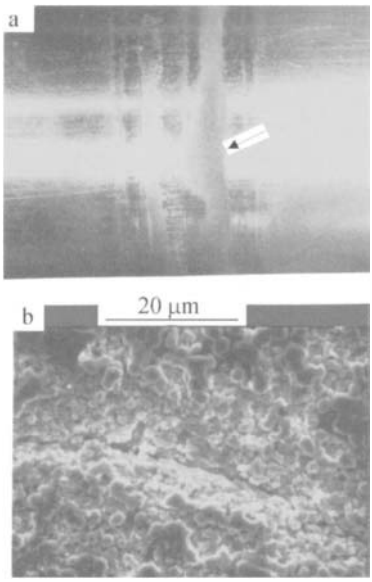

Figure 23.13. Border zone between the electrolyte and the gas atmosphere of the electrolyzer, (a): general appearance of the membrane, the arrow indicates the bordering zone (visual examination), (b): appearance of the bordering zone by Scanning Electron Microscopy indicating loss of cohesion and cracking of the alloy by $^3H_2$.

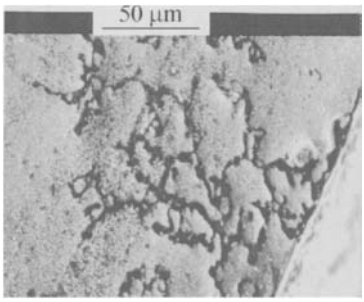

Figure 23.14. Scanning Electron Microscopy of the cross-section of a PdAg membrane in the bordering zone between the electrolyte and the gas atmosphere of the electrolyzer showing the intergranular cracks and loops due to $^3H_2$.

the surface at the gas atmosphere/electrolyte bordering zone appears to be embrittled with loops that result from tritium back-diffusion in the course of the tritiation cycles. The Pd membrane dimensions change due to a modification of the size of the lattice in the face-centered cubic system; this could be the result of the presence of two tritiated phases in palladium. Nevertheless, the PdAg alloy is the less sensitive to embrittlement.

Chapter 24

FINDINGS AND PRACTICAL APPLICATIONS

This work is divided into three parts; the first concerns thermonuclear fusion reactors and preparation and reprocessing of tritium for fusion technology. All aspects of corrosion in tritium processing industrial installations are presented within the second part with significant results obtained from various areas of the world. This part also concerns the metallurgical aspects of stainless steels and alloys studied world-wide in the field of nuclear corrosion with practical applications relating to tritium technology. It is thus aimed at the professional experts working in the nuclear and corrosion fields and the equipment manufacturers. In the third part, analytical results for corrosion induced by tritium and its radiolytic and decay products formed in nuclear installations are given. In this discussion selected stainless steels and alloys are linked to the findings presented in chapter 4, i.e. the strategy for controlling corrosion. This analytical part describing radiolytic products and alloys aids in avoiding and limiting corrosion; it also provides a basis for protection in the tritium reprocessing industrial installations. It should be of great interest to corrosion and electrochemistry scientists.

Before presenting remedies, we remind ourselves (chapters 2 and 3), that storage and reprocessing of low energy radioactive products, in particular waste from nuclear power plants, require compliance with strict safety demands. For this, it is necessary to confine products in containers, or operating systems (first barrier) at the lowest possible corrosion rates and the highest possible tightness. The equipment used must have high mechanical strength or ductility and optimum resistance to corrosion. This requirement will become increasingly important with the progression of fusion technology, as it requires high tritium concentrations; the same may be applied to nuclear reactors generating tritium. One of the problems associated with the use of nuclear fuel in power production and particularly where reprocessing is concerned is the safe handling of tritium compounds. This tritium, in the form of gas or tritiated water, should be enriched by such techniques as electrolysis, gas purification and isotopic separation to lead to the depletion of tritiated waste.

The purpose of this chapter is therefore to provide methods in which tritium and substances containing it can be reliably stored with no corrosion and reprocessed without difficulty at any time. First, one problem has been solved by not storing tritium as a gas, but as tritide thus avoiding eventual loss by permeation through the metal equipment and storage containers. Another possible measure is that of oxidizing the tritium in tritiated water so that it can be absorbed on a molecular sieve enclosed in a container. The container

may consist of high-grade stainless steels or alloys. It must be hermetic regarding tritium diffusivity and furthermore be corrosion-proof. The materials used must be insensitive to radiolysis products and tritiated water. To achieve completely tight sealing, that is reliable, the container should be provided with a hardened flange or be welded. Welding is preferably carried out by electron beams. The containers can hold up to 200 liter of tritiated water.

As our results show, tritiated water contains various forms of peroxides and non-negligible concentrations of carbonate, chloride, fluoride and nitrate ions; its pH can be acid, neutral or alkaline. It was therefore necessary to study the influence of these different radiolytic species on corrosion. This work was undertaken under a specific brief, corresponding to actual tritium processes, and it is possible to introduce further improvements. Proposed methods for avoiding or limiting corrosion are therefore intended to cover any variations, uses, adaptations and improvements following the general principles and essential features in the tritium processes. In accordance with our work, we *claim* the following easy and attractive methods for limiting and avoiding localized corrosion. In the same way, we indicate specific properties and behavior limiting the passivity of metals. These should be taken into account to avoid corrosion. These *claims* and specific items follow on from our experimental results. They are described below.

1. Design of the medium to avoid corrosion

1.1. Energy released by tritium including that in metals

These effects cannot be suppressed because they are inherent in radioactive media and their effects can only be limited by a suitable choice of alloys or stainless steels. Such a choice will be indicated in the last section of this chapter.

1.2. Non-peroxygenated medium with and without species responsible for localized corrosion

- The species responsible for localized corrosion are adsorbed by and then diffuse in the tritiated oxide. They accelerate the vacancy accumulations at interfaces and occupy oxygen sites in the oxide. In this case the oxide layer will have defects corresponding to the incubation time for localized corrosion with formation of transients. If there is pitting, this will be stable and should increase with formation of crevices.
- In the absence of species responsible for localized corrosion, the kinetics of passive oxide layer formation are slow. These are dependent on pH, and the oxide layer is produced by adsorbed intermediate species which are not eliminated in stagnant tritiated water.

The formation of transients has been clearly evidenced by our voltammetric curve-plotting instrument that is equipped with a numerical analyzer. This arrangement has the advantage that curves are not incremented, but digitized in pixels in real time since no artifact is introduced for averaging. However, interpretation of curves is more tedious and

necessitates more time than that with the standard system. We can thus obtain unusual hysteresis that provides an easier interpretation of metastable pits.

1.3. Peroxide media

1.3.1. Acid and alkaline pH

- At low peroxide concentration, the corrosion potential will be in the active region thus inducing instabilities in formation of the passive oxide layer.
- At intermediate peroxide concentration, the corrosion potential will be in the passive region, and studied alloys are thus protected. It ensues that the oxide layer will be more difficult to destroy. At a peroxide concentration of 0.05 mol dm^{-3}, the oxide layer is protective.
- At high peroxide concentration, the corrosion potential will be near the transpassive region thus bringing about internal stresses leading to future ruptures in the oxide layer. In this case, the displacements of the pitting potential towards lower values and the corrosion potential towards higher values are critical. The passivity domain is therefore smaller. Moreover, this is again emphasized with acid pH. The presence of peroxide facilitates pitting and crevice corrosion.
- Flowing tritiated water should decrease the pitting domain. Here, an inverted effect can be observed. This result is explained by the continual peroxide contribution thus increasing the localized corrosion. Pitting is therefore strongly dependent on the peroxide contribution at the surface and the flow velocity.
- During pitting, grain boundaries can be attacked. Such attack depends on the strongly oxidizing medium and the difference in chemistry between grains and grain boundaries.

1.3.2. Alkaline pH It is more difficult to obtain reduction of peroxide in passivity at alkaline pH. This is explained by changes in thickness, structure, composition and the number of carriers in the passive oxide layer. The oxide layer formed at alkaline pH protects alloys better. Analysis has shown that this oxide is enriched in chromium and it is well known that chromium favors passivity. Changes of thickness in the oxide layer indicate that its formation depends on passivity and peroxide concentration. The concentration of carrier in oxide corresponds to the theoretical value of a protective passive oxide layer.

1.4. Carbonate and peroxide media at slightly alkaline pH, with or without species leading to localized corrosion

- Carbonates and slightly alkaline pH show an inhibiting effect on pitting and crevice corrosion. By buffering, carbonates keep pH at the initial value on the surface and thus avoid local acidification. Moreover, if the oxide layer is formed in slightly alkaline media, it should offer greater protection than that obtained at other pH values.
- Carbonate and peroxide create a protective duplex oxide layer. The pitting current decreases and the repassivation potential increases with the peroxide concentration.

Clearly, peroxide and carbonate act together: one buffering the surface alkaline pH of steel, and the other favoring the formation of a protective internal oxide layer. The external layer is initially porous before passivation by peroxide introduced in pores. The internal passive oxide layer grows in the presence of peroxide and depends on passive potentials, whereas the external oxide layer depends on carbonate being present and forms mainly in prepassivity. The number of carriers in the internal oxide is close to the theoretical value, thus signifying the formation of a protective internal oxide. There is no development of metastable pits—these repassivate. Vacancy diffusion and formation of pits have been formulated for this medium.

1.5. Nitrate and peroxide media at slightly alkaline pH, with or without localized corrosion

- In presence of nitrates, pitting and repassivation potentials move towards higher values. Because nitrates render the repassivation potential more positive, they improve passivity by suppressing initiation of pitting and slowing propagation. In reality, the oxide layer contains NH_4^+ buffering the surface pH and thus avoids acidification in the bottom of pits. Pitting cannot occur without acid pH. In this way, it has been noted that the flat band potential is lower indicating that nitrates effectively buffer the surface at alkaline pH.
- In the case of nitrate and peroxide at slightly alkaline pH, the corrosion potential does not change. In practice, generalized corrosion due to the introduction of solid oxide transported material able to settle on tube walls is not a real problem in tritium installation. This remark is significant in the sense that the surface remains buffered, and the pitting potential is displaced in the positive direction. However, this is not the case for the repassivation potential. It is concluded that in presence of peroxide and nitrate, new pits do not form, but propagation of existing pits is possible. However, if this result is compared with that obtained in the presence of a pitting species alone, it is seen that peroxides nevertheless aid in repassivation. It can be useful to introduce these two species while controlling their concentration. The criterion of vacancy diffusion and pitting formation has been formulated for these media.

It is also necessary to avoid corrosion in other ways. Chlorides and fluorides must be eliminated in tritiated water by suppressing all organic polymer seals.

To apply our laboratory results, localized corrosion inhibitors (H_2O_2, CO_3^{2-} and NO_3^-) were tested in tritium installation piping in the order to monitor our tests in the production section. However, the flow regime, flow velocity, and nuclear chemistry may vary from one line to another and can be completely different from the data anticipated in the development field. If the hydrodynamic flow changes from turbulent to stagnant, it is very likely that the selected inhibitors will still be effective. Experience indicates that inhibition in turbulent conditions provides an acceptable level of protection in stagnant conditions. The inhibitor efficiency was tested under actual use in turbulent conditions of the recirculating loop between the electrolyzer and condensers used for reprocessing tritiated water (Figs 3.10

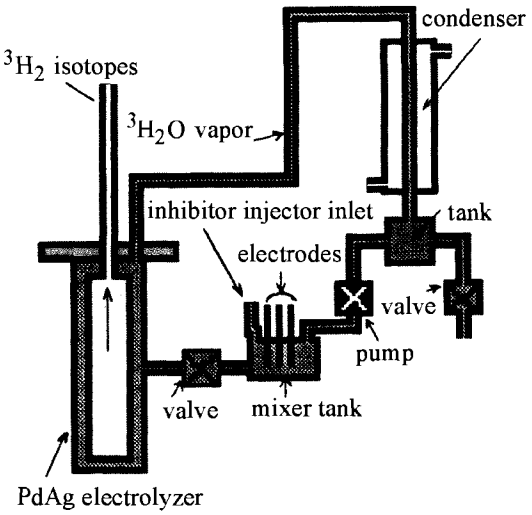

Figure 24.1. Flow loop for dynamic tests.

and 24.1). This electrolyzer combines exceptional high-field, is very easy to use and has a wide versatility in recycling tritium.

First, concentrations of natural inhibitors in tritiated water were verified. After measurements, these concentrations were corrected by injection using a jet impingement system integrated in the loop [287], until the corrosion rate was reduced or became constant. In this case, electrochemical measurements were made in the flow area [288]. Concentrations of the selected inhibitors were 1.5×10^{-2} mol dm^{-3} H_2O_2, 5×10^{-2} mol dm^{-3} CO_3^{2-} and 3×10^{-2} mol dm^{-3} NO_3^-. Oxide layer quality was evaluated by televisual examinations as described previously (chapter 4.2). With corrosion inhibitor injection, localized corrosion rates decreased by 50% in the line between the circulating pump and condensers. Six similar locations were inspected, but no localized corrosion was detected. Investigations showed that the high corrosion rates were caused by failure of the inhibitor injection system. During two years of operations, two flow lines were automatically monitored and no significant corrosion was detected. In the presence of an efficient inhibitor, a thin layer of oxide was formed. This layer was quite compact and protective in the presence of inhibitors.

2. Design with regard to alloys and stainless steels to avoid corrosion

As mentioned in the introduction of this book, materials selection is a difficult and complex but essential process, and many problems are caused by an inappropriate choice leading to corrosion-related failures. Our assessments of the 15 alloys/stainless steels and deposits we examined while taking into account their mechanical characteristics and respective applications are listed below. The selection is the following.

- Concerning furnaces used for cracking tritiated water, for recycling of gases by purification and separation, the selected stainless steel is the type austenitic 310SS having a high chromium concentration and low diffusibility of tritium. This steel has good resistance to embrittlement.
- The super-Duplex and super-austenitic stainless steels exhibited the best behavior with respect to localized corrosion in tritiated water. This results from better corrosion resistance of their passive oxide layer; this involves an oxide layer with the smallest amounts of defects. Consequently, stainless steel assemblies for storing or circulating tritiated water are made using type N08932, S31803 and S32550 stainless steels.
- Containers for tritium gas storage should be made of type 316L stainless steel in order that tritium diffusibility is low at ambient temperature. This is effective in reducing embrittlement by tritium.
- For particular equipment such as flanges and valves, stainless steels should be bulk or surface hardened. Consequently, we have retained two martensite types; these are Maraging and 630 stainless steels (17-4-PH steel). The assembly of high strength stainless steel with a ductile superalloy is necessary. In this case Hastelloy and R30003 alloys are ideal while they exhibit high resistance to localized corrosion.
- Metallic seals and bellows equipping flanges and valves have to be ductile. To avoid the formation of corroding species and crevice corrosion, elastomer seals are prohibited. The same is true for copper, a source of galvanic corrosion. Type 316L stainless steel seals and bellows have been selected (see chapter 3.4).
- Turbulent flows are often responsible for corrosion-erosion. To avoid this attack, the internal walls are protected by a titanium nitride deposit. Since this deposit is porous, the underlying steel must have a high resistance to localized corrosion; it should be one of previously selected super-alloys or stainless steels.
- Distillation column packing is 316L stainless steel spirals on which a Ni-Cr layer has been deposited. This deposit was annealed with oxygen so as to improve characteristics of the oxide layer.
- For the cathode used in the electrolyzer to reduce tritiated water, the alloy selected is 25% silver–palladium. However, so as to restrain embrittlement, electrolysis is carried out with the optimum operating conditions.

All these selected stainless steels and alloys have been tested under actual operating conditions in gaseous tritium loops and tritiated water installations. Satisfactory results have been obtained over several years.

Part IV

APPENDIX

This Page Intentionally Left Blank

Chapter 25

3D SURFACE TOPOGRAPHIES IN TRITIATED MEDIA

The illustrations that make up this chapter are available in colour on the (accompanying) CD-ROM.

Figure 25.1. 3D surface morphology, (left top): peeled oxide, (right top): roughness and scratches, (left bottom): cracked oxide, (right bottom): peeled oxide.

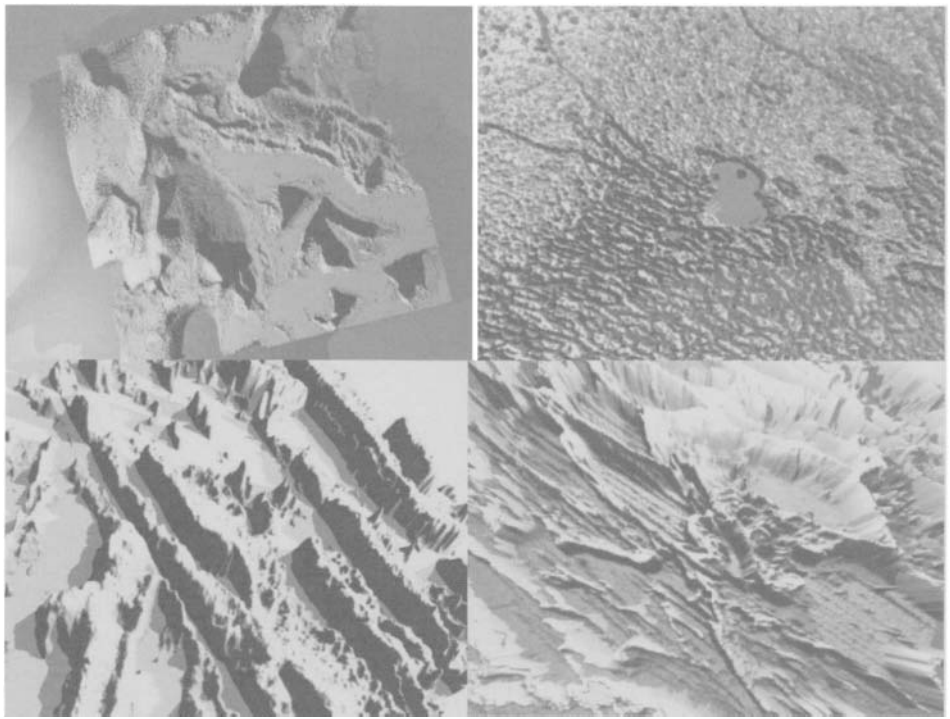

Figure 25.2. 3D surface morphology, (left top): cavities induced by helium, (right top): sub-critical microscopic helium cavities, (left bottom): cracking in form of planar slips, (right bottom): over-oxidized scales.

Figure 25.3. 3D surface morphology, (left top): cavities and cracks induced by tritium, (right top): embrittlement of palladium by tritium, (left bottom): embrittlement and cleavage of titanium, (right bottom): oxide covering cleavage.

Figure 25.4. 3D surface morphology, (left top): pits and grain boundaries corrosion, (right top and right bottom): grain boundaries corrosion, (left bottom): cracked oxide.

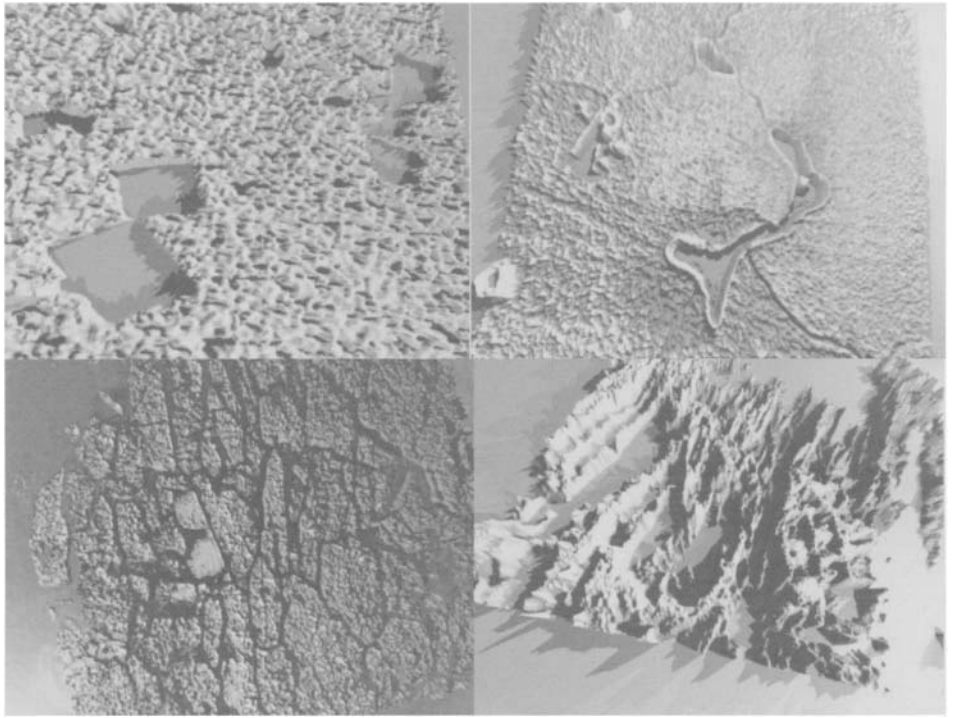

Figure 25.5. 3D surface morphology, (left top): loosening titanium carbide crystallite, (right top): loosening ferrite crystallite, (left bottom): grain boundaries corrosion, (right bottom): microcracks induced by tritium in weld.

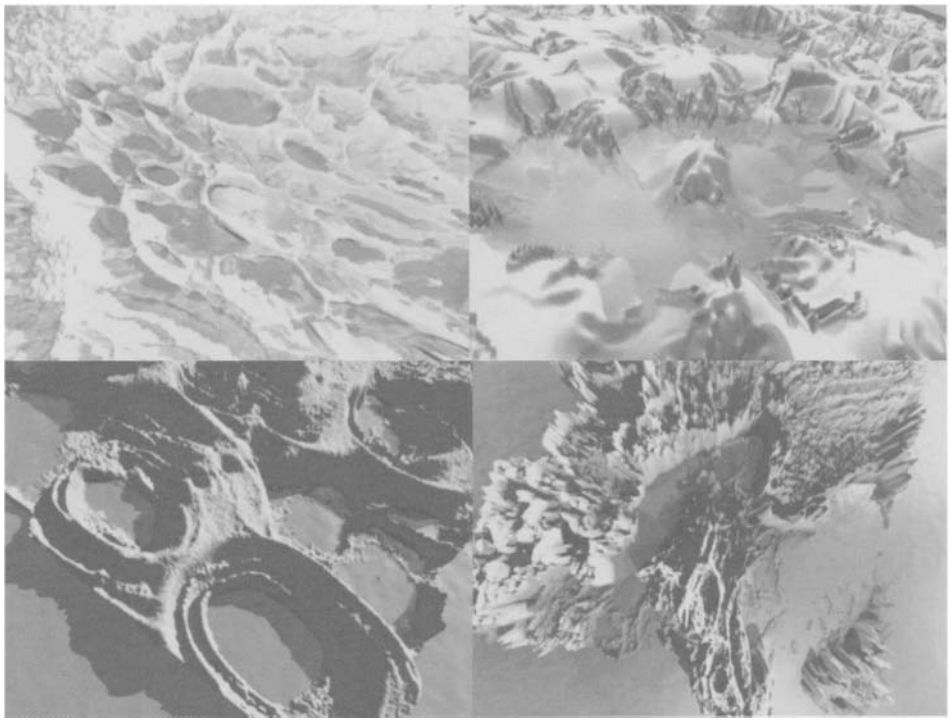

Figure 25.6. 3D surface morphology, (left and right top, left and right bottom): pits.

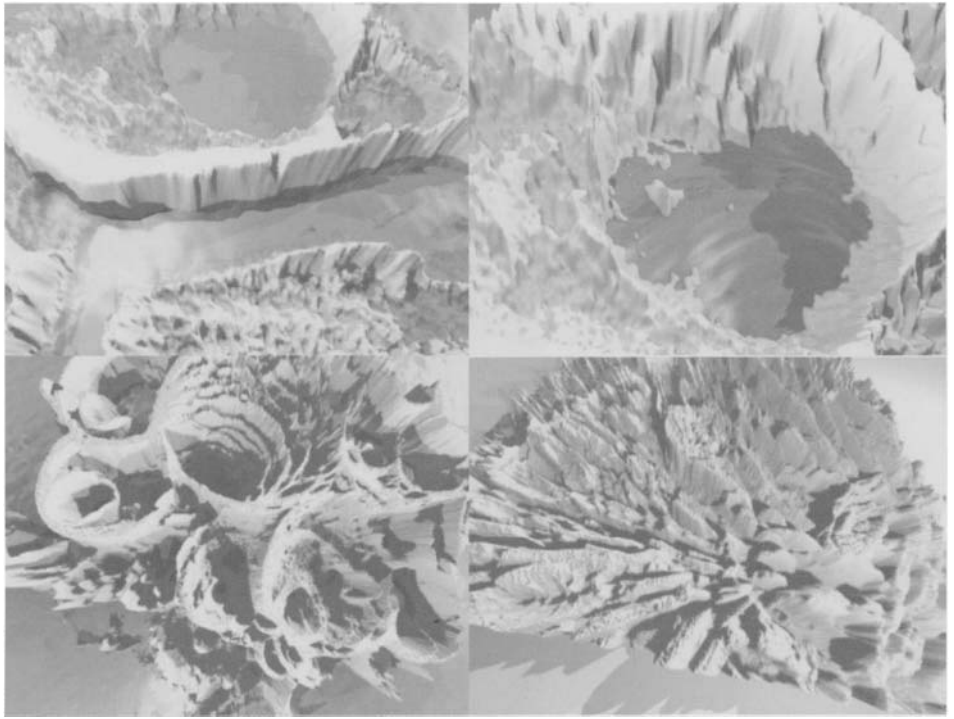

Figure 25.7. 3D surface morphology, (left top): pits and grain boundaries corrosion, (right top and left bottom): pits, (right bottom): crystallized corrosion products on pit.

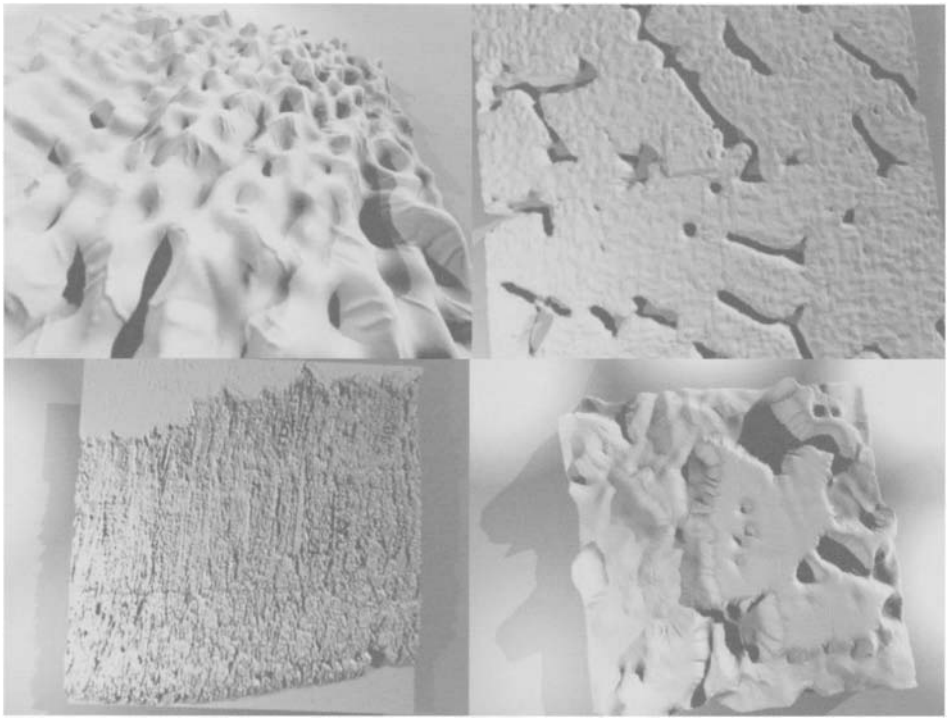

Figure 25.8. 3D surface morphology, (left top): dendrites on weld, (right top): vermicular ferrite, (left bottom): thin hardened surface, (right bottom): polygonisation of steel.

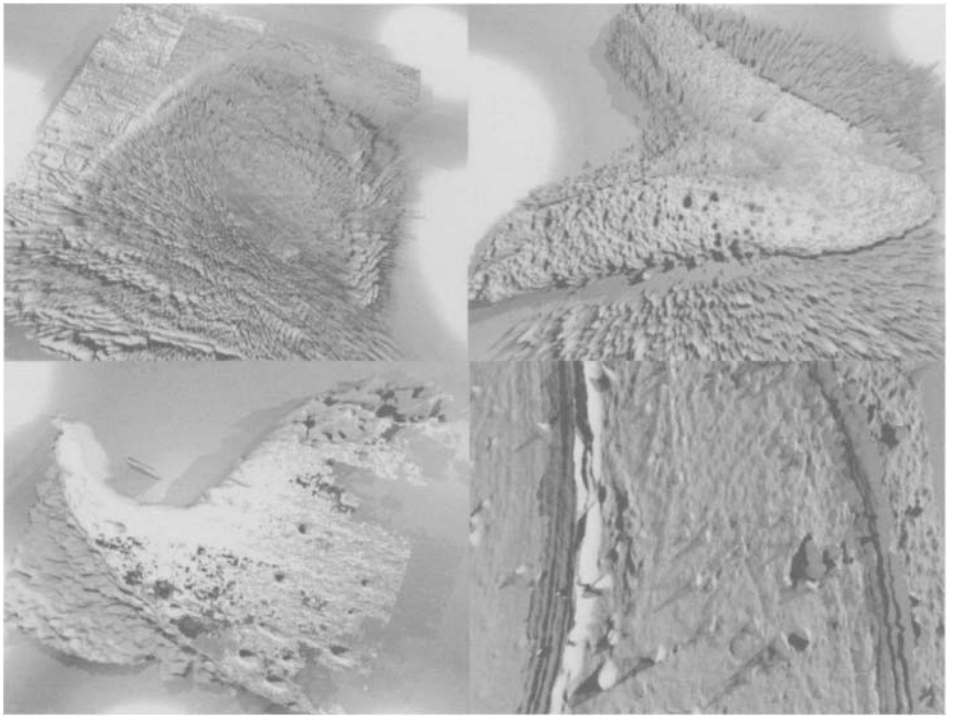

Figure 25.9. 3D surface morphology, (left top): weld made by tungsten inert gas, (right top): melted zone, thermally affected zone and sensitized zone, (left bottom): melted hemisphere with furrow during welding, (right bottom): weld made point by point using a laser beam.

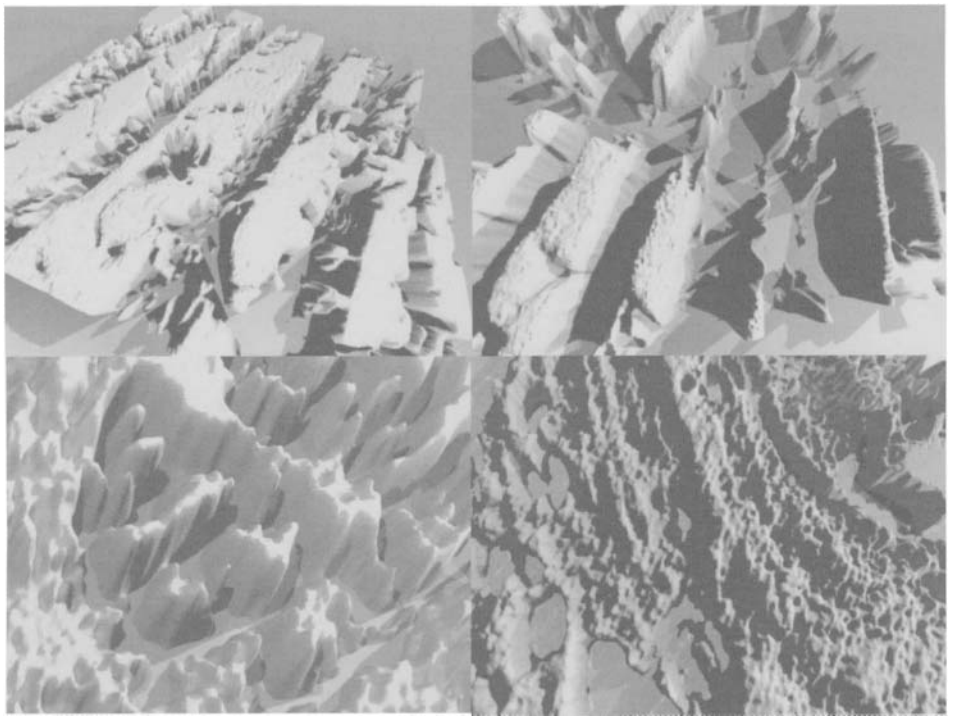

Figure 25.10. 3D surface morphology, (left and right top): transformation of austenite to martensite phase by shock pressure, (left bottom): embrittlement of PdAg with cavity loops interconnected by channels, (right bottom): cavities and cracks induced by tritium.

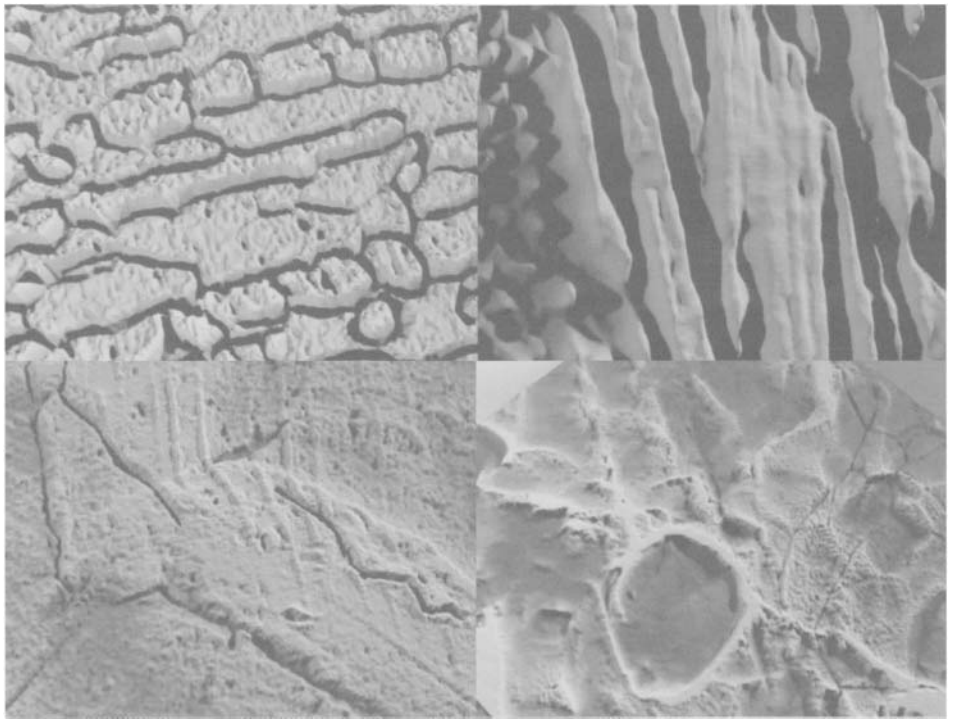

Figure 25.11. 3D surface morphology, (left top): austenite and ferrite grains, (right top): pure ferrite grains, (left bottom): transgranular and intergranular fractures, (right bottom): thin oxide dome covering a pit.

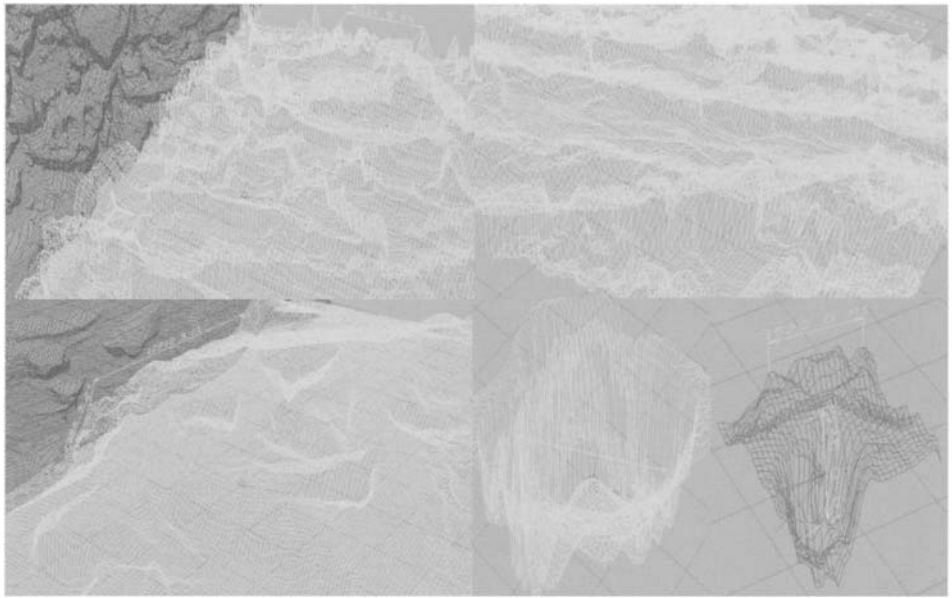

Figure 25.12. Meshing surface morphology where 3500 points represent 20 μm (Scanning Laser Profilometer), (left top): numerous and large pits, (right top): brittle ledges and fractures, (left bottom): cavities and cracks, (right bottom): external and internal views of extruded pit.

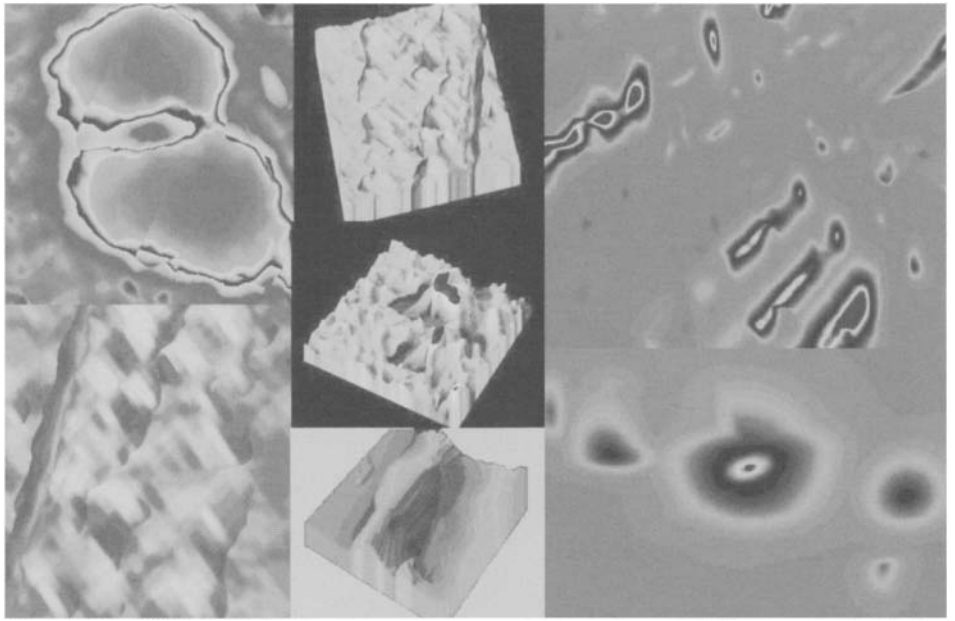

Figure 25.13. Model elevation digital, (left top): planar view showing a thin oxide dome covering a pit, (middle top): 400 nm^2 topographic image showing a nearly hexagonal plane oxide lattice with parallel alignment in terraces (Scanning Tunneling Microscopy), (right top): planar view showing craters formation before cracking (Scanning Vibrating Probe SRET System), (middle): three dimensional topographic view showing a cone-capped pit, (left bottom): 400 nm^2 planar image showing a nearly hexagonal plane oxide lattice with parallel alignment in terraces (Scanning Tunneling Microscopy), (middle bottom): three dimensional topographic view showing a pit, (right bottom): planar view showing craters formation before pitting (Scanning Vibrating Probe SRET System).

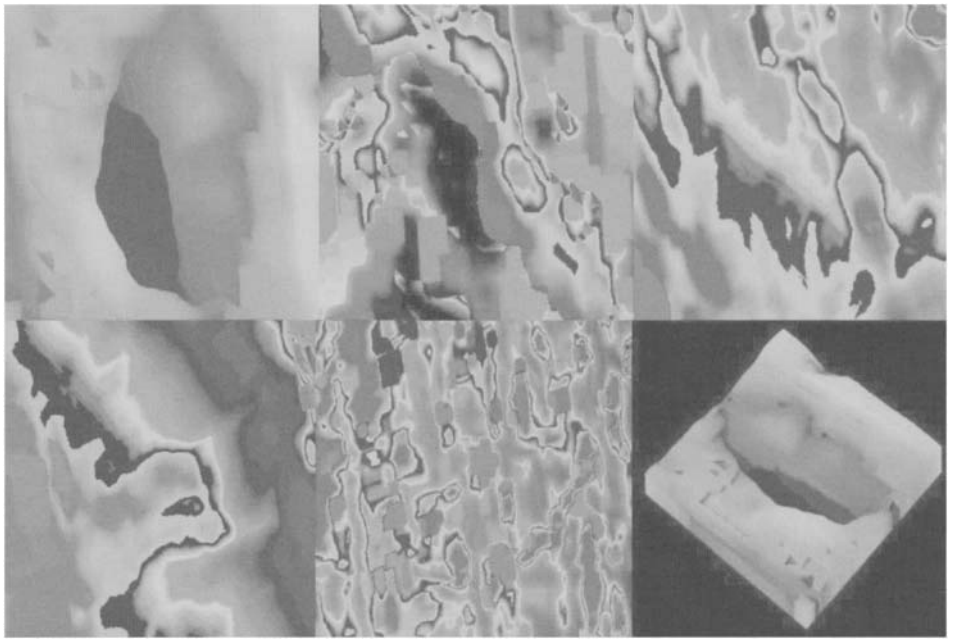

Figure 25.14. Model elevation digital, (left top): planar view showing pit morphology, (middle top): planar view showing digitized fracture morphology revealing thereby details of the inner oxide, (right top): planar view showing digitized fracture morphology, (left bottom): planar view showing digitized fracture morphology. Changes in color characterize also topography, (middle bottom): planar view showing digitized fracture morphology, (right bottom): three dimensional topographic view showing digitized pit morphology.

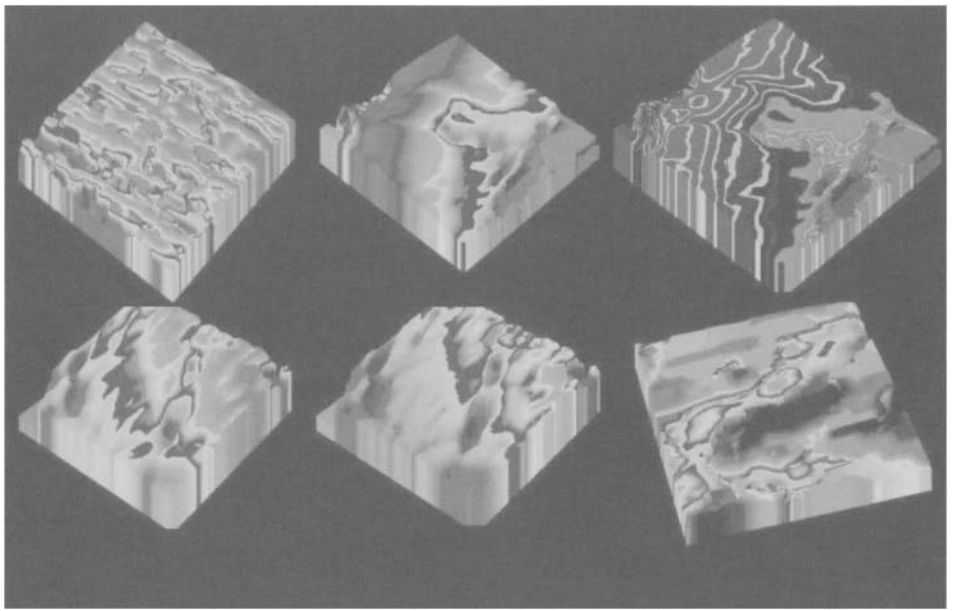

Figure 25.15. Model elevation digital, (left top): three dimensional topographic view showing digitized fracture morphology, (middle top): three dimensional topographic view showing digitized fracture morphology, (right top): three dimensional topographic view showing contour lines during stress corrosion, (left bottom): three dimensional topographic view showing digitized fracture morphology, (middle bottom): three dimensional topographic view showing digitized fracture morphology, (right bottom): three dimensional topographic view showing digitized fracture morphology.

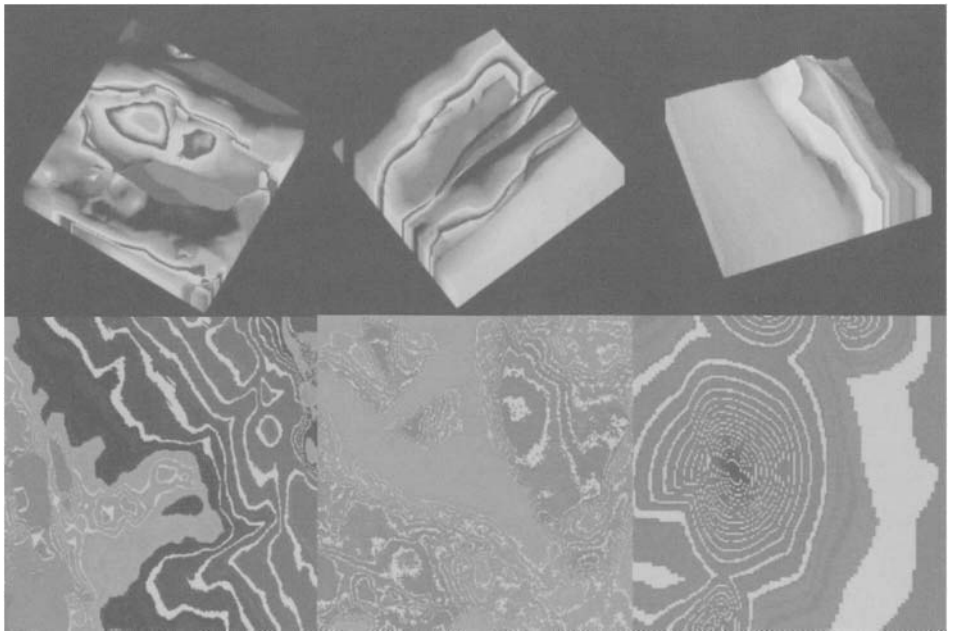

Figure 25.16. Model elevation digital, (left top): three dimensional topographic view showing digitized pit morphology, (middle top): three dimensional topographic view showing digitized dislocation and edge morphology, (right top): three dimensional topographic view showing digitized edge and constraint morphology. Each fringe indicates change in elevation, (left bottom): planar view showing contour lines during cracking, (middle bottom): planar view showing contour lines of excessive thickness oxide, (right bottom): planar view showing contour lines during pitting.

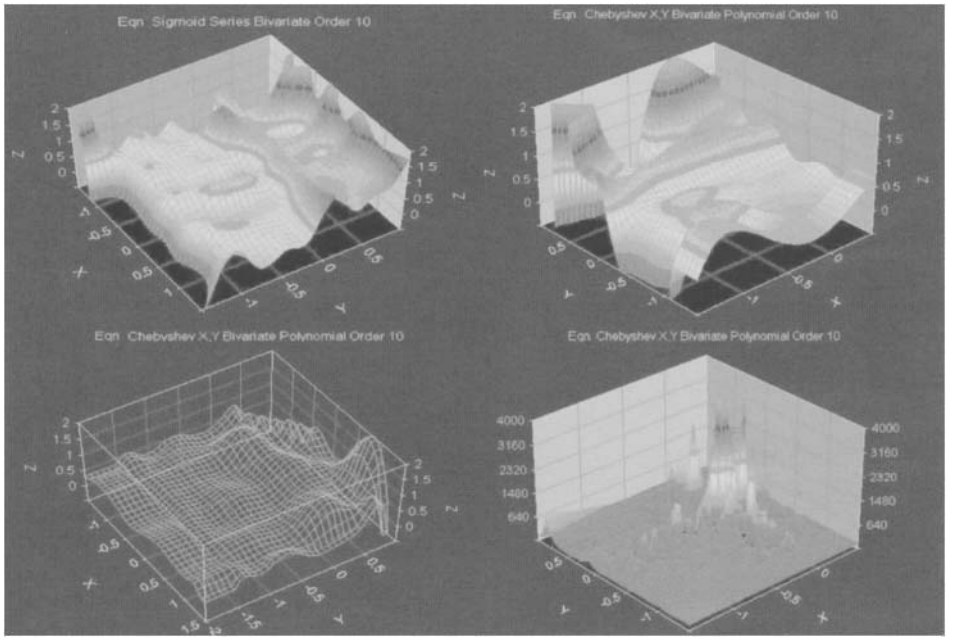

Figure 25.17. Oxide deformation network model (chapter 6), arbitrary graduation, (left top): stress distribution in the deformed oxide, (right top): stress distribution in the deformed oxide, (left bottom): mapping in the vertex mode, (right bottom): numerically calculated stress concentration for the principal void.

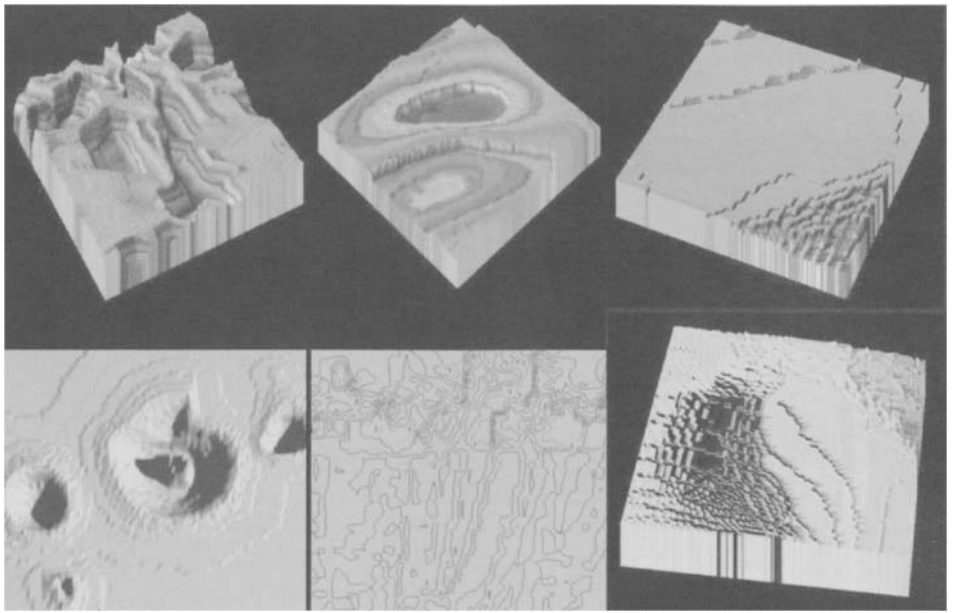

Figure 25.18. Localized corrosion, (left top): three dimensional topographic view showing cracks and pits, (middle top): three dimensional topographic view showing pits, (right top): three dimensional topographic view showing contours of deformed oxide, (left bottom): planar view showing pits, (middle bottom): contours visualization of image in the left top, (right bottom): three dimensional topographic view showing contours of deformed oxide.

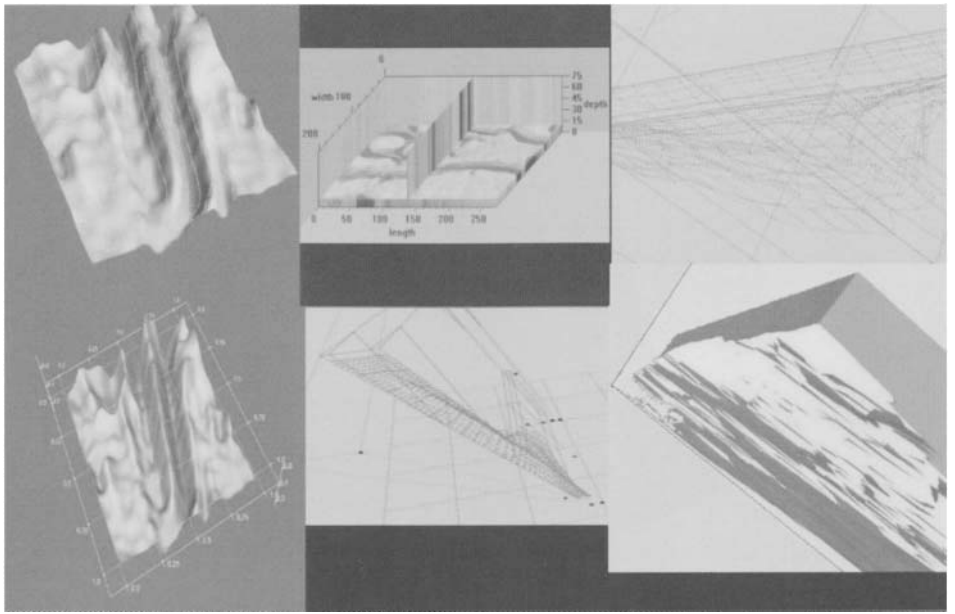

Figure 25.19. Localized corrosion network model and sampling sectors, (left top): MS Macrosystem Open GL, contours of the cracked and deformed oxide, (middle top): determination of orthogonal cut planes in the slicer before analysis, (right top): sampling sector by sector in the $x-y$ horizontal plane (slicer), (left bottom): MS Macrosystem Open GL, cracks in the deformed oxide, arbitrary graduation, (middle bottom): sampling sector by sector in the z vertical plane (slicer), (right bottom): global result for the chosen sector showing crevice distribution.

Figure 25.20. Views of analyzed sectors showing crevice evolution depending of its position (depth—z axis and horizontal $x-y$ axis displacements).

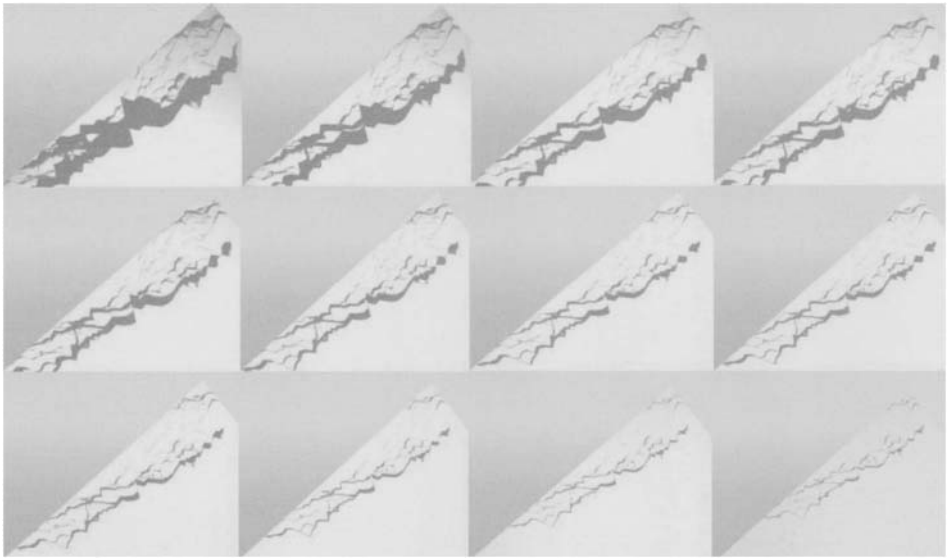

Figure 25.21. Views of analyzed sectors showing crevice evolution depending of its position (depth—z axis and horizontal $x-y$ axis displacements).

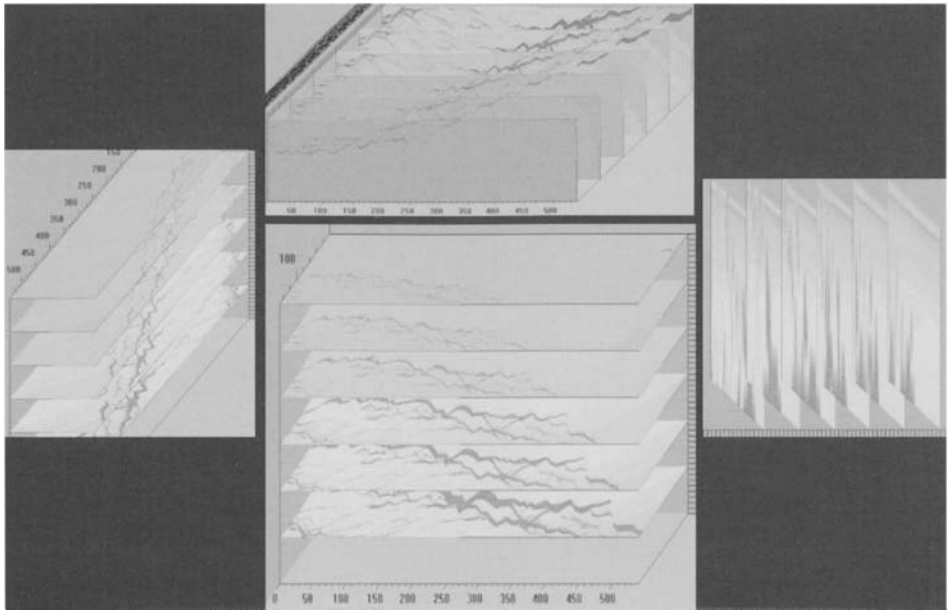

Figure 25.22. Cracking metal by tritium, arbitrary graduation, (top, left, bottom): crack distribution in metal, (right): ray intensity depending on crack concentration.

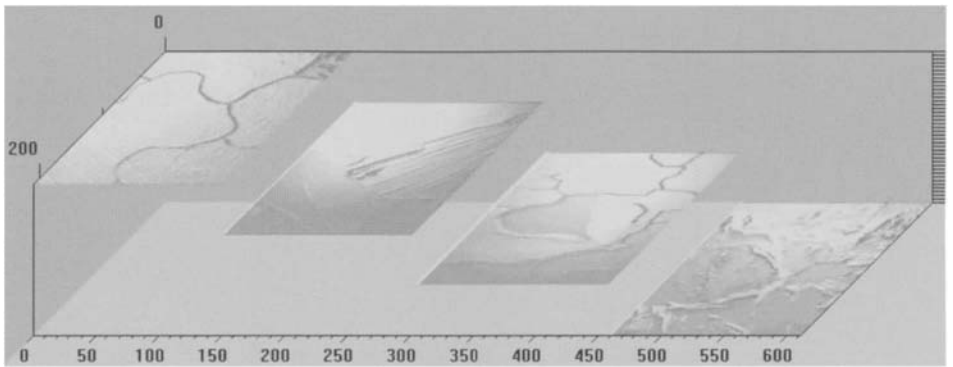

Figure 25.23. Views of analyzed depth—sectors showing localized corrosion evolution depending on tritium concentration in oxide and time, arbitrary graduation (in first cracked and crisped oxide, then exfoliation and walls formation).

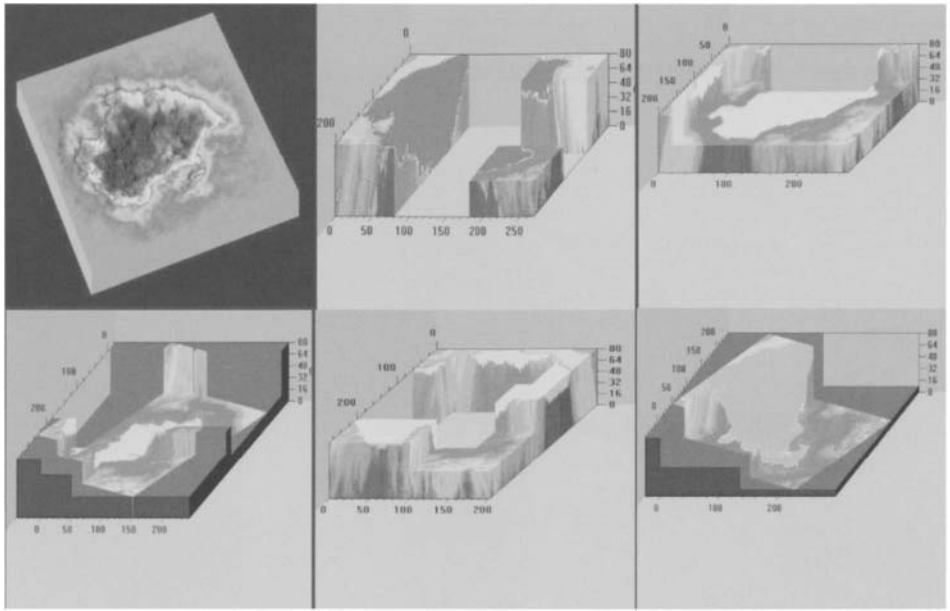

Figure 25.24. Localized corrosion network model and cut planes in the slicer, (left top): three dimensional topographic view showing a pit, (middle and right top, left, middle and right bottom): cut planes of the previous pit obtained by slicer.

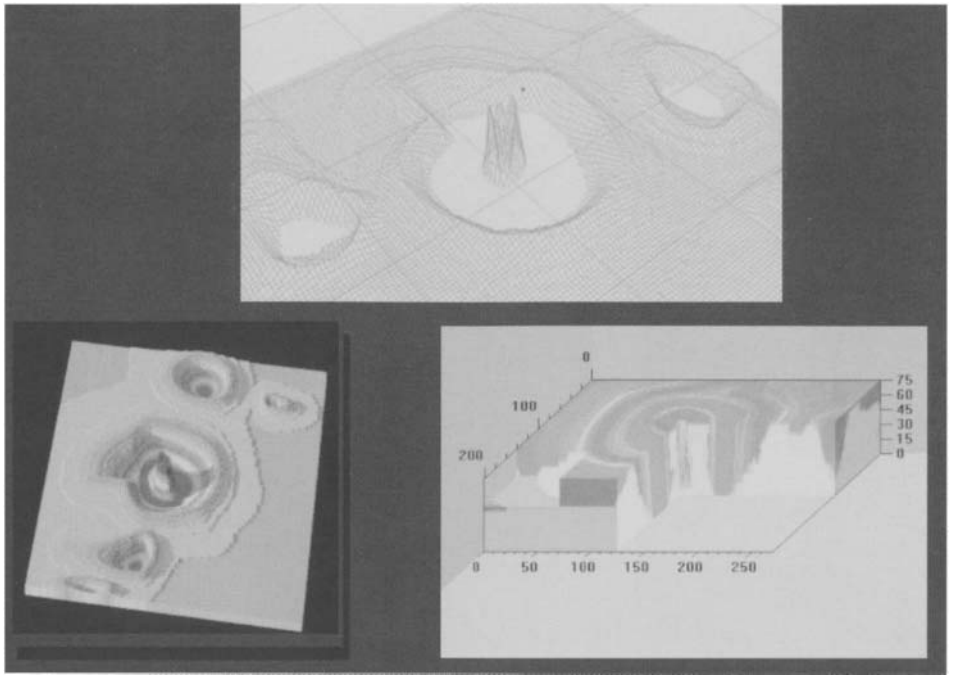

Figure 25.25. Oxide crystal centered into a pit, (top): pit and crystal in the vertex mode, (left bottom): three dimensional topographic view showing the pit and the crystal, (right bottom): cut plane of the pit obtained by slicer.

Chapter 26

FRACTAL REPRESENTATION FOR TRITIATED OXIDE

The illustrations that make up this chapter are available in colour on the (accompanying) CD-ROM.

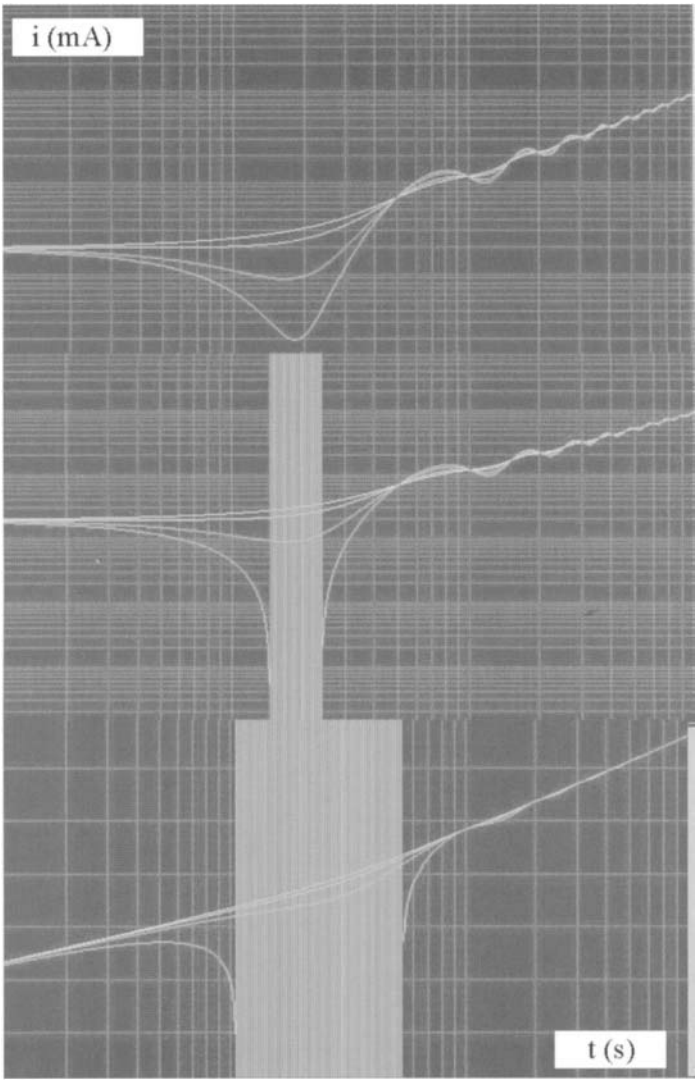

Figure 26.1. Erratic oscillations depending on time and aging.

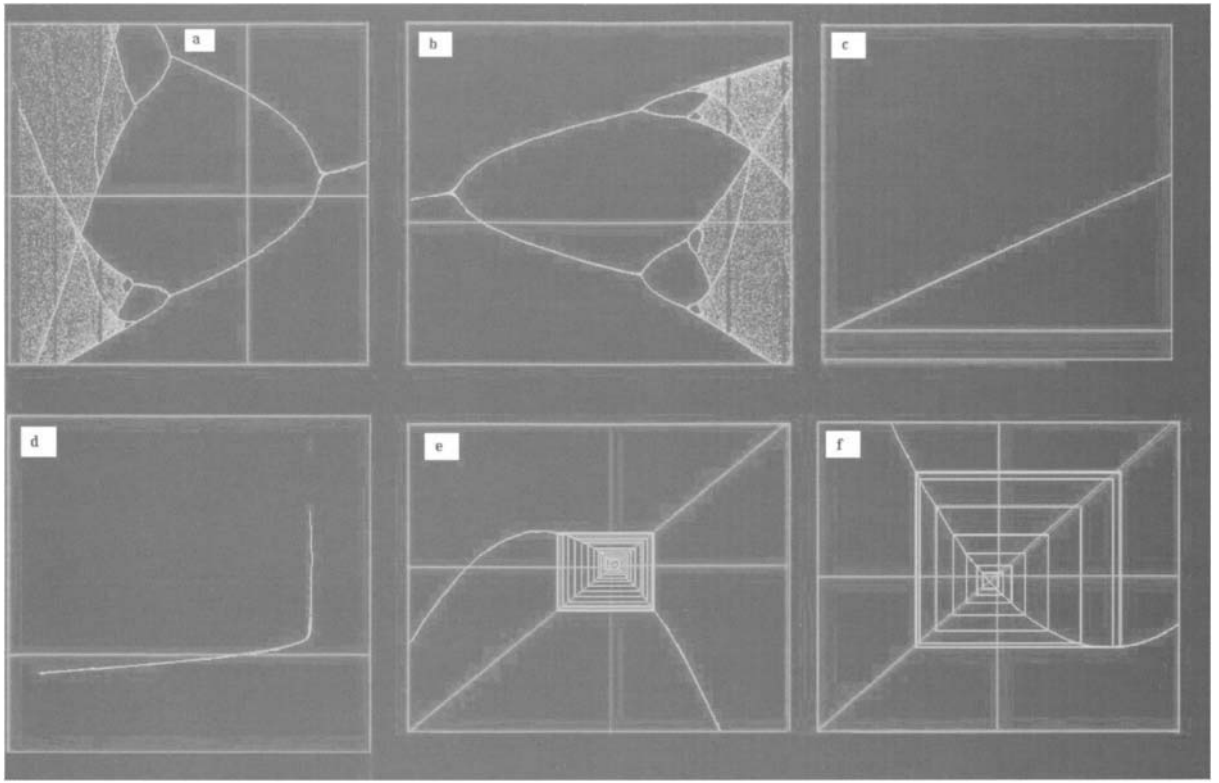

Figure 26.2. Quadratic and geometry chaos depending on corrosion along grains (b, e) and eruption (d) in oxide by excited holes (a, e, f) and time, x: arbitrary value of time, y: current.

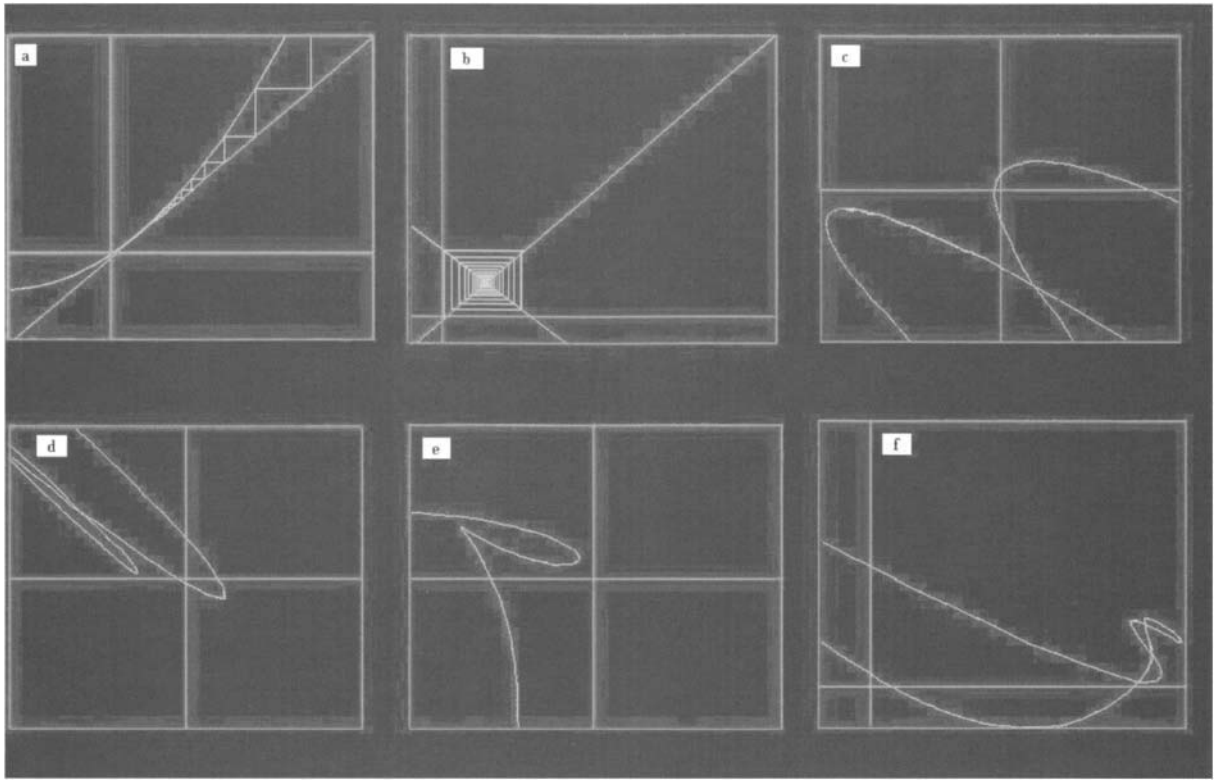

Figure 26.3. Geometry and 2D chaos depending on corrosion along grains (e) and eruption (a, f) in oxide by excited holes (b, c, d) and time, x: arbitrary value of time, y: current.

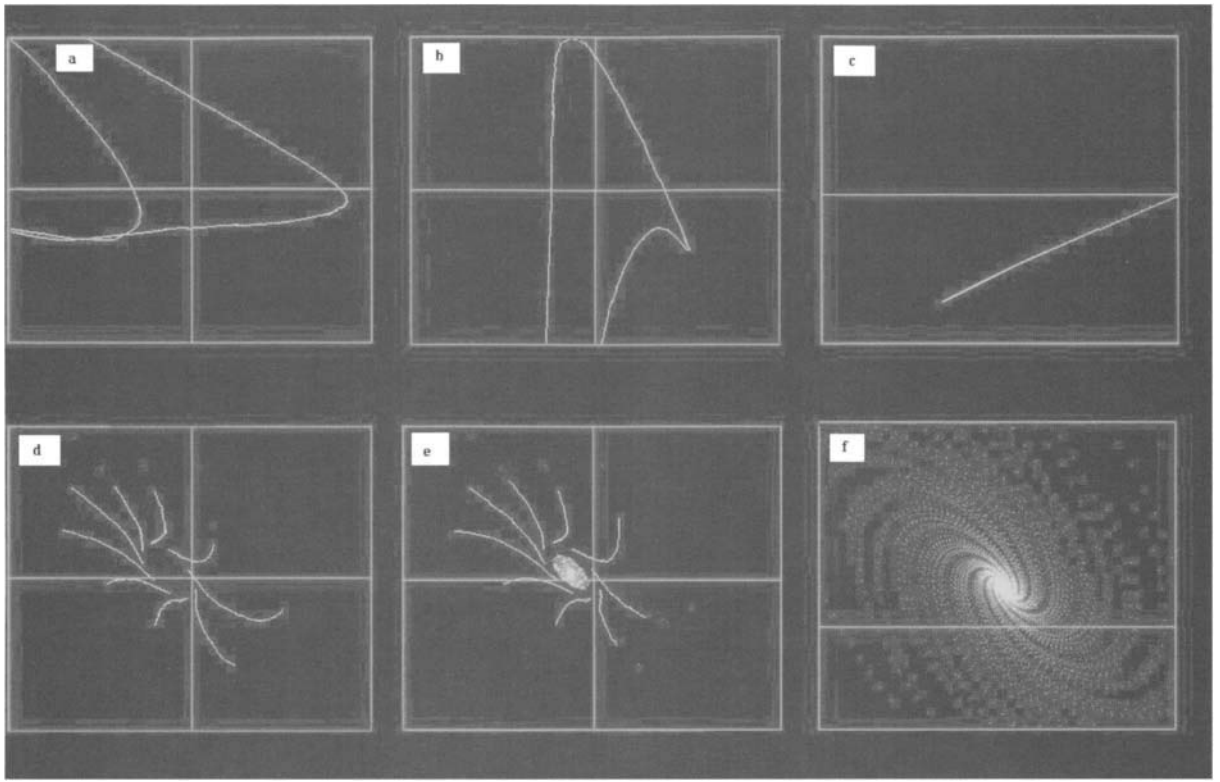

Figure 26.4. 2D chaos depending on corrosion along grains (b) and eruption (a) in oxide by excited holes (c, d, e, f) and time, x: arbitrary value of time, y: current.

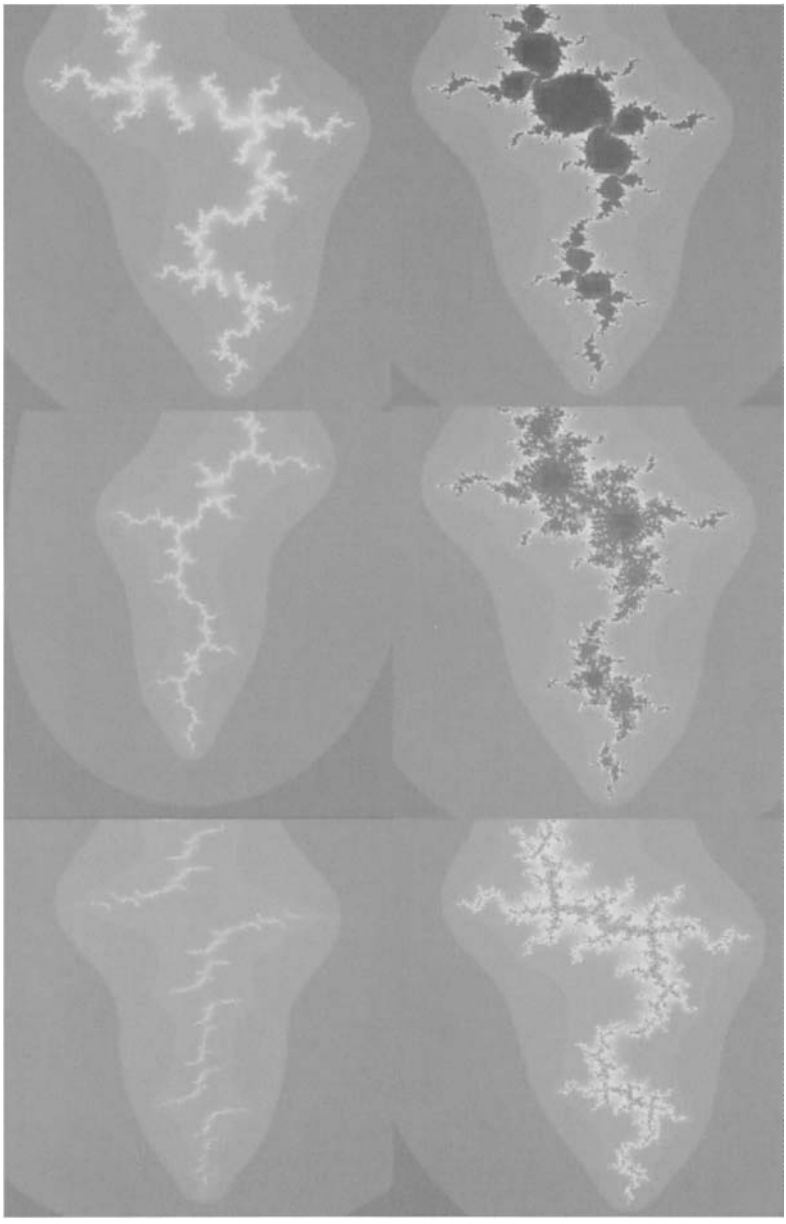

Figure 26.5. Bassin chaos depending on time and aging.

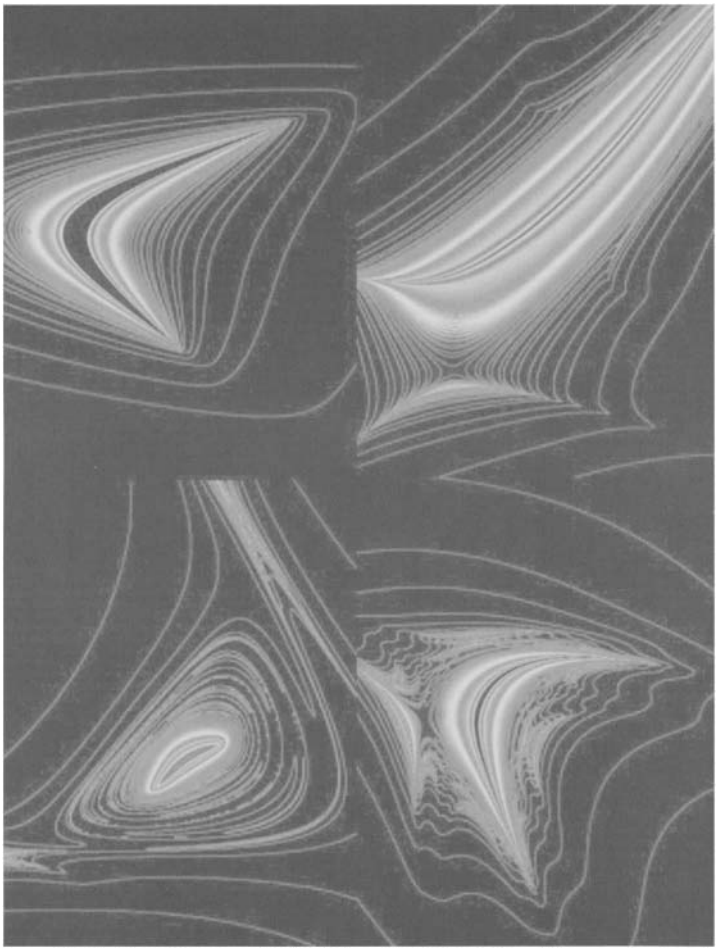

Figure 26.6. Fractal corrosion by blister obtained from dynamic mathematical system.

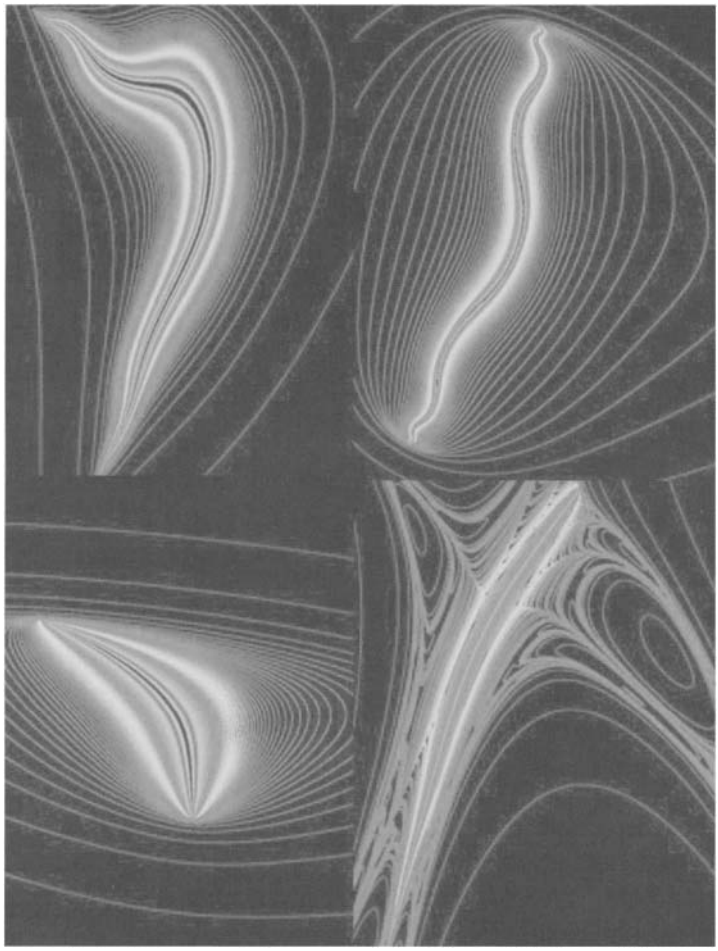

Figure 26.7. Fractal corrosion by blister.

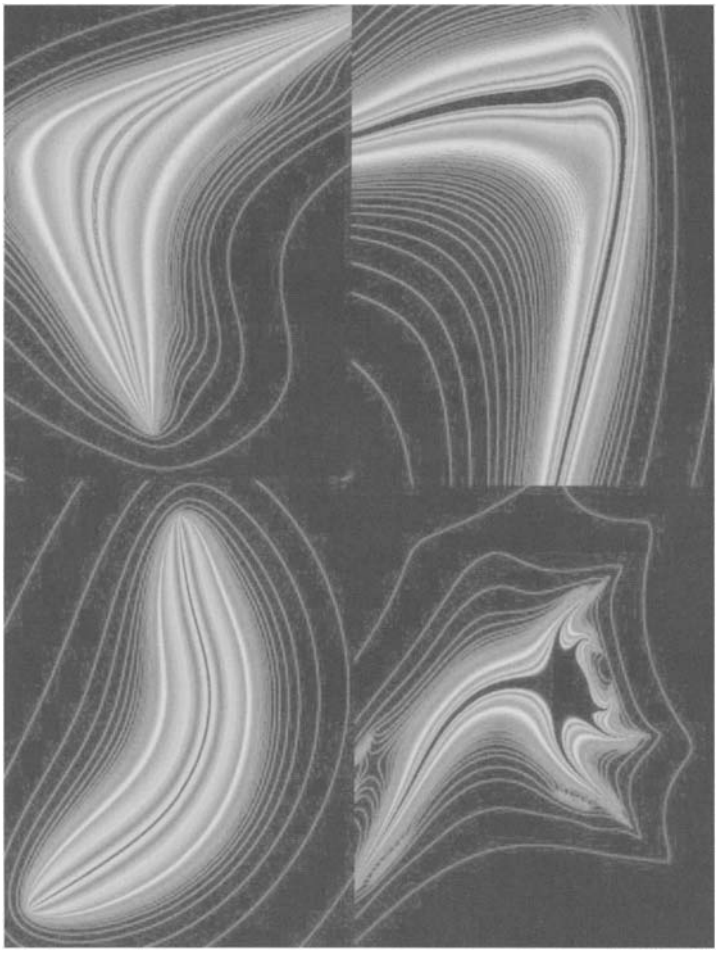

Figure 26.8. Fractal corrosion by blister.

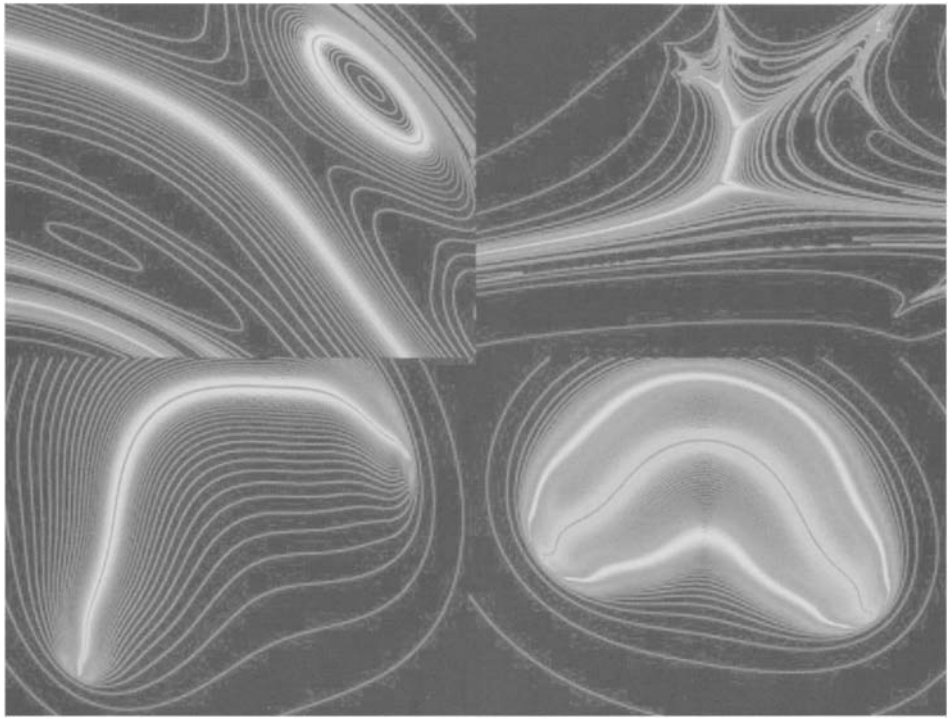

Figure 26.9. Fractal corrosion by blister.

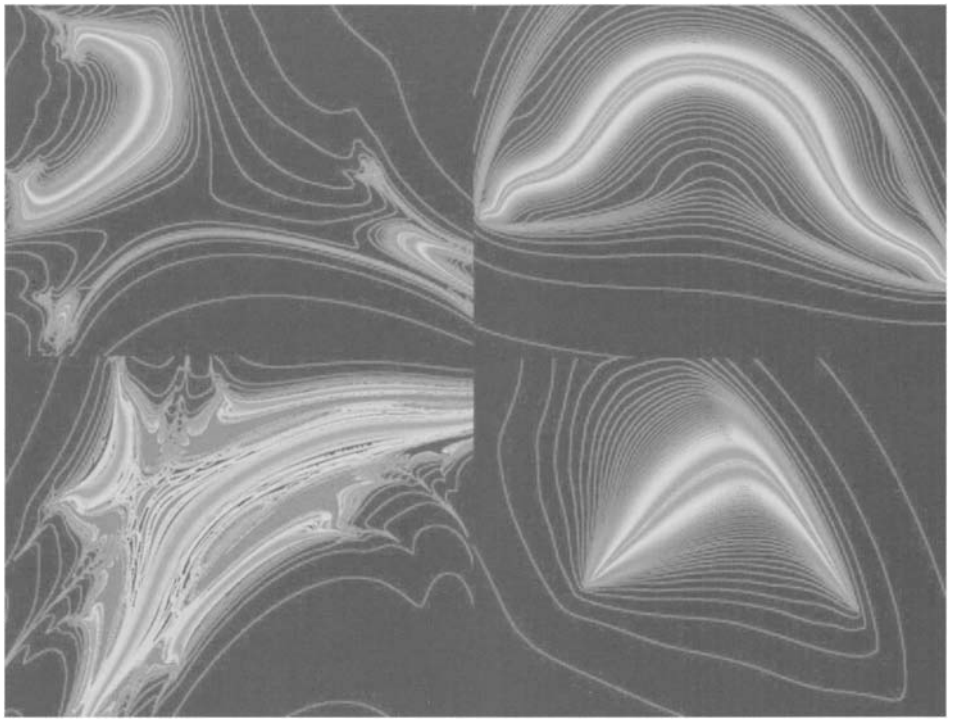

Figure 26.10. Fractal corrosion by blister.

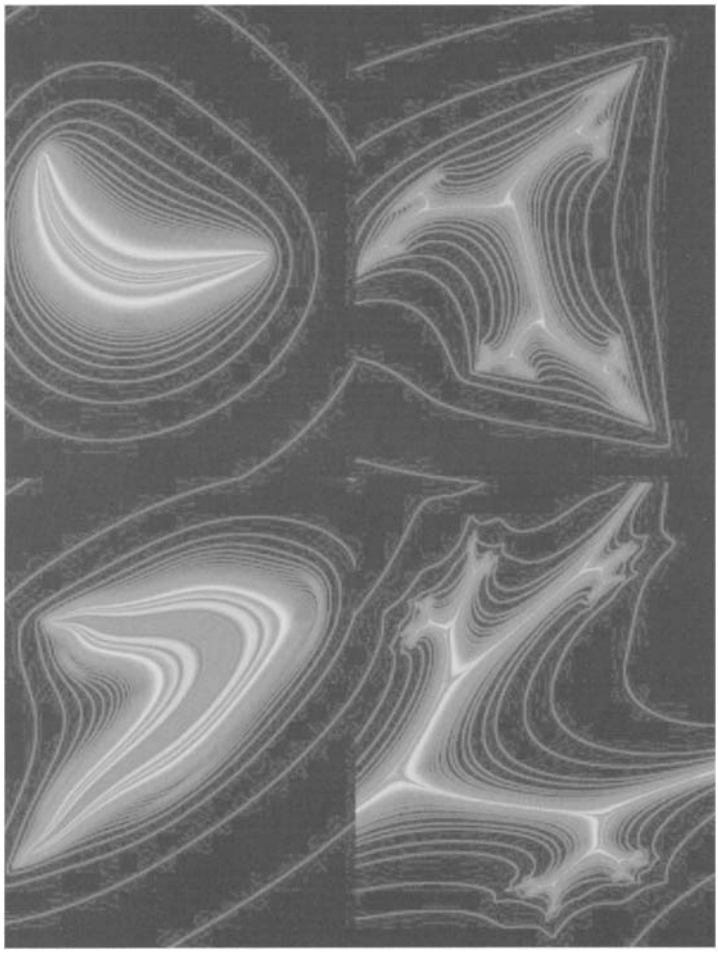

Figure 26.11. Fractal corrosion by blister and along the oxide crystals.

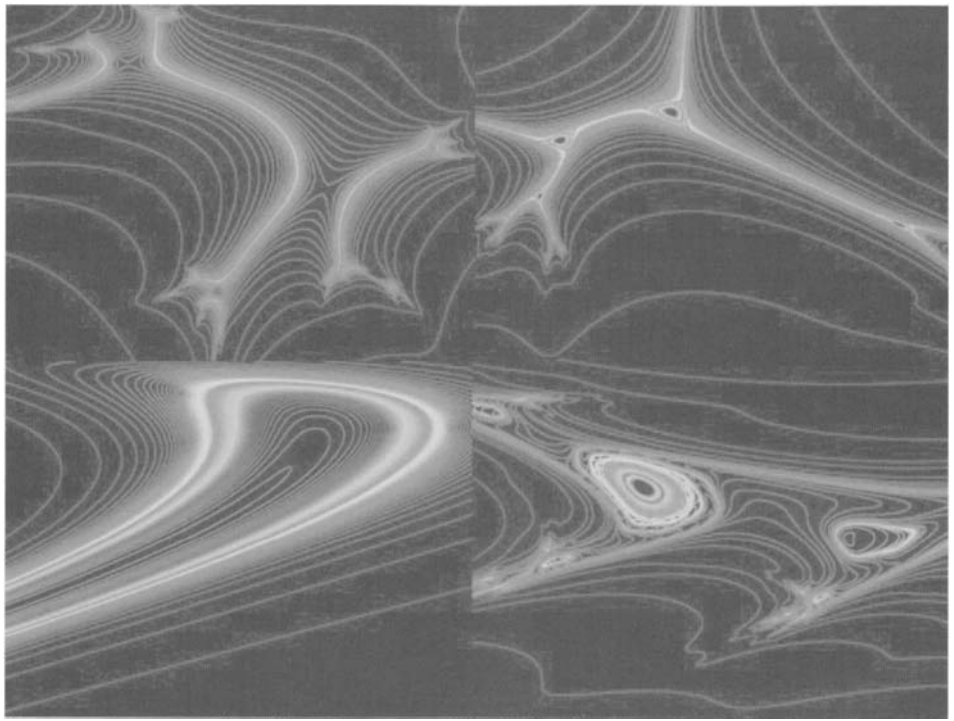

Figure 26.12. Fractal corrosion by void, blister and along the oxide crystals.

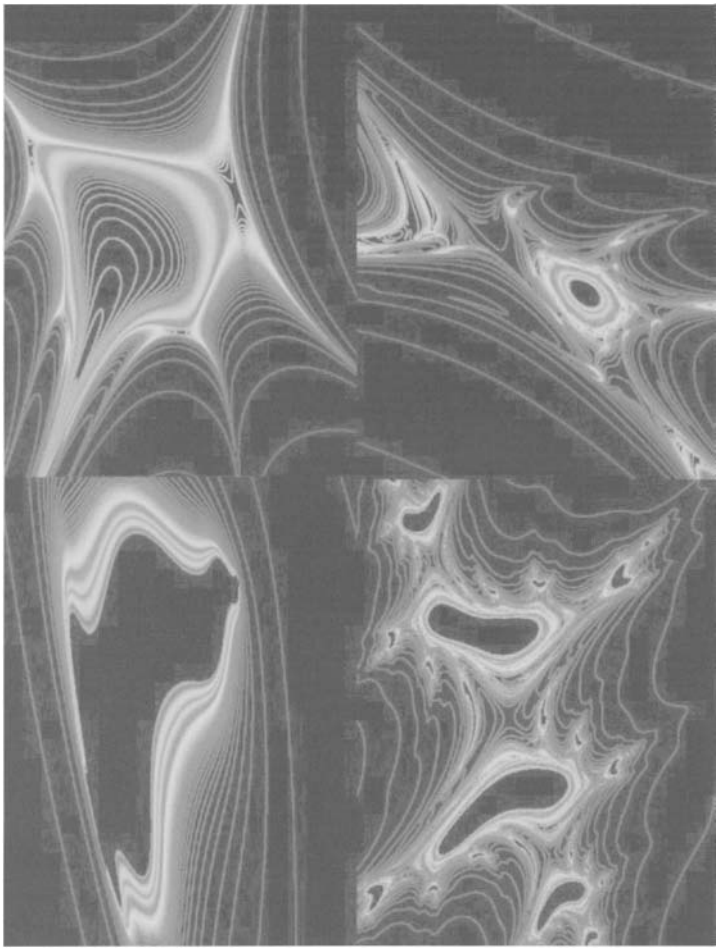

Figure 26.13. Fractal corrosion by void, blister and along the oxide crystals.

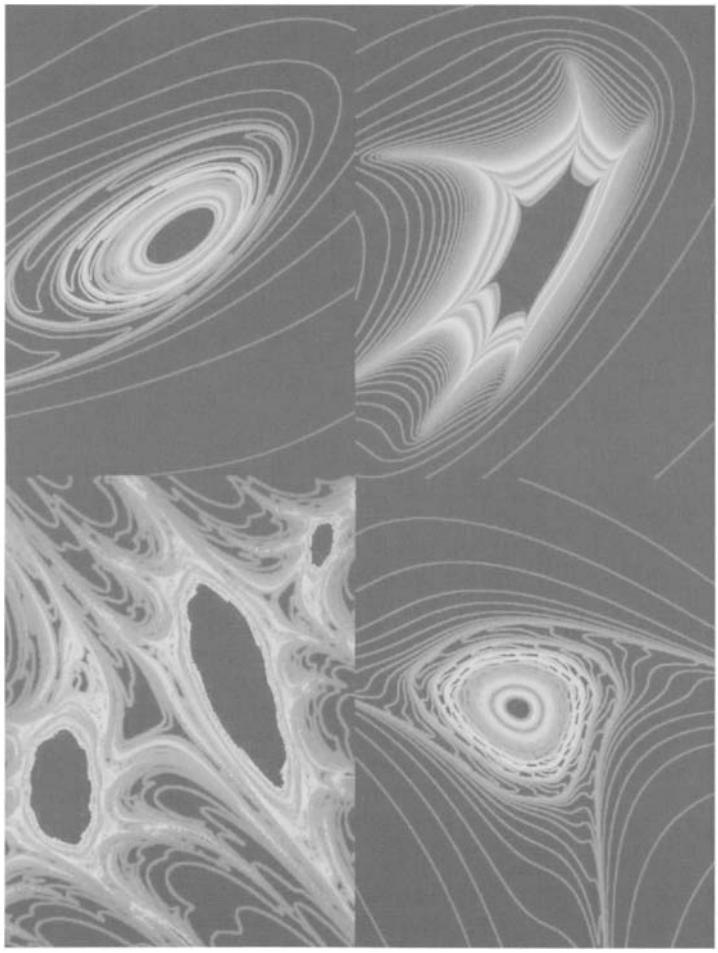

Figure 26.14. Fractal corrosion by exploded void before formation of blister.

This Page Intentionally Left Blank

REFERENCES

[1] S. Nakagawa, T. Shimokawa, Radiat. Phys. Chem. 63 (2002) 151.

[2] E. Janata, M. Kelm, B.G. Ershov, Radiat. Phys. Chem. 63 (2002) 157.

[3] T. Matsui, T. Takano, S. Takayama, M. Ito, I. Narisawa, Radiat. Phys. Chem. 63 (2002) 193.

[4] R. Mukundan, E.L. Brosha, S.A. Birdsell, A.L. Costello, F.H. Garzon, R.S. Willms, J. Electrochem. Soc. 146 (1999) 2184.

[5] P.H. Rebut, B.E. Keen, Fusion Technol. 11 (1987) 13.

[6] R. Dautray, La Fusion Thermonucléaire contrôlée par confinement magnétique. Collection du Commissariat à l'Energie Atomique, Série Scientifique, Masson, Paris (1987).

[7] R. Dautray, J.P. Watteau, La Fusion Thermonucléaire Inertielle par Laser. Collection du Commissariat à l'Energie Atomique, Série Scientifique, Eyrolles, Paris (1993).

[8] C.E. Johnson, J. Nucl. Mat. 270 (1999) 212.

[9] F. Abraham, P. Blouet, J.C. Boivin, M. Boncoeur, B. Rasneur, N. Roux, French Patent: FR2733975 (1997).

[10] B. Hircq, Proceedings of the 16th Symposium on Fusion Technology—London, 3–7 September 1990, eds B.E. Keen, M. Huguet, R. Hemsworth, Elsevier Science Publishers, Amsterdam, 161 (1991) 1.

[11] J. Chabot, J. Lecomte, C. Grumet, J. Sannier, Fusion Technol. 14 (1988) 614.

[12] B. Hircq, Proceedings of the 3th Symposium on Tritium Technology in Fission, Fusion and Isotopic Applications—Toronto, 1–6 May 1988, Fusion Technol. 424 (1988) 14.

[13] F. Botter, J. Gowman, J.L. Hemmerich, B. Hircq, R. Lässer, D. Leger, S. Tistchenko, M. Tschudin, Fusion Technol. 14 (1988) 562.

[14] R. Lässer, Tritium and Helium-3 in Metals, Springer Series in Materials Science 9, Springer-Verlag, New-York (1989).

[15] G. Bellanger, French patent n° FR2609352, foreign application: Canada (1988), EEC (1992), Japan (1988), USA (1989).

[16] G. Bellanger, P. Giroux, French patent n° FR2517663, foreign application: Canada (1985), EEC (1992), Japan (1990), USA (1984).

[17] S. Rosanvallon, G. Marbach, A.M. Brass, J. Chene, J.P. Daclin, 5th Symposium on the Nuclear Fusion, p4-7-26, organized by the Agency for New Technologies, Energy and Environment, Rome, 19–24 September, 1999.
[18] Th. Pelletier, P. Giroux, M. Maj, Fusion Technol. 21 (1992) 560.
[19] J. Bourdon, F. Mannone, A. Aytekin, I.S. Wheelton, Fusion Technol. 21 (1992) 352.
[20] J. Chabot, J. Montel, J. Sannier, Fusion Technol. 14 (1988) 933.
[21] R.A. Jalbert, Fusion Technol. 8 (1985) 2077.
[22] P.J. Allsop, J.A. Senohrabek, J.M. Miller, E.F. Romaniszyn, Fusion Technol. 21 (1992) 599.
[23] D.P. Wong, J.L. Hemmerich, J.J. Monahan, Fusion Technol. 21 (1992) 572.
[24] J. Chene, A.M. Brass, F.P. Ford, Corrosion sous Contrainte, Phénoménologie et Mécanismes, eds D. Desjardins, R. Oltra (Les Editions de Physique, Paris, 1992) p. 159, 833.
[25] T. Magnin, A. Chambreuil, J.P. Chateau, D. Delafosse, B. Bayle, or. 3, Eurocorr'96, session 4, International Conference on Corrosion–Deformation Interaction, Nice, 24–26 September, 1996.
[26] T. Cassagne, Corrosion sous Contrainte, Phénoménologie et Mécanismes, eds D. Desjardins, R. Oltra (Les Editions de Physique, Paris, 1992) p. 685.
[27] I.M. Bernstein, A.W. Thompson, p. 412, Int. Conferences of Mechanisms of Environment Sensitive Cracking of Materials, Surrey, U.K., 4–7 April, 1977.
[28] J. Sedriks, Corrosion of stainless steels, Wiley-Interscience, New York (1979).
[29] J.P. Audouard, Les Aciers Inoxydables, eds P. Lacombe, B. Baroux, G. Béranger (Les Editions de Physique, Paris, 1990) p. 255.
[30] H. Mazille, eds F. Dabosi, G. Béranger, B. Baroux, Corrosion Localisée (Les Editions de Physique, Paris, 1994) p. 383.
[31] P. Combrade, eds F. Dabosi, G. Béranger, B. Baroux, Corrosion Localisée (Les Editions de Physique, Paris, 1994) p. 241.
[32] G. Mankowski, C. Lemaître, H.H. Strehblow, eds F. Dabosi, G. Béranger, B. Baroux, Corrosion Localisée (Les Editions de Physique, Paris, 1994) p. 173.
[33] G. Béranger, J.C. Charbonnier, V. Cihal, eds F. Dabosi, G. Béranger, B. Baroux, Corrosion Localisée (Les Editions de Physique, Paris, 1994) p. 303.
[34] H. Pickering, C. Wagner, J. Electrochem. Soc. 114 (1967) 698.
[35] H. Uhlig, Corros. Sci. 19 (1979) 777.
[36] B. MacDougall, M.J. Graham, eds P. Marcus, J. Oudar, Corrosion Mechanisms in Theory and Practice (Marcel Dekker Inc., New York, 1995) p. 143.
[37] A. Petit, L. Vincent, eds F. Dabosi, G. Béranger, B. Baroux, Corrosion Localisée (Les Editions de Physique, Paris, 1994) p. 353.
[38] C. Duret-Thual, R. Oltra, J.C. Bosson, eds F. Dabosi, G. Béranger, B. Baroux, Corrosion Localisée (Les Editions de Physique, Paris, 1994) p. 321.
[39] J. Galland, P. Onthiaux, Corrosion Localisée (Les Editions de Physique, Paris, 1994) p. 361.
[40] P. Lacombe, G. Béranger, Les Aciers Inoxydables, eds P. Lacombe, B. Baroux, G. Béranger (Les Editions de Physique, Paris, 1990) p. 11.

[41] P. Berge, Corrosion sous Contraintes-Phénoménologie et Mécanismes, eds D. Desjardins, R. Oltra (Les Editions de Physique, Paris, 1992) p. 735.
[42] F.P. Ford, Corrosion sous Contraintes-Phénoménologie et Mécanismes, eds D. Desjardins, R. Oltra (Les Editions de Physique, Paris, 1992) p. 833.
[43] F.P. Ford, Corrosion sous Contraintes-Phénoménologie et Mécanismes, eds D. Desjardins, R. Oltra (Les Editions de Physique, Paris, 1992) p. 307.
[44] J.I. Dickson, S. Li, J.P. Bailon, Corrosion sous Contraintes-Phénoménologie et Mécanismes, eds D. Desjardins, R. Oltra (Les Editions de Physique, Paris, 1992) p. 425.
[45] A. Turnbull, Corrosion sous Contrainte-Phénoménologie et Mécanismes, eds D. Desjardins, R. Oltra (Les Editions de Physique, Paris, 1992) p. 75.
[46] F.P. Ford, P. Andresen, Corrosion sous Contrainte-Phénoménologie et Mécanismes, eds D. Desjardins, R. Oltra (Les Editions de Physique, Paris, 1992) p. 501.
[47] R.C. Newman, Corrosion Mechanisms in Theory and Practice, eds P. Marcus, J. Oudar (Marcel Dekker Inc., New York, 1995) p. 311.
[48] K.W. Andrews, J. Iron Steel Inst. 184 (1956) 44.
[49] J. Charles, International Congress Duplex stainless steels'91, 28–30 October 1991, Beaune, France, eds J. Charles, S. Bernhardsson (Les Editions de Physique, Paris, 1992) p. 3.
[50] J. Desestret, J. Charles, Les Aciers Inoxydables, eds P. Lacombe, B. Baroux, G. Béranger (Les Editions de Physique, Paris, 1990) p. 631.
[51] R. Oltra, C. Bouillot, T. Magnin, p. 32, Eurocorr'96, session 4, International Conference on Corrosion–Deformation Interaction, Nice, 24–26 September, 1996.
[52] P.J. Cunat, Les Aciers Inoxydables, eds P. Lacombe, B. Baroux, G. Béranger (Les Editions de Physique, Paris, 1990) p. 795.
[53] J.C. Lippold, I. Varol, W.A. Baeslack, International Congress Duplex Stainless Steels'91, Beaune, France, 28–30 octobre, 1991, eds J. Charles, S. Bernhardsson (Les Editions de Physique, Paris, 1992) p. 383.
[54] L. van Nassau, H. Meelker, J. Hilkes, International Congress Duplex Stainless Steels'91, Beaune, France, 28–30 octobre, 1991, eds J. Charles, S. Bernhardsson, (Les Editions de Physique, Paris, 1992) p. 303.
[55] B. Bonnefois, J. Charles, P. Soulignac, International Congress Duplex Stainless Steels'91, Beaune, France, 28–30 octobre, 1991, eds J. Charles, S. Bernhardsson (Les Editions de Physique, Paris, 1992) p. 469.
[56] T.G. Gooch, International Congress Duplex Stainless Steels'91, Beaune, France, 28–30 octobre, 1991, eds J. Charles, S. Bernhardsson (Les Editions de Physique, Paris, 1992) p. 325.
[57] J. Bourrat, C. Goux, Les Aciers Inoxydables, eds P. Lacombe, B. Baroux, G. Béranger (Les Editions de Physique, Paris, 1990) p. 679.
[58] B.I. Gromov, M.V. Erofeev, A.A. Kalin, V.A. Moiseev, Soviet. Tech. Phys. Lett. 16 (1990) 301.
[59] O.B. Naimark, V.V. Belyaev, Probl. Prochn. (in Russian) 7 (1989) 26.

[60] V.I. Averin, V.I. Gromov, M.V. Erofeev, A.A. Kalin, M.S. Kuznetsov, V.A. Moiseev, V.P. Ostafitchuk, E.P. Pitchurin, Bulletin of the Academy of Sciences of the U.S.S.R. 55 (1991) 1409.
[61] V.V. Belyaev, V.V. Silberschmidt, O.B. Naimark, L.V. Filimonova, Proceedings on the Kinetics of Polymorphic Transformations in Metals under High Pressure in Detonation—All Union Symposium on Combustion and Explosion, 153, p. 66, Tchernogolovka (1989) (in Russian).
[62] V.V. Silberschmidt, O.B. Naimark, L.V. Filimonova, Phys. Met. Metallogr. 69 (1990) 32.
[63] V.V. Silberschmidt, K. Tanaka, Memoirs of Tokyo Metropolitan Institute of Technology 7 (1993) 95.
[64] A.X. Clauer, J.H. Holbrook, B.P. Fairand, Shock Waves and High-Strain-Rate Phenomena in Metals, eds M.A. Meyers, L.E. Murr (Plenum Press, New York, 1981) p. 675.
[65] J.P. Romain, M. Hallodin, M. Gerland, F. Cottet, L. Marty, Schock Waves in Condensed Matter, eds S.C. Schmidt, N.C. Holmes (Elsevier Science Publishers, Oxford, 1988) p. 787.
[66] W.D. Manly, W.H. Bridges, Nickel and its alloys, Reactor Handbook, vol. 1, Materials, ed. C.R. Tipton (Interscience Publishers, Inc., New York, 1960) p. 636.
[67] P.M. Scott, Corrosion 56 8 (2000) 771.
[68] H.J. Grabke, Corrosion 56 8 (2000) 801.
[69] P. Kritzer, N. Boukis, E. Dinjus, Corrosion 56 11 (2000) 1093.
[70] M. Casales, M.A. Espinoza-Medina, A. Martinez-Villafañe, V.M. Salinas-Bravo, Corrosion 56 11 (2000) 1133.
[71] P. Kritzer, N. Boukis, E. Dinjus, Corrosion 56 3 (2000) 265.
[72] W.C. Moshier, C.M. Brown, Corrosion 56 3 (2000) 307.
[73] W.D. Manly, W.H. Bridges, Cobalt-base alloys, Reactor Handbook, vol. 1, Materials, ed. C.R. Tipton (Interscience Publishers, Inc., New York, 1960) p. 520.
[74] R. Tricot, Le Zirconium, Matériau pour Industries Chimiques, eds G. Béranger, P. Lacombe, R. Tricot (Les Editions de Physique, Paris, 1992) p. 7.
[75] G. Béranger, Le Zirconium, Matériau pour Industries Chimiques, eds G. Béranger, P. Lacombe, R. Tricot (Les Editions de Physique, Paris, 1992) p. 93.
[76] J. Schmuck, Le Zirconium, Matériau pour Industries Chimiques, eds G. Béranger, P. Lacombe, R. Tricot (Les Editions de Physique, Paris, 1992) p. 219.
[77] J.R. Keeler, Chromium and its Alloys, Reactor Handbook, vol. 1, Materials, ed. C.R. Tipton (Interscience Publishers, Inc., New York, 1960) p. 547.
[78] D.J. Maykuth, R.I. Jaffee, J.M. Blocher, The Effect of Metal Purity on Chromium-Base Alloys, WADC-TR-56-33 (Battelle Memorial Institute, 1956).
[79] F. Armanet, P. Moulin, A.M. Huntz, A. Vejux, G. Béranger, Mém. Sci. Rev. Met. 2 (1979) 32.
[80] P. Moulin, F. Armanet, G. Béranger, P. Lacombe, Mém. Sci. Rev. Met. 3 (1977) 60.
[81] J. Moreau, J. Benard, C. R. Acad. Sci., Paris, p. 1659 (1954).

[82] N. Jallerat, S. Mischler, D. Landolt, Symp. Modifications of Passive Films, 1993, Paris, France (Institute of Materials, London, 1994) p. 26.
[83] M.M. Hukovic, S. Omanovic, R. Babic, V51, 45th Annual Meeting of the International Society of Electrochemistry, Porto, Portugal, 1994, University of Porto.
[84] J. Hampikian, p. 66, conf. Materials week, TMS and ASM, Chicago, 2–6 October, 1994.
[85] C.E. Lowell, Oxid. Met. 7 (1973) 114.
[86] J.C. Pivin, C. Roques-Carmes, P. Lacombe, Mém. Sci. Rev. Mat. 3 (1977) 75.
[87] P. Lacombe, B. Baroux, G. Béranger, Les Aciers Inoxydables (Les Editions de Physique, Paris, 1990).
[88] D.S. Bloom, N.J. Grant, Trans. Am. Inst. Mining Met. Engrs. 191 (1951) 1009.
[89] E.P. Abrahamson, N.J. Grant, Ductile Chromium, chapter 21, The Chromium-Nickel-Nitrogen Ternary Diagram (American Society for Metals, Cleveland, 1957).
[90] B. Elsener, A. Rota, H. Böhni, Electrochemical Methods in Corrosion Research Proceedings, published by Mater. Sci. Forum 44 (1989) 29.
[91] J. Piippo, B. Elsener, H. Böhni, Surface and Coating Technology 61 (1993) 43.
[92] I. Milosev, H.H. Strehblow, B. Navinsek, II25, 45th Annual Meeting of the International Society of Electrochemistry, Porto (1994), University of Porto.
[93] F.A. Lewis, The Palladium Hydrogen System (Academic Press, New York, 1967).
[94] N.A. Galaktionowa, Hydrogen-Metal Systems databook, ed. A. Abraham (Ordentlich, Holon, Israel, 1981).
[95] P.L. Levine, K.E. Weale, Trans. Faraday Soc. 56 (1960) 357.
[96] T.J. Tiedema, B.C. de Jong, W.G. Burgers, Proc. K. Ned. Akad. Wet. 63 (1960) 422.
[97] A.J. Maeland, Gibb, J. Phys. Chem. 65 (1961) 1270.
[98] H. Numata, I. Ohno, Fusion Technology 28 (2000) 205.
[99] H. Brodowsky, E. Poeschel, Z. Phys. Chem. 44 (1965) 143.
[100] G. Bellanger, J.J. Rameau, J. Nucl. Mat. 228 (1996) 24.
[101] M. Pourbaix, Atlas of Electrochemical Equilibrium in Aqueous Solution, Pergamon Press (1966).
[102] P.E. Morris, R.C. Scarberry, Corrosion 26 (1970) 169.
[103] A.J. Bard, L.R. Faulker, Electrochemical Methods. Fundamentals and Applications, Wiley, New York (1980).
[104] C.-C. Huang, W.-T. Tsai, J.-T. Lee, Mater. Sci. and Engineering A196 (1995) 243.
[105] M.W. Breiter, Electrochim. Acta 15 (1970) 1145.
[106] Kerrec, D. Devilliers, H. Groult, M. Chemla, Electrochim. Acta 40 (1995) 719.
[107] P. Schmuki, M. Büchler, S. Virtanen, H. Böhni, J. Electrochem. Soc. 142 (1995) 3336.
[108] E.B. Castro, J.R. Vilche, Electrochim. Acta 38 (1993) 1567.
[109] A.M.P. Simoes, M.G.S. Ferreira, B. Rondot, M. da Cunha Belo, J. Electrochem. Soc. 137 (1990) 1.
[110] R.-H. Song, S.-I. Pyun, R.A. Oriani, J. Appl. Electrochem. 21 (1991) 181.
[111] G. Barral, F. Njanjo-Eyoke, S. Maximovitch, Electrochim. Acta 40 (1995) 17.
[112] F.M. Al Kharafi, W.A. Badawy, Electrochim. Acta 40 (1995) 1811.

[113] B.H. Erné, D. Vanmaekelbergh, J.J. Kelly, J. Electrochem. Soc. 143 (1996) 305.
[114] H.H. Strehblow, 'Mechanisms of Pitting Corrosion', Corrosion Mechanisms in Theory and Practice, eds P. Marcus, J. Oudar, Marcel Dekker, New York, p. 201 (1995).
[115] C.Y. Chao, L.F. Lin, D.D. Macdonald, J. Electrochem. Soc. 128 (1981) 1187.
[116] C.Y. Chao, L.F. Lin, D.D. Macdonald, J. Electrochem. Soc. 128 (1981) 1194.
[117] J.R. Macdonald, Impedance Spectroscopy, Wiley, New York (1987).
[118] K. Jüttner, Electrochim. Acta 35 (1990) 1501.
[119] C.-N. Cao, Electrochim. Acta 35 (1990) 5.
[120] Z. Stoynov, Electrochim. Acta 38 (1993) 14.
[121] P. Agarwal, M.E. Orazem, L.H. Garcia-Rubio, Electrochemical Impedance, eds Scully, Silverman, Kendig, ASTM-1993, Philadelphia (USA), p. 115.
[122] C. Gabrielli, M. Keddam, H. Takenouti, Electrochemical Impedance, eds Scully, Silverman, Kendig, ASTM-1993, Philadelphia (USA), p. 140.
[123] B.J. Dougherty, S.I. Smedley, Electrochemical Impedance, eds Scully, Silverman, Kendig, ASTM-1993, Philadelphia (USA), p. 154.
[124] J.M. Bastidas, J.L. Polo, C.L. Torres, E. Cano, Corros. Sci. 43 (2001) 269.
[125] F.P. Ford, Corrosion sous constraintes, eds D. Desjardins, R. Oltra, Bombannes, Physique, Les Ulis, France (1992).
[126] L. Ma, J.E. Vitt, J. Electrochem. Soc. 146 11 (1999) 4152.
[127] G. Bourceanu, V. Melnig, J. Vatamanu, R. Vasiliu, Electrochim. Acta 43 9 (1998) 1031.
[128] E.N. Lorenz, The Essence of Chaos, University of Washington Press, U.S.A., 1993, p. 148.
[129] O.E. Rössler, Phys. Lett. 57 5 (1976) 397.
[130] J.C. Sprott, Phys. Rev. 50 2 (1994) R647.
[131] S.M. Seltzer, M.J. Berger, Energy Loss Straggling of Protons and Mesons, Penetration of Charged Particles in Matter, Nuclear Science Series 39, Nat. Academy of Sciences, Washington DC, 1964.
[132] A. Causey, L.M. Steck, J. Nucl. Mat. 122 (1984) 1518.
[133] J.D. Braun, G.L. Downs, G.W. Powell, Metallography 4 (1971) 231.
[134] T. Hirabayashi, M. Saeki, E. Tachikawa, Proceedings of the international symposium on fusion reactor blanket and fuel cycle technology, p. 213, Takahashi, Tanaka Satoru, Tokyo (1987).
[135] F.M. Kimmerle, J. Chevalet, J. Electroanal. Chem. 21 (1969) 237.
[136] Y. Sakamoto, H. Katayama, 3° Congrès international hydrogène et matériaux, Science et Industrie, 359, Paris (1982).
[137] G. Bellanger, E. Laviron, J. Nucl. Mat. 189 (1992) 14.
[138] D.A. Vaughan, D.I. Phales, Met. Eng. Quart. 8 (1965) 39.
[139] M.R. Louthan, J.A. Donovan, G.R. Caskey, Nuclear Technol. 26 (1975) 192.
[140] T. Hirabayashi, M. Saeki, E. Tachikawa, Int. Symp. Fusion Reactor Blanket and Fuel Cycle Technology, Tokai-mura, Japan, October 27 (1986).
[141] W.G. Burns, P.B. Moore, Radiat. Effects 30 (1976) 233.
[142] T. Hirabayashi, M. Saeki, J. Nucl. Mat. 120 (1984) 309.

[143] J.H. Austin, T.S. Elleman, K. Verghese, J. Nucl. Mat. 48 (1973) 307.
[144] P. Tison, J.P. Fidelle, CEA-N-2231 report, Commissariat à l'Energie Atomique (1981).
[145] P. Tison, Thèse de Doctorat, Paris 6 (1983).
[146] M.R. Louthan, G.R. Caskey, D.E. Rawl, Conf. Radiation Effects and Tritium Technology for Fusion Reactors, Gatlinburg, Tennessee, September 30–October 3 (1975).
[147] G. Bellanger, Thèse de Doctorat, Dijon (1989).
[148] I. Olefjord, B. Brox, U. Jelvestam, J. Electrochem. Soc. 132 (1985) 12.
[149] C. Ho, I.D. Raistrick, R.A. Huggins, J. Electrochem. Soc. 127 (1980) 343.
[150] S. Bourkane, C. Gabrielli, F. Huet, M. Keddam, Electrochim. Acta 38 (1993) 1023.
[151] C. Lemaignan, J. Nucl. Mat. 187 (1992) 122.
[152] T.E. Perez, A. Funes, J. Ovejero-Garcia, Third International Congress of Hydrogen, conf. I14, vol. 2, 923, Paris, France (1982).
[153] J.A. Brooks, A.J. West, Metal. Trans. A 12A (1981) 213.
[154] T.E. Perez, M. Solari, J. Ovejero-Garcia, Miami International Symposium on Metal-Hydrogen Systems (1981).
[155] A. Bruggeman, M. Snykers, P. de Regge, Fusion Technol. 14 (1988) 828.
[156] J.K. Linacre, W.R. Marsh, Chemistry Division, Atomic Energy Research Establishment, Harwel, Report R 10027 (1981).
[157] M.R. Tarasevich, A. Sadkowski, E. Yeager, Comprehensive Treatise of Electrochemistry, 301, vol. 7, Kinetics and Mechanisms of Electrode Processes, eds J.O'M. Bockris, B.E. Conway, E. Yeager, S.U.M. Khan, R.E. White, Plenum Press, New York, 1983.
[158] W.H. Smyrl, Comprehensive Treatise of Electrochemistry, 97, vol. 4, Electrochemical Materials Science, eds J.O'M. Bockris, B.E. Conway, E. Yeager, R.E. White, Plenum Press, New York, 1981.
[159] S. Zecevic, D.M. Drazic, S. Gojkovic, Electrochim. Acta 36 (1991) 5.
[160] R.S. Glass, G.E. Overturf, R.A. Van Konynenburg, R.D. McCright, Corros. Sci. 26 (1986) 577.
[161] D.W. Shoesmith, S. Sunder, J. Nucl. Mat. 190 (1992) 20.
[162] N. Sato, G. Okamoto, Comprehensive Treatise of Electrochemistry, 193, vol. 4, Electrochemical Materials Science, eds J.O'M. Bockris, B.E. Conway, E. Yeager, R.E. White, Plenum Press, New York, 1981.
[163] J.A. Cox, R.W. Jaworski, Anal. Chem. 61 (1989) 2176.
[164] E. Bednarkiewicz, Z. Kublik, Electrochim. Acta 24 (1979) 121.
[165] V.M. Berenblit, V.A. Guskow, Zh. Prikl. Khim. 46 (1973) 2111.
[166] P. Lorbeer, W.J. Lorenz, Electrochim. Acta 25 (1980) 375.
[167] Z. Galus, Fundamentals of Electrochemical Analysis, eds P.W.N. Warszawa, E. Horwood, Chichester, 1976, p. 316.
[168] M.R. de Tacconi, A.J. Calandra, A.J. Arvia, Electrochim. Acta 18 (1973) 571.
[169] R.S. Schrebler Guzman, J.R. Vilche, A.J. Arvia, J. Appl. Electrochem. 11 (1981) 551.

[170] F. Beck, R. Kauss, Oberst, Electrochim. Acta 30 (1985) 173.
[171] C. Sarasola, T. Fernandez, Y. Jimenez, Electrochim. Acta 33 (1988) 1295.
[172] G. Bellanger, J. Nucl. Mat. 210 (1994) 63.
[173] O. Gebhardt, Electrochim. Acta 38 (1993) 633.
[174] D. Garriga Majo, P. Vaillant, J.C. Van Duysen, conf. PWR/3, proc. 12th Scandinavian Corrosion Congress and Eurocorr'92, Uusimaa Oy, Porvoo, Finland (1992).
[175] M.O. Speidel, R. Magdowski, proc. Corrosion-Deformation Interactions, Physique, Les Ulis, France (1992).
[176] M.-Y. Chang, G.-P. Yu, J. Nucl. Mat. 202 (1993) 145.
[177] V.S. Muralidharan, M. Veerashanmugamani, C. Selvanayagi, Transactions SAEST 22 1 (1987).
[178] G. Bellanger, J. Nucl. Mat. 217 (1994) 187.
[179] C.-C. Huang, W.-T. Tsai, J.-T. Lee, Mater. Sci. and Engineering A190 (1995) 199.
[180] W.A. Badawy, Kh.M. Ismail, Electrochim. Acta 38 (1993) 2231.
[181] Yu.V. Pleskow, Comprehensive Treatise of Electrochemistry, vol. 1, The Double Layer, eds J.O'M. Bockris, B.E. Conway, E. Yeager, Plenum Press, New York (1981).
[182] J.P. Randin, Comprehensive Treatise of Electrochemistry, vol. 4, Electrochemical Materials Science, eds J.O'M. Bockris, B.E. Conway, E. Yeager, Plenum Press, New York (1984).
[183] J. Bessone, L. Karakaya, P. Lorbeer, W.J. Lorenz, Electrochim. Acta 22 (1977) 1147.
[184] V.S. Muralidharan, M. Veerashanmugamani, C. Selvanayagi, Transactions of the SAEST 22 (1987) 55.
[185] J. Titz, G.H. Wagner, W.J. Lorenz, Electrochim. Acta 37 (1992) 2309.
[186] J.-Y. Zou, D.-T. Chin, Electrochim. Acta 32 (1987) 1751.
[187] J.-Y. Zou, D.-T. Chin, Electrochim. Acta 33 (1988) 477.
[188] D.D. Mac Donald, B. Roberts, Electrochim. Acta 23 (1978) 781.
[189] A.J. Calandra, N.R. De Tacconi, R. Pereiro, A.J. Arvia, Electrochim. Acta 19 (1974) 901.
[190] F. Mansfeld, Electrochim. Acta 38 (1993) 1891.
[191] M. Aubay, E. Lojou, J. Electrochem. Soc. 141 (1994) 865.
[192] R.D. Armstrong, D. Wright, Electrochim. Acta 38 (1993) 1799.
[193] F. Deflorian, L. Fedrizzi, P.L. Bonora, Electrochim. Acta 38 (1993) 1609.
[194] F. Deflorian, L. Fedrizzi, A. Locaspi, P.L. Bonora, Electrochim. Acta 38 (1993) 1945.
[195] A.J. Griffin, F.R. Brotzen, C.F. Dunn, J. Electrochem. Soc. 141 (1994) 3473.
[196] S. Haruyama, M. Asari, T. Tsuru, Corrosion Protection by Organic Coatings, eds M. Kendig, H. Leidhaiser, Proc. vol. 87-2, p. 197, Electrochemical Society, Pennington, NJ (1987).
[197] G. Bellanger, J.J. Rameau, Electrochim. Acta 40 (1995) 2519.
[198] A.M. Farvaque-Béra, S. Leistikow, J. Nucl. Mat. 185 (1991) 1.
[199] P.J. Kinlen, D.C. Silverman, J. Electrochem. Soc. 140 (1993) 3140.

[200] H.S. Isaacs, Localized Corrosion Congres, p. 158, vol. 3, eds R. Staechle, B.F. Brown, J. Kruger, A. Agrawal, Nace, Houston (1974).
[201] I. Milosev, H.H. Strehblow, B. Navinsek, 45th Annual Meeting of the International Society of Electrochemistry, Porto (1994), University of Porto.
[202] C.B. In, S.P. Kim, Y.I. Kim, I.H. Kuk, S.S. Chun, W.J. Lee, J. Nucl. Mat. 211 (1994) 223.
[203] B. Siemensmeyer, K. Bade, J.W. Schultze, Ber. Bunsenges. Phys. Chem. 95 (1991) 1461.
[204] Y. Massiani, A. Medjahed, J.P. Crousier, P. Gravier, I. Rebatel, Surface and Coatings Technology 45 (1991) 115.
[205] C.Q. Cui, S.P. Jiang, A.C.C. Tseung, J. Electrochem. Soc. 139 (1992) 6.
[206] T.P. Moffat, R.M. Latanision, J. Electrochem. Soc. 139 (1992) 7.
[207] T.E. Pou, O.J. Murphy, V. Young, J.O'M. Bockris, International Congress on Metallic Corrosion, Toronto, 1984, ed. H.P. Godard, Conseil National de Recherches du Canada, Ottawa, 1984, 2, p. 141.
[208] M.Y. Chang, G.P. Yu, J. Nucl. Mat. 202 (1993) 145.
[209] R. Oltra, M. Keddam, First International Symposium on Electrochemical Impedance Spectroscopy, Electrochim. Acta 35 (1990) 10.
[210] A.W. Hassel, M.M. Lohrengel, Electrochim. Acta 40 (1995) 433.
[211] P. Moulin, F. Armanet, G. Béranger, P. Lacombe, Mém. Sci. Rev. Mét. 74 (1977) 3.
[212] J. de Damborenea, A.J. Vazquez, B. Fernandez, Materials & Design 15 (1994) 1.
[213] A. Jouanneau, M. Keddam, M.C. Petit, Electrochim. Acta 21 (1976) 287.
[214] R.A. Huggins, I.D. Raistrick, C.K. Ho, J. Electrochem. Soc. 127 (1980) 343.
[215] G. Bellanger, Conf. CA 46, Journées d'Electrochimie de Grenoble (France) (1993).
[216] B. Trémillon, Electrochimie analytique et réactions en solution, Masson, Paris, France, 1993.
[217] M. Rouby, Les Aciers Inoxydables, eds P. Lacombe et al., Physique, Les Ulis, France, 1990, p. 915.
[218] P. Houlle, Corrosion Localisée, eds F. Dabosi et al., Physique, Les Ulis, France, 1994, p. 621.
[219] F. Dupoiron, M. Vernon, Corrosion Localisée, eds F. Dabosi et al., Physique, Les Ulis, France, 1994, p. 605.
[220] A. Wieckowski, E. Ghali, H.H. Le, J. Electrochem. Soc. 131 (1984) 9.
[221] A. Sehgal, B.G. Ateya, H.W. Pickering, J. Electrochem. Soc. 142 (1995) 198.
[222] R.G. Ballinger, R.M. Latanision, W.C. Moshier, K.N. Siebein, International congress on metallic corrosion, Toronto, 1984, ed. H.P. Godard, National Research Council of Canada, Ottawa, 1984, 1, p. 265.
[223] G. Pinard-Legry, H. Coriou, L. Grall, A. Besnard, 1er conf. int. Hydrogène dans les métaux, Paris, 1972, ed. P. Bastien, Science et Industrie, Paris, 1972, 1, p. 241.
[224] P. Delahay, New Instrumental Methods in Electrochemistry, Interscience Publishers, New York, 1954.
[225] H.W. Pickering, Mat. Sc. and Eng. A198 (1995) 213.
[226] K. Cho, H.W. Pickering, J. Electrochem. Soc. 138 (1991) 10.

[227] S. Laihonen, T. Laitinen, G. Sundholm, A. Yli-Pentti, Electrochim. Acta 35 (1990) 229.
[228] S. Rouquette-Sanchez, P. Cowache, P. Boncorps, J. Vedel, Electrochim. Acta 38 (1993) 2043.
[229] M. Keddam, Corrosion Mechanisms in Theory and Practice, ed. P. Marcus, J. Oudar, Marcel Dekker Inc., New York, 1995, p. 55.
[230] I. Epelboin, C. Gabrielli, M. Keddam, H. Takenouti, Comprehensive Treatise of Electrochemistry, vol. 4, Electrochemical Materials Science, eds J.O'M. Bockris et al., Plenum Press, New York, 1981, p. 151.
[231] C.-N. Cao, Electrochim. Acta 35 (1990) 831.
[232] C.-N. Cao, Electrochim. Acta 35 (1990) 837.
[233] J.B. Bessone, D.R. Salinas, C.E. Mayer, M. Ebert, W.J. Lorenz, Electrochim. Acta 37 (1990) 2283.
[234] J.P. Diard, P. Landaud, B. Le Gorrec, C. Montella, Deuxième Forum sur les Impédances Electrochimiques, Montrouge, 1987, ed. C. Gabrielli, University P. et M. Curie, Paris.
[235] F.M. Al-Kharafi, W.A. Badawy, Electrochim. Acta 40 (1995) 2623.
[236] G. Nogami, R. Shiratsuchi, J. Electrochem. Soc. 140 (1993) 919.
[237] P. Schmuki, H. Böhni, Electrochim. Acta 40 (1995) 775.
[238] C.L. McBee, J. Kruger, Localized Corrosion, eds R.W. Staehle et al., NACE, Houston, 1974, p. 252.
[239] B. Normand, A. Pierre, J. Pagetti, Corros. Sci. 37 (1995) 1537.
[240] C.O.A. Olsson, Corros. Sci. 37 (1995) 467.
[241] I. Olefjord, L. Wegrelius, Corros. Sci. 38 (1996) 1203.
[242] C.R. Clayton, G.P. Halada, J.R. Kearns, Mater. Sci. and Engineering A198 (1995) 135.
[243] C.C. Huang, W.T. Tsai, J.T. Lee, Corros. Sci. 37 (1995) 769.
[244] M. Pourbaix, N. de Zoubov, Atlas of Electrochemical Equilibria in Aqueous Solutions, ed. M. Pourbaix, Pergamon Press, Oxford, U.K., 1966, p. 493.
[245] M. Abdelmoula, Ph. Refait, S.H. Drissi, J.P. Mihe, J.M. Génin, Corros. Sci. 38 (1996) 623.
[246] S.H. Drissi, Ph. Refait, M. Abdelmoula, J.M.R. Genin, Corros. Sci. 37 (1995) 2025.
[247] J.M. Blengino, M. Keddam, J.P. Labbe, L. Robbiola, Corros. Sci. 37 (1995) 621.
[248] K. Ravindranath, S.N. Malhotra, Corros. Sci. 37 (1995) 121.
[249] G. Bohnsack, D.A. Johnson, E. Buss, Proceedings of Corrosion/90, 1990, p. 439, NACE, Houston, 1990.
[250] H. Sontheimer, W. Koelle, R. Rudek, Korrosionsschutzschichter auf Metall von Wasser 52 (1979) 1.
[251] E.B. Castro, J.R. Vilche, A.J. Arvia, Corros. Sci. 32 (1991) 37.
[252] J.C. Rubim, J. Dunnwald, J. Electroanal. Chem. 258 (1989) 327.
[253] L.M. Gassa, H.T. Mishima, B.A. Lopez de Mishima, J.R. Vilche, Electrochim. Acta 42 (1997) 1717.
[254] M. Dolata, P. Kedzierzawski, J. Augustynski, Electrochim. Acta 41 (1996) 1287.

[255] P. Schmuki, M. Beuchler, H. Boehni, R. Miller, L.J. Gauckler, Oxide Films on Metals and Alloys, session VII, Proceedings of 186th Meeting Electrochem. Soc. 1994, Miami Beach, J. Electrochem. Soc., 1994.
[256] E. Sikola, J. Sikola, D.D. Macdonald, Electrochim. Acta 41 (1996) 783.
[257] G. Bellanger, J.J. Rameau, Corros. Sci. 39 (1997) 209.
[258] G. Bellanger, J.J. Rameau, Corros. Sci. 36 (1994) 545.
[259] G. Bellanger, J.J. Rameau, J. Mat. Sc. 30 (1995) 1259.
[260] G. Bellanger, J. Nucl. Mat. 210 (1994) 63.
[261] G. Bellanger, J.J. Rameau, J. Nucl. Mat. 240 (1996) 1.
[262] I. Olefjord, P. Falkenberg, L. Wegrelius, A. Velon, Conf. Eurocorr'96, session mechanisms of localized corrosion, Nice, September 24–26, 1996, p. OR20.
[263] G. Barral, F. Njanjo-Eyokep, S. Maximovitch, Electrochim. Acta 40 (1995) 2815.
[264] D.C. Silverman, Proceedings of Electrochemical Impedance, Analysis and Interpretation, 4–5 November 1991, San Diego, eds J.R. Scully et al., ASTM, Philadelphia, 1993, p. 192.
[265] H.J. Miao, D.L. Piron, Electrochim. Acta 38 (1993) 1079.
[266] G. Bellanger, Fusion Technol. 27 (1995) 46.
[267] F.D. Quarto, S. Piazza, M. Yang, C. Sunseri, S.-M. Cai, Electrochim. Acta 41 (1996) 2511.
[268] V. Horvat-Radoševic, K. Kvastek, Electrochim. Acta 42 (1997) 1403.
[269] C. Bataillon, S. Brunet, Electrochim. Acta 39 (1994) 455.
[270] E.M. Patrito, R.M. Torresi, E.P.M. Leiva, V.A. Macagno, Electrochim. Acta 37 (1992) 281.
[271] H. Göhr, J. Schaller, C.-A. Schiller, Electrochim. Acta 38 (1993) 1961.
[272] C.R. Clayton, I. Olefjord, Passivity of Austenitic Stainless Steels, Corrosion Mechanisms in Theory and Practice, eds P. Marcus, J. Oudar, Marcel Dekker, New York (1995).
[273] E. Fujioka, H. Nishihara, K. Aramaki, Corros. Sci. 35 (1996) 1915.
[274] W.A. Badawy, F.M. Al-Kharafi, Corros. Sci. 39 (1997) 681.
[275] S.A.M. Refaey, S.S. Abg El Rehim, Electrochim. Acta 42 (1997) 667.
[276] F.D. Quarto, V.O. Aimiuwu, S. Piazza, C. Sunseri, Electrochim. Acta 36 (1991) 1817.
[277] J. Van Muylder, Comprehensive Treatise of Electrochemistry, vol. 4, p. 1–96, Electrochemical Materials Science, eds J.O'M. Bockris, B.E. Conway, E. Yeager, R.E. White, Plenum Press, New York (1981).
[278] D.J. Duquette, K.L. Wrisley, E. Coomer, D. Steiner, J. Nucl. Mat. 194 (1992) 992.
[279] S. Magaino, M. Matlosz, D. Landolt, J. Electrochem. Soc. 140 (1993) 5.
[280] I. Epelboin, M. Keddam, Electrochim. Acta 17 (1972) 177.
[281] H.G. Feller, H.J. Ratzer-Scheibe, W. Wendt, Electrochim. Acta 17 (1972) 187.
[282] B.C. Pound, C.H. Becker, J. Electrochem. Soc. 138 (1991) 696.
[283] I. Olefjord, B. Brox, U. Jelvestam, J. Electrochem. Soc. 132 (1985) 2854.

[284] M.A. Habib, J.O'M. Bockris, Comprehensive Treatise of Electrochemistry, vol. 1, The Double Layer, eds J.O'M. Bockris, B.E. Conway, E. Yeager, R.E. White, Plenum Press, New York (1980).
[285] J.S. Chen, R. Durand, C. Montella, J. Chim. Phys. 91 (1994) 383.
[286] R. Durand, J.C. Chen, J.P. Diard, C. Montella, Symposium on Electrochemistry and Materials Science of Cathodic Hydrogen Absorption and Adsorption, San Francisco, 1994, proc. vol. 94-21, The Electrochemical Society (Pennington).
[287] Y.M. Gunaltun, T. Chevrot, conf. NACE-CORROSION, p. 6, San Antonio, Texas, April 25–30, 1999.
[288] J. Kolts, M.W. Joosten, P.G. Humble, J. Clapham, conf. NACE-CORROSION, p. 37, San Diego, California, April 15–17, 1998.

SUBJECT INDEX

This Page Intentionally Left Blank